Радови Драгана К. Маркушев

Часописи

М21а+

Results in Engineering 27 (2025) 106988

Contents lists available at ScienceDirect

Results in Engineering

journal homepage: www.sciencedirect.com/journal/results-in-engineering

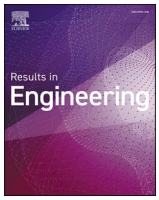

Research paper

Optical manipulation of the heat flow followed by the thermoelastic photoacoustic response of *n*-type silicon

Dragana K. Markushev [a,*], Slavica M. Kovacevic [a], Jose Ordonez-Miranda [b], Dragan D. Markushev [a]

[a] Institute of Physics, University of Belgrade, Pregrevica 118, 11080 Belgrade-Zemun, Serbia
[b] Sorbonne Université, CNRS, Institut des Nanosciences de Paris, INSP, F-75005 Paris, France

ARTICLE INFO

Keywords:
Photoacoustics
Heat flow
Temperature difference
Thermoelastic
Absorption coefficient
Penetration depth

ABSTRACT

We model and quantify the combined impact of the free carriers and absorption coefficient of *n*-type silicon on the heat flux generated by its light illumination periodically modulated in time. The light penetration depth is shown to significantly affect the temperature difference between the illuminated and unilluminated surfaces of the sample. Consequently, the frequency response of the thermoelastic component of the photoacoustic signal changes and becomes a reliable indicator of the heat flux variations. Our numerical calculations illustrate how these variations can be achieved by adjusting the wavelength of the light source.

1. Introduction

Heat transfer in various materials has long captured the interest of engineers across different research fields, particularly regarding the processes involved in this transfer [1–3]. The efficiency of heat transfer is characterized by the heat flux, which describes the movement of thermal energy from a hot area to a cold one [4–6]. In solids, characterizing heat flow is crucial for applications in electrical engineering, energy management, and medicine, particularly in micro- and nanomaterials that undergo overheating [7–13]. The heat flow in semiconductors is a topic of ongoing interest, particularly regarding the role of generated free carriers (electrons and holes) as heat carriers in heat flow dynamics within illuminated samples [14–19]. An analysis of the photoacoustic response, specifically thermoelastic one, of *n*-type silicon with a thickness smaller than the diffusion length of free carriers (referred to as plasma-thin samples) has shown that heat flow is significantly influenced by the recombination of excess carriers at the sample surfaces [20–24]. Whether passivated or not, the condition of these surfaces plays a critical role. A non-passivated surface, characterized by dangling bonds acting as heat sources and sites of high local recombination, behaves like a thin layer of material accumulating heat. Our recent research indicates that this heat accumulation effect is most pronounced when the passivated front side is illuminated while the non-passivated back side is not. In this scenario, heat accumulated at the non-passivated side, due to intense carrier recombination at the surface, leads to a sharp increase in temperature at the back of the sample [22, 23]. This alteration changes the direction of the temperature gradient and heat flow within the sample. Consequently, the amplitude of the thermoelastic component of the photoacoustic signal in plasma-thin samples experiences a sudden drop at low frequencies. This drop creates a structure at higher frequencies resembling a resonant peak, allowing the thermodiffusion component to dominate the total photoacoustic amplitude across the entire measurement range, from 20 Hz to 20 kHz [23–25].

There are several ways to alter the dynamics of free carriers and heat flow in *n*-type silicon. Most of these methods require mechanical interventions on the sample, such as changing the surface state or applying thin films with specific absorption properties to the illuminated surfaces [26–29]. These interventions can significantly alter the experimental conditions and often necessitate a more complex theoretical model, such as one for multilayer structures. This paper will present, using numerical simulations, a simple method for changing heat flow in *n*-type silicon without any interventions on the sample. Such an approach relies on varying the light penetration depth, which describes how deeply light penetrates the silicon before absorption. Parameter variations are achieved by adjusting the wavelength of the light source while maintaining a theoretical model of a volume absorber with a single-layer structure. Simply, changes in the wavelength of the illumination light source result

* Corresponding author.
E-mail addresses: dragana.markusev@ipb.ac.rs (D.K. Markushev), slavica.kovacevic@ipb.ac.rs (S.M. Kovacevic), jose.ordonez@cnrs.fr (J. Ordonez-Miranda), dragan.markushev@ipb.ac.rs (D.D. Markushev).

https://doi.org/10.1016/j.rineng.2025.106988
Received 7 July 2025; Received in revised form 24 August 2025; Accepted 28 August 2025
Available online 30 August 2025

in variations in the absorption coefficient, β, affecting the depth to which light penetrates the sample. For example, when using n-type silicon as the sample, a higher frequency of the illumination light leads to a greater penetration depth due to a lower β. Suppose we denote the thickness of the sample as l. In that case, we find that when optical absorbance $\beta l \rightarrow (1–2)$, the effects of peak-like structures in the sample's thermoelastic response in the frequency domain completely disappear. However, the mentioned disappearance does not signify a loss of free carriers' influence on the heat flow, but their more pronounced impact across the entire range of examined modulation frequencies.

2. Theoretical background

Photoacoustic experiments conducted in transmission mode, especially with an open-cell photoacoustic setup, are valuable tools for characterizing materials. However, some limitations are associated with measurements involving changes in the wavelength of the optical excitation source. Firstly, heat carriers' effects become more significant at higher frequencies, particularly those well above the standard modulation frequency range used in photoacoustics (20 Hz - 20 kHz). Secondly, when using excitation wavelengths from the optical source exceeding 700 nm, plasma-thin n-type silicon becomes increasingly transparent. As a result, much of the excitation radiation directly stimulates the microphone membrane, distorting the detected sound signals and obscuring those generated within the material being probed. Direct excitation of the detector membrane interferes with the conditions needed for solving the relevant equations, making it difficult to reliably compare the sound produced by visible and infrared excitation. For these reasons, most of the results presented here are based on numerical simulations related to the theoretical model of the composite piston. This model is well-established in photoacoustics and has been experimentally validated multiple times, both in our open-cell research [20–25] and in the published work of other authors [30–33].

According to our previous work [36], the most significant heat flow parameters are the temperature difference (ΔT_s) between the illuminated $(T_s(-l/2))$ and non-illuminated $(T_s(-l/2))$ sides of the investigated sample (see Fig. 1) and the thermoelastic component of the photoacoustic signal $(\delta p_{TE}(j\omega))$, which depends on both the value and sign of ΔT_s. Consequently, our present work will focus on the behavior of these two parameters with frequency, relying on the composite piston theory, specifically the mechanical piston model [34,35]. This model establishes that $\delta p_{TE}(j\omega)$ is given by [22,36]:

$$\delta p_{TE}(j\omega) = 3\pi \frac{\gamma_g p_0 \alpha_T R_s^4}{l^3 V_0} \int_{-\frac{l}{2}}^{\frac{l}{2}} x T_s(x) \mathrm{d}x, \tag{1}$$

where γ_g is the adiabatic ratio of the gas (air) in the photoacoustic cell, p_0 and V_0 are the respective gas pressure and volume, l is the sample thickness, D_g is the sample thermal diffusivity, α_T is the sample coefficient of linear expansion, R_s is the sample radius, and $T_s(x)$ is the temperature distribution within the homogeneous one-layer sample along the x-axes (Fig. 1). For a sample of n-type silicon as volume absorber, the 1D dynamic solution of the parabolic heat conduction equation (PHCE) yields [22,37]:

$$\frac{\partial^2 T_s(x)}{\partial x^2} - \sigma_\omega^2 T_s(x) = -\frac{\beta I_0}{k} e^{-\beta x} \frac{\varepsilon - \varepsilon_g}{\varepsilon} - \frac{\varepsilon_g}{k\tau_p} \delta n_p(x). \tag{2}$$

Here, I_0 is the excitation light intensity, $\sigma_\omega = (1+j)\sqrt{\omega/2D_T}$ is the complex wave vector of heat diffusion, $\omega = 2\pi f$, f is the modulation frequency, $D_T = k/(\rho c)$ is the thermal diffusivity of the sample (k is the heat conductivity, ρ is the density, c is the heat capacity), ε is the photon energy, ε_g is the semiconductor band gap energy, $\delta n_p(x)$ is the minority excess carrier density (see Appendix I), and β is the absorption coefficient of silicon at excitation light wavelength.

As a result of our semiconductor response investigation obtained with open-cell experimental set-up, it was shown that the thermoelastic component of the photoacoustic signal is very sensitive to the influence of excess free carriers, especially in the case of plasma-thin samples, whose thickness is smaller than the diffusion length L_p of the minority carriers (holes, p, in the case of n-type silicon), defined as $L_p = \sqrt{D_p \tau_p}$, where D_p is the holes diffusivity, and τ_p is the holes lifetime [20–25]. Solving Eq. (2), it was shown that in plasma-thin samples the 1D temperature profile $T_s(x)$ along the direction of heat propagation (Fig. 1, x-axis) is shaped by the contributions of rapid thermalization component $T_{therm}(x)$ (corresponding to the β-dependent direct conversion of light energy into heat) and excess carrier surface recombination component $T_{sr}(x)$. Considering plasma-thin samples, the thinner the sample is, the bulk recombination component $T_{br}(x)$ can be regarded as negligible. This is the reason why $T_s(x)$, in the case of plasma-thin samples, can be written as [22,25,37]:

$$T_s(x) = T_{therm}(x) + T_{sr}(x), \tag{3}$$

where

$$T_{therm}(x) = \frac{I_0}{k} \frac{\varepsilon - \varepsilon_g}{\varepsilon} \frac{\beta}{\beta^2 - \sigma_\omega^2} \left[\frac{\beta}{\sigma_\omega} \frac{\cosh[\sigma_\omega(x - l/2)] - e^{-\beta l} \cosh[\sigma_\omega(x + l/2)]}{\sinh(\sigma_\omega l)} - e^{-\beta(x+l/2)} \right], \tag{4}$$

and

$$T_{sr}(x) = \frac{\varepsilon_g}{k\sigma_\omega} \frac{s_1 \delta n_p(-l/2) \cosh[\sigma_\omega(x - l/2)] + s_2 \delta n_p(l/2) \cosh[\sigma_\omega(x + l/2)]}{\sinh(\sigma_\omega l)}, \tag{5}$$

assuming that s_1 and s_2 are the front and back surface recombination velocities, respectively, $\delta n_p(-l/2)$ is the minority excess carrier density at front, and $\delta n_p(l/2)$ is the minority excess carrier density at back of the sample (see Appendix I).

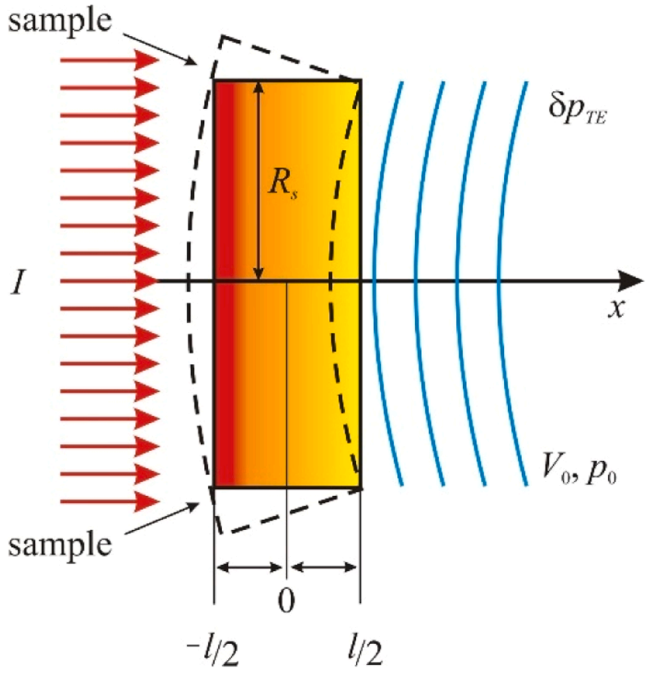

Fig. 1. Simple scheme of the 1D heat propagation and thermoelastic component $\delta p_{TE}(j\omega)$ generation within the periodically illuminated n-type silicon sample of thickness, l, and radius, R_s.

As complex numbers, the frequency response of $\delta p_{TE}(j\omega)$ (Eq. (1)) and $T_s(x)$ Eqs. (3–5) is usually represented by their amplitudes ($A_{TE} = |\delta p_{TE}(j\omega)|$ and $A_T = |T_s(x)|$), and phases ($\varphi_{TE} \leq (\delta p_{TE}(j\omega))$ and $\varphi_T \leq (T_s(x))$) in the modulation frequency f domain. For the sake of simplicity, only the amplitudes will be analyzed and presented in this work.

3. Results and discussion

Before any analysis, the following points should be noted. The values of the assumed n-type silicon parameters for numerical simulations are presented in Table I [9,10], which follow our standard measurement conditions ($s_1 > s_2$) and results at room temperature ($T = 300$ K). A sample thickness of $l = 40$ μm (plasma-thin sample) is the thickness that has been found to give the clearest picture of the most intensive effects of free carriers as heat carriers when measured [20–23,36]. The noticeable effects of heat carriers can be observed by monitoring changes in the $\delta p_{TE}(j\omega)$ response in both the modulation frequency (f) and absorbance (βl) domains (see Appendix II). From the absorbance analysis of the $\delta p_{TE}(j\omega)$ amplitude (A_{TE}) and sensitivity ($\partial(A_{TE})/\partial(\beta l)$), three key points can be distinguished, corresponding to absorbance values of $\beta_1 l = 10.32 \gg 1$ ($\lambda_1 = 660$ nm), $\beta_2 l = 5.00 > 1$ ($\lambda_2 = 755$ nm) and $\beta_3 l = 1.53 \rightarrow 1$ ($\lambda_3 = 880$ nm). The significance of these points will be explained in the following analysis. The absorbance value of $\beta_1 l$ corresponds to the red (R) light excitation frequently utilized in our experiments to validate the composite piston theoretical model within the (20 Hz - 20 kHz) experimental f range. The $\beta_2 l$ and $\beta_3 l$ values correspond to the beginning of the infrared (IR_a) and close to the band gap (IR_b), respectively. All simulations are performed in the 1 Hz – 10^7 Hz, the frequency range in which the validity of the composite piston theory has been confirmed [22].

Fig. 2 shows the results of numerical simulations and typical relationships between the temperature amplitudes A_T^R and A_T^{IR} of $T_s(x)$ and its components $T_{therm}(x)$ and $T_{sr}(x)$ as a function of the modulation frequency f, under the strong influence of excess carriers, using red (R, λ_1) and infrared (IR_a, λ_2, and IR_b, λ_3) irradiation sources. Simulations are performed (solid lines) using Eqs. (3–5) applied on the illuminated front ($x = -l/2$) and non-illuminated back ($x = +l/2$) sides of an $l = 40$ μm tick n-type silicon sample (plasma-thin sample). Experimental validation (solid squares) was performed using a red excitation light source R within the 20 Hz-20 kHz frequency range (Appendix III). The values of s_1 and s_2 indicate that the front sample side (1) is passivated, while the back side (2) is not [25,37].

It must be pointed out here that, in the so called “no carrier” scenario, only thermalization component $T_{therm}(x)$ exists, representing the case of temperature distribution in silicon $T_s(x)$ without the influence of free carriers: $T_s(x) = T_{therm}(x)$.

It is clear from Fig. 2 that the $T_{therm}(x)$ component (red line) experiences the most significant changes due to variations in the absorption coefficient, which affects the penetration depth of the excitation light due to its wavelength changes. These alterations occur more prominently on the back of the sample compared to the front. Also, $T_{sr}(x)$ component (green line) experiences significant changes, especially on the back side. Such $T_{therm}(x)$ and $T_{sr}(x)$ changes impact the values of $T_s(x)$ on both sides. These effects are most apparent when we examine the amplitude ratios $A_T^{IR_a}/A_T^R$ and $A_T^{IR_b}/A_T^R$ of $T_s(x)$ and its $T_{therm}(x)$ and $T_{sr}(x)$ components, as illustrated in Fig. 3, indicating the net effect: $T_s(x)$ amplitudes (black lines) on the illuminated front side decreases, while they increases on the non-illuminated back side, at high modulation frequencies. More significant changes are observed in the case of $A_T^{IR_b}/A_T^R$.

To understand the implications of presented temperature behavior on heat flow, one has to analyze the temperature differences of $\Delta T_s = |T_s(-l/2)| - |T_s(l/2)|$ and its components $\Delta T_{therm} = |T_{therm}(-l/2)| - |T_{therm}(l/2)|$ and $\Delta T_{sr} = |T_{sr}(-l/2)| - |T_{sr}(l/2)|$ between the illuminated and non-illuminated sides of the sample and how this difference affects the thermoelastic component’s amplitude A_{TE} response of the corresponding photoacoustic signal. This type of analysis is depicted in Figs. 4–6.

Fig. 4a shows “no excess carriers” scenario simulations having $\Delta T_s > 0 (|T_s(-l/2)| > |T_s(l/2)|)$ for all investigated R (solid), IR_a (dash) and IR_b (dot) cases in the entire modulation frequency f domain. The corresponding thermoelastic amplitude responses A_{TE} are shown in Fig. 4b. They can be called "standard" thermoelastic responses - constant at low and sharply falling with small differences in slope at high frequencies, without any spikes or peaks.

Fig. 5 shows the “excess carriers” scenario simulations (solid lines) for the same R (a,b), IR_a (c,d) and IR_b (e,f) cases. Bearing in mind the mentioned limitations of photoacoustics, experimental validations (solid squares) were performed only for the R case, within the range of 20 Hz - 20 kHz.

Fig. 5a,c (R and IR_a cases) shows that the contributions of thermalization (red) and surface recombination (blue) are nearly equal but have opposite signs ($\Delta T_{therm} > 0 \rightarrow |T_{therm}(-l/2)| > |T_{therm}(l/2)|$ and ($\Delta T_{sr} < 0 \rightarrow |T_{sr}(-l/2)| < |T_{sr}(l/2)|$). A slightly lower contribution of ΔT_{therm} is noticed in IR_a case, while ΔT_{sr} contribution remains the same. The combined effect of these contributions (black line) results in $\Delta T_s < 0$ at low frequencies, and $\Delta T_s > 0$ at higher ones. Negative temperature differences in all cases indicate that the temperature of the illuminated side of the sample is lower than that of the non-illuminated side. This suggests that by altering the modulation frequency, one can change the intensity of the heat flow and its direction. Additionally, it seems possible to even halt heat flow at a specific frequency ($\Delta T_s = 0$), although the processes of light absorption and carrier generation within the sample did not stop. Because of such ΔT_s behaviour, the A_{TE} amplitude (Fig. 5b and d) changes drastically compared to the "no carrier” scenario (Fig. 4b), obtaining a peak-like structure at higher frequencies. We emphasized that the drop in the A_{TE} value at lower frequencies is the largest one for the IR_a case, accompanied by the most pronounced peak. Such behavior is indicated by point $\beta l = 5$ in Fig. 6 (Appendix II).

Fig. 5e clearly shows the dominant influence of ΔT_{sr} on $\Delta T_s (\Delta T_s \approx \Delta T_{sr} < 0)$, because a smaller value of β_3 ($\beta_3 \rightarrow 1$) significantly reduces ΔT_{therm} due to an increasingly transparent sample (larger penetration depth). The dominance of one process is characterized by the unchanged sign of ΔT_s at almost all frequencies (the change at higher frequencies has a negligible contribution), which results in the return of the A_{TE} to the "standard” response as in the “no carriers” scenario (Fig. 5f), as indicated by point $\beta l \rightarrow 1.3$ in Fig. 6 (Appendix II). A small reduction of ΔT_{sr} influence arises from the strong influence of β on the values of $\delta n_p(-l/2)$ and $\delta n_p(l/2)$ at longer wavelengths. A sharp decrease in the $\delta n_p(-l/2)$ and $\delta n_p(l/2)$ values at IR_b wavelength is

Table I
Si n-type sample parameters.

Lifetime of minority carriers	$\tau_p = 6$ μs	Coefficient of minority carrier diffusion	$D_p = 12 \times 10^{-4}$ m^2•s^{-1}
Density	$\rho = 2.33 \times 10^3$ kg•m^{-3}	Specific heat	$c = 715$ J•kg^{-1}•K^{-1}
Thermal conductivity	$k = 150$ W•m^{-1}•K^{-1}	Thermal diffusivity	$D_T = 0.90 \times 10^{-4}$ m^2•s^{-1}
Linear thermal expansion	$\alpha_T = 2.60 \times 10^{-6}$ K^{-1}	Optical absorption coefficients	$\beta_1 = 0.258$μm^{-1} $\beta_2 = 0.125$μm^{-1} $\beta_3 = 0.038$μm^{-1}
Excitation energy	$\varepsilon_1 = 1.88$ eV $\varepsilon_2 = 1.64$ eV $\varepsilon_3 = 1.41$ eV	Energy gap	$\varepsilon_g = 1.12$ eV
Front surface recombination velocity	$s_1 = 2$ m•s^{-1}	Rear surface recombination velocity	$s_2 = 24$ m•s^{-1}

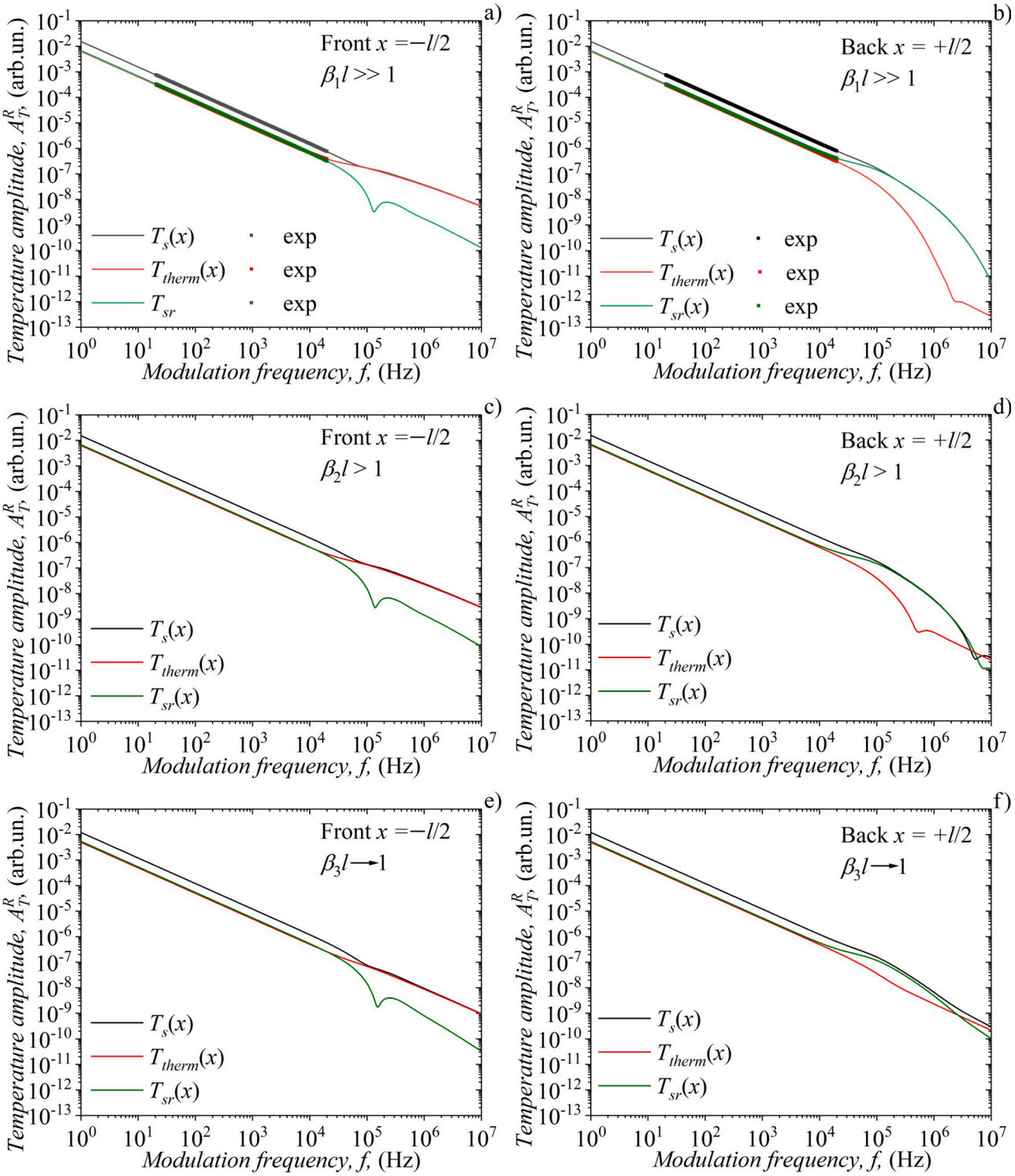

Fig. 2. The temperature amplitudes A_T of $T_s(x)$ (black solid) and its components $T_{therm}(x)$ (red solid) and $T_{sr}(x)$ (green solid) calculated at front and back of the $l = 40$ μm thick n-type silicon sample, obtained with Eqs. (1–3) and parameters from Table I, in the case of red (a, b – ($\lambda_1 = 660$ nm), infrared IR_a (c, d – ($\lambda_2 = 660$ nm) and infrared IR_b (c, d – ($\lambda_3 = 880$ nm) excitation light. Experimental validations (a,b) are given with asterisks.

expected (see Appendix I and Eq. (5)), comparing to *R* and IR_a case.

Changing the wavelength of the excitation light from red to infrared reduces the absorption coefficient, allowing light to penetrate deeper into the sample. As a result, a greater amount of heat sources (points of light absorption) builds up at the back side of the sample, producing significant heat and causing a sharp rise in surface temperature (while the illuminated front side experiences no significant temperature change). This process causes ΔT_{therm} to approach zero, so ΔT_{sr} enables a complete heat flow through the sample (Fig. 5e, $\Delta T_s \approx \Delta T_{sr}$). Consequently, the thermoelastic amplitude response, A_{TE}, returns to its original "standard" form (Fig. 5f), losing its peak-like structure. The response of A_{TE} is independent of the sign of ΔT_s. In photoacoustics, the negative or positive sign of ΔT_s merely indicates whether the sample's bending is concave or convex. An analogous effect of heat flow reversal and the

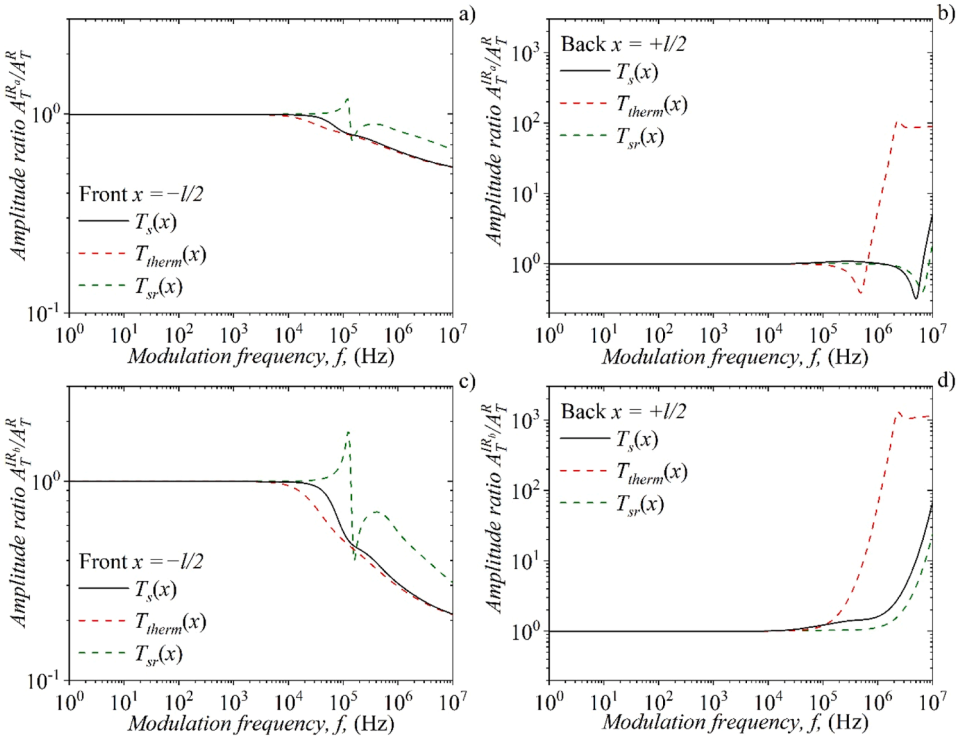

Fig. 3. The amplitude ratios a,b) A_T^{IRa} / A_T^R and c,d) A_T^{IRb} / A_T^R of $T_s(x)$ (black solid) and its components $T_{therm}(x)$ (red dashed) and $T_{sr}(x)$ (green dashed) calculated at a, c) front and b,d) back of the $l = 40$ μm thick n-type silicon sample.

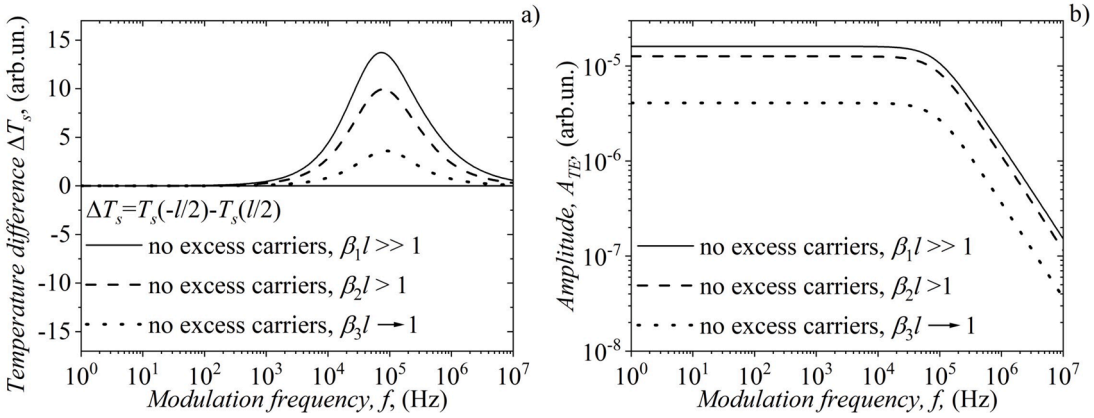

Fig. 4. The n-type silicon $l = 40$ μm sample a) temperature differences, $\Delta T_s(x)$, and b) photoacoustic thermoelastic component amplitude, A_{TE}, "standard" responses, in the "no excess carriers" influence scenario, as functions of modulation frequency, f, in the case of red R ($\lambda_1 = 660$ nm, $\beta_1 l$, solid), and infrared IR_a ($\lambda_2 = 755$ nm, $\beta_2 l$, dash) and IR_b ($\lambda_3 = 880$ nm, $\beta_3 l$, dots) excitation light.

subsequent A_{TE} responses can be observed when a thin, non-transparent absorption layer is attached to the back of a transparent material [38, 39]. This technique is frequently employed in experimental photoacoustics, where the thin layer prevents the excitation light from reaching the microphone, thereby reducing distortion of the measured signal.

4. Conclusions

Based on the results presented so far, the primary process influencing heat flow in the *n*-type silicon sample, besides the recombination of free carriers on the sample surfaces, is the direct conversion of light energy into heat within the sample. We have demonstrated that the most effective method for monitoring this process is through photoacoustics. This involves changing the wavelength (absorption coefficient) of the excitation light source and monitoring the temperature differences of the total temperature and its components between the illuminated and unilluminated sides of the sample, together with the behavior of the thermoelastic amplitude of the photoacoustic frequency response.

Our numerical simulations, conducted in the modulation frequency range of 1 to 10^7 Hz, have shown that the behavior of the thermoelastic amplitude is intrinsically linked to the temperature differences and their sign. Specifically, if the total temperature differences do not change sign within the investigated frequency range, the amplitude of the thermoelastic component exhibits a "standard" response, characterized by a smooth curve that sharply declines at higher frequencies. Conversely, if the temperature differences change sign within the investigated frequency range, the thermoelastic response becomes "nonstandard" (distorted), taking on a peak-like shape at higher frequencies before dropping sharply.

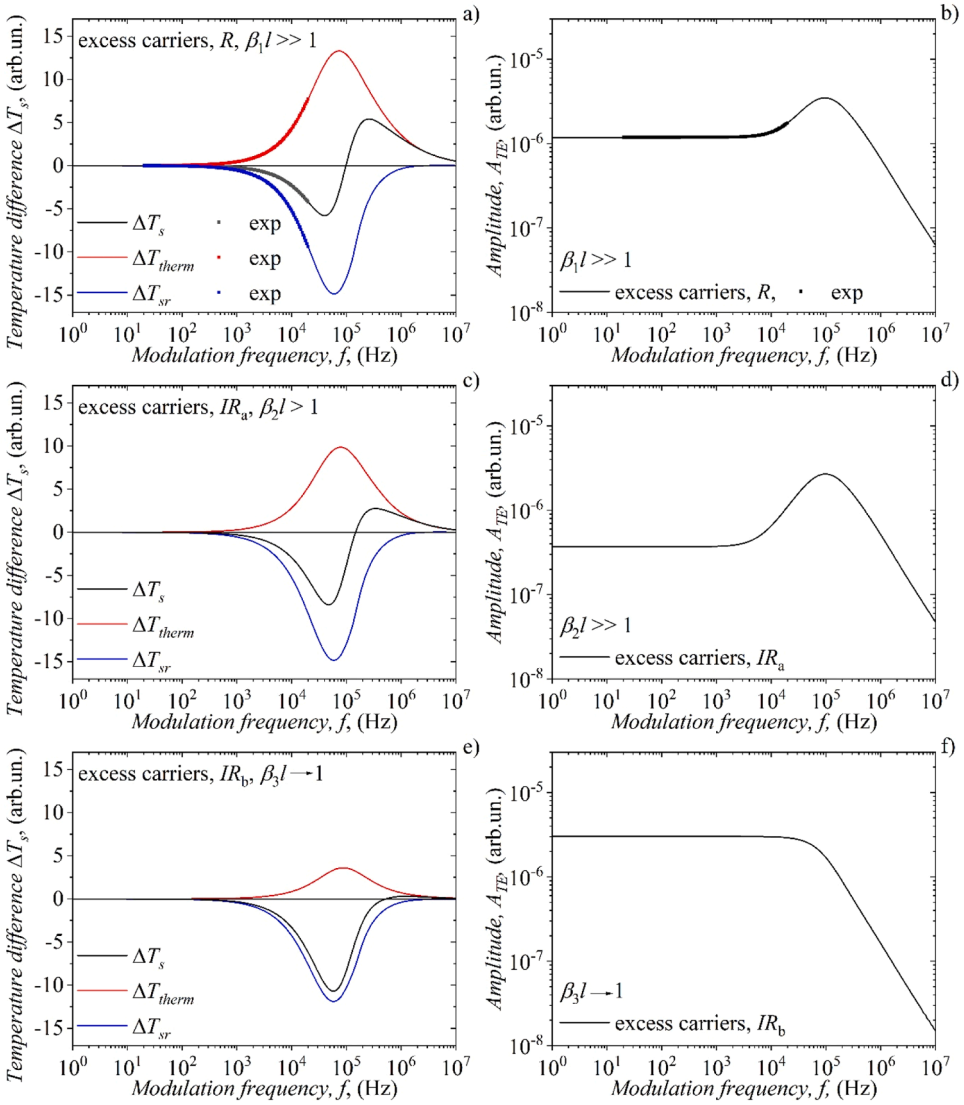

Fig. 5. The n-type silicon $l = 40$ μm sample a,c,e) temperature differences of $T_s(x)$ (black solid) and its components $T_{therm}(x)$ (red solid) and $T_{sr}(x)$ (blue solid), and corresponding b,d,f) photoacoustic thermoelastic component amplitude response A_{TE} (black solid), calculated in the case of "carrier influence" scenario and a,b) $\lambda_1 =$ 660 nm (R), c,d) $\lambda_1 = 755$ nm (IR_a), c,d) 880 nm (IR_b). Experimental verification of the composite piston model was done with red excitation (a,b,R), within the 20 Hz – 20 kHz modulation frequency range (solid squares).

These results indicate that distortions in the behavior of the thermoelastic amplitude (from smooth to peak-like and vice versa) reliably signal a change in the sign of the thermal gradient and the direction of heat flow in the sample. Such changes can help define the modulation frequency range in which silicon can function as either a heat reservoir or a heat sink. In addition, the change in the sign of the thermal gradient indicates the existence of a modulation frequency at which it is possible to stop the heat flow, despite the intense reactions of thermalization and surface recombination that continuously take place on the surfaces of the tested silicon. This possibility is very important when it comes to the efficient operation of electronic components in various devices.

Data availability

The data that support the findings of this study are available from the corresponding author upon reasonable request.

CRediT authorship contribution statement

Dragana K. Markushev: Writing – original draft, Supervision, Methodology, Investigation, Formal analysis, Data curation, Conceptualization. **Slavica M. Kovacevic:** Methodology, Investigation, Formal analysis, Data curation. **Jose Ordonez-Miranda:** Writing – original draft, Supervision, Methodology, Formal analysis, Conceptualization. **Dragan D. Markushev:** Writing – original draft, Methodology, Investigation, Formal analysis, Data curation, Conceptualization.

Declaration of competing interest

The authors declare that they have no known competing financial interests or personal relationships that could have appeared to influence the work reported in this paper.

Acknowledgements

The authors acknowledge funding provided by the Institute of Physics Belgrade, through a grant by the Ministry of Science, Technological Development and Innovations of the Republic of Serbia.

Appendix I. Excess carrier density distribution

The *n*-type silicon has an abundance of free electrons. In other words, the density of electrons in it, n_{n0}, is much higher than the density of holes, n_{p0} ($n_{n0} \gg n_{p0}$). Suppose the energy of the photons from the modulated light source (Fig. 1), denoted as ε, is equal to or greater than the energy band gap of the semiconductor, ε_g. In that case, the illumination of silicon can generate excess carriers (electrons and holes) in pairs at equal rates. This means that the densities of excess electrons, denoted as $\delta n_n(x,t)$, and excess holes, denoted as $\delta n_p(x,t)$, are equal: $\delta n_n(x,t) = \delta n_p(x,t)$. In the case of low-level injection approximation $\left(n_{n0} \gg \delta n_n(x,t), \delta n_p(x,t) \gg n_{p0}\right)$, excess carrier diffusion and recombination processes are driven by the minority carrier density $\delta n_p(x,t)$, which dynamics is explained by the 1D diffusion equation [22,25,37]

$$\frac{\partial \delta n_p(x,t)}{\partial t} = D_p \frac{\partial^2 \delta n_p(x,t)}{\partial x^2} + -\frac{\beta I_0}{\varepsilon} e^{-\beta x}\left(1 + e^{j\omega t}\right) - \frac{\delta n_p(x,t)}{\tau_p}, \tag{A1.1}$$

and its solution, which implies modulated light excitation, part of the written as [22,25,37]:

$$\frac{d^2 \delta n_p(x)}{dx^2} - \frac{\delta n_p(x)}{L_p^2} = -\frac{\beta I_0}{\varepsilon D_p} e^{-\beta x}, \tag{A1.2}$$

where I_0 is the incident light intensity, β is the silicon absorption coefficient, $L = L_p/\sqrt{(1 + j\omega\tau)}$, $L_p = \sqrt{D_p \tau_p}$ is the excess carrier (holes) diffusion length characterized by their diffusion coefficient D_p and lifetime τ_p, $\omega = 2\pi f$, and f is the light source modulation frequency. The solution of this equation is given by [22,25]:

$$\delta n_p(x) = A_+ e^{(x+l/2)/L} + A_- e^{-(x+l/2)/L} - A e^{-\beta(x+l/2)}, \tag{A.1.3}$$

where $A = I_0/\left(\varepsilon D_p \beta\right)$, and the integration constants $A_\pm$ are defined by [22,25]:

$$A_\pm = \frac{A}{\nu_D} \frac{\nu_\beta(\nu_D \pm s_2)e^{\mp l/L} - \nu_D(\nu_\beta - s_2)e^{-\beta l}}{(\nu_D + s_2)e^{l/L} - (\nu_D - s_2)e^{-l/L}}, \tag{A1.4}$$

depending strongly on β, the relative values of the characteristic diffusion speeds $\nu_D = D_p/L$ and $\nu_\beta = \beta D_p \left(\nu_\beta > \nu_D\right)$, and recombination speeds s_1 and s_2 at investigated sample irradiated and nonirradiated surface, respectively. Surface defects (dangling bonds) and impurities are factors that affect *s* values. Reducing the number of dangling bonds also reduces *s* values. The process used for such reduction is called "surface passivation". Passivation could be mechanical or chemical. In our experiments, silicon sample surfaces are mechanically passivated (polished), significantly changing *s* values, from unpolished $s_2 = 24$ ms^{-1} to polished $s_1 = 2$ ms^{-1}. Higher *s* values indicate higher surface recombination rates, while lower *s* values indicate lower surface recombination rates. In all our experiments with plasma-thin silicon samples, a necessary condition for the visibility of free carrier effects is always $s_1 < s_2$.

Appendix II. Thermoelastic amplitude component sensitivity to the optical absorbance βl

According to Eqs. (1–4) and (A1.1), the temperatures $T_s(x)$, $T_{therm}(x)$, and $T_{sr}(x)$, and therefore the thermoelastic component $\delta p_{TE}(j\omega)$ of the photoacoustic signal depend on the optical absorbance βl. The amplitude $A_{TE} = |\delta p_{TE}(j\omega)|$ and its first derivative $\partial(A_{TE})/\partial(\beta l)$ are respectively shown in Fig. 6a and 6b, as functions of βl. Two points stand out in these figures: $\beta l = 1.3$ and $\beta l = 5$ originating from the influence of ΔT_{therm}, and ΔT_{sr}, respectively. This behavior of A_{TE} thus supports our finding that the light-to-heat conversion driving the temperature difference between the illuminated and non-illuminated sides of the sample, becomes significant when βl is between 1 and 2, mainly.

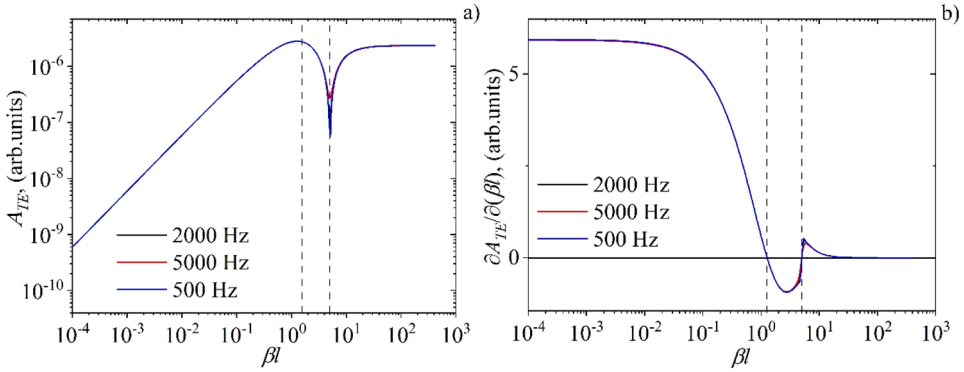

Fig. 6. The dependences of (a) amplitudes A_{TE}, and (b) thermoelastic component sensitivity on optical absorbance βl. Calculations were done for a sample of thickness $l = 40$ μm, modulation frequencies of 2000 Hz, 5000 Hz and 500 Hz, and absorption coefficient β varying in the range $(10^{-6} - 10)$ μm^{-1}.

Appendix III. Experimental procedure for obtaining thermal and electronic parameters of the sample

Using the open-cell experimental setup [20–25,36], the measured sound response $S(j\omega)$ (Fig. 7a, asterisks) and its fit $S_{\text{fit}}(j\omega)$ (black line) of

periodically illuminated *n*-type silicon with a thickness of 40 μm can be obtained across modulation frequencies ranging from 20 Hz to 20 kHz. The figure illustrates the significant impact of the microphone acting as an *RC* high-pass filter in the low-frequency ($H_e(j\omega)$), and as an *RCL* low-pass filter in the high-frequency range ($H_a(j\omega)$).

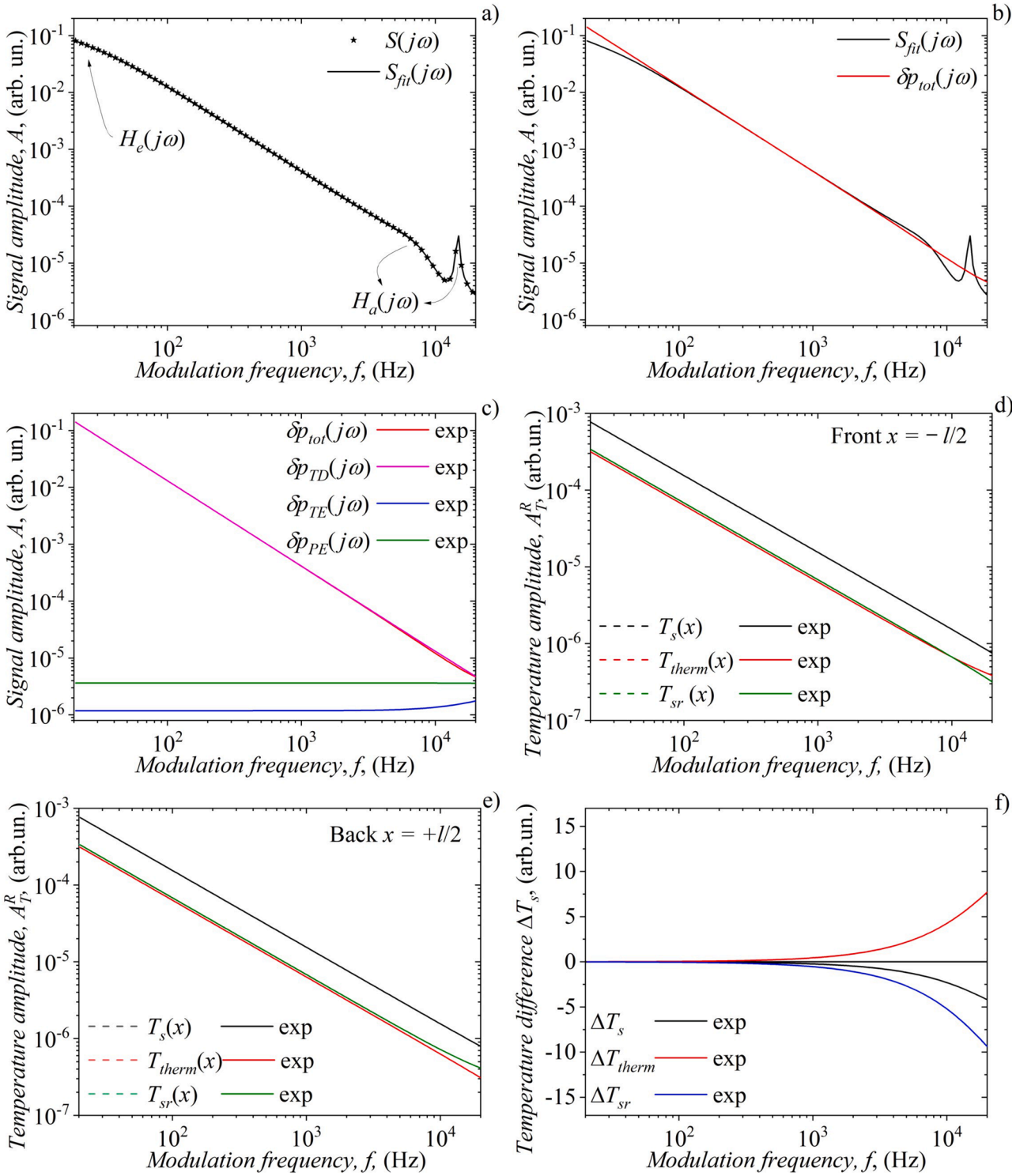

Fig. 7. a) Raw measurement results $S(j\omega)$ and their fit $S_{fit}(j\omega)$, together with b) the "real" photoacoustic signal $\delta p_{tot}(j\omega)$ and c) its components $\delta p_{TD}(j\omega)$, $\delta p_{TE}(j\omega)$ and $\delta p_{PE}(j\omega)$, d) the total temperature $T_s(x)$ and its components $T_{therm}(x)$ and $T_{sr}(x)$ on the illuminated and non-illuminated sides, as well as their e) the temperature differences $\Delta T_s(x)$, $\Delta T_{therm}(x)$ and $\Delta T_{sr}(x)$.

The relationship between the measured sound response $S(j\omega)$ and the "real" $\delta p_{tot}(j\omega)$ signal that originates solely from the sample is expressed as [36]

$$S_{fit}(j\omega) = \delta p_{tot}(j\omega) H_e(j\omega) H_e(j\omega). \tag{A.3.1}$$

Using $S_{fit}(j\omega)$ and Eq.(A.3.1), the influences of $H_e(j\omega)$ and $H_a(j\omega)$ can be accounted for and eliminated, thereby yielding the $\delta p_{tot}(j\omega)$ signal (Fig. 7b, red line) along with all relevant thermal and electronic parameters of the sample (Table I). Since the fitting process is based on the theoretical model of

a composite piston, it allows us to obtain not only $\delta p_{tot}(j\omega)$ but also all of its components (Fig. 7c): thermodiffusion $\delta p_{TD}(j\omega)$, thermoelastic $\delta p_{TE}(j\omega)$, and plasmaelastic $\delta p_{PE}(j\omega)$. Additionally, temperature distributions within the sample ($T_s(x)$, $T_{therm}(x)$, and $T_{sr}(x)$, Fig. 7d,e and f) are derived, which are essential for analyzing heat flow.

This methodology for acquiring $\delta p_{tot}(j\omega)$, thermal parameters, signal components and temperature distributions has been validated through numerous experiments. This extensive validation gives us confidence to extrapolate the obtained results (Fig. 8. dashed lines) to a much wider frequency domain (1–10^7 Hz) while still adhering to the principles of Fourier's law and the assumptions regarding the diffusion character of heat flow.

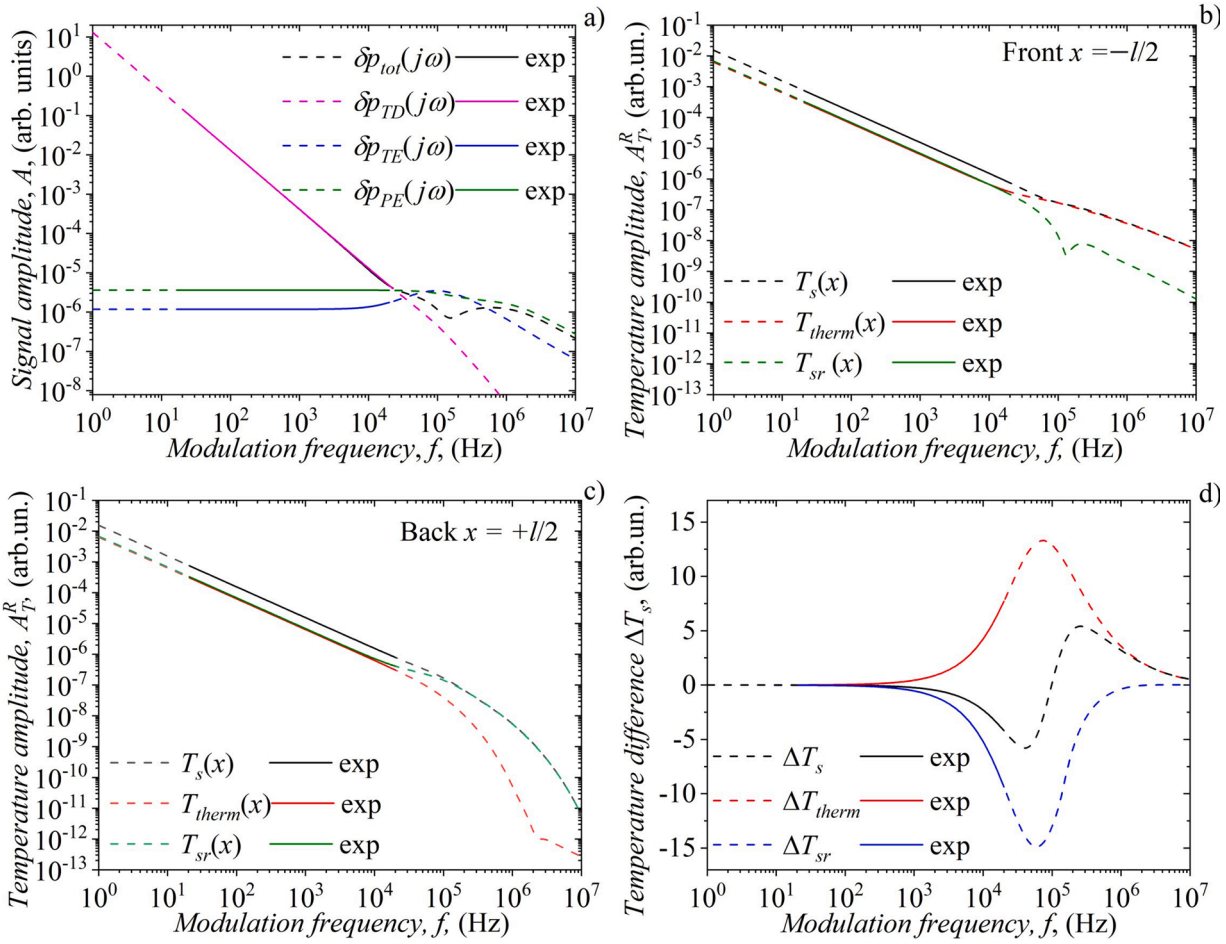

Fig. 8. Extrapolations (dashed) of a) $\delta p_{tot}(j\omega)$ and its components $\delta p_{TD}(j\omega)$, $\delta p_{TE}(j\omega)$ and $\delta p_{PE}(j\omega)$, b) $T_s(x)$ and its components $T_{therm}(x)$ and $T_{sr}(x)$ at illuminated sample side, c) $T_s(x)$ and its components $T_{therm}(x)$ and $T_{sr}(x)$ at nonilluminated sample side, and d) temperature differences $\Delta T_s(x)$, $\Delta T_{therm}(x)$ and $\Delta T_{sr}(x)$ in a wide frequency domain from 1 Hz to 10 MHz, respectively.

References

[1] C. Ximin, R. Qifeng, Z. Xiaolu, X. Xinyue, Hu Jingtian, Fu Runfang, Li Yang, W. Jianfang, Xu Hongxing, Photothermal nanomaterials: a powerful light-to-heat converter, Chem. Rev. 123 (11) (2023), https://doi.org/10.1021/acs.chemrev.3c00159.

[2] M.-J. He, Ya-S Sun, Z.-L. Wang, Bo-X Wang, Micro/nanomaterials for heat transfer, energy storage and conversion, Coatings 13 (1) (2023) 11, https://doi.org/10.3390/coatings13010011.

[3] A.P. Moreira, A.G.S. Vilaronga, J.D. Oliveira, E.M. Cardoso, Heat transfer and two-phase flow of deionized water in heat sink with micro-pin fins, Results. Eng. 27 (2025) 106378, https://doi.org/10.1016/j.rineng.2025.106378.

[4] G. Lebon, Heat conduction at micro and nanoscales: a review through the prism of Extended Irreversible Thermodynamics, J. Non-Equilibr. Thermodynamics 39 (1) (2014) 35, https://doi.org/10.1515/jnetdy-2013-0029.

[5] T.L. Bergman, A.S. Lavine, F.P. Incropera, D.P. DeWitt, Fundamentals of Heat and Mass Transfer, 7th ed., John Wiley, New York, 2011.

[6] M. Sivagnanam, AK. Mehrotra, ID. Gates, Flow rate perturbations for enhanced heat transfer and fouling mitigation in once-through steam generators, Results. Eng. 26 (2025) 104651, https://doi.org/10.1016/j.rineng.2025.104651.

[7] S. Suresh, S. Nanomaterials, Methods and applications: a review, Nanosci. Nanotechnol. 3 (3) (2013) 62–74. http://article.sapub.org/10.5923.j.nn.20130303.06.html.

[8] N. Hossain, Md Hosne Mobarak, M. Akter Mimona, MdA Islam, A. Hossain, Fatema Tuz Zohura, Mohammad Asaduzzaman Chowdhury, advances and significances of nanoparticles in semiconductor applications – A review, Results. Eng. 19 (2023) 101347, https://doi.org/10.1016/j.rineng.2023.101347.

[9] M. Zeeshan Siddique, JAl Hossain, BoH Kim, Nanoscale thermal transport at metal-semiconductor interfaces: size-dependent exponential scaling, Results. Eng. 27 (2025) 106632, https://doi.org/10.1016/j.rineng.2025.106632.

[10] L. Yang, W. Jiang, W. Ji, O. Mahian, S. Bazri, R. Sadri, I. Anjum Badruddin, S. Wongwises, A review of heating/cooling processes using nanomaterials suspended in refrigerants and lubricants, Int. J. Heat. Mass Transf. 153 (2020) 119611, https://doi.org/10.1016/j.ijheatmasstransfer.2020.119611.

[11] H. Alkhatib, Enhancing performance and mitigating overheating in flat plate solar collectors: a UV-selective coating approach-experimental analysis, Results. Eng. 25 (2025) 103766, https://doi.org/10.1016/j.rineng.2024.103766.

[12] D.- Kim, S. Choi, J. Cho, M. Lim, B.J. Lee, Boosting thermal conductivity by surface plasmon polaritons propagating along a thin Ti film, Phys. Rev. Lett. 130 (2023) 176302, https://doi.org/10.1103/PhysRevLett.130.176302.

[13] AB.M. Ali, S.F.H. Alhamdi, M.M.S. Al-Azawii, N.S.S. Singh, M.A. Fazilati, S. Salahshour, S. Ali Eftekhari, Thermal management in a phase change material-based microchannel heat sink manifold system for cooling electronic boards, Results. Eng. 26 (2025) 104914, https://doi.org/10.1016/j.rineng.2025.104914.

[14] H S. Chatterjee, Hu Paras, M. Chakraborty, A review of nano and microscale heat transfer: an experimental and molecular dynamics perspective, Processes 11 (9) (2023) 2769, https://doi.org/10.3390/pr11092769.

[15] J.V.T. Silveira, H. Nakamizo, K. Fushinobu, R. Yasui, T. Shinoda, Estimation of heat generation in semiconductors by inverse heat transfer analysis, IEEE Trans. Compon., Packag. Manuf. Technol. 13 (3) (2023) 315–322, https://doi.org/10.1109/TCPMT.2023.3257309. March.

[16] G. Bakan, N. Khan, H. Silva, et al., High-temperature thermoelectric transport at small scales: thermal generation, transport and recombination of minority carriers, Sci. Rep. 3 (2013) 2724, https://doi.org/10.1038/srep02724.
[17] M. Borghi, D. Bazzanella, M. Mancinelli, L. Pavesi, On the modeling of thermal and free carrier nonlinearities in silicon-on-insulator microring resonators, Opt. Express. 29 (2021) 4363–4377, https://doi.org/10.1364/OE.413572.
[18] M.W. Shura, A simple method to differentiate between free-carrier recombination and trapping centers in the bandgap of the p-type semiconductor, Adv. Mater. Sci. Eng. 2021 (1) (2020) 5568880, https://doi.org/10.1155/2021/5568880.
[19] G. Sliaužys, K. Arlauskas, V. Gulbinas, Photogeneration and recombination of charge carrier pairs and free charge carriers in polymer/fullerene bulk heterojunction films, Physica. Status. Solidi(a) 209 (7) (2012) 1302–1306, https://doi.org/10.1002/pssa.201127512.
[20] D.K. Markushev, N. Branković, S.M. Aleksić, D.S. Pantić, S.P. Galović, D. D. Markushev, J. Ordonez-Miranda, The influence of excess free carriers as heat carriers on the n-type silicon thermoelastic photoacoustic responses explained by electro-acoustic analogies, Int. J. Thermophys. 45 (2024) 107, https://doi.org/10.1007/s10765-024-03406-3.
[21] N. Stanojevic, D.K. Markushev, S.M. Aleksić, D.S. Pantić, S.P. Galović, D. D. Markushev, J. Ordonez-Miranda, Thermal characterization of n-type silicon based on an electro-acoustic analogy, J. Appl. Phys. 133 (2023) 245102, https://doi.org/10.1063/5.0152495.
[22] D.K. Markushev, D.D. Markushev, S.M. Aleksic, D.S. Pantic, S.P. Galovic, D. M. Todorovic, J. Ordonez-Miranda, Effects of the photogenerated excess carriers on the thermal and elastic properties of n-type silicon excited with a modulated light source: theoretical analysis, J. Appl. Phys. 126 (18) (2019) 185102, https://doi.org/10.1063/1.5100837.
[23] D.K. Markushev, D.D. Markushev, S.M. Aleksic, D.S. Pantic, S.P. Galovic, D. M. Todorovic, J. Ordonez-Miranda, Experimental photoacoustic observation of the photogenerated excess carrier influence on the thermoelastic response of n-type silicon, J. Appl. Phys. 128 (2020) 095103, https://doi.org/10.1063/5.0015657.
[24] S.P. Galovic, D.K. Markushev, D.D. Markushev, K.L.j. Djordjevic, M.N. Popovic, E. Suljovrujic, D.M. Todorovic, Time-resolved photoacoustic response of thin semiconductors measured with minimal volume cell: influence of photoinduced charge carriers, Appl. Sci. 15 (13) (2025) 7290, https://doi.org/10.3390/app15137290.
[25] D.K. Markushev, D.D. Markushev, S. Galović, S. Aleksić, D.S. Pantić, D. M. Todorović, The surface recombination velocity and bulk lifetime influences on photogenerated excess carrier density and temperature distributions in n-type silicon excited by a frequency-modulated light source, Facta Univ., Series: Electr. Energet. 31 (2) (2018) 313–328, https://doi.org/10.2298/FUEE1802313.
[26] S.M. Aleksić, D.K. Markushev, D.D. Markushev, D.S. Pantić, D.V. Lukić, M. N. Popović, S.P. Galović, Photoacoustic analysis of illuminated Si-TiO_2 sample bending along the heat-flow axes, Silicon 14 (2022) 9853–9861, https://doi.org/10.1007/s12633-022-01723-6.
[27] N. Jovančić, D.K. Markushev, D.D. Markushev, S.M. Aleksić, D.S. Pantić, D. Korte, M. Franko, Thermal and elastic characterization of nanostructured Fe_2O_3 polymorphs and TiO_2-coated Fe_2O_3 using open photoacoustic cell, Int. J. Thermophys. 41 (2020) 90, https://doi.org/10.1007/s10765-020-02669-w.
[28] M.S. Nadeem, M. Baoji, M.M. Alam, N.N. Riaz, AG. Al-Sehemi, T. Munawar, F. Mukhtar, A.W. Rabbani, A. Naz, MA. Al-Tahan, F. Iqbal, Sr-doped ZnO thin film on a silicon substrate (100) grown by sol-gel method: structural and optical study, Opt Mater 157 (2024) 116106, https://doi.org/10.1016/j.optmat.2024.116106. ISSN 0925-3467.
[29] G. Hamaoui, N. Horny, Z. Hua, et al., Electronic contribution in heat transfer at metal-semiconductor and metal silicide-semiconductor interfaces, Sci. Rep. 8 (2018) 11352, https://doi.org/10.1038/s41598-018-29505-4.
[30] M. Isaiev, G. Mussabek, P. Lishchuk, K. Dubyk, N. Zhylkybayeva, G. Yar-Mukhamedova, D. Lacroix, V. Lysenko, Application of the photoacoustic approach in the characterization of nanostructured materials, Nanomaterials 12 (4) (2022) 708, https://doi.org/10.3390/nano12040708.
[31] A. Somer, F. Camilotti, G.F. Costa, C. Bonardi, A. Novatski, A.V.C. Andrade, V. A. Kozlowski Jr., G.K. Cruz, The thermoelastic bending and thermal diffusion processes influence on photoacoustic signal generation using open photoacoustic cell technique, J. Appl. Phys. 114 (2013) 063503, https://doi.org/10.1063/1.4817655.
[32] J.L. Pichardo-Molina, J.J. Alvarado-Gil, Heat diffusion and thermolastic vibration influence on the signal of an open photoacoustic cell for two layer systems available to purchase, J. Appl. Phys. 114 (2004) 6450–6456, https://doi.org/10.1063/1.1711182.
[33] J.A. Balderas-López, A. Mandelis, Thermal diffusivity measurements in the photoacoustic open-cell configuration using simple signal normalization techniques, J. Appl. Phys. 90 (2001) 2273–2279, https://doi.org/10.1063/1.1391224.
[34] A. Rosencwaig, A. Gersho, Theory of the photoacoustic effect with solids, Acoustical Society Am. 58 (S1) (1975) S52, https://doi.org/10.1121/1.2002181, v. n.
[35] F. Alan McDonald, Photoacoustic cell for liquids and solids: generalization of one-dimensional models, J. Opt. Soc. Am. 70 (5) (1980) 555–557, https://doi.org/10.1364/JOSA.70.000555.
[36] D.K. Markushev, N.Lj. Brankovic, S.P. Galovic, K.Lj. Djordjevic, S.M. Aleksic, D. S. Pantic, D.D. Markushev, The cut-off frequency – a key concept in the heat flow measurements based on the thermoelastic photoacoustic response, Measurement 248 (2025) 116902, https://doi.org/10.1016/j.measurement.2025.116902.
[37] M.D. Dramićanin, P.M. Nikolić, Z.D. Ristovski, D.G. Vasiljević, D.M. Todorović, Photoacoustic investigation of transport in semiconductors: theoretical and experimental study of a Ge single crystal, Phys. Rev. B 51 (1995) 14226, https://doi.org/10.1103/PhysRevB.51.14226.
[38] V.V. Miletić, M.N. Popović, S.P. Galović, D.D. Markushev, M.V. Nešić, Estimation of linear expansion coefficient and thermal diffusivity by photoacoustic numerical self-consistent procedure, J. Appl. Phys. 133 (2023) 075101, https://doi.org/10.1063/5.0134313.
[39] M. Popovic, D. Milicevic, L.T. Kostic, V. Miletic, S. Galovic, Influence of the high absorbing nonilluminated surface of the sample on the photothermally induced thermoelastic bending, Int. J. Thermal Sci. 211 (2) (2025) 109689, https://doi.org/10.1016/j.ijthermalsci.2025.109689.

Радови Драгана К. Маркушев

Часописи

М21а

Measurement 248 (2025) 116902

Contents lists available at ScienceDirect

Measurement

journal homepage: www.elsevier.com/locate/measurement

The cut-off frequency – a key concept in the heat flow measurements based on the thermoelastic photoacoustic response

DK Markushev [a,*], NLj Brankovic [b], SP Galovic [c], KLj Djordjevic [c], SM Aleksic [b], DS Pantic [b], DD Markushev [a]

[a] Institute of Physics Belgrade-National Institute of the Republic of Serbia University of Belgrade Belgrade Serbia
[b] Department of Microelectronics Faculty of Electronic Engineering University of Nis Nis Serbia
[c] Vinca Institute of Nuclear Sciences-National Institute of the Republic of Serbia Belgrade Serbia

ARTICLE INFO

Keywords:
Photoacoustics
Heat flow
Thermal conductivity
Thermal diffusivity
Thermoelastic
RC filters
Light-matter interaction
Diffusion

ABSTRACT

This article discusses the thermoelastic photoacoustic response cut-off frequency, a key concept for measuring and quality-controlling solid materials. It links the cut-off frequency to the maximum temperature difference across the sample and its thickness, enabling detailed monitoring of heat flow parameters. The presented model and numerical simulations were validated by measuring 735 μm and 120 μm aluminium and its alloy samples, revealing significant changes in thermal diffusion (−43 %) and conductivity (−40 %) that helped identify the alloy type.

1. Introduction

The efficient transfer of thermal energy is a critical issue in various fields, including solid-state physics. This problem becomes particularly complex when dealing with a wide range of electronic and aerospace materials, polymers, composites and ceramics. The proper manufacturing of new aircraft and spacecraft devices, electronic switchers and heat sinks, is based on the knowledge of behaviour of multilayer systems and layered structures that have different thermal and electrical conductivities in their layers [1–4]. To address these challenges, theoretical models based on the analysis of multilayer systems are necessary, alongside various experimental non-destructive techniques, including laser flash, IR thermography, beam deflection, and so on [5–9]. Special attention must be given to the interactions that occur at the interfaces between the layers. This is why there is a need for a simpler approach that would not be so theoretically demanding but would satisfy the needs for quality and reliable heat flow analysis. One such approach is suggested in this paper, based on photoacoustics.

Photoacoustics is a part of photothermal sciences that uses sound generated in a material illuminated by a modulated light source to analyse its periodic thermal state changes. The thermal state changes lead to the temperature gradient generation implying temperature differences between the material illuminated and non-illuminated surfaces. Therefore, photoacoustics can be considered a powerful technique for heat flow measurements because heat transfer occurs whenever a temperature difference exists [10,11]. A simple theoretical model of surface absorber (Appendix I) in photoacoustics could help one to analyse measurement data and calculate important thermophysical properties of the material, generally referred to as transport and thermodynamic parameters. In heat flow measurements, the coefficients of thermal conductivity, k, and thermal diffusivity, D_t, are the most important parameters, knowing that k is the heat transport property of the sample material, while D_t measures the ability of a material to conduct thermal energy relative to its ability to store it [12–19]. It is not easy to compare photoacoustics with other measurement techniques because comparative characteristics, such as sensitivity and selectivity, strongly depend on sample characteristics (measured parameters) and measurement conditions. In general, sensitivity across the entire range of modulation frequencies for any material is 10^{-15}K/Hz [20,21], while high selectivity concerning the material being tested is achieved by adjusting the wavelength of the excitation light source throughout the visible spectrum. One of the unique advantages of photoacoustics is its ability to accurately calculate temperature fluctuations in the range of 10^{-1}K to 10^{-9}K for nearly all types of solids by measuring the amplitude and

* Corresponding author.
E-mail address: dragana.markusev@ipb.ac.rs (D. Markushev).

https://doi.org/10.1016/j.measurement.2025.116902
Received 11 October 2024; Received in revised form 12 January 2025; Accepted 30 January 2025
Available online 31 January 2025

phase of the produced sound. Additionally, the photoacoustic measurement system does not require consumables and has low maintenance needs.

Even based on the simple theoretical model, the photoacoustic heat flow measurements in solid samples in the frequency domain suggest multi-parametric analysis managing to extract, besides mentioned, more thermophysical and mechanical parameters of the investigated samples simultaneously, using the total photoacoustic signal and its components [22–30]. To avoid the complexity of multiparameter fitting and simplify the heat flow analysis we have recently developed a new method based on the electro-acoustic analogies between the low-pass *RC* filter and the thermoelastic (TE) photoacoustic response of the sample [31,32]. This method implies the analysis of only one photoacoustic signal component, a thermoelastic one, introducing only one fitting parameter, the cut-off frequency, f_c, as the single characteristic value of the thermoelastic response.

Our investigations have shown that the f_c depends on the thickness of the sample, l: $f_c = f(l)$ where $f_c \ l^{-2}$, having the D_t of the sample material as a proportionality factor. Thus, obtained $f_c = f(l)$ dependence enables us to establish the reference curves of the tested materials and develop methods of their characterization or quality control [31]. While electroacoustic analogies have the advantage of simplicity, they are only an approximation. The f_c values determined by the *RC* filter transfer function or Bode plot method imply the existence of some level of uncertainty. Also, *RC* analogies partially explain f_c nature, but its concept in terms of physics was not fully clarified.

Previously, the concept of cut-off frequency was introduced in photoacoustics as the limiting frequency between thermally thick and thin regimes [18], relying on analysing all photoacoustic signal components. In our case, the cut-off frequency concept is the novel one, exclusively related to the thermoelastic photoacoustic component. It refers to the frequency at which the temperature difference, ΔT, between the illuminated and non-illuminated sides of the sample, is maximized for a given sample thickness. Such a concept relies on the composite piston theoretical model where the temperature variations within the sample and its surfaces are calculated by applying the dynamic solution of the parabolic heat conduction equation (PHCE), assuming aluminium as a surface absorber and heat flow as a diffusion process [22,23,30]. This approach provides insight into the heat flow efficiency in materials at different modulation frequencies and allows measurement of the investigated material's thermal conductivity and thermal diffusivity.

2. Theoretical background

Following the simple 1D model scheme presented in Fig. 1 and based on the theoretical model of the composite piston [23], the total photoacoustic signal $\delta p_{total}(j\omega)$ and its components, thermodiffusion $\delta p_{TD}(j\omega)$ and thermoelastic $\delta p_{TE}(j\omega)$, can be written in the form:

$$\delta p_{total}(j\omega) = \delta p_{TD}(j\omega) + \delta p_{TE}(j\omega) \tag{1}$$

where

$$\delta p_{TD}(j\omega) = \frac{\gamma_g p_0 \sqrt{D_g}}{l_c T_0 \sqrt{j\omega}} T_s(l) \tag{2}$$

$$\delta p_{TE}(j\omega) = 3\pi \frac{\gamma_g p_0 \alpha_T R_s^4}{l^3 V_0} M \tag{3}$$

$$M = \int_0^l (x - l/2) T_s(x) \mathrm{d}x \tag{4}$$

and

$$T_s(x) = \frac{I_0}{k\sigma \sinh(\sigma l)} \cosh[\sigma(x - l)] \tag{5}$$

Here, $\omega = 2\pi f$, f is the modulation frequency, j is an imaginary unit, $T_s(l)$ is the temperature at the non-illuminated sample surface, γ_g, D_g, p_0, V_0 and T_0 are the adiabatic coefficient, coefficient of thermal diffusion, pressure, volume and temperature of the air inside the microphone, respectively, α_T is the coefficient of linear thermal expansion, l and R_s are the sample thickness and radius, respectively, M is the temperature moment, $T_s(x)$ is the temperature distribution along the heat-flow axes (see Fig. 1, x-axes), $\sigma = (1+j)(\omega/2D_t)^{1/2}$ is the complex thermal diffusion coefficient of the sample, $D_t = k/\rho c$ is the coefficient of thermal diffusivity, k is the coefficient of thermal conductivity, ρ is the sample density, and c is the specific heat capacity of the sample. The $T_s(x)$ and $T_s(l)$ are calculated by applying a 1D PHCE dynamic solution (see Appendix A) [22,23,30].

Utilising Eqs. (1–3) during the data fitting procedure, all the sample physical parameters mentioned so far can be obtained. Although the thermoelastic response (Eq. (3)) carries many sample parameters, we have shown in our previous articles [31–33] that the same response can be described more simply, with only one parameter. That parameter is the so-called cut-off frequency f_c $(\omega_c = 2\pi f_c)$, which occurs in simple equations for the amplitude, $|\delta p_{TE}(j\omega)|$, and phase, $< (\delta p_{TE}(j\omega))$, of the thermoelastic response in the frequency domain, based on the electroacoustic analogies with a low-pass *RC* filter [31,32]:

$$|\delta p_{TE}(j\omega)| = \frac{1}{\sqrt{1 + \left(\frac{\omega}{\omega_c}\right)^2}} \tag{6}$$

and

$$< (\delta p_{TE}(j\omega)) = -\arctan\left(\frac{\omega}{\omega_c}\right) \tag{7}$$

In basic electronics, the cut-off frequency is a characteristic of filtering devices like *RC* circuits. In simple words, the cut-off frequency is the point where the amount of attenuation due to the filter increases swiftly. In literature, the cut-off frequency is usually defined as the frequency at which the power output of a circuit has fallen to a certain proportion of the power in the passband, often one-half. This proportion is also known as the 3 dB point, referring to the fact that a 3 dB fall corresponds approximately to half power. In terms of voltage ratio, this is a fall to approximately 0.707.

From the analytical solution of Eq.(3) (Appendix B), we found a relationship between f_c and the parameters of the tested sample (D_t and l) in the form [18,31–33]:

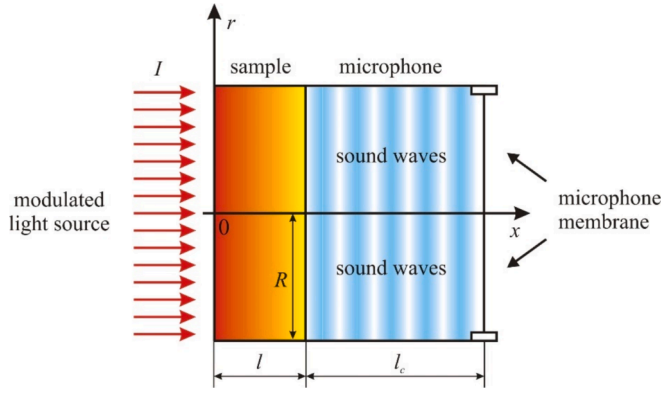

Fig. 1. A simple scheme of our theoretical model based on the open-cell photoacoustic set-up where the sample, having the thickness l and radius R_s, is mounted on the top of the microphone which acts as a photoacoustic cell and the sound detector in the same time, filled with air, having the length l_c.

$$f_c = \frac{2}{\pi}\cdot\frac{D_T}{l^2}m^2 \tag{8}$$

where $\sqrt{2} \le m \ll \sqrt{6}$ is a calibration factor depending on the method of determining f_c (RC analogy or Bode plot). Following the previous consideration about thermally thick and thin limiting frequency [18], we found that the last equation (Eq. (8)) can be generalized and used to create unique reference curves of the investigated materials calculated from the adopted values in the literature. Such obtained reference curves can be represented by a straight line in a log–log scale and used for material characterization or quality control purposes [18,31–33].

To quantify the heat flow processes in investigated material one can use appropriate rate equations. Our theoretical model of composite piston [23] relies on the well-known rate equation, the so-called Fourier's law of heat conduction. It allows us to use the rate of heat flow, H, defined as the amount of heat, Q, that is transferred per unit of time, Δt, in a given material. Following Fourier's law and Fig. 1, assuming steady-state conditions of a 1D heat flow, H can be expressed as [30,34]:

$$H = \frac{Q}{\Delta t} = kS\frac{\Delta T}{\Delta x} \tag{9}$$

where k is the coefficient of thermal conductivity, S is the cross-sectional area of the sample, and $\Delta x = l$ is the sample thickness. In most suitable form for our investigation, last equation can be written as:

$$\Delta T = \frac{H}{kS}l \tag{10}$$

3. Results and discussion

Since we use previously electroacoustic analogies with RC filters to describe the thermoelastic response, a basic question can be asked: what is the physical nature of the cut-off frequency in thermoelastic photoacoustic response? To answer that question, we need to refer back to Equation (3) and consider the presence of the temperature moment M in it (see Equation (4)). Equation (3) explains the thermoelastic response of a periodically illuminated sample resulting from the sample bending (mechanical piston). In solid mechanics, a bending moment is a force exerted at a certain distance that causes the sample to bend. In Equation (4), the role of force is taken over by the temperature difference, ΔT, between the illuminated ($x = 0$) and the non-illuminated ($x = l$) side of the sample (see Fig. 1): $\Delta T = T_s(0) - T_s(l)$. In photoacoustics, ΔT is a frequency-dependent quantity that changes its value following a bell-shaped curve. At a certain frequency, ΔT reaches its maximum, corresponding to the so-called cut-off frequency of the thermoelastic component of the photoacoustic signal. This fact is the essence of the thermoelastic response cut-off frequency physical nature.

To explain the concept of cut-off frequency and outline a methodology for material characterization or quality control, we utilized numerical simulations of the thermoelastic photoacoustic response using pure aluminium data [35,36]. To validate the proposed method, experimental measurements were conducted using samples of pure aluminium and its alloys [37,38], chosen as the most suitable materials which can be completely described by the simplest theoretical model of the surface absorber (Appendix I). Although the phases also influenced the processing of the results, for clarity, only the results for the signal amplitudes are provided.

4. A. Numerical simulations

Our numerical simulations are based on calculations running on our computer, following a program in MATLAB – MathWorks. This program implements a mechanical piston theoretical model (Eqs.(3–5)) for an investigated physical system: periodically irradiated aluminium plates. The main purpose of the numerical simulations is to indicate the physical nature of the cut-off frequency by connecting it with the maximum temperature difference between the illuminated and non-illuminated sides of the sample, and the sample thickness. Using the mentioned interconnections, the ultimate goal of the simulations is to establish a simple methodology for measuring the basic transport and thermodynamic parameters of heat flow in solids using standard literature data.

4.1. Simulation procedure

A persuasive representation of the applied f_c concept is shown in Figs. 2 and 3. In Fig. 2 numerically simulated frequency responses of $T_s(0)$ and $T_s(l)$ amplitudes are presented, obtained using Eq. (5) in the case of thick ($l = 1000\mu m$) and thin ($l = 10\mu m$) aluminium samples (Table 1) in the form of circular plates ($R_s = 3mm$) at room temperature. Temperature differences, ΔT, and difference maximums, ΔT_{max}, are also presented in the same Figure. The position of ΔT_{max} in the frequency domain can be understood as a position of cut-off frequency, f_c, ($f_c^{1000} = 127Hz$ and $f_c^{10} = 1.27 \times 10^6 Hz$), the point after which the amplitude of the temperature moment M (Eq(4)) attenuates swiftly (Fig. 3.a). Both f_c values match −5 dB or 0.770 falls in electronic terms. According to Eq. (3), the same behaviour also applies to the amplitude of thermoelastic photoacoustic response, $TE = |\delta p_{TE}(j\omega)|$ (Fig. 3.b).

Obviously, there is a strong correlation between the position of ΔT_{max} and f_c for different sample thicknesses, and the corresponding behaviour of temperature moments (M_{1000} and M_{10}) and thermoelastic responses (TE_{1000} and TE_{10}) in the modulated frequency domain.

The same ΔT analysis was carried out for other aluminium sample thicknesses ranging from 10 to 1000 μm. The obtained results are presented in Table 2 and Fig. 4, having 5 % relative error for both ΔT_{max} and f_c values. Presented analysis shows that ΔT_{max} and corresponding f_c are dependent on l: $\Delta T_{max} = \Delta T_{max}(l)$ and $f_c = f_c(l)$. Here, besides ΔT_{max} and f_c corresponding values, f_{crc} values are given for comparison, previously calculated using RC analogies (Eq. (6), $m = 1.545 > \sqrt{2}$) [31–33]. The position of f_c obtained using the ΔT_{max} position has smaller values compared to f_{crc}, which is expected because the RC analogy is a rough approximation.

When plotted on a log–log scale, $\Delta T_{max}(l)$ and $f_c(l)$ values from Table 2 form a straight line (Fig. 5). In the case of a) $\Delta T_{max} = \Delta T_{max}(l)$, the line follows Eq. (10) $\left(H = 2.12 \times 10^{-3} W\right)$, and in the case of b) $f_c = f_c(l)$, the line follows Eq. (8) $\left(m \to \sqrt{2}\right)$.

The results presented in Fig. 5 allow one to establish the simple methodology for heat flow analysis, and material characterization or quality control. In Fig. 5.a, the graph allows one to calculate the value of k (ΔT_{max} $1/k$, Eq. (10)) directly from the measurements of $\Delta T_{max} = \Delta T_{max}(l)$. Similarly, in Fig. 5.b, the graph allows one to calculate the value of D_t (f_c D_t, Eq. (8)) defining $f_c = f_c(l)$ directly from the measured positions of $\Delta T_{max} = \Delta T_{max}(l)$ in the frequency domain. These graphs can also be used to characterize and control the quality of solid materials. This is especially true when $\delta p_{total}(j\omega)$ for two different measurements does not differ much, implying additional analysis.

Any deviation on either graph obtained using literature values would indicate the nature of D_t changes, helping one to understand whether such changes are caused by k (changes in ΔT_{max} values and positions) or ρc (changes in ΔT_{max} positions only). Sensitivity analysis based on Eqs. (8) & (10) indicate that the overall sensitivities of ΔT_{max} ($\sim 10^{-7}$ K/m) and f_c (~ 1 Hz/μm^2) to sample thickness l demonstrate high reliability and robustness of the obtained values for k and D_t in the measurement range of sample thicknesses from 100 to 1000 μm. This range of sample thicknesses is recommended to be used in the measurements. In the case of thinner samples, the sensitivity of f_c to l and f changes significantly, which leads to unreliable and weaker results.

When talking about the measurements, in photoacoustics, the modulation frequency range that corresponds to the applied theoretical model validity includes ($10 - 10^7$) Hz [31,32]. Experimental range of modulation frequencies corresponds to typically electret microphone frequency response range from 20 Hz to 20 kHz [36,37]. Based on the

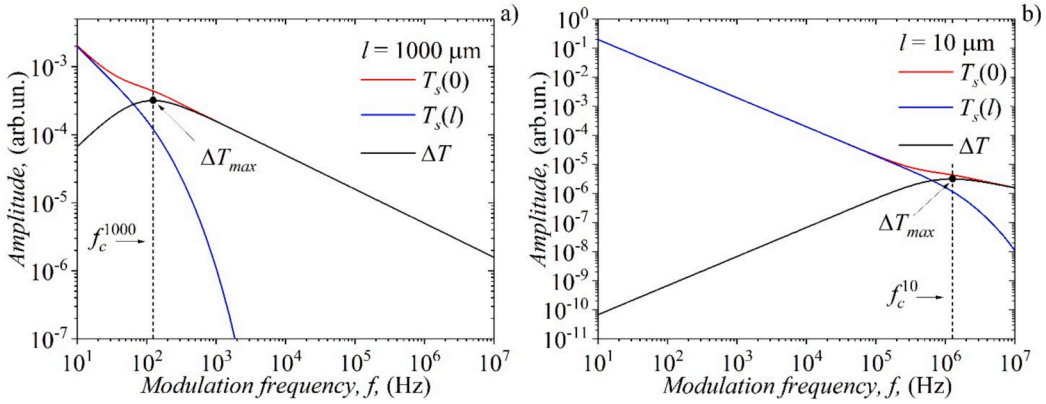

Fig. 2. Amplitude responses of $T_s(0)$, $T_s(l)$ and ΔT as the functions of modulation frequency f, with assumed ΔT_{max} and cut-off frequency f_c positions in the case of thick a) 1000 μm and thin b) 10 μm aluminium samples.

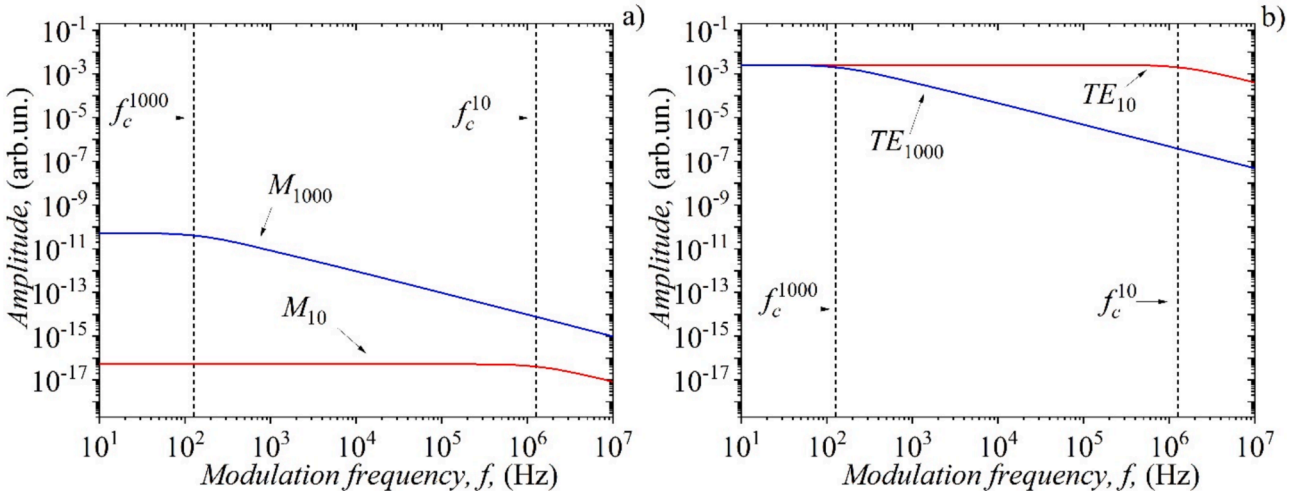

Fig. 3. Amplitude responses of a) temperature moments (M_{1000}, M_{10}), and b) thermoelastic photoacoustic components (TE_{1000} and TE_{10}) with corresponding cut-off frequencies positions in the case of thick (1000 μm) and thin (10 μm) aluminium samples, as a functions of modulation frequency f.

Table 1
Aluminium sample parameters used in Eq.(1–3) [24,25].

Thermal conductivity, k / (W/mK)	237
Heat capacity, C / (J/kgK)	900
Density, ρ / (kg/m^3)	2700
Thermal diffusivity Dt / (10^{-5} m^2/s)	9.75
Linear thermal expansion, α_T / (10^{-6} 1/K)	23.1

numerical simulation results (Table 2), it is evident that direct measurement of f_c can only be done for aluminium samples with a thickness greater than 70μm. For thinner samples, indirect measurements are required: extrapolation after the fitting procedure is needed.

5. B. Experimental measurements

Our experience suggests that experimental confirmation of the previously described methods can best be performed by measuring the photoacoustic frequency response of aluminium and its alloys. Alloying elements in solid aluminium usually change (weaken) its thermal conductivity rather than volumetric heat capacity. Therefore, it is expected that in the case of alloys, an increase in the intensity of the ΔT_{max} value (decrease in k) is expected, followed by a decline in the corresponding f_c position in the frequency domain (decrease in D_t).

Table 2
ΔT_{max} values and corresponding f_c positions of investigated aluminium samples as a function of their thickness l.

l / ($\times 10^{-6}$ m)	ΔT_{max} / ($\times 10^{-6}$ K)	f_c / (Hz)	f_{crc} / (Hz)
10	3	1,271,698	1,482,388
20	6	317,924	370,597
30	9	141,299	164,709
40	12	79,481	92,649
50	15	50,867	59,295
60	19	35,324	41,177
70	22	25,953	30,252
80	25	19,870	23,162
90	28	15,699	18,301
100	31	12,716	14,823
200	63	3179	3705
300	95	1412	1647
400	126	794	926
500	158	508	592
600	190	353	411
700	222	259	302
800	253	198	231
900	285	156	183
1000	317	127	148

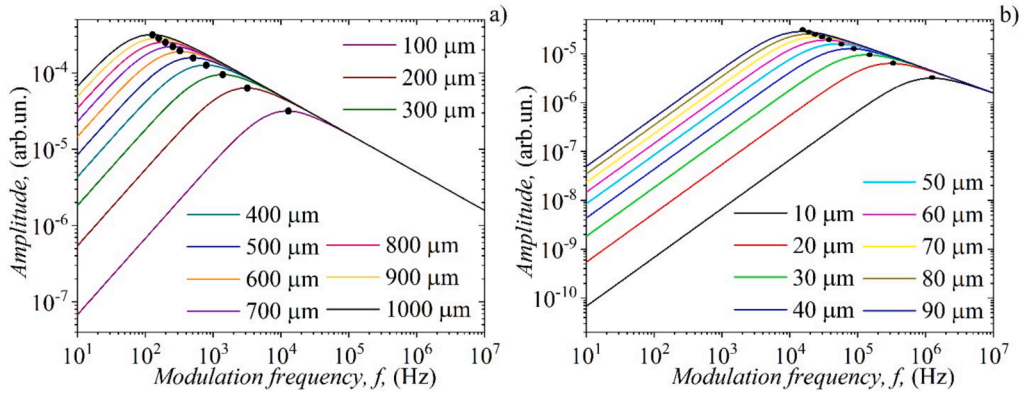

Fig. 4. Temperature differences ΔT (solid lines) and corresponding ΔT_{max} positions (solid points) as a functions of modulation frequency f, in the case of thick a) (200–1000) μm and thin b) (10–100) μm aluminium samples.

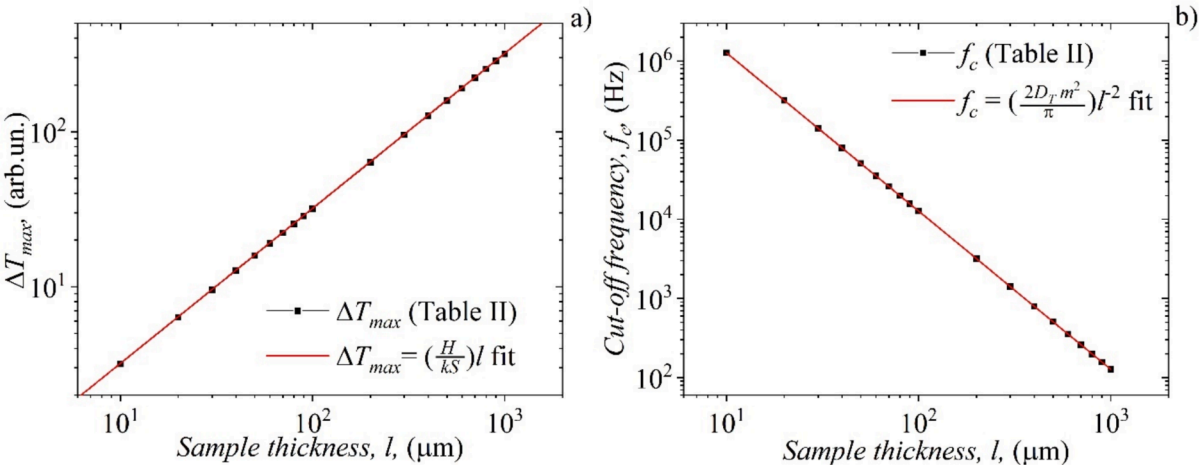

Fig. 5. A) temperature difference ΔT_{max} values and corresponding b) f_c positions as a functions of aluminium sample thickness l, and appropriate straight-line fits obtained by a) Eq. (10), and b) Eq. (8).

5.1. Experimental set-up and measurement procedure

The experimental set-up used in this investigation is presented with the schematic diagram in Fig. 6 [19,29,31,32,36,37]. It corresponds to a standard open-cell configuration that implies transmission photoacoustic measurements (modulated light source-sample-microphone) with a minimal volume cell (microphone body as a photoacoustic cell). The control box, powered by batteries, contains all the electronics needed for signal amplification and light source supervision. The PC is used as a complex instrument; it acts as a function generator and lock-in generator. Appropriate software is used to generate the signal for laser diode modulation in the 20 Hz – 20 kHz range and to perform data acquisition. All experimental conditions are well-controlled. Measurements were made at room temperature without significant fluctuations. The intensity of the laser diode is controlled by a photodiode. The microphone is well protected from external noise by a duralumin shield.

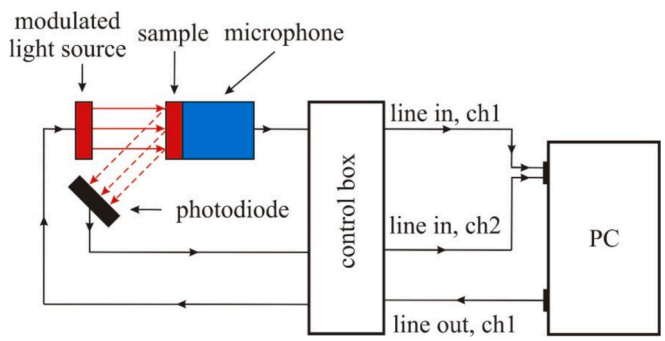

Fig. 6. A simple scheme of the open-cell photoacoustic set-up.

In brief, samples are mounted on the front of an electret microphone (ECM30B) and uniformly irradiated with the red laser diode (15 mW, 660 nm) modulated and controlled by the PC sound card (Intel 82801Ib/ir/ih hd) and laser diode driver. Usually, photoacoustic signals generated by the sample are quite weak (tens to hundreds of nanovolts), which indicates the need for their amplification. High-speed operational amplifiers OP37 are used to amplify the signal in the low- (x10) and high-(x100) modulation frequency range. The photodiode (BPW34) of high speed and radiant sensitivity is used to monitor how the laser diode works. For clarity, the signal from the photodiode is amplified ten times. The PC sound card (with appropriate software) is used to record amplitudes and phases of the low-level photoacoustic signals picked up by the microphone, acting as a homemade lock-in amplifier, using the signal from the photodiode as the referent one. Actual figure of the descripted set-up is presented in Fig. 7.

5.2. Signal correction procedure

It's widely recognized that measuring instruments can sometimes alter the signals we are studying due to their inherent imperfections or incorrect usage. In photoacoustics, the most significant distortions in the measured signal are caused by the microphone as a detector (usually an

Fig. 7. Actual figure of the descripted set-up.

electret microphone) and the accompanying instruments (in our case, sound cards). Our detailed analyses show that the signal distortion caused by the influence of measuring instruments can be described as unwanted *RC* and *RCL* filtering of sound signals originating from the illuminated sample [31,32,37]. This is the reason why signal distortions can be classified into two groups: low-frequency (*RC* filtering, 20 Hz – 1 kHz)) and high-frequency (*RCL* filtering, 1 kHz – 20 kHz) distortions.

Low-frequency distortions result in a gradual reduction in amplitude without abrupt changes. The mathematical description of such signal distortion in the modulation frequency f domain ($\omega = 2\pi f$) can be given using the transfer function $H_e(j\omega)$ of the high-pass *RC* filters cascade connection [37]

$$H_e(j\omega) = -\frac{\left(\frac{\omega}{\omega_{e1}}\right)}{1+\frac{j\omega}{\omega_{e1}}} \bullet \frac{\left(\frac{\omega}{\omega_{e2}}\right)}{1+\frac{j\omega}{\omega_{e2}}} \tag{11}$$

where ω_{e1} and ω_{e2} are the microphone and sound-card characteristic cut-off frequencies, respectively.

High-frequency distortions, on the other hand, are typical microphone distortions and lead to sudden changes in amplitude, referred to as peaks, which may occur more than once, depending on the type of microphone. Their mathematical description in modulation frequency range uses the transfer function $H_a(j\omega)$ of the low-pass *RCL* filters connection [37]

$$H_e(j\omega) = \frac{{\omega_{a1}}^2}{{\omega_{a1}}^2 + j\delta_{a1}\omega_{a1}\omega + \omega^2} + \frac{{\omega_{a2}}^2}{{\omega_{a2}}^2 + j\delta_{a2}\omega_{a2}\omega + \omega^2} \tag{12}$$

where ω_{a1} and ω_{a2} are the characteristic frequencies, and δ_{a1} and δ_{a2} are dumping factors of the existing peaks.

Fig. 7 depicts how $H_e(j\omega)$ and $H_a(j\omega)$ amplitude distortions appear. The blue arrows indicate the total photoacoustic signal distortion tendency, $\delta p_{total}(j\omega)$. The amplitude of the measured signal, $S(j\omega)$, in the low-frequency range, illustrates how the $\delta p_{total}(j\omega)$ weakens under the influence of the microphone and sound card, both acting as high-pass *RC* filters described by $H_e(j\omega)$ (Eq.(11)). Furthermore, $S(j\omega)$ in the high-frequency range demonstrates how the $\delta p_{total}(j\omega)$ suddenly changes its amplitude behaviour, forming two peaks with different damping factors. These peaks are primarily due to the microphone's influence, indicating that the microphone acts as a low-pass *RCL* filter characterised by $H_a(j\omega)$ (Eq.(12)).

Based on the previous discussion and Fig. 7, the connection between $\delta p_{total}(j\omega)$ and $S(j\omega)$ can be easily established [37]:

$$S(j\omega) = \delta p_{total}(j\omega) H_e(j\omega) H_a(j\omega) \tag{13}$$

Here, $H_e(j\omega)$ and $H_a(j\omega)$ could be understood as the calibration factors. The idea in all our measurements is to fit $S(j\omega)$ and find the characteristic frequencies and dumping factors of the microphone and sound card. Such procedure, given in detail somewhere else [37], will allow us to remove $H_e(j\omega)$ and $H_a(j\omega)$ from Eq.(13), aiming only $\delta p_{total}(j\omega)$ for analysis.

5.3. Measurement data analysis

Open-cell measurements were carried out in the modulation frequency range, f, from 20 Hz to 20 kHz, and samples in the form of circular plates (R_s = 3mm) of pure aluminium (Al) and its alloys (AlA) with thicknesses of 120 μm (Al120 and AlA120) and 735 μm (Al735 and AlA735). The measurement results are presented in Fig. 8. Following the

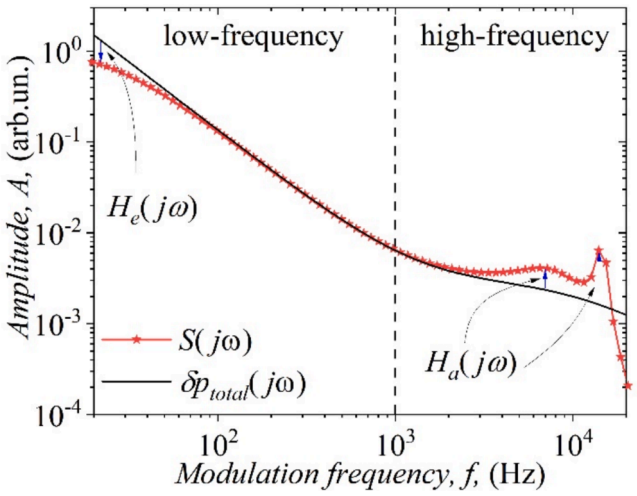

Fig. 8. Photoacoustic signal amplitude distortions due to measuring instruments influence in the modulation frequency domain.

Table 3
Measuring chain characteristic parameters.

parameter	value
microphone characteristic frequency, f_{e1} (Hz)	24 ± 1
PC sound card characteristic frequency, f_{e2} (Hz)	16 ± 1
microphone characteristic first peak frequency, f_{a1} (kHz)	7.8 ± 0.1
microphone characteristicsecond peak (cut-off) frequency, f_{a2} (kHz)	14.7 ± 0.2
first peak damping factor, δ_{a1}	0.80 ± 0.05
second peak damping factor, δ_{a2}	0.02 ± 0.01

signal correction procedure, the measured signal, $S(j\omega)$, for all investigated samples was corrected to the influence of the measuring chain (Table 3) to obtain $\delta p_{total}(j\omega)$, a signal originating only from the illuminated sample.

Applying the composite piston theoretical model, both $\delta p_{TD}(j\omega)$ and $\delta p_{TE}(j\omega)$ signal components are obtained, too, together with corresponding temperature differences ΔT, ΔT_{max} and f_c positions. The integrated results of the presented analysis are shown in Table 3, having ΔT_{max} and f_c relative errors in the range of 7 %.

Based on the results presented in Fig. 9 and Table 4, it is evident that, in the case of alloys, the maximum temperature difference, ΔT_{max}, for both thicknesses increases by almost twice compared to pure aluminium. At the same time, the value of the cut-off frequency f_c decreases by nearly the same amount. This behaviour of the mentioned parameters indicates that the alloying elements have significantly reduced the sample's thermal conductivity. The relative error of the results obtained for D_t and f_c is approximately 8 %, primarily arising from the signal correction procedure. To determine precisely whether the thermal conductivity changes in the investigated sample, we will use the dependencies $\Delta T_{max} = \Delta T_{max}(l)$ and $f_c = f_c(l)$ obtained earlier for

Table 4
The measurement results obtained from Fig. 7.

	ΔT_{max} / ($\times 10^{-6}$ K)	f_c / (Hz)
Al 120	38	8687
AlA 120	61	4903
Al 735	233	232
AlA 735	381	133

pure aluminium in numerical simulations, considering them as reference curves. It is observed (see Fig. 10) that the results of pure aluminium samples (red circles) completely match the reference curves (red solid lines). In contrast, the results of aluminium alloys (blue circles) deviate significantly from them. Using Eqs.(8) and (6), we obtain new dependencies for alloys (blue solid lines) that yield values of $k = 150\mathrm{Wm^{-1}K^{-1}}$ and $D_t = 5.75 \times 10^{-5}\mathrm{m^2s^{-1}}$, indicating the 7 % increase in ρc value. Searching for such an alloy in the literature, we found that the closest is 2014-T4 ($\rho = 3000\mathrm{kgm^{-3}}$, and $c = 870\mathrm{Jkg^{-1}K^{-1}}$) [24].

Here we have presented only one of the possible ways of using the proposed methodology for the characterization and quality control of materials. In addition to the production of alloys and their application in different industrial branches [39–41], we believe that this methodology can be easily extended to a much wider field of new and advanced materials technologies, particularly in the development of nanostructured materials, especially when exploring new approaches to manipulate the nanostructure to decrease or increase its thermal conductivity [42–44]. We need to keep in mind that there are some limitations when examining nanostructures using photoacoustics with our open-cell setup. These structures can't be studied directly as single-layered due to their transparency, but only indirectly as two- or multi-layered structures. This makes the calculation a bit more complicated, but it doesn't reduce the effectiveness of the methodology we're proposing. Also, the thickness of the nanostructures must not be less than

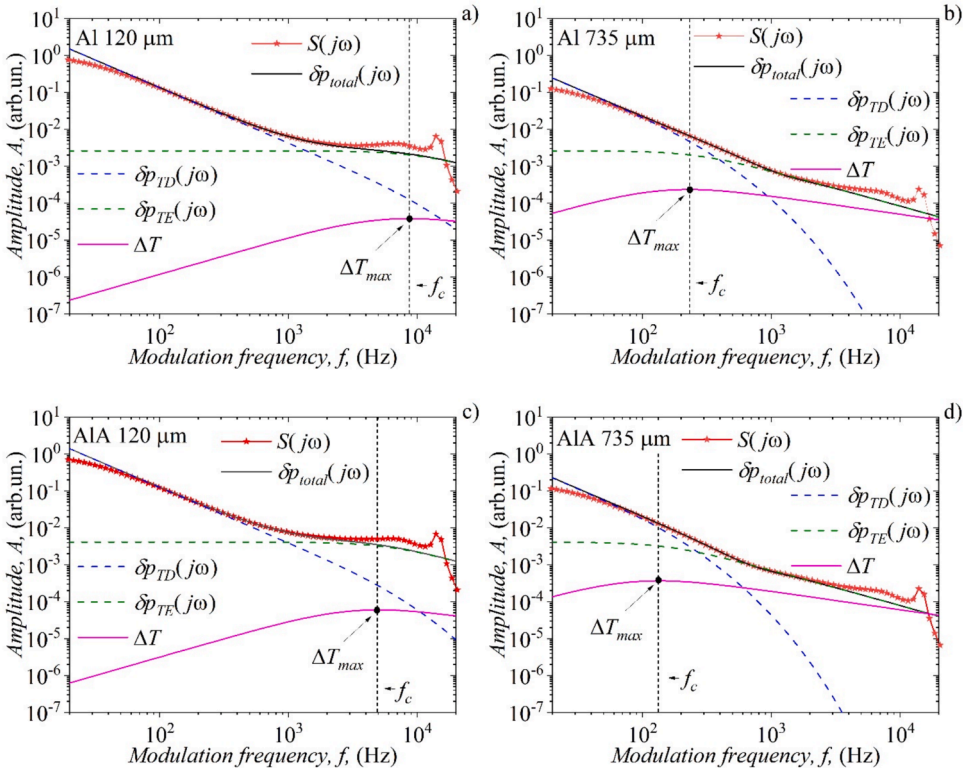

Fig. 9. Measured signal $S(j\omega)$ together with total signal $\delta p_{total}(j\omega)$ obtained after signal correction procedure and its corresponding components $\delta p_{TD}(j\omega)$ and $\delta p_{TE}(j\omega)$, temperature differences ΔT with their maximal values ΔT_{max} and corresponding f_c positions as a functions of a), b) pure aluminium (Al), and c), d) aluminium alloys (AlA) samples, having the thicknesses of 120 μm and 735 μm, in the modulation frequency f domain.

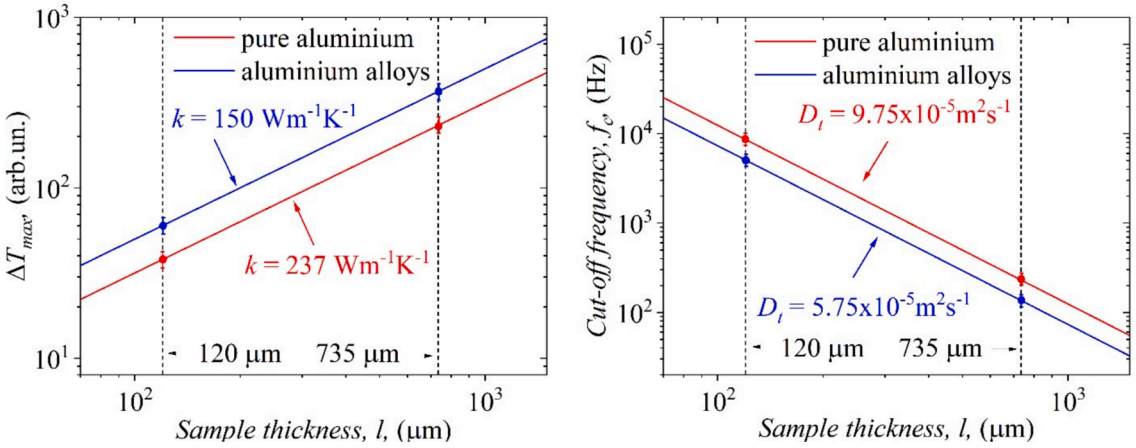

Fig. 10. A) temperature differences ΔT_{max} values and corresponding b) f_c positions as a functions of aluminium sample thickness l, and appropriate straight-line fits obtained by a) Eq. (10), and b) Eq. (8).

10 nm, the established theoretical limit below which the examined samples cannot be considered thermodynamic systems [18].

The cut-off frequency approach is new and has yet to be validated. This paper gives only the basics and the simplest theory to understand the cut-off principle of determining thermal conductivity and diffusivity. A detailed comparison with conventional methods is yet to follow, especially when dealing with solid dielectrics, semiconductors, composites and substrate + thin film samples [45–48].

6. Conclusions

In this article, we introduced the cut-off frequency (f_c) concept in heat flow measurements and analysis based on the numerical simulations and experimental measurements of the thermoelastic photoacoustic response of aluminium samples. We discovered that the temperature difference (ΔT) between the illuminated and non-illuminated sides of the investigated sample at a specific thickness in the modulation frequency domain is characterized by its maximal value, ΔT_{max}, which determines the position of f_c. We showed how these three parameters (ΔT, ΔT_{max}, and f_c) influenced the frequency response of the temperature moment (M) and thermoelastic photoacoustic component (TE). Additionally, we demonstrated that all mentioned parameters depend on the sample thickness (l) and how these dependencies can be used to establish a simplified methodology for heat flow analysis and material quality control or its characterization. Based on the dependencies of ΔT_{max} and f_c on sample thickness, we proposed two independent methods in heat flow analysis to determine the sample's thermal conductivity and thermal diffusivity, respectively. The applicability of the proposed methods is confirmed by measuring pure aluminium and aluminium alloy photoacoustic responses in the standard modulation frequency range, from 20 Hz to 20 kHz. The cut-off frequency concept has the potential to be generalised to all types of materials, especially those with complex thermal behaviours, such as composites and anisotropic materials. To achieve this, the concept must be extended to a new theoretical model, which implies taking into account the optical properties of the material.

CRediT authorship contribution statement

DK Markushev: Writing – original draft, Validation, Supervision, Methodology, Investigation, Formal analysis, Data curation, Conceptualization. **NLj Brankovic:** Writing – original draft, Methodology, Investigation, Formal analysis, Data curation. **SP Galovic:** Validation, Supervision, Methodology, Formal analysis, Data curation. **KLj Djordjevic:** Methodology, Investigation, Formal analysis. **SM Aleksic:** Methodology, Investigation, Formal analysis. **DS Pantic:** Supervision, Methodology, Investigation, Formal analysis. **DD Markushev:** Writing – original draft, Validation, Supervision, Methodology, Investigation, Formal analysis, Data curation, Conceptualization.

Funding

This research was funded by the Ministry of Science, Technological Development and Innovation of the Republic of Serbia (Contract No. 451-03-47/2024-01/200017).

Declaration of competing interest

The authors declare that they have no known competing financial interests or personal relationships that could have appeared to influence the work reported in this paper.

Acknowledgement

The authors acknowledge funding provided by the Institute of Physics Belgrade, through a grant by the Ministry of Science, Technological Development and Innovations of the Republic of Serbia.

Appendix A:. Temperature field in irradiated solid sample

Detailed knowledge of the temperature field in the solid sample from Fig. 1 is essential in photoacoustics. Once this temperature distribution is known, the photoacoustic signal and its components can be derived, interconnecting the sound frequency response characteristics and the thermophysical characteristics of the irradiated sample as the sound source. In classical physics, the temperature field can be calculated using the heat conduction equation. Assuming 1D heat flow along the x-axis and the geometry presented in Fig. 1, the heat equation can be derived from Fourier's law and energy conservation law in the form

$$\frac{\partial T_s(x,t)}{\partial t} = D_t \frac{\partial^2 T_s(x,t)}{\partial x^2} \tag{A1}$$

where $T_s(x,t)$ is the temperature within the sample and on its surfaces, $D_t = k/\rho c$ is the coefficient of thermal diffusivity, k is the coefficient of thermal conductivity, ρ is the sample density and c is the specific heat capacity of the sample. The last equation is known as the 1D parabolic heat conduction equation − PHCE or, more general, 1D heat diffusion (time-dependent conduction) equation, a parabolic partial differential equation that describes heat distribution (in terms of temperature) in an investigated sample (considered as surface absorber) over time.

In photoacoustics, if the modulated light source illuminates a sample, it is reasonable to expect the sample's thermal state to change in the light source's "rhythm". This means that if the intensity of the modulated light, I, can be represented as $I = I_0\exp(j\omega t)$, where I_0 is the intensity amplitude, j is the imaginary unit, $\omega = 2\pi f$, f is the modulation frequency, and t is time, the temperature changes within the sample and on its surfaces can be defined with

$$T_s(x,t) = T_{amb} + T_s(x)\exp(j\omega t) \tag{A2}$$

where T_{amb} is an ambient (room) temperature, and $T_s(x)$ is the sample cross-section temperature at distance x (Fig. 1, the constant temperature is assumed on the sample cross-sections). Combining Eq. (A1) and Eq. (A2), two equations could be obtained: the static

$$\frac{\partial^2 T_s(x)}{\partial x^2} = 0 \tag{A3}$$

and dynamic one

$$\frac{\partial^2 T_s(x)}{\partial x^2} = \sigma^2 T_s(x) \tag{A4}$$

Here $\sigma = (1+j)(\omega/2D_t)^{1/2}$. Photoacoustics is only interested in dynamic, so called harmonic thermal-wave 1D equations because static ones do not contribute to sound generation. The solution of Eq. (A4) can be found in the form

$$T_s(x) = A_1 e^{\sigma x} + A_2 e^{-\sigma x} \tag{A5}$$

where A_1 and A_2 are the constants which can be found from the boundary conditions:

$$\text{a)}\ \ -k\frac{\partial T_s(x)}{\partial x}\bigg|_{x=0} = I_0 \text{ and b) } -k\frac{\partial T_s(x)}{\partial x}\bigg|_{x=l} = 0. \tag{A6}$$

Combining Eq.(A5) and Eq.(A6) leads to.

$A_1 = \frac{I_0}{2k\sigma}\frac{e^{-\sigma l}}{\sinh\sigma l}$, and $A_2 = \frac{I_0}{2k\sigma}\frac{e^{\sigma l}}{\sinh\sigma l}$. (A7).

Taking into account Eq.(A7), the temperature field within the solid sample and on its surfaces (Eq.(A5)), can be calculated in spatial (x) and frequency (f) domains using

$$T_s(x) = \frac{I_0}{k\sigma\sinh(\sigma l)}\cosh[\sigma(x-l)] \tag{A8}$$

Appendix B. . Analytical solution of the thermoelastic photoacoustic component

The analytical solution of the thermoelastic photoacoustic component allows one to explicitly show the analogy between the thermoelastic response and the low-pass *RC* filter. The Eq.(3) can be given in the analytical form as:

$$\delta p_{TE}(j\omega) = \frac{3\pi}{2}\frac{I_0\gamma_g p_0\alpha_T R_s^4}{V_0 k(\sigma l)^2}\left[\frac{\tanh(\sigma l/2)}{(\sigma l/2)} - 1\right] \tag{B1}$$

Applying the series expansion of $\tanh(\sigma l/2)/(\sigma l/2)$ in the most suitable form for our analysis

$$\frac{\tanh(\sigma l/2)}{(\sigma l/2)} = \frac{1}{(\sigma l/2)}\frac{\sinh(\sigma l/2)}{\cosh(\sigma l/2)} = \frac{1+\frac{(\sigma l/2)^2}{3!}+\frac{(\sigma l/2)^4}{5!}+\cdots}{1+\frac{(\sigma l/2)^2}{2!}+\frac{(\sigma l/2)^4}{4!}+\cdots} \tag{B2}$$

one can obtain $\left(\frac{\left(\frac{\sigma l}{2}\right)^2}{3!} \ll 1 \rightarrow m \ll \sqrt{6}\right)$

$$\delta p_{TE}(j\omega) \rightarrow \frac{3\pi}{2}\frac{I_0\gamma_g p_0\alpha_T R_s^4}{V_0 k}\left[\frac{1}{1+j\frac{f}{f_c}}\right] \tag{B3}$$

where f is the modulation frequency, f_c is the cut-off frequency defined with Eq.(8), and $m \rightarrow \sqrt{2}$. The last equation, Eq.(B3), can be understood as a $j\omega$-domain transfer function, presenting a mathematical description of the frequency-domain behaviour of a first-order low-pass filter. Knowing the transfer function, one can easily obtain the amplitude, $|\delta p_{TE}(j\omega)|$, and phase, $< (\delta p_{TE}(j\omega))$, of the thermoelastic response as:

$$|\delta p_{TE}(j\omega)| \rightarrow \frac{1}{\sqrt{1+\left(\frac{f}{f_c}\right)^2}} \tag{B4}$$

and

$$< (\delta p_{TE}(j\omega)) \rightarrow -\arctan\left(\frac{f}{f_c}\right) \tag{B5}$$

having the same form as the amplitudes (Eq.(6)) and phases (Eq.(7)) of the low-pass *RC* filter.

Data availability

Data will be made available on request.

References

[1] O. Ye, O.V. Pogorelov, E.M. Filatov, I.V.K. Rudenko, M.V. Dyakin, Characterization methods of heat flows in solids, Progress Phys. Met. 24 (2) (2023) 239–281, https://doi.org/10.15407/ufm.24.02.239.

[2] K. Hirata, T. Matsunaga, S. Singh, M. Matsunami, T. Takeuchi, Capacitor-type thin-film heat flow switching device, Jpn. J. Appl. Phys. 60 (12) (2021) 124004, https://doi.org/10.35848/1347-4065/ac3723/meta.

[3] T. Matsunaga, K. Hirata, S. Singh, M. Matsunami, T. Takeuchi, A field effect heat flow switching device, Mater. Trans. 62 (1) (2021) 16–19, https://doi.org/10.2320/matertrans.E-M2020844.

[4] Saurabh Singh, Bed Poudel, Amin Nozariasbmarz, Tsunehiro Takeuchi, Shashank Priya, Chapter 4: Constructive Approach Towards Design of High-Performance Thermoelectrics, Thermal Diodes, and Thermomagnetic Devices for Energy Generation Applications, Thoutam, L.R., Ajayan, J., & Nirmal, D. (Eds.). (2023). Energy Harvesting and Storage Devices: Sustainable Materials and Methods (1st ed.). CRC Press, DOI: 10.1201/9781003340539.

[5] R.R. Souza, V. Faustino, I.M. Gonçalves, A.S. Moita, M. Bañobre-López, R. Lima, A review of the advances and challenges in measuring the thermal conductivity of nanofluids, Nanomaterials 12 (15) (2022) 2526, https://doi.org/10.3390/nano12152526.

[6] A. Lunev, V. Zborovskii, T. Aliev, Complexity matters: Highly-accurate numerical models of coupled radiative–conductive heat transfer in a laser flash experiment, Int. J. Therm. Sci. 160 (2021) 106695, https://doi.org/10.1016/j.ijthermalsci.2020.106695.

[7] M. Yumnam, H. Gupta, D. Ghosh, J. Jaganathan, Inspection of concrete structures externally reinforced with FRP composites using active infrared thermography: A review, Constr. Build. Mater. 310 (2021) 125265, https://doi.org/10.1016/j.conbuildmat.2021.125265.

[8] S. Gholizadeh, A review of non-destructive testing methods of composite materials, Procedia Struct. Integrity 1 (2016) 50–57, https://doi.org/10.1016/j.prostr.2016.02.008.

[9] D. Korte, G. Carraro, F. Fresno, M. Franko, Thermal properties of surface-modified α- and ε-Fe2O3 photocatalysts determined by beam deflection spectroscopy, Int. J. Thermophys. 35 (2014) 2107–2114, https://doi.org/10.1007/s1076 5-014-1739-5.

[10] S. Manohar, D. Razansky, Photoacoustics: a historical review, Adv. Opt. Photon. 8 (4) (2016) 586–617, https://doi.org/10.1364/AOP.8.000586.

[11] S.E. Bialkowski, N.G.C. Astrath, M.A. Proskurnin, Photothermal spectroscopy methods for chemical analysis, 2nd ed., John Wiley, New York, 2019.

[12] M.I. Sarkar, M.M. Upadhyay, K. Kumar, Fabrication of a photoacoustic cell and thermal diffusivity measurement of graphene oxide using photoacoustic spectroscopy, Proc. Inst. Mech. Eng. C J. Mech. Eng. Sci. 238 (8) (2022) 3184–3189, https://doi.org/10.1177/09544062221135528.

[13] C. Glorieux, J. De Groote, J. Fivez, et al., Application of photoacoustic and photothermal techniques for heat conduction measurements in a free-standing chemical vapor-deposited diamond film, Int J Thermophys 14 (1993) 1201–1214, https://doi.org/10.1007/BF02431284.

[14] J. Ordonez-Miranda, Y. Guo, J.J. Alvarado-Gil, S. Volz, M. Nomura, T.-W. Diode, Phys. Rev. Appl 16 (2021) L041002, https://doi.org/10.1103/PhysRevApplied.16.L041002.

[15] A. Alkurdi, J. Lombard, F. Detcheverry, S. Merabia, Enhanced heat transfer with metal-dielectric core-shell nanoparticles, Phys. Rev. Appl 13 (2020) 034036, https://doi.org/10.1103/PhysRevApplied.13.034036.

[16] T.L. Bergman, A.S. Lavine, F.P. Incropera, D.P. DeWitt, Fundamentals of Heat and Mass Transfer, 7th ed., John Wiley, New York, 2011.

[17] G. Vera-Medina, E. Marín, A. Calderón, J.A.I. Díaz Góngora, G. Peña-Rodríguez, O. Delgado-Vasallo, A method for heat capacity measurement by photoacoustics, *Measurement*, **46** (3), (2013), pp: 1208–1211, DOI: 10.1016/j.measurement.2012.10.032.

[18] A. Bedoya, E. Marín, A.M. Mansanares, M.A. Zambrano-Arjona, I. Riech, A. Calderón, On the thermal characterization of solids by photoacoustic calorimetry: thermal diffusivity and linear thermal expansion coefficient, Thermochim Acta 614 (2015) 52–58, https://doi.org/10.1016/j.tca.2015.06.009.

[19] K.Lj. Djordjević, Z.Z. Stoisavljević, M.A. Dragaš, I. Stanimirović, Z. Stanimirović, E. Suljovrujic, S.P. Galović, Application of neural network to study of frequency range effect to photoacoustic measurement of thermoelastic properties of thin aluminum samples, *Measurement*, **236**, (2024), 115043, DOI: 10.1016/j.measurement.2024.115043.

[20] D.M. Todorović, M.D. Rabasović, D.D. Markushev, M. Sarajlić, Photoacoustic elastic bending in thin film-substrate system: Experimental determination of the thin film parameters, J. Appl. Phys. 116 (2014) 053506, https://doi.org/10.1063/1.4890346.

[21] D.D. Markushev, J. Ordonez-Miranda, M.D. Rabasovic, M. Chirtoc, D. M. Todorovic, S.E. Bialkowski, D. Korte, M. Franko, Thermal and elastic characterization of glassy carbon thin films by photoacoustic measurements, The European Phys. J. plus 132 (33) (2017) 1–9, https://doi.org/10.1140/epjp/i2017-11307-2.

[22] A. Rosencwaig, A. Gersho, Theory of the photoacoustic effect with solids, J. Appl. Phys. 47 (1976) 64–69, https://doi.org/10.1063/1.322296.

[23] F. McDonald, G. Wetsel, Generalized theory of the photoacoustic effect, J. Appl. Phys. 49 (1978) 2313, https://doi.org/10.1063/1.325116.

[24] E. Gutiérrez-Reyes, C. García-Segundo, A. García-Valenzuela, Roberto Ortega, Christian Buj and Frank Filbir, Heat transport considerations in the mathematical analysis of the photoacoustic and photothermal effects,, J. Phys. Commun. 3 (2019) 085007, https://doi.org/10.1088/2399-6528/ab376d.

[25] A.A. Obukhov, T.A. Novikova, V.G. Lebedev, et al., Determination of temperature dependence of thermophysical parameters in solids: Numerical solution of the problem, Tech. Phys. 65 (2020) 1922–1929, https://doi.org/10.1134/S106378422012018X.

[26] G. D'Alessandro, M. Potenza, S. Corasaniti, S. Sfarra, P. Coppa, G. Bovesecchi, F. de Monte, Modeling and measuring thermodynamic and transport thermophysical properties: a review, Energies 15 (23) (2022), https://doi.org/10.3390/en15238807.

[27] M. Isaiev, G. Mussabek, P. Lishchuk, K. Dubyk, N. Zhylkybayeva, G. Yar-Mukhamedova, D. Lacroix, V. Lysenko, Application of the Photoacoustic Approach in the Characterization of Nanostructured Materials, *Nanomaterials*, **12**, (2022),708. DOI: 10.3390/nano12040708.

[28] M.V. Nesic, M.N. Popovic, S.P. Galovic, K. Lj, M.I. Djordjevic, V.V. Jordovic-Pavlovic, Miletic and D. D. Markushev,, Estimation of linear expansion coefficient and thermal diffusivity by photoacoustic numerical self-consistent procedure, *J. Appl. Phys.* 131 (2022) 105104, https://doi.org/10.1063/5.0075979.

[29] K.Lj.Djordjevic, S.P. Galović, M.N. Popović, M.V. Nešić, I.P. Stanimirović, Z.I. Stanimirović, D.D. Markushev,, Use neural network in photoacoustic measurement of thermoelastic properties of aluminum foil, Measurement 119 (2022), https://doi.org/10.1016/j.measurement.2022.111537.

[30] A. Mandelis, Diffusion-wave fields, Springer, New York, 2001.

[31] N. Stanojevic, D.K. Markushev, S.M. Aleksić, D.S. Pantić, S.P. Galović, D. D. Markushev, J. Ordonez-Miranda, Thermal characterization of n-type silicon based on an electro-acoustic analogy, J. Appl. Phys. 133 (2023), https://doi.org/10.1063/5.0152495.

[32] D.K. Markushev, N. Branković, S.M. Aleksić, D.S. Pantić, S.P. Galović, D. D. Markushev, J. Ordonez-Miranda, The influence of excess free carriers as heat carriers on the n-type silicon thermoelastic photoacoustic responses explained by electro-acoustic analogies, Int. J. Thermophys. 45 (2024) 107, https://doi.org/10.1007/s10765-024-03406-3.

[33] S. Galovic, Z. Soskic, M. Popovic, Analysis of photothermal response of thin solid films by analogy with passive linear electric networks, Therm. Sci. 13 (4) (2009) 129–142, https://doi.org/10.2298/TSCI0904129G.

[34] E. Marín, Characteristic dimensions for heat transfer, *Latin-American Journal of Physics Education*, **4** (1), pp. 56-60, (2010), ISSN 1870-9095, http://www.lajpe.org/index_jan10.html.

[35] David R. Lide (ed), CRC Handbook of Chemistry and Physics, 84th Edition. CRC Press. Boca Raton, Florida, 2003; Section 12, Properties of Solids.
[36] D.D. Markushev, J. Ordonez-Miranda, M.D. Rabasović, S. Galović, D.M. Todorović, S.E. Bialkowski, Effect of the absorption coefficient of aluminium plates on their thermoelastic bending in photoacoustic experiments, J. Appl. Phys. 117 (2015) 245309, https://doi.org/10.1063/1.4922718.
[37] D.D. Markushev, M.D. Rabasović, D.M. Todorović, S. Galović, S.E. Bialkowski, Photoacoustic signal and noise analysis for Si thin plate: Signal correction in frequency domain, Rev. Sci. Instrum. 86 (2015) 035110, https://doi.org/10.1063/1.4914894.
[38] J.R. Davis, Alloying: Understanding the Basics, Copyright © 2001 ASM International®, p351-416, ISBN: 978-0-87170-744-4, DOI:10.1361/autb2001p351.
[39] M. Tisza, I. Czinege, Comparative study of the application of steels and aluminium in lightweight production of automotive parts, Int. J. Lightweight Mater. Manufacture 1 (4) (2018) 229–238, https://doi.org/10.1016/j.ijlmm.2018.09.001.
[40] Mohamed Toumi Nasri, Fethi Abbassi, Tasnime Hamdeni, Murat Demiral, Mohamed Ali Rezgui, Mahfoudh Ayadi, Novel approach for sheet metal constitutive parameters identification based on shape index and multiple regression, Results in Engineering, **22**, 2024, 102267, ISSN 2590-1230, DOI: 10.1016/j.rineng.2024.102267.
[41] Fayaz Ahmad Mir, Noor Zaman Khan, Lubaid Nisar, Haseeb A. khan, Salman H. Alrokayan, Analyzing microstructural evolution and wear behavior of friction stir welded dissimilar joints of SS304 and 2024-T3 Al alloy, *Materials Letters*, **366**, 2024, 136493, ISSN 0167-577X, DOI: 10.1016/j.matlet.2024.136493.
[42] V.P. Carey, G. Chen, C. Grigoropoulos, M. Kaviany, A. Majumdar, A review of heat transfer physics, Nanoscale Microscale Thermophys. Eng. 12 (1) (2008) 1–60, https://doi.org/10.1080/15567260801917520.
[43] Lizhu Guan, Xuemin Zhao, Zengren Ji, Mengyuan Jiang, Yongai Cui, Ling Weng, Xuan Wang & Junwang Liu, Preparation of 3D BN-BT/PVDF skeleton structure composites for high thermal conductivity and energy storage. Polymer Testing, **125**, (2023), pages 108126.
[44] Chih-Chun Chang & Chih-Che Chueh, Effective conductivity of composite materials made of randomly packed densified core-shell particles, *Powder Technology*, **428**, (2023), pages 118840.
[45] Giorgia Fugallo and Luciano Colombo, Calculating lattice thermal conductivity: a synopsis, 2018, *Physica Scripta*, **93**, 043002, https://iopscience.iop.org/article/10.1088/1402-4896/aaa6f3.
[46] Narayan Gaonkar and R G Vaidya, Electronic thermal conductivity of few-layer black phosphorus, 2023, *Physica Scripta*, **98**, 125990, https://dx.doi.org/10.1088/1402-4896/ad09a4.
[47] G. Wang, Y. Huang, M. Gao, et al., Micromechanics of thermal conductive composites: review, developments and applications, Acta Mech. Solida Sin. 37 (2024) 215–237, https://doi.org/10.1007/s10338-024-00469-5.
[48] M. Grilli, D. Ristau, M. Dieckmann, U. Willamowski, Thermal conductivity of e-beam coatings, Appl. Phys. A 71 (2000) 71–76, https://doi.org/10.1007/PL00021094.

Радови Драгана К. Маркушев

Часописи

М21

International Journal of Thermophysics (2026) 47:24
https://doi.org/10.1007/s10765-025-03695-2

Role of Excess Free Carriers in the Plasma–Elastic Photoacoustic Response of Semiconductors

D. K. Markushev[1] · S. M. Kovacevic[1] · J. Ordonez-Miranda[2] · D. D. Markushev[1]

Received: 1 November 2025 / Accepted: 11 December 2025

Abstract
We numerically and experimentally investigate the impact of photogenerated minority excess carriers on the plasma–elastic and total photoacoustic response of semiconductors. The frequency domain behavior of photoacoustic signals is examined as a function of the surface conditions, optical absorbance, and material thickness. For a visible-light excitation, distinct peak-like features in the plasma–elastic amplitude emerge at high modulation frequencies and for thin enough samples. These trends are attributed to carrier density asymmetries between the illuminated and non-illuminated surfaces. These findings highlight the key role of carrier dynamics in shaping plasma–elastic coupling to optimize and interpret photoacoustic measurements in semiconductor characterization.

Keywords Absorption coefficient · Carrier density · Photoacoustics · Photogenerated carriers · Plasma–elastic response · Semiconductors

1 Introduction

One of the most widely used theoretical models in the photoacoustics of solids is the composite piston model [1–7]. This model, based on relatively simple mathematical formulations, describes the generation of the total photoacoustic signal from a regularly illuminated sample, which results from the combined actions of thermal and mechanical pistons. The thermal piston is created by the periodic expansion and contraction of a thin layer of gas on the non-illuminated side of the sample, while the mechanical piston arises from the periodic bending of the sample due to the different expansion between its illuminated and non-illuminated surfaces. The interaction between these two pistons determines the overall photoacoustic response, which

✉ D. K. Markushev
dragana.markusev@ipb.ac.rs

[1] Institute of Physics, University of Belgrade, Pregrevica 118, Zemun, 11080 Belgrade, Serbia

[2] Sorbonne Université, CNRS, Institut des Nanosciences de Paris, INSP, 75005 Paris, France

Published online: 23 December 2025

is influenced by the thermal and mechanical properties of the sample. Because of this sensitivity, the composite piston model provides a reliable theoretical basis for the precise thermal characterization of materials [8–14].

Semiconductors, when illuminated, especially within the visible spectrum, exhibit unique behavior compared to other materials due to the generation of excess free carriers, including both majority and minority electrons and holes. This illumination primarily affects the density and dynamics of minority carriers, whose transport and recombination govern the overall behavior of the excess carriers in the semiconductor. These photogenerated excess free carriers serve a dual purpose in photoacoustics: first, as heat carriers, they modify the temperature distribution within the semiconductor's volume and surfaces [15–17]. Second, as charge carriers, they generate additional mechanical stress through interactions between electrons and the lattice [18–21]. The resulting asymmetry in carrier densities between the illuminated and non-illuminated sides produces differential stress, leading to additional periodic bending of the sample. This effect adds a purely electronic component to the mechanical piston. Consequently, excess free carriers, acting as both heat and charge carriers, influence the material's photoacoustic response through interconnected modifications of both the thermal and mechanical pistons [22–26].

In our previous work [27], we provided a detailed analysis of how excess free carriers, acting as heat carriers, influence the thermoelastic photoacoustic response of *n*-type silicon in the frequency domain. Temperature variations highlighted the significant role of surface recombination, while amplitude changes appeared as peak-like features that indicate strong carrier effects. These effects are most pronounced in plasma-thin samples with a passivated illuminated side and a non-passivated rear surface. More recently, we demonstrated that the plasma–elastic component in thin semiconductor samples significantly influences the time-domain photoacoustic response [28–30]. A model was developed to account for surface temperature variations due to surface charge-carrier recombination, revealing the dependence of the temperature response on surface recombination velocity and electronic parameters for both plasma-opaque and plasma-transparent samples.

In this article, we extend our previous analyses by examining the influence of excess free carriers as charge carriers on the purely electronic photoacoustic frequency response of solid *n*-type silicon. By analyzing the formation of an additional part of a mechanical piston, the plasma–elastic component of the photoacoustic signal, we investigate the relationship between carrier density variations on the illuminated and non-illuminated sides and their effects on amplitude behavior in the frequency domain. Special attention is given to elucidating how changes in surface conditions, such as polishing or passivation, govern the emergence and disappearance of peak-like amplitudes associated with plasma–elastic coupling.

2 Theoretical Background

The generation of a photoacoustic signal in a material arises from the non-radiative de-excitation processes that follow the absorption of energy from modulated light. These localized non-radiative transitions initiate transport phenomena that

give rise to thermal, elastic, and electronic effects responsible for the acoustic response of the illuminated material. Consequently, the resulting acoustic signal encodes information about the material's optical, thermal, elastic, and electronic properties.

The first theoretical description of photoacoustic signals in solids was formulated through the thermal piston model, which explains the phenomenon as periodic expansion and contraction of the gas layer adjacent to the sample (Fig. 1(a)) [1]. This gas layer acts as a piston relative to the surrounding medium, inducing pressure fluctuations that generate sound waves. Subsequently, this model was extended to include a mechanical piston that models the sound generation of the mechanical vibrations of the sample's surface, caused by bending (Fig. 1(b)) [2]. Initially, the mechanical piston was attributed solely to thermoelastic effects within the solid [31]. However, subsequent studies revealed that in semiconductors, an additional contribution arises from bending induced by electron–lattice interactions [22]. Together, these thermal and mechanical pistons form the basis of the composite piston model, which provides a comprehensive framework for describing photoacoustic signal generation in solids.

Relying on the composite piston model and Fig. 1, the total photoacoustic signal $\delta p_{tot}(j\omega)$ is usually written as [2, 23]:

$$\delta p_{tot}(j\omega) = \delta p_{tp}(j\omega) + \delta p_{mp}(j\omega), \tag{1}$$

where $\delta p_{tp}(j\omega)$ is the signal component created by the thermal piston, so-called thermodiffusion component, $\delta p_{TD}(j\omega)$, and $\delta p_{mp}(j\omega)$ is the signal component created by the mechanical piston, recognized as the thermoelastic component, $\delta p_{TE}(j\omega)$. Both are usually represented as [1, 2, 23]:

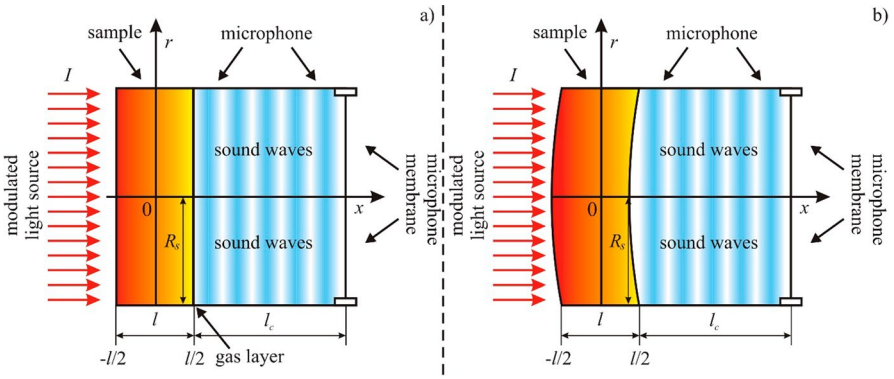

Fig. 1 Scheme of our composite piston model made up of (a) thermal and (b) mechanical pistons generating the photoacoustic signal within an open-cell experimental set-up. The sample of thickness l and radius R_s, is mounted on the top of the microphone which acts as both a sound detector and an air photoacoustic cell of length l_c

$$\delta p_{TD}(j\omega) = \frac{\gamma_g p_0 \sqrt{D_g}}{l_c T_0 \sqrt{j\omega}} T_\beta(l/2), \tag{2}$$

$$\delta p_{TE}(j\omega) = 3\pi \frac{\gamma_g p_0 \alpha_T R_s^4}{l^3 V_0} M, \tag{3}$$

where j is an imaginary unit, γ_g is the adiabatic ratio of the gas (air) in the photoacoustic cell, p_0, V_0 and T_0 are the respective cell gas pressure, volume and temperature, l is the sample thickness, D_g is the air thermal diffusivity, $T_\beta(l/2)$ is the temperature of the sample at non-illuminated side, α_T is the sample coefficient of linear thermal expansion, R_s is the sample radius, M is temperature moment defined as [13, 23, 31]:

$$M = \int_{-l/2}^{l/2} x T_\beta(x) \mathrm{d}x, \tag{4}$$

and $T_\beta(x)$ is the 1D temperature distribution in the sample along the heat flow axis (x-axis), acting like the volume absorber ("Appendix 1").

Analyzing Eqs. 2 and 3, it is evident that periodic variations of the sample temperature distribution $T_\beta(x)$ generate photoacoustic signal components. The $\delta p_{TD}(j\omega)$ component arises from the periodic temperature change $T_\beta(l/2)$ on the non-illuminated side of the sample, while the $\delta p_{TE}(j\omega)$ component results from the periodic temperature differences ΔT_β between the illuminated $T_\beta(-l/2)$ and non-illuminated $T_\beta(l/2)$ sample sides ($M \sim \Delta T_\beta = \left|T_\beta(-l/2)\right| - \left|T_\beta(l/2)\right|$). These two components can be used to thermally characterize any opaque material in the form of a thin elastic plate, assuming its homogeneous and isotropic optical, thermal and elastic properties.

In the case of semiconductors, the temperature distribution $T_s(x)$ ("Appendix 1") is not as simple as in the previous case, but is made up of several components, taking into account, in addition to the direct conversion of absorbed light energy into heat, $T_{therm}(x)$ ($T_{therm}(x) = T_\beta(x)$), the influence of excess carriers as heat carriers that change the thermal image of the sample, both on the surface, $T_{sr}(x)$, and in the bulk, $T_{br}(x)$. That is why $T_s(x)$ is usually represented as [22, 23]:

$$T_s(x) = T_{\mathrm{therm}}(x) + T_{\mathrm{sr}}(x) + T_{\mathrm{br}}(x). \tag{5}$$

Excess carrier diffusion and recombination processes are explained by the 1D diffusion equation along the x-axes (Fig. 1) [22, 23, 27]:

$$\frac{\partial \delta n_p(x,t)}{\partial t} = D_p \frac{\partial^2 \delta n_p(x,t)}{\partial x^2} + \frac{\beta I}{\varepsilon} e^{-\beta x} - \frac{\delta n_p(x,t)}{\tau_p}. \tag{6}$$

Here, I is the excitation light intensity, $\delta n_p(x,t)$ is the minority carriers (holes) density, D_p is holes diffusion coefficient and τ_p is holes lifetime, β is the absorption coefficient of silicon, and ε is the excitation light photon energy.

Implying modulated light excitation $I = I_0\left(1 + e^{j\omega t}\right)$, where I_0 is an excitation light intensity amplitude, and assuming periodical density changes $\delta n_p(x,t) = \delta n_p(x)\left(1 + e^{j\omega t}\right)$, Eq. 6 can be simplified and written in the form [22, 23, 27]:

$$\frac{d^2\delta n_p(x)}{dx^2} - \frac{\delta n_p(x)}{L_\omega^2} = -\frac{\beta I_0}{\varepsilon D_p} e^{-\beta x}, \tag{7}$$

where $L_\omega = L_p/\sqrt{(1 + j\omega\tau)}$, and $L_p = \sqrt{D_p\tau_p}$ is the minority excess carrier (holes) diffusion length.

The solution of Eq. 7 is given by [22, 23, 27]:

$$\delta n_p(x) = A_+ e^{(x+l/2)/L_\omega} + A_- e^{-(x+l/2)/L_\omega} - Ae^{-\beta(x+l/2)}, \tag{8}$$

where $A = \frac{I_0\beta}{\varepsilon D_p}\frac{1}{\beta^2 - L_\omega^{-2}}$, and the integration constants $A_\pm$ are defined by:

$$A_\pm = A\frac{\left(v_\beta + s_1\right)\left(v_D \pm s_2\right)e^{\mp l/L_\omega} - \left(v_D + s_1\right)\left(v_\beta - s_2\right)e^{-\beta l}}{\left(v_D + s_1\right)\left(v_D + s_2\right)e^{l/L_\omega} - \left(v_D - s_1\right)\left(v_D - s_2\right)e^{-l/L_\omega}}, \tag{9}$$

depending on absorbance, βl, the surface recombination velocities at the illuminated front, s_1, and non-illuminated back, s_2, sample surfaces, and the relative values of the characteristic diffusion velocities $v_D = D_p/L_\omega$ and $v_\beta = \beta D_p\left(v_\beta > v_D\right)$.

In earlier articles, we stated that the excess free carriers behave as a heat carriers, changing the temperature of the semiconductor sample *via* $T_{sr}(x)$ and $T_{br}(x)$, more precisely *via* the parameters $\delta n_p(x)$, τ_p, s_1 and s_2. This distribution of temperature in relation to other materials also changes the components of the photoacoustic signal. The thermal piston gives a thermodiffusion component that has the same form as in Eq. 2, but instead of $T_\beta(l/2)$ now stands $T_s(l/2)$ [1, 23]:

$$\delta p_{TD}(j\omega) = \frac{\gamma_g p_0\sqrt{D_g}}{l_c T_0\sqrt{j\omega}} T_s(l/2). \tag{10}$$

In the case of mechanical piston, the situation is a bit more complicated. The bending of the semiconductor sample, as the main characteristic of the mechanical piston, can occur for two reasons: (a) unequal temperatures, and (b) unequal carrier densities on the illuminated and non-illuminated side of the sample. Therefore, the mechanical piston in semiconductors produces two components of the photoacoustic signal, the thermoelastic $\delta p_{TE}(j\omega)$ and the plasma–elastic $\delta p_{PE}(j\omega)$ one, which are usually written in the form [22, 23, 27–30]:

$$\delta p_{TE}(j\omega) = 3\pi\frac{\gamma_g p_0\alpha_T R_s^4}{l^3 V_0} M_T, \tag{11}$$

and

$$\delta p_{PE}(j\omega) = 3\pi \frac{\gamma_g p_0 d_e R_s^4}{l^3 V_0} M_n, \tag{12}$$

where d_e is the coefficient of electronic deformation, and temperature $\left(M_T\right)$ and electronic-excess free carrier $\left(M_n\right)$ moments, respectively, are given as [22, 23, 27]

$$M_T = \int_{-l/2}^{l/2} x T_s(x) \mathrm{d}x, \text{ and } M_n = \int_{-l/2}^{l/2} x \delta n_p(x) \mathrm{d}x. \tag{13}$$

It should be noted here that

$$M_T \sim \Delta T_s = \left|T_s(-l/2)\right| - \left|T_s(l/2)\right|, \tag{14}$$

and

$$M_n \sim \Delta \delta n_p = \left|\delta n_p(-l/2)\right| - \left|\delta n_p(l/2)\right|. \tag{15}$$

Equations 11 and 12 demonstrate that the mechanical piston plays multiple roles in the analysis of semiconductors through its generation of $\delta p_{TE}(j\omega)$ and $\delta p_{PE}(j\omega)$ components. First, it allows for the investigation of how excess free carriers function as both heat $[\delta p_{TE}(j\omega)]$ and charge $[\delta p_{PE}(j\omega)]$ carriers. Second, it contributes to the formation of the total photoacoustic signal $[\delta p_{tot}(j\omega)]$ emitted by the periodically illuminated sample, which is recorded by the microphone. This highlights the piston's crucial role in the accurate and reliable thermal, optical, mechanical, and electronic characterization of semiconductors.

3 Results and Discussion

To better understand the results and analysis presented in this chapter, several key points should be considered. The *n*-type silicon was chosen as a typical representative of semiconductors because it proved to be highly suitable for photoacoustic analysis for several reasons, which we highlight: (a) silicon has excellent elastic properties and is an ideal material for elastic bending analysis; (b) silicon allows for reliable validation of the composite piston theory within the experimental modulation frequency f range of 20 Hz to 20 kHz; (c) such validation enables accurate extrapolation of theoretical predictions over a much wider frequency range from 1 MHz to 10 MHz, in the so-called domain of the diffusion character of heat flow and free carrier movement. The numerical simulations and experimental results discussed in this article are based on the photoacoustic transmission setup of an open-cell, which utilizes the microphone body as a minimal photoacoustic cell. This setup supports the standard solid sample–gas (air)–microphone arrangement, belonging to the typical, so-called, gas–microphone signal detection configuration. It should also be noted that silicon samples are assumed to have standard thermal and electronic parameters presented in Table 1 [27]. For simplicity, all samples are considered

as isotropic circular discs with thicknesses l ranging from 10 μm to 1000 μm, and radius $R_s = 3$mm. This thickness/radius ratio satisfies the condition that each sample can be analyzed as an elastic thin plate $\left(l \ll 2R_s\right)$, whose bending behavior in frequency domain is described by Eqs. 15 and 16.

When discussing the state of illuminated front and non-illuminated back surfaces of a semiconductor sample, it is important to recognize that surfaces are places where the crystal lattice is significantly disrupted. Recombination processes are often enhanced by such defects (dangling bonds) or by the presence of impurities. As a result, semiconductor surfaces can be seen as areas with particularly high recombination rates. The surface recombination velocity, s, is a key parameter that describes the recombination occurring at the surfaces and is closely related to the dynamics of minority carriers within the sample. The value of s can be reduced by minimizing the number of dangling bonds through a process known as surface passivation. The surface passivation process is most often achieved mechanically (our case, through polishing), chemically (*via* hydrogen passivation), or thermally (through high-temperature oxidation). Passivated surfaces exhibit a significantly lower number of broken bonds, resulting in s-values that approach zero (2 $\mathrm{m{\cdot}s^{-1}}$ in our case). In contrast, non-passivated surfaces are marked by a high density of broken bonds, leading to s-values greater than 10 $\mathrm{m{\cdot}s^{-1}}$ (24 $\mathrm{m{\cdot}s^{-1}}$ in our case).

Analyzing the thickness of semiconductor samples, we should also mention the characteristic thickness defined by the diffusion length of minority carriers, L_p (see Table 1) [23]. In our case, it is $L_p = \sqrt{D_p \tau_p} \approx 85$ μm, and it was previously used in analyzing the response of the amplitude of the thermoelastic component as a boundary between the so-called plasma-thin ($l < L_p$, visible peak-like structures) and plasma-thick ($l > L_p$, no peak-like structures) samples [32]. In the context of analyzing the response of the amplitude of the plasma–elastic component, L_p was applied as the boundary for defining the so-called opaque ($l \gg L_p$, no peak-like structures) and transparent ($l < L_p$, visible peak-like structures) semiconductor samples [28], which we confirm in this article.

Due to the nature of their origin, it is understood that the total photoacoustic signal [$\delta p_{tot}(j\omega)$, Eq. 1] and its components [$\delta p_{TD}(j\omega)$, $\delta p_{TE}(j\omega)$, $\delta p_{PE}(j\omega)$, Eqs. 14–16] can be represented as complex numbers, usually given in the form $\delta p(j\omega) = Ae^{j\varphi}$. Their analysis is reduced to the study of the behavior of their amplitudes, $A = |\delta p(j\omega)|$, and phases, $\varphi =< (\delta p(j\omega))$, in the modulation frequency $f = \omega/2\pi$ domain. In this paper, for the sake of simplicity, we will focus only on the analysis of amplitudes.

3.1 Photoacoustic Signal Response *vs.* Conditions at Sample Surfaces

When analyzing the response of the photoacoustic signal in the frequency domain, it is important to acknowledge the limitations of the experiment. Reliable operation occurs within the modulation frequency range of 20 Hz to 20 kHz (Fig. 2, vertical dashed), which is where most microphones used in open-cell (minimal-volume cells) configurations operate effectively. We have previously noted that, theoretically, the composite piston theory can be applied to modulation frequencies ranging

Table 1 Si *n*-type sample parameters ($T_0 = 300$ K) [27]

Density	$\rho = 2.33 \times 10^3$ kg·m^{-3}	Specific heat	$c = 715$ J·kg^{-1}·K^{-1}
Thermal conductivity	$k = 150$ W·m^{-1}·K^{-1}	Coefficient of thermal diffusivity	$D_T = 9.0 \times 10^{-5}$ m^2·s^{-1}
Coefficient of linear thermal expansion	$\alpha_T = 2.60 \times 10^{-6}$ K^{-1}	Coefficient of optical absorption	$\beta = 0.258$ μm^{-1}
Excitation energy	$\varepsilon = 1.88$ eV	Energy gap	$\varepsilon_g = 1.12$ eV
Minority carrier lifetime	$\tau_p = 6$ μs	Coefficient of minority carrier diffusion	$D_p = 12 \times 10^{-4}$ m^2·s^{-1}
Coefficient of electronic deformation	$d_e = -9 \times 10^{-31}$ m^3	Minority excess carrier diffusion length	$L_p = 84.85$ mm

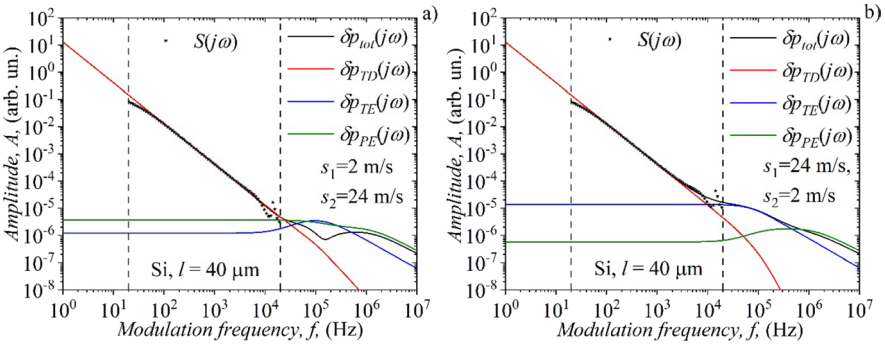

Fig. 2 The amplitudes A of the experimental data [$S(j\omega)$, asterisks], total photoacoustic signal [$\delta p_{tot}(j\omega)$, Eq. 1, black] and its components [$\delta p_{TD}(j\omega)$ red, $\delta p_{TE}(j\omega)$ blue, $\delta p_{PE}(j\omega)$ green, Eqs. 14–16] as a function of the modulation frequency (f), in the case (a) $s_1/s_2 < 1$ [27] and (b) $s_1/s_2 > 1$, for a 40-μm-thick n-type silicon sample (Color figure online)

from 1 Hz to 10 MHz, and its experimental validation can be successfully conducted within the microphone's operational frequency range. In earlier work [27, 33], we outlined the main steps for obtaining experimental data and validating the total photoacoustic signal for a 40 mm thick n-type silicon sample, with the illuminated side being passivated [Fig. 2(a)]. In this current work, we present the same procedure for the same sample, but with only the non-passivated side illuminated (see "Appendix 2"). The results of this procedure (the total signal) and the comprehensive application of composite piston theory (which accounts for all components of the total signal) are illustrated in Fig. 2(b).

Figure 2 illustrates the amplitudes A of the total photoacoustic signal [$\delta p_{tot}(j\omega)$, Eq. 1] and its components [$\delta p_{TD}(j\omega)$, $\delta p_{TE}(j\omega)$, $\delta p_{PE}(j\omega)$, Eqs. 10–12] as a function of the modulation frequency (f) for a 40 mm plasma-thin n-type silicon sample, obtained after careful fitting of the measuring points and removal of instrumental deviations. Sample is examined in two cases: (a) the illuminated side is passivated ($s_1 = 2$ m·s^{-1}) and the non-illuminated side is not ($s_2 = 24$ m·s^{-1}), and (b) the illuminated side is non-passivated ($s_1 = 24$ m·s^{-1}), and the non-illuminated side is passivated ($s_2 = 2$ m·s^{-1}).

The differences in responses and the mutual relationship between $\delta p_{TE}(j\omega)$ and $\delta p_{PE}(j\omega)$ in these two cases are immediately noticeable. In case (a), a change in the behavior of $\delta p_{TE}(j\omega)$ is clearly observed, displaying a peak-like structure at higher frequencies. In contrast, $\delta p_{PE}(j\omega)$ shows the typical response of a mechanical piston, characterized by a constant amplitude response at low frequencies followed by a sharp drop in values at higher ones. In case (b), $\delta p_{TE}(j\omega)$ assumes the standard shape of the mechanical piston response, while $\delta p_{PE}(j\omega)$ exhibits a peak-like structure.

The total signal, in case a) and in the range of experimental frequencies (20 Hz to 20 kHz), is completely defined by the $\delta p_{TD}(j\omega)$ component [$\delta p_{tot}(j\omega) \approx \delta p_{tp}(j\omega)$], because $\delta p_{TE}(j\omega)$ suffers a sudden drop at $f < 20$kHz due to the influence of photogenerated carriers as heat carriers. The $\delta p_{PE}(j\omega)$ component affects $\delta p_{tot}(j\omega)$ at the ends of the experimental frequency range (~20 kHz). This fact indicates the

possibility that, in the case of plasma-thin samples, both the electronic parameters of the sample [d_e, $\delta n_p(x)$] and the direct influence of $\delta p_{PE}(j\omega)$ on the total signal, $\delta p_{tot}(j\omega)$, can be measured, which, in many cases, especially for plasma-thick samples, was not possible due to the relatively low values of the $\delta p_{PE}(j\omega)$ amplitude compared to the $\delta p_{TD}(j\omega)$ and $\delta p_{TE}(j\omega)$. In case (b), the total signal $\delta p_{tot}(j\omega)$ is defined by the $\delta p_{TD}(j\omega)$ component in most of the experimental frequency range, but already in the area $f > 1$kHz it suffers a strong influence of the $\delta p_{TE}(j\omega)$ component.

From the results shown in Fig. 2, it is clear that $\delta p_{PE}(j\omega)$ influence on $\delta p_{tot}(j\omega)$ must be taken into account if $s_1/s_2 < 1$, because only in this way the high-quality thermal and electronic characterization of semiconductors can be performed, which leading to reliable and precisely determined sample parameters.

3.2 Plasma–Elastic Component Response *vs.* Sample Thickness

In previous articles, we detailed the reasons behind the peak-like behavior of the $\delta p_{TE}(j\omega)$ component and the role of photogenerated carriers at sample surfaces as heat carriers. Now, let's examine the same behavior of $|\delta p_{PE}(j\omega)|$ in two scenarios (Fig. 3): (a) $s_1/s_2 < 1$, and (b) $s_1/s_2 > 1$, for different sample thicknesses ranging from 10 mm to 1000 mm. If we simulate $|\delta p_{PE}(j\omega)|$'s behavior under the same conditions and normalized it to unity, we can clearly see that in case (a), $|\delta p_{PE}(j\omega)|$ maintains a standard response across all thicknesses. In case (b), the standard response is evident for thicknesses greater than 400 mm, while for thinner samples, we observe the development of a peak-like structure. This peak-like structure reaches its maximum at approximately 21 mm, and with a further reduction in thickness, its prominence decreases.

The behavior of $|\delta p_{PE}(j\omega)|$ in case (b) is consistent with the results of our previous analysis in the time-domain where we define plasma-opaque and plasma-transparent semiconductor samples: a $|\delta p_{PE}(j\omega)|$ response without peak-like structures

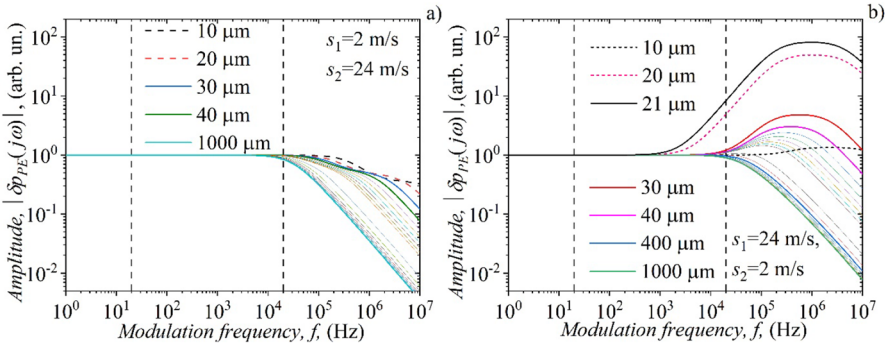

Fig. 3 Normalized plasma–elastic amplitude $|\delta p_{PE}(j\omega)|$ response in the case (a) ($s_1/s_2 < 1$) and (b) ($s_1/s_2 > 1$), as a function of the modulation frequency f. Calculations were done n-type Si sample with thicknesses 10 μm $\le l \le$ 1000 μm. Thicker lines represent sample thicknesses relevant to this study, while thinner lines correspond to thicknesses within the specified range

can be expected in the case of plasma-opaque samples ($l \gg L_p \approx 85$ μm). In contrast, peak-like structures are strongly expressed in the case of plasma-transparent samples ($l < L \approx 85$ μm).

3.3 Plasma–Elastic Component Response *vs.* Excess Free Carrier Density

As previously established, the formation of the peak-like structure in the amplitude of the thermoelastic component is related to the relationship and difference in temperatures on the illuminated and non-illuminated sides of the sample (Eq. 14, $M_T \sim \Delta T_s$). Similarly, one can assume that the formation of a peak-like structure in the $\delta p_{PE}(j\omega)$ component amplitude is connected to the relationship and difference in photogenerated carrier densities on those same sides (Eq. 15, $M_n \sim \Delta\delta n_p$). Based on the results shown in the previous section, the analysis of $\delta n_p(x)$ in the frequency domain will be divided into two groups: (1) for sample thicknesses $l \geq 400$ μm (Fig. 4) with representative thicknesses of 400 μm, 500 μm, and 1000 μm, and (2) for sample thicknesses $l < 400$ μm (Fig. 5) with representative thicknesses of 10 μm, 20 μm, 21 μm, 30 μm, and 40 μm.

The results presented in the first group (Fig. 4) show that the amplitude values of $\left|\delta n_p(-l/2)\right|$ (solid lines) are approximately the same for all shown sample thicknesses, while the amplitude values of $\left|\delta n_p(l/2)\right|$ (dashed lines) are significantly lower, and gets lower as the thickness of the sample increases. It means that $\Delta\delta n_p > 0$ for all thicknesses, all frequencies, and all cases (a) ($s_1/s_2 < 1$) and (b) ($s_1/s_2 > 1$), assuring standard plasma–elastic amplitude response without peak-like structures.

The results shown in the second group (Fig. 5) show that differences between $\left|\delta n_p(-l/2)\right|$ (solid lines) and $\left|\delta n_p(l/2)\right|$ (dashed lines) are getting smaller as we move towards thinner samples. In case (a), the values of $\Delta\delta n_p$ are in a wider range, and $\Delta\delta n_p > 0$, up to the thinnest samples. In case (b), the values of $\Delta\delta n_p$

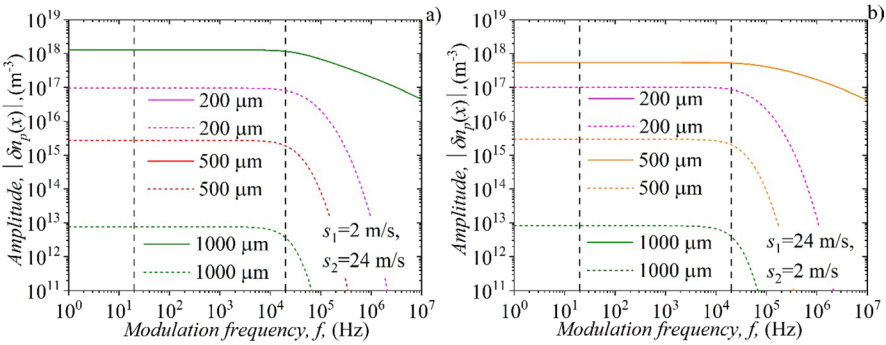

Fig. 4 The amplitude values of $\left|\delta n_p(-l/2)\right|$ (solid lines) and $\left|\delta n_p(l/2)\right|$ (dashed lines) in the case of (a) ($s_1/s_2 < 1$) and (b) ($s_1/s_2 > 1$), as a function of the modulation frequency f. Calculations were done for a Si n-type sample with thicknesses 400 μm ≤ l ≤ 1000 μm

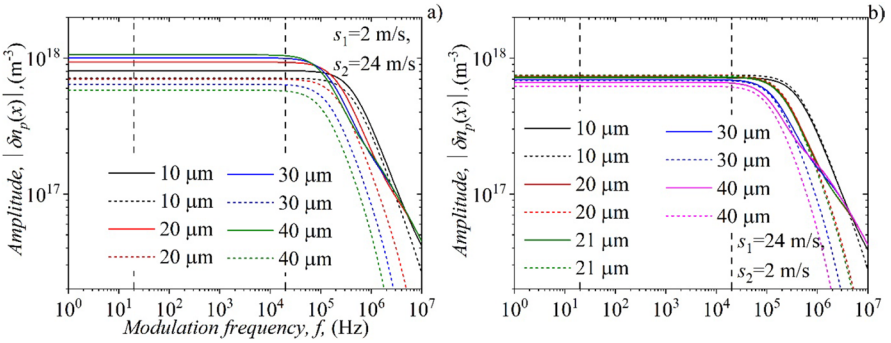

Fig. 5 The amplitude values of $\left|\delta n_p(-l/2)\right|$ (solid lines) and $\left|\delta n_p(l/2)\right|$ (dashed lines) in the case of (a) $(s_1/s_2 < 1)$ and (b) $(s_1/s_2 > 1)$, as a function of the modulation frequency f. Calculations were done for a Si n-type sample with thicknesses 10 μm ≤ l ≤ 40 μm

are in a much narrower range, simultaneously changing their sign ($\Delta\delta n_p < 0$) to the thinnest samples (21 mm, 20 mm, and 10 mm). Such behavior of $\Delta\delta n_p$ (narrowing the values range) is the reason for the appearance of a peak-like structure in the $\left|\delta p_{PE}(j\omega)\right|$ response [Fig. 3, case (b)].

To obtain a clearer understanding of these effects, Fig. 6 displays the calculated amplitude ratio $R_n = \left|\delta n_p(-l/2)\right| / \left|\delta n_p(l/2)\right|$ for the thinnest samples. It is evident that in case (a) $(s_1/s_2 < 1)$, $R_n > 1.1$ for all the shown thicknesses, meaning no peak-like structures in $\left|\delta p_{PE}(j\omega)\right|$ response. In case (b) $(s_1/s_2 > 1)$, the change from $1.0 < R_n < 1.1$ (30 mm and 40 mm) to $0.9 < R_n < 1.0$ (21 mm, 20 mm, 10 mm) is clearly observable, meaning the emergence of peak-like structures in $\left|\delta p_{PE}(j\omega)\right|$ response. This result confirms the assumption that the tendency of δn_p to narrow the R_n values range around unity ($1 \pm 10\,\%$) is one of the causes of the peak-like structure appearance in the $\left|\delta p_{PE}(j\omega)\right|$ response.

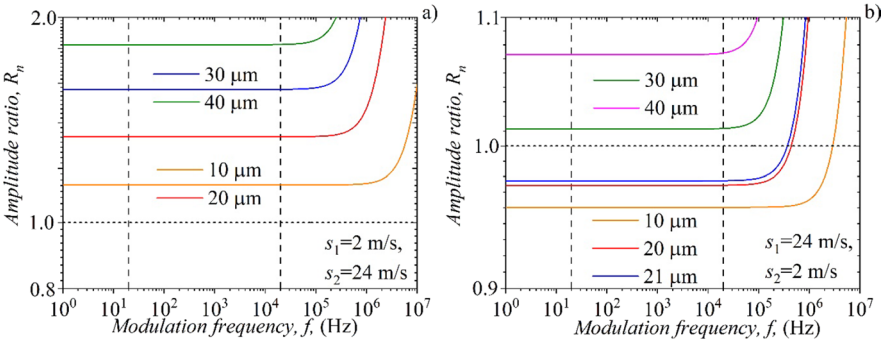

Fig. 6 The calculated amplitude ratio $R_n = \left|\delta n_p(-l/2)\right| / \left|\delta n_p(l/2)\right|$ in the case of (a) $(s_1/s_2 < 1)$ and (b) $(s_1/s_2 > 1)$, as a function of the modulation frequency f. Calculations were done for a Si n-type sample with thicknesses 10 μm ≤ l ≤ 40 μm

3.4 Plasma–Elastic Component Response *vs.* Sample Absorbance

The absorption coefficient measures how deeply light of a specific wavelength can penetrate a semiconductor before being absorbed. In materials with a low absorption coefficient, light is weakly absorbed, and if the material is sufficiently thin, it may appear transparent to that wavelength. The absorption coefficient depends on factors such as temperature, doping level, wavelength, and the intensity of the light being absorbed. Therefore, it is possible to alter a semiconductor's absorption coefficient by adjusting the operating temperature, increasing the doping concentration to enhance free carrier absorption, modifying its bandgap energy through changes in material composition, or increasing light intensity to induce nonlinear absorption.

In the field of photoacoustics, the total photoacoustic signal and its components, particularly the thermoelastic component, are influenced by the absorption coefficient, which we refer to as beta. In our previous work, we examined the behavior of the thermoelastic component in the frequency domain through a phenomenological analysis of its sensitivity to β (more precisely βl), but without detailed elaboration (all results were normalized to the red-light excitation). It was demonstrated that, within the optical and near-infrared spectrum, the amplitude of the thermoelastic component changes its shape, a peak-like structure may form or disappear depending on the temperature difference and the contributions of thermalization and surface recombination temperatures on both the illuminated and non-illuminated sides of the sample. We emphasized that all findings suggested the illuminated side was passivated, while the non-illuminated side was not. Furthermore, under other passivation conditions, the peak-like effect was not observed. It was also emphasized that the temperature component of surface recombination strongly depends on the density of photogenerated minority carriers, $\delta n_p(x)$, on the illuminated and non-illuminated side.

Here, a phenomenological analysis of the 40 mm Si *n*-type thick sample plasma–elastic $\delta p_{PE}(j\omega)$ component behavior in the frequency domain is presented (Fig. 7), based on its sensitivity to β (Table 2, red, infrared IR_a, infrared IR_b) and

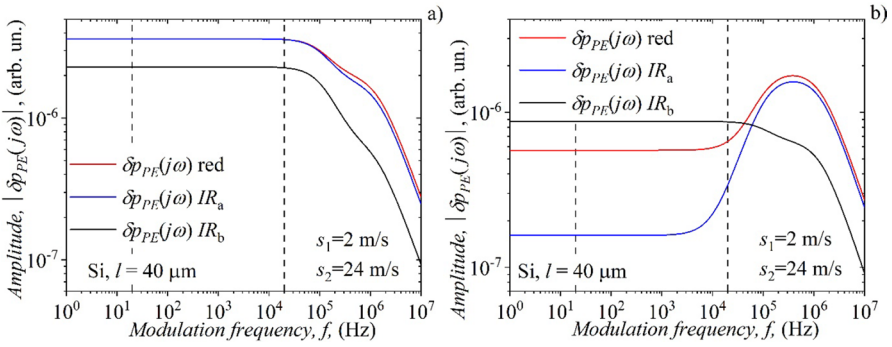

Fig. 7 Plasma–elastic amplitude $|\delta p_{PE}(j\omega)|$ response in the case (a) ($s_1/s_2 < 1$) and (b) ($s_1/s_2 > 1$), as a function of modulation frequency, f, and 40 mm thick Si *n*-type sample excitation light wavelengths: 660 nm (red), 755 nm (IR_a) and 880 nm (IR_b) (Color figure online)

Table 2 Si *n*-type sample parameters for *b* analysis

Light wavelengths	$l_{red}=660$ nm $l_{IRa}=755$ nm $l_{IRb}=880$ nm	Optical absorption coefficients	$b_{red}=0.258$ mm^{-1} $b_{IRa}=0.125$ mm^{-1} $b_{IRb}=0.038$ mm^{-1}
Excitation energies	$e_{red}=1.88$ eV $e_{IRa}=1.64$ eV $e_{IRb}=1.41$ eV	Energy gap	$\varepsilon_g=1.12$ eV

s_1/s_2 ratio, using density of carriers dependences at illuminated ($\left|\delta n_p(-l/2)\right|$) and non-illuminated ($\left|\delta n_p(l/2)\right|$) sample surfaces (Fig. 8), and their ratios $R_n = \left|\delta n_p(-l/2)\right| / \left|\delta n_p(l/2)\right|$ (Fig. 9).

In Fig. 7, plasma–elastic amplitude $\left|\delta p_{PE}(j\omega)\right|$ frequency responses are given, presenting "standard" response without peak-like structure in the case (a) ($s_1/s_2 < 1$),

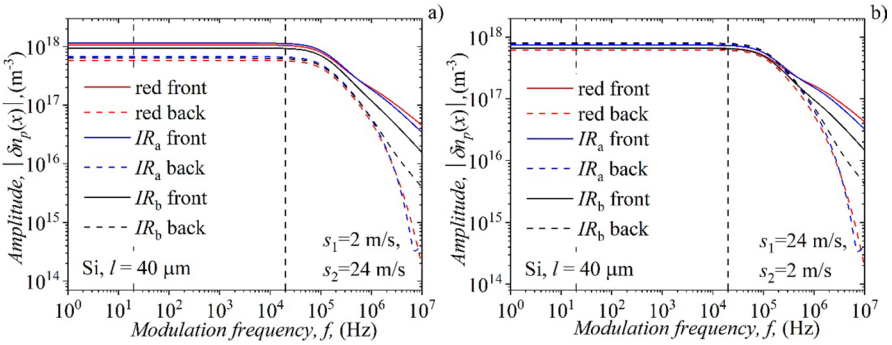

Fig. 8 The amplitude values of $\left|\delta n_p(-l/2)\right|$ (solid lines) and $\left|\delta n_p(l/2)\right|$ (dashed lines) in the case of (a) ($s_1/s_2 < 1$) and (b) ($s_1/s_2 > 1$), as a function of modulation frequency, f, and 40 mm thick Si *n*-type sample excitation light wavelengths: 660 nm (red), 755 nm (IR_a) and 880 nm (IR_b) (Color figure online)

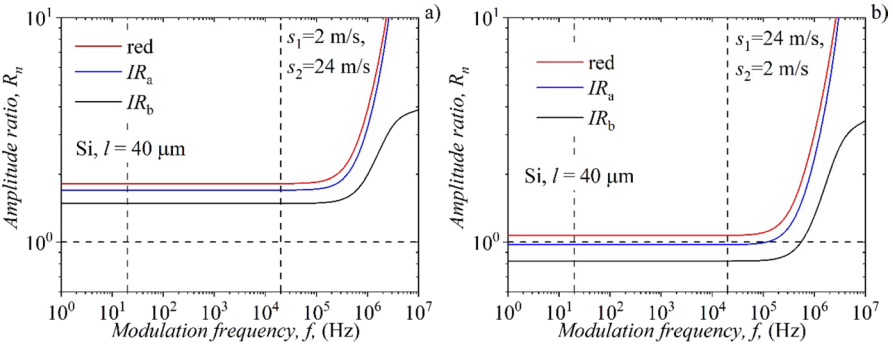

Fig. 9 The calculated amplitude ratio $R_n = \left|\delta n_p(-l/2)\right| / \left|\delta n_p(l/2)\right|$ in the case of (a) ($s_1/s_2 < 1$) and (b) ($s_1/s_2 > 1$), as a function of modulation frequency, f, and 40 mm thick Si *n*-type sample excitation light wavelengths: 660 nm (red), 755 nm (IR_a) and 880 nm (IR_b) (Color figure online)

and red and IR_a peak-like structure in the case (b) ($s_1/s_2 > 1$), returning to the "standard" response at IR_b. Such behavior is similar to the thermoelastic amplitude component in reverse s_1/s_2 order. It must be noted that the plasma–elastic peak-like structure is wider than the thermoelastic one, which is expected, because the nature and behavior of temperature and carrier density in the frequency domain are not the same.

In Fig. 8, the amplitude values of $\left|\delta n_p(-l/2)\right|$ (solid lines) and $\left|\delta n_p(l/2)\right|$ (dashed lines) in the case of (a) ($s_1/s_2 < 1$) and (b) ($s_1/s_2 > 1$), as a function of modulation frequency, f, and different excitation light b values and wavelengths. It is clear that $\Delta\delta n_p$, in case (a) maintains a noticeable difference and does not change sign ($\Delta\delta n_p > 0$) for each b. In the case (b), $\Delta\delta n_p$ values are significantly smaller and changes sign: in the case of red, $\Delta\delta n_p > 0$ in the entire f-domain; in the case of IR_a, $\Delta\delta n_p \cong 0$ in the largest part of the f-domain, while at higher frequencies $\Delta\delta n_p > 0$; in the case of IR_b $\Delta\delta n_p < 0$ in the largest part of the f-domain, and at higher frequencies $\Delta\delta n_p > 0$.

To enhance our understanding of the behavior of $\Delta\delta n_p$, Fig. 9 introduces the results presented in Fig. 8; however, the ratio R_n is given instead of $\Delta\delta n_p$. It is evident that, in both scenarios (a) and (b), a peak-like structure will only appear when $R_n \cong 1 \pm 10\,\%$ (almost the same density on both sides) for a significant portion of the f-domain.

The obtained results indicate that the effects of carriers, shown by the peak-like structures in the plasma–elastic component of the photoacoustic signal, are only clearly visible at frequencies above the measurement range of standard photoacoustics. Therefore, it is necessary to find a technique that can experimentally observe these effects. Photothermal radiometry is a promising technique which generally operates up to 10 MHz [34].

4 Conclusions

Using numerical simulations and experimental measurements, we have shown that the influence of photogenerated minority excess carriers on plasma–elastic photoacoustic responses is significantly affected by the surface conditions of the semiconductor, particularly regarding recombination rates. When carrier influence is substantial, the photoacoustic response is determined by two key effects. The first one involves the high-frequency contribution of the plasma–elastic component to the overall signal when the illuminated surface is passivated, while the rear surface is not. The second one is characterized by peak-like structures of the plasma–elastic amplitudes when the non-illuminated surface is passivated and the illuminated surface is not. Peaks occur when the carrier densities on both surfaces are nearly equal and diminish as their differences increase, similar to the temperature-driven changes observed in thermoelastic responses. Amplitude peak-like behavior primarily occurs in plasma-thin and plasma-transparent samples with non-passivated illuminated surfaces, whereas plasma-thick and plasma-opaque samples do not exhibit such behavior. Additionally, increasing the excitation light wavelength reduces absorption and suppresses these peaks by

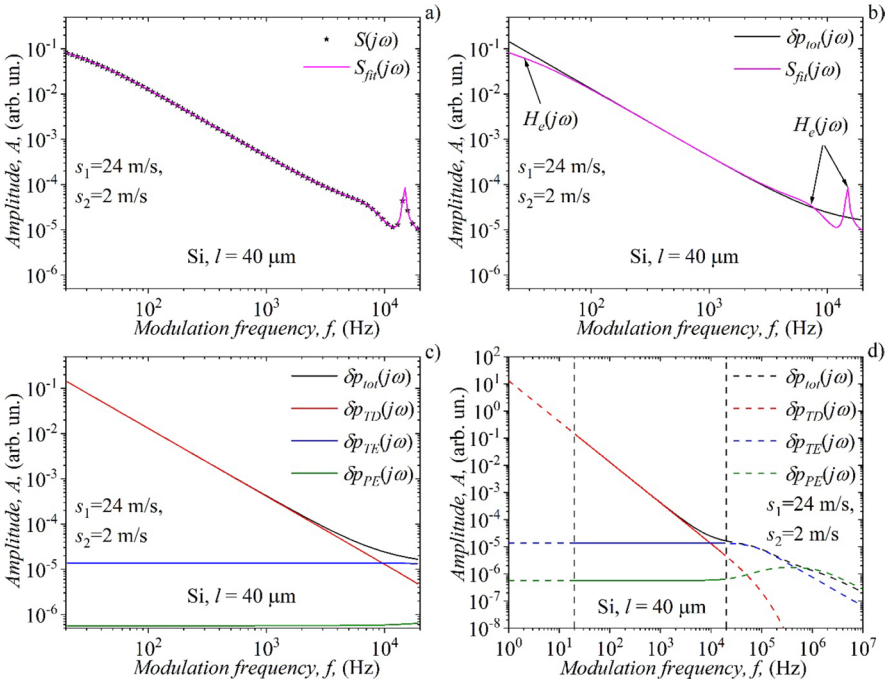

Fig. 10 Experimental validation and extrapolation procedure based on measured photoacoustic signal $S(j\omega)$ amplitudes (asterisks): (a) fitting procedure with $S_{fit}(j\omega)$ (solid pink), (b) removing $H_e(j\omega)$ and $H_a(j\omega)$ deviations targeting $\delta p_{tot}(j\omega)$ (solid black), (c) obtaining signal components: $\delta p_{TD}(j\omega)$, $\delta p_{TE}(j\omega)$, and $\delta p_{PE}(j\omega)$ (red, blue and olive, respectively), and (d) extrapolation of all total signal and signal components to the wider frequency range (dashed lines). Vertical dashed lines indicate experimental frequency range (Color figure online)

Table 3 Measuring chain characteristic parameters

Fitting parameters	Value
$H_e(j\omega)$	
Microphone characteristic frequency, f_{e1} (Hz)	24 ± 1
PC sound card characteristic frequency, f_{e2} (Hz)	16 ± 1
$H_a(j\omega)$	
Microphone characteristic first peak frequency, f_{a1} (kHz)	7.8 ± 0.1
Microphone characteristic second peak (cut-off) frequency, f_{a2} (kHz)	14.7 ± 0.2
First peak damping factor, δ_{a1}	0.80 ± 0.05
Second peak damping factor, δ_{a2}	0.02 ± 0.01

enhancing the sample's transparency. Overall, plasma–elastic features are sensitive to surface passivation, sample thickness, and excitation light wavelength. This sensitivity emphasizes the importance of optimizing experimental conditions to accurately

identify the electronic and recombination properties during semiconductor photoacoustic characterization.

Appendix 1: Temperature Distributions in Irradiated Solid Sample

Detailed knowledge of the temperature distributions in the solid sample based on the geometry from Fig. 1 is essential in photoacoustics. Following the classical physics approach and one-dimensional case of heat flow along the x-axis, the temperature distributions can be calculated using the parabolic heat conduction equation adopted in three basic cases:

Surface Absorber

$$D_T \frac{\partial^2 T(x,t)}{\partial x^2} - \frac{\partial T(x,t)}{\partial t} = 0, \tag{16}$$

where $T(x,t)$ is the temperature within the sample and on its surfaces, assuming that light absorption occurs only on the sample surface.

Volume Absorber

$$D_T \frac{\partial^2 T_\beta(x,t)}{\partial x^2} - \frac{\partial T_\beta(x,t)}{\partial t} = -\frac{D_T}{k}\beta I e^{-\beta x}, \tag{17}$$

where $T_\beta(x,t)$ is the temperature within the sample and on its surfaces, assuming that absorption occurs on the sample surface and within the samples' volume.

Semiconductor Absorber

$$D_T \frac{\partial^2 T_s(x,t)}{\partial x^2} - \frac{\partial T_s(x,t)}{\partial t} = -\frac{D_T}{k}\beta I \bullet \frac{\varepsilon - \varepsilon_g}{\varepsilon} \bullet e^{-\beta x} - \frac{D_T \varepsilon_g}{k\tau_p} \bullet \delta n_p(x), \tag{18}$$

where $T_s(x,t)$ is the temperature within the sample and on its surfaces, assuming that absorption occurs on the sample surface and within the sample's volume, followed by the intensive photogeneration of excess free carriers.

In the case of modulated light excitation of the sample $I = I_0\left(1 + e^{j\omega t}\right)$, where I_0 is an excitation light intensity amplitude, periodical changes of the temperature distributions $T(x,t)$, $T_\beta(x,t)$ and $T_s(x,t)$ are expected, so Eqs. 16–18 can be simplified in the forms

$$\frac{\partial^2 T(x)}{\partial x^2} - \sigma_\omega^2 T(x) = 0, \tag{19}$$

$$\frac{\partial^2 T_\beta(x)}{\partial x^2} - \sigma_\omega^2 T_\beta(x) = -\frac{\beta I_0}{k} \bullet e^{-\beta x}, \tag{20}$$

and

$$\frac{\partial^2 T_s(x)}{\partial x^2} - \sigma_\omega^2 T_s(x) = -\frac{\beta I_0}{k} \bullet \frac{\varepsilon - \varepsilon_g}{\varepsilon} \bullet e^{-\beta x} - \frac{\varepsilon_g}{k\tau_p} \bullet \delta n_p(x), \tag{21}$$

respectively.

Solution of the Eq. 19 can be written as:

$$T(x) = \frac{I_0 \cosh\left[\sigma_\omega (x-l)\right]}{k\sigma_\omega \sinh\left(\sigma_\omega l\right)}. \tag{22}$$

Solution of the Eq. 20 is usually represented as:

$$T_\beta(x) = \frac{I_0}{k} \frac{\beta}{\beta^2 - \sigma_\omega^2} \left[\frac{\beta}{\sigma_\omega} \frac{\cosh\left[\sigma_\omega (x - l/2)\right] - e^{-\beta l} \cosh\left[\sigma_\omega (x + l/2)\right]}{\sinh\left(\sigma_\omega l\right)} - e^{-\beta(x+l/2)} \right]. \tag{23}$$

Here, $\sigma_\omega = (1+j)\sqrt{\omega/2D_T}$ is the complex wave vector of heat diffusion, $\omega = 2\pi f$, f is the modulation frequency, $D_T = k/(\rho c)$ is the thermal diffusivity of the sample (k is the thermal conductivity, ρ is the density, c is the specific heat), and β is the absorption coefficient of silicon at excitation light wavelength.

Solution of the Eq. 21 has the form equal to Eq. 6:

$$T_s(x) = T_{\text{therm}}(x) + T_{\text{sr}}(x) + T_{\text{br}}(x), \tag{24}$$

where

$$T_{\text{therm}}(x) = \frac{I_0}{k} \frac{\varepsilon - \varepsilon_g}{\varepsilon} \frac{\beta}{\beta^2 - \sigma_\omega^2} \left[\frac{\beta}{\sigma_\omega} \frac{\cosh\left[\sigma_\omega (x - l/2)\right] - e^{-\beta l} \cosh\left[\sigma_\omega (x + l/2)\right]}{\sinh\left(\sigma_\omega l\right)} - e^{-\beta(x+l/2)} \right], \tag{25}$$

$$T_{\text{sr}}(x) = \frac{\varepsilon_g}{k\sigma_\omega} \frac{s_1 \delta n_p(-l/2) \cosh\left[\sigma_\omega (x - l/2)\right] + s_2 \delta n_p(l/2) \cosh\left[\sigma_\omega (x + l/2)\right]}{\sinh\left(\sigma_\omega l\right)}, \tag{26}$$

and

$$T_{\text{br}}(x) = \frac{\varepsilon_g B_1}{\tau_p k \sigma_\omega^2} \left\{ \frac{B_2 e^{\sigma_\omega (x+l/2)} + B_3 e^{-\sigma_\omega (x+l/2)}}{e^{\sigma_\omega l} - e^{-\sigma_\omega l}} - \frac{1}{c^2 - 1} \left[\frac{\delta n_p(x)}{B_1} + \frac{b^2 - c^2}{b^2 - 1} e^{-\beta(x+l/2)} \right] \right\}. \tag{27}$$

Here, ε is the photon energy, ε_g is the semiconductor band gap energy, s_1 and s_2 are the surface recombination velocities at the illuminated front and non-illuminated back sample surfaces, respectively, while the other constants are given by

$$b = \frac{\beta}{\sigma_\omega}, c = \frac{1}{L_\omega \sigma_\omega},$$

$$B_1 = -\frac{\beta I_0}{\varepsilon D_p\left(\beta^2 - L_\omega^{-2}\right)},$$

$$B_2 = B_4 e^{-\sigma_\omega l} + B_5,$$

$$B_3 = B_4 e^{\sigma_\omega l} + B_5,$$

$$B_4 = -c\frac{\frac{1}{B_1}\left[\delta n_p\left(\frac{l}{2}\right) - \delta n_p\left(-\frac{l}{2}\right)\cosh\left(\frac{l}{L_\omega}\right)\right] - \cosh\left(\frac{l}{L_\omega}\right) + e^{-\beta l}}{\sinh\left(\frac{l}{L_\omega}\right)\cdot\left(c^2-1\right)} - \frac{b}{b^2-1},$$

$$B_5 = c\frac{\frac{1}{B_1}\left[\delta n_p(l/2)\cosh\left(l/L_\omega\right) - \delta n_p(-l/2)\right] - 1 + e^{-\beta l}\cosh\left(l/L_\omega\right)}{\sinh\left(l/L_\omega\right)\cdot\left(c^2-1\right)} + \frac{be^{-\beta l}}{b^2-1},$$

where $L_\omega = L_p/\sqrt{(1+j\omega\tau)}$, $L_p = \sqrt{D_p\tau_p}$ is the minority excess carrier (holes) diffusion length characterized by their diffusion coefficient D_p and lifetime τ_p, parameter $\delta n_p(x)$ is the holes density, $\delta n_p(-l/2)$ is the holes density at front, and $\delta n_p(l/2)$ is the holes density at back of the sample.

Appendix 2: Experimental Validation and Extrapolation Procedure

When discussing the theoretical background, we highlighted a crucial fact. The scheme in Fig. 1, which illustrates the theoretical model of the composite piston, fully aligns with the experimental setup of an open-cell (minimal-volume cell) operating in transmission mode. This experimental setup, described in detail multiple times in our previous works [27, 32, 33], allows measurements of the amplitudes and phases of the total photoacoustic signal in the frequency domain, by selecting modulation frequencies of the light source so that they evenly (on a logarithmic scale) cover the standard measurement range from 20 Hz to 20 kHz, with about 70 points. These measurements, among other purposes, serve to validate the theoretical model used, enabling us to extend our research through extrapolation from the measured range to 1 Hz to 10 MHz, in which we assume the model remains valid. Through this extrapolation, the effects occurring within the sample (e.g., changes in heat or carrier flow) are included, which only display their full potential at high frequencies, well beyond the measurement range where only end effects are observable.

In a previous study [27], we analyzed the total photoacoustic signal, $\delta p_{tot}(j\omega)$, obtained by periodically illuminating an *n*-type silicon sample that is 40 μm thick (see Table 1). We investigated this sample when the illuminated side was passivated

($s_1 = 2\ \mathrm{m{\cdot}s^{-1}}$), and the non-illuminated side was non-passivated ($s_2 = 24\ \mathrm{m{\cdot}s^{-1}}$). In this work, we will examine the behavior of the plasma–elastic component of the photoacoustic signal by rotating the sample along its vertical axis. As a result, the illuminated side is now non-passivated ($s_1 = 24\ \mathrm{m{\cdot}s^{-1}}$), while the non-illuminated side is passivated ($s_2 = 2\ \mathrm{m{\cdot}s^{-1}}$). For clarity, we will focus on analyzing only the measured amplitudes, assuming that the signal level is significantly above the existing background noise (flicker noise) and/or parasitic signals (coherent noise), which have been measured and confirmed multiple times under the current experimental conditions [33]. We must remain aware of unavoidable deviations in the measured signal, resulting from the electronic and acoustic characteristics of the microphone used as a detector, as well as some devices within the measurement chain, such as a computer sound card that emulates a lock-in amplifier.

We found that the influence of the measuring chain, primarily the microphone and the lock-in amplifier, is manifold [33]. In the low-frequency range, this influence is reflected in the attenuation of the measured signal, similar to the behavior of *RC* filters. Consequently, this attenuation can be represented by the transfer function $H_e(j\omega)$, which consists of a cascade connection of two high-pass *RC* filters (the first from the microphone and the second from the sound card). In the high-frequency range, this influence is manifested through peaks due to acoustic resonances of the microphone, displaying characteristics typical of the response from *RCL* filters. This behavior can be represented by the transfer function $H_a(j\omega)$, which includes two connected low-pass *RCL* filters (our microphone exhibits two peaks).

With this understanding, the measured signal $S(j\omega)$ can be fitted using the function $S_{fit}(j\omega) = \delta p_{tot}(j\omega)H_e(j\omega)H_a(j\omega)$ (see Fig. 10(a)) [33]. This fitting allows us to determine the necessary parameters for the *RC* and *RCL* filters, presented in Table 3. With these parameters, we can remove the deviations contributed by $H_e(j\omega)$ and $H_a(j\omega)$, isolating the signal $\delta p_{tot}(j\omega)$ (see Fig. 10(b)). Based on the composite piston theory (Eq. 1), we can then derive all the components of this signal: $\delta p_{TD}(j\omega)$, $\delta p_{TE}(j\omega)$, and $\delta p_{PE}(j\omega)$ (see Fig. 10(c)), together with sample parameters presented in Table 1.

The thermal and electronic parameters of the sample obtained through this process can be used to extrapolate the components and the signal itself across a frequency range from 1 Hz to 1 kHz [Fig. 10(d)], assuming that the theoretical model in use is valid. This approach allows simulation of various experimental conditions (such as sample thickness and/or illumination wavelength) and investigation of the effects observed through these simulations.

Acknowledgments The authors acknowledge funding provided by the Institute of Physics Belgrade, through a Grant by the Ministry of Science, Technological Development and Innovations of the Republic of Serbia.

Author Contributions The authors confirm their contribution to the paper as follows: (1) study conception and design: D. K. Markushev, D. D. Markushev; (2) data collection: D. K. Markushev, S. M. Kovacevic; (3) analysis and interpretation of results: D. K. Markushev, S. M. Kovacevic, J. Ordonez-Miranda, D. D. Markushev; (4) draft manuscript preparation: D. K. Markushev, J. Ordonez-Miranda, D. D. Markushev; All authors reviewed the results and approved the final version of the manuscript.

Funding This research was funded by the Ministry of Science, Technological Development and Innovation of the Republic of Serbia.

Data Availability The data that supports the findings of this study are available from the corresponding author upon reasonable request.

Declarations

Conflict of interest The authors declare that they have no known competing financial interests or personal relationships that could have appeared to influence the work reported in this paper.

References

1. A. Rosencwaig, A. Gerscho, Theory of the photoacoustic effect with solids. J. Appl. Phys. **47**, 64–69 (1976). https://doi.org/10.1063/1.322296
2. F.A. McDonald, G.C. Wetsel, Generalized theory of the photoacoustic effect. J. Appl. Phys. **49**, 2313–2322 (1978). https://doi.org/10.1063/1.325116
3. H. Hu, X. Wang, X. Xu, Generalized theory of the photoacoustic effect in a multilayer material available to purchase. J. Appl. Phys. **86**, 3953–3958 (1999). https://doi.org/10.1063/1.371313
4. S. Manohar, D. Razansky, Photoacoustics: a historical review. Adv. Opt. Photonics **8**, 586–617 (2016). https://doi.org/10.1364/AOP.8.000586
5. X. Wang, B.A. Cola, T.L. Bougher, S.L. Hodson, T.S. Fisher, X. Xu, Chapter 5, photoacoustic technique for thermal conductivity and thermal interface measurements. In *Annual Review of Heat Transfer*, vol. 16, ed. by Z.M. Zhang, V. Prasad, Y. Jaluria (Begell House, Inc., 2013). ISBN 978-1-56700-313-0 (Print), ISBN 978-1-6700-297-3 (Online), ISSN 1049-0787
6. S.E. Bialkowski, N.G.C. Astrath, M.A. Proskurnin, *Photothermal Spectroscopy Methods* (Wiley, Hoboken, 2019). ISBN 978-1-119-27907-5
7. B.K. Bein, J. Pelzl, Theory of signal generation in a photoacoustic cell. J. Phys. Colloq. **44**, C6-27-C6-34 (1983). https://doi.org/10.1051/jphyscol:1983604
8. J. Zakrzewski, M. Maliński, Ł Chrobak, M. Pawlak, Comparison of theoretical basics of microphone and piezoelectric photothermal spectroscopy of semiconductors. Int. J. Thermophys. **38**, 2 (2017). https://doi.org/10.1007/s10765-016-2137-y
9. D.D. Markushev, M.D. Rabasović, M. Nesic, M. Popovic, S. Galovic, Influence of thermal memory on thermal piston model of photoacoustic response. Int. J. Thermophys. **33**, 2210–2216 (2012). https://doi.org/10.1007/s10765-012-1229-6
10. D.M. Todorovic, Photoacoustic study of elastic deformations in silicon membranes, special collection: semiconductor physics: plasma, thermal, elastic, and acoustic phenomena. J. Appl. Phys. **134**, 095703 (2023). https://doi.org/10.1063/5.0151402
11. A. Somer, S. Galovic, M.N. Popovic, E.K. Lenzi, A. Novatski, K. Djordjevic, Thermoelastic component of photoacoustic response calculated by the fractional dual-phase-lag heat conduction theory. Int. J. Heat Mass Transf. **223**, 125233 (2024). https://doi.org/10.1016/j.ijheatmasstransfer.2024.125233
12. K. Herrmann, N.W. Pech-May, M. Retsch, Photoacoustic thermal characterization of low thermal diffusivity thin films. Photoacoustics **22**, 100246 (2021). https://doi.org/10.1016/j.pacs.2021.100246
13. D.K. Markushev, N.L. Brankovic, S.P. Galovic, K.L. Djordjevic, S.M. Aleksic, D.S. Pantic, D.D. Markushev, The cut-off frequency—a key concept in the heat flow measurements based on the thermoelastic photoacoustic response. Measurement **248**, 116902 (2025). https://doi.org/10.1016/j.measurement.2025.116902
14. N.C. Fernelius, Extension of the Rosencwaig–Gersho photoacoustic spectroscopy theory to include effects of a sample coating available to purchase. J. Appl. Phys. **51**, 650–654 (1980). https://doi.org/10.1063/1.327320
15. M.D. Dramićanin, P.M. Nikolić, Z.D. Ristovski, D.G. Vasiljević, D.M. Todorović, Photoacoustic investigation of transport in semiconductors: theoretical and experimental study of a Ge single crystal. Phys. Rev. B **51**, 14226 (1995). https://doi.org/10.1103/PhysRevB.51.14226
16. K.M. Gupta, N. Gupta, *Carrier Transport in Semiconductors in Advanced Semiconducting Materials and Devices: Part of the Series Engineering Materials* (Springer, Cham, 2016), pp.87–144. https://doi.org/10.1007/978-3-319-19758-6
17. J. Zakrzewski, M. Maliński, A. Bachiri, K. Strzałkowski, Photothermal determination of the optical and thermal parameters of $Cd_xZn_{1-x}Se$ mixed crystals. Mater. Sci. Eng. B **271**, 115305 (2021). https://doi.org/10.1016/j.mseb.2021.115305

18. Y. Sun, S.E. Thompson, T. Nishida, Physics of strain effects in semiconductors and metal–oxide–semiconductor field-effect transistors. J. Appl. Phys. **101**, 104503 (2007). https://doi.org/10.1063/1.2730561
19. M. Chu, Y. Sun, U. Aghoram, S.E. Thompson, Strain: a solution for higher carrier mobility in nanoscale MOSFETs. Annu. Rev. Mater. Res. **39**, 203–229 (2009). https://doi.org/10.1146/annurev-matsci-082908-145312
20. S. Tiwari, *Stress and Strain Effects, Semiconductor Physics: Principles, Theory and Nanoscale*, online edition (Oxford Academic, 2020). https://doi.org/10.1093/oso/9780198759867.003.0017
21. Y. Sun, S.E. Thompson, T. Nishida, *Strain Effect in Semiconductors—Theory and Device Applications* (Springer, 2010). https://doi.org/10.1007/978-1-4419-0552-9
22. D.M. Todorovic, P.M. Nikolic, Chapter 9, carrier transport contribution to thermoelastic and electronic deformation in semiconductors. In *Semiconductors and Electronic Materials Progress in Photothermal and Photoacoustic, Science and Technology*, vol. PM74 (Optical Engineering Press, New York, 2000), pp. 273–318. ISBN 9780819435064
23. D.K. Markushev, D.D. Markushev, S.M. Aleksic, D.S. Pantic, S.P. Galovic, D.M. Todorovic, J. Ordonez-Miranda, Effects of the photogenerated excess carriers on the thermal and elastic properties of *n*-type silicon excited with a modulated light source: theoretical analysis. J. Appl. Phys. **126**, 185102 (2019). https://doi.org/10.1063/1.5100837
24. K.L. Djordjevic, S.P. Galović, ŽM. Ćojbašić, D.D. Markushev, D.K. Markushev, S.M. Aleksic, D.S. Pantic, Electronic characterization of plasma-thick *n*-type silicon using neural networks and photoacoustic response. Opt. Quantum Electron. **54**, 485 (2022). https://doi.org/10.1007/s11082-022-03808-3
25. D.M. Todorovic, M.D. Rabasovic, D.D. Markushev, V. Jovic, K.T. Radulovic, Study of silicon cantilevers by the photoacoustic elastic bending method. Int. J. Thermophys. **38**, 40 (2017). https://doi.org/10.1007/s10765-016-2175-5
26. J. Zakrzewski, M. Pawlak, O. Matsuda, D. Todorovic, J. Liu, Semiconductor physics: plasma, thermal, elastic, and acoustic phenomena. J. Appl. Phys. **136**, 120401 (2024). https://doi.org/10.1063/5.0234837
27. D.K. Markushev, S.M. Kovacevic, J. Ordonez-Miranda, D.D. Markushev, Optical manipulation of the heat flow followed by the thermoelastic photoacoustic response of *n*-type silicon. Results Eng. **27**, 106988 (2025). https://doi.org/10.1016/j.rineng.2025.106988
28. S. Galovic, D.K. Markushev, D.D. Markushev, K. Djordjevic, M. Popovic, E. Suljovrujic, D.M. Todorovic, Time-resolved photoacoustic response of thin semiconductors measured with minimal volume cell: influence of photoinduced charge carriers. Appl. Sci. **15**, 7290 (2025). https://doi.org/10.3390/app15137290
29. S.P. Galovic, K.L. Djordjevic, M.V. Nesic, M.N. Popovic, D.D. Markushev, D.K. Markushev, D.M. Todorovic, Time-domain minimum-volume cell photoacoustic of thin semiconductor layer. I. Theory. J. Appl. Phys. **133**, 245701 (2023). https://doi.org/10.1063/5.0152519
30. I. Stanimirović, D. Markushev, Z. Stanimirović, S. Galović, K. Djordjević, Analysis of plasma–elastic component of time-domain photoacoustic response. J. Appl. Phys. **133**, 235701 (2023). https://doi.org/10.1063/5.0152713
31. G. Rousset, F. Lepoutre, L. Bertrand, Influence of thermoelastic bending on photoacoustic experiments related to measurements of thermal diffusivity of metals. J. Appl. Phys. **54**, 2383–2391 (1983). https://doi.org/10.1063/1.332352
32. D.K. Markushev, D.D. Markushev, S.M. Aleksic, D.S. Pantic, S.P. Galovic, D.M. Todorovic, J. Ordonez-Miranda, Experimental photoacoustic observation of the photogenerated excess carrier influence on the thermoelastic response of *n*-type silicon. J. Appl. Phys. **128**, 095103 (2020). https://doi.org/10.1063/5.0015657
33. D.D. Markushev, M.D. Rabasović, D.M. Todorović, S. Galović, S.E. Bialkowski, Photoacoustic signal and noise analysis for Si thin plate: signal correction in frequency domain. Rev. Sci. Instrum. **86**, 035110 (2015). https://doi.org/10.1063/1.4914894
34. G. Hamaoui, N. Horny, C.L. Gomez-Heredia et al., Thermophysical characterisation of VO_2 thin films hysteresis and its application in thermal rectification. Sci. Rep. **9**, 8728 (2019). https://doi.org/10.1038/s41598-019-45436-0

applied sciences

MDPI

Article

Time-Resolved Photoacoustic Response of Thin Semiconductors Measured with Minimal Volume Cell: Influence of Photoinduced Charge Carriers

Slobodanka P. Galovic [1,*], Dragana K. Markushev [2], Dragan D. Markushev [2], Katarina Lj. Djordjevic [1], Marica N. Popovic [2], Edin Suljovrujic [1] and Dragan M. Todorovic [3]

[1] Vinca Institute of Nuclear Sciences-National Institute of the Republic of Serbia, University of Belgrade, 11001 Belgrade, Serbia; katarina.djordjevic@vin.bg.ac.rs (K.L.D.); edin@vin.bg.ac.rs (E.S.)
[2] Institute of Physics-National Institute of the Republic of Serbia, University of Belgrade, 11001 Belgrade, Serbia; dragana.markushev@ipb.ac.rs (D.K.M.); dragan.markushev@ipb.ac.rs (D.D.M.); maricap@ipb.ac.rs (M.N.P.)
[3] Institute for Multidisciplinary Research, University of Belgrade, 11001 Belgrade, Serbia; dmtodor@afrodita.rcub.bg.ac.rs
* Correspondence: bobagal@vin.bg.ac.rs

Abstract

When a semiconducting sample is illuminated by an intensity-modulated monochromatic light beam with photon energy exceeding the band gap, part of the absorbed energy is directly converted into heat through photon–lattice interactions. This gives rise to a heat source that closely follows the temporal profile of the optical excitation, known as the fast heat source. Simultaneously, another portion of the absorbed energy is used to generate electron-hole pairs. These charge carriers diffuse together and recombine via electron–electron and electron–hole interactions, transferring their kinetic energy to the lattice and producing additional heating of the sample. This indirect heating mechanism, associated with carrier recombination, is referred to as the slow heat source. In this study, we develop a model describing surface temperature variations on the non-illuminated side of a thermally thin semiconductor exposed to a rectangular optical pulse, explicitly accounting for the contribution of surface charge carrier recombinations. Using this model, we investigate the influence of surface recombination velocity and the material's plasma properties on the time-domain temperature response for both plasma-opaque and plasma-transparent samples. Our results demonstrate that charge carrier recombinations can significantly affect the transient photoacoustic signal recorded using a minimum volume cell, highlighting the potential of time-resolved photoacoustic techniques for probing the electronic properties of semiconductors.

Keywords: time-domain photoacoustic; minimum volume cell; semiconductors; plasma effects; surface recombinations

Academic Editor: Franco Mutinelli

Received: 29 April 2025
Revised: 19 June 2025
Accepted: 22 June 2025
Published: 28 June 2025

Citation: Galovic, S.P.; Markushev, D.K.; Markushev, D.D.; Djordjevic, K.L.; Popovic, M.N.; Suljovrujic, E.; Todorovic, D.M. Time-Resolved Photoacoustic Response of Thin Semiconductors Measured with Minimal Volume Cell: Influence of Photoinduced Charge Carriers. *Appl. Sci.* **2025**, *15*, 7290. https://doi.org/10.3390/app15137290

1. Introduction

Frequency-domain photoacoustic (PA) techniques for semiconductors have been under development for more than four decades. Their primary objective is to enable non-destructive characterization of key material properties—optical, thermal, elastic, and electronic—which are crucial for the design and optimization of microelectronic, photonic, sensor, and biosensor devices, as well as for solar cells and thermal management in VLSI circuits [1–9].

Photoacoustic (PA) phenomena arise when a sample is illuminated by an intensity-modulated optical beam, leading to time-dependent heating and subsequent generation

of pressure waves (acoustic waves). The resulting acoustic signal can be detected using a variety of techniques: deflection-based photothermal (PT) methods [10,11], ultrasonic detectors [12,13], or gas–microphone configurations, either in reflection or in transmission using a minimum volume cell [14].

The generation of acoustic waves is a consequence of the PT effect, wherein absorbed electromagnetic energy from the excitation beam is converted into heat. In addition to generating acoustic waves, the PT effect also produces other detectable phenomena that do not rely on acoustic sensors [10,11,15–17]. For example, it may cause changes in the infrared spectrum of the sample, which can be captured via radiometry; induce gradients in the optical refractive index within the sample (utilized in thermal lens spectroscopy methods) or in the surrounding medium (mirage techniques); or be directly observed as surface temperature changes using calorimetric methods.

This study focuses on the gas–microphone technique implemented using a minimum volume cell. This configuration has been developed in parallel with the more widespread reflection-mode PA techniques [14], and it has proven especially effective for the characterization of metals, semiconductors, and semiconductor devices [1].

In recent years, special attention has been given to developing time-domain PA techniques for real-time electronic characterization of semiconductor structures. However, a critical challenge in this domain is the deconvolution of signal contributions arising from charge carrier dynamics and those due to the detection system. This challenge motivates our current study.

Previous studies have shown that frequency-domain PA spectroscopy [18] can be used to measure the electronic properties of semiconductors. However, these methods are generally not suitable for real-time measurements, which are increasingly important for industrial and biomedical applications [19]. In contrast, time-domain PA methods [20–23] offer the potential for real-time characterization, but they require more advanced models and signal-processing techniques [22].

There are three main approaches to modeling PT and PA effects in semiconductors. The first approach assumes that photogenerated carriers influence the thermal conductivity, diffusivity, or relaxation times of the semiconductor, thereby affecting the temperature distribution and, ultimately, the generated pressure wave [24–27]. The second approach utilizes the two-temperature model, treating electrons and lattice as separate thermal systems; this is particularly suited for highly doped or degenerate semiconductors [28–31]. The third approach, which we adopt in this study, considers two types of heat sources: fast heat sources resulting from immediate photon–lattice interactions and nonradiative relaxation, and slow heat sources resulting from recombination of photogenerated carriers [18,32–34]. Among these, the third approach—based on distinguishing fast and slow heat sources—is particularly well-suited for the PA analysis of moderately doped semiconductors. This model forms the theoretical basis of our study.

The first type of heat source, referred to as the fast heat source, is characteristic of all solid-state materials. It originates from the interaction of the excitation electromagnetic radiation with lattice vibrations and non-radiative de-excitation processes. These mechanisms rapidly convert the absorbed photon energy into heat and operate on timescales much shorter than those relevant to photothermal detection. As a result, the temporal profile of this heat generation closely follows that of the incident optical pulse. However, due to the electronic band structure of semiconductors—which includes a filled valence band, a partially empty conduction band, and a band gap in between—photons with energy exceeding the band gap can excite electrons into the conduction band, leaving behind holes in the valence band [35]. These electron-hole pairs (quasi-free charge carriers), bound by Coulomb attraction, diffuse through the material driven by concentration gradients and

eventually recombine after a characteristic time known as the carrier lifetime. During recombination, their kinetic energy is transferred to the lattice, generating additional heat. These recombination events are distributed in space and time, and form what is known as the slow heat source. The overall temperature distribution in the semiconductor is therefore a superposition of the contributions from fast and slow heat sources. This dual-source model is especially appropriate for moderately doped, narrow-band gap semiconductors, where the Fermi level remains within the band gap and the photoinduced plasma plays a significant role in thermal dynamics.

From the perspective of PA research and device characterization, this approach provides a physically realistic and experimentally relevant description of how photogenerated carriers influence the PA signal. It links electronic properties, carrier dynamics, and recombination processes to the optically induced heating and the resulting acoustic response detectable in gas–microphone or other PA configurations [18,32–34].

Using the third modeling approach, where photogenerated charge carriers contribute to additional heating via recombination (slow heat sources), frequency-domain PA measurements have already enabled the electronic characterization of semiconductors. However, despite having an original time-domain PA setup with gas microphones and validated knowledge from frequency-domain studies, the use of time-domain gas–microphone PA techniques for the electronic characterization of semiconductors remains challenging. The main obstacle lies in the complexity of the system's transfer characteristics in the time domain—specifically, the transformation of optically induced temperature variations on the non-illuminated surface into acoustic signals, and subsequently into the final electrical signal detected by the microphone. This transformation process is not yet fully understood [22,36], and as a result, it is currently not possible to deconvolve the contributions of charge carrier dynamics from those of the detection system response with sufficient accuracy. Therefore, although our broader research goal is to establish time-domain PA methodologies for the electronic characterization of semiconductor structures, this cannot be realized without first addressing a fundamental intermediate step: quantifying the influence of photogenerated charge carriers on the transient temperature response at the non-illuminated surface.

In this study, we investigate how photo-induced quasi-free carriers affect surface temperature variations in a thin, moderately doped semiconductor when illuminated by square optical pulses. We analyze the transient temperature response at the non-illuminated surface using parameters introduced in our previous work [22,36]: rise time, fall time, settling time, and steady-state value, which are commonly used in system dynamics and signal processing. This provides a quantitative and physically interpretable way to assess the role of photogenerated carriers in shaping the thermal response detectable via time-domain PA measurements.

The paper is structured as follows. Section 2 presents a theoretical model of temperature variations caused by fast and slow heat sources using the Laplace transform and electro-thermal analogies. Section 3 analyzes the impact of thickness, surface recombination velocity, and electronic properties on the time-domain PA signal. Section 4 summarizes our conclusions. Technical details of the calculations are provided in Appendices A and B.

2. Photoinduced Heat Transfer Across Thin Semiconductor: Theoretical Model

The model of photoinduced heat propagation is derived under the following assumptions:

- The sample is excited by an optical pulse of irradiance $I(t) = I_0 f(t)$ [W/m^2], where $f(t)$ describes the time dependence of the incident irradiance:

$$f(t) = h(t) - h(t - T) \tag{1}$$

where $h(t)$ is denoted the Heaviside step function and with T [s] is the pulse duration.
- Before the excitation of optical radiation, the whole structure and its environment are at the same temperature—T_{amb} [K].
- The deexcitation–relaxation processes due to photon–phonon interactions are assumed to be much faster than the rate of change of the rising edge of the optical pulse. Thus, the heat sources formed by these processes follow the temporal shape of the optical pulse [37].
- We consider a semiconductor disk uniformly illuminated across its cross-sectional surface normal to the direction of light propagation (Figure 1), allowing the entire problem of optically generated heat propagation to be analyzed using a one-dimensional approximation.
- It is assumed that the surrounding gas does not absorb the incident radiation. Heat sources are generated solely within the sample; however, the resulting thermal disturbance affects the surrounding area.
- The sample is considered optically opaque, i.e., $\beta l_s \gg 1$, where β is the optical absorption coefficient [m^{-1}] and l_s [m] is the sample thickness. Thus, the excitation optical beam penetrates only a thin layer of the semiconductor near its illuminated surface. The optically generated heat due to photon–phonon interactions can be described as a surface heat source [38]:

$$H_T(t) = (1 - R) I_0 \delta(x) f(t) = S_0 \delta(x) f(t) \tag{2}$$

where R is the sample's reflectance, δ is the Dirac delta function, and $S_0 = (1 - R) I_0$.

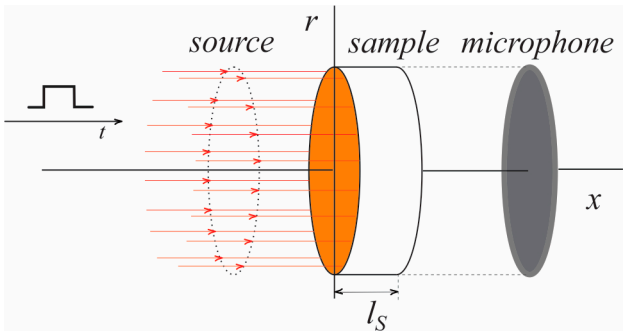

Figure 1. The geometry of the problem of optically excited temperature variations in semiconductors.

Consequently, the optically generated concentration flux of charge carriers can also be described as surface excitation [39]:

$$g(t) = (1 - R) I_0 \frac{E_G}{E} \delta(x) f(t) = S_0 \frac{E_G}{E} \delta(x) f(t) \tag{3}$$

where E_G and E signify the energy gap of semiconductor and photon energy, respectively, and $E \geq E_G$ [18].

- The slow heat sources generated by charge carrier recombinations, denoted as $H_g^{SR}(t)$, $H_b^{SR}(t)$, and $H^{BR}(x,t)$, can be described by [18,32–34]

$$H_g^{SR}(t) = E_G s_g n(0,t) \tag{4}$$

$$H_b^{SR}(t) = E_G s_b n(l_s,t) \tag{5}$$

$$H^{BR}(x,t) = E_G \frac{n(x,t)}{\tau} \tag{6}$$

where s_g and s_b are parameters describing the surface recombination velocity at the illuminated (g) and non-illuminated (b) surfaces of the semiconductor sample. The terms $n(x,t)$, $n(0,t)$, and $n(l_s,t)$ represent the concentration of photoinduced minority carriers within the sample and at the sample surfaces, illuminated and unilluminated, respectively, obtained by solving the diffusion equation for minority charge carriers induced by a surface source, as described by by Equation (3).

The surface recombination velocity depends strongly on the surface treatment of the semiconductor. Chemically etched surfaces typically exhibit low recombination velocities due to the removal of surface defects, while untreated or contaminated surfaces can have significantly higher recombination rates. Additional passivation techniques—such as thermal oxidation, hydrogenation, or dielectric layer deposition (e.g., SiO_2, Al_2O_3)—are commonly employed to further reduce surface defect density and electronically stabilize the surface [40]. However, surface recombination velocities are generally higher than volumetric recombination rates, which are intrinsic to the semiconductor and primarily depend on the doping level.

- Due to the significantly lower rates of volumetric recombination compared to surface recombination [39], the intensity of the volumetric heat source described by Equation (6) is much smaller than that of surface-related heat sources [18,34] and can thus be neglected in the thermal analysis
- The semiconductor sample is surrounded by air, which is a much poorer thermal conductor than the semiconductor itself. Therefore, adiabatic boundary conditions for the heat flux are assumed.
- Nonlinear effects in heat conduction, transport of photogenerated charge carriers through the semiconductor, thermal relaxation effects, and effects of dissipation of heat caused by charge carrier recombination are neglected because these effects are not expected to be significant in gas–microphone photoacoustic experiments [18,32,33].

Under these assumptions, the conduction of photogenerated heat through the semiconductor sample can be described by the one-dimensional classical Fourier's theory of heat conduction [41], leading to the following system of linear partial differential equations:

$$\frac{\partial^2 \vartheta(x,t)}{\partial x^2} - \frac{1}{D_T}\frac{\partial \vartheta(x,t)}{\partial t} = 0 \tag{7}$$

$$q(x,t) = -k\frac{\partial \vartheta(x,t)}{\partial x} \tag{8}$$

With the following inhomogeneous boundary conditions [18]:

$$q(x=0,t) = H_T(t) + H_g^{SR}(t) \tag{9}$$

$$q(x=l_s,t) = H_b^{SR}(t) \tag{10}$$

and zero initial conditions.

In the above equations (Equations (5)–(8)), $\vartheta(x,t)$ denotes the temperature variation in relation to the ambient (initial) temperature, $\vartheta(x,t) = T(x,t) - T_{amb}$, $q(x,t)$ is the heat flux, D_T is the thermal diffusivity of the semiconductor, and k is the thermal conductivity.

Since the problem is linear, the temperature distribution in the illuminated semiconductor sample can be obtained by applying the Laplace transform to Equations (7)–(10). In this case, the system of Equations (7)–(10) reduces to a system of ordinary differential equations in the complex domain:

$$\frac{d^2\overline{\vartheta}(x)}{dx^2} - \overline{\sigma}^2\overline{\vartheta}(x) = 0 \tag{11}$$

$$\overline{q}(x) = -\frac{1}{\overline{\sigma}\overline{Z}_c}\frac{d\overline{\vartheta}(x)}{dx} \tag{12}$$

with the following boundary conditions:

$$\overline{q}(x=0) = S_0\overline{F}(s) + \overline{H}_g^{SR} \tag{13}$$

$$\overline{q}(x=l_s) = \overline{H}_b^{SR} \tag{14}$$

In Equations (11)–(14), the variables with an overline denote the Laplace transforms of the temperature, heat flux, the time function describing the modulation of the excitation beam's amplitude, and the recombination heat sources on the illuminated and non-illuminated surfaces. Here, s is denoted the complex frequency $s = \alpha + j\omega$ and $j = \sqrt{-1}$ is the imaginary unit (see Appendix B).

The symbols $\overline{\sigma}$ and $\overline{Z}_c$ represent the complex coefficient of heat propagation and thermal impedance, respectively, defined as follows:

$$\overline{\sigma} = \frac{\sqrt{s}}{\sqrt{D_T}} \tag{15}$$

$$\overline{Z}_c = \frac{\sqrt{D_T}}{k}\frac{1}{\sqrt{s}} \tag{16}$$

As can be seen from Equations (11) and (12), heat propagation through the semiconductor sample is described by equations analogous to those governing the propagation of current and voltage through an electrical transmission line [42–44] (see Figure 2), with propagation coefficient $\overline{\sigma}$ and characteristic impedance $\overline{Z}_s$, defined as

$$\overline{\sigma} = \sqrt{\overline{z}\,\overline{y}} \tag{17}$$

$$\overline{Z}_s = \sqrt{\frac{\overline{z}}{\overline{y}}} \tag{18}$$

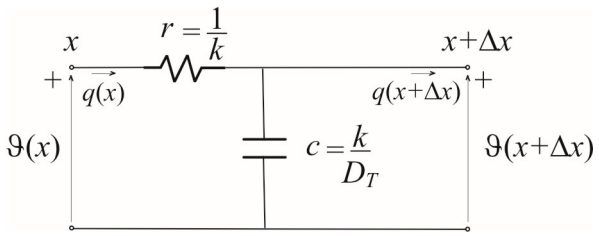

Figure 2. Equivalent transmission line for the description of heat transfer problem based on classical Fourier heat conduction theory.

With symbols $\overline{z}$ and $\overline{y}$, we denote complex series impedance and complex parallel admittance of a transmission line segment (Figure 2):

$$\overline{z} = r + sl = \frac{1}{k} \tag{19}$$

$$\overline{y} = g + sc = s\frac{k}{D_T} \tag{20}$$

As can be seen from the boundary conditions (Equations (13) and (14)), heat propagation is driven by surface heat fluxes, which is analogous to the excitation of an electrical transmission line by current sources:

$$\overline{I}_1 = S_0\overline{F} + \overline{H}_g^{SR} = \overline{I}_T + \overline{I}_g^{SR} \tag{21}$$

$$\overline{I}_2 = \overline{H}_b^{SR} = \overline{I}_b^{SR} \tag{22}$$

To calculate surface temperature variations on the unilluminated side, it is convenient to use the representation of an electrical transmission line via a symmetrical electrical T-network with two ports (quadripole) [43–49]. The analogous electrical circuit for calculating surface temperature variations on the unilluminated surface is shown in Figure 3.

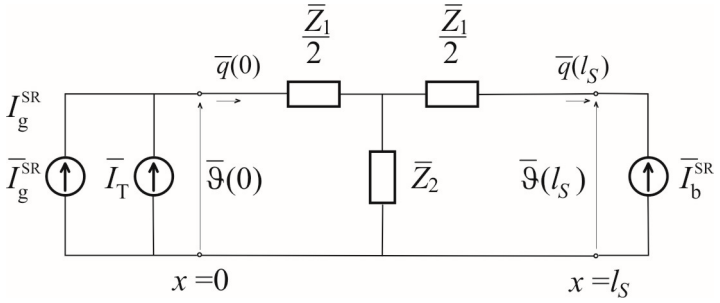

Figure 3. The equivalent quadripole for the calculation of surface temperature variations in the semiconducting sample.

The impedances of the equivalent electrical circuit shown in Figure 3 are given by the following expressions [43,44]:

$$\overline{Z}_1 = \overline{Z}_c\frac{1}{sh(\overline{\sigma}l_s)} = \sqrt{\frac{\overline{Z}}{\overline{Y}}}\frac{1}{sh(\overline{ZY})} \tag{23}$$

$$\overline{Z}_2 = \overline{Z}_c\frac{ch(\overline{\sigma}l_s) - 1}{sh(\overline{\sigma}l_s)} = \sqrt{\frac{\overline{Z}}{\overline{Y}}}th(\frac{\overline{ZY}}{2}) \tag{24}$$

where $\overline{Z}$ and $\overline{Y}$ denote the equivalent longitudinal impedance and the equivalent longitudinal admittance, respectively:

$$\overline{Z} = \overline{z}l_s = \frac{l_s}{k} \tag{25}$$

$$\overline{Y} = \overline{y}l_s = s\frac{k}{D_T}l_s \tag{26}$$

The equivalent current sources are given by the following expression:

$$\overline{I}_T = \overline{H}_T = S_0\overline{F} = S_0\frac{1}{s}(1 - e^{-sT}) \tag{27}$$

$$\overline{I}_g^{SR} = \overline{H}_g^{SR} = E_G s_g \overline{n}(0) \tag{28}$$

$$\overline{I}_b^{SR} = \overline{H}_b^{SR} = E_G s_b \overline{n}(l_s) \tag{29}$$

The symbols $\overline{n}(0)$ and $\overline{n}(l_s)$ signify the spectral functions of the concentrations of minority charge carriers at illuminated and non-illuminated surfaces, respectively.

Spectral functions of charge carrier concentrations are obtained by solving the diffusion equation for minority charge carriers [18,34] (see Appendix A):

$$\overline{n}(0) = \frac{S_0}{E}\overline{F}(s)\overline{G}_g(s) \tag{30}$$

$$\overline{n}(l_s) = \frac{S_0}{E}\overline{F}(s)\overline{G}_b(s) \tag{31}$$

In the above equations, $\overline{G}_g(s)$ and $\overline{G}_b(s)$ represent complex functions given by the following relations (see Appendix A and [18,34]):

$$\overline{G}_g(s) = \frac{1}{\left(\frac{D_{e/p}}{\overline{L}} + s_g\right)} \tag{32}$$

$$\overline{G}_b(s) \approx 0 \tag{33}$$

for $l_s/\mu_{\max} >> 1$ (plasma opaque sample), where

$$\overline{L} = \sqrt{\frac{D_{e/p}\tau}{1+s\tau}} \tag{34}$$

and

$$\overline{G}_g(s) = \frac{\frac{1}{s_g}\frac{l_s}{D_{e/p}}}{\left(\frac{l_s}{D_{e/p}} + \frac{1}{s_g}\right)} \frac{sl_s + \frac{l_s}{\tau} + \frac{\frac{l_s}{D_{e/p}} + \frac{1}{s_b}}{\frac{l_s}{D_{e/p}}\frac{1}{s_b}}}{sl_s + \frac{l_s}{\tau} + \frac{\frac{l_s}{D_{e/p}} + \frac{1}{s_b} + \frac{1}{s_g}}{\left(\frac{l_s}{D_{e/p}} + \frac{1}{s_g}\right)\frac{1}{s_b}}} \tag{35}$$

$$\overline{G}_b(s) = \frac{\frac{1}{s_g}}{\left(\frac{l_s}{D_{e/p}} + \frac{1}{s_g}\right)} \frac{1}{sl_s + \frac{l_s}{\tau} + \frac{\frac{l_s}{D_{e/p}} + \frac{1}{s_b} + \frac{1}{s_g}}{\left(\frac{l_s}{D_{e/p}} + \frac{1}{s_g}\right)\frac{1}{s_b}}} \tag{36}$$

for $l_s/\mu_{\max} < 1$ (plasma transparent sample).

In the above relations, the symbol $D_{e/p}$ signifies the coefficient of diffusion of minority charge carriers—electrons in p-doped semiconductors (index e) or holes in n-doped semiconductors (index p). The symbol τ denotes the lifetime of photoinduced charge carriers. The maximum diffusion length of minority carriers is given by $\mu_{\max} = \sqrt{D_{e/p}\tau}$ [34,50],

By substituting Equations (30) and (31) into Equations (28) and (29), a mathematical description of the spectral functions of recombination heat sources in the illuminated semiconductor is obtained:

$$\overline{I}_g^{SR} = \overline{H}_g^{SR} = S_0\overline{F}(s)\frac{E_G}{E}s_g\overline{G}_g(s) = \frac{E_G}{E}s_g\overline{H}_T(s)\overline{G}_g(s) \tag{37}$$

$$\overline{I}_b^{SR} = \overline{H}_b^{SR} = S_0\overline{F}(s)\frac{E_G}{E}s_b\overline{G}_b(s) = \frac{E_G}{E}s_b\overline{H}_T(s)\overline{G}_b(s) \tag{38}$$

As can be seen from Equations (37) and (38), the recombination sources can be described as a convolution of the function that represents the thermalization source and the functions $\overline{G}_g(s)$ and $\overline{G}_b(s)$, which depend on the diffusion of minority carriers in the semiconductor.

By applying the superposition principle in solving the circuit shown in Figure 3, we obtain the spectral functions of the total temperature variations on the unilluminated surface as a sum of temperature variations generated by each of the sources described in Equations (27), (37), and (38):

$$\overline{\vartheta}(l_S) = \overline{\vartheta}_T(l_s) + \overline{\vartheta}_g^{SR}(l_s) + \overline{\vartheta}_b^{SR}(l_s) = \overline{\vartheta}_T(l_s) + \overline{\vartheta}^{SR}(l_s) \tag{39}$$

It is important to note that there are two limiting cases considering the frequency of excitation harmonic: the thermally thin sample ($\mathrm{Re}\{1/\overline{\sigma}l_s\} = \mathrm{Im}\{1/\overline{\sigma}l_s\} \gg 1$) and the thermally thick sample ($1/\mathrm{Re}\{\overline{\sigma}l_s\} = 1/\mathrm{Im}\{\overline{\sigma}l_s\} < 1$).

Considering the definition of $\overline{\sigma}$ (Equation (15)) the following relation is obtained:

$$\mathrm{Re}\{\overline{\sigma}l_s\} = \mathrm{Im}\{\overline{\sigma}l_s\} = l_s\sqrt{\frac{\pi f}{D_T}} \tag{40}$$

From the above equation (Equation (40)), it can be easily concluded that for low frequencies, below a certain cutoff frequency f_c (which depends on l_s and D_T), every sample is thermally thin. Conversely, for high frequencies, above the cutoff frequency f_c, every sample is thermally thick, where f_c is given by:

$$f_c = \frac{1}{l_s^2}\frac{D_T}{\pi} \tag{41}$$

In further considerations, we assume that the sample is geometrically thin, such that the excitation harmonics span a wide frequency range, and that the sample is thermally thin. In this case, the equivalent circuit from Figure 3 is reduced to the equivalent circuit shown in Figure 4 [43].

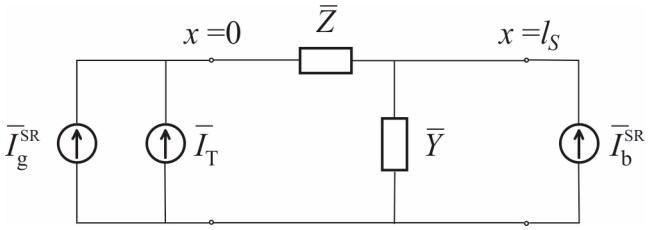

Figure 4. Equivalent electrical circuit for the calculation of temperature variations in a thermally thin semiconducting sample.

By solving the circuit shown in Figure 4, we obtain the spectral functions of surface temperature variations caused by photon–lattice interactions, as well as the spectral functions of temperature variations resulting from surface recombination of photogenerated excess charge carriers, as follows (Equations (42)–(44)):

$$\overline{\vartheta}_T(l_s) = \overline{H}_T\frac{1}{\overline{\overline{Y}}} \tag{42}$$

$$\overline{\vartheta}_g^{SR}(l_s) = \overline{H}_g^{SR}\frac{1}{\overline{\overline{Y}}} \tag{43}$$

$$\overline{\vartheta}_b^{SR}(l_s) = \overline{H}_b^{SR}\frac{1}{\overline{\overline{Y}}} \tag{44}$$

By substituting Equations (26) and (27) into Equation (42), the spectral function of surface temperature variations caused by lattice thermalization at the non-illuminated side

of the semiconductor sample exposed to the action of a square optical pulse of duration T is obtained:

$$\overline{\vartheta}_T(l_s) = S_0 \frac{D_T}{kl_s} \frac{1}{s^2} \left(1 - e^{-sT}\right) \tag{45}$$

By substituting Equations (26), (30), and (31) into Equations (43) and (44), the spectral function of surface temperature variations due to recombination sources at the surface of the semiconductor, is obtained:

$$\overline{\vartheta}^{SR}(l_s) = \frac{E_G}{E} \overline{\vartheta}_T(l_s) \left(s_g \overline{G}_g(s) + s_b \overline{G}_b(s)\right) \tag{46}$$

By finding the inverse Laplace transform of Equation (45), we obtain [44,46]:

$$\vartheta_T(l_s, t) = S_0 \frac{D_T}{kl_s} [th(t) - (t - T)h(t - T)] \tag{47}$$

Considering heat sources generated by recombinations of minority carriers at the sample surfaces depend on the ratio between the sample thickness and the diffusion length of the minority carriers (i.e., plasma transparency (Equations (32)–(36)) [28], we further observe two limiting cases: thermally thin and plasma opaque, and thermally thin and plasma transparent samples.

2.1. Surface Temperature Variations in Thermally Thin and Plasma Opaque Semiconductor Samples

Using Equations (32)–(34), the spectral functions of recombination heat sources in plasma opaque samples can be described as follows [34]:

$$s_g \overline{G}_g(s) = \frac{b}{\sqrt{s + a} + b} \tag{48}$$

$$s_b \overline{G}_b(s) \approx 0 \tag{49}$$

where

$$a = 1/\tau \tag{50}$$

$$b = \frac{s_g}{\sqrt{D_{e/p}}} \tag{51}$$

In this case, the temperature variations generated by surface recombination (based on Equation (46)) becomes

$$\overline{\vartheta}^{SR}(l_s) = \vartheta_g^{SR}(l_s, s) + \vartheta_b^{SR}(l_s, s) = S_0 \frac{D_T}{kl_s} \frac{E_G}{E} \frac{1}{s^2} \frac{b}{\sqrt{s + a} + b} (1 - e^{-sT}) \tag{52}$$

By finding the inverse Laplace transform of Equation (52), we obtain (see Appendix B):

$$\vartheta^{SR}(l_s, t) = S_0 \frac{D_T}{kl_s} \frac{E_G}{E} [g_1(t)h(t) - g_1(t - T)h(t - T)] \tag{53}$$

where the function g_1 is defined by

$$g_1(t) = c_3 b \left[c_1 t + \frac{e^{-at}\sqrt{t}}{b\sqrt{\pi}} - c_2 erf\left(\sqrt{at}\right) - c_3 e^{-(a-b^2)t} erfc(b\sqrt{t}) - t\frac{\sqrt{a}}{b} erfc(\sqrt{at}) + c_3\right] \tag{54}$$

and

$$c_1 = \frac{\sqrt{a} - b}{b} \tag{55}$$

$$c_2 = \frac{b}{\sqrt{a}(a-b^2)} + \frac{1}{2b\sqrt{a}}, \quad c_3 = \frac{1}{a-b^2} \tag{56}$$

2.2. Surface Temperature Variations in Thermally Thin and Plasma Transparent Semiconductor Samples

Using Equations (35) and (36), the spectral functions of recombination heat sources in plasma-transparent samples are given by [34]

$$s_g \overline{G}_g(s) = r_1 \frac{s+p}{s+q} \tag{57}$$

$$s_b \overline{G}_b(s) = r_2 \frac{1}{s+q} \tag{58}$$

Parameters r_1, r_2, p, and q are defined by the following expressions:

$$r_1 = \frac{\left(l_s/D_{e/p}\right)}{\left((1/s_g) + \left(l_s/D_{e/p}\right)\right)} \tag{59}$$

$$r_2 = \frac{\left(s_b/s_g\right)}{\left(\left(l_s/D_{e/p}\right) + \left(1/s_g\right)\right)l_s} \tag{60}$$

$$p = \frac{(l_s/D_{e/p}) + (1/s_b)}{(l_s/s_b)(l_s/D_{e/p})} + \frac{1}{\tau} \tag{61}$$

$$q = \frac{\left((l_s/D_{p/e}) + 1/s_g + 1/s_b\right)}{(l_s/s_b)\left((l_s/D_{p/e}) + (1/s_g)\right)} + \frac{1}{\tau} \tag{62}$$

By substituting Equations (57) and (58) into Equation (46), we obtain the spectral function of temperature variations in a thermally thin and plasma-transparent semiconductor sample, caused by surface recombination heat sources:

$$\overline{\vartheta}^{SR}(l_s) = S_0 \frac{D_T}{k l_s} \frac{E_G}{E} r_1 \frac{1}{s^2} \frac{s+r_3}{s+q}\left(1-e^{-sT}\right) \tag{63}$$

with the parameter r_3 defined by

$$r_3 = \frac{(l_s/D_{e/p}) + (1/s_b)}{(l_s/s_b)(l_s/D_{e/p})} + \frac{1}{\tau} + \frac{s_b}{s_g({l_s}^2/D_{e/p})} \tag{64}$$

By finding the inverse Laplace transform of Equation (63) (see Appendix B), we obtain the following:

$$\vartheta^{SR}(l_s,t) = S_0 \frac{D_T}{k l_s} \frac{E_G}{E} r_1 [g_2(t)h(t) - g_2(t-T)h(t-T)] \tag{65}$$

where the function $g_2(t)$ is defined by

$$g_2(t) = \left(\frac{q-r_3}{q^2} + \frac{r_3}{q}t + \frac{r_3-q}{q^2}e^{-qt}\right) \tag{66}$$

3. Analysis and Discussion

PA measurements with a minimal volume cell record pressure fluctuations in the gas column located on the non-illuminated side of the sample. The measurement configuration is transmission-based, as the source and the detector are on opposite sides of the sample

being examined [51]. The literature indicates that in this type of measurement configuration, the spectral function of the resulting pressure fluctuations in the closed cell can be described by a composite piston model [52]. Specifically, these pressure fluctuations are a consequence of the thermal piston effect, which involves the expansion and contraction of the thin layer of air adjacent to the illuminated surface of the sample [53,54]. Additionally, the bending of the sample surface due to the generation of a thermal moment within the sample [52] acts as a mechanical piston, producing the thermoelastic (TE) component of the PA response.

In semiconductors, due to the photogeneration of charge carriers, there exists a plasma-elastic component resulting from the bending of the sample surface caused by the concentration gradient of excess charge carriers in illuminated semiconductor samples [18,39]. If the sample is thin, both the TE and plasma-elastic components can be neglected [22,55]. In such cases, it can be assumed that the pressure fluctuations are caused solely by the thermal piston effect and are consequently proportional to the surface temperature variations [55–57].

However, the thermal piston model is not suitable for time-domain photoacoustics [22,36,58–60]. In this case, it is more appropriate to use models derived in [22,36,58–60], which indicate that temperature changes at the non-illuminated surface generate pressure variations in a closed PA cell. However, the thermal thickness of the gas column in the closed PA cell [36] and the transfer characteristics of the microphone [22,36] can alter the time profile of the recorded time-resolved electrical signal.

$$\overline{p}_{th}(s) = \overline{\vartheta}(l_S)\overline{T}_{gas-column}(s) \tag{67}$$

$$S_{mic}(t) = L^{-1}\{\overline{p}_{th}(s)\overline{T}_{mic}(s)\} \tag{68}$$

As can be seen from Equations (67) and (68), the recorded photoacoustic signal is a convolution of the temperature variations at the non-illuminated side of the sample and the system's transfer characteristics, described by $\overline{T}_{gas-column}(s)$ and $\overline{T}_{mic}(s)$. This implies that a complete understanding of the measured time-domain signal [23] requires the deconvolution of these effects. However, in order to determine the electronic properties of the semiconductor, it is essential to first investigate the influence of photogenerated charge carriers on the surface temperature variations $\overline{\vartheta}(l_S)$.

In this study, we analyze the evolution of temperature changes at the non-illuminated surface and the influence of photogenerated charge carriers on the magnitude and slope of these changes based on the derived model (hereafter referred to as the time-domain temperature signal). However, modeling the transfer function of the gas column ($\overline{T}_{gas-column}(s)$) and the microphone ($\overline{T}_{mic}(s)$), which is essential for a complete understanding and accurate processing of the recorded time-resolved PA signal in semiconductors [23], remains the focus of our future research.

In the calculations, it was assumed that the optical source has a nondestructive irradiance, with the power of the employed LED diodes typically below 20 mW and the illuminated surface area approximately 25π mm^2 (see Figure 1) [18,22]. Furthermore, the excitation takes place in the visible part of the electromagnetic spectrum, where the photon energy is approximately equal to the energy bandgap of narrow-gap semiconductors such as silicon. Under these conditions, E/E_G is close to unity [18]. The normalized components were evaluated relative to a constant reference value, $K = S_0 D_T / k l_s$.

The time interval was selected to match the excitation pulse duration, which reflects our experimental conditions. This pulse width corresponds to the excitation used in our PA setup and was chosen based on our real measurements on silicon membranes (see Refs. [22,23]). In the analysis, it was assumed that the pulse duration is T = 50 ms. The normalized signal was observed over a time interval of $t = 2T$.

The values of surface recombination velocity (Table 1) were chosen based on the analysis of frequency-domain PA measurements on semiconductors [18].

Table 1. Electronic, thermal, and geometrical properties of silicon samples used in the analysis of the model [18,61].

Parameter	Value
Coefficient of diffusion of holes D_p	1.2×10^{-3} m^2s^{-1}
Coefficient of diffusion of electrons D_e	3.6×10^{-3} m^2s^{-1}
Lifetime of excess charge carriers τ	5×10^{-6} s
Energy gap E_G	1.12 eV
Velocity of surface recombination $S_{g/b}$	2–24 ms^{-1}
Coefficient of thermal diffusivity D_T	9×10^{-5} m^2s^{-1}
Thermal conductivity k	150 $Wm^{-1}K^{-1}$

The parameters of the Si sample used in the calculations are provided in Table 1 [18,61].

Let us consider the thicknesses of the Si sample for which the assumptions of the derived model are satisfied (the absorption coefficient is significantly larger than the inverse of the sample thickness, justifying the assumption of strong absorption in the thin layer close to the illuminated region—practically surface absorption).

The optical absorption coefficient of silicon is 10^5 m^{-1} for light in the visible part of the electromagnetic spectrum [62]. Consequently, the approximation of an optically opaque sample is reasonable for silicon samples thicker than 10 μm.

Since the thermal diffusivity of silicon is $9 \cdot 10^{-5}$ m^2s^{-1} [18], the cutoff frequency between thermally thin and thermally thick regimes for a sample thicker than 10 μm can be calculated from Equation (41). It ranges from approximately 5 kHz for a 90 μm thick sample to 300 kHz for a 10 μm thick sample. For samples with a thickness of about 100 μm, the cutoff frequency varies from 50 Hz for a 900 μm thick sample to 3000 Hz for a 100 μm thick sample. This implies that in the PA measurement range (from 50 Hz to a few kHz), silicon samples with a thickness of 10–150 μm can be considered thermally thin.

Finally, in our model, we considered two cases related to the ratio of the maximum diffusion length of minority carriers to the geometric thickness of the sample. These include the plasma-opaque case, where this ratio is less than one, and the plasma-transparent case, where the ratio is greater than one.

Since the maximum diffusion length of minority carriers is given by the square root of the product of their diffusion coefficient and lifetime (see Appendix B), it can be estimated based on the parameters given in Table 1 that a p-doped silicon sample with a thickness greater than 135 μm is plasma-opaque, while an n-doped silicon sample is plasma-opaque if it is thicker than 75 μm. This means that Si samples, whether p- or n-doped, with a thickness below 75 μm are plasma-transparent, whereas samples thicker than 135 μm are plasma-opaque.

In the further analysis, we considered silicon samples with a thickness of 20 μm as representatives of plasma-transparent, thermally thin, and optically opaque semiconductor samples, and samples with a thickness of 140 μm as representatives of plasma-opaque, thermally thin, and optically opaque semiconductor samples.

Figure 5 shows the normalized time-domain temperature signal (evolution of temperature change on the non-illuminated side) for a thermally thin, plasma-opaque n-doped silicon sample (l_s = 140 μm, D_p = 1.2×10^{-3} m^2s^{-1}). The red line represents the signal originating from lattice thermalization (fast thermal source), while the blue lines correspond to signals influenced by surface recombination for different values of s_g. The green

lines depict the total signal resulting from both sources. (Legend: s_g = 6 ms^{-1} (solid line), s_g = 10 ms^{-1} (dashed line), s_g = 14 ms^{-1} (dash-dot line)).

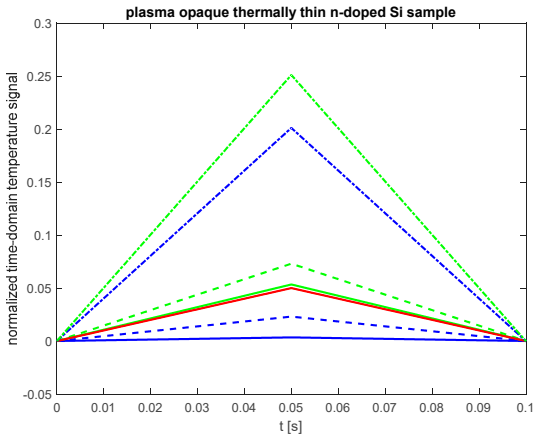

Figure 5. The normalized time-domain temperature signal for a thermally thin and plasma opaque n-doped silicon sample. The red line represents the signal resulting from lattice thermalization (fast heat source), while the blue lines indicate the signal from surface recombinations at different s_g values. The green lines represent the total signal caused by both sources: s_g = 6 ms^{-1} (solid line), s_g = 10 ms^{-1} (dashed line), and s_g = 14 ms^{-1} (dash-dotted line).

As shown in Figure 5, in plasma-opaque and thermally thin samples, carrier recombination does not alter the shape of the signal but does affect its maximum value (blue and green lines). When the parameter s_g is low (below 6 ms^{-1}), the contribution of recombination sources is negligible, and the signal is primarily determined by lattice thermalization (solid red and green lines). However, as s_g increases, recombination effects become more significant. For s_g = 14 ms^{-1}, recombination sources play a dominant role in temperature change (dash-dot green and blue lines in Figure 5).

From Figure 5, it can also be observed that the time-domain temperature signal for a thermally thin semiconductor sample reaches a steady value of zero after a time equal to $2T$. This indicates that the settling time is equal to twice the duration of the optical pulse.

In cases where the signal does not reach a peak during the pulse duration, it is not appropriate to work with parameters such as rising time or falling time; instead, it is much more suitable to consider the slope of the rising or falling curve. Figure 5 shows that the slopes of the rise after the leading edge of the excitation and the slope of the fall after the trailing edge of the pulse are equal and depend on the surface recombination velocities.

To investigate the impact of the charge carrier diffusivity (the semiconductor electronic property) on the shape of the time-domain temperature signal, Figure 6 presents the signal for a thermally thin and plasma-opaque p-doped Si sample (l_s = 140 µm, D_e = 3.6 × 10^{-3} m^{2}s^{-1}). The red line represents the signal resulting from lattice thermalization (fast heat source), while the blue lines indicate the signal from surface recombinations at different s_g values. The green lines show the total signal caused by both sources: s_g = 6 ms^{-1} (solid lines), s_g = 10 ms^{-1} (dashed lines), and s_g = 14 ms^{-1} (dash-dotted lines).

As seen in Figure 6, for the plasma-opaque and thermally thin p-doped sample, the recombination of charge carriers similarly affects the time domain temperature signal as in the n-doped sample (Figure 5). Specifically, it does not influence the shape or settling time, but it does impact the maximum value of the signal in the time domain (indicated by the blue and green lines in Figures 5 and 6) and the slopes of both the rising and falling curves.

However, in the case of the p-doped sample, minority carriers are electrons, which have a diffusion coefficient three times larger (as shown in Table 1). Therefore, at the same

surface recombination velocities, the dominance of recombination sources does not occur for the $s_g > 10$ ms^{-1} (Figure 6).

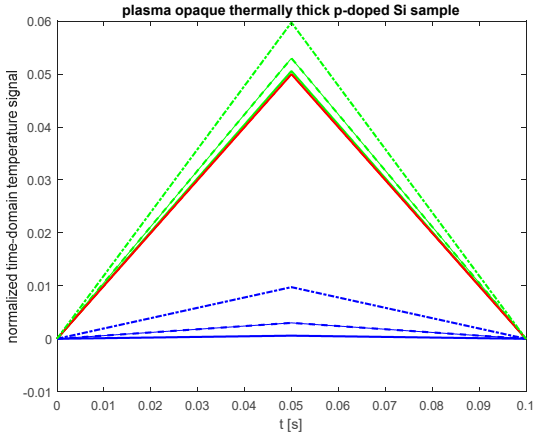

Figure 6. The normalized time-domain temperature signal for a thermally thin and plasma opaque p-doped silicon sample. The red line represents the signal resulting from lattice thermalization (fast heat source), while the blue lines indicate the signal from surface recombinations at different s_g values. The green lines represent the total signal caused by both sources: $s_g = 6$ ms^{-1} (solid line), $s_g = 10$ ms^{-1} (dashed line), and $s_g = 14$ ms^{-1} (dash-dotted line).

Based on this observation, it can be concluded that the slopes of the time-domain temperature signal—both the rising slope following the leading edge of the optical pulse and the falling slope following the trailing edge—are influenced by the electronic properties of the semiconductor, particularly the diffusion coefficient of the minority carriers. An increase in the diffusion coefficient results in a slower rise and fall of the signal and consequently a smaller maximum value for the same surface recombination velocities.

It is interesting to note that the results presented in Figures 5 and 6 indicate that the complex function describing the time-domain temperature signal in thermally thin and plasma-opaque samples (Equation (47)) can, in fact, be approximated by a linear function. The electronic parameters of silicon (such as the minority carrier lifetime and their diffusion coefficient) primarily influence the slope of the linear function.

Figure 7 illustrates the normalized time-domain temperature signal for a thermally thin and plasma-transparent n-doped silicon sample ($l_s = 20$ µm, $D_p = 1.2 \times 10^{-3}$ m^{2}s^{-1}). The red line represents the signal originating from the thermalization of the lattice (a fast heat source), while the blue lines show the signal resulting from surface recombinations for $s_b = 6$ ms^{-1} and various s_g values. The green lines depict the total signal generated by both sources ($s_g = 6$ ms^{-1} as a solid line and $s_g = 14$ ms^{-1} as a dashed line)

As seen in Figure 7, the time-domain temperature signal from the plasma-transparent sample behaves similarly to that of the plasma-opaque sample in terms of shape, settling time, and dependence on s_g. However, for the plasma-transparent sample, the slopes of both the rising and falling edges are also affected by the surface recombination velocity s_b. This results in a slower rise of the signal, leading to significantly lower maximum signal values when all other electronic and thermal parameters remain constant.

To further investigate the impact of s_b, Figure 8 presents the time-domain temperature signal for a thermally thin and plasma-transparent n-doped silicon sample ($l_s = 20$ µm, $D_p = 1.2 \times 10^{-3}$ ms^{-1}) with a fixed $s_g = 2$ ms^{-1}. The value of the surface recombination velocity on the unilluminated side, s_b, was varied. The red line indicates the signal resulting from thermalization of the lattice (a fast heat source), while the blue lines show the signal from surface recombinations for $s_g = 2$ m/s at different s_b values. The green lines represent

the total signal caused by both sources, with s_b = 6 ms^{-1} indicated by a solid line and s_b = 24 ms^{-1} by a dashed line.

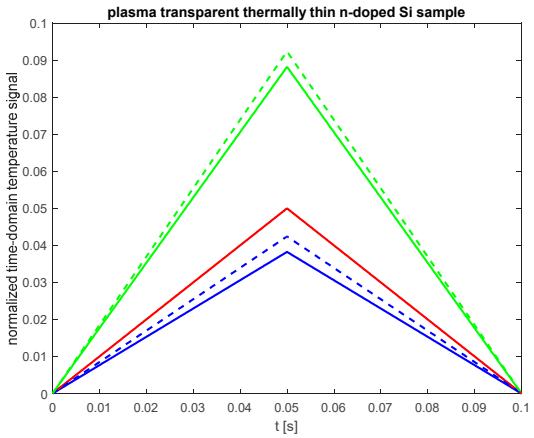

Figure 7. The normalized time-domain temperature signal for a thermally thin and plasma-transparent n-doped silicon sample (l_s = 20 µm, D_p = 1.2 × 10^{-3} m^{2}s^{-1}). The red line represents the signal originating from the thermalization of the lattice (a fast heat source), while the blue lines depict the signal resulting from surface recombinations for s_b = 6 m/s and various s_g values. The green lines illustrate the total signal produced by both sources, with s_g = 6 ms^{-1} represented by a solid line and s_g = 14 ms^{-1} by a dashed line.

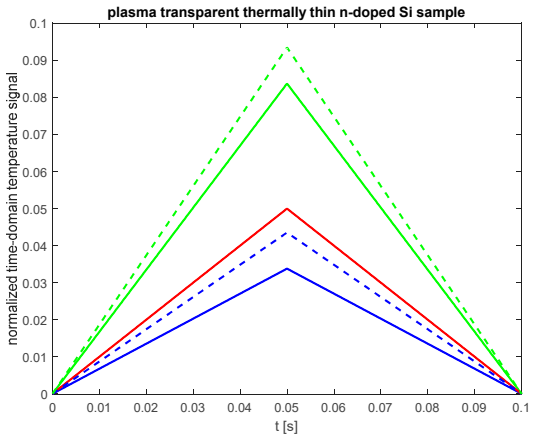

Figure 8. The normalized time-domain temperature signal for a thermally thin and plasma-transparent n-doped silicon sample (l_s = 20 µm, D_p = 1.2 × 10^{-3} m^{2}s^{-1}). The red line represents the signal originating from the thermalization of the lattice (a fast heat source), while the blue lines show the signal from surface recombinations for s_g = 2 ms^{-1} at different s_b values. The green lines depict the total signal caused by both sources, with s_b = 6 ms^{-1} indicated by a solid line and s_b = 24 ms^{-1} by a dashed line.

As seen in Figure 8, the increase in s_b influences both the slope of the time-domain temperature signal and the maximum value the signal reaches just before the falling edge of the optical pulse, similar to the effect observed with an increase in s_g.

Finally, Figure 9 presents the normalized time-domain temperature signal for a thermally thin and plasma-transparent p-doped Si sample (l_s = 20 µm, D_p = 3.6 × 10^{-3} ms^{-1}) at s_g = 2 ms^{-1}, s_b = 2 ms^{-1} and s_g = 24 ms^{-1}, s_b = 24 ms^{-1}. This analysis aims to investigate the influence of the electronic properties on the time-domain temperature signal of the thermally thin and plasma transparent semiconductor samples.

By comparing the results shown in Figures 6 and 8, it is evident that an increase in the diffusion coefficient of minority carriers—similar to the case of plasma-opaque samples—influences both the maximum value that the time-domain temperature signal can achieve during the pulse

duration and the steepness of the nearly linear rising and falling curves. However, this increase does not affect the settling time.

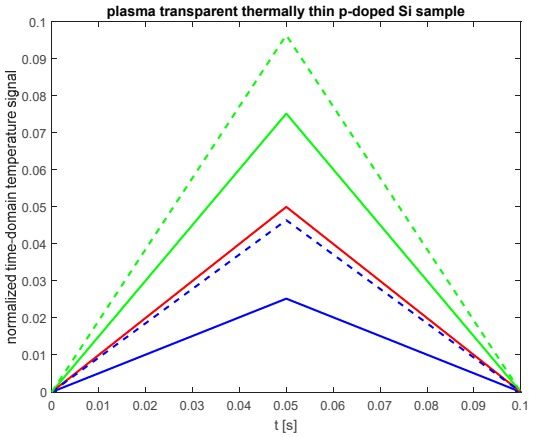

Figure 9. The normalized time-domain temperature signal for a thermally thin and plasma-transparent p-doped silicon sample. The red line represents the signal originating from the thermalization of the lattice (a fast heat source), while the blue lines denote signals resulting from surface recombinations at various values of s_g and s_b. The green lines indicate the total signal contributed by both sources, with the solid line corresponding to $s_g = 2$ ms^{-1} and $s_b = 2$ ms^{-1} and the dashed line corresponding to $s_g = 24$ ms^{-1} and $s_b = 24$ ms^{-1}.

4. Conclusions

In this paper, we developed a model to describe the temperature variation on the non-illuminated side of thermally thin semiconductor samples exposed to rectangular optical pulses. The model incorporates the effects of surface recombination of photo-generated charge carriers.

Using the derived expressions, we analyzed how recombination heat sources and the electronic properties of semiconductors influence the surface temperature response, with moderately doped n-type and p-type silicon as representative cases.

Our results demonstrate that, depending on the surface recombination velocity—which is strongly influenced by surface treatment methods—recombination heat sources can substantially affect both the amplitude of surface temperature changes and the dynamics of its rise and decay, particularly in plasma-opaque samples with high recombination velocity at the illuminated surface.

At low surface recombination velocities, lattice thermalization remains the dominant heating mechanism, and the contribution of recombination sources becomes negligible in thermally thin and plasma-opaque samples, especially for low recombination rates at the illuminated surface. In contrast, for plasma-transparent samples, recombination remains a non-negligible contributor to heating, regardless of surface recombination velocity.

Additionally, we show that the electronic properties of the semiconductor, particularly the minority carrier diffusion coefficient, affect the slopes of the temperature signal and its maximum value, but have little influence on the overall shape or settling time of the response.

These findings indicate that carrier recombination can significantly influence the thermal response at the non-illuminated surface and, consequently, the time-domain PA signal. The observed dependence of temperature dynamics on sample thickness, surface processing, and electronic transport parameters suggests that this method could be used to extract the electronic properties of semiconductor materials.

The developed model and conclusions of this study may be applied not only to improve the time-domain PA characterization of semiconductors but also in the broader

context of non-destructive time-resolved techniques for the electronic characterization of semiconductor materials, nanoelectronic devices, and sensors.

For a complete interpretation and accurate processing of experimentally recorded time-resolved PA signals in thin semiconductor membranes [23], further investigations are needed to fully understand the transformation of transient surface temperature changes into pressure fluctuations, and their subsequent conversion into detectable electrical signals. This remains an open challenge and a subject of our ongoing research.

Author Contributions: Conceptualization, S.P.G.; methodology, S.P.G.; software, S.P.G.; validation, S.P.G., M.N.P. and D.M.T.; formal analysis, S.P.G., D.K.M., D.D.M., K.L.D., M.N.P. and E.S., investigation, S.P.G., D.K.M., D.D.M., K.L.D., M.N.P., E.S. and D.M.T.; resources, S.P.G. and E.S.; data curation, S.P.G. and D.M.T.; writing—original draft preparation, S.P.G.; writing—review and editing, S.P.G., K.L.D., M.N.P. and D.M.T.; visualization, S.P.G. and K.L.D.; supervision, D.M.T. and E.S.; project administration, S.P.G. and E.S.; funding acquisition, S.P.G. and E.S. All authors have read and agreed to the published version of the manuscript.

Funding: This research was funded by the Ministry of Science, Technological Development and Innovations of the Republic of Serbia (Contract No. 451-03-136/2025-03/200017).

Institutional Review Board Statement: Not applicable.

Informed Consent Statement: Not applicable.

Data Availability Statement: The raw data supporting the conclusions of this article will be made available by the authors on request.

Acknowledgments: We would like to express our gratitude to ChatGPT with GPT-4o for its assistance in improving the clarity and coherence of the manuscript. However, it is important to emphasize that the authors retain full responsibility for all content, analyses, and conclusions presented in this work. The role of artificial intelligence in this context was limited to providing language enhancement and stylistic suggestions and does not imply that any part of the manuscript was generated by AI.

Conflicts of Interest: The authors declare no conflicts of interest.

Appendix A. Photogenerated Diffusion of Charge Carriers in Semiconductor

The equation describing the transport of photogenerated charge carriers in a semiconductor, under the low-level injection approximation, is a linear, one-dimensional spatial diffusion equation for minority carriers. By applying the Laplace transform, this equation is reduced to the second-order differential equation in the complex domain [12].

In the case where optical absorption occurs in a thin layer near the illuminated semiconductor surface (i.e., when the sample is optically opaque and has a high optical absorption coefficient), the transport problem of photogenerated charge carriers is described by the following system of homogeneous differential equations (Equations (A1) and (A2)), with inhomogeneous boundary conditions (Equations (A3) and (A4)) [34]:

$$\frac{d^2\overline{n}(x)}{dx^2} - \frac{1}{\overline{L}^2}\overline{n}(x) = 0 \tag{A1}$$

$$\overline{j}(x) = -D_{p/e}\frac{d\ \overline{n}(x)}{dx} \tag{A2}$$

$$\overline{j}(0) = \overline{G}(s) - s_g\overline{n}(0) \tag{A3}$$

$$\overline{j}(l_s) = s_b\overline{n}(l_s) \tag{A4}$$

In the above equations, $\overline{G}(s) = (S_0/E)\overline{F}(s)$ denotes the spectral function of the optically generated source of excess carriers, under the assumption that the semiconductor is optically opaque (it is important to note that the model is derived under the assumption of shallow optical penetration depth, meaning that the generation of charge carriers occurs within a spatially confined region near the illuminated surface—practically at the surface itself) [34].

By solving the problem described by Equations (A1)–(A4), the following expression for the spectral function of concentration distribution of photogenerated minority carriers is obtained:

$$\overline{n}(x) = \frac{S_0}{E}\overline{F}(s)\frac{\left(\frac{D_{e/p}}{\overline{L}} - s_b\right)e^{\frac{x-l_s}{\overline{L}}} + \left(\frac{D_{e/p}}{\overline{L}} + s_b\right)e^{-\frac{x-l_s}{\overline{L}}}}{\left(\frac{D_{e/p}}{\overline{L}} + s_g\right)\left(\frac{D_{e/p}}{\overline{L}} + s_b\right)e^{\frac{l_s}{\overline{L}}} - \left(\frac{D_{e/p}}{\overline{L}} - s_g\right)\left(\frac{D_{e/p}}{\overline{L}} - s_b\right)e^{-\frac{l_s}{\overline{L}}}} \tag{A5}$$

Based on Equation (A5), expressions describing the carrier concentrations at the semiconductor surfaces can be readily derived [34].

$$\overline{n}(0) = \frac{S_0}{E}\overline{F}(s)\frac{\left(\frac{D_{e/p}}{\overline{L}} - s_b\right)e^{-\frac{l_s}{\overline{L}}} + \left(\frac{D_{e/p}}{\overline{L}} + s_b\right)e^{\frac{l_s}{\overline{L}}}}{\left(\frac{D_{e/p}}{\overline{L}} + s_g\right)\left(\frac{D_{e/p}}{\overline{L}} + s_b\right)e^{\frac{l_s}{\overline{L}}} - \left(\frac{D_{e/p}}{\overline{L}} - s_g\right)\left(\frac{D_{e/p}}{\overline{L}} - s_b\right)e^{-\frac{l_s}{\overline{L}}}} \tag{A6}$$

$$\overline{n}(l_s) = \frac{S_0}{E}\overline{F}(s)\frac{2\frac{D_{e/p}}{\overline{L}}}{\left(\frac{D_{e/p}}{\overline{L}} + s_g\right)\left(\frac{D_{e/p}}{\overline{L}} + s_b\right)e^{\frac{l_s}{\overline{L}}} - \left(\frac{D_{e/p}}{\overline{L}} - s_g\right)\left(\frac{D_{e/p}}{\overline{L}} - s_b\right)e^{-\frac{l_s}{\overline{L}}}} \tag{A7}$$

In this work, we analyzed two asymptotic cases—the plasma-opaque and the plasma-transparent semiconductor sample—using an analogy with propagation processes. If the complex frequency is written as $s = j\omega$ (stationary propagation), where the symbol j denotes the imaginary unit, the real part of the inverse of the complex propagation coefficient (Equation (34)) corresponds to the diffusion length of charge carriers [34,50].

$$\mathrm{Re}\left\{\frac{1}{\overline{L}}\right\} = \mu(\omega) = \sqrt{\frac{2D_{e/p}\tau}{1+\sqrt{1+\omega^2\tau^2}}} \tag{A8}$$

As can be seen from Equation (A8), the carrier diffusion length depends on the frequency of the harmonic excitation. As the frequency increases, the diffusion length decreases to zero, while for a frequency of zero, it reaches its maximum value [34,50]:

$$\mu_{\max} = \sqrt{D_{e/p}\tau} \tag{A9}$$

If the sample thickness is much greater than the maximum diffusion length ($l_s/\mu(\omega) >> 1$), the sample is plasma opaque. Conversely, if the sample thickness is smaller than the maximum diffusion length ($l_s/\mu(\omega) < 1$), the sample is plasma transparent [34].

Following the results of [34], in the case of optically opaque samples, Equations (A6) and (A7) can be reduced, and the theoretical model of surface recombination heat sources is described by Equations (52) and (63) in the paper.

Appendix B. Inverse Laplace Transform: Method of Partial Fraction and Irrational Function

To obtain the evolution of a function $f(t)$, given its spectral function $\overline{F}(s)$, one should solve the inverse Laplace transform. The inverse Laplace transform of functions of a complex argument is defined as follows [63,64]:

$$f(t) = L^{-1}\{\overline{F}(s)\}(t) = \frac{1}{2\pi j}\lim_{T\to\infty}\int_{\beta-jT}^{\beta+jT} e^{sT}\overline{F}(s)ds \tag{A10}$$

where $s = \alpha + j\omega$ is complex plane and α is a real number greater than the real part of all singularities of $\overline{F}(s)$.

The integral formula given by Equation (A10) is called the Bromwich integral, also known as Mellin's inverse formula or the Fourier–Mellin integral. In many cases, the complex integral can be evaluated using the Cauchy residue theorem.

In practice, it is not necessary to solve the complex integral given by Equation (A10). Instead, existing tables of inverse Laplace transforms can be used [65,66], along with various methods of representing a complex function in forms for which Bromowich integral solutions are known, such as method partial fractions for rational functions of complex argument s [34,65].

For solving the inverse Laplace transform of the irrational function obtained in this study, the known solutions given in table bellow were used [65].

Complex Function	Inverse Laplace Transform
$\frac{1}{\sqrt{s}+b}$	$\frac{1}{\sqrt{\pi t}} - be^{b^2t}erfc(b\sqrt{t})$

Additionally, the following properties of the Laplace transform were used [67–69]:

$$L^{-1}\{\overline{F}(s+a)\} = e^{-at}f(t) \tag{A11}$$

$$L^{-1}\{\overline{F}(s)\overline{G}(s)\} = \int_0^t f(t-t')g(t')dt' \tag{A12}$$

References

1. Zakrzewski, J.; Pawlak, M.; Matsuda, O.; Todorovic, D.; Liu, J. Semiconductor physics: Plasma, thermal, elastic, and acoustic phenomena. *J. Appl. Phys.* **2024**, *136*, 120401. [CrossRef]
2. Miranda, L.C.M. Theory of the photoacoustic effect in semiconductors influence of carrier diffusion and recombination. *Appl. Opt.* **1982**, *21*, 2923–2928. [CrossRef] [PubMed]
3. Isaiev, M.; Kuryliuk, V.; Kuzmich, A.; Burbelo, R. Photothermal Transformation In Heterogeneous Semiconductors Structures Under Its Pulse Laser Irradiation: Role of Electron-Hole Diffusion. *Arch. Metall. Mater.* **2013**, *58*, 1351–1354. [CrossRef]
4. Lishchuk, P.; Andrusenko, D.; Isaiev, M.; Lysenko, V.; Burbelo, R. Investigation of Thermal Transport Properties of Porous Silicon by Photoacoustic Technique. *Int. J. Thermophys.* **2015**, *36*, 2428–2433. [CrossRef]
5. Bychto, L.; Maliński, M.; Chrobak, L.; Zakrzewski, J.; Boumhamdi, M. Investigations of optical and thermal properties of surface layers of Cd1−xBexTe samples by the photoacoustic method. *Opto-Electron. Rev.* **2024**, *32*, e150186. [CrossRef]
6. Zakrzewski, J.; Maliński, M.; Bachiri, A.; Strzałkowski, K. Photothermal determination of the optical and thermal parameters of CdxZn1-xSe mixed crystals. *J. Mater. Sci. Eng. B* **2021**, *271*, 115305. [CrossRef]
7. Todorovic, D.M.; Cretin, B.; Song, Y.Q.; Vairac, P. Photothermal elastic vibration method: Investigation of the micro-electro-mechanical-systems. *J. Phys. Conf. Ser.* **2010**, *214*, 012105. [CrossRef]
8. Cyr, B.; Sumaria, V.; Long, Y.; Tadigadapa, S.; Sugawara, T.; Fu, K. How Lasers Exploit Photoacoustic and Photoelectric Phenomena to Inject Signals into MEMS Microphones. *Preprint* **2024**. [CrossRef]

9. Pawlak, M.; Pal, S.; Ludwig, A.; Wieck, A.D. On the infrared absorption coefficient measurement of thick heavily Zn doped GaAs using spectrally resolved modulated photothermal infrared radiometry. *J. Appl. Phys.* **2017**, *122*, 135109. [CrossRef]
10. Bialkowski, S.E.; Astrath, N.G.C.; Proskurnin, M.A. *Photothermal Spectroscopy Methods*; John Wiley & Sons: Hoboken, NJ, USA, 2019.
11. Vargas, H.; Miranda, L.C.M. Photoacoustic and related photothermal techniques. *Phys. Rep.* **1988**, *161*, 43–101. [CrossRef]
12. Escamilla-Herrera, L.F.; Derramadero-Domínguez, J.M.; Medina-Cázares, O.M.; Alba-Rosales, J.E.; García-Rodríguez, F.J.; Gutiérrez-Juárez, G. On the dual-phase-lag thermal response in the pulsed photoacoustic effect: A theoretical and experimental 1D-approach. *J. Appl. Phys.* **2024**, *136*, 175105. [CrossRef]
13. Neprokin, A.; Broadway, C.; Myllyla, T.; Bykov, A.; Meglinski, I. Photoacoustic Imaging in Biomedicine and Life Sciences. *Life* **2022**, *12*, 588. [CrossRef] [PubMed]
14. Park, H.K.; Grigoropoulos, C.P.; Tam, A.C. Optical measurements of thermal diffusivity of a material. *Int. J. Thermophys.* **1995**, *16*, 973–995. [CrossRef]
15. Bertolotti, M.; Li Voti, R. A note on the history of photoacoustic, thermal lensing, and photothermal deflection techniques. *J. Appl. Phys.* **2020**, *128*, 230901. [CrossRef]
16. Skvortsov, L.A. Laser photothermal spectroscopy of light-induced absorption. *Quantum Electron.* **2013**, *43*, 1–13. [CrossRef]
17. Zakrzewski, J.; Maliński, M.; Chrobak, Ł.; Pawlak, M. Comparison of Theoretical Basics of Microphone and Piezoelectric Photothermal Spectroscopy of Semiconductors. *Int. J. Thermophys.* **2017**, *38*, 2. [CrossRef]
18. Todorović, D.M.; Nikolić, P.M. Chapter 9—Carrier Transport Contribution to Thermoelastic and Electronic Deformation in Semiconductors. In *Semiconductors and Electronic Materials Progress in Photothermal and Photoacoustic, Science and Technology*; Optical Engineering Press: New York, NY, USA, 2000; Volume PM74, pp. 273–318; ISBN 9780819435064.
19. Sarode, A.P.; Mahajan, O.H. Theoretical Aspects of Photoacoustic Effect with Solids: A Review. *Int. J. Sci. Adv. Res. Technol.* **2018**, *4*, 1237–1242.
20. Telenkov, S.; Mandelis, A. Signal-to-noise analysis of biomedical photoacoustic measurements in time and frequency domains. *Rev. Sci. Inst.* **2010**, *81*, 124901. [CrossRef]
21. Lashkari, B.; Mandelis, A. Comparison between pulsed laser and frequency-domain photoacoustic modalities: Signal-to-noise ratio, contrast, resolution, and maximum depth detectivity. *Rev. Sci. Inst.* **2011**, *82*, 094903. [CrossRef]
22. Galovic, S.P.; Stanimirovic, Z.; Stanimirovic, I.; Djordjevic, K.L.; Milicevic, D.; Suljovrujic, E. Time-resolved photoacoustic response of thin solids measured using minimal volume cell. *Int. Commun. Heat Mass Transf.* **2024**, *155*, 107574. [CrossRef]
23. Djordjevic, K.L.; Galovic, S.P.; Nesic, M.V.; Todorovic, D.M.; Popovic, M.N.; Markushev, D.D.; Markushev, D.K. Transmission pulse photoacoustic set-up for characterization of solids. In Proceedings of the 21st International Symposium INFOTEH-JAHORINA, East Sarajevo, Bosnia and Herzegovina, 16–18 March 2022.
24. Gärtner, W.W. Photothermal Effect in Semiconductors. *Phys. Rev.* **1961**, *122*, 419–424. [CrossRef]
25. Fournier, D.; Boccara, C.; Skumanich, A.; Amer, N.M. Photothermal investigation of transport in semiconductors: Theory and experiment. *J. Appl. Phys.* **1986**, *59*, 787–795. [CrossRef]
26. Forgot, B.C.; Fournier, D. Photothermal characterization of semiconductors. In *Progress in Photothermal and Photoacoustic Science and Technology*; Mandelis, A., Hess, P., Eds.; SPIE Press: Washington, DC, USA, 2000; Chapter 7, Volume 4, p. 200. ISBN 9780819435064.
27. Stanimirović, Z.; Stanimirović, I.; Galović, S.; Djordjević, K.; Suljovrujić, E. Transmission pulse photoacoustic response of thin semiconductor plate. *J. Appl. Phys* **2023**, *133*, 195701. [CrossRef]
28. Titov, O.Y.; Gurevich, Y.G. Recombination and temperature distribution in semiconductors. *Semicond. Sci. Technol.* **2012**, *27*, 055014. [CrossRef]
29. Titov, O.Y.; Gurevich, Y.G. Temperature gradient and transport of heat and charge in a semiconductor structure. *J. Low Temp. Phys.* **2021**, *47*, 550–554. [CrossRef]
30. Sobolev, S.L. Nonlocal two-temperature model: Application to heat transport in metals irradiated by ultrashort laser pulses. *Int. J. Heat Mass Transf.* **2016**, *94*, 138–144. [CrossRef]
31. Sobolev, S.L.; Dai, W. Heat Transport on Ultrashort Time and Space Scales in Nanosized Systems: Diffusive or Wave-like? *Materials* **2022**, *15*, 4287. [CrossRef]
32. Mandelis, A. Laser infrared photothermal radiometry of semiconductors: Principles and applications to solid state elec-tronics. *Solid-State Electron.* **1998**, *42*, 1–15. [CrossRef]
33. Rojas-Trigos, J.B.; Calderón, A.; Marín, E.A. Practical model for the determination of transport parameters in semiconductors. *J. Mater. Sci.* **2011**, *46*, 7799–7805. [CrossRef]
34. Galovic, S.; Djordjevic, K.; Dragas, M.; Milicevic, D.; Suljovrujic, E. Dynamics of Photoinduced Charge Carrier and Photothermal Effect in Pulse-Illuminated Narrow Gap and Moderate Doped Semiconductors. *Mathematics* **2025**, *13*, 258. [CrossRef]
35. Wang, S. *Fundamentals of Semiconductor Theory and Device Physics*; Prentice Hall, Inc.: Hoboken, NJ, USA, 1989; ISBN 0-13-344425-2.

36. Galovic, S.P.; Djordjevic, K.L.; Nesic, M.V.; Popovic, M.N.; Markushev, D.D.; Markushev, D.K.; Todorovic, D.M. Time-domain minimum-volume cell photoacoustic of thin semiconductor layer. I. Theory. *J. Appl. Phys.* **2023**, *133*, 245701. [CrossRef]
37. Sablikov, V.A.; Sandomirskii, V.A. The Photoacoustic Effect in Semiconductors. *Phys. Status Solidi (b)* **1983**, *120*, 471–480. [CrossRef]
38. Balderas-Lopez, J.A.; Mandelis, A. Thermal diffusivity measurements in the photoacoustic open-cell configuration using simple signal normalization techniques. *J. Appl. Phys.* **2001**, *90*, 2273–2279. [CrossRef]
39. Stanimirović, I.; Markushev, D.; Stanimirović, Z.; Galović, S.; Djordjević, K. Analysis of plasma-elastic component of time-domain photoacoustic response. *J. Appl. Phys.* **2023**, *133*, 235701. [CrossRef]
40. Aberle, A.G. Surface passivation of crystalline silicon solar cells: A review. *Prog. Photovolt. Res. Appl.* **2000**, *8*, 473–487. [CrossRef]
41. Carslaw, H.S.; Jaeger, J.C. *Conduction of Heat in Solids*; Oxford University Press: Oxford, UK, 1959; ISBN 0198533683.
42. McCord Morse, P.; Feshbach, H. *Methods of Theoretical Physics*; McGraw-Hill: New York, NY, USA, 1953; ISBN 0070433178/9780070433175.
43. Galovic, S.; Soskic, Z.; Popovic, M. Analysis of Photothermal Response of Thin Solid Films By Analogy with Passive Linear Electric Networks. *Therm. Sci.* **2009**, *13*, 129–142. [CrossRef]
44. Maillet, D.; André, C.; Batsale, J.-C.; Degiovanni, A.; Moyne, C. *Thermal Quadrupoles, Solving the Heat Equation Through Integral Transforms*; John Wiley and Sons: Hoboken, NJ, USA, 2000; ISBN 0 471 98320 9.
45. Suszyński, Z. Thermal model based on the electrical analogy of the thermal processes. In Proceedings of the 10th International Conference on Photoacoustic and Photothermal Phenomena, Rome, Italy, 23–27 August 1998; pp. 197–199.
46. Chen, G.; Hui, P. Pulsed photothermal modeling of composite samples based on transmission-line theory of heat conduction. *Thin Solid Films* **1999**, *339*, 58–67. [CrossRef]
47. Krapez, J.C.; Dohou, E. Thermal quadrupole approaches applied to improve heat transfer computations in multilayered materials with internal heat sources. *Int. J. Therm. Sci.* **2014**, *81*, 38–51. [CrossRef]
48. Pailhes, J.; Pradere, C.; Battaglia, J.L.; Toutain, J.; Kusiak, A.; Aregba, W.; Batsale, J.C. Thermal quadrupole method with internal heat sources. *Int. J. Therm. Sci.* **2012**, *53*, 49–55. [CrossRef]
49. Salazar, A.; Celorrio, R. Application of the thermal quadrupole method to the propagation of thermal waves in multilayered cylinders. *J. Appl. Phys.* **2006**, *100*, 113535. [CrossRef]
50. Nestoros, M. Photothermal Techniques in Material Characterization. In *Materials Science—Advanced Topics*; Mastai, Y., Ed.; InTech: London, UK, 2013; Chapter 14. [CrossRef]
51. Pichardo-Molina, J.L.; Alvarado-Gil, J.J. Heat diffusion and thermolastic vibration influence on the signal of an open photoacoustic cell for two layer systems. *J. Appl. Phys.* **2004**, *95*, 6450–6456. [CrossRef]
52. Rousset, G.; Lepoutre, F.; Bertrand, L. Influence of thermoelastic bending on photoacoustic experiments related to measurements of thermal diffusivity of metals. *J. Appl. Phys.* **1983**, *54*, 2383–2391. [CrossRef]
53. Rosencwaig, A.; Gersch, A. Theory of the photoacoustic effect with solids. *J. Appl. Phys.* **1976**, *47*, 64–69. [CrossRef]
54. McDonald, F.A.; Wetsel, G.C. Generalized theory of the photoacoustic effect. *J. Appl. Phys.* **1978**, *49*, 2313–2322. [CrossRef]
55. Bonno, B.; Zeninari, V.; Joly, L.; Parvitte, B. Study of a Thermophysical System with Two Time Constants Using an Open Photoacoustic Cell. *Int. J. Thermophys.* **2011**, *32*, 630–640. [CrossRef]
56. Tam, A.C. Applications of photoacoustic sensing techniques. *Rev. Mod. Phys.* **1986**, *58*, 381–431. [CrossRef]
57. Bein, B.K.; Pelzl, J. Theory of signal generation in a photoacoustic cell. *J. Phys.-Colloq.* **1983**, *44*, C6-27–C6-34. [CrossRef]
58. Mandelis, A.; Royce, B.S.H. Time-domain photoacoustic spectroscopy of solids. *J. Appl. Phys.* **1979**, *50*, 4330–4338. [CrossRef]
59. Mandelis, A.; Royce, B.S.H. Relaxation time measurements in frequency and time-domain photoacoustic spectroscopy of condensed phases. *J. Opt. Soc. Am.* **1980**, *70*, 474–480. [CrossRef]
60. Domanowska, R.; Bukowski, J. Theoretical Analysis of Pulsed Photoacoustic Effect in Solids. *Int. J. Thermophys.* **2009**, *30*, 1536–1556. [CrossRef]
61. Volovichev, I.N.; Logvinov, G.N.; Titov, O.Y.; Gurevich, Y.G. Recombination and lifetimes of charge carriers in semiconductors. *J. Appl. Phys.* **2004**, *95*, 4494–4496. [CrossRef]
62. Adachi, S. *The Handbook on Optical Constants of Semiconductors: In Tables and Figures*; World Scientific Publishing: Singapore, 2006; ISBN 978-981-4405-97.
63. Davies, B.J. *Integral Transforms and Their Applications*; Springer: Berlin, Germany; New York, NY, USA, 2002; ISBN 978-0-387-95314-4.
64. Available online: https://eqworld.ipmnet.ru/en/auxiliary/aux-inttrans.htm (accessed on 2 April 2004).
65. Chen, Y.Q.; Petras, L.; Vinagre, B.M. A List of Laplace and Inverse Laplace Transforms Related to Fractional Order Calculus. Available online: https://ivopetras.tripod.com/foc_laplace.pdf (accessed on 30 November 2001).
66. Oberhettinger, F.; Badii, L. *Tables of Laplace Transforms*; Springer: Berlin/Heidelberg, Germany, 1973; ISBN 978-3-642-65645-3.
67. Stojic, M. *Continuous System of Automatic Control*; Naucna Knjiga-Komerc: Belgrade, Serbia, 1991. (In Serbian)

68. Lynn, P.A. The Laplace Transform and the z-transform. In *Electronic Signals and Systems*; Macmillan Education: London, UK, 1986; pp. 225–272. ISBN 978-0-333-39164-8. [CrossRef]
69. Galovic, S.; Djordjević, A.; Djordjević, K. Analytical Solution of the Inverse Laplace Transform for Combined Shifted Quasi-Rational Radical Functions of Power 1/2 with a Decaying Potential Term. *J. Comput. Appl. Math.* 2025; *under review*.

International Journal of Thermophysics (2024) 45:107
https://doi.org/10.1007/s10765-024-03406-3

The Influence of Excess Free Carriers as Heat Carriers on the *n*-Type Silicon Thermoelastic Photoacoustic Responses Explained by Electro-Acoustic Analogies

D. K. Markushev[1] · N. Branković[2] · S. M. Aleksić[2] · D. S. Pantić[2] · S. P. Galović[3] · D. D. Markushev[1] · J. Ordonez-Miranda[4]

Received: 12 June 2024 / Accepted: 3 July 2024

Abstract

The explanation of the *n*-type silicon thermoelastic photoacoustic response is given by electro-acoustic analogies, which clarify the influence of excess free carriers as heat carriers. It was found that electro-acoustic analogies could interconnect different theoretical models of heat flow and carrier dynamics aiming to find the optimal experimental conditions for the efficient free carrier influence analysis of the sample thermoelastic photoacoustic response. Theoretical analysis was based on the comparison between the composite piston, surface recombination, and *RC* filter frequency response models, extrapolating the behavior of the photoacoustic response much beyond the experimental frequency domain. Experimental analysis was based on the open-cell photoacoustic setup operating under the transmission configuration within the modulation frequencies range from 20 Hz to 20 kHz. The accuracy of our predictions and the validity of electro-acoustic analogies are confirmed by measuring 875 μm plasma-thick and 35 μm plasma-thin silicon samples.

Keywords Electro-acoustic analogies · Excess carriers · Lead compensator · Photoacoustics · *RC* filtering · Thermoelastic response

✉ D. K. Markushev
dragana.markusev@ipb.ac.rs

[1] Institute of Physics, University of Belgrade, Pregrevica 118, 11080 Belgrade-Zemun, Serbia

[2] Faculty of Electronic Engineering, University of Niš, Aleksandra Medvedeva 14, 18000 Niš, Serbia

[3] Vinča Institute of Nuclear Sciences, P.O. Box 522, 11001 Belgrade, Serbia

[4] LIMMS, CNRS-IIS IRL 2820, The University of Tokyo, Tokyo 153-8505, Japan

Published online: 11 July 2024

1 Introduction

Within the framework of photothermal sciences, photoacoustics is established as a very sensitive and convenient nondestructive method for investigating thermal and electronic transport in semiconductor materials and micro- and nanostructures based on them [1–9]. Special attention has been paid to the generation and dynamics of excess carriers as well as to their participation in thermal transport processes that profile the thermal states of the investigated samples [10–14]. By using an open-cell photoacoustic setup with a simply supported circular plate sample, we observed that it is possible to measure the effects of excess carriers, for modulation frequencies from 20 Hz to 20 kHz. In our recent photoacoustic studies of *n*-type silicon [14–17], we found that the influence of excess carriers, acting as heat carriers, can be observed in the amplitude and phase patterns of both the total photoacoustic signal and its components at higher modulation frequencies and thin samples. Those patterns show up for silicon thicknesses around the excess free carrier diffusion length L_p, the average distance that carrier can diffuse before recombination (see Appendix I). This is the reason why we introduced the division into the so-called a) plasma-thick and b) plasma-thin semiconductors, whose thickness l is larger $\left(l > L_p\right)$, or smaller $\left(l < L_p\right)$ than L_p, respectively. For plasma-thick samples, the frequency dependence of the amplitude and phase patterns of the photoacoustic signal are the same as the corresponding ones in absence of excess carriers. On the contrary, the photoacoustic amplitude and phase of plasma-thin samples are strongly driven by excess carriers [14, 17].

A particularly interesting case of heat transport in semiconductors driven by excess carriers is visible in the frequency response of the thermoelastic photoacoustic signal component [18]. For plasma-thin samples, its amplitude strongly decreases at low frequencies, forming a peak-like shape at higher ones. These features are absent in plasma-thick samples [14, 17]. On the other hand, our latest results show that any thermoelastic response of a photoacoustic system without the influence of excess carriers can be described, through electro-acoustic analogies, by the transfer functions of a low-pass *RC* filter [19]. In such a way, the analogies between different parameters, such as the photoacoustic signal (amplitude and phase), thermal characteristics of the sample (temperature, heat flux, thermal conductivity, heat capacity), and electrical parameters of the filter (voltage, current, resistance, capacitance), could be established [20]. By analyzing the amplitudes and phases of the silicon thermoelastic response, using transfer functions of the *RC* low-pass filter (which takes into account surface absorption and no excess carriers), it is possible to identify some characteristic cut-off frequencies. These frequencies can be used to create a calibration curve for the material being investigated. This approach demonstrates how electro-acoustic analogies can enhance photoacoustic measurement techniques and provide a better understanding of cut-off frequencies.

In this study, we have used electro-acoustic analogies to create a method for understanding the behavior of the *n*-type silicon thermoelastic response under the

presence of excess carriers. This method enables one to find optimal experimental conditions to measure the surface recombination effects, most significant effects of free carriers as heat carriers in semiconductors. To analyze plasma-thick samples, we have used a low-pass *RC* filter with a characteristic cut-off frequency that depends on the thickness of the sample. For plasma-thin samples, we have used a cascade connection of the low-pass *RC* filter and lead compensator, which has additional characteristic frequencies connected to the surface lifetime of the excess carriers and their recombination speeds on both illuminated and non-illuminated sample surfaces. We have experimentally confirmed our results by measuring both plasma-thick and plasma-thin samples of the same material using a standard open-cell photoacoustic setup operating under the transmission configuration.

2 Theoretical Background

2.1 Photoacoustic Response

The simplest explanation of the photoacoustic response in solids relies on the composite piston model (thermal and mechanical) and the setup geometry presented in Fig. 1. The sample, presented as a homogeneous and circular thin plate of thickness l and radius R_s $\left(l \ll R_s\right)$, is heated up with the modulated (sinusoid) light beam having the intensity $I = I_0\exp(-j\omega t)$, where j is an imaginary unit, t is the time, and $\omega = 2\pi f$, where f is the modulation frequency. Assuming that the light source spot is greater than R_s, allows one to consider that heat propagates mainly along the x -axis—1D case.

The total photoacoustic signal $\delta p_{total}(j\omega)$, generated by a sample and detected by a microphone membrane M (Fig. 1), is theoretically described as a combination of thermal and mechanical piston responses resulting from the thermal state changes of the sample and the surrounding gas (air) [21–25]. A thermal piston generates a thermodiffusion response, the so-called thermodiffusion component $\delta p_{TD}(j\omega)$ of the total photoacoustic signal,

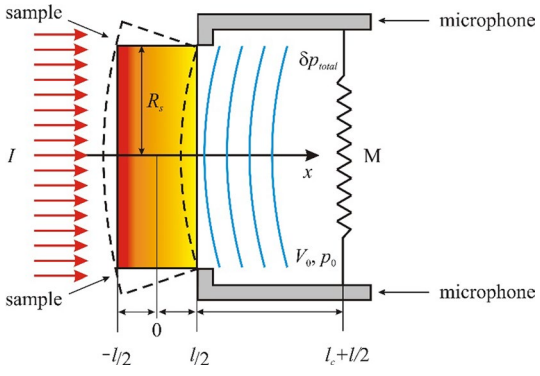

Fig. 1 Simple scheme of the photoacoustic setup under consideration

while a mechanical piston generates a thermoelastic response, the so-called thermoelastic component $\delta p_{TE}(j\omega)$ of the total photoacoustic signal. In the case of semiconductors, the mechanical piston generates an additional plasmaelastic response caused by excess free carrier influence, the so-called plasmaelastic component $\delta p_{PE}(j\omega)$ of the total photoacoustic signal. It is important to keep in mind that excess free carriers affect the behavior of all three components in completely different ways. In $\delta p_{TD}(j\omega)$ and $p_{TE}(j\omega)$, excess free carriers impact temperature distributions as heat carriers, while their influence as charged particles is ignored. In $p_{PE}(j\omega)$, their influence is primarily through their properties as charged particles, while their role as heat carriers is ignored (their influence on temperature distributions is not considered). Typically, the $\delta p_{total}(j\omega)$ is represented as the sum of its independent components [14–17]:

$$\delta p_{total}(j\omega) = \delta p_{TD}(j\omega) + \delta p_{TE}(j\omega) + \delta p_{PE}(j\omega) \tag{1}$$

Analytical expressions of all $\delta p_{total}(j\omega)$ components are given in the form [14–17, 21–25]:

$$\delta p_{TD}(j\omega) = \frac{\gamma_g p_0 \sqrt{D_g}}{l_c T_0 \sqrt{j\omega}} T_s(l/2) \tag{2}$$

$$\delta p_{TE}(j\omega) = 3\pi \frac{\gamma_g p_0 \alpha_T R_s^4}{l^3 V_0} \int_{-\frac{l}{2}}^{\frac{l}{2}} x T_s(x) dx \tag{3}$$

$$\delta p_{PE}(j\omega) = 3\pi \frac{\gamma_g p_0 d_n R_s^4}{l^3 V_0} \int_{-\frac{l}{2}}^{\frac{l}{2}} x \delta n_p(x) dx, \tag{4}$$

where γ_g is the adiabatic ratio of the gas (air) in the cell, p_0 and T_0 are the ambient pressure and temperature, respectively, l_c is the cell length, D_g is the sample thermal diffusivity, α_T is the sample coefficient of linear expansion, $T_s(l/2)$ is the sample temperature variation at non-illuminated surface, $T_s(x)$ is the sample temperature variation distribution along the heat propagation axes, d_n is the coefficient of electronic deformation, and $\delta n_p(x)$ is the minority excess carrier density (holes, p, in the case of n-type silicon) along the propagation axes. As complex numbers, the responses of the total signal and its components are usually represented by their amplitudes and phases in the frequency domain.

Obviously, Eq. 4 is obtained after $\delta n_p(x)$ calculation using the theoretical model presented in Appendix I. Equations 2 and 3 are obtained after knowing the temperature variations $T_s(x)$ inside the sample of thickness l. The explicit expressions of $T_s(x)$ for (i) a surface absorber without excess carriers, $T_s(x) = T_{s,a}(x)$, and (ii) a volume absorber under the influence of excess carriers, $T_s(x) = T_{s,b}(x)$, are derived in the Appendix II.

2.2 Surface Recombination

The electron–hole recombination process occurs in the bulk as well as on both surfaces of the sample giving up the energy to produce heat. The surfaces play an important role in recombination of free carriers and temperature variations of the semiconductor samples [14–17, 26–28]. Any defects or impurities within or at the sample surface promote recombination. Recombination at the surfaces is usually described by a surface recombination lifetime τ_s, which is a function of the surface recombination velocities s_1 at illuminated, and s_2 at non-illuminated surface, the sample thickness l, and the minority carrier diffusivity D_p. Our earlier research showed that the states of semiconductor surfaces define the dynamics of heat flow in it. It turns out that the most interesting case of studying the influence of excess carriers as heat carriers on the photoacoustic response (especially thermoelastic) is the one that implies $s_1 \to 0$ and $s_2 \gg s_1$. In this work, we investigate how τ_s, more precisely, the surface recombination frequency $f_s = 1/(2\pi\tau_s)$ affects the thermoelastic photoacoustic response. For this purpose, we use the approximate expression for f_s, given by (see Appendix III) [27, 28]:

$$f_s = \frac{(s_1 + s_2)D_p + s_1 s_2 l}{2\pi D_p l} \tag{5}$$

For plasma-thick samples of n-type silicon excited with red light and $s_2 \gg s_1 (s_1 \to 0)$, the heat flow is driven by the temperature variations on the front (illuminated) side: $T_{s,b}(x) \to T_{\text{therm}}(x) \to T_{s,a}(x)$ [29]. In plasma-thin samples, the heat flow is determined by the temperature variations on the back (non-illuminated) side: $T_{s,b}(x) \to T_{\text{therm}}(x) + T_{\text{sr}}(x)$ [29]. Such spatial distribution of temperature is a direct consequence of the surfaces state of the sample, where the illuminated front is passivated (small value of s_1), and the unilluminated back is not (large value of s_2) [29]. In other words, the back surface serves as a heat reservoir: in the case of plasma-thin samples, intensive recombination of carriers occurs on it, which leads to the release of a larger amount of heat and an increase in the temperature on that surface.

2.3 Thermoelastic response

Recently, we showed that the thermoelastic response of n-type silicon is very sensitive to the influence of excess carriers, which can be seen on the frequency spectra of the amplitude and phase (they take the shape of resonant peaks) of $\delta p_{\text{TE}}(j\omega)$ for plasma-thin samples [14, 17, 29]. Combining Eq. (3) and the assumption of the volume absorber $(T_s(x) = T_{s,b}(x), \text{Eq.(A2.2)})$, one can calculate, using parameters from Table 1, the corresponding amplitudes $|\delta p_{TE}(j\omega)|$ and phases $< (\delta p_{TE}(j\omega))$ in modulation frequency f domain, as a function of sample thickness, l,. Obtained results are presented in Fig. 2. Note that the thermoelastic responses of a plasma-thick sample $(l > L_p)$, $\delta p_{TE,1}(j\omega)$, are the same as the

Table 1 Si *n*-type sample parameters at $T_{amb}=300$ K and $\lambda=660$ nm [14, 17]

Lifetime of minority carriers	$\tau_p=6\mu s$	Coefficient of minority carrier diffusion	$D_p=12\ cm^2 \bullet s^{-1}$
Density	$\rho=2.33\times10^3\ kg \bullet m^{-3}$	Specific heat	$c=715\ J \bullet kg^{-1} \bullet K^{-1}$
Thermal conductivity	$k=150\ W \bullet m^{-1} \bullet K^{-1}$	Thermal diffusivity	$D_T=0.90\ cm^2 \bullet s^{-1}$
Linear thermal expansion	$\alpha_T=2.60\times10^{-6}\ K^{-1}$	Optical absorption coefficient	$\beta=0.258\mu m^{-1}$
Excitation energy	$\varepsilon=1.88$ eV	Energy gap	$\varepsilon_g=1.12$ eV
Front surface recombination velocity	$s_1=2\ m \bullet s^{-1}$	Rear surface recombination velocity	$s_2=24\ m \bullet s^{-1}$

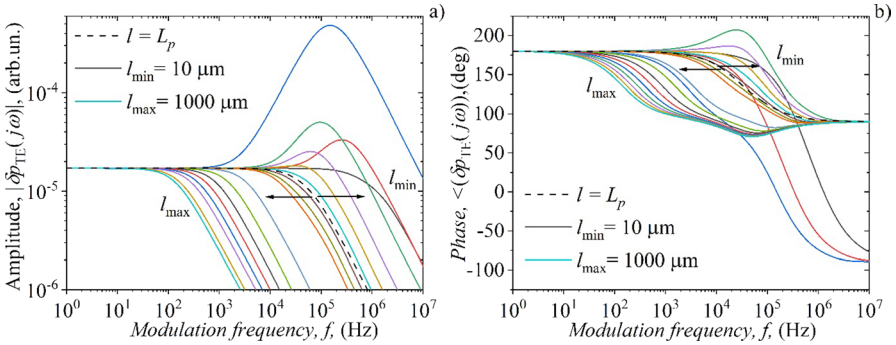

Fig. 2 Frequency spectra of the (a) amplitude and (b) phase of the δp_{TE} response for an *n*-type silicon sample with thicknesses in the (10–1000) μm range, showing its patterns for plasma-thick and plasma-thin regimes. Calculations were done taking the data from Table 1. The minority excess carrier diffusion length $l = L_p = \sqrt{D_p \tau_p} = 85\mu m$ defines the border line (dashed) between plasma-thick and plasma-thin samples

thermoelastic responses of surface absorbers are $\left(T_{s,b}(x) \rightarrow T_{s,a}(x), \text{Eq.}(A2.1)\right)$ without the excess carrier influence [14, 17, 29]:

$$\delta p_{TE,1}(j\omega) = 3\pi \frac{\gamma_g p_0 \alpha_T R_s^4}{l^3 V_0} \int_{-\frac{l}{2}}^{\frac{l}{2}} x T_{s,a}(x) dx \tag{6}$$

On the other hand, the plasma-thin sample $\left(l < L_p\right)$ thermoelastic responses, $\delta p_{TE,2}(j\omega)$, are more complicated $\left(T_{s,b}(x) \rightarrow T_{\text{therm}}(x) + T_{\text{sr}}(x), \text{Eq.}(A2.1), T_{br}(x) \text{ almost negligible}\right)$, exhibiting the peak-like structure generated by the excess carrier recombination at the sample surfaces [14, 17, 29]:

$$\delta p_{TE,2}(j\omega) = 3\pi \frac{\gamma_g p_0 \alpha_T R_s^4}{l^3 V_0} \int_{-\frac{l}{2}}^{\frac{l}{2}} x\left(T_{therm}(x) + T_{sr}(x)\right) dx \tag{7}$$

2.4 Electro-acoustic analogies

In this work, we focus on the analysis of the $\delta p_{\text{TE}}(j\omega)$ component under the strong influence of excess carriers as heat carriers, trying to find an electro-acoustic analogy for describing their effects on photoacoustic measurements. Based on the temperature-voltage analogy (Appendix IV), we aim to describe any photoacoustic system like an ordinary LTI system (Fig. 3), with an input ($U_{\text{in}}(t) = x(t)$) and output ($U_{\text{out}}(t) = y(t)$) voltages varying with time.

Typical plasma-thick response (Eq. 6, Fig. 2) can be simulated by the low-pass *RC* filter (Fig. 3) response, and fitted (so-called *RC* fit) by the corresponding transfer function amplitude and phase in the form [19]:

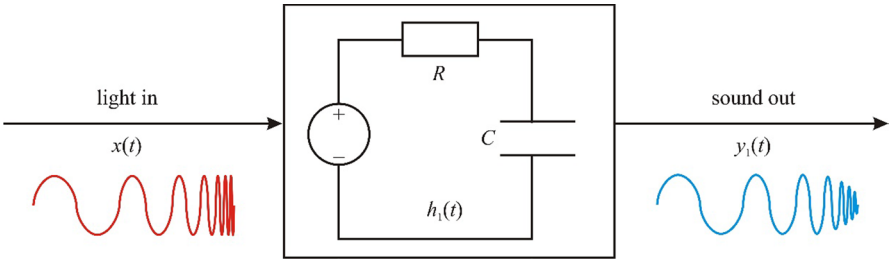

Fig. 3 The linear time-invariant system presentation of the low-pass *RC* filter as an analog to the thermoelastic photoacoustic response of plasma-thick *n*-type silicon. The light input $x(t)$ will give the sound out $y_1(t)$ generated by the heated sample, characterized by its thermal properties—system response function $h_1(t)$

$$\left|\delta p_{TE,1}(j\omega)\right| = \frac{1}{\sqrt{1+\left(\frac{\omega}{\omega_{01}}\right)^2}} \tag{8}$$

and

$$< \left(\delta p_{TE,1}(j\omega)\right) = -\arctan\left(\frac{\omega}{\omega_{01}}\right) \tag{9}$$

respectively. Here, $\omega = 2\pi f$, f is the modulation frequency of the input signal, $\omega_{01} = 2\pi f_{01} = 1/RC$, and f_{01} is the filter cut-off frequency.

Typical plasma-thin response (Eq. 7, Fig. 2) is more complicated dependence due to the strong excess carrier influence. We found that $\delta p_{TE,2}(j\omega)$ can be simulated by the cascade connection between the same low-pass *RC* filter (Fig. 3) and lead compensator (Fig. 4), and fitted (so-called *RCC* fit) by the amplitude and phase of the corresponding transfer functions in the form:

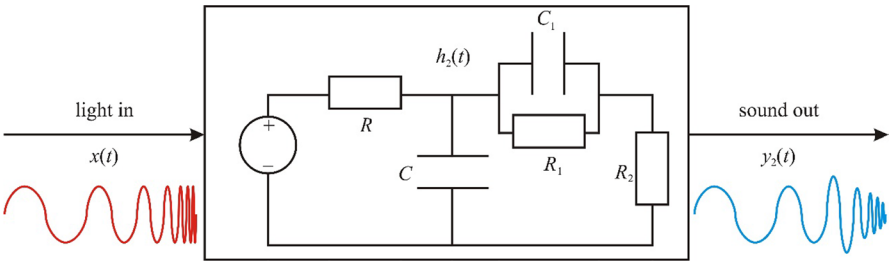

Fig. 4 The linear time-invariant system presentation of a cascade connection between the low-pass *RC* filter (R, C) and phase lead compensator (R_1, C_1, R_2), as an analog to the thermoelastic photoacoustic response of plasma-thin *n*-type silicon. The light input $x(t)$ will give the sound out $y_2(t)$ generated by the heated sample, characterized by its thermal properties under the strong excess carrier influence—system response function $h_2(t)$

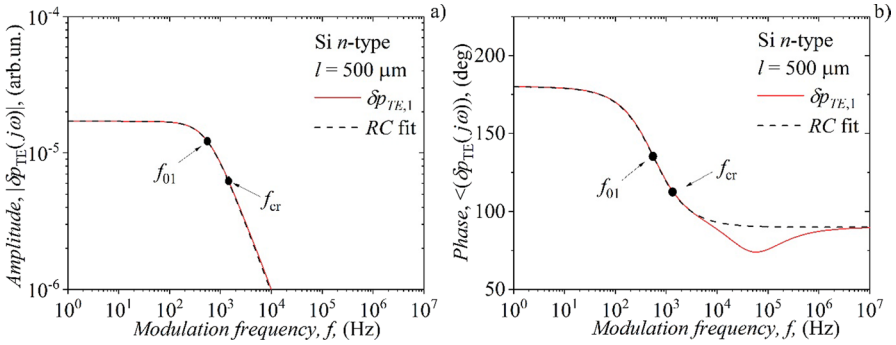

Fig. 5 Typical (a) amplitude and (b) phase of the $\delta p_{TE,1}$ response (red line) of a plasma-thick samples and *RC* filter fit (black dashed), with marked characteristic cut-off f_{01} and critical f_{cr} frequencies. Red solid lines represent the numerical simulations obtained with Eq. 6, and black dashed lines stand for *RC* (Eqs. 8 and 9) fits

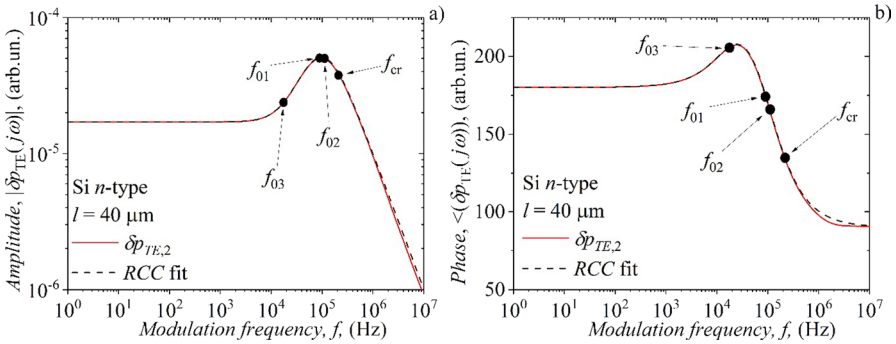

Fig. 6 Typical (a) amplitude and (b) phase of the $\delta p_{\mathrm{TE},2}$ response (red line) of plasma-thin samples and *RCC* filter fit (black dashed), with marked characteristic cut-off f_{01}, f_{02}, f_{03}, and critical f_{cr} frequencies. Red solid lines represent the numerical simulations obtained with Eq. 7, and black dashed lines stand for *RCC* (Eqs. 10 & 11) fits

$$\left|\delta p_{TE,2}(j\omega)\right| = \frac{\left(1+\left(\frac{\omega}{\omega_{03}}\right)^2\right)^{1/2}}{\left(1+\left(\frac{\omega}{\omega_{01}}\right)^2\right)^{1/2}\left(1+\left(\frac{\omega}{\omega_{02}}\right)^2\right)^{1/2}} \tag{10}$$

and

$$< \left(\delta p_{TE,2}(j\omega)\right) == -\arctan\left(\frac{\omega}{\omega_{01}}\right) - \arctan\left(\frac{\omega}{\omega_{02}}\right) + \arctan\left(\frac{\omega}{\omega_{03}}\right) \tag{11}$$

respectively. Here, $\omega_{01} = 2\pi f_{01} = 1/RC$ (Fig. 3), $\omega_{02} = 2\pi f_{02} = (R_1 + R_2)/(R_1 R_2 C_1)$ and $\omega_{03} = 2\pi f_{03} = 1/R_1 C_1$.

To illustrate how the analogy works, we selected samples with thicknesses of 500 μm and 40 μm from the data set shown in Fig. 2 as typical examples of plasma-thick and plasma-thin n-type silicon. The related amplitudes and phases are seen in Figs. 5 and 6, respectively.

The *RC* fit from Fig. 5 provides finding the thermoelastic cut-off frequency $f_{\mathrm{TE}} = f_{01} = (560 \pm 8)$ Hz using Eqs. 8 and 9, allowing one to establish the referent curve for investigated material $f_{01} = f(l)$, using well-known equation [19]

$$f_{TE} = f_{01} = \frac{2}{\pi} \cdot \frac{D_T}{l^2} \cdot m^2, \tag{12}$$

where $\sqrt{2} \le m < \sqrt{6}$ [19, 20] is a calibration factor depending on the assumed *RC* approximation validity. Critical frequency $f_{\mathrm{cr}} = (1375 \pm 20)$ Hz can be calculated, also, when $m = \sqrt{6}$ [20].

The *RCC* fit from Fig. 6 provides not only the thermoelastic cut-off frequency $f_{\mathrm{TE}} = f_{01} = (91500 \pm 1500)$ Hz, but $f_{02} = (110000 \pm 1500)$ Hz, and $f_{03} = (17000 \pm 300)$ Hz as well, using Eqs. 10 and 11. The critical frequency was found to be

Table 2 Fitting results of an Si n-type semiconductor samples estimation of f_{01}, f_{02}, f_{03}, frequency difference Δf, and quality factor Q (height of a pick-like structure) as a function of sample thickness l

Sample thickness l / ($\times 10^{-6}$ m)	f_{01} / (Hz)	f_{02} / (Hz)	$\Delta f = f_{02} - f_{01}$ / (Hz)	f_{03} / (Hz)	f_{cr} / (Hz)	Q	Q*
10	1 467 250	420 382.16561	– 1 046 867.83439	–	3 439 490	–	
20	352 064.0	213 375.79618	– 138 688.20382	71 007	859 872	1.97	0.51
30	150 994.8	144 373.67304	– 6621.12696	2600	382 165	22.30	0.39
40	91 465.38	109 872.61146	18 407.23146	17 007	214 968	8.08	0.92
50	58 578.48	89 171.97452	30 593.49452	26 000	137 579	2.36	0.85
60	40 865.79	75 371.54989	34 505.75989	32 000	95 541	1.61	0.93
70	28 097.52	65 514.10373	37 416.58373	34 000	70 193	1.14	0.91
80	21 687.13	58 121.01911	36 433.88911	35 000	53 742	0.97	0.96
90	17 231.35				42 462		
100	14 013.44				34 394		
200	3475.289				8598		
300	1578.390				3821		
400	871.7279				2149		
500	558.1317				1375		
600	387.6765				955		
700	284.8613				701		
800	217.3823				537		
900	172.3485				424		
1000	139.6089				343		

$f_{cr} = (214000 \pm 4000)$ Hz $\left(m = \sqrt{6}\right)$ [20]. In both *RC* and *RCC* approximations, the critical frequency represents the limiting frequency of their validity.

The results of such fitting procedures, obtained for all sample thicknesses from 10 to 1000 microns, are shown in Table 2. Relative errors for all frequencies are laying in the (1.5–2.0)% range. *RC* fit was used for all sample thicknesses ≥ 90 microns. For thicknesses < 90 microns, *RCC* fit is used.

The chart in Fig. 7 illustrates the meanings of all the acquired frequencies and their differences. The symbols, including circles, squares, asterisks, and polygons, were determined using *RC* and *RCC* fits as per Eqs. 8 and 10. The solid blue and red lines were computed by solving Eqs. 12 and 5 using the parameters listed in Table 1. The green line indicates the difference between the blue and red lines.

Comparing the f_{01} values obtained from *RC* and *RCC* fitting with the f_{TE} values represented by the blue line (according to Eq. 12), one can conclude that f_{01} is equal to f_{TE}. Similarly, comparing the f_{02} values (squares) obtained from the *RCC* fit with the f_s (red line, according to Eq. 5), one can conclude that f_{02} is equal to f_s. The minimum value of $|\Delta f| = \left|f_{02} - f_{01}\right|$ (green solid) gives the thickness $l_p = 31.4\mu m$ at which the influence of the carriers in the thermoelastic response is most visible (the most intense amplitude of the peak-like structure). There is also clear connection between $f_{03}/|\Delta f| = Q^*$, where Q^* is a quality factor showing the system (thermoelastic response) dumping level at lower modulation frequencies f. The parameter which follows the amplitude peak-like structure behavior is the quality factor $Q = \sqrt{f_{01} f_{02}}/|\Delta f|$.

The purpose of the presented analysis (Fig. 7) is to show (a) how the cut-off frequency can be used to confirm that the sample material belongs to the *n*-type silicon reference curve (blue line, Table 1), and, (b) how the most favorable measurement conditions intended to study the thermal influence of the excess carriers (for example, sample thickness) can be found by combining cut-off and surface recombination frequencies. In our case, if we follow the minimal values of $|\Delta f|$, we can find the sample thicknesses $\left(l_p \pm 10\mu m\right)$ on which the effects of excess free carriers as heat carriers (surface carrier recombination) on $\delta p_{TE}(j\omega)$ will be most visible.

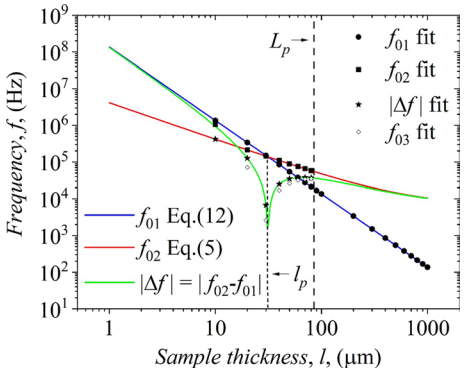

Fig. 7 Typical results of our *RC* and *RCC* fitting procedures used to calculate f_{TE}=f_{01} (black circles), f_{02} (black squares), Δf (black asterisks), and f_{03} (white polygons), together with the theoretical predictions of Eqs. 12 (f_{01}, blue solid), and (5) (f_{02} and $|\Delta f|$). Also, the limit thickness L_p is shown with l_p, the thickness at which the influence of excess carriers is most visible

3 Experimental Setup

The practice has shown that the experimental setup that best fits the theoretical model of the composite piston explained in previous paragraphs (Fig. 1) is the so-called transmission configuration of an open photoacoustic cell—OPC [17, 30, 31]. Simple scheme of the experimental setup based on the OPC configuration used in our investigation is presented in Fig. 8. This configuration uses the microphone body as a minimal-volume photoacoustic cell. To ensure no air leaks from the cell, the sample is mounted to the front of an electret microphone (ECM 30B, Jin In Electronic Co., Ltd) and secured with vacuum grease. The microphone's cylindrical shape and circular front opening prefers the examined sample's circular shape, having the radius $R_s = 4\text{mm}$. In order to preserve the real relationship between the components of the photoacoustic signal, the sample is simply supported at the ends of the microphone opening (clamping would disturb that relationship increasing the bending). A low-power 10 mW red laser diode (660 nm XL7090- RED, RF Communication Electronic Technology Co., Ltd.) having the spot radius of 5 mm is used as a sample illuminator, modulated with the homemade current modulator within the 20 Hz–20 kHz frequency range. Sensitive photodiode (BPW34 Vishay Telefunken) controls the illumination of the sample. The amplitude and phase of the photoacoustic signal measured by the microphone are extracted from the noisy environment using a PC sound card (Intel 82,801 Ib/ir/ih hd audio controller) which emulates a lock-in amplifier, using a photodiode signal as a reference [30].

Because our samples are made of *n*-type silicon (Si) from the same wafer (Table 1), the light source wavelength corresponds to the absorption coefficient of $\beta = 2.58 \times 10^5 \text{m}^{-1}$, which, for a given range of sample thicknesses $l = (10 - 1000) \times 10^{-6}\text{m}$, ensures that $\beta l > 2$, justifying the approximation of the surface absorber in the case of plasma-thick samples. Measurements have been conducted for two Si circular plates, having the thicknesses $l = 875\mu m$ and $35\mu m$. Illuminated (front) side is mechanically passivated to reduce surface recombination, while non-illuminated (rear) side is mechanically roughened to assure high surface recombination rate. By focusing on the role of surface recombination in the photoacoustic response, we can now accurately measure it by studying the behavior of the total signal and its components within a given

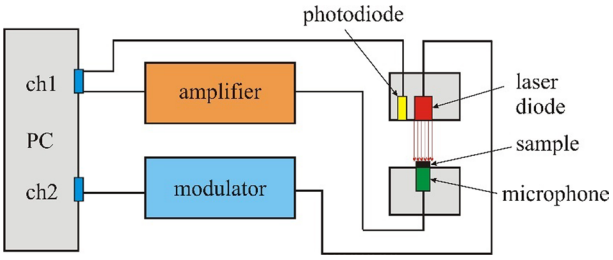

Fig. 8 Simple scheme of the experimental setup based on the open photoacoustic cell configuration

modulation frequency range. To avoid any disruptions caused by the public electrical network, the amplifier, photodiode, and modulator are powered by batteries.

4 Results and Discussion

To validate the *RC* and *RCC* analogy method presented in 2.4, we conducted an experimental check using an OPC setup (see Fig. 8) and two *n*-type silicon plasma-thick and plasma-thin samples having 875- and 35- micron thicknesses, respectively. With the plasma-thick sample, we will try to verify how the cut-off frequency can be used to confirm that the sample material belongs to the *n*-type silicon reference curve. With the plasma-thin sample, we will try to verify how properly picked-up sample thickness can be used to show the thermal influence of the excess carrier through the cut-off and surface recombination frequencies. Details about our measurement procedures applied to obtain $\delta p_{total}(j\omega)$ and its components, $\delta p_{TD}(j\omega)$ and $\delta p_{TE}(j\omega)$, are given in Appendix V [31].

After extraction from $\delta p_{total}(j\omega)$(Fig. 12), the $\delta p_{TE}(j\omega)$ components are obtained at different sample thicknesses (Fig. 9, nonnormalized ones) and analyzed based on the electro-acoustic analogies. Plasma-thick sample $\delta p_{TE875}(j\omega)$ amplitudes and phases are fitted by *RC* fit (Eq. 8 and 9), giving $f_{01} = (180 \pm 5)$Hz as a result. Plasma-thin sample $\delta p_{TE35}(j\omega)$ amplitudes and phases are fitted by *RCC* fit (Eq. 10 and 11) giving $f_{01} = (110000 \pm 2500)$Hz, $f_{02} = (123000 \pm 2600)$Hz, and $f_{03} = (9200 \pm 200)$Hz as the results. Critical frequencies are obtained as follows: $f_{cr875} = (460 \pm 20)$Hz and $f_{cr35} = (290000 \pm 6000)$Hz.

To ensure a precise measurement quality assessment, all the experimental results with different sample thicknesses are displayed in Fig. 10, a simplified version of Fig. 7. The accurate reproduction of the experimental data shows that our theoretical assumptions and analysis through electro-acoustic analogies are correct. Similar

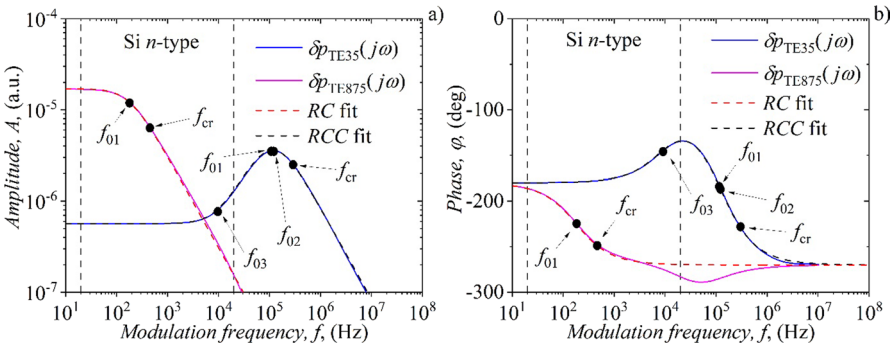

Fig. 9 Extracted $\delta p_{TE}(j\omega)$ (a) amplitude and (b) phase responses of a plasma-thick ($\delta p_{TE875}(j\omega)$, 875 μm, solid blue) and plasma-thin ($\delta p_{TE35}(j\omega)$, 35 μm, solid magenta) samples in frequency domain, together with the *RC* (dash red) and *RCC* (dash black) fits and calculated characteristic frequencies. Vertical dashed lines indicate the range of experimental modulation frequencies *f*

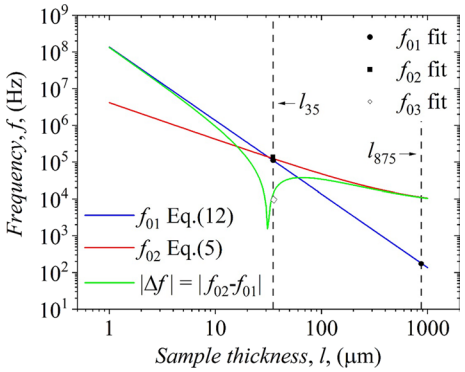

Fig. 10 Simplified form of Fig. 7 with typical results of our *RC* and *RCC* fitting of the δp_{TE875} $(j\omega)$ and δp_{TE875} $(j\omega)$ amplitudes and phases calculated from the measured signal, presented as f_{01} (black circles), f_{02} (black squares), and f_{03} (white polygon), together with theoretical predictions for the same frequencies obtained with Eq. 12 (f_{01}, blue solid), Eq. 5 (f_{02}, red solid) and $|\Delta f|$ (green solid). Also, plasma-thick thickness l_{875} is presented together with plasma-thin one, l_{35}

analogies can also be applied to gases, as was recently proposed [32]. To build a reliable and simple experimental setup and measure how carriers affect heat flow and temperature changes in *n*-type silicon with standard properties at 300 K, one therefore must follow the proposed numerical analysis. This involves illuminating a circular plate-shaped sample with modulated light from the visible spectrum, ensuring the spot is larger than the sample, with a thickness of $l_p \pm 10\mu m$, and a radius similar to the opening of the microphone. The sample should be passivated on the illuminated side and non-passivated on the non-illuminated side. Further, to accurately analyze the thermoelastic component for different sample thicknesses, the sample should be freely supported without any side clamps.

5 Conclusions

We have developed a method for accurately determining the experimental conditions needed to analyze the impact of free excess carriers as heat carriers on the heat flow and thermal response of an *n*-type silicon sample. By numerically testing its photoacoustic response in the frequency domain, and analyzing it with the composite piston model, we have confirmed that the thermoelastic component of the photoacoustic signal is the most sensitive to the carrier influence, especially in plasma-thin samples. Through electro-acoustic analogies, we have discovered that this component can be used to identify characteristic cut-off frequencies needed to establish the calibration curve of the tested material. Furthermore, we have found that surface recombination frequencies are the most important parameters for describing the thermal influence of excess carriers. We have also identified the sample thickness l_p at which the influence of excess carriers is most significant for our experimental setup. This influence can only be observed if a) $\beta l > 2$, and b) the

illuminated surface of the sample is passivated while the non-illuminated surface is not.

Although our measurements of the free carriers' heat carrier effects on the thermoelastic component of plasma-thin samples are indirect and based on extrapolation outside the measurement range of modulation frequencies, we have found that the obtained results are highly reliable and consistent with the predictions of the theoretical model of the composite piston. This reliability is also observed in plasma-thick samples, where the explanations and predictions of the electro-acoustic analogies are much simpler. We believe that the methodology presented can be applied generally to analyze the impact of excess free carriers on heat flow and temperature changes in all types of semiconductors under the same experimental conditions (transmission measurements, passivation of the illuminated side, and non-passivation of the non-illuminated side).

Appendix

See Fig. 11 and 12

Appendix I. Excess carrier density distribution

Following the simple scheme of the photoacoustic system under consideration (Fig. 1), one can say that excess carriers (electrons and holes) can be generated in semiconductors illuminated by the modulated light source if the energy of the light photon is larger than the band gap of the semiconductor. Both minority and majority carriers are generated when a photon is absorbed. After they are generated, both types of excess carriers diffuse from regions of high

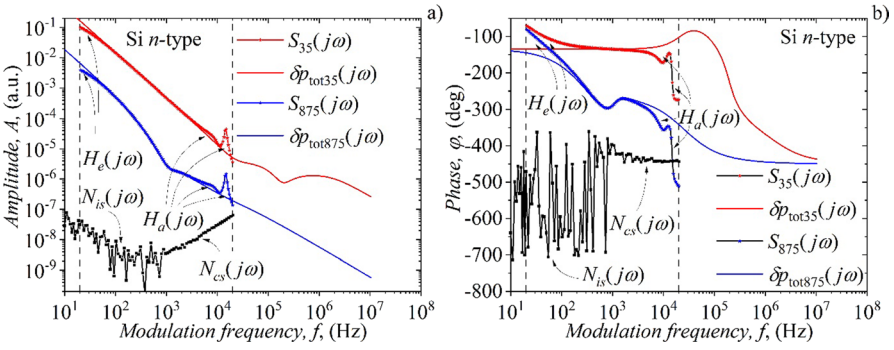

Fig. 11 Typical measured $S(j\omega)$ (a) amplitude and (b) phase responses (asterisks) in frequency domain, together with $\delta p_{total}(j\omega)$ responses obtained by composite piston model fitting (solid lines) of a plasma-thick (875 μm, blue) and plasma-thin (35 μm, red) samples. Coherent ($N_{cs}(j\omega)$) and incoherent ($N_{is}(j\omega)$) signals are presented with black square-lines. Vertical dashed lines indicate the range of experimental modulation frequencies f

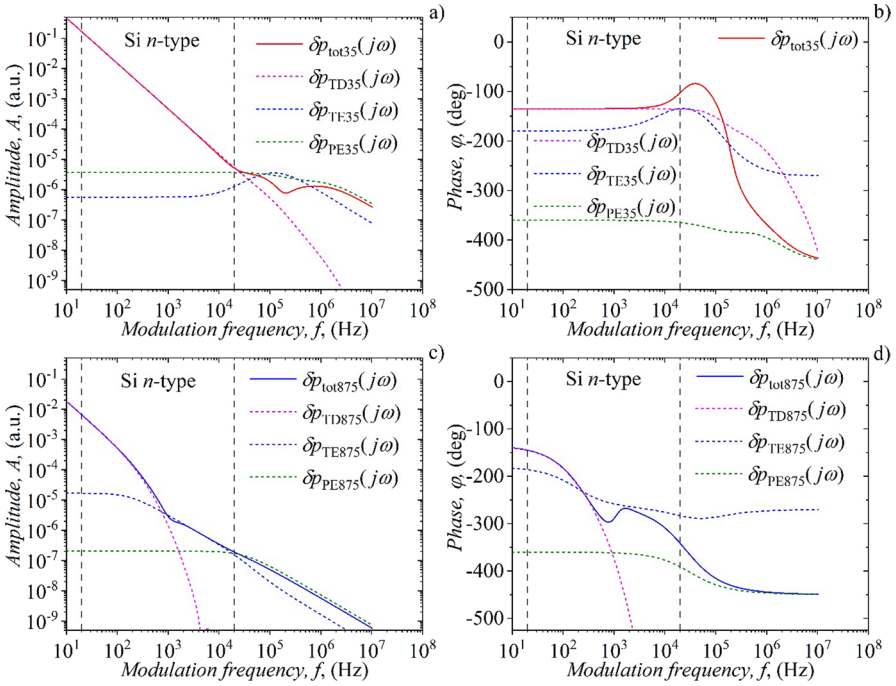

Fig. 12 The $\delta p_{total}(j\omega)$ (a, c) amplitude and (b, d) phase responses (solid lines) of a plasma-thick (875 μm, blue) and plasma-thin (35 μm, red) samples in frequency domain, obtained by composite piston model fitting of measured $S(j\omega)$, together with corresponding δp_{TD} $(j\omega)$, δp_{TE} $(j\omega)$, and δp_{PE} $(j\omega)$ component responses (dashed lines). Vertical dashed lines indicate the range of experimental modulation frequencies f

density to ones of low density, changing the temperature distribution within the semiconductor and on its surfaces. In the case of n-type semiconductor, carrier diffusion and recombination processes are driven by the minority carrier density $\delta n_p(x)$, which dynamics is explained by the dynamic part of the 1D diffusion equation written as

$\frac{d^2\delta n_p(x)}{dx^2} - \frac{\delta n_p(x)}{L_p^2} = -\frac{\beta I_0}{\varepsilon D_p} e^{-\beta x}$, (A1.1). where I_0 is the incident light intensity, ε is the light photon energy, β is the semiconductor material absorption coefficient, $L = L_p/\sqrt{(1+j\omega\tau)}$, $L_p = \sqrt{D_p\tau_p}$ is the excess free carrier (holes) diffusion length characterized by their diffusion coefficient D_p and lifetime τ_p, $\omega = 2\pi f$, and f is the light source modulation frequency. The solution of this equation is given by [22, 23]:

$\delta n_p(x) = A_+ e^{(x+l/2)/L} + A_- e^{-(x+l/2)/L} - Ae^{-\beta(x+l/2)}$, (A.1.2). where $A = I_0/(\varepsilon D_p \beta)$, and the integration constants $A_\pm$ are defined by [22, 23]:

$A_\pm = \frac{A}{v_D} \frac{v_\beta(v_D \pm s_2)e^{\mp l/L} - v_D\left(v_\beta - s_2\right)e^{-\beta l}}{(v_D+s_2)e^{l/L} - (v_D - s_2)e^{-l/L}}$, (A1.3).

depending strongly on the relative values of the characteristic diffusion speeds $v_D = D_p/L$ and $v_\beta = \beta D_p \left(v_\beta > v_D\right)$, and recombination speeds s_1 and s_2 at sample irradiated and nonirradiated surface, respectively.

Appendix II. Temperature variations

In the case of surface absorber without the excess carrier influence, the 1D temperature profile in semiconductors is given by [14–17, 19] as a solution of Eq. (A4.1):

$T_{s,a}(x) = \frac{I_0}{k\sigma_\omega}\frac{\cosh\left[\sigma_\omega(x-l/2)\right]}{\sinh\left(\sigma_\omega l\right)}$, (A2.1). where I_0 is the light intensity, $_{\sigma_\omega = (1+j)\sqrt{\pi f/D_T}}$ is the complex wave vector of heat diffusion, and $D_T = k/(\rho c)$ is the thermal diffusivity of the sample (k is the heat conductivity, ρ is the density, c is the heat capacity). The equation of temperature variations in semiconductors as a volume absorber under the influence of excess carriers, $T_{s,b}(x)$, is more complex, having three contributions: $T_{\text{therm}}(x)$—direct light-heat conversion (immediate excess carrier thermalization), $T_{\text{br}}(x)$—nonradiative excess carrier recombination in the bulk, and $T_{\text{sr}}(x)$—nonradiative excess carrier recombination at surfaces. This is the reason why $T_{s,b}(x)$ can be written as [14–17]:

$$T_{s,b}(x) = T_{\text{therm}}(x) + T_{\text{br}}(x) + T_{\text{sr}}(x), \tag{A2.2}$$

where

$$T_{\text{therm}}(x) = \frac{I_0}{k}\frac{\varepsilon-\varepsilon_g}{\varepsilon}\frac{\beta}{\beta^2-\sigma_\omega^2}\left[b\frac{\cosh\left[\sigma_\omega(x-l/2)\right]-e^{-\beta l}\cosh\left[\sigma_\omega(x+l/2)\right]}{\sinh\left(\sigma_\omega l\right)} - e^{-\beta(x+l/2)}\right], \tag{A2.3a}$$

$$T_{\text{br}}(x) = \frac{\varepsilon_g B_1}{\tau_p k\sigma_\omega^2}\left\{\frac{B_2 e^{\sigma_\omega(x+l/2)} + B_3 e^{-\sigma_\omega(x+l/2)}}{e^{\sigma_\omega l} - e^{-\sigma_\omega l}} - \frac{1}{c^2-1}\left[\frac{\delta n_p(x)}{B_1} + \frac{b^2-c^2}{b^2-1}e^{-\beta(x+l/2)}\right]\right\}, \tag{A2.3b}$$

$$T_{\text{sr}}(x) = \frac{\varepsilon_g}{k\sigma_\omega}\frac{s_1\delta n_p(-l/2)\cosh\left[\sigma_\omega(x-l/2)\right] + s_2\delta n_p(l/2)\cosh\left[\sigma_\omega(x+l/2)\right]}{\sinh\left(\sigma_\omega l\right)}. \tag{A2.3.c}$$

Here, ε is the photon energy, ε_g is the semiconductor band gap energy, s_1 and s_2 are the surface recombination velocities at the illuminated front and non-illuminated back sample surfaces, respectively, while the other constants are given by

$$b = \frac{\beta}{\sigma_\omega}, c = \frac{1}{L_\omega\sigma_\omega},$$

$$B_1 = -A_\omega,$$

$$B_2 = B_4 e^{-\sigma_\omega l} + B_5,$$

$$B_3 = B_4 e^{\sigma_\omega l} + B_5,$$

$$B_4 = -c\frac{\frac{1}{B_1}\left[\delta n_p\left(\frac{l}{2}\right) - \delta n_p\left(-\frac{l}{2}\right)\cosh\left(\frac{l}{L_\omega}\right)\right] - \cosh\left(\frac{l}{L_\omega}\right) + e^{-\beta l}}{\sinh\left(\frac{l}{L_\omega}\right)\cdot\left(c^2-1\right)} - \frac{b}{b^2-1},$$

$$B_5 = c\frac{\frac{1}{B_1}\left[\delta n_p(l/2)\cosh\left(l/L_\omega\right) - \delta n_p(-l/2)\right] - 1 + e^{-\beta l}\cosh\left(l/L_\omega\right)}{\sinh\left(l/L_\omega\right)\cdot\left(c^2-1\right)} + \frac{be^{-\beta l}}{b^2-1}.$$

Appendix III. Surface recombination

There are various recombination mechanisms within even a uniformly doped piece of semiconductor. In bulk materials, the carriers recombine by either radiative (also known as band-to-band) recombination, Auger recombination or defect recombination (via traps within the energy gap). For an indirect bandgap semiconductor such as silicon, radiative recombination time is very large and usually neglected. The direct measurement of the bulk lifetime is usually complicated due to the influence of surface recombination described by the surface lifetime τ_s, or surface recombination frequency $f_s = 1/\left(2\pi\tau_s\right)$. These parameters are the function of the surface recombination velocities s_1 and s_2, the sample thickness l and the minority carrier diffusivity D_p. General equation that allows one to calculate τ_s is given by [27, 28]:

$$\tan\left(\sqrt{\frac{1}{\tau_s D_p}}\bullet l\right) = \frac{s_1 + s_2}{\sqrt{\frac{1}{\tau_s D_p}}\bullet D_p - \frac{s_1 \bullet s_2}{\sqrt{\frac{1}{\tau_s D_p}}\bullet D_p}}. \tag{A3.1}$$

While the exact solution (A3.1) may be complex, there are approximate solutions available for specific scenarios that are accurate enough for most needs. One of them has the form:

$$\tau_s = \frac{D_p l}{\left(s_1 + s_2\right)D_p + s_1 s_2 l}, \tag{A3.2}$$

obtained under the approximation $\tan x \approx x$ (our case).

Appendix IV. The basics of electro-acoustic analogies

Using the electro-acoustic analogy, it is possible to create models of acoustic systems with basic electrical elements. This allows for the use of established electrical network theory to study, design, and characterize complex systems like

photoacoustics. Through this elegant modeling, the behavior of the photoacoustic system can be explained in the electrical domain, and the interactions between electrical and acoustical parameters can be accurately predicted [20].

In photoacoustics, as one of the methods of photothermal science, it is very important to determine the thermal state of a periodically illuminated sample, so that its acoustic response can be correctly interpreted. The simplest way to do this is to analyze the absorption of light by a sample that behaves as a surface absorber. In this case, the temperature variation distribution $T_s(x)$ within the sample, can be obtained by solving the dynamic part of the 1D parabolic heat conduction equation (PHCE) along the x-axes (Fig. 1):

$$\frac{\partial^2 T_s(x,t)}{\partial x^2} = \frac{1}{D_T}\frac{\partial T_s(x,t)}{\partial t}, \tag{A4.1}$$

where $T_s(x,t) = T_{\text{amb}}(x) + T_s(x)\left(1 + e^{j\omega t}\right)$, $T_{\text{amb}}(x)$ is the ambient temperature, ω is the modulation circular frequency, $D_T = k/(\rho C_V)$, k is the thermal conductivity, ρ is the density, and C_V is the volumetric thermal capacity of the medium. This is, so called, parabolic heat conduction equation (PHCE), depicting heat transfer process in medium as a diffusion process.

To make the analogy with the electrical system, one can find in literature that Eq. (A4.2) is similar in form to the (telegraph) equation, which, given in terms of the voltage $u(x,t)$ along the transmission lines, reads [20, 33]:

$$\frac{\partial^2 u(x,t)}{\partial x^2} = rc\frac{\partial u(x,t)}{\partial t}, \tag{A4.2}$$

where r is the distributed resistance, and c—the distributed capacitance of the line. One can establish an analogy between Eq. (A4.1) and Eq. (A4.2) as an analogy between two distributed parameter systems, by introducing the following relationships: $u \leftrightarrow T$, $c \leftrightarrow \rho C_V$, and $r \leftrightarrow 1/k$.

Previously it was found that the electric network which consists of the elements with lumped (not anymore distributed) parameters can be established to describe the system defined with Eq. (A4.2) [20, 34]. The thermal system (and therefore the photoacoustic one) can be analogously described through an *RC* electrical system. The analogies are, of course, approximations, only valid in a limited frequency domain.

Appendix V. Signal correction procedure

Our experience has shown that photoacoustic measurements can be distorted due to the measuring chain, which is a series of connected instruments (detectors, modulators, and amplifiers) that transmit the signal from the sample to the PC as a receiver [31]. This distortion can be caused by various factors, such as electronic and acoustic filtering properties of the microphone and accompanying electronics, random noise, and parasitic currents that can interfere with the measurement signal

at higher frequencies and significantly alter the results. To address this issue, we follow the established signal correction procedure (SCP) to detect and eliminate any signal disturbances [31]. This ensures that only the relevant signal remains, which can then be fitted to a well-known theoretical model.

Measurements performed in this work, $Y(j\omega)$, can be expressed by the sum of the total measured signal $S(j\omega)$ (Fig. 11, asterisks), and noise $N(j\omega)$ (Fig. 11, black square-lines), as it is explained in details in [31]:

$$Y(j\omega) = S(j\omega) + N(j\omega). \tag{A5.1}$$

The noise $N(j\omega)$ is measured using the apparatus without sample irradiation, showing the existence of random noise as an incoherent signal $N_{is}(j\omega)$, and parasitic coherent signal $N_{cs}(j\omega)$ [31]: $N(j\omega) = N_{is}(j\omega) + N_{cs}(j\omega)$. It is obvious from our measurements that signal-to-noise ratio is always large enough to ensure that our $S(j\omega)$ can be fitted as a signal clear from noise, but under the strong influence of the measuring chain.

The $S(j\omega)$ can be written as [17, 31]:

$$S(j\omega) = A \bullet \exp(j\varphi) = \delta p_{total}(j\omega)H(j\omega), \tag{A5.2}$$

where A and φ are the measured amplitudes and phases, respectively, $\delta p_{total}(j\omega)$ is the total signal (Fig. 11, solid lines) generated by the illuminated sample (Eq. 1), and $H(j\omega) = H_e(j\omega) \bullet H_a(j\omega)$ is the response of a measuring chain. The $H_e(j\omega)$ and $H_a(j\omega)$ influence are indicated in Fig. 11 with arrows. The $H_e(j\omega)$ alters the signal at low frequencies (decreasing it), while $H_a(j\omega)$ shows sharp peaks at high frequencies. Both $H_e(j\omega)$ and $H_a(j\omega)$ are given in the form [17, 31]

$$H_e(j\omega) = -\frac{\frac{\omega}{\omega_{e1}}}{1+j\frac{\omega}{\omega_{e1}}} \bullet \frac{\frac{\omega}{\omega_{e2}}}{1+j\frac{\omega}{\omega_{e2}}}, \text{and} H_a(j\omega) = \frac{1}{1+\theta_1\frac{\omega}{\omega_{a1}}+\frac{\omega^2}{\omega_{a1}^2}} + \frac{1}{1+\theta_2\frac{\omega}{\omega_{a2}}+\frac{\omega^2}{\omega_{a2}^2}}, \tag{A5.3}$$

where ω_{e1}, ω_{a1}, and ω_{a2} are characteristic microphone frequencies, ω_{e2} is characteristic PC sound-card frequency, and θ_1 and θ_2 are corresponding dumping factors.

Fitting the $S(j\omega)$ with Eq. (A5.2) one can find $H_e(j\omega)$ and $H_a(j\omega)$ frequencies and dumping factors (A5.3) and remove it, leaving only $\delta p_{total}(j\omega)$ which can be extrapolated using a composite piston theoretical model beyond the experimental range of modulation frequencies (Fig. 11, vertical dashed lines).

The same theoretical model could be used to obtain all $\delta p_{total}(j\omega)$ components ($\delta p_{TD}(j\omega), \delta p_{TE}(j\omega) and \delta p_{PE}(j\omega)$, Fig. 12, dashed lines). We are interested in the thermoelastic components for both thicknesses, $\delta p_{TE35}(j\omega)$ and $\delta p_{TE875}(j\omega)$, and we will continue to analyze them in Chapter 4.

Here, we will briefly refer to the obtained results. Analyzing Fig. 12 one can say that our previous investigation findings are confirmed [14, 17]. The effects of photogenerated carriers have been found to be intensive in cases when the illuminated side is passivated and the non-illuminated side is not. Also, the intense drop in $\delta p_{TE}(j\omega)$ amplitude and growth in its phase in plasma-thin samples

$\left(\delta p_{TE35}(j\omega)\right)$ is confirmed in the range of experimental modulation frequencies. Such behavior of $\delta p_{TE35}(j\omega)$ has the consequence that the $\delta p_{TD35}(j\omega)$ component is dominant in the $\delta p_{total}(j\omega)$ signal of plasma-thin samples ($\delta p_{tot35}(j\omega)$) in the entire domain of experimental frequencies. In the case of plasma-thick samples, $\delta p_{TD875}(j\omega)$ is dominant in $p_{tot875}(j\omega)$ at lower frequencies ($l < 1000$Hz), while $\delta p_{TE875}(j\omega)$ dominates at $f > 1000$Hz, resulting in a unique saddle shape in both amplitude and phase of the $p_{tot875}(j\omega)$.

Acknowledgements The authors acknowledge funding provided by the Institute of Physics Belgrade, through a grant by the Ministry of Science, Technological Development and Innovations of the Republic of Serbia.

Author Contributions The authors confirm contribution to the paper as follows:1) study conception and design: Dragana K. Markushev, Dragan D. Markushev;2) data collection: Dragana K. Markushev, Neda Branković, Sanja M. Aleksić, Dragan S. Pantić;3) analysis and interpretation of results: Dragana K. Markushev, Neda Branković, Sanja M. Aleksić, Dragan S. Pantić, Dragan D. Markushev, Slobodanka P. Galović, Jose Ordonez-Miranda;4) draft manuscript preparation: Dragana K. Markushev, Dragan D. Markushev, Jose Ordonez-Miranda;All authors reviewed the results and approved the final version of the manuscript.

Funding This research was funded by the Ministry of Science, Technological Development and Innovation of the Republic of Serbia (Contract No. 451–03-47/2024–01/200017).

Data Availability The data that support the findings of this study are available from the corresponding author upon reasonable request.

Declarations

Competing Interests The authors declare that they have no known competing financial interests or personal relationships that could have appeared to influence the work reported in this paper.

References

1. Krishnaswamy, S. (2008). Photoacoustic Characterization of Materials. In: Sharpe, W. (eds) Springer Handbook of Experimental Solid Mechanics. Springer Handbooks. Springer, Boston, MA. https://doi.org/10.1007/978-0-387-30877-7_27
2. V. Gusev, M. Franko, Editorial for the special collection on non-invasive and non-destructive methods and applications, I: Festschrift—A tribute to Andreas Mandelis. J. Appl. Phys. **132**, 230401 (2022). https://doi.org/10.1063/5.0133988
3. B. Abad, D.-A. Borca-Tasciuc, M.S. Martin-Gonzalez, Non-contact methods for thermal properties measurement. Renew. Sustain. Energy Rev. **76**, 1348–1370 (2017). https://doi.org/10.1016/j.rser.2017.03.027
4. P. Lishchuk, D. Andrusenko, M. Isaiev et al., Investigation of thermal transport properties of porous silicon by photoacoustic technique. Int. J. Thermophys. **36**, 2428–2433 (2015). https://doi.org/10.1007/s10765-015-1849-8
5. Z. Šoškic, S. Ciric-Kostic, S. Galovic, An extension to the methodology for characterization of thermal properties of thin solid samples by photoacoustic techniques. Int. J. Therm. Sci. **109**, 217–230 (2016)
6. J. Zhou, Xu. Shen, J. Liu, Review of photothermal technique for thermal measurement of micro-/nanomaterials. Nanomaterials **12**(11), 1884 (2022). https://doi.org/10.3390/nano12111884

7. M. Isaiev, G. Mussabek, P. Lishchuk, K. Dubyk, N. Zhylkybayeva, G. Yar-Mukhamedova, D. Lacroix, V. Lysenko, Application of the photoacoustic approach in the characterization of nanostructured materials. Nanomaterials **12**, 708 (2022). https://doi.org/10.3390/nano12040708
8. D.M. Todorovic, M.D. Rabasovic, D.D. Markushev, V. Jovic, K.T. Radulovic, Photoacoustic elastic bending method: characterization of thin films on silicon membranes. Int. J. Thermophys. **36**, 1016–1028 (2015). https://doi.org/10.1007/s10765-014-1801-3
9. S.J. Zelewski, R. Kudrawiec, Photoacoustic and modulated reflectance studies of indirect and direct band gap in van der Waals crystals. Sci. Rep. **7**, 15365 (2017). https://doi.org/10.1038/s41598-017-15763-1
10. Y.U. Oleg et al., Temperature gradient and transport of heat and charge in a semiconductor structure. Low Temp. Phys. **47**, 550–554 (2021). https://doi.org/10.1063/10.0005182
11. Photoacoustic and Thermal Wave Phenomena in Semiconductors by A. Mandelis (Editor), 1987 (North-Holland)
12. K.M. Gupta, Nishu Gupta, "Carrier Transport in Semiconductors" in Advanced Semiconducting Materials and Devices, Part of the series Engineering Materials (2016) (Springer International Publishing Switzerland), pp 87–144
13. M. Pawlak, Photothermal, photocarrier, and photoluminescence phenomena in semiconductors studied using spectrally resolved modulated infrared radiometry: physics and applications editors-pick. J. Appl. Phys. **126**, 150902 (2019). https://doi.org/10.1063/1.5114719
14. D.K. Markushev et al., Effects of the photogenerated excess carriers on the thermal and elastic properties of n-type silicon excited with a modulated light source: theoretical analysis. J. Appl. Phys. **126**(18), 185102 (2019). https://doi.org/10.1063/1.5100837
15. D.K. Markushev, D.D. Markushev, S.M. Aleksić, D.S. Pantić, S.P. Galović, D.V. Lukić, J. Ordonez-Miranda, Enhancement of the thermoelastic component of the photoacoustic signal of silicon membranes coated with a thin TiO2 film. J. Appl. Phys. **131**, 085105 (2022). https://doi.org/10.1063/5.0079902
16. S.M. Aleksić, D.K. Markushev, D.D. Markushev, D.S. Pantić, D.V. Lukić, M.N. Popović, S.P. Galović, Photoacoustic analysis of illuminated Si-TiO2 sample bending along the heat-flow axes. SILICON **14**, 9853–9861 (2022). https://doi.org/10.1007/s12633-022-01723-6
17. D.K. Markushev et al., Experimental photoacoustic observation of the photogenerated excess carrier influence on the thermoelastic response of n-type silicon. J. Appl. Phys. **128**, 095103 (2020). https://doi.org/10.1063/5.0015657
18. D.M. Todorovic, M.D. Rabasovic, D.D.J. Markushev, V., Radulovic K.T., Study of silicon cantilevers by the photoacoustic elastic bending method. Int. J. Thermophys. **38**, 40 (2017). https://doi.org/10.1007/s10765-016-2175-5
19. N. Stanojevic, D.K. Markushev, S.M. Aleksić, D.S. Pantić, S.P. Galović, D.D. Markushev, J. Ordonez-Miranda, Thermal characterization of n-type silicon based on an electro-acoustic analogy. J. Appl. Phys. **133**, 245102 (2023). https://doi.org/10.1063/5.0152495
20. S. Galovic, Z. Soskic, M. Popovic, Analysis of photothermal response of thin solid films by analogy with passive linear electric networks. Therm. Sci. **13**(4), 129–142 (2009). https://doi.org/10.2298/TSCI0904129G
21. S.E. Bialkowski, N.G.C. Astrath, M.A. Proskurnin, *Photothermal Spectroscopy Methods for Chemical Analysis*, 2nd edn. (Wiley, 2019)
22. A. Rosencwaig, A. Gersho, Theory of the photoacoustic effect with solids. J. Appl. Phys. **47**, 64–69 (1976). https://doi.org/10.1063/1.322296
23. A. Rosencwaig, *Photoacoustics and Photoacoustic Spectroscopy* (Wiley, 1980)
24. F.A. McDonald, Photoacoustic, photothermal, and related techniques: a review. Can. J. Phys. **64**, 1023–1029 (1986). https://doi.org/10.1139/p86-174
25. F. McDonald, G. Wetsel, Generalized theory of the photoacoustic effect. J. Appl. Phys. **49**, 2313 (1978). https://doi.org/10.1063/1.325116
26. J. Zakrzewski, K. Strzałkowski, M. Boumhamdi, A. Marasek, A. Abouais, D.M. Kaminski, Photothermal determination of the surface treatment of $Cd_{1-x}Be_xTe$ mixed crystals. Appl. Sci. **13**, 2113 (2023). https://doi.org/10.3390/app13042113
27. F. Kløwa, H. Hauga, Sean erik fossa, surface recombination velocity measurements of metallized surfaces by photoluminescence imaging, 4th workshop on metallization for crystalline silicon solar cells. Energy Procedia **43**, 18–26 (2013). https://doi.org/10.1016/j.egypro.2013.11.084
28. A.B. Sproul, Dimensionless solution of the equation describing the effect of surface recombination on carrier decay in semiconductors. J. Appl. Phy. (1994). https://doi.org/10.1063/1.357521

29. D.K. Markushev, D.D. Markushev, S. Galović, S. Aleksić, D.S. Pantić, D.M. Todorović, The surface recombination velocity and bulk lifetime influences on photogenerated carrier density and temperature distributions in n-type silicon excited by a frequency-modulated light source. FACTA UNIVERSITATIS Series: Electron. Energ. **31**(2), 313–328 (2018). https://doi.org/10.2298/FUEE1802313M
30. M.D. Rabasović, M.G. Nikolić, M.D. Dramićanin, M. Franko, D.D. Markushev, Low-cost, portable photoacoustic setup for solid samples. Measurement Sci. Technol. (2009). https://doi.org/10.1088/0957-0233/20/9/095902
31. D.D. Markushev, M.D. Rabasović, D.M. Todorović, S. Galović, S.E. Bialkowski, Photoacoustic signal and noise analysis for Si thin plate: Signal correction in frequency domain. Rev. Sci. Instrum. **86**, 035110 (2015). https://doi.org/10.1063/1.4914894
32. X. Liu, Wu. Hongpeng, L. Dong, Methodology and applications of acousto-electric analogy in photoacoustic cell design for trace gas analysis. Photoacoustics **30**, 100475 (2023). https://doi.org/10.1016/j.pacs.2023.100475
33. Thermal quadrupoles: solving the heat equation, by Denis Maillet, (2000), John Wiley & Sons, Chichester, West Sussex, ISBN: 9780471983200, 0471983209
34. S.P. Galovic, K.L. Djordjevic, M.V. Nesic, M.N. Popovic, D.D. Markushev, Time-domain minimum-volume cell photoacoustic of thin semiconductor layer I. Theory. J. Appl. Phy. (2023). https://doi.org/10.1063/5.0152519

materials

IMPACT FACTOR 3.748

Indexed in: PubMed

Article

Photoacoustic Characterization of TiO_2 Thin-Films Deposited on Silicon Substrate Using Neural Networks

Katarina Lj Djordjević, Dragana K. Markushev, Marica N. Popović, Mioljub V. Nesić, Slobodanka P. Galović, Dragan V. Lukić and Dragan D. Markushev

Special Issue

Characterization of Thin Films and Superlattice Using Thermal Wave Methods

Edited by

Prof. Dr. Michał Pawlak

MDPI

https://doi.org/10.3390/ma16072865

materials

MDPI

Article

Photoacoustic Characterization of TiO_2 Thin-Films Deposited on Silicon Substrate Using Neural Networks

Katarina Lj Djordjević [1], Dragana K. Markushev [2], Marica N. Popović [2], Mioljub V. Nesić [1], Slobodanka P. Galović [1,*], Dragan V. Lukić [2] and Dragan D. Markushev [2,*]

[1] "Vinča" Institute of Nuclear Sciences, National Institute of the Republic of Serbia, University of Belgrade, P.O. Box 522, 11000 Belgrade, Serbia
[2] Institute of Physics Belgrade, National Institute of the Republic of Serbia, Pregrevica 118, University of Belgrade, Zemun, 11080 Belgrade, Serbia
* Correspondence: bobagal@vin.bg.ac.rs (S.P.G.); dragan.markushev@ipb.ac.rs (D.D.M.)

Abstract: In this paper, the possibility of determining the thermal, elastic and geometric characteristics of a thin TiO_2 film deposited on a silicon substrate, with a thickness of 30 μm, in the frequency range of 20 to 20 kHz with neural networks were analysed. For this purpose, the geometric (thickness), thermal (thermal diffusivity, coefficient of linear expansion) and electronic parameters of substrates were known and constant in the two-layer model, while the following nano-layer thin-film parameters were changed: thickness, expansion and thermal diffusivity. Predictions of these three parameters of the thin-film were analysed separately with three neural networks. All of them together were joined by a fourth neural network. It was shown that the neural network, which analysed all three parameters at the same time, achieved the highest accuracy, so the use of networks that provide predictions for only one parameter is less reliable. The obtained results showed that the application of neural networks in determining the thermoelastic properties of a thin film on a supporting substrate enables the estimation of its characteristics with great accuracy.

Keywords: thin-film; TiO_2; photoacoustic; artificial neural networks; thermal diffusion; thermal expansion; inverse problem

Citation: Djordjević, K.L.; Markushev, D.K.; Popović, M.N.; Nesić, M.V.; Galović, S.P.; Lukić, D.V.; Markushev, D.D. Photoacoustic Characterization of TiO_2 Thin-Films Deposited on Silicon Substrate Using Neural Networks. *Materials* **2023**, *16*, 2865. https://doi.org/10.3390/ma16072865

Academic Editor: Michał Pawlak

Received: 22 February 2023
Revised: 24 March 2023
Accepted: 31 March 2023
Published: 4 April 2023

1. Introduction

The photoacoustic effect is the effect of the appearance of sound in the gaseous environment of a sample that is illuminated. This effect was discovered by A. G. Bell in 1880 [1], and explained by A. Rosencwaig almost 100 years later, in 1975 [2–4]. If the sample is exposed to the effect of electromagnetic radiation, part of the excitation energy is absorbed and part of the absorbed energy is transformed into heat through a non-radiative de-excitation relaxation process. This process is also called the photothermal effect. The heated sample generates a disturbance of the thermodynamic equilibrium with the environment and, as a result, there is a fluctuation of pressure, density and temperature in both the sample itself and in its gaseous surrounding. These fluctuations affect the appearance of several phenomena that can be detected in different ways [4]. Numerous non-destructive methods, known as photothermal methods, based on the recording of these phenomena, have been developed in the last half-century and are increasingly used for the characterization of various materials, electronic devices, sensors, biological tissues, etc. Pressure fluctuations are, in fact, a sound signal, the so-called photoacoustic effect, which can be detected using piezoelectric or ultrasonic sensors as well as a microphone [5–11]. The gas microphone photoacoustic was the first developed and today is one of the most widespread experimental techniques. The implementation of this measuring technique with a cell of minimal volume, proposed in the early 1980s, ensures that acoustic losses are attenuated as much as possible in detection.

In the last decade, TiO_2 has had a wide range of applications in coatings, medicines, plastics, food, inks, cosmetics, and textiles. In the form of thin-film, TiO_2 has been used for a great variety of applications, including photocatalytic degradation of organic pollutants in water as well as in air, dye-sensitized solar cells, anti-fogging, super hydrophilic, micro- and nano-mechanical sensors, etc. [12–15]. To be able to measure the physical properties of such thin films, it is usually necessary to deposit such a film on a thicker wafer.

The analysis of thin-films on substrates has always been a challenge for photoacoustic because film thicknesses ranges from a few tens to several hundred nanometres. Depending on the thickness of the substrate (usually more than tens of microns), such film thicknesses are usually at the limit of experimental detection [16–19]. This means, for example, that the differences in the amplitude of the photoacoustic signals (PAS), generated by a two-layer sample (substrate + thin-film) in the case where only the thickness of the film is changed, are extremely small [20–28]. The analysis of such two-layer samples is also theoretically demanding.

For photoacoustic measurements to be used in the characterization of materials, it is necessary to develop a theoretical model that well describes all the processes involved in the formation of the measured signal: the process of absorption and its conversion into heat, which depends on the optical properties of the sample, the processes of heat conduction and sound propagation, which depend on the thermal and elastic properties of the sample and the thermodynamic pressure change in the gaseous environment of the sample, that is, the sound signal formed by the heated sample and recorded by a microphone. The inverse solution of the photoacoustic problem is essentially a multi-parameter fitting of the sample properties based on the developed model, which should lead to the best matching of the theoretical model with the experimentally measured signal. Since it is a multi-parameter problem, which is also a non-linear and ill-posed problem of mathematical physics due to the limited measurement range, the inverse photoacoustic problem is still the subject of intensive research, especially in the case of multi-layered structures or semiconductors where an increased number of parameters influence the recorded increase in signals (in semiconductors, photogenerated carriers affect the recorded signal. In multi-layered structures, the same processes occur in all layers, but they are controlled by properties of each layer). This makes solving the inverse photoacoustic problem extremely difficult.

Recently, machine learning has been introduced to solve the inverse photoacoustic problem. The achieved results are encouraging because they show that the application of neural networks allows a very high accuracy of the multi-parameter fitting.

The earlier developed procedure based on neural networks [10,11,29–31] for processing of experimentally recorded photoacoustic signals of silicon samples by the open photoacoustic cell [32–35] shows effective recognition and removal of instrumental influence [33–40], and, consequently, provides a detailed and precise characterization of the sample [41–46]. On the other hand, a very thin TiO_2 layer (nano-layer) is easily deposited in a silicon substrate. Therefore, we selected a well-photoacoustically characterized silicon sample as the substrate, open photoacoustic cell photoacoustic set-up for measurement, and neural networks for solving the inverse PA photoacoustic problem and determining the thin-film's properties.

In order to avoid additional normalizations and the calculation of effective values, we resorted to the use of the two-layer model for determining thin-film parameters where the properties of the silicon substrate are known [21,47–62]. Neural networks were formed for the analysis of photoacoustic signals generated from the Si substrate and the TiO_2 thin-film system.

Based on previous experiences in PAS processing, we expected that they would recognize differences in signals caused by only changing film parameters (thickness, thermal diffusivity, coefficient of thermal expansion). We also expected that neural networks can determine the specified parameters of TiO_2 thin-film with satisfactory accuracy and reliability. To do this, we created a relatively small database of photoacoustic signals for training and four types of networks; three of them serve as the individual predictions of only one

parameter of the film, and the fourth, which serves as the prediction of all three parameters simultaneously.

In Section 2, a brief description of the theoretical model for the PAS measured on a two-layer structure is given. In Section 3, the network architecture used in the work is explained. Section 4 explains in detail how the base upon which the networks were trained and tested was formed. In Section 5, the results are given and discussed. In the end, the most important conclusions were drawn. The obtained results show that the application of neural networks in determining the thermoelastic properties of a thin-film on a supporting substrate enables the estimation of thin-film characteristics with great accuracy.

2. Experimental Procedure

The open-cell experimental photoacoustic set-up in a transmission configuration is illustrated in Figure 1. Excitation is performed by a low-power 10 mW laser/LED (XL7090-RED, RF Communication Electronic Technology Co., Ltd., Xiamen, China) diode regulated by a frequency generator in the range of 20 Hz to 20 kHz and which illuminates the sample with a red light of a wavelength of 660 nm with a distance that ensures homogeneous (uniform) surface illumination. Illumination control is performed by a sensitive photodiode (BPW34 Vishay Telefunken).

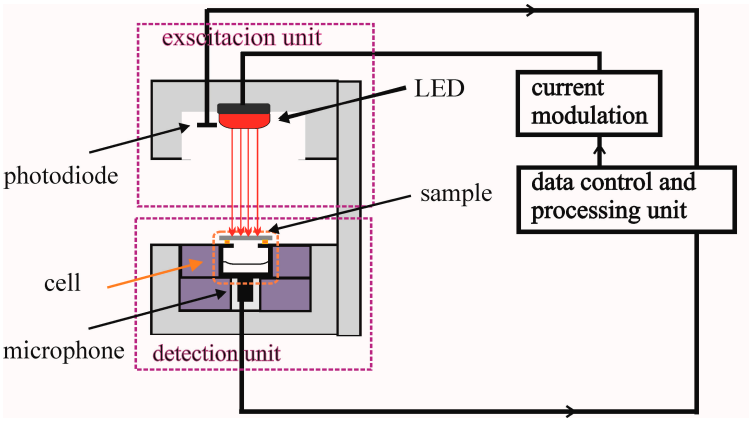

Figure 1. Open-cell experimental set-up in transmission configuration.

After absorption and excitation of the sample structural units, thermal energy is released through a non-radiative relaxation process, causing changes in the temperature profile of the sample. Periodic excitation generates a periodic change in the temperature distribution of the sample, which leads to periodic change in the pressure in the microphone hole that serves as a photoacoustic cell [32]. The sample is placed directly on the photoacoustic cell. The pressure changes are very small, ~10^{-6} bar, but the MC60 microphone, due to its sensitivity, detects their amplitudes and phase deviations from excitation optical signals recorded by the photodiode at each modulation frequency. The photoacoustic response is finally given in an amplitude-phase characteristic in a wide range of frequencies, from 10 Hz to 20 kHz.

The open photoacoustic cell [32], is formed so that the inside of the microphone represents a cell. Thus, the measurement takes place with a minimum volume, which enables the recording of weak sound signals. In the measuring set-up from Figure 1, the computer sound card (Intel 82,801 Ib/ir/ihhd) is used for making the lock-in amplifier. The sampling of the modulation frequencies is programmed in a regular logarithmic equidistant step. The photoacoustic response recorded in this way is suitable for the analysis of silicon samples up to 1 mm thick, with layers of thin-films with a thickness of up to several 100 nm, or the analysis of thin layers of multilayer structures.

One of the problems of photoacoustics is that the entire measurement frequency range is most often not used due to the influence of the accompanying measurement instrumen-

tation in the low and high-frequency ranges. The influence of the used instruments is reflected in the fact that the amplitude of the photoacoustic signal of the sample is distorted in the low and high frequency parts, and the phase shifts its position, as is shown in Figure 2. With the developed methodology of removing the instrumental influence [35–40], from the microphone to the accompanying electronics, it was shown that it is possible from the recorded photoacoustic response $S(f)$ to obtain the photoacoustic signal $\delta p_{\text{total}}(f)$, with a wide frequency range of 20 to 20 kHz, which can be used for further precise characterization [36–40]. The instrumental influence in the photoacoustic experiment can be described by the transfer function $H(f)$, which distorts the photoacoustic signal of the sample $\delta p_{\text{total}}(f)$, in the following way:

$$S(f) = \delta p_{\text{total}}(f) H(f) \tag{1}$$

$$H(f) = H^{\text{e}}_{\text{total}}(f) H^{\text{a}}_{\text{total}}(f) \tag{2}$$

The form of the function $H(f) = H^{\text{e}}_{\text{total}}(f) H^{\text{a}}_{\text{total}}(f)$ used for filtering in the low-frequency part represents the transfer functions, which characterize the influences of the microphone and accompanying electronics:

$$H^{\text{e}}_{\text{total}}(f) = -\frac{\omega \tau_{c1}}{(1 + i\omega \cdot \tau_{c1})} \cdot \frac{\omega\, \tau_{c2}}{(1 + i\omega \cdot \tau_{c2})}, \tag{3}$$

where time constants are $\tau_{c1} = (2\pi f_{c1})^{-1}$ and $\tau_{c2} = (2\pi f_{c2})^{-1}$, the attenuation factor is δj ($j = c3, c4$), the peak frequency is denoted by ω_{c3} and cut- by ω_{c4} ($\omega = 2\pi f$) (blue arrows, Figure 2). The function of form $H^{\text{a}}_{\text{total}}(f)$ is used for filtering in the high-frequency part. It is a combination of second-order transfer functions:

$$H^{\text{a}}_{\text{total}}(f) = \frac{\omega^2_{c3}}{\omega^2_{c3} + \delta_{c3} i\omega - \omega^2} + \frac{\omega^2_{c4}}{\omega^2_{c4} + \delta_{c4} i\omega - \omega^2}, \tag{4}$$

The correction procedure of the experimentally recorded photoacoustic response of multilayer samples produces a signal that can be further analyzed using a theoretical model and all frequency ranges of the measurement.

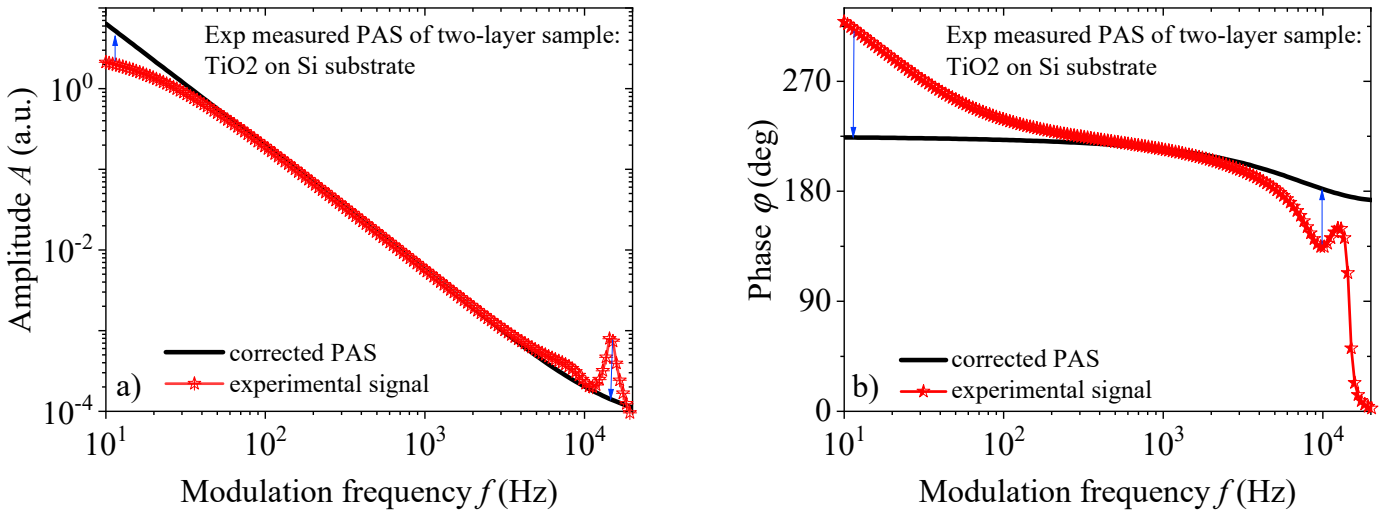

Figure 2. Frequency dependence of (**a**) amplitude and (**b**) phase of experimentally measured photoacoustic signal TiO_2 placed on Si substrate (red asterisk) and the corresponding amplitude and phase of the photoacoustic signal $\delta p_{\text{total}}(f)$ (black line), correction on the instrument input (blue arrows).

3. Theoretical Background

Using uniform illumination of the two-layer sample (Figure 3) with a modulated light source, the electromagnetic radiation is absorbed and produces a periodic change in the thermal state of both the thin-film and the substrate. The layer of TiO_2 is considered dielectric because there is no effect of photogenerated charge carriers due to the larger energy gap of TiO_2 in comparison to the photon energy of the exciting beam, while the photogenerated charge carriers affect the temperature profile of the silicon substrate $T_2(z,f)$. Temperature changes of the non-illuminated side of the sample $T_2(l,f)$ and the temperature gradient between the illuminated and non-illuminated sides of the sample causes the change in the thermodynamic state in the air behind the sample. Such fluctuations create three different components of sound that result from thermal transfer from the elastic bending of the sample (composite piston theory) that the microphone detects as a total photoacoustic signal $\delta p_{\text{total}}(f)$, defined as [10,11,21,30,63–66]:

$$\delta p_{\text{total}}(f) = \delta p_{\text{TD}}(f) + \delta p_{\text{TE}}(f) + \delta p_{\text{PE}}(f), \tag{5}$$

where f is the modulation frequency, and $\delta p_{\text{TD}}(f)$, $\delta p_{\text{TE}}(f)$ and $\delta p_{\text{PE}}(f)$ are the thermodiffusion (TD), thermoelastic (TE) and plasmaelastic (PE) photoacoustic signal components, respectively. The thermodiffusion component arises as a result of periodic heating of the non-illuminated surface of the sample, which periodically heats the air layer, causing it to periodically expand and contract. The periodic expansion and contraction of the air layer create a disturbance that is detected by the microphone. The thermoelastic component arises due to the temperature gradient between the illuminated and non-illuminated sides of the sample, which leads to the bending of the sample. Due to the modulation of the illumination, the bending is periodic, which pushes the pressure in the air that is detected by the microphone. The plasmaelastic component is caused by the photogeneration of carriers due to illumination, which leads to the additional bending of the sample, caused by a concentration gradient of charge carrier that pushes the pressure in the air which is then detected by the microphone. These components can be written as [10,11,21,30,63–66]:

$$\delta p_{\text{TD}}(f) = \frac{p_0 \gamma_g}{\sigma_g l_c} \frac{T_2(l_2, f)}{T_0}, \tag{6}$$

$$\delta p_c(f) = \frac{\gamma_g p_0}{V_0} \int_0^{R_s} 2\pi r U_{z,c}(r,z) \mathrm{d}r \; c = \text{TE, PE} \tag{7}$$

where γ_g is the adiabatic constant, p_0 and T_0 represent the standard pressure and temperature of the air in the microphone, $\sigma_g = (1+i)/\mu_g$, μ_g is the thermal diffusion length of the air, l_c is the photoacoustic cell length, $T_2(l_2,f)$ is the dynamic temperature variation at the substrate rear (non-illuminated) surface [10,11,21,30,63–66] (see Appendix A), V_0 is the open photoacoustic cell volume and $U_{z,c}(r,z)$ is the sample displacement along the z-axes (see Appendix B).

The total photoacoustic sound signals $\delta p_{\text{total}}(f)$, (Equation (5)) are usually represented using its amplitudes $A(f)$ and phases $\varphi(f)$. Therefore, $\delta p_{\text{total}}(f)$, can be written as a complex number in the form:

$$\delta p_{\text{total}}(f) = A(f) e^{i\varphi(f)}, \tag{8}$$

where i is the imaginary unit. The theoretically calculated photoacoustic signal $\delta p_{\text{total}}(f)$ is comparable to the experimentally recorded amplitude and phase from which the instrumental influence has been removed (Equations (1)–(4)). Thus, by analytically developing the model and numerical simulations, a standard method can be used for making the base of signals required for neural networks. The application of neural networks in photoacoustics

for characterization requires an adjusted value of amplitude in order to be comparable with the values of phase. A formula used for this purpose has a form:

$$A_{scale}(f) = 20\log_{10} A(f). \quad (9)$$

The theoretically determined photoacoustic signal $\delta p_{\text{total}}(f)$, is compared with the experimentally recorded amplitude and phase, and is used for material characterization.

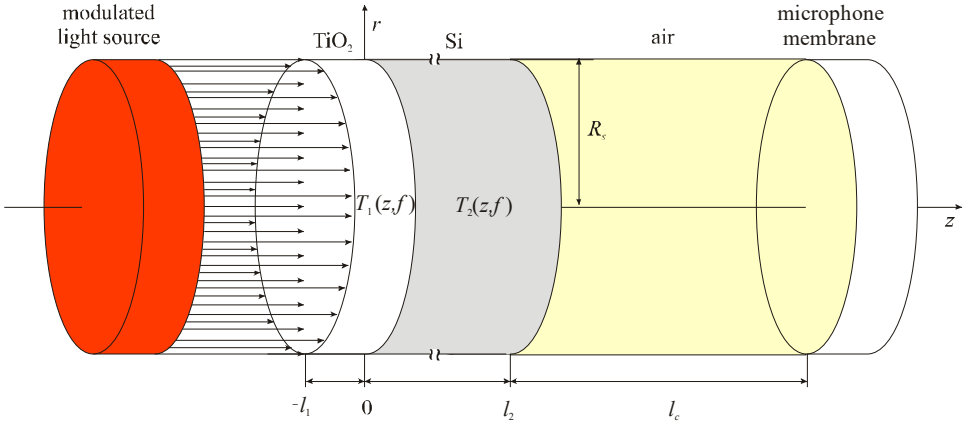

Figure 3. The simplest scheme of the two−layer sample irradiated by modulated light source. l_1 and l_2 ($l_1 << l_2$) are the thicknesses of the thin−film (TiO_2) and substrate (Si), respectively. R_s is the sample radius, $T_1(z,f)$ and $T_2(z,f)$ is the temperature distribution in the thin-film and substrate.

4. Networks Structure

The structure of the networks used to characterize the thin-films on the substrate is shown in Figure 4. All networks used in this paper have the same structure: 2 × 72 input neurons (72 amplitudes and 72 phases) and 15 neurons in the hidden layer. The three networks, labeled NN1, NN2 and NN3, have one neuron each in the output layer that serves to predict the l_1, α_{T_1} and D_{T_1} thin-film parameters, respectively. The network designated as NN4 has three neurons in the output layer that simultaneously predict all three mentioned parameters. The bases formed for the training of the first three networks were made individually (Base 1, Base 2 and Base 3), while the training base NN4 (Base 4) was made by merging all three individual bases [67–70].

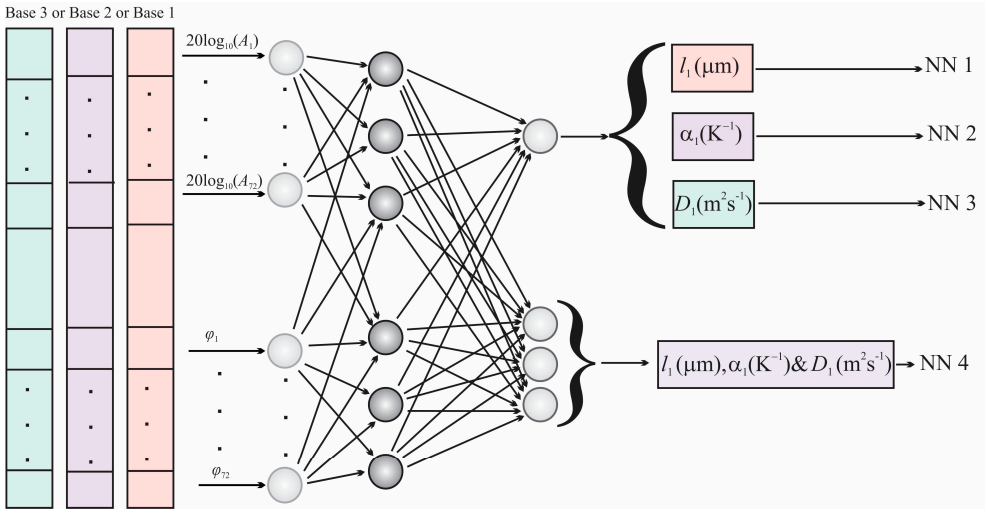

Figure 4. A representation of the structure of a single−layer neural network used for the training and prediction of TiO_2 thin−film parameters.

The training process involved neural network training on theoretical signal Bases 1–4, amplitude-phase characteristics and the connection with the parameters of the thin-film, performed by an algorithm that uses statistical models of machine learning that enable prediction, as shown in Figure 4. In the prediction process, thin-film parameters are determined from the test signal or the experimentally recorded photoacoustic signal.

5. Formation of the Networks Training Bases

The accuracy of the neural network largely depends on the selection of the basis for training, testing and validation. The bases have been obtained numerically using Equations (5)–(9). It is assumed that all these signals are generated by the Si substrate and TiO_2 thin-film two-layer system presented in Figure 3. All bases consist of 41 photoacoustics and one basic. The rest of them were obtained by changing 10% of the TiO_2 thin-film parameters. The basic parameters as a system property that affects the photoacoustic signal include: geometric (thickness), thermal (thermal diffusivity, coefficient of linear expansion) and electronic, which depend on the level of doping and the purity of Si and the properties of the TiO_2 thin-film, which are shown in Table 1, with standard temperature and pressure. Base 1 was formed for NN1 training, changing the thickness of TiO_2 film in the range of l_1 = (475–525) nm with a step of 5 nm. Base 2 was formed for NN2 training, obtained by changing the coefficient of thermal expansion of TiO_2 film in the range of $\alpha_1 = (1.045–1.55) \times 10^{-5}$ K^{-1} with a step of 5×10^{-8} K^{-1}. Base 3 was formed for NN3 training, changing the thermal diffusivity of TiO_2 film in the range of $D_1 = (3.515–3.885) \times 10^{-6}$ m^2s^{-1} with a step of 18.5×10^{-8} m^2s^{-1}. Base 4 was formed for NN4 training, obtained by collecting 3×41 signals from all three previously mentioned bases. Since all bases are very similar, we will show only one of them, Base 4, bearing in mind that, by one photoacoustic signal, we mean two curves presented in the networks: one for amplitude and another for phase (Equation (9) and Figure 5).

Table 1. Values of basic parameters used for PA simulation TiO_2 thin-film deposed on Si substrate.

Parameters	Labels	Values
Air thermal diffusivity	$D_g[m^2s^{-1}]$	2.0566×10^{-5}
Air thermal conductivity	$k_g[W(mK)^{-1}]$	0.0454
Relaxation time of air	$\tau_g[s]$	2×10^{-10}
Air adiabatic index	γ_g	1.4223
Si Thermal diffusivity	$D_{T2}[m^2s^{-1}]$	9×10^{-5}
TiO_2 Thermal diffusivity	$D_{T1}[m^2s^{-1}]$	3.7×10^{-6}
Si Thermal conductivity	$k_2[Wm^{-1}K^{-1}]$	150.0
TiO_2 Thermal conductivity	$k_1[Wm^{-1}K^{-1}]$	11.0
Si Thermal expansion coefficient	$\alpha_{T2}[K^{-1}]$	2.6×10^{-6}
TiO_2 Thermal expansion coefficient	$\alpha_{T1}[K^{-1}]$	1.1×10^{-5}
Si absorption coefficient	β_2	2.58×10^5
TiO_2 absorption coefficient	β_1	1.8×10^5
Si reflexing coefficient	R_2	0.3
TiO_2 reflexing coefficient	R_1	0.2
Si Young's modulus	Ey_2	1.37×10^{11}
TiO_2 Young's modulus	Ey_1	1.0×10^{11}
Si Poison coefficient	v_2	0.35
TiO_2 Poison coefficient	v_1	0.30

By displaying the photoacoustics of a silicon substrate thickness of l_2 = 30 μm, with different applied layers l_1 of TiO_2 thin-film, it is observed that there is no clear visual difference in the frequency dependence of the amplitudes, A, and that the factor of precise characterization by neural networks can be a visible difference in signal phases, φ, especially in the range from 10^3 Hz to 20 kHz, shown in Figure 5. The difference that exists in the phases is sufficient to train neural networks NN1-4 on the amplitude-phase characteristics

and to correctly determine the parameters of a thin layer that is two orders of magnitude thinner than the substrate.

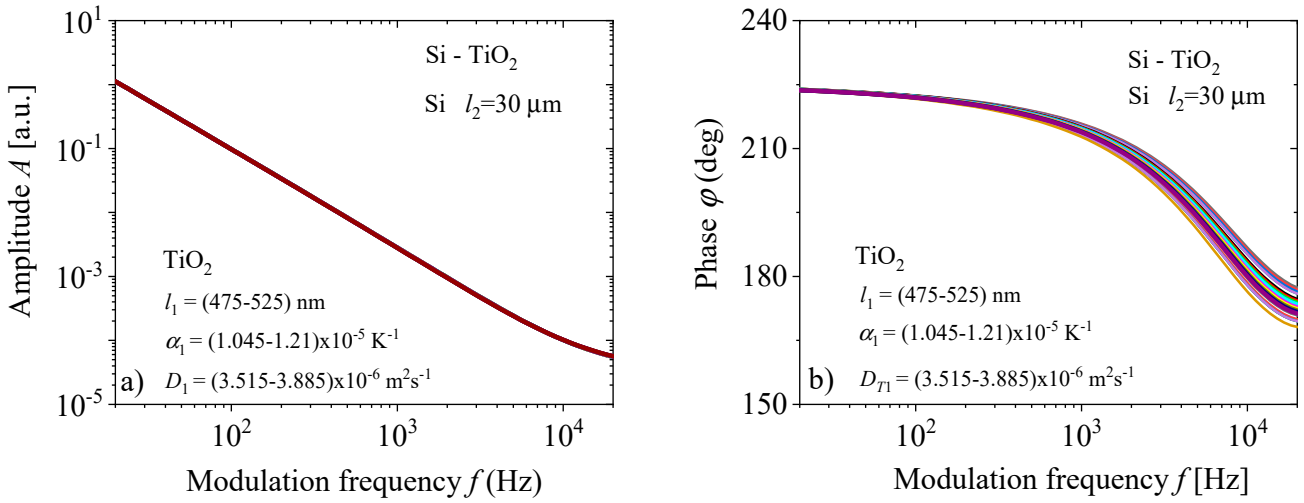

Figure 5. (**a**) Amplitudes, A, and (**b**) phases, φ, of the two−layer model: TiO_2 thin−films deposited on the Silicon substrate, obtained by changing parameters of the thin−film, diffusivity D_{T1}, expansion α_{T1} and thickness l_1.

6. Results and Discussion

The training results of the NN1-4 neural networks are given in Figure 6a–d, showing the Mean Square Error (MSE) of training, test and validation, depending on the number of epochs, and obtaining the best training performance. From each base for NN1-3 training, four signals were extracted for later testing. In the case of NN4 training, $3 \times 4 = 12$ signals were also extracted from Base 4 for later testing. Network training interruption is activated by the deviation criterion of Mean Square Error training in relation to validation and testing. The performance achieved by network NN1 is 4.1292×10^{-4} in 5 epochs, network NN2 achieved 9.5639×10^{-6} in 5 epochs, network NN3 achieved 3.6325×10^{-5} in 3 epochs and network NN4 achieved 9.8558×10^{-6} in 7 epochs. It can be seen by comparing these values that the best performance was obtained by the NN4 and NN2 networks for determining all three parameters and expansion, respectively. The NN1 network obtained the weakest performance for determining the thin-film thickness parameter.

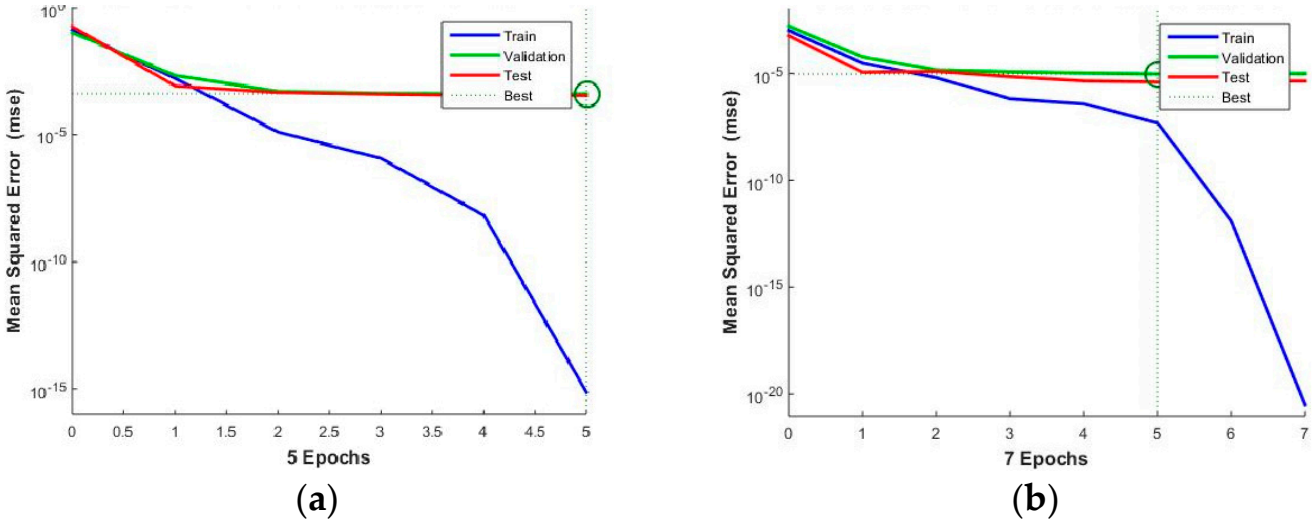

Figure 6. *Cont.*

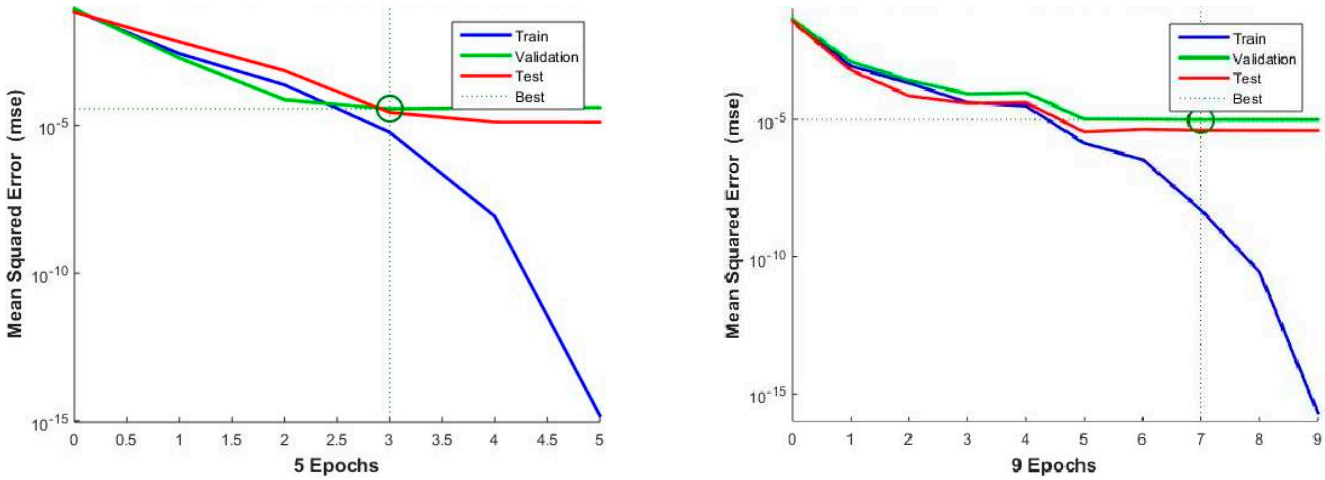

Figure 6. Network training: (**a**) NN1, (**b**) NN2, and (**c**) NN3 for determining the parameters of thickness, expansion, and diffusivity of the TiO_2 thin−film, respectively, and (**d**) NN4 for determining all three data, simultaneously.

6.1. Networks Testing with In-Step, Out-Step of Photoacoustic Signal

As we said in the previous paragraph, four signals that did not participate in the training were separated from each training base of the NN1-3 networks. A similar thing was carried out with the training base for the NN4 network, from which 12 signals were separated and did not participate in the training. All four networks were tested with these "in-step" signals and the results of such tests are shown in Tables 2 and 3. Relative error predictions (%) presented in these tables show that the most accurate networks are NN2 for the prediction of α_{T1} and NN4 for the prediction of D_{T1}.

Table 2. Relative (%) error prediction of TiO_2 thin-film parameters on 4 test photoacoustic signals that are in step by NN1, NN2 and NN3 networks.

Type of Network	**NN1**	**NN2**	**NN3**
Base	**1**	**2**	**3**
Parameter	l_1^{NN1}	α_{T1}^{NN2}	D_{T1}^{NN3}
TiO_2 film no.1	0.4060	0.1041	0.3424
TiO_2 film no.2	0.1681	0.1270	0.1526
TiO_2 film no.3	0.1414	0.0690	0.2317
TiO_2 film no.4	0.0658	0.1583	0.0764
Relative % error	0.1953	0.1146	0.2008

Table 3. Relative (%) error prediction of TiO_2 thin-film parameters NN4 on 4 signals from three bases "in-step" of training network.

Type of Network	**NN4**								
Base	**1**			**2**			**3**		
Parameters	l_1^{NN4}	α_{T1}^{NN4}	D_{T1}^{NN4}	l_1^{NN4}	α_{T1}^{NN4}	D_{T1}^{NN4}	l_1^{NN4}	α_{T1}^{NN4}	D_{T1}^{NN4}
TiO_2 film no.1	0.7878	0.8782	0.4542	0.3579	0.1592	0.9610	0.2958	0.0951	0.0152
TiO_2 film no.2	0.0130	0.2941	0.3980	0.4126	0.4990	0.0564	0.0165	0.1059	0.2139
TiO_2 film no.3	0.0187	0.2002	0.1512	0.7414	1.1077	1.3738	0.0932	0.0016	03694
TiO_2 film no.4	0.1578	0.0588	0.2811	0.4206	0.8822	0.8822	0.1298	0.1278	0.0663
Relat % error	0.2443	0.3578	0.3211	0.4831	0.6434	0.8183	0.1325	0.0831	0.1661

Our next step is to check the quality of the prediction of neural networks with "out-step" signals—signals outside the training step but within the framework of parameter changes. For this purpose, 12 signals were randomly generated. Four for each changed parameter l, α_T and D_T individually. The prediction results for all four networks are given in Table 4 (NN1-3) and Table 5 (NN4). It is interesting to note that the NN1 network gives the worst prediction of sample thickness, while the NN4 network gives relatively satisfactory predictions for all three parameters.

Table 4. Relative (%) error prediction of TiO_2 thin-film parameters NN1-3 on 4 signals from three bases "out of step" of training network.

Type of Network	**NN1**	**NN2**	**NN3**
Parameter	l_1^{NN1}	α_{T1}^{NN2}	D_{T1}^{NN3}
TiO_2 film no.1	2.4890	0.0186	0.0777
TiO_2 film no.2	2.4584	0.0293	0.0927
TiO_2 film no.3	5.4138	0.0011	0.2593
TiO_2 film no.4	4.8427	0.0031	0.0116
Relative % error	3.8099	0.0130	0.1103

Table 5. Relative (%) prediction error of TiO_2 thin-film parameters by NN4 for 4 signals "out of step".

Type of Network	**NN4**								
Base	**1**			**2**			**3**		
Parameter	l_1^{NN4}	α_{T1}^{NN4}	D_{T1}^{NN4}	l_1^{NN4}	α_{T1}^{NN4}	D_{T1}^{NN4}	l_1^{NN4}	α_{T1}^{NN4}	D_{T1}^{NN4}
TiO_2 film no.1	0.1184	0.0422	1.33552	0.0173	0.0081	0.0164	0.0070	0.0049	0.0245
TiO_2 film no.2	0.0422	0.0116	1.3516	0.0055	0.0183	0.0153	0.0182	0.0140	0.0104
TiO_2 film no.3	0.0066	0.0599	1.3880	0.0080	0.0058	0.0270	0.0097	0.0215	0.0104
TiO_2 film no.4	0.1213	0.0044	1.3685	0.0781	0.0225	0.0520	0.0245	0.0238	0.0059
Relative% error	0.0721	0.0368	1.3658	0.0272	0.0137	0.0277	0.0149	0.0161	0.0128

6.2. Networks Testing with Experimental Signals

The final part of our analysis is to test the ability to predict our networks on experimental signals. For this purpose, we measured, by the standard method of an open photoacoustic cell, the frequency response of a circular plate of a two-layer sample (silicon + TiO_2). Amplitudes and phases of the measured response (red stars) are shown in Figure 1. By removing the influence of the measuring chain (measuring instruments, especially detectors), corrected amplitudes and phases (black line) are obtained which can be analyzed by Equations (1)–(4) by the standard fitting method. The results of such analysis of the corrected signal give values of silicon (l_1 = 30 μm), which corresponds to standard silicon substrate (thin plate) thicknesses, titanium-dioxide (l_2 = 500 nm), which corresponds to standard thin-film thicknesses, and radius R = 3 mm, while other parameters correspond to the parameters from Table 1, with an error of 5%. The corrected signals from Figure 2 are further presented in our networks and the results of their prediction are given in Tables 6 and 7. The relative error in these tables is the result of comparing network predictions and standard fitting of the existing theoretical model.

Table 6. Parameters l_1^{NN1}, α_{T1}^{NN2} and D_{T1}^{NN3} obtained by prediction of NN1-3, with relative (%) errors are calculated according to the parameters obtained from standard photoacoustics techniques.

Parameter	l_1^{NN1}	α_{T1}^{NN1}	D_{T1}^{NN3}
NN exp prediction	4.8018×10^2 nm	1.0955×10^{-5} K^{-1}	3.57913×10^{-6} m^2s^{-1}
relative (%) error	3.9644	0.4066	2.9372

Table 7. Parameters l_1^{NN4}, α_{T1}^{NN4} and D_{T1}^{NN4} obtained by prediction of NN4, with relative (%) errors are calculated according to the parameters obtained from standard photoacoustics techniques.

Parameter	l_1^{NN4}	α_{T1}^{NN4}	D_{T1}^{NN4}
NN4 exp prediction	4.8690×10^2 nm	1.1166×10^{-5} K^{-1}	3.7189×10^{-6} m^2s^{-1}
relative (%) error	2.6196	1.5106	0.5105

Based on the results of the prediction by neural networks NN1–3, (Table 6), the most accurate network is NN2 in the prediction of the thermal expansion coefficient α_{T1}^{NN2} of a thin-film TiO_2, with a relative (%) error <1%, while the precision in the prediction of the thermal diffusivity D_{T1}^{NN3} and thickness l_1^{NN1} is with relative (%) errors <5%.

In the simultaneous prediction of the parameters of thickness l_1^{NN4}, thermal expansion coefficient α_{T1}^{NN4} and thermal diffusivity D_{T1}^{NN4} (Table 7), the NN4 network gives satisfactory results comparable to the prediction results of NN1–3.

Despite the expectations based on the consideration of the theoretical model, which is reflected in the small visual difference of the amplitude characteristics and stratification of signal phases in the high-frequency part (1–20) kHz, neural networks based on the coupled amplitudes and phases in the frequency domain (20–20 k) Hz can determine the parameters of the thin-layer TiO_2. The results of neural networks show that more precise and accurate results are obtained in networks in which multiple parameters are determined at the same time (Tables 3 and 5) than in networks in the prediction of individual parameters (Tables 2 and 4). This conclusion is also valid for the prediction of the thin-film parameter from the experimental results, where the reduction of the relative % error in the prediction of the network NN4 in relation to NN1–3 is observed, which can represent one of the methods of optimizing the work of networks in prediction the parameter of thin-films. It should be noted that the derived model is made for the expected ranges that each of the three parameters of the thin layer can have. If some of the parameters are outside this range, e.g., thickness of the thin-film, it could lead to incorrect determination of all three parameters of the thin-film using the proposed model.

This consideration is particularly valid due to the analysis of a thin layer of TiO_2 placed on a well-characterized substrate, in this case, silicon. The method of characterization of TiO_2 developed in this way can be applied and analyzed on other well-characterized optically transparent and non-transparent substrates. By applying TiO_2 to optically transparent substrates, and by characterizing it, we obtain a suitable material for protecting the detectors of the measuring system.

7. Conclusions

The results presented in this paper indicate one very important fact—if in the measurement range, there is an influence of the thin-film on the total photoacoustic signal, neural networks easily can recognize these changes, even if they are negligibly small. Theoretical analyses of two-layer samples Si (substrate) and TiO_2 (thin-film) showed relatively easy recognition of changes in the film of a thickness of ± 5 nm, with the coefficient of thermal expansion of $\pm 5 \times 10^{-8}$ K^{-1} and coefficient of thermal diffusion of $\pm 18.5 \times 10^{-8}$ m^2s^{-1}.

In addition, it has been shown that neural networks for predicting thin-film parameters can be well-trained with a relatively small database, either to predict one or three parameters simultaneously. Furthermore, all networks give approximately the same accuracy of prediction in both theoretically generated signals and experimental data. Therefore, it can be recommended that, for the analysis of thin-films on different substrates, it is enough to form one network that simultaneously predicts several of its parameters instead of a separate network for determining each parameter.

Author Contributions: Conceptualization, K.L.D. and D.K.M.; methodology, S.P.G. and D.D.M.; software, K.L.D.; validation, S.P.G., M.N.P. and D.D.M.; formal analysis, D.K.M. and M.N.P.; investigation, K.L.D.; resources, M.V.N. and D.V.L.; data curation, K.L.D.; writing—original draft preparation, D.D.M.; writing—review and editing, K.L.D. and S.P.G.; visualization, K.L.D. and M.V.N.; supervision, S.P.G.; project administration, D.D.M.; funding acquisition, M.V.N. and D.V.L.; All authors have read and agreed to the published version of the manuscript.

Funding: This research was funded by the Ministry of Science, Technological Development and Innovation of the Republic of Serbia, contract number 451-03-47/2023-01/200017.

Data Availability Statement: The data that support the findings of this study are available from the corresponding author upon reasonable request.

Acknowledgments: The authors are grateful to Dragan Todorovic for the knowledge and support provided in their progress. We are thankful for the financial support of this research by the Ministry of Science, Technological Development and Innovation of the Republic of Serbia, contract number 451-03-47/2023-01/200017.

Conflicts of Interest: The authors declare no conflict of interest.

Appendix A. Temperature Distributions in Two-Layer Sample

Periodic temperature distributions in the thin-film (label 1 forTiO_2) and substrate (label 2 for Si) illuminated by the modulated light source (Figures 1 and 3) can be obtained by solving the thermal-diffusion equations in the form [21,31,59,62]:

$$\frac{\partial^2 T_1(z,f)}{\partial z^2} - \frac{i\omega}{D_{T1}} T_1(z,f) = -\frac{1}{k_1}\beta_1(1-R_1)I_0 e^{-\beta_1 z} \tag{A1}$$

and

$$\frac{\partial^2 T_2(z,f)}{\partial z^2} - \sigma_2^2 T_2(z,f) = -\frac{\varepsilon_g}{k_2\tau_2} n_{p2}(z,f) - \frac{\beta_2 I}{k_2}\cdot\frac{\varepsilon-\varepsilon_g}{\varepsilon} e^{-\beta_2 z} \tag{A2}$$

where $\omega = 2\pi f$, f is the modulation frequency, I_0 is the incident light intensity, $I = (1-R_1)(1-R_2)e^{-\beta_1 l_1} I_0$, R_1 is the film reflection coefficient, R_2 is the substrate reflection coefficient, $\sigma_1 = \sqrt{i\omega/D_{T1}}$ is the film complex thermal diffusivity, D_{T1} is the film thermal diffusion coefficient, $\sigma_2 = \sqrt{i\omega/D_{T2}}$ is the substrate complex thermal diffusivity, D_{T2} is the substrate thermal diffusion coefficient, k_1 is the thin-film heat conduction coefficient, k_2 is the substrate heat conduction coefficient, β_1 is the film absorption coefficient, β_2 is the substrate absorption coefficient, and $\delta n_{p2}(z,f)$ is the substrate photo-generated minority carrier dynamic density component (Equation (A2)).

The general solutions of Equations (A1) and (A2) can be written in the form [21,31,59,62]:

$$T_1(z,f) = A_1 e^{\sigma_1 z} + A_2 e^{-\sigma_1 z} + A_3 e^{-\beta_1 z}, \tag{A3}$$

and

$$T_2(z,f) = B_1 e^{\sigma_2 z} + B_2 e^{-\sigma_2 z} + B_3\delta n_p(z,f) + B_4 e^{-\beta_1 z}, \tag{A4}$$

where the constants A_3, B_3 and B_4 are given as:

$$A_3 = -\frac{\beta_1 I_0(1-R_1)}{k_1(\beta_1^2-\sigma_1^2)},\ B_3 = -\frac{\varepsilon_g}{k_2\tau_{p2}\left(\sigma_2^2 - \frac{1}{L_2^2}\right)},\ B_4 = -\frac{\beta_2(1-R_1)(1-R_2)e^{-\beta_1 l_1} I_0}{\varepsilon(\beta_2^2-\sigma_2^2)}\left(\frac{B_3}{D_{p2}} - \frac{\varepsilon-\varepsilon_g}{k_2}\right).$$

Here $L_2 = \sqrt{\frac{D_{p2}\tau_{p2}}{1+i\omega\tau_{p2}}}$ is the complex minority carrier diffusion length, D_{p2} is the diffusion coefficient of minority carriers (holes p in the n-type substrate), and τ_{p2} is the bulk minority carrier lifetime. Constants A_1, A_2, B_1 and B_2 can be found solving the boundary conditions [21,31,59,62]:

$$(a) - k_1 \frac{\partial T_1(z,f)}{\partial z}\bigg|_{z=-l_1} = 0,\ (b)\ T_1(0,f) = T_2(0,f),$$

$$(c) - k_2 \frac{\partial T_2(z,f)}{\partial z}\bigg|_{z=0} = s_F n_{p2}(0,f)\varepsilon_g - k_1 \frac{\partial T_1(z,f)}{\partial z}\bigg|_{z=0},$$

$$(d) - k_2 \frac{\partial T_2(z,f)}{\partial z}\bigg|_{z=l_2} = -s_R n_{p2}(l_2,f)\varepsilon_g, \tag{A5}$$

where s_F and s_R are the substrate surface recombination speeds at the front ($z = 0$) and rear ($z = l_2$) surfaces, respectively.

Based on our previous investigations, the analysis of the two-layer optical properties shows that the multiple optical reflections can be neglected in the Si substrate [31], but must be taken into account in the case of thin TiO_2 film. This is the reason why the film reflection coefficient R_1 is calculated here using [21,62]:

$$R_1 = r_F + (1 - r_F)^2 r_R \cdot \frac{e^{-2\beta_1 l_1}}{1 - r_F r_R e^{-2\beta_1 l_1}}, \tag{A6}$$

where r_F and r_R are the front and rear thin-film reflectivity coefficients, respectively.

Appendix B. Two-Layer Sample Displacement along the Heat-Flow Axes

The $U_{z,c}(r,z)$ of the two-layer sample at the back surface, $z = l_2$, important in transmission photoacoustic measurements, can be written in a general form as:

$$U_{z,c}(r,z) = \frac{C_c}{2}\left(R_s^2 - r^2\right),\ c = TE, PE, \tag{A7}$$

where R_s is the sample radius and

$$C_{TE} = 6\frac{A_1 + A_2 + E_1E_2[\alpha_{T1}l_2(2M_{T1} - l_2N_{T1}) + \alpha_{T2}l_1(2M_{T2} + l_1N_{T2})]}{E_1^2l_1^4 + E_2^2l_2^4 + 2E_2E_1l_2l_1\left(2l_2^2 + 3l_2l_1 + 2l_1^2\right)}, \tag{A8a}$$

$$C_{PE} = 6d_nE_2\frac{[E_1l_1(2M_n + l_1N_n) + E_2l_2(2M_n - l_2N_n)]}{E_2^2l_2^4 + E_1^2l_1^4 + 2E_2E_1l_2l_1\left(2l_2^2 + 3l_2l_1 + 2l_1^2\right)}. \tag{A8b}$$

Here $A_1 = E_1^2l_1(2M_{T1} + l_1N_{T1})\alpha_{T1}, A_2 = E_2^2l_2(2M_{T2} - l_2N_{T2})\alpha_{T2}$, E_1 and E_2 are Young's modulus of the film and substrate, respectively, d_n is the coefficient of electronic deformation and M_{T1}, M_{T2}, M_n, N_{T1}, N_{T2} and N_n are defined as:

$$M_{T1} = \int_{-l_1}^{0} z \cdot T_1(z,f)\mathrm{d}z, M_{T2} = \int_{0}^{l_2} z \cdot T_2(z,f)\mathrm{d}z, M_n = \int_{0}^{l_2} z \cdot \delta n_{p2}(z,f)\mathrm{d}z, \tag{A9}$$

$$N_{T1} = \int_{-l_1}^{0} T_1(z,f)\mathrm{d}z. N_{T2} = \int_{0}^{l_2} T_2(z,f)\mathrm{d}z, N_n = \int_{0}^{l_2} \delta n_{p2}(z,f)\mathrm{d}z, \tag{A10}$$

where $T_1(z,f)$ is the temperature in the thin-film and $T_2(z,f)$ is the temperature in the substrate and $\delta n_{p2}(z,f)$ is the photo-generated minority carrier density. The M_{T1}, and M_{T2} are the first moments of the temperature change, and the M_n is the first moment of the photo-generated minority carriers change along the z-axis. The N_{T1} and N_{T2} are the average temperature changes and N_n is the average photo-generated minority carriers change along the z-axes [21,31,59,62].

References

1. Bell, A.G. On the production and reproduction of sound by light. *Am. J. Sci.* **1880**, *20*, 20305–20324. [CrossRef]
2. Rosencwaig, A. Photoacoustic spectroscopy of solids. *Opt. Commun.* **1973**, *7*, 305–308. [CrossRef]
3. Rosencwaig, A.; Gersho, A. Photoacoustic effect with solids: A theoretical treatment. *Science* **1975**, *19*, 556–557. [CrossRef]
4. Vargas, H.; Miranda, L.C.M. Photoacoustic and related photothermal techniques. *Phys. Rep.* **1988**, *161*, 43–101. [CrossRef]
5. McDonald, F.; Wetsel, G. Generalized theory of the photoacoustic effect. *J. Appl. Phys.* **1978**, *49*, 2313. [CrossRef]
6. McDonald, F.A.; Wetsel, G.C. Theory of Photothermal and Photoacoustic Effects in Condensed Matter. In *Physical Acoustics*; Academic Press: Cambridge, MA, USA, 1988. [CrossRef]
7. Fournier, D.; Boccara, A.C.; Skumanich, A.; Amer, N.M. Photothermal investigation of transport in semiconductors: Theory and experiment. *J. Appl. Phys.* **1986**, *59*, 787. [CrossRef]
8. Sablikov, V.A.; Sandomirskii, V.B. The photoacoustic effect in semiconductors. *Phys. Status Solidi (B)* **1983**, *120*, 471. [CrossRef]
9. Pinto Neto, A.; Vargas, H.; Leite, N.F.; Miranda, L.C.M. Photoacoustic investigation of semiconductors: Influence of carrier diffusion and recombination in PbTe and Si. *Phys. Rev. B* **1989**, *40*, 3924–3930. [CrossRef]
10. Todorović, D.M.; Nikolić, P.M.; Dramićanin, M.D.; Vasiljević, D.G.; Ristovski, Z.D. Photoacoustic frequency heat-transmission technique: Thermal and carrier transport parameters measurements in silicon. *J. Appl. Phys.* **1995**, *78*, 5750–5755. [CrossRef]
11. Todorović, D.M.; Nikolić, P.M. *Semiconductors and Electronic Materials Progress in Photothermal and Photoacoustic, Science and Technology Chapter 9*; Optical Engineering Press: New York, NY, USA, 2000; Volume PM74, pp. 273–318. ISBN 9780819435064.
12. Delgado, L.P.; Figueroa-Torres, M.Z.; Ceballos-Chuc, M.C.; García-Rodríguez, R.; Alvarado-Gil, J.J.; Oskam, G.; Rodriguez-Gattorno, G. Tailoring the TiO_2 phases through microwave-assisted hydrothermal synthesis: Comparative assessment of bactericidal activity. *Mater. Sci. Eng. C* **2020**, *117*, 111290. [CrossRef]
13. Trejo-Tzab, R.; Alvarado-Gil, J.J.; Quintana, P.; Bartolo-Pérez, P. N-doped TiO_2 P25/Cu powder obtained using nitrogen (N_2) gas plasma. *Catal. Today* **2012**, *193*, 179–185. [CrossRef]
14. Ceballos-Chuc, M.C.; Ramos-Castillo, C.M.; Alvarado-Gil, J.J.; Oskam, G.; Rodríguez-Gattorno, G. Influence of Brookite Impurities on the Raman Spectrum of TiO_2 Anatase Nanocrystals. *J. Phys. Chem. C* **2018**, *122*, 19921–19930. [CrossRef]
15. Patil, M.K.; Shaikh, S.; Ganesh, I. Recent Advances on TiO_2 Thin Film Based Photocatalytic Applications (A Review). *Curr. Nanosci.* **2015**, *11*, 271–285. [CrossRef]
16. Mandelis, A.; Batista, J.; Pawlak, M.; Gibkes, J.; Pelzl, J. Space charge layer dynamics at oxide-semiconductor interfaces under optical modulation: Theory and experimental studies by non-contact photocarrier radiometry. *J. Phys. IV* **2005**, *125*, 565–567. [CrossRef]
17. Somer, A.; Camilotti, F.; Costa, G.F.; Bonardi, C.; Novatski, A.; Andrade, A.V.C.; Kozlowski, V.A., Jr.; Cruz, G.K. The thermoelastic bending and thermal diffusion processes influence on photoacoustic signal generation using open photoacoustic cell technique. *J. Appl. Phys.* **2013**, *114*, 063503. [CrossRef]
18. Dubyk, K.; Chepela, L.; Lishchuk, P.; Belarouci, A.; Lacroix, D.; Isaiev, M. Features of photothermal transformation in porous silicon based multilayered structures. *Appl. Phys. Lett.* **2019**, *115*, 021902. [CrossRef]
19. Maliński, M.; Pawlak, M.; Chrobak, L.; Pal, S.; Ludwig, A. Monitoring of amorfization of the oxygen implanted layers in silicon wafers using photothermal radiometry and modulated free carrier absorption methods. *Appl. Phys. A* **2014**, *118*, 1009–1014. [CrossRef]
20. Larson, K.B.; Koyama, K. Measurement by the Flash Method of Thermal Diffusivity, Heart Capacity, and Thermal Conductivity in Two-Layer Composite Samples. *J. Appl. Phys.* **1968**, *39*, 4408–4416. [CrossRef]
21. Todorović, D.M.; Rabasović, M.D.; Markushev, D.D. Photoacoustic elastic bending in thin film—Substrate system. *J. Appl. Phys.* **2013**, *114*, 213510. [CrossRef]
22. Aguirre, N.M.; Pérez, L.M.; Garibay-Febles, V.; Lozada-Cassou, M. Influence of the solid–gas interface on the effective thermal parameters of a two-layer structure in photoacoustic experiments. *J. Phys. D Appl. Phys.* **2003**, *37*, 128–131. [CrossRef]
23. Salazar, A.; Sánchez-Lavega, A.; Terrón, J.M. Effective thermal diffusivity of layered materials measured by modulated photothermal techniques. *J. Appl. Phys.* **1998**, *84*, 3031–3041. [CrossRef]
24. Somer, A.; Novatski, A.; Cruz, C.B.K.; Serbena, F.C.; Cruz, G.K.D. The Influence of the Surface Micro-structure Change on the Stainless Steel Effective Thermal Diffusivity. *Int. J. Thermophys.* **2022**, *43*, 151. [CrossRef]
25. Medina, J.; Gurevich, Y.G.; Logvinov, G.N.; Rodríguez, P.; de la Cruz, G.G. Photoacoustic investigation of the effective diffusivity of two-layer semiconductors. *Mol. Phys.* **2002**, *100*, 3133–3138. [CrossRef]
26. Sánchez-Lavega, A.; Salazar, A.; Ocariz, A.; Pottier, L.; Gomez, E.; Villar, L.M.; Macho, E. Thermal diffusivity measurements in porous ceramics by photothermal methods. *Appl. Phys. A Mater. Sci. Process.* **1997**, *65*, 15–22. [CrossRef]
27. Somer, A.; Camilotti, F.; Costa, G.F.; Jurelo, A.R.; Assmann, A.; de Souza, G.B.; Cintho, O.M.; Bonardi, C.; Novatski, A.; Cruz, G.K. Effects of thermal oxidation on the effective thermal diffusivity of titanium alloys. *J. Phys. D Appl. Phys.* **2014**, *47*, 385306. [CrossRef]
28. Mandelis, A.; Batista, J.; Gibkes, J.; Pawlak, M.; Pelzl, J. Noncontacting laser photocarrier radiometric depth profilometry of harmonically modulated band bending in the space-charge layer at doped SiO_2-Si interfaces. *J. Appl. Phys.* **2005**, *97*, 083507. [CrossRef]
29. Gunha, J.V.; Gonçalves, A.; Somer, A.; de Andrade, A.V.K.; Dias, D.T.; Novatski, A. Thermal, structural and optical properties of TeO_2–Na_2O–TiO_2 glassy system. *J. Mater. Sci. Mater. Electron.* **2019**, *30*, 16695–16701. [CrossRef]

30. Markushev, D.K.; Markushev, D.D.; Galović, S.; Aleksić, S.; Pantić, D.; Todorović, D.M. The surface recombination velocity and bulk lifetime influences on photogenerated excess carrier density and temperature distributions in n-type silicon excited by a frequency-modulated light source. *Facta Univ. Ser. Electron. Energetics* **2018**, *31*, 313–328. [CrossRef]
31. Jovančić, N.; Markushev, D.K.; Markushev, D.D.; Aleksić, S.M.; Pantić, D.S.; Korte, D.; Franko, M. Thermal and Elastic Characterization of Nanostructured Fe_2O_3 Polymorphs and TiO_2-Coated Fe_2O_3 Using Open Photoacoustic Cell. *Int. J. Thermophys.* **2020**, *41*, 90. [CrossRef]
32. Rabasović, M.D.; Nikolić, M.G.; Dramićanin, M.D.; Franko, M.; Markushev, D.D. Low-cost, portable photoacoustic setup for solid state. *Meas Sci. Technol.* **2009**, *20*, 095902. [CrossRef]
33. Perondi, L.F.; Miranda, L.C.M. Minimal-volume photoacoustic cell measurement of thermal diffusivity: Effect of the thermoelastic sample bending. *J. Appl. Phys.* **1997**, *62*, 2955–2959. [CrossRef]
34. Korte, D.; Pavlica, E.; Bratina, G.; Franko, M. Characterization of Pure and Modified TiO_2 Layer on Glass and Aluminum Support by Beam Deflection Spectrometry. *Int. J. Thermophys.* **2014**, *35*, 1990–2000. [CrossRef]
35. Markushev, D.D.; Rabasović, M.D.; Todorović, D.M.; Galović, S.; Bialkowski, S.E. Photoacoustic signal and noise analysis for Si thin plate: Signal correction in frequency domain. *Rev. Sci. Instrum.* **2015**, *86*, 035110. [CrossRef] [PubMed]
36. Popović, M.N.; Nešić, M.V.; Cirić-Kostić, S.; Zivanov, M.; Markushev, D.D.; Rabasovic, M.D.; Galovic, S.P. Helmholtz resonances in photoacoustic experiment with laser-sintered polyamide including thermal memory of samples. *Int. J. Thermophys.* **2016**, *37*, 116. [CrossRef]
37. Aleksić, S.M.; Markushev, D.K.; Pantić, D.S.; Rabasović, M.D.; Markushev, D.D.; Todorović, D.M. Electro-acoustic influence of the measuring system on the photoacoustic signal amplitude and phase in frequency domain. *Facta Univ. Ser. Phys. Chem. Technol.* **2016**, *14*, 9–20. [CrossRef]
38. Jordović-Pavlović, M.I.; Stanković, M.M.; Popović, M.N.; Ćojbašić, Ž.M.; Galović, S.P.; Markushev, D.D. The application of artificial neural networks in solid-state photoacoustics for the recognition of microphone response effects in the frequency domain. *J. Comput. Electron.* **2020**, *19*, 1268–1280. [CrossRef]
39. Jordovic-Pavlovic, M.I.; Kupusinac, A.D.; Djordjevic, K.L.; Galovic, S.P.; Markushev, D.D.; Nesic, M.V.; Popovic, M.N. Computationally intelligent description of a photoacoustic detector. *Opt. Quantum Electron.* **2020**, *52*, 246. [CrossRef]
40. Jordovic Pavlovic, M.I.; Markushev, D.D.; Kupusinac, A.D.; Djordjevic, K.L.; Nesic, M.V.; Galovic, S.P.; Popovic, M.N. Deep Neural Network Application in the Phase-Match Calibration of Gas–Microphone Photoacoustics. *Int. J. Thermophys.* **2020**, *41*, 73. [CrossRef]
41. Popovic, M.N.; Furundzic, D.; Galovic, S.P. Photothermal depth profiling of optical gradient materials by neural network. *Publ. Astron. Obs. Belgrade* **2010**, *89*, 2015.
42. Nesic, M.; Popovic, M.; Djordjevic, K.; Miletic, V.; Jordovic-Pavlovic, M.; Markushev, D.; Galovic, S. Development and comparison of the techniques for solving the inverse problem in photoacoustic characterization of semiconductors. *Opt. Quantum Electron.* **2021**, *53*, 381. [CrossRef]
43. Lukić, M.; Ćojbašić, Z.; Markushev, D.D. Trace gases analysis in pulsed photoacoustics based on swarm intelligence optimization. *Opt. Quantum Electron.* **2022**, *54*, 674. [CrossRef]
44. Lukić, M.; Ćojbašić, Z.; Rabasović, M.D.; Markushev, D.D.; Todorović, D.M. Genetic Algorithms Application for the Photoacoustic Signal Temporal Shape Analysis and Energy Density Spatial Distribution Calculation. *Int. J. Thermophys.* **2013**, *34*, 1466–1472. [CrossRef]
45. Nesic, M.V.; Popovic, M.N.; Galovic, S.P.; Djordjevic, K.L.; Jordovic-Pavlovic, M.I.; Miletic, V.V.; Markushev, D.D. Estimation of linear expansion coefficient and thermal diffusivity by photoacoustic numerical self-consistent procedure. *J. Appl. Phys.* **2022**, *131*, 105104. [CrossRef]
46. Nesic, M.; Popovic, M.; Galovic, S. Developing the Techniques for Solving the Inverse Problem in Photoacoustics. *Atoms* **2019**, *7*, 24. [CrossRef]
47. Lopez, T.; Picquart, M.; Aguirre, G.; Arriola, G.; Freile, Y.; Aguilar, D.H.; Quintana, P.; Alvarado-Gil, J.J.; Vargas-Luna, F.M. Thermal Characterization of Agar Encapsulated in TiO_2 Sol-Gel. *Int. J. Thermophys.* **2004**, *25*, 1483–1493. [CrossRef]
48. Mansanares, A.M.; Vargas, H.; Galembeck, F.; Buijs, J.; Bicanic, D. Photoacoustic characterization of a two-layer system. *J. Appl. Phys.* **1991**, *70*, 7046–7050. [CrossRef]
49. Lima, C.A.S.; Miranda, L.C.M.; Vargas, H. Photoacoustics of Two-Layer Systems: Thermal Properties of Liquids and Thermal Wave Interference. *Instrum. Sci. Technol.* **2006**, *34*, 191–209. [CrossRef]
50. Gurevich, Y.G.; Logvinov, G.N.; de la Cruz, G.G.; López, G.E. Physics of thermal waves in homogeneous and inhomogeneous (two-layer) samples. *Int. J. Therm. Sci.* **2003**, *42*, 63–69. [CrossRef]
51. Nogueira, E.; Pereira, J.R.; Baesso, M.; Bento, A. Study of layered and defective amorphous solids by means of thermal wave method. *J. Non-Cryst. Solids* **2003**, *318*, 314–321. [CrossRef]
52. Popovic, M.N.; Nesic, M.V.; Zivanov, M.; Markushev, D.D.; Galovic, S.P. Photoacoustic response of a transmission photoacoustic configuration for two-layer samples with thermal memory. *Opt. Quantum Electron.* **2018**, *50*, 330. [CrossRef]
53. Pichardo, J.L.; Alvarado-Gil, J.J. Open photoacoustic cell determination of the thermal interface resistance in two layer systems. *J. Appl. Phys.* **2001**, *89*, 4070–4075. [CrossRef]
54. Pichardo-Molina, J.L.; Alvarado-Gil, J.J. Heat diffusion and thermolastic vibration influence on the signal of an open photoacoustic cell for two layer systems. *J. Appl. Phys.* **2004**, *95*, 6450–6456. [CrossRef]

55. Alvarado-Gil, J.; Zelaya-Angel, O.; Sánchez-Sinencio, F.; Vargas, H.; Lucio, J. Photoacoustic thermal characterization of a semiconductor (CdTe)-glass two layer system. *Vacuum* **1995**, *46*, 883–886. [CrossRef]
56. Somer, A.; Popovic, M.N.; da Cruz, G.K.; Novatski, A.; Lenzi, E.K.; Galovic, S.P. Anomalous thermal diffusion in two-layer system: The temperature profile and photoacoustic signal for rear light incidence. *Int. J. Therm. Sci.* **2022**, *179*, 107661. [CrossRef]
57. Alekseev, S.; Andrusenko, D.; Burbelo, R.; Isaiev, M.; Kuzmich, A. Photoacoustic thermal conductivity determination of layered structures PS-Si: Piezoelectric detection. *J. Phys. Conf. Ser.* **2011**, *278*, 012003. [CrossRef]
58. Popovic, M.N.; Markushev, D.D.; Nesic, M.V.; Jordovic-Pavlovic, M.I.; Galovic, S.P. Optically induced temperature variations in a two-layer volume absorber including thermal memory effects. *J. Appl. Phys.* **2021**, *129*, 015104. [CrossRef]
59. Aleksić, S.M.; Markushev, D.K.; Markushev, D.D.; Pantić, D.S.; Lukić, D.V.; Popović, M.N.; Galović, S.P. Photoacoustic Analysis of Illuminated Si-TiO_2 Sample Bending along the Heat-Flow Axes. *Silicon* **2022**, *14*, 23. [CrossRef]
60. Markushev, D.D.; Rabasović, M.D.; Nesic, M.; Popovic, M.; Galovic, S. Influence of Thermal Memory on Thermal Piston Model of Photoacoustic Response. *Int. J. Thermophys.* **2012**, *33*, 2210–2216. [CrossRef]
61. Korte, D.; Franko, M. Photothermal Deflection Experiments: Comparison of Existing Theoretical Models and Their Applications to Characterization of TiO_2-Based Thin Films. *Int. J. Thermophys.* **2014**, *35*, 2352–2362. [CrossRef]
62. Todorović, D.M.; Rabasović, M.D.; Markushev, D.D.; Franko, M.; Štangar, U.L. Study of TiO_2 thin films on Si substrate by the photoacoustic elastic bending method. *Sci. China Phys. Mech. Astron.* **2013**, *56*, 1285–1293. [CrossRef]
63. Markushev, D.K.; Markushev, D.D.; Aleksić, S.M.; Pantić, D.S.; Galović, S.P.; Todorović, D.M.; Ordonez-Miranda, J. Experimental photoacoustic observation of the photogenerated excess carrier influence on the thermoelastic response of n-type silicon. *J. Appl. Phys.* **2020**, *128*, 095103. [CrossRef]
64. Markushev, D.K.; Markushev, D.D.; Aleksić, S.; Pantić, D.S.; Galović, S.; Todorović, D.M.; Ordonez-Miranda, J. Effects of the photogenerated excess carriers on the thermal and elastic properties of n-type silicon excited with a modulated light source: Theoretical analysis. *J. Appl. Phys.* **2019**, *126*, 185102. [CrossRef]
65. Nešić, M.; Gusavac, P.; Popović, M.; Šoškić, Z.; Galović, S. Thermal memory influence on the thermoconducting component of indirect photoacoustic response. *Phys. Scr.* **2012**, *T149*, 014018. [CrossRef]
66. Galović, S.; Šoškić, Z.; Popović, M.; Čevizović, D.; Stojanović, Z. Theory of photoacoustic effect in media with thermal memory. *J. Appl. Phys.* **2014**, *116*, 024901. [CrossRef]
67. Ma, Y.; Liu, X.; Gu, P.; Tang, J. Estimation of optical constants of thin film by the use of artificial neural networks. *Appl. Opt.* **1996**, *35*, 5035. [CrossRef]
68. Jakatdar, N.H.; Niu, X.; Spanos, C.J. Neural network approach to rapid thin film characterization. In *Flatness, Roughness, and Discrete Defects Characterization for Computer Disks, Wafers, and Flat Panel Displays II*; SPIE: Bellingham, WA, USA, 1998. [CrossRef]
69. Castellano-Hernandez, E.; Sacha, G.M. Characterization of thin films by neural networks and analytical approximations. In Proceedings of the 12th IEEE International Conference on Nanotechnology (IEEE-NANO), Birmingham, UK, 20–23 August 2012. [CrossRef]
70. Fan, L.; Chen, A.; Li, T.; Chu, J.; Tang, Y.; Wang, J.; Zhao, M.; Shen, T.; Zheng, M.; Guan, F.; et al. Thin-film neural networks for optical inverse problem. *Light Adv. Manuf.* **2021**, *2*, 395–402. [CrossRef]

Optical and Quantum Electronics (2022) 54:485
https://doi.org/10.1007/s11082-022-03808-3

Electronic characterization of plasma-thick n-type silicon using neural networks and photoacoustic response

K. Lj Djordjević[1] · S. P. Galović[1] · Ž. M. Ćojbašić[2] · D. D. Markushev[3] · D. K. Markushev[3] · S. M. Aleksić[4] · D. S. Pantić[4]

Received: 14 September 2021 / Accepted: 6 May 2022

Abstract
In this paper, electronic semiconductor characterization using reverse-back procedure was applied to different photoacoustic responses aiming to find effective ambipolar diffusion coefficient and a bulk lifetime of the minority carriers. The main idea was to find the small fluctuations in investigated parameters due to detecting possible unwanted sample contaminations and temperature variations during the measurements. The mentioned procedure was based on the application of neural networks. Knowing that in experiments the contaminated surfaces of the sample can play a significant role in the global recombination process that we are measuring and that the unintentionally introduced defects of the sample crystal lattice could vary the carrier lifetime by several orders of magnitude, a method of PA signal adjustment by the reverse-back procedure is developed, based on the changes of the carrier electronic parameters.

Keywords Photoacoustic · Semiconductors · Coefficient of ambipolar diffusion · Carrier lifetime · Artificial neural networks · Inverse problem · n-type silicon · Reverse-back procedure

This article is part of the Topical Collection on Photonics:Current Challenges and Emerging Applications.

Guest edited byJelena Radovanovic, Dragan Indjin, Maja Nesic, Nikola Vukovic andMilena Milosevic.

✉ K. Lj Djordjević
katarina.djordjevic@vinca.bg.ac.rs

[1] "VINČA" Institute of Nuclear Sciences - National Institute of the Republic of Serbia, University of Belgrade, PO box 522, 11000 Belgrade, Serbia

[2] Mechanical Engineering Faculty, University of Niš, Aleksandra Medvedeva 14, 18000 Niš, Serbia

[3] Institute of Physics Belgrade, National Institute of the Republic of Serbia, University of Belgrade, Pregrevica 118, 11080 Belgrade (Zemun), Serbia

[4] Faculty of Electronic Engineering, University of Niš, Aleksandra Medvedeva 14, 18000 Niš, Serbia

Published online: 29 June 2022

1 Introduction

For many applications of semiconductors in microelectronics, photonics, sensor and converter development, it is very important to know the electronic properties of semiconductors, using well-known parameters such as the diffusion coefficients of charge carriers and their lifetime, because the dynamics of charge carriers represent the basics of operation of all electronic devices (Wang 1989). Researchers have been working for more than half a century to improve old and develop new techniques for the characterization of semiconductors and semiconductor devices. Of particular importance are non-destructive and non-contact techniques suitable for use in the semiconductor industry and the electronics industry (Mandelis and Hess 2000; Todorovic et al. 1995; Dramićanin et al. 1995; Todorović et al. 2014). It was shown that photoacoustics (PA) and other photothermal (PT) techniques could be very suitable for such application (Fournier et al. 1986), not only as non-destructive and non-contact but the techniques that require minimal or practically no sample preparation.

The general theoretical framework for the interpretation of PT and PA signals produced in a semiconductor has been developed by many authors in the last forty years (Wang 1989; Todorović et al. 2014; Sablikov and Sandomirskii 1983; Neto et al. 1989; Stearns and Kino 1987; Yu and Gurevich 2021; Melnikov et al. 2021). Based on these investigations, it can be concluded that the dynamic of photogenerated charge carriers, generated by the modulated light beam, can have a significant influence on the PA and PT response of semiconductors (Wang 1989; Mandelis and Hess 2000; Todorovic et al. 1995; Dramićanin et al. 1995; Todorović et al. 2014; Sablikov and Sandomirskii 1983; Neto et al. 1989; Stearns and Kino 1987; Yu and Gurevich 2021; Melnikov et al. 2021). It means that PA and PT techniques can be established as a diagnostic method with good sensitivity to the photogenerated charge carrier changes described by material-dependent electronic parameters such as lifetime and ambipolar diffusion coefficient.

As the group of model-dependent techniques, the PA and other PT techniques comprise the development and improvement of fast and accurate inverse solving techniques, which should work in real-time. It has been shown that the use of neural networks in the inverse solution of the photoacoustic problem can determine those properties of the material that dominate the recorded signal in real-time with high accuracy (Lukić et al. 2013, 2014; Ćojbašić et al. 2011; Albu et al. 2019; Glorieux et al. 1993; Djordjevic et al. 2020a, b, c; Aleksić et al. 2016). In the case of semiconductors, the thermoelastic and heat diffusion properties of the sample have been determined first (Djordjevic et al. 2020a, b).

In our previous paper, a neural network-supported reverse-back procedure for the additional determination of optical parameters of silicon samples is proposed (Djordjevic et al. 2020c). Here, in this article, electronic parameters of plasma-thick samples are proposed for determination within the same reverse-back procedure, trying to find some typical patterns in parameters behavior due to sample thickness and overall influence of photogenerated carriers. A method of PA signal adjustment by the reverse-back procedure applied here is based on the changes of the carrier electronic parameters. The presented method can be used, besides the others, in the quality control procedure of the investigated samples, active control of the experimental conditions, and within the general characterization process of semiconductors.

2 Theory

Our theoretical consideration of excess carrier influence on photoacoustic response relies on the theory of the one-dimensional (1D) ambipolar transport (Wang 1989; Neamen 2002; Markushev et al. 2018, 2019). Within this theory, if an external light excitation is applied to the semiconductor, excess carriers (electrons and holes) could be generated (at equal rates, in pairs) if the light photon energy ε is equal or larger than the semiconductor energy band-gap ε_g. Both excess electrons $\left(\delta n_n(x,t)\right)$ and holes $\left(\delta n_p(x,t)\right)$ concentrations exist as an addition to the thermal equilibrium concentrations. They do not move independently of each other due to the existence of the internal electric field E_{int} between the excess carriers. This field creates a force attracting the electrons and holes, holding them together, so they diffuse, drift, and recombine with the same effective ambipolar diffusion coefficient D_{eff} and drift mobility μ_{eff}. Their movement within the semiconductor due to an applied constant external electric field E ($E>>E_{\text{int}}$) can be explained using the time-dependent diffusion equation in a homogeneous semiconductor (the doping concentration of electrons n_{n0} and holes n_{p0} is uniform throughout the semiconductor), written as (Wang 1989; Neamen 2002):

$$\frac{\partial \delta n(x,t)}{\partial t} = D_{eff}\frac{\partial^2 \delta n(x,t)}{\partial x^2} + \mu_{eff}E\frac{\partial \delta n(x,t)}{\partial x} + G(x,t) - R(x,t) \tag{1}$$

where

$$D_{eff} = \frac{\mu_n n D_p + \mu_p p D_n}{\mu_n n + \mu_p p} \text{ and } \mu_{eff} = \frac{\mu_n \mu_p (p-n)}{\mu_n n + \mu_p p} \tag{2}$$

D_n is the electron diffusion coefficient, D_p is the hole diffusion coefficient, μ_n is the electron mobility, μ_p is the hole mobility, and $G(x,t)$ and $R(x,t)$ are the excess carriers generation and recombination rates, respectively, equal for both electrons and holes. Considering that excess carriers are generated in pairs (charge neutrality), it is assumed that $\delta n_p(x,t) = \delta n_n(x,t) = \delta n(x,t)$.

In the case of n-type semiconductors $\left(n_{n0} >> n_{p0}\right)$ and low-level injection approximation $\left(n_{n0} >> \delta n_n(x,t), \delta n_p(x,t) >> n_{p0}\right)$, Eq. (1) can be written in the form (Wang 1989; Neamen 2002), ($D_{eff} \cong D_p, \mu_{eff} \cong -\mu_p, G(x,t) = G_p(x,t), R(x,t) = R_p(x,t)$):

$$\frac{\partial \delta n_p(x,t)}{\partial t} = D_p\frac{\partial^2 \delta n_p(x,t)}{\partial x^2} - \mu_p E\frac{\partial \delta n_p(x,t)}{\partial x} + G_p(x,t) - R_p(x,t) \tag{3}$$

The last Equation leads to the general conclusion: in the low-level injection n-type semiconductors, the dynamics of excess carriers can be described using the concentration changes of the minority ones—$\delta n_p(x,t)$.

Within the photoacoustics excess carriers are usually light-generated (so-called photogenerated carriers) (Mandelis and Hess 2000; Todorovic et al. 1995; Dramićanin et al. 1995; Todorović et al. 2014). Their concentration calculations are based on Fick's second law of diffusion, assuming that electrons and holes are identical particles neglecting their electrical nature ($E_{\text{int}}=0$), generating in pairs described by $G_p(x,t) = \beta I_0 e^{-\beta x}\left(1 + e^{i2\pi ft}\right)/2\varepsilon$ (modulated light source of intensity I_0, modulation frequency f and absorption coefficient of silicon β), and recombining by $R_p(x,t) = \delta n_p(x,t)/\tau_p$($\tau_p$ is the bulk lifetime of minority carriers). Including all the mentioned assumptions, taking that $E=0$, 1D time-dependent diffusion equation of

photogenerated carrier transport, used in photoacoustics for low-level injection n-type semiconductors, can be written in the form (Tyagi and Overstraeten 1983, Markushev et al. 2018, 2019):

$$\frac{\partial \delta n_p(x,t)}{\partial t} = D_p \frac{\partial^2 \delta n_p(x,t)}{\partial x^2} + \frac{\beta I_0 e^{-\beta x}}{\varepsilon}\left(1 + e^{i2\pi ft}\right) - \frac{\delta n_p(x,t)}{\tau_p} \tag{4}$$

Last Equation is identical to Eq. (3) in the case of $E = E_{\text{int}} = 0$. The dynamic part of Eq. (4) (important for PA sound generation), is given in the form:

$$\frac{\mathrm{d}^2 \delta n_p(x,f)}{\mathrm{d}x^2} - \frac{\delta n_p(x,f)}{L^2} = -\frac{\beta I_0}{\varepsilon D_p} e^{-\beta x}, \tag{5}$$

where $L = L_p/\left(1 + i2\pi f\tau_p\right)^{1/2}$ is the complex excess carrier diffusion length, $L_p = \sqrt{D_p \tau_p}$ is the excess carrier diffusion length, and $\delta n_p(x,f)$ is the photogenerated minority dynamic concentration component. The solution $\delta n_p(x,f)$ of Eq. (5) (Appendix 1) shows a very complex dependence on the D_p and τ_p. These parameters can be easily extracted and calculated from the experimental data during the standard fitting procedure.

The importance of the D_p and τ_p calculation lies in the fact that they allow L_p calculation, the parameter that can be used to define the thickness of a semiconductor in relation to the influence of photogenerated carriers on its thermal and mechanical characteristics (Markushev et al. 2018, 2019). All semiconductor samples with a thickness: (a) larger than L_p are named plasma-thick samples; (b) lower than L_p are named plasma-thin samples. Under the same conditions of the influence of photogenerated carriers on thermal distributions within the investigated sample, plasma-thick samples have different patterns of behaviour of temperatures and/or photoacoustic signals in relation to plasma-thin ones. The word "plasma" here refers to the excess carriers which are characterized by two main properties of plasma: acting like a swarm of charged particles, possessing the property of charge neutrality.

As we mentioned earlier, measured carriers ambipolar diffusivity and lifetime in the experiment could be understood as the effective minority carrier ambipolar diffusivity D_{eff} and lifetime τ_{eff}. These values sometimes do not correspond to the PA model predicted D_p and τ_p due to the fact that Fick's model (Eq. (4)) does not recognize the difference between electrons and holes. Another thing that supports D_{eff} and τ_{eff} definition of effective parameters is the fact that Eq. (5) is a dynamic part of Eq. (4) responsible for PA sound generation. Also, one must bear in mind that in most experiments the silicon samples really have higher levels of contaminants (or structural growing defects) so the lower lifetimes than theoretically predicted τ_p can be expected.

Photogenerated minority carrier concentration $\delta n_p(x,t)$ is important because it also appears in the heat diffusion equations:

$$\frac{\partial^2 T_s(x,t)}{\partial x^2} - \frac{1}{D_T}\frac{\partial T_s(x,t)}{\partial t} = -\frac{\varepsilon - \varepsilon_g}{k\varepsilon}\beta I e^{-\beta x} - \frac{\varepsilon_g}{k\tau_p}\delta n_p(x,t), \tag{6}$$

where $T_s(x,t)$ is the temperature of the irradiated sample, $I = I_0\left(1 + e^{i2\pi ft}\right)$ is the intensity of the modulated light source, k is the coefficient of thermal conduction, and D_T is the heat diffusion coefficient. Following the modulated irradiation of the sample it is assumed that $T_s(x,t) = T_s(x)\left(1 + e^{i2\pi ft}\right)$ and $\delta n_p(x,t) = \delta n_p(x)\left(1 + e^{i2\pi ft}\right)$ are changed in the rhythm of

modulation, so dynamic part of Eq. (6) (responsible for sound generation) can be written in the form (Markushev et al. 2018, 2019):

$$\frac{\mathrm{d}^2 T_s(x,f)}{\mathrm{d}x^2} - \sigma_i^2 T_s(x,f) = -\frac{\varepsilon - \varepsilon_g}{k\varepsilon}\beta I_0 e^{-\beta x} - \frac{\varepsilon_g}{k\tau_p}\delta n_p(x,f), \tag{7}$$

where $T_s(x,f)$ is the dynamic temperature component, $\sigma_i = (1+i)\mu^{-1}$ is the complex thermal diffusion length and $\mu = \sqrt{D/(\pi f)}$ is the thermal diffusion length. It is obvious that $T_s(x,f)$ strongly depend on the photogenerated minority dynamic concentration component $\delta n_p(x,f)$.

The solution $T_s(x,f)$ of the Eq. (7) is given in Appendix 2. It is expected that $T_s(x,f)$ is a function of D_p and τ_p, too.

Both $T_s(x,f)$ and $\delta n_p(x,f)$ are used to calculate photoacoustic signal thermodiffusion $\delta p_{\mathrm{TD}}(f)$, thermoelastic $\delta p_{\mathrm{TE}}(f)$ and plasmaelastic $\delta p_{\mathrm{PE}}(f)$ components (Todorovic et al. 1995; Dramićanin et al. 1995; Todorović et al. 2014; Markushev et al. 2018, 2019; Rabasović et al. 2009; Markushev et al. 2015):

$$\delta p_{\mathrm{TD}}(f) = \frac{\gamma p_0}{\sigma_{ig} l_{\mathrm{c}}} \frac{T_s(l,f)}{T_0}, \tag{8}$$

$$\delta p_{\mathrm{TE}}(f) = \alpha_T \frac{\gamma p_0}{V_0} \frac{3\pi R^4}{l^3} \int_0^l \left(x - \frac{l}{2}\right) T_s(x,f)\mathrm{d}x, \tag{9}$$

$$\delta p_{\mathrm{PE}}(f) = d_{\mathrm{n}} \frac{\gamma p_0}{V_0} \frac{3\pi R^4}{l^3} \int_0^l \left(x - \frac{l}{2}\right) n_p(x,f)\mathrm{d}x. \tag{10}$$

where l is the sample thickness, l_{c} is the photoacoustic cell length, α_T is the coefficient of linear expansion of the sample, d_{n} the coefficient of electronic deformation, γ is the adiabatic ratio, R is the sample effective radius, p_0 and T_0 are the gas pressure and temperature in the photoacoustic cell, respectively, and σ_{ig} is the complex thermal diffusion length of the gas surrounding the sample (usually air). All these components represent constitutive parts of the total photoacoustic signal $\delta p_{\mathrm{total}}(f)$, the measured value in the experiments, usually represented in the form (Todorovic et al. 1995; Dramićanin et al. 1995; Todorović et al. 2014; Markushev et al. 2018, 2019; Rabasović et al. 2009; Markushev et al. 2015):

$$\delta p_{\mathrm{total}}(f) = \delta p_{\mathrm{TD}}(f) + \delta p_{\mathrm{TE}}(f) + \delta p_{\mathrm{PE}}(f). \tag{11}$$

The standard procedure for processing the $\delta p_{\mathrm{total}}(f)$ involves fitting it with Eqs. (8–11) and extracting the wanted thermal (D_T,k,α_T) and electronic (D_p,τ_p) parameters of the sample. With the help of these parameters the minority carrier diffusion length $L_p = \sqrt{D_p \tau_p}$ can be calculated as the average length a carrier moves between generation and recombination. Our goal here is to extract mentioned electronic parameters from the PA experiment as an effective one using standard PA procedures and neural networks as a powerful tool within the semiconductor characterization. Later, effective L_p will be calculated to establish plasma-thick—plasma-thin boundaries.

3 Parameter determination procedures

Conditioned by multiparameter nonlinear dependences of photoacoustic signals on sample parameters (Eqs. 8–11), a goal of this work is to implement computational intelligence and machine learning for electronic parameter determination and precise sample characterization. Supervised machine learning is used to provide an algorithm that connects the input photoacoustic signals and the output values of the sample parameters, stored in the artificial neural network structure which was developed and optimized previously (Djordjevic et al. 2020a, b, c). In such a way an optimal tool for precise sample parameter prediction in real-time is devised and efficiently used, utilizing the advantages of the artificial neural networks (NN) based approach. In order to emphasize the possibilities of developing analyzes of physical processes and application to experimental results, deep machine learning and other computationally demanding approaches have been avoided but instead network structure has been optimized and kept simple to provide for easy hardware and software implementation, high precision and very fast performance.

To determine heat diffusion, thermoelastic and geometric parameters of the investigated samples in real-time ($\sim 7.1\mu s$) and with high precision (performance of NN $\sim 10^7$) (Djordjevic et al. 2020a, b, c), a neural network with optimized structure containing single hidden layer with 50 neurons was used. By training the NN with theoretically obtained photoacoustic signals (Eqs. 8–11) generated in thick samples (1 mm–100 μm), characterized with the heat diffusion coefficient D_T, the coefficient of linear expansion α_T and the sample thickness l, a model for determining mentioned semiconductor parameters was formed, which predicts D^{NN}, α_T^{ANN} and l^{ANN}. The learning process is based on the modification of weights $w_{j,i}^1$ and biases θ_i^1 matrices to reach the minimum of mean square error (MSE) (Djordjevic et al. 2020a):

$$\mathrm{MSE} = \frac{1}{2}\sum_{k\in K}\left(Q_k - T_k\right)^2, \quad T_k \in \left\{D_T, \alpha_T, l\right\} \tag{12}$$

where Q_k (with $k = 1, 2, 3$) are the calculated values of the output layer of the neural network, which are compared at the end of each epoch with the values T_k ($k = 1, 2, 3$):

$$Q_k = \sigma\left(\sum_{i=1}^{50} w_{i,k}^2 \sigma\left(\sum_{j=1}^{72}\left(w_{j,i}^1 20\log A_{\mathrm{total}}\left(f_j\right) + w_{j+72,i}^1 \phi_{\mathrm{total}}\left(f_j\right)\right) + \theta_i^1\right) + \theta_k^2\right), k = 1, 2, 3. \tag{13}$$

where $A_{\mathrm{total}}\left(f_j\right)$ and $\phi_{\mathrm{total}}\left(f_j\right)$ are the $\delta p_{\mathrm{total}}(f)$ amplitudes and phases (Eq. (11)) respectively, which numerical values are in the ranges of several orders of magnitude for amplitude and between 0 and 360 deg for phases. To improve network performances scaling of the input amplitude data was performed with the $20\log A_{\mathrm{total}}\left(f_j\right)$ function aiming to "equalize" amplitude and phase numerical values. Selecting the simple perceptron feed-forward neural network with 50 neurons in a single hidden layer, which is very fast and optimized for real-time operation, we obtained a network model with optimal characteristics (Djordjevic et al. 2020a, b, c). This NN model predicts D^{NN}, α_T^{ANN} and l^{ANN} parameters from experimentally measured PA signals. Predicted parametars are used to obtain amplitude $A_{\mathrm{total}}^{\mathrm{ANN}}\left(f_j\right)$ and phase $\phi_{\mathrm{total}}^{\mathrm{ANN}}\left(f_j\right)$ curves of the predicted signal that differs slightly from the measured one ($A_{\mathrm{total}}^{\mathrm{exp}}(f_i)$ and $\phi_{\mathrm{total}}^{\mathrm{exp}}$) (Djordjevic et al. 2020b). The esence of the reverse-back procedure (RBP) is to find such small differences between network prediction and measured PA and use it to determine the deviation parameter MSD in the following way:

$$\mathrm{MSD} = \xi = \sqrt{\sum_{i-1}^{72} \frac{\left((20\log A_{\mathrm{total}}^{\mathrm{ANN}}(f_i) - 20\log A_{\mathrm{total}}^{\mathrm{exp}}(f_i))^2 + (\phi_{\mathrm{total}}^{\mathrm{ANN}}(f_i) - \phi_{\mathrm{total}}^{\mathrm{exp}}(f_i))^2\right)}{n}} \tag{14}$$

MSD is iteratively reduced until the network prediction and measured PA curves coincide. Assuming that experiment is well controlled due to the optical stability of the radiation source (Djordjevic et al. 2020c), founded differences are joined to the minority carrier dynamic electronic parameters: diffusivity D_p^{RBP} and bulk-life time τ_p^{RBP}. Based on these values, the excess carrier diffusion length L_p^{RBP} was determined, too. One can assume (Djordjevic et al. 2020c) that the RBP allows us to determine mentioned parameters precisely, accurately and in real-time (Fig. 1).

4 Application of the reverse-back procedure to experimental photoacoustic measurements

In our research, we will use the photoacoustic experimental results (Fig. 1, asterisks) taken by measuring the two thicknesses of silicon plates made from the same wafer. Using standard signal correction procedure (Rabasović et al. 2009) the corrected experimental signals (Corrected PA), also called the "true" PA signals, are obtained indicating (Fig. 1, solid) the same mutual parameter values of $D_T^{\mathrm{exp}} = 9.0\times10^{-5}\mathrm{m^2s^{-1}}$, $\alpha_T^{\mathrm{exp}} = 2.6\times10^{-6}\mathrm{K^{-1}}$, $\tau_p^{\mathrm{exp}} = 5.0\times10^{-6}\mathrm{s}$, $D_p^{\mathrm{exp}} = 1.2\times10^{-3}\mathrm{m^2s^{-1}}$ (same wafer) for all sample thicknesses: $l_1 = 227$ μm, and $l_2 = 690$ μm (Fig. 2s).

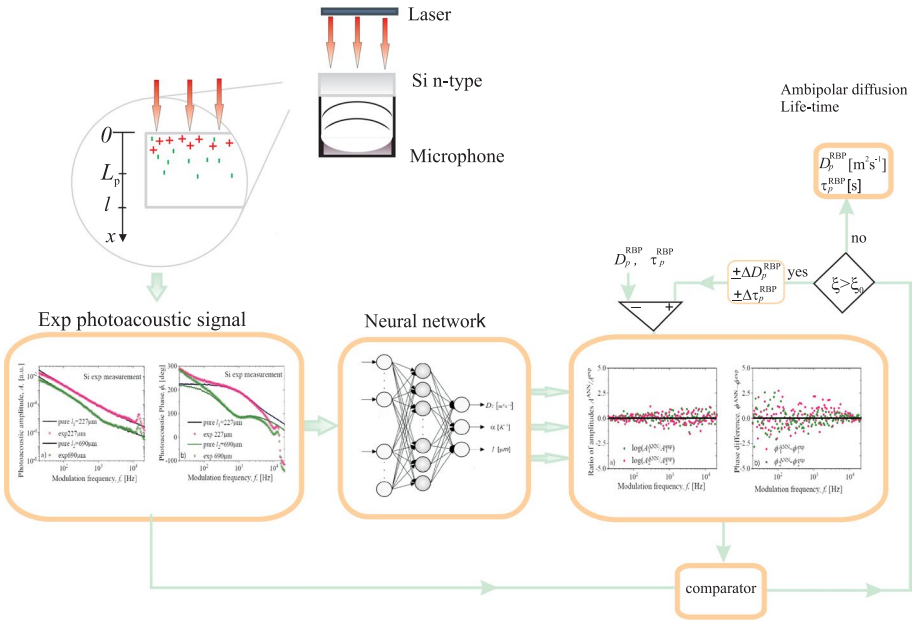

Fig. 1 Reverse-back procedure (RBP) scheme for the minority carrier dynamic electronic parameters D_p^{RBP} and τ_p^{RBP}, by reducing the deviation of the neural network prediction from the experimentally measured signal

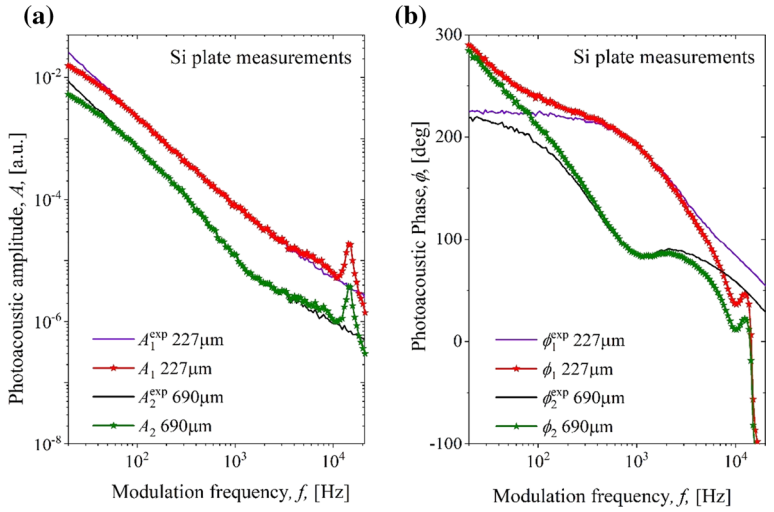

Fig. 2 The photoacoustic experimental results (asterics) in frequency range 20 Hz–20 kHz: (**a**) amplitudes A_i and (**b**) phases ϕ_t of two n-type silicon samples thickness (690 μm, 227 μm) and corresponding Corrected PA signals a) amplitudes A_i^{exp} and b) phases ϕ_i^{exp} obtained with standard signal correction procedure (Markushev et al. 2015) ($i=1, 2$)

The corrected photoacoustic signals with mutual parameters (Table 1, Standard PA) are presented to our network, so the ANN can predict D^{NN}, α_T^{ANN} and l^{ANN} (Table 1, ANN prediction). The ANN prediction/Corrected PA ratio is used to calculate relative error (Table 1, relative % error) (Djordjevic et al. 2020a; b).

The parameters obtained by the ANN prediction were returned into the theoretical model. The PA signals thus calculated are slightly different from the Corrected PA obtained in experiment. In our previous article we have seen that these differences can be used to check the stability of the radiation source and the purity of the sample surface calculating changes in the sample optical parameters (absorption β and reflection R_{ref} coefficient) within the RBP (Djordjevic et al. 2020c). Now, assuming that mentioned β and R_{ref} changes are negligibly small (well controlled experimental conditions), we can go a step further and all RBP calculated changes join to the electronic characteristics of the semiconductor sample, getting D_p^{RBP} and/or τ_p^{RBP}. It must be noted here that D_p^{RBP} and τ_p^{RBP} have be considered as an effective values which are the combination of different effects on surface or in the bulk of the investigation sample.

Usually, reverse-back procedure comprises the analysis of amplitude ratios $\left(A_i^{ANN}/A_i^{exp}\right)$ and phase differences $\left(\phi_i^{ANN}-\phi_i^{exp}\right)$ between ANN prediction and Corrected PA signals (Fig. 3, i=1,2) (Djordjevic et al. 2020a, b, c). In our case, for all sample thicknesses 1 (227 μm) and 2 (690 μm), the reverse-back procedure results are presented in Table 2, where D_p^{RBP} and τ_p^{RBP} are the parameters obtained directly, and $L_p^{RBP}=\sqrt{D_p^{RBP}\tau_p^{RBP}}$.

Based on the results presented in Table 2 it is obvious that the reverse-back procedure gives very accurate results for D_p^{RBP} and τ_p^{RBP}, with an error of less than 0.2%. It means that the performed experiment is reliable, the investigated samples are not accidentally contaminated and the temperature fluctuations during the experiment are negligible. The D_p^{RBP} and τ_p^{RBP} values are in accordance with the literature ones obtained with the same (Markushev et al. 2018, 2019; Rabasović et al. 2009; Markushev et al. 2015) and other established

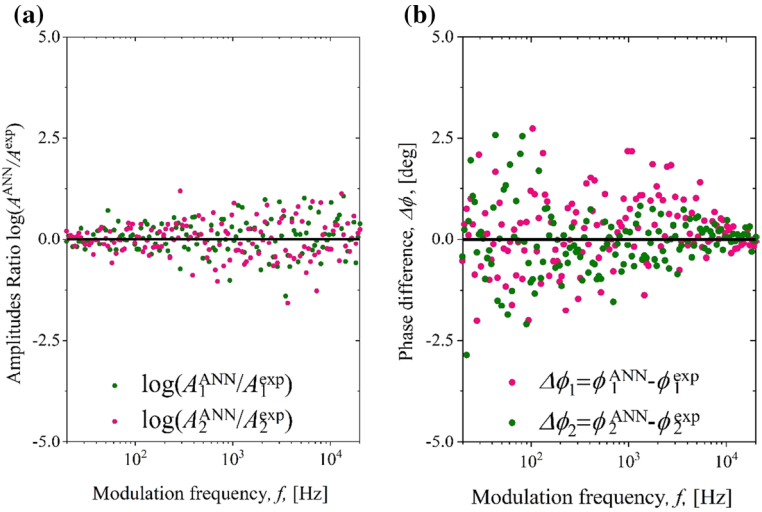

Fig. 3 (**a**) Ratio of amplitudes and (**b**) difference of phases of ANN prediction and Corrected PA (exp) signal in frequency domain

Table 1 Neural network prediction parameters D^{NN}, α_T^{ANN} and l^{ANN} with corresponding relative % error in relation to the values of standard photoacoustic measurements

Parameters	Sample no. 1 227 μm			Sample no.2 690 μm		
	D_T^{ANN}	α_T^{ANN}	l^{ANN}	D_T^{ANN}	α_T^{ANN}	l^{ANN}
Units	$[10^{-5}m^2s^{-1}]$	$[10^{-6}K^{-1}]$	$[10^2\mu m]$	$[10^{-5}m^2s^{-1}]$	$[10^{-6}K^{-1}]$	$[10^2\mu m]$
Corrected PA	9.0000	2.6000	2.27	9.0000	2.6000	6.90
ANN predict	8.9823	2.6246	2.2804	9.0492	2.5831	6.8918
rel. % error	0.1967	0.9462	0.4881	0.5467	0.6500	0.1188

Table 2 The electronic characteristics of semiconductor sample in reverse-back procedure, the minority diffusion coefficient D^{RBP}, and their lifetimes τ_p^{RBP} determined with corresponding relative % errors. From these values is determined the effective value of the minority carrier diffusion length L_p^{RBP}

Parameters & relative errors	Sample no. 1 227 μm	Sample no. 2 690 μm
$D_p^{RBP}\ [10^{-3}m^2s^{-1}]$	1.20999	1.19511
Relative % error	0.83250	0.40750
$\tau_p^{RBP}\ [10^{-6}s]$	5.05599	4.99911
Relative % error	1.11980	0.01780
$L_p^{RBP}\ [10^{-5}m]$	7.82157	7.72948
Relative % error	0.97561	0.21327

characterization systems (Popovic et al. 2010; Palais et al. 2000; Cuevas and Daniel 2003; Alamo and Swanson 1987). The obtained values of $L_p^{RBP} \approx 77\mu m$ confirms that all investigated samples are plasma-thick ($l > L_p$), meaning that one can expect the bulk recombination to dominate over the surface ones, so the τ_p^{RBP} parameter can be considered as an

effective carrier bulk lifetime where SRH (Shockley–Read–Hall) recombination dominates (Popovic et al. 2010; Palais et al. 2000; Cuevas and Daniel 2003; Alamo and Swanson 1987). Higher values of the τ_p^{RBP} relative error in thinner samples indicate the fact that, as the sample becomes thinner the effect of surface recombination slowly becomes more and more important (Popovic et al. 2010; Alamo and Swanson 1987). This result could be understood as a typical pattern of effective τ_p behavior approaching the L_p boundary value in the case of plasma-thick samples. Calculating the photogenerated carrier density $\delta n_p(x,f)$ from obtained Corrected PA signals we found that $\delta n_p(x,f) = (1-2)\times 10^{18}$ m^{-3}. It means that $\delta n_p(x,f) << N_T$, so the low-injection approximation (Tyagi and Overstraeten 1983; Wang 1989; Neamen 2002) in our experiment is always justified.

5 Conclusion

It is shown in this paper that the proposed reverse-back procedure leads to the solution of the inverse photoacoustic problem enabling one to determine the changes in the electronic properties of semiconductors with high accuracy. The obtained results of the diffusion coefficient and the lifetime of minority carriers can help one to check the reliability of the experimental samples of low-level injection n-type silicon having two different thicknesses: 227 μm and 690 μm. The small deviations of D_p^{RBP} and τ_p^{RBP} from standard PA response and literature values indicate that investigated samples are not accidentally contaminated. Also, the temperature fluctuations during the experiment are negligible. Knowledge of D_p^{RBP} and τ_p^{RBP} is essential for L_p^{RBP} calculation needed for determining the boundary thickness of the semiconductor samples that separates plasma-thick from plasma-thin ones. The obtained numerical value of $L_p^{\mathrm{RBP}} \approx 77\mu m$ justifies our assumption that all samples are plasma-thick, meaning that τ_p^{RBP} parameter can be considered as an effective carrier bulk lifetime where SRH recombination dominates. At the same time, higher values of τ_p^{RBP} relative error in thinner samples indicate the larger influence of surface recombination on the measured (effective) lifetime of carriers, which is expected and theoretically predicted. The methodology presented here was found to be effective not only as a powerful tool for the control of the experimental condition changes but, also, for the complete electronic characterization of semiconductors, too, based on the theory of ambipolar diffusion.

The development of procedures for the determination of the semiconductor electronic parameter from photoacoustic measurement, especially silicon, is of particular interest because it provides a direct possibility of implementing photoacoustic as a precise and non-destructive method in engineering of properties of semiconductors for various applications in the semiconductor industry.

Appendix 1: Photogenerated density calculation

The Solution of the Eq. (5) can be found in the form (Markushev et al. 2018; 2019):

$$\delta n_p(x,f) = A_+ e^{xL^{-1}} + A_- e^{-xL^{-1}} + A_\beta e^{-\beta x}, \tag{15}$$

The A_β is the solution of the inhomogeneous part of the differential equation, and A_+ and A_- are the integration constants which are given in the form:

$$A_\pm = \pm\frac{A_\beta}{A_L}\left[\left(1\mp\sigma_1\right)\left(1+\beta L\sigma_2\right)e^{-\beta l} - \left(1\pm\sigma_2\right)\left(1+\beta L\sigma_1\right)e^{\pm lL^{-1}}\right] \tag{16}$$

$$A_L = \left(1+\sigma_1\right)\left(1+\sigma_2\right)e^{lL^{-1}} - \left(1-\sigma_1\right)\left(1-\sigma_2\right)e^{-lL^{-1}} \tag{17}$$

$$A_\beta = \frac{I_0}{\varepsilon v_D}\frac{\beta L}{L^{-2}-\beta^2} \tag{18}$$

calculated using the boundary conditions.

$$D_p\frac{\mathrm{d}\delta n_p(x)}{\mathrm{d}x}\bigg|_{x=0} = s_1\delta n_p(0) \text{ and } D_p\frac{\mathrm{d}\delta n_p(x)}{\mathrm{d}x}\bigg|_{x=l} = -s_2\delta n_p(l) \tag{19}$$

where $\sigma_i = D_p\left(s_m L\right)^{-1}$ is the dimensionless parameter which depends on the surface recombination speed s_m at front ($m=1$) and back side ($m=2$) surfaces of the sample, and $v_D = D_p L^{-1}$ is the diffusion velocity of the photogenerated minority carriers.

Appendix 2: Temperature calculation

The solution of the Eq. (6) can be written as (Markushev et al. 2018; 2019):

$$T_s(x,f) = b_1 e^{\sigma_i x} + b_2 e^{-\sigma_i x} + b_3\delta n_p(x,f) + b_4 e^{-\beta x}, \tag{20}$$

where

$$\begin{aligned} b_1 = \frac{\coth\left(\sigma_i l\right)-1}{2k\sigma_i}\left[b_3 k\left(\frac{\mathrm{d}\delta n_p(x)}{\mathrm{d}x}\right)_{x=0} - e^{-\sigma_i l}\left(\frac{\mathrm{d}\delta n_p(x)}{\mathrm{d}x}\right)_{x=l}\right] + \\ +\varepsilon_g\left[\delta n_p(0)s_1 + \delta n_p(l)s_2 e^{\sigma_i l}\right] + b_4 k\beta\left[e^{l(\sigma_i-\beta)}-1\right] \end{aligned} \tag{21}$$

$$\begin{aligned} b_2 = \frac{1}{2k\sigma_i\sinh\left(\sigma_i l\right)}\left\{-b_3 k\left(\frac{\mathrm{d}\delta n_p(x)}{\mathrm{d}x}\right)_{x=l} + \varepsilon_g\delta n_p(l)s_2 + b_4 k\beta\, e^{-\beta l} + \right. \\ \left. +e^{-\sigma_i l}\left[b_3 k\left(\frac{\mathrm{d}\delta n_p(x)}{\mathrm{d}x}\right)_{x=0} + \varepsilon_g\delta n_p(0)s_1 - b_4 k\beta\right]\right\} \end{aligned} \tag{22}$$

$$b_3 = \frac{\varepsilon_g}{k\tau_p\left(\sigma_i^2 - L^{-2}\right)} \text{ and } b_4 = \frac{\beta I_0}{\varepsilon\left(\beta^2-\sigma_i^2\right)}\left(\frac{b_3}{D_p} - \frac{\varepsilon-\varepsilon_g}{k}\right) \tag{23}$$

are constants calculated using the boundary conditions !!!!!

$$-k\frac{\mathrm{d}T_s(x)}{\mathrm{d}x}\bigg|_{x=0} = s_1\delta n_p(0)\varepsilon_g \text{ and } -k\frac{\mathrm{d}T_s(x)}{\mathrm{d}x}\bigg|_{x=l} = -s_2\delta n_p(l)\varepsilon_g \tag{24}$$

Here s_1 and s_2 are the surface recombination speeds at illuminated front (1) and nonilluminated back (2) sample surface.

Acknowledgements We are thankful for the financial support of this research by the Ministry of Education, Science and Technology development of the Republic of Serbia, contract number 451-03-9/2021-14/200017.

Funding The authors have not disclosed any funding.

Declarations

Conflict of interest The authors have not disclosed any competing interests.

References

Alamo, J.A.D., Swanson, R.M.: Measurement of steady-state minority-carrier transport parameters in heavily doped n-type silicon. IEEE Trans. Electron Dev. **34**, 1580–1589 (1987). https://doi.org/10.1109/T-ED.1987.23122

Albu, A., Precup, R.E., Teban, T.E.: Results and challenges of artificial neural networks used for decision-making and control in medical applications. Facta Univ. Series: Mech. Eng. **17**(3), 285–308 (2019)

Aleksić, S.M., Markushev, D.K., Pantić, D.S., Rabasović, M.D., Markushev, D.D., Todorović, D.M.: Electro-Acoustic influence of the measuring system on the photoacoustic signal amplitude and phase in frequency domain. Facta Univ. Series Phys. Chem. Technol. **14**(1), 9–20 (2016). https://doi.org/10.2298/FUPCT1601009A

Cuevas, A., Daniel, M.D.: Measuring and interpreting the lifetime of silicon wafers. Sol. Energy **76**(1–3) 255–262 (2003). https://doi.org/10.1016/j.solener.2003.07.033

Ćojbašić, Z., Nikolić, V., Ćirić, I., Lj, Ć: Computationally intelligent modelling and control of fluidized bed combustion process. Therm. Sci. **15**(2) 321–338 (2011). https://doi.org/10.2298/TSCI101205031C

Djordjevic, K.Lj., Markushev, D.D., Ćojbašić, ŽM., Galović, S.P.: Photoacoustic measurements of the thermal and elastic properties of n-type silicon using neural networks. SILICON **12** 1289–1300 (2020a). https://doi.org/10.1007/s12633-019-00213-6

Djordjevic, K.Lj., Markushev, D.D., Ćojbašić, ŽM., Galović, S.P.: Inverse problem solving in semiconductor photoacoustics by neural networks. Inverse Probl. Sci. Eng. **29**(2) 248–262 (2020b). https://doi.org/10.1080/17415977.2020.1787405

Djordjevic, K.Lj, Galovic, S.P., Jordovic-Pavlovic, M.I., Nesic, M.V., Popovic, M.N., Ćojbašić, ŽM., Markushev, D.D.: Photoacoustic optical semiconductor characterization based on machine learning and reverse-back procedure. Opt. Quant. Electron. **52**(5) 247 1–9 (2020c). https://doi.org/10.1007/s11082-020-02373-x

Dramićanin, M.D., Nikolić, P.M., Ristovski, Z.D., Vasiljević, D.G., Todorović, D.M.: Photoacoustic investigation of transport in semiconductors: theoretical and experimental study of a Ge single crystal. Phys. Rev. B **51**, 14 226–233 (1995). https://doi.org/10.1103/PhysRevB.51.14226

Fournier, D., Boccara, C., Skumanich, A., Amer, N.M.: Photothermal investigation of transport in semiconductors: theory and experiment. J. Appl. Phys. **59**(3) 787–795 (1986). https://doi.org/10.1063/1.336599

Glorieux, G., Fivez, J., Thoen, J.: Photoacoustic investigation of the thermal properties of layered materials: calculation of the forward signal and numerical inversion procedure. J. Appl. Phys. **73**, 684–690 (1993). https://doi.org/10.1063/1.353352

Lukić, M., Čojbašić, Ž, Rabasović, M.D., Markushev, D.D., Todorović, D.M.: Neural networks-based real-time determination of laser beam spatial profile and vibrational-to-translational relaxation time within pulsed photoacoustics. Int. J. Thermophys. **34**(8–9), 1795–1802 (2013). https://doi.org/10.1007/s10765-013-1507-y

Lukić, M., Čojbašić, Ž, Rabasović, M.D., Markushev, D.D.: Computationally intelligent pulsed photoacoustics. Measur. Sci. Technol. **25**(12), 125203–125209 (2014). https://doi.org/10.1088/0957-0233/25/12/125203

Mandelis, A., Hess, P. (eds.): Semiconductors and Electronic Materials, Vol. IV in the series: progress in photothermal and photoacoustic science and technology (SPIE Press, Bellingham, 2000) Available form: ISBN: 9780819435064

Markushev, D.D., Rabasović, M.D., Todorović, D.M., Galović, S., Bialkowski, S.E.: Photoacoustic signal and noise analysis for Si thin plate: signal correction in frequency domain. Rev. Sci. Instrum. **86**(3) 035110 1–9 (2015). https://doi.org/10.1063/1.4914894

Markushev, D.K., Markushev, D.D., Galović, S., Aleksić, S., Pantić, D.S., Todorović, D.M.: The surface recombination velocity and bulk lifetime influences on photogenerated excess carrier density and temperature distributions in n-type silicon excited by a frequency-modulated light source. Facta Univ. Electron. Energ. **31**(2), 313–328 (2018). https://doi.org/10.2298/FUEE1802313M

Markushev, D.K., Markushev, D.D., Aleksic, S.M., Pantic, D.S., Galovic, S.P., Todorovic, D.M., Ordonez-Miranda, J.: Effects of the photogenerated excess carriers on the thermal and elastic properties of n-type silicon excited with a modulated light source: theoretical analysis. J. Appl. Phys. **126**(8) 185102 1–12 (2019). https://doi.org/10.1063/1.5100837

Melnikov, A., Mandelis, A., Soral, A., Zavala-Lugo, C., Pawlak, M.: Quantitative imaging of defect distributions in CdZnTe wafers using combined deep-level photothermal spectroscopy, photocarrier radiometry, and lock-in carrierography. ACS Appl. Electron. Mater. **3**, 2551–2563 (2021). https://doi.org/10.1021/acsaelm.1c00100

Neamen, D. A.: Semiconductor physics and devices (McGraw–Hill, Boston, 2002)

Neto, A.P., Vargas, H., Leite, N.F., Miranda, L.C.M.: Photoacoustic investigation of semiconductors: influence of carrier diffusion and recombination in PbTe and Si. Phys. Rev. B Condens. Matter **40**(6), 3924–3930 (1989). https://doi.org/10.1103/physrevb.40.3924

Palais, O., Gervais, J., Clerc, L., Martinuzzi, S.: High resolution lifetime scan maps of silicon wafers. Mater. Sci. Eng. B **71**(1–3), 47–50 (2000). https://doi.org/10.1016/S0921-5107(99)00347-5

Popovic, M. N., Furundzic, D., Galovic, S. P.: Photothermal depth profiling of optical gradient materials by neural network, Publications of the Astronomical Observatory of Belgrade, 89 147–150 (2010)

Rabasović, M.D., Nikolić, M.G., Dramićanin, M.D., Franko, M., Markushev, D.D.: Low-cost, portable photoacoustic setup for solid state. Measur. Sci. Technol. **20**(9) 1−6 (2009). https://doi.org/10.1088/0957-0233/20/9/095902

Sablikov, V.A., Sandomirskii, V.B.: The photoacoustic effect in semiconductors. Phys. Status Solidi (b) **120**(2) 471–480 (1983). https://doi.org/10.1002/pssb.2221200203

Stearns, R. G., Kino, G. S.: Photoacoustic techniques for the measurement of electronic properties of semiconductors, Chap.9 in Photoacoustic and thermal wave phenomena in semiconductors, A. Mandelis Ed., Elsivier Sci.Pub.Co., North-Holland, N.York, p.201, (1987)

Todorovic, D.M., Nikolic, P.M., Dramicanin, M.D., Vasiljevic, D.G., Ristovski, Z.D.: Photoacoustic frequency heat transmission technique: thermal and carrier transport parameters measurements in silicon. J. Appl. Phys. **78**(9) 5750–5755 (1995). https://doi.org/10.1063/1.359637

Todorović, D.M., Rabasović, M.D., Markushev, D.D., Sarajlic, M.: Photoacoustic elastic bending in thin film-substrate system: experimental determination of the thin film parameters. J. Appl. Phys. **116**(6) 053506 1–9 (2014). https://doi.org/10.1063/1.4890346

Tyagi, M.S., Van Overstraeten, R.: Minority carrier recombination in heavily-doped silicon. Solid-State Electron **26**(6) 577–597 (1983). https://doi.org/10.1016/0038-1101(83)90174-0

Wang, S.: Fundamentals of semiconductr theory and device physics, Prentice-Hall International Editions, NJ USA 1989 Available form: ISBN 0–13–344425–2

Yu, T.O., Gurevich, Y.G.: Temperature gradient and transport of heat and charge in a semiconductor structure. Low Temp. Phys./fizika Nizkih Temp. **47**(7), 596–601 (2021). https://doi.org/10.1063/10.0005182

Terms and Conditions

Springer Nature journal content, brought to you courtesy of Springer Nature Customer Service Center GmbH ("Springer Nature").

Springer Nature supports a reasonable amount of sharing of research papers by authors, subscribers and authorised users ("Users"), for small-scale personal, non-commercial use provided that all copyright, trade and service marks and other proprietary notices are maintained. By accessing, sharing, receiving or otherwise using the Springer Nature journal content you agree to these terms of use ("Terms"). For these purposes, Springer Nature considers academic use (by researchers and students) to be non-commercial.

These Terms are supplementary and will apply in addition to any applicable website terms and conditions, a relevant site licence or a personal subscription. These Terms will prevail over any conflict or ambiguity with regards to the relevant terms, a site licence or a personal subscription (to the extent of the conflict or ambiguity only). For Creative Commons-licensed articles, the terms of the Creative Commons license used will apply.

We collect and use personal data to provide access to the Springer Nature journal content. We may also use these personal data internally within ResearchGate and Springer Nature and as agreed share it, in an anonymised way, for purposes of tracking, analysis and reporting. We will not otherwise disclose your personal data outside the ResearchGate or the Springer Nature group of companies unless we have your permission as detailed in the Privacy Policy.

While Users may use the Springer Nature journal content for small scale, personal non-commercial use, it is important to note that Users may not:

1. use such content for the purpose of providing other users with access on a regular or large scale basis or as a means to circumvent access control;
2. use such content where to do so would be considered a criminal or statutory offence in any jurisdiction, or gives rise to civil liability, or is otherwise unlawful;
3. falsely or misleadingly imply or suggest endorsement, approval , sponsorship, or association unless explicitly agreed to by Springer Nature in writing;
4. use bots or other automated methods to access the content or redirect messages
5. override any security feature or exclusionary protocol; or
6. share the content in order to create substitute for Springer Nature products or services or a systematic database of Springer Nature journal content.

In line with the restriction against commercial use, Springer Nature does not permit the creation of a product or service that creates revenue, royalties, rent or income from our content or its inclusion as part of a paid for service or for other commercial gain. Springer Nature journal content cannot be used for inter-library loans and librarians may not upload Springer Nature journal content on a large scale into their, or any other, institutional repository.

These terms of use are reviewed regularly and may be amended at any time. Springer Nature is not obligated to publish any information or content on this website and may remove it or features or functionality at our sole discretion, at any time with or without notice. Springer Nature may revoke this licence to you at any time and remove access to any copies of the Springer Nature journal content which have been saved.

To the fullest extent permitted by law, Springer Nature makes no warranties, representations or guarantees to Users, either express or implied with respect to the Springer nature journal content and all parties disclaim and waive any implied warranties or warranties imposed by law, including merchantability or fitness for any particular purpose.

Please note that these rights do not automatically extend to content, data or other material published by Springer Nature that may be licensed from third parties.

If you would like to use or distribute our Springer Nature journal content to a wider audience or on a regular basis or in any other manner not expressly permitted by these Terms, please contact Springer Nature at

onlineservice@springernature.com

Радови Драгана К. Маркушев

Часописи

М22

Journal of Applied Physics

RESEARCH ARTICLE | JUNE 22 2023

Thermal characterization of *n*-type silicon based on an electro-acoustic analogy

N. Stanojevic ; D. K. Markushev ; S. M. Aleksić ; D. S. Pantić ; S. P. Galović ; D. D. Markushev ; J. Ordonez-Miranda

Journal of Applied Physics 133, 245102 (2023)
https://doi.org/10.1063/5.0152495

Journal of Applied Physics ARTICLE scitation.org/journal/jap

Thermal characterization of *n*-type silicon based on an electro-acoustic analogy

Cite as: J. Appl. Phys. **133**, 245102 (2023); doi: 10.1063/5.0152495
Submitted: 30 March 2023 · Accepted: 31 May 2023 ·
Published Online: 22 June 2023

N. Stanojevic,[1] D. K. Markushev,[2] S. M. Aleksić,[1,a)] D. S. Pantić,[1] S. P. Galović,[3] D. D. Markushev,[2] and J. Ordonez-Miranda[4]

AFFILIATIONS

[1]Faculty of Electronic Engineering, University of Niš, Aleksandra Medvedeva 14, 18000 Niš, Serbia
[2]Institute of Physics, National Institute of the Republic of Serbia, University of Belgrade, Pregrevica 118, 11080 Belgrade-Zemun, Serbia
[3]Vinča Institute of Nuclear Sciences, National Institute of the Republic of Serbia, P.O. Box 522, 11001 Belgrade, Serbia
[4]LIMMS, CNRS-IIS IRL 2820, The University of Tokyo, Tokyo 153-8505, Japan

Note: This paper is part of the Special Topic on Semiconductor Physics: Plasma, Thermal, Elastic, and Acoustic Phenomena.

[a)]**Author to whom correspondence should be addressed:** sanja.aleksic@elfak.ni.ac.rs

ABSTRACT

Based on the analogy between resistor–capacitor (RC) filters and the thermoelastic component of a photoacoustic signal, the complex thermoelastic response of an open photoacoustic cell is described as a simple linear time-invariant system of a low-pass *RC* filter. This description is done by finding a linear relation between the thermoelastic cut-off frequency and sample material thickness within the range of 10–1000 μm. Based on the theory of a composite piston, we run numerical simulations of the proposed method for *n*-type silicon, described as either a surface or volume absorber. Theoretical predictions are experimentally validated by using an open photoacoustic cell setup to record the signal of an 850-μm-thick *n*-type silicon wafer illuminated by a blue light source modulated with frequencies from 20 Hz to 20 kHz. The obtained experimental results confirm the linear dependence of the thermoelastic cut-off frequency on the sample thickness, and, therefore, they lay the foundation of a new method for the thermal characterization of materials.

I. INTRODUCTION

Although photoacoustics is a powerful method that has been used for decades for the thermal characterization of solids and liquids,[1–8] it also provides a platform for the development of new methods based not only on the analysis of its total signal but also on its signal components for semiconductors.[9–11] By analyzing the frequency spectrum of the thermoelastic component of the photoacoustic signal generated by semiconductors, some research groups[12–14] recently showed that its patterns can be used to probe the influence of free carriers. Such analysis can be used in different areas, such as the design of heat sinks in electronic devices[15–17] and silicon membranes suitable for micro electromechanical systems (MEMSs) sensors.[18–20]

The practice has shown that analog electrical networks are a suitable tool for representing systems and processes of diverse physical nature.[21–23] In particular, linear time-invariant (LTI) systems are widely used to process signals modeling physical phenomena and implementing the desired effects on data. For instance, a simple LTI system made of analog passive RC (resistor–capacitor) filters is commonly applied to pass data through and eliminate unwanted frequencies.[24,25]

In this article, we show that a photoacoustic cell can be considered as a LTI system composed of an analog passive *RC* low-pass filter.[26] By finding the characteristic cut-off frequency (f_{TE}) of the thermoelastic component, this electro-acoustic analogy is used to develop a new methodology for the thermal characterization of semiconductors. This methodology provides the cut-off frequency f_{TE} (l) as a function of the sample thickness l, a unique curve for a given material. Numerical simulations of the frequency response of *n*-type silicon are performed to determine its characteristic curve in the presence of surface or volume absorption and without the influence of free carriers. Furthermore, the proposed method is experimentally validated by using an open-cell photoacoustic setup to measure the photoacoustic signal of *n*-type silicon samples of different thicknesses. We selected this silicon sample because of its ability to act both as a surface (blue light, low absorption depth) and volume

absorber (red light, high absorption depth) by changing the wavelength of the illumination light. This material behavior allows us to treat the thermoelastic response of silicon in the simplest way (surface absorber) needed to establish the RC analogy.

II. THEORETICAL BACKGROUND

A. Fundamentals of linear time-invariant systems

Following the definition of a signal as the description of how one parameter varies with another, and the definition of the system as a process that maps an input signal to an output one, practice shows that the most useful systems fall into the LTI category.[24,25] This is the reason why LTI systems are primary signal-processing tools, mostly represented as filters of different kinds. A LTI system has the following properties: homogeneity, additivity, and time invariance. Homogeneity means that a change in the input signal's amplitude results in a corresponding change in the output signal's amplitude, additivity means that the signals added at the input produce signals that are added to the output, and time invariance means that the system responds in the same way now or later.[25]

Static linearity, sinusoidal fidelity, and commutativity are the other useful properties of LTI systems[25] to understand the analogy between low-pass *RC* filters and photoacoustics. Static linearity defines how a LTI system reacts when the signals do not change (DC or static signals): the output is the input multiplied by a constant. Sinusoidal fidelity establishes that if the input to a LTI system is a sinusoidal wave, the output will also be a sinusoidal wave oscillating with the same frequency as the input. If two or more systems are combined in a cascade (the output of one system is the input to the next), and if each system is linear, then the overall combination will also be linear. The commutative property states that the order of the systems in the cascade can be rearranged without affecting the characteristics of the overall combination. As one of the most used ways of describing a LTI system is its frequency response, in this article, we study this frequency in relation to a photoacoustic signal.

B. Analog passive low-pass RC filters

Filters are electronic circuits that reject a band of frequencies and allow others to pass through. They alter a signal's amplitude

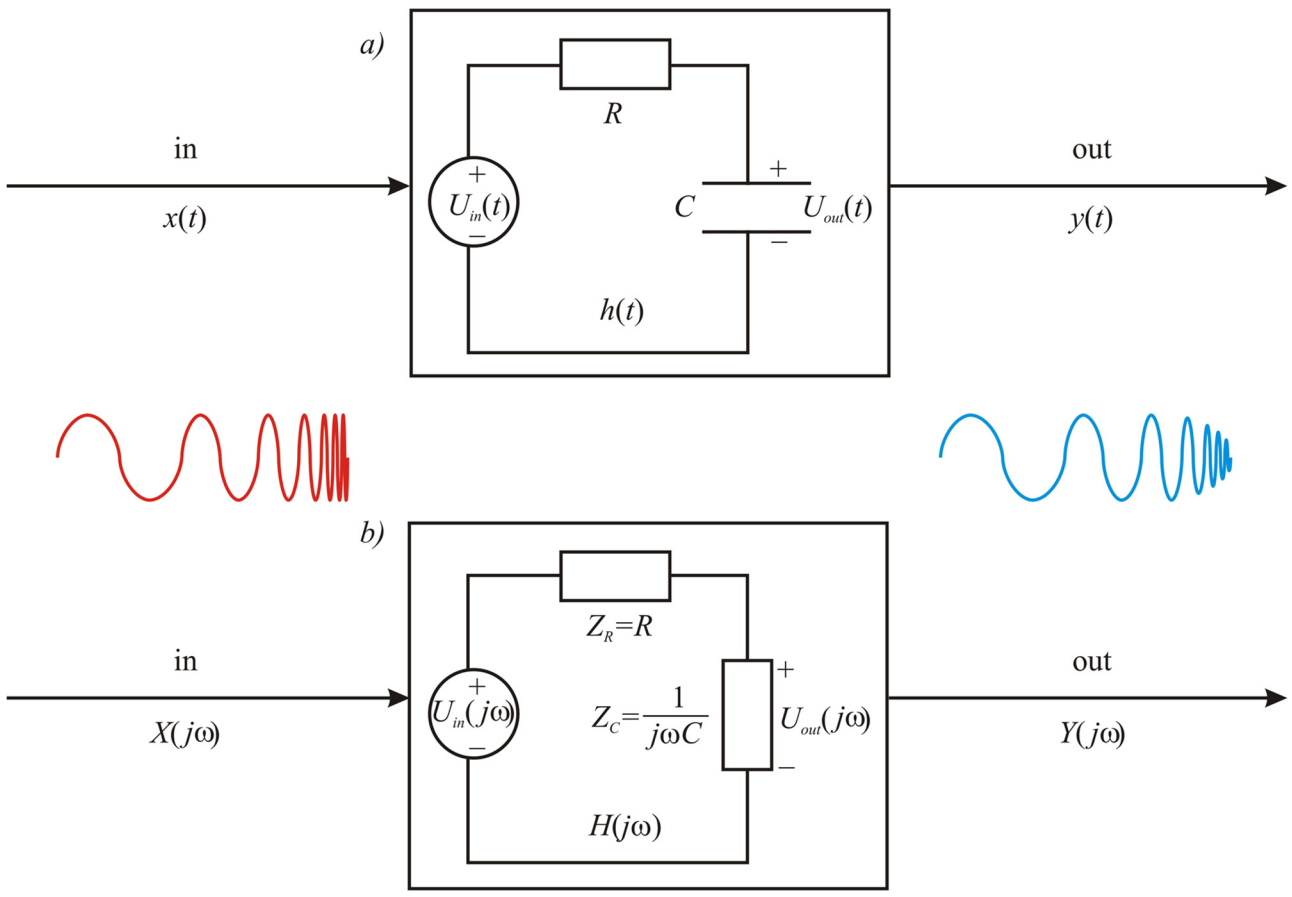

FIG. 1. Typical LTI schemes of the low-pass *RC* filter on (a) time and (b) frequency domains. The red and blue lines stand for the usual sinusoidal input and output signals of the same frequencies.

and/or phase characteristics with respect to frequency in the way that the LTI system does. A filter circuit that consists of passive components such as resistors, capacitors, and inductors, is called a passive filter.[27–29] Considering that the operating frequency range of a filter is determined by the components used to build its circuit, a filter can be categorized based on the operating frequency of a particular circuit. The basic categories are low-pass, high-pass, bend-pass, and bend-stop filters. Here, we present fundamentals of the analog passive low-pass *RC* filter (LPRCF). This filter provides a constant output (gain) from zero up to the cut-off frequency f_0, by attenuating all frequencies above f_0. The schemes of a LPRCF on time and frequency domains are shown in Figs. 1(a) and 1(b), respectively.

Mathematically, a LPRCF is often described in terms of its transfer function $H(j\omega)$ (frequency response), which is given by the ratio of the Fourier transforms $Y(j\omega)$ and $X(j\omega)$ of its respective output and input signals, as follows:

$$H(j\omega) = \frac{Y(j\omega)}{X(j\omega)} = \frac{U_{out}(j\omega)}{U_{in}(j\omega)} = \frac{1}{1 + j\frac{\omega}{\omega_0}}, \tag{1}$$

where j is the imaginary unit, $\omega = 2\pi f$, f is the modulation frequency of the input signal, $\omega = 2\pi f_0 = 1/RC$, with f_0 being the filter cut-off frequency, R the electrical resistance, C the capacitance, $U_{in}(j\omega)$ the input voltage (ideal voltage source), and $U_{out}(j\omega)$ the output voltage. As a complex quantity, the amplitude $|H(j\omega)|$ and phase φ of $H(j\omega)$ are given by

$$|H(j\omega)| = \frac{1}{\sqrt{1 + \left(\frac{\omega}{\omega_0}\right)^2}} \tag{2}$$

and

$$\varphi = -\arctan\left(\frac{\omega}{\omega_0}\right). \tag{3}$$

To plot $|H(j\omega)|$ and φ for $0 < \omega < \infty$, we obtain their values at the following characteristic points: (1) when $\omega \to 0$ then $|H(j\omega)| \to 1$ and $\varphi \to 0°$; (2) when $\omega \to \infty$ then $|H(j\omega)| \to 0$ and $\varphi \to 90°$; and (3) when $\omega = \omega_0$ then $|H(j\omega)| = 1/\sqrt{2}$ and $\varphi = -45°$. According to Eqs. (2) and (3) and these characteristic points (black dots), the LPRCF frequency response is plotted and shown in Fig. 2.

To locate the crucial features of the amplitude and phase of the transfer function, we follow the standard practice to use Bode plots, semi-log plots of the amplitude (in decibels), and phase (in degrees) of a transfer function vs frequency. To obtain these Bode plots (Fig. 2), we transformed the amplitude $|H(j\omega)|$ [Eq. (2)] into A_{dB} (in decibels) given by

$$A_{\mathrm{dB}} = 20\log|H(j\omega)|. \tag{4}$$

A_{dB} is shown in the right vertical axis in Fig. 2(a) and contains the same information as the logarithmic plot of $|H(j\omega)|$, but it is much easier to construct and interpret. The phase φ, on the other hand, is shown in Fig. 2(b) and its Bode plot remains the same.

C. Photoacoustic thermoelastic component

As it is well known, photoacoustics relies on the photoacoustic effect dealing with the generation of sound waves due to the modulated light absorption in a material.[30–32] Sound waves are usually detected by different kinds of sensors, usually microphones, in the form of the total photoacoustic signal—the time variation of the microphone electric output (voltage or current). Based on the

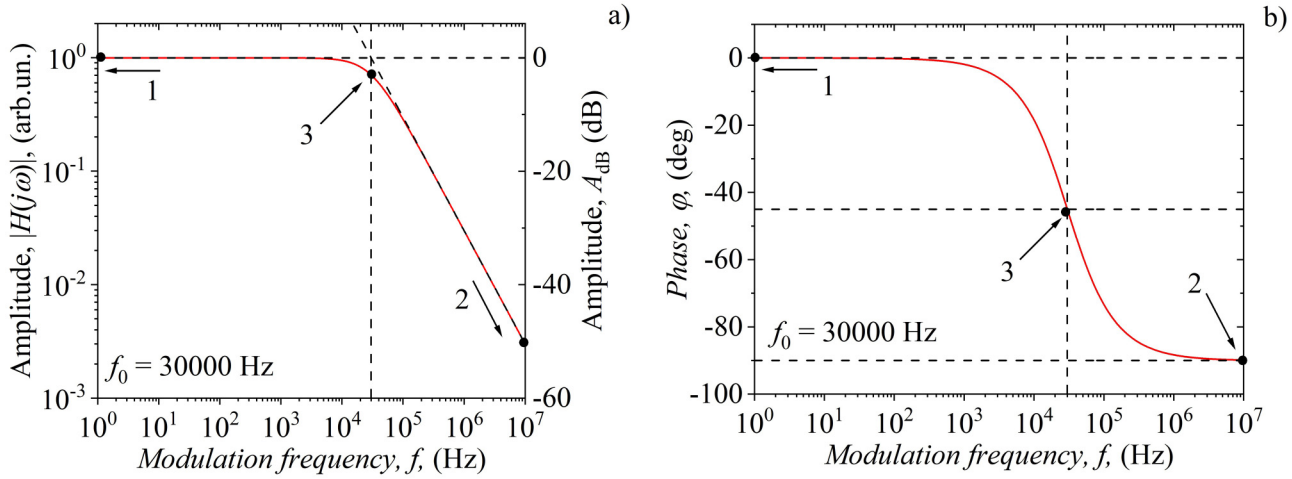

FIG. 2. Frequency response of the (a) amplitude and (b) phase of a typical LPRCF. Calculations were done for f_0 = 30 000 Hz and the amplitude in arbitrary units and decibels in (a).

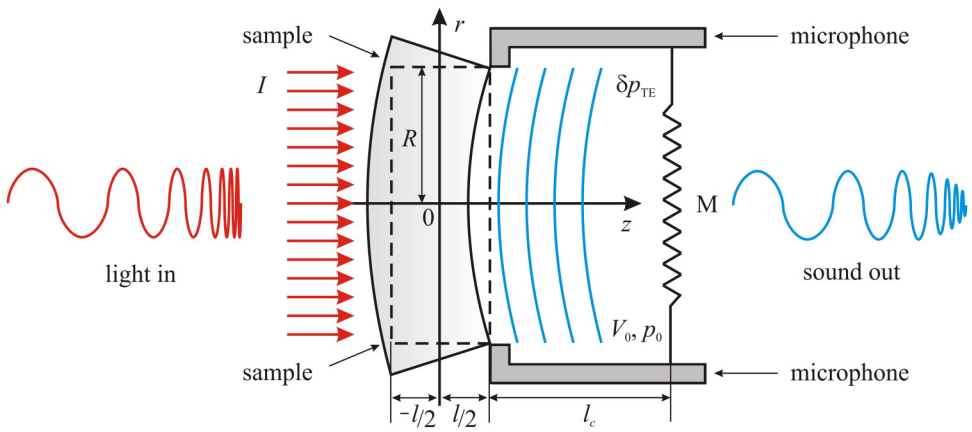

FIG. 3. Scheme of a LTI for the photoacoustics thermoelastic frequency response. The red and blue lines represent the sinusoidal input (modulated light) and output (sound) signals oscillating at the same frequencies, as processed by an open photoacoustic cell.

theoretical model of the composite piston,[33,34] the total photoacoustic signal $\delta p_{\text{total}}(j\omega)$ of the semiconductor, excited without the excess carrier influence, consists of two components: one generated by the thermal piston (thermo-diffusion component, $\delta p_{\text{TD}}(j\omega)$) and another one generated by the mechanical piston [thermoelastic component, $\delta p_{\text{TE}}(j\omega)$]. Mathematically, the total photoacoustic semiconductor signal is a complex function composed of its two components as follows:

$$\delta p_{\text{total}}(j\omega) = \delta p_{\text{TD}}(j\omega) + \delta p_{\text{TE}}(j\omega). \tag{5}$$

Being complex quantities, all components have amplitudes and phases. For our analysis, we will single out the thermoelastic component, $\delta p_{\text{TE}}(j\omega)$, of the semiconductor as the one whose frequency response, based on our experience, most closely matches the response of the low-pass *RC* filter—LPRCF.

A schematic representation of the most used setup of photoacoustics, the so-called open-cell setup, is shown in Fig. 3. The microphone is the detector of the photoacoustic cell having a length l_c and volume V_0. Open cell fairly represents the photoacoustic setup as a LTI system, with all its aforementioned characteristics. The modulated light source (red lines and sinusoids) uniformly illuminates the front side of the semiconductor sample with a circular shape of thickness l and radius R (dashed sample lines). The energy of absorbed light on the illuminated surface and in the nearby volume is transformed into thermal energy that is

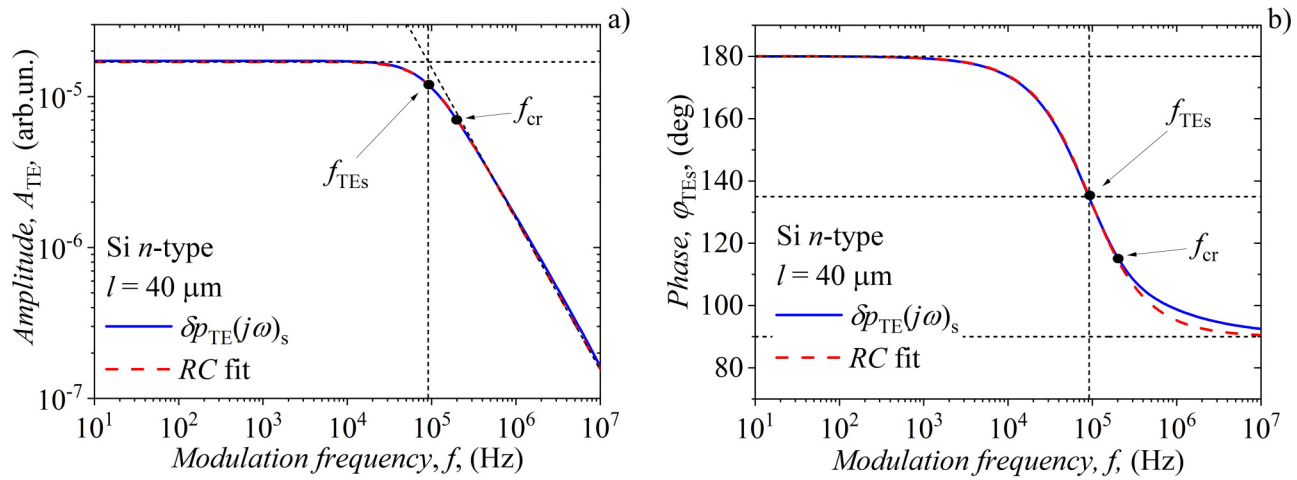

FIG. 4. Frequency response of the (a) amplitude and (b) phase of $\delta p_{\text{TE}}(j\omega)_s$ (black solid lines) for a n-type Si sample of thickness $l = 40\,\mu$m, together with their *RC* fit (red dashed lines).

TABLE I. Si n-type sample parameters used in Eq. (16).

Thermal conductivity, k (W/mK)	150
Heat capacity, C (J/kgK)	715
Density, ρ (kg/m^3)	2329
Thermal diffusivity, D_T (mm^2/s)	90.0
Linear thermal expansion, α_T (10^{-6} 1/K)	2.60

transferred through the sample along the z axis (1D transfer) changing the thermal state of the semiconductor. Such a change leads to different temperatures on the illuminated and non-illuminated sides of the sample, which leads to its, so-called, thermoelastic bending (solid sample lines). The bending is periodic, consistently follows the rhythm of the light source, and periodically changes the air pressure in the immediate vicinity of the unilluminated side of the sample (mechanical piston). A change in air pressure creates sound, i.e., the thermoelastic component $\delta p_{\mathrm{TE}}(j\omega)$ of the photoacoustic signal is formed (blue curves). The sound propagates through the air (at atmospheric pressure p_0) and it is registered by the microphone membrane (M), having the typical frequency response (blue sinusoids) of the semiconductor illumination without the influence of free carriers (electrons and holes).

From a physics point of view, there are two different classical ways to describe the temperature distribution of a semiconductor during its illumination (Fig. 1): (1) surface absorption and (2) volume absorption, both without the excess carrier influence. Avoiding deeper analysis and derivation of the main temperature distribution equations, we present the final expressions and the underlying ideas about the new methods of thermal characterization based on electro-acoustic analogies between RC filters and photoacoustics. Based on the model of the composite piston[33,34] and the theory of thermoelastic bending,[35,36] the thermoelastic component $\delta p_{\mathrm{TE}}(j\omega)_{\mathrm{i}}$ of the photoacoustic signal is given by

$$\delta p_{\mathrm{TE}}(j\omega)_{\mathrm{i}} = 3\pi \frac{\gamma_g p_0 \alpha_T R^4}{l^3 V_0} \int_{-l/2}^{l/2} z T_{\mathrm{i}}(z) dz, \tag{6}$$

where $T_{\mathrm{i}}(z)$ is the temperature distribution within the sample in the case of surface (i = s) or volume (i = v) absorber, p_0 is the air pressure in the cell volume V_0, γ_{g} is the ratio of the heat capacities of the intracell air, and α_{T} is the coefficient of thermal linear expansion of the sample.

D. Surface absorber without excess carrier influence

In this section, we will show how electro-acoustic analogies can be established between the frequency response of the thermoelastic component of the photoacoustic signal and the low-pass RC filter. In the case of n-type semiconductor surface absorption without excess carrier influence, solving the parabolic heat conduction equation (PHCE), the temperature distribution $T_{\mathrm{s}}(z)$ within the illuminated semiconductor (1D heat transport along the z axis and geometry presented in Fig. 1) can be written by a simple

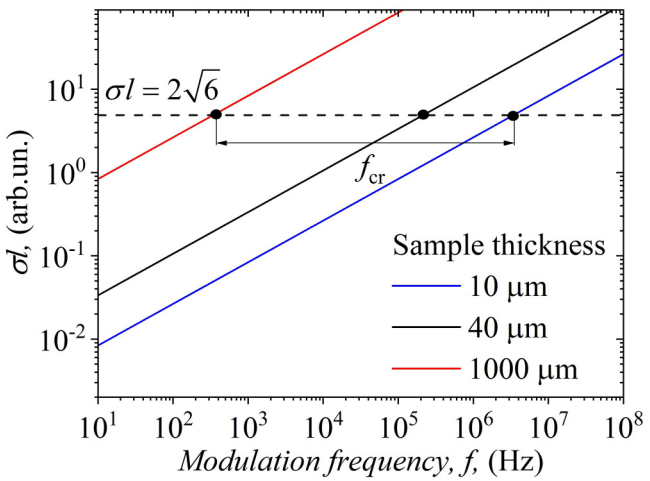

FIG. 5. The values of σl as a function of modulation frequencies, f, in the case of n-type silicon (Table I) different thicknesses and the corresponding range of critical frequencies, f_{cr}, (between red and blue solid lines).

expression,[37,38]

$$T_{\mathrm{s}}(z) = \frac{I_0}{k\sigma} \frac{\cosh[\sigma(l/2 - z)]}{\sinh(\sigma l)}, \tag{7}$$

where I_0 is the amplitude of the incident light intensity I, $\sigma = (1 + j)\mu^{-1}$ is the complex wave vector of heat diffusion, $\mu = \sqrt{2D_T/\omega}$ is the thermal diffusion length, $\omega = 2\pi f$, f is the light source modulation frequency, D_{T} is the thermal diffusivity, and k is the thermal conductivity of the sample.

Solving the integral in Eq. (6) with $T_{\mathrm{s}}(z)$ [Eq. (7)] yields a simple analytical expression for the thermoelastic component $\delta p_{\mathrm{TE}}(j\omega)_{\mathrm{s}}$,[37,38]

$$\delta p_{\mathrm{TE}}(j\omega)_{\mathrm{s}} = 3\pi \frac{I_0 \gamma_g p_0 \alpha_T R^4}{2kV_0(\sigma l)^2} \left\{ \frac{\tanh(\sigma l/2)}{\sigma l/2} - 1 \right\}, \tag{8}$$

which can be easily analyzed in detail. The amplitude $A_{\mathrm{TE}}(f)_{\mathrm{s}}$ and phase $\varphi_{\mathrm{TE}}(f)_{\mathrm{s}}$ of $\delta p_{\mathrm{TE}}(j\omega)_{\mathrm{s}}$ [Eq. (8)] as a function of light source modulation frequency f are numerically obtained using MATLAB and presented in Fig. 4 (blue solid lines), in the case of $l = 40\,\mu$m thick n-type silicon (Si) sample with basic parameters given in Table I. The resulting $\delta p_{\mathrm{TE}}(j\omega)_{\mathrm{s}}$ responses are very similar to the $|H(j\omega)|$ [Eq. (2)] and φ [Eq. (3)] responses of the RC filter (Fig. 3). Based on such obvious similarity, the RC fit is performed on amplitude $A_{\mathrm{TE}}(f)_{\mathrm{s}}$ and phase $\varphi_{\mathrm{TE}}(f)_{\mathrm{s}}$ [Eqs. (2) and (3), respectively, Fig. 4, red dashed lines] which reveals that $\delta p_{\mathrm{TE}}(j\omega)_{\mathrm{s}}$ has the cut-off frequency $f_{\mathrm{TEs}} = (9.1 \pm 0.1) \times 10^4$ Hz. Small discrepancies were observed between $\delta p_{\mathrm{TE}}(j\omega)_{\mathrm{s}}$ and RC fit at higher frequencies, roughly $f_{\mathrm{cr}} > 2 \times 10^5$ Hz, both in amplitude and phase.

Here, the question arises whether the obtained fitting results have justification and meaning, knowing that our photoacoustic system is a system described by partial differential equations, the

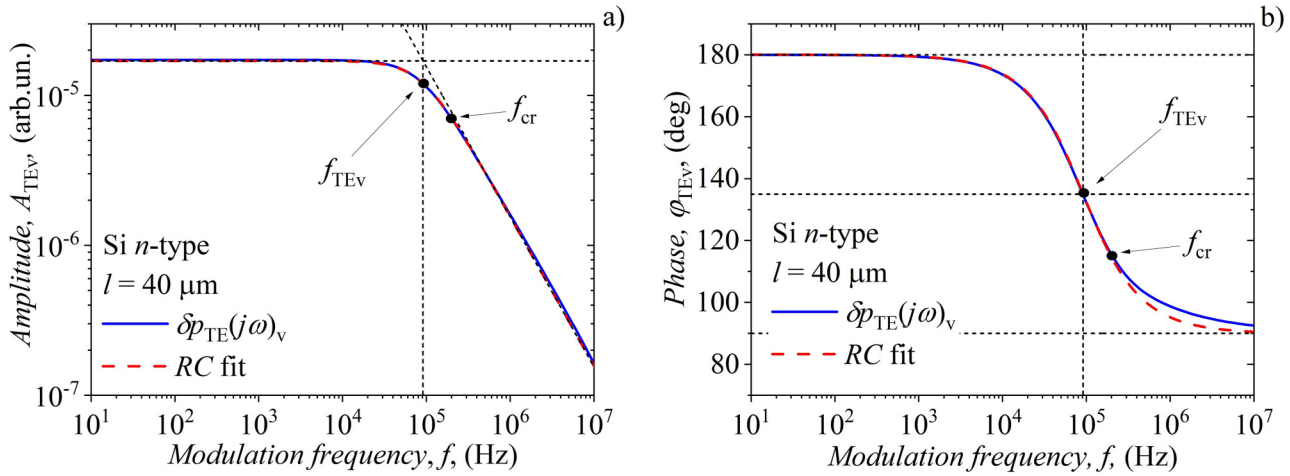

FIG. 6. Typical $\delta p_{TE}(j\omega)_v$ (a) amplitude and (b) phase frequency responses (black solid lines) in the case of Si n-type sample having the thickness, $l = 40\,\mu$m, together with their *RC* fit (red dashed lines).

so-called distributed parameter system (DPS), while *RC* filters are typical representatives of systems described by ordinary differential equations, the so-called lumped-parameter system (LPS).

Without going into the details, the justification and meaning of obtained results are as follows: in a previous article,[26] the condition that should be met to make the photothermal induced temperature variations of a solid sample analogous to the voltage variations of the electric network with passive linear elements is presented. Temperature variations are calculated using the hyperbolic heat conduction equation (HHCE) if the relaxation time τ of thermal processes in the medium exists ($\tau \neq 0$). It was found that HHCE based photothermal (photoacoustic) system (DPS) can be represented as a linear passive electrical network (LPS) under certain conditions $|\sigma|l < \sqrt{6}$[26] (see Appendix A), where σ is defined by a *RLC* filter. Taking our PHCE case ($\tau \to 0$), these conditions remain, but σ is reduced to the *RC* filter. In addition, our photoacoustic thermoelastic system can be described only with resistors and capacitors[26] (see Appendix A). Considering the description of σ by passive electrical elements (resistor, capacitor, and coil), a similar condition for the modeling of the TE component by a passive linear electrical network can be obtained: $|\sigma|l/2 < \sqrt{6}$ (see Appendix A). For $\tau = 0$ (our case), this electrical network becomes the *RC* filter (see Appendix A).

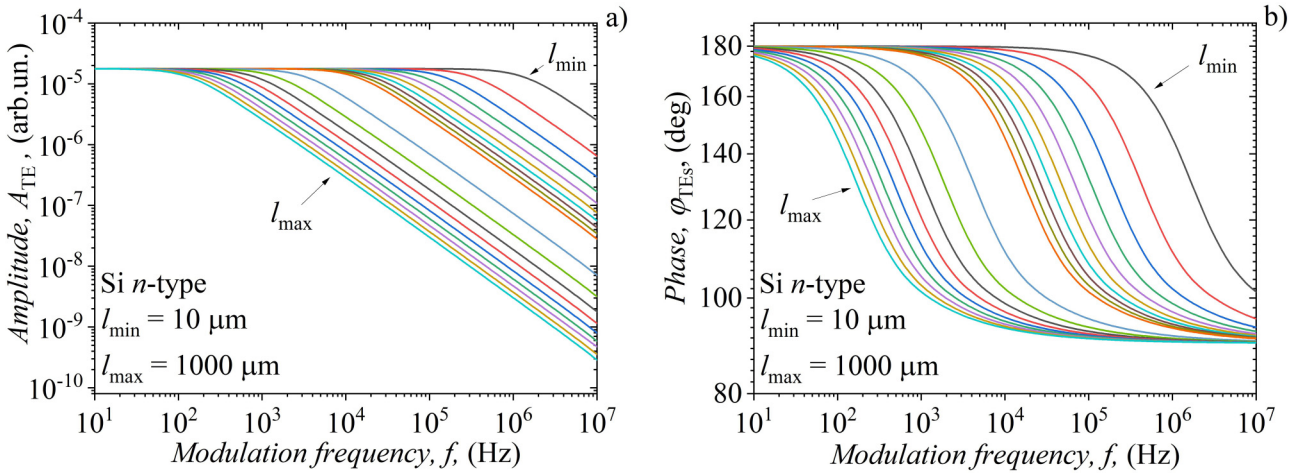

FIG. 7. Frequency response of the (a) amplitude and (b) phase of $\delta p_{TE}(j\omega)_s$ for a *n*-type Si sample. Calculations were done for a sample thickness in the range 10–1000 μm, which is used to find f_{TEs} applying a *RC* fit [Eqs. (2) and (3)].

TABLE II. Cut-off frequency f_{TEs} determined by fitting for a *n*-type Si semiconductor of different thicknesses.

Sample thickness l ($\times 10^{-6}$ m)	Cut-off frequency f_{TEs} (Hz)
10	1 467 250
20	352 064.0
30	150 994.8
40	91 465.38
50	58 578.48
60	40 865.79
70	28 097.52
80	21 687.13
90	17 231.35
100	14 013.44
200	3 475.289
300	1 578.390
400	871.7279
500	558.1317
600	387.6765
700	284.8613
800	217.3823
900	172.3485
1000	139.6089

The stated condition can be adapted to our analysis (Fig. 5), where for the range of Si sample thicknesses from 10 to 1000 μm, the range of critical modulation frequencies $4 \times 10^2 < f_{cr} < 4 \times 10^6$ Hzis determined (DPS–LPS approximation). When $l = 40\,\mu$m (Fig. 4), the photoacoustic system thermoelastic response can be described only by resistors and capacitors—a low-pass *RC* filter—LPRCF, at frequencies $f_{cr} < 2 \times 10^5$ Hz.

The final results show the possibility to develop an electric network—*RC* low-pass filter (Fig. 1) that will be the analog of the photoacoustic system under consideration (Fig. 3). More precisely, the illuminated sample is modeled by LPRCF, where the values of voltages and electric currents in this filter are analog to the values of temperature distribution and heat flux at the respective points of the sample. The resistor corresponds to the reciprocal value of the sample thermal conductivity, and the capacitor corresponds to the sample thermal capacity.

E. Volume absorber without excess carrier influence

In the case of *n*-type semiconductor volume absorption without free carrier influence, under the same excitation condition as in the surface absorber case, the temperature distribution $T_v(z)$ (1D case) within the semiconductor can be written as[37,38]

$$T_v(z) = \frac{I_0}{k\sigma}\frac{\beta^2}{\beta^2-\sigma^2} \times \left\{\frac{\cosh[\sigma(l/2-z)] - e^{-\beta l}\cosh(\sigma(l/2+z))}{\sinh(\sigma l)} - \frac{\sigma}{\beta}e^{-\beta(l/2+z)}\right\}. \quad (9)$$

Here, β is the absorption coefficient of the sample. Solving the integral in Eq. (6) with $T_v(z)$ [Eq. (11)] yields a slightly more complicated analytical expression for the thermoelastic component $\delta p_{TE}(j\omega)_v$,[37,38]

$$\delta p_{TE}(j\omega)_v = 3\pi\frac{I_0\gamma_g p_0\alpha_T R^4}{2kV_0(\sigma l)^2}\frac{\beta^2}{\beta^2-\sigma^2} \times \left\{\left(1+e^{-\beta l}\right)\left[\frac{\tanh(\sigma l/2)}{\sigma l/2}-1\right] - \left(\frac{\sigma}{\beta}\right)^2\frac{C}{\beta l}\right\}, \quad (10)$$

where $C = 2 - \beta l - (2+\beta l)e^{-\beta l}$. The amplitude $A_{TE}(f)_v$ and phase $\varphi_{TE}(f)_v$ of $\delta p_{TE}(j\omega)_v$ as a function of light source modulation frequency f are presented in Fig. 6 (blue solid lines), in the case of $l = 40\,\mu$m, a thick n-type Si sample with basic parameters given in Table I, adding $\beta = 2,41 \times 10^6\,\mathrm{m}^{-1}$ and excess carrier lifetime $\tau \approx 10^{-9}$ s (ultrafast recombination—no excess carriers influence).

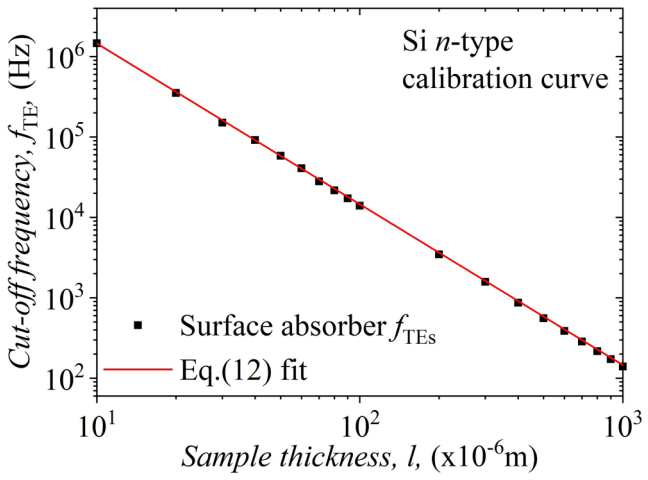

FIG. 8. The calibration curve of *n*-type Si, showing the cut-off frequencies f_{TEs} of $\delta p_{TE}(j\omega)_s$ as a function of the sample thickness (Table II).

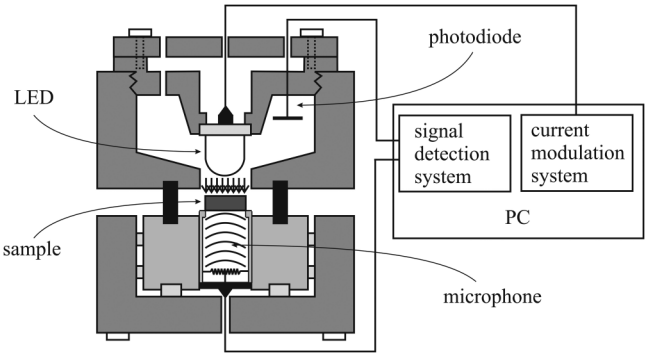

FIG. 9. Scheme of the open-cell photoacoustic setup.

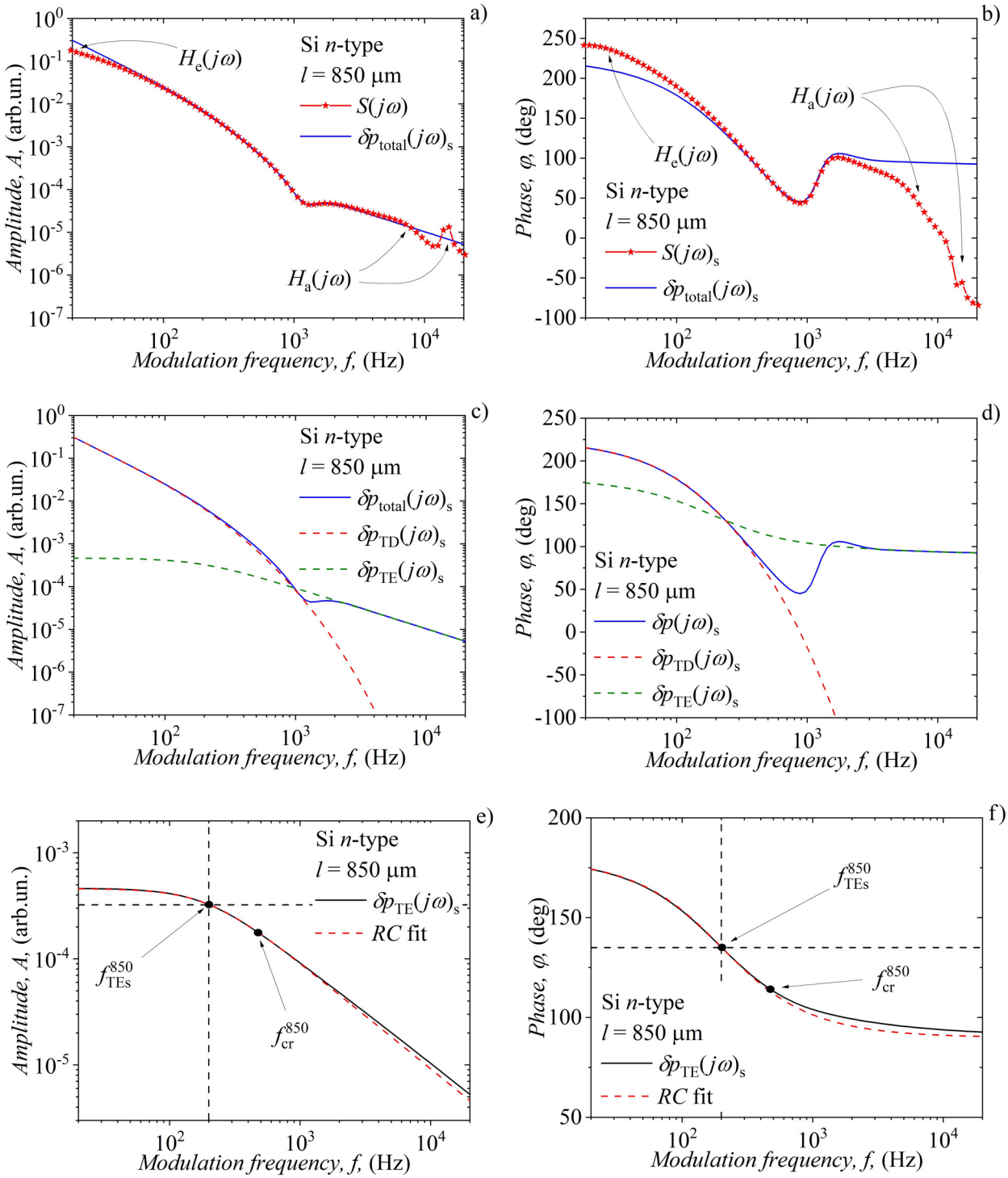

FIG. 10. Measured photoacoustic signal $S(j\omega)_s$ of a *n*-type Si sample together with its "true" signal $\delta p(j\omega)_s$. (a) Amplitude A and (b) phase φ are plotted together with $\delta p(j\omega)_s$ components in (c) and (d) $\delta p_{TD}(j\omega)_s$ and $\delta p_{TE}(j\omega)_s$, as a function of modulated frequency f. *RC* fits [Eqs. (2) and (3)] are depicted on (e) amplitude A and (f) phase φ together with the characteristic frequencies f_{TE}^{850} and f_{cr}^{850}.

It is obvious that $A_{TE}(f)_v$ and phase $\varphi_{TE}(f)_v$ of $\delta p_{TE}(j\omega)_v$ are the same as in the surface absorber case ($\beta l \to \infty$). It means that the *RC* fit [Eqs. (2) and (3), Fig. 6, red dashed line] reveals the same value of $f_{TEv} = f_{TEs} = (9.1 \pm 0.1) \times 10^4$ Hz. Also, it reveals the same values of f_{cr} as in the surface absorption case at $l = 40\,\mu$m ($f_{cr} < 2 \times 10^5$ Hz) and in the whole investigated range of thicknesses (10^3 Hz $< f_{cr} < 10^7$ Hz).

III. NEW METHOD FOR MATERIAL CHARACTERIZATION

In the previous paragraphs (Sec. II), we found the essential characteristics of our thermoelastic photoacoustic system: f_{TE}, f_{cr} (Figs. 4 and 6), and dependence of f_{cr} on the sample thickness, l (Fig. 5). In this paragraph, we will find another essential characteristic of our system, which is the dependence of f_{TEs} on l. This dependence is the basis of establishing a new material characterization method that connects the external parameters (f_{TEs}, l) that can be changed in the experiment, with the internal essential one (thermal diffusivity, D_T), a natural material characteristic. It can be found from the $\sigma l/2$ value in square brackets of Eq. (8) when $f = f_{TEs}$. In this case, one can write

$$\frac{|\sigma| l}{2} = m \tag{11}$$

or

$$f_{TEs} = \frac{2}{\pi} \frac{D_T}{l^2} m^2, \tag{12}$$

considering that $|\sigma| = \sqrt{\omega/D_T}$, $\omega = \omega_{TEs} = 2\pi f_{TEs}$, and $\sqrt{2} \le m < \sqrt{6}$ (see Appendix A).[26]

Applying the identical procedure as in Fig. 6, f_{TEs} values can be found from $\delta p_{TE}(j\omega)_s$ [Eq. (8)], for a wide range of silicon sample thicknesses (from 10 to 1000 μm, Fig. 7, Table II), with the same characteristics as it was given in Table I. Thicknesses are taken from $l_{min} = 10$ to 100 μm in steps of 10 μm and from 100 to $l_{max} = 1000\,\mu$m in steps of 100 μm.

Using the results presented in Table II, one can plot the dependence of f_{TEs} on the thickness of the sample, l, in a log–log scale (Fig. 8). By fitting these results with Eq. (12), the value of $m = (1.513 \pm 0.002)$ is obtained. This result, in a general sense, represents a reference curve for a certain material (n-type Si, in our case, with parameter D_T from Table I) and can be used as a calibration curve within the framework of material characterization. In other words, a new method for material characterization (not only semiconductors), based on the analysis of $\delta p_{TE}(j\omega)_s$ frequency response and its f_{TEs} dependence on the thickness of the sample, can be established. Such a methodology can be advantageous when it comes to the development of non-destructive methods of material characterization, investigation of semiconductor wafers as substrates for thin film analysis, as well as the role of photogenerated excess carriers both at surfaces and in bulk.[39–43]

IV. EXPERIMENTAL CONFIRMATION

To experimentally confirm the validity of the calibration method described in Sec. III, let us use the measurement results of

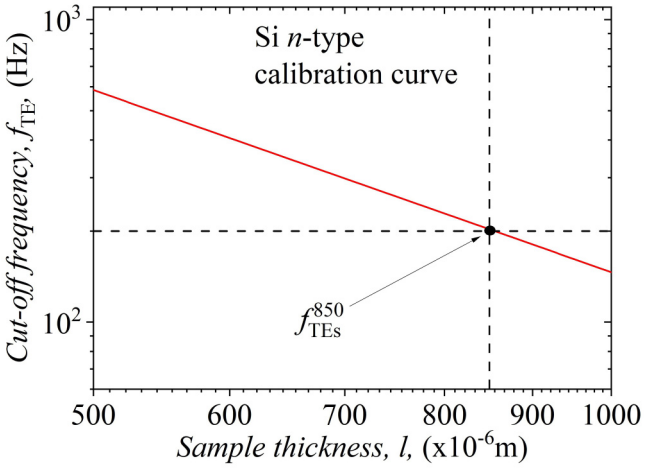

FIG. 11. Cut-off frequency f_{TE}^{850} experimentally obtained (black dot) for an 850-μm-thick circular silicon wafer compared to the n-type silicon calibration curve (solid red line) predicted by theory (Fig. 8).

a circular n-type silicon wafer with a radius of $R = 3$ mm and a thickness of $l = 850\,\mu$m. Measurements were made by the open-cell photoacoustic setup (Fig. 9), explained in detail somewhere else,[12,13] with a blue LED light source (450 nm), and corresponding wafer absorption coefficient $\beta = 2,41 \times 10^6$ m^{-1} ($\beta l >> 1$, surface absorption) and excess carriers relaxation time, $\tau \approx 10^{-6}$ s, insufficient for their influence on the photoacoustic signal (and its components) in the 20 Hz to 20 kHz modulation frequency f range.

The obtained measured signal $S(j\omega)_s$, its amplitude A, and phase φ [red asterisks, Figs. 9(a) and 9(b)] are cleaned from the influence of the experimental instruments in the low-frequency [$H_e(j\omega)$] and high-frequency [$H_a(j\omega)$] regions, in order to obtain the "true" signal $\delta p_{total}(j\omega)_s$ amplitudes and phases (solid blue lines, Figs. 10(a) and 10(b)], the signal originating directly from the illuminated sample[13,44] (see Appendix B).

The obtained $\delta p_{total}(j\omega)_s$ is fitted using the composite piston model [solid blue, Figs. 10(c) and 10(d)]. Besides the basic sample parameters (matching those from Table I), such a fitting procedure leads to the signal components: $\delta p_{TD}(j\omega)_s$ from the thermal (dashed red) and $\delta p_{TE}(j\omega)_s$ from the mechanical (dashed blue) piston.[13,33,34,44]

Singling out $\delta p_{TE}(j\omega)_s$ [solid black, Figs. 10(e) and 10(f)], it is clear that the analogy with *RC* circuits can be applied to this component, i.e., its amplitudes and phases can be fitted with Eqs. (2) and (3), respectively (red dashed). The results of that fitting give the value of cut-off frequency $f_{TEs}^{850} = (200 \pm 10)$ Hz and $f_{cr}^{850} = (480 \pm 20)$ Hz. The value of f_{TEs}^{850} matches to the Si n-type calibration curve (Fig. 11), and $f < f_{cr}^{850}$ defines the frequency range where the *RC* fit of $\delta p_{TE}(j\omega)_s$ is fully applicable.

The results obtained from the experimental data confirm the applicability of the new method aimed at the thermal characterization of n-type silicon based on electro-acoustic analogies between passive low-pass *RC* filters and thermoelastic components of the photoacoustic signals.

V. CONCLUSIONS

We have demonstrated that the thermoelastic response of n-type silicon recorded via an open photoacoustic cell can be described as a simple linear time-invariant system made of a passive *RC* filter. This analogy is driven by the linear relation between the silicon sample thickness and the modulation frequency of its thermal excitation. For both surface and volume excitations without the influence of free carriers, we have obtained the values of the critical frequencies, below which the analogy between the photoacoustic (temperature, heat flux, thermal conductivity, and heat capacity) and electrical (voltage, current, resistance, and capacitance) quantities is complete. Based on the proposed analogy, the frequency spectrum of the amplitude and phase of the thermoelastic component of the silicon photoacoustic signal has been analyzed like a passive low-pass *RC* filter to determine the characteristic thermoelastic cut-off frequencies. By correlating the obtained cut-off frequencies with the thickness of the examined *n*-type silicon, we have determined that its linear calibration curve is driven by thermal diffusivity. Such linearity has been experimentally validated using an open-cell setup to measure the photoacoustic response of the 850-μm-thick silicon wafer excited with a blue light source within the 20 Hz–20 kHz modulation frequency range. Thus, the proposed method is expected to be useful for the thermal characterization of materials.

ACKNOWLEDGMENTS

The authors acknowledge the financial support provided by the Institute of Physics Belgrade, through Grant No. 660-01-00015/69, of the Ministry of Science, Technological Development, and Innovations of the Republic of Serbia.

AUTHOR DECLARATIONS

Conflict of Interest

The authors have no conflicts to disclose.

Author Contributions

N. Stanojevic: Investigation (equal). **D. K. Markushev:** Methodology (equal). **S. M. Aleksić:** Formal analysis (equal). **D. S. Pantić:** Supervision (equal). **S. P. Galović:** Supervision (equal). **D. D. Markushev:** Conceptualization. **J. Ordonez-Miranda:** Conceptualization (equal).

DATA AVAILABILITY

The data that support the findings of this study are available within the article.

APPENDIX A: PHOTOTHERMAL RESPONSE AND ANALOGY WITH PASSIVE LINEAR ELECTRIC NETWORKS

The thermal response of the sample illuminated by a modulated light source is described by the temperature distribution $T_s(z)$ within the sample [Eq. (7)], obtained by solving the dynamic part of the 1D diffusion equation of heat transport along the z axis,

$$\frac{\partial^2 T_s(z,t)}{\partial z^2} = \frac{1}{D_T}\frac{\partial T_s(z,t)}{\partial t}, \tag{A1.1}$$

where $T_s(z,t) = T_{amb}(z) + T_s(z)(1+e^{j\omega t})$, $T_{amb}(z)$ is the ambient temperature, ω is the modulation circular frequency, $D_T = k/(\rho C_V)$, k is the thermal conductivity, ρ is the density, and C_V is the volumetric thermal capacity of the medium. This equation is the so-called parabolic heat conduction equation (PHCE), which is always stable, depicting a heat transfer process in the medium as a diffusion process. It assumes an infinite speed of heat propagation or, in other words, the zero-relaxation time ($\tau \to 0$) of thermal processes in the medium. On the other hand, the 1D hyperbolic heat conduction equation (HHCE) along the z axis,[26]

$$\frac{\partial^2 T_s(z,t)}{\partial z^2} = \frac{1}{D_T}\frac{\partial T_s(z,t)}{\partial t} + \frac{\tau}{D_T}\frac{\partial^2 T_s(z,t)}{\partial t^2}, \tag{A1.2}$$

acknowledges the finite speed of heat propagation, or finite value of τ ($\tau \neq 0$), describing the heat transfer process in the medium as a wave propagation process. Equation (A1.2) is similar in form to the Maxwell (telegraph) equation of an electromagnetic field, which, given in terms of voltage $u(z,t)$ between the lines has the form[26]

$$\frac{\partial^2 u(z,t)}{\partial z^2} = rc\frac{\partial u(z,t)}{\partial t} + l_z c\frac{\partial^2 u(z,t)}{\partial t^2}, \tag{A1.3}$$

where $r = \mathrm{d}R/\mathrm{d}z$ is the distributed resistance, $c = \mathrm{d}C/\mathrm{d}z$—the distributed capacitance, and $l_Z = \mathrm{d}L/\mathrm{d}z$—the distributed inductance of the line. An analogy between Eqs. (A1.2) and (A1.3) can be established, as an analogy between two distributed parameter systems, by introducing the following relationships: $u \leftrightarrow T$, $c \leftrightarrow \rho C_V$, $r \leftrightarrow 1/k$, and $l_Z \leftrightarrow \tau/k$.

However, the electric network which consists of the elements with lumped (not anymore distributed) parameters can be established to describe the system defined with Eq. (A1.3). Such a system consists of the equivalent impedance Z_{eq} and admittance Y_{eq}, given in the forms,[26]

$$Z_{eq} = Z\frac{\tanh\left(\frac{\sqrt{ZY}}{2}\right)}{\frac{\sqrt{ZY}}{2}} \text{ and } Y_{eq} = Y\frac{\sinh\left(\sqrt{ZY}\right)}{\sqrt{ZY}}, \tag{A1.4}$$

where

$$Z = l_l(r + j\omega l_z) \text{ and } Y = j\omega c l_l \tag{A1.5}$$

and l_l is the length of the line. If one wants to represent Z_{eq} and Y_{eq} with real electric elements (resistors, capacitors, and coils), Eq. (A1.4) must be simplified to

$$Z_{eq} = Z \text{ and } Y_{eq} = Y. \tag{A1.6}$$

This can be done if the condition $ZY \ll 6$ is satisfied, as shown in Ref. 26.

If $\tau = 0$ is the case we are considering, the equivalent electric circuit that describes the optically induced surface temperature variations is an *RC* filter (the coil as an element is lost). The equivalent impedance Z_{eq} and the equivalent admittance Y_{eq} are given by the expressions:

$$Z_{eq} = Z = l_l r = \frac{1}{k} l_l \text{ and } Y_{eq} = Y = j\omega c l_l = j\omega \rho C_v l_l. \tag{A1.7}$$

Using the knowledge that the properties of materials in relation to heat conduction can, under certain conditions, be described as equivalent to resistance and capacitance [Eq. (A1.7)], the condition under which the TE component of the PA signal [Eq. (8)] can be described with *RC* filters is $ZY << 24$ (obtained following the series expansion of $\tanh(\sqrt{ZY}/2)/(\sqrt{ZY}/2)$).[26] The condition can be written as

$$ZY = l_l r j\omega c l_l = j\omega r c l_l^2 \ll 24 \tag{A1.8}$$

or rewritten in terms of sample properties using established analogies (sample thickness $l = l_l$),[26]

$$j\omega \frac{1}{D_T} l^2 \ll 24. \tag{A1.9}$$

This condition in terms of real numbers can be written as

$$\omega \frac{1}{D_T} l^2 = (|\sigma| l)^2 \ll 24, \tag{A1.10}$$

which leads to the final form of $|\sigma| l \ll 2\sqrt{6}$. Taking into account the obtained limits and series expansion, the analytical expression of $\delta p_{TE}(j\omega)_s$ [Eq. (8)] can be simplified as

$$\delta p_{TE}(j\omega)_s = 3\pi \frac{I_0 \gamma_g p_0 \alpha_T R^4}{8 m^2 k V_0} \left[\frac{1}{1 + (j\omega/\omega_{TE})}\right], \tag{A1.11}$$

where

$$A_{TE}(j\omega)_s = |\delta p_{TE}(j\omega)_s| \sim \frac{1}{\sqrt{1 + (\omega/\omega_{TE})^2}}, \text{ and } \varphi = -\arctan\left(\frac{\omega}{\omega_{TE}}\right). \tag{A1.12}$$

Here, $\omega_{TE} = D_T/(l/2m)^2$ and $\sqrt{2} \le m < \sqrt{6}$, depending on the number of terms in the series expansion.

APPENDIX B: THE CLEANING OF EXPERIMENTAL SIGNAL FROM THE INFLUENCE OF THE MEASURING CHAIN

The measuring chain of photoacoustics consists of many devices with associated electronics that measure not only the desired signal but also control the conditions of the experiment, especially the sources of excitation. All these devices, in addition to their good features, carry with them (as electronic devices) plenty of bad features that are reflected in different types of noise and strong signal deviations in the entire frequency domain of interest for our research.[44]

In our case, the microphone as a detector, with its associated electronics, introduces the most interference and affects the shape of the measured signal in the entire range of modulation frequencies f from 20 Hz to 20 kHz. In the low-frequency range ($f < 10^3$ Hz), the microphone and the lock-in, which is emulated by the computer's sound card, act like two cascaded high-pass *RC* filters, decreasing the measured signal more and more, as we move toward lower frequencies. In a mathematical sense, their influence can be described by a transfer function $H_e(j\omega)$ of the first order having the form

$$H_e(j\omega) = -\frac{\left(\frac{\omega}{\omega_1}\right)}{\left(1 + j\frac{\omega}{\omega_1}\right)} \times \frac{\left(\frac{\omega}{\omega_2}\right)}{\left(1 + j\frac{\omega}{\omega_2}\right)}, \tag{A2.1}$$

where $\omega = 2\pi f$, $\omega_1 = 2\pi f_1$, where f_1 is the microphone cut-off frequency, and $\omega_2 = 2\pi f_2$, where f_2 is the lock-in (sound card) cut-off frequency. In the high-frequency range, the microphone acts like two second-order high-pass *RC* filters, altering the measured signal in the form of peaks (resonances) more and more as we move toward higher frequencies. In a mathematical sense, microphone influence (acoustic response) can be described by a transfer function $H_a(j\omega)$ of the second order having the form[44]

$$H_a(j\omega) = \frac{1}{1 - \left(\frac{\omega}{\omega_3}\right)^2 + j\delta_3 \frac{\omega}{\omega_3}} + \frac{1}{1 - \left(\frac{\omega}{\omega_4}\right)^2 + j\delta_4 \frac{\omega}{\omega_4}}. \tag{A2.2}$$

Here, $\omega_3 = 2\pi f_3$ and $\omega_4 = 2\pi f_4$, where f_3 and f_4 are the characteristic cut-off frequencies of the first and second peaks of the microphone, while δ_3 and δ_4 are their corresponding dumping factors.

The measured photoacoustic signal $S(j\omega)_s$ is the product of the "real" photoacoustic signal $\delta p_{total}(j\omega)_s$ originating from the sample, multiplied by the aforementioned effects of $H_e(j\omega)$ and $H_a(j\omega)$ in the entire frequency domain,[44]

$$S(j\omega)_s = \delta p(j\omega)_s H_e(j\omega) H_a(j\omega). \tag{A2.3}$$

The basic idea of cleaning the measured signal is to recognize all the mentioned cut-off frequencies of the microphone and lock-in (sound card), e.g., by fitting the $S(j\omega)_s$. In this way, $H_e(j\omega)$ and $H_a(j\omega)$ can be fully recognized and removed from the measured signal, leaving only the "real" signal $\delta p_{total}(j\omega)_s$ that carries information about the illuminated sample. The "real" signal, now, can be the subject of fitting based on, for example, the theory of composite piston, searching for the signal components, especially, the thermoelastic one.

REFERENCES

[1] S. Engel, C. Wenisch, F. A. Müller, and S. Gräf, "A new photoacoustic method based on the modulation of the light induced absorption coefficient," Meas. Sci. Technol. **27**(4), 045202 (2016).

[2]A. Somer, A. Gonçalves, T. V. Moreno, G. K. da Cruz, M. L. Baesso, N. G. C. Astrath, and A. Novatski, "Photoacoustic signal with two heating sources: Theoretical predictions and experimental results for the open photoacoustic cell technique," Meas. Sci. Technol. **31**(7), 075202 (2020).
[3]D. Gasca-Figueroa, G. Gutiérrez-Juárez, F. J. García-Rodríguez, L. Polo-Parada, A. Pérez-Pacheco, and M. G. Bravo-Sánchez, "Direct measurement of solids thermal effusivity by cw photoacoustic technique," Results Phys. **42**, 105986 (2022).
[4]M. Sarkar and K. Kumar, "Fabrication of photoacoustic cell and thermal diffusivity measurement of coal carbon black using it," Mater. Today Proc. **52**(3), 1812–1816 (2022).
[5]A. Somer, S. Galovic, E. K. Lenzi, A. Novatski, and K. Djordjevic, "Temperature profile and thermal piston component of photoacoustic response calculated by the fractional dual-phase-lag heat conduction theory," Int. J. Heat Mass Transf. **203**, 123801 (2023).
[6]A. Somer, A. Novatski, and E. K. Lenzi, "Theoretical predictions for photoacoustic signal: Fractionary thermal diffusion with modulated light absorption source," Eur. Phys. J. Plus **134**(12), 593 (2019).
[7]D. S. Volkov, O. B. Rogova, and M. A. Proskurnin, "Photoacoustic and photothermal methods in spectroscopy and characterization of soils and soil organic matter," Photoacoustics **17**, 100151 (2020).
[8]M. Isaiev, G. Mussabek, P. Lishchuk, K. Dubyk, N. Zhylkybayeva, G. Yar-Mukhamedova, D. Lacroix, and V. Lysenko, "Application of the photoacoustic approach in the characterization of nanostructured materials," Nanomaterials **12**(4), 708 (2022).
[9]S. J. Zelewski and R. Kudrawiec, "Photoacoustic and modulated reflectance studies of indirect and direct band gap in van der Waals crystals," Sci. Rep. **7**, 15365 (2017).
[10]L. Bychto and M. Malinski, "Photoacoustic spectroscopy analysis of thin semiconductor samples," Opto-Electron. Rev. **26**, 217–222 (2018).
[11]K. L. Djordjevic, D. D. Markushev, Ž. M. Ćojbašić, and S. P. Galović, "Inverse problem solving in semiconductor photoacoustics by neural networks," Inverse Problems Sci. Eng. **29**, 248–262 (2021).
[12]D. K. Markushev, D. D. Markushev, S. M. Aleksić, D. S. Pantić, S. P. Galović, D. V. Lukić, and J. Ordonez-Miranda, "Enhancement of the thermoelastic component of the photoacoustic signal of silicon membranes coated with a thin TiO_2 film," J. Appl. Phys. **131**, 085105 (2022).
[13]D. K. Markushev, D. D. Markushev, S. M. Aleksic, D. S. Pantic, S. P. Galovic, D. M. Todorovic, and J. Ordonez-Miranda, "Experimental photoacoustic observation of the photogenerated excess carrier influence on the thermoelastic response of n-type silicon," J. Appl. Phys. **128**, 095103 (2020).
[14]D. K. Markushev, D. D. Markushev, S. M. Aleksic, D. S. Pantic, S. P. Galovic, D. M. Todorovic, and J. Ordonez-Miranda, "Effects of the photogenerated excess carriers on the thermal and elastic properties of n-type silicon excited with a modulated light source: Theoretical analysis," J. Appl. Phys. **126**(18), 185102 (2019).
[15]P. Ci, M. Sun, M. Upadhyaya, H. Song, L. Jin, B. Sun, M. R. Jones, J. W. Ager, Z. Aksamija, and J. Wu, "Giant isotope effect of thermal conductivity in silicon nanowires," Phys. Rev. Lett. **128**(8), 085901 (2022).
[16]B. L. Rakshith, L. G. Asirvatham, A. A. Angeline, S. Manova, J. R. Bose, J. P. Selvin Raj, O. Mahian, and S. Wongwises, "Cooling of high heat flux miniaturized electronic devices using thermal ground plane: An overview," Renew. Sustain. Energy Rev. **170**, 112956 (2022).
[17]J. Khan, S. A. Momin, and M. Mariatti, "A review on advanced carbon-based thermal interface materials for electronic devices," Carbon **168**, 65–112 (2020).
[18]J. Su, X. Zhang, G. Zhou, C. Xia, W. Zhou, and Q. Huang, "A review: Crystalline silicon membranes over sealed cavities for pressure sensors by using silicon migration technology," J. Semicond. **39**(7), 071005 (2018).
[19]P. G. Ullmann, C. Bretthauer, M. Schneider, and U. Schmid, "Stress analysis of circular membrane-type MEMS microphones with piezoelectric read-out," Sens. Actuators A **349**, 114003 (2023).
[20]A. Bagolini, R. Correale, A. Picciotto, M. Di Lorenzo, and M. Scapinello, "MEMS membranes with nanoscale holes for analytical applications," Membranes **11**(2), 74 (2021).
[21]G. Bertuccio, "On the physical origin of the electro-mechano-acoustical analogy," J. Acoust. Soc. Am. **151**, 2066 (2022).
[22]E. Brandão, W. D'Andrea Fonseca, and P. H. Mareze, "An algorithmic approach to electroacoustical analogies," J. Acoust. Soc. Am. **152**, 667 (2022).
[23]W. M. Taha, A. E. M. Taha, and J. Thunberg, "Modeling physical systems," in *Cyber-Physical Systems: A Model-Based Approach* (Springer, Cham, 2021).
[24]D. Sundararajan, *Digital Signal Processing, An Introduction* (Springer Nature Switzerland AG, 2021).
[25]S. W. Smith, *The Scientist and Engineer's Guide to Digital Signal Processing*, 2nd ed. (California Technical Publishing, 1999), see https://www.dspguide.com/.
[26]S. Galovic, Z. Soskic, and M. Popovic, "Analysis of photothermal response of thin solid films by analogy with passive linear electric networks," Therm. Sci. **13**(4), 129–142 (2009).
[27]G. Ellis, "Chapter 8—Filters in control systems," in *Control System Design Guide*, 4th ed. (Butterworth-Heinemann, 2012), pp. 165–183.
[28]L. F. Chaparro and A. Akan, "Chapter 12—Introduction to the design of discrete filters," in *Signals and Systems Using MATLAB*, 3rd ed. (Academic Press, 2019), pp. 721–802.
[29]A. S. Morris and R. Langari, "Chapter 8—Principles of data acquisition and signal processing," in *Measurement and Instrumentation*, 3rd ed. (Academic Press, 2021), pp. 211–241.
[30]A. Rosencwaig and A. Gersho, "Theory of the photoacoustic effect with solids," J. Appl. Phys. **47**, 64–69 (1976).
[31]A. Rosencwaig, *Photoacoustics and Photoacoustic Spectroscopy* (John Wiley & Sons, New York, 1980), pp. 1–309.
[32]S. E. Bialkowski, N. G. C. Astrath, and M. A. Proskurnin, *Photothermal Spectroscopy Methods for Chemical Analysis*, 2nd ed. (John Wiley, New York, 2019).
[33]F. A. McDonald, "Photoacoustic, photothermal, and related techniques: A review," Can. J. Phys. **64**, 1023–1029 (1986).
[34]F. McDonald and G. Wetsel, "Generalized theory of the photoacoustic effect," J. Appl. Phys. **49**, 2313 (1978).
[35]B. A. Boley and J. H. Weiner, *Theory of Thermal Stresses* (Wiley, New York, 1960).
[36]G. Roussett, F. Lepoutre, and L. Bertrand, J. Appl. Phys. **54**, 2383 (1983).
[37]D. D. Markushev, J. Ordonez-Miranda, M. D. Rabasovic, M. Chirtoc, D. M. Todorovic, S. E. Bialkowski, D. Korte, and M. Franko, "Thermal and elastic characterization of glassy carbon thin films by photoacoustic measurements," Eur. Phys. J. Plus **132**, 33 (2017).
[38]D. D. Markushev, J. Ordonez-Miranda, M. D. Rabasović, S. Galović, D. M. Todorović, and S. E. Bialkowski, "Effect of the absorption coefficient of aluminium plates on their thermoelastic bending in photoacoustic experiments," J. Appl. Phys. **117**, 245309 (2015).
[39]V. Gusev and M. Franko, "Editorial for the special collection on non-invasive and non-destructive methods and applications, I: Festschrift—A tribute to Andreas Mandelis," J. Appl. Phys. **132**, 230401 (2022).
[40]K. Herrmann, N. W. Pech-May, and M. Retsch, "Photoacoustic thermal characterization of low thermal diffusivity thin films," Photoacoustics **22**, 100246 (2021).
[41]A. Melnikov, A. Mandelis, A. Soral, C. Zavala-Lugo, and M. Pawlak, "Quantitative imaging of defect distributions in CdZnTe wafers using combined deep-level photothermal spectroscopy, photocarrier radiometry, and lock-in carrierography," ACS Appl. Electron. Mater. **3**(6), 2551–2563 (2021).
[42]M. Pawlak, "Photothermal, photocarrier, and photoluminescence phenomena in semiconductors studied using spectrally resolved modulated infrared radiometry: Physics and applications editors-pick," J. Appl. Phys. **126**, 150902 (2019).
[43]J. Zakrzewski, K. Strzałkowski, M. Boumhamdi, A. Marasek, A. Abouais, and D. M. Kaminski, "Photothermal determination of the surface treatment of $Cd_{1-x}Be_xTe$ mixed crystals," Appl. Sci. **13**(4), 2113 (2023).
[44]D. D. Markushev, M. D. Rabasović, D. M. Todorović, S. Galović, and S. E. Bialkowski, "Photoacoustic signal and noise analysis for Si thin plate: Signal correction in frequency domain," Rev. Sci. Instrum. **86**, 035110 (2015).

Journal of Applied Physics

RESEARCH ARTICLE | JUNE 22 2023

Time-domain minimum-volume cell photoacoustic of thin semiconductor layer. I. Theory

S. P. Galovic ; K. Lj. Djordjevic ; M. V. Nesic ; M. N. Popovic ; D. D. Markushev ; D. K. Markushev ; D. M. Todorovic

Journal of Applied Physics 133, 245701 (2023)
https://doi.org/10.1063/5.0152519

Journal of Applied Physics ARTICLE pubs.aip.org/aip/jap

Time-domain minimum-volume cell photoacoustic of thin semiconductor layer. I. Theory

Cite as: J. Appl. Phys. **133**, 245701 (2023); doi: 10.1063/5.0152519
Submitted: 30 March 2023 · Accepted: 4 June 2023 ·
Published Online: 22 June 2023

S. P. Galovic,[1,a)] K. Lj. Djordjevic,[1] M. V. Nesic,[1] M. N. Popovic,[2] D. D. Markushev,[2] D. K. Markushev,[2] and D. M. Todorovic[3]

AFFILIATIONS

[1]"Vinča" Institute of Nuclear Sciences—National Institute of the Republic of Serbia, University of Belgrade, P.O. Box 522, Belgrade 11000, Serbia
[2]Institute of Physics Belgrade, National Institute of the Republic of Serbia, University of Belgrade, Pregrevica 118, Belgrade (Zemun) 11080, Serbia
[3]Institute for Multidisciplinary Research, University of Belgrade, P.O. Box 33, Belgrade 11030, Serbia

Note: This paper is part of the Special Topic on Semiconductor Physics: Plasma, Thermal, Elastic, and Acoustic Phenomena.

[a)]**Author to whom correspondence should be addressed:** bobagal@vin.bg.ac.rs

ABSTRACT

The model of a photoacoustic gas-microphone signal in the time domain recorded in a transmission configuration using a minimum volume cell is derived. This model takes into account the inertial thermal relaxations of both the sample and the gas filling the cell by means of the generalized hyperbolic theory of heat conduction. With the introduction of electro-thermal analogy for the thin sample and short microphone length cavity, characteristic quantities are defined, which can be used in solving the inverse problem in time-domain photoacoustic in both cases, when thermal relaxations are neglected as well as when they are considered. The derived model that includes thermal relaxation explains the experimentally observed occurrence of overshoots and undershoots as well as an oscillatory approach to the steady values of the recorded signal in high-resolution time-domain photoacoustic measurements of thin semiconductor membranes, which will be presented in detail in Paper II of the paper.

I. INTRODUCTION

If a sample is illuminated by an electromagnetic (EM) beam, one part of the incident EM energy is absorbed by the sample and part of the absorbed energy is transformed into heat. The heated sample generates pressure fluctuations and the propagation of sound in its gaseous or fluid surrounding, which depends on optical, thermal, elastic, electronic, and other related physical properties of the sample. This effect of optically generated sound is called photoacoustic (PA) effect, and it is suitable for the development of experimental non-contact and non-destructive methods allowing for the examination of various properties of solids and soft matter.[1–42]

In the so-called solid–gas–microphone (SGM) photoacoustics, pressure fluctuations in the gas column of a closed cell are recorded by a microphone; i.e., the acoustic response is detected. The time variation in the electric output from the microphone is the well-known *PA signal*.

The PA signal can be recorded in the frequency domain[1–30] or in the time-domain.[31–42]

In frequency PA methods, the excitation optical signal of a given wavelength is periodically modulated, while the amplitude and the phase of the PA signal at each modulation frequency are the subjects of the measurement. The characteristics of frequency domain PA are periodically modulated optical sources with modulation frequency matched to frequency-phase selected signal detection (lock-in amplifier, boxcar integrator), cost efficient setup, high signal-to-noise ratio (SNR), low laser fluence, and the technical simplicity of EM sources. On the other hand, the acoustic response

in the frequency domain is narrowband and many processes that become observable at high frequencies cannot be detected.

A monochromatic source is usually modulated by current–voltage control of its electrical supply. Then, a series of optical pulses appear as an optical output where two cases can be distinguished. If the frequencies of this periodical series are higher than 10 Hz, the excess energy in the system is not completely relaxed (dissipated) for most materials and structures, and a quasi-stationary regime is established. Typically, this is the case in the frequency-domain solid–gas–microphone detection. The other case is when the excitation pulse is short enough compared to the pause until the next pulse so that the system has enough time to fully relax and return to the unexcited state before the next pulse; this is when the PA signal is to be measured in time domain. There are two types of time-domain photoacoustics: optoacoustics, for pulse durations less than 10 ns, and thermoacoustics, for pulse duration between 500 ns and 1 ms.[35–37] The characteristics of time-domain photoacoustics are pulsed sources, broadband response, time of flight measurement, high SNR, and high energy pulses (10–100 mJ/pulse), relatively high costs. The most common applications of time-domain photoacoustics are given in Refs. 30–42.

The response of an experimental system to pulse excitation, as well as the acoustic response to periodical modulation, contains information on optical (light absorption) and thermal properties of the material under investigation, but due to broadband response, such experimental configurations allow the measurement of additional high-rate relaxation properties, which affect the PA signal at very high frequencies.[33,43–48]

The time-domain or pulse gas-microphone PA experiments may be carried out using the modified frequency gas-microphone setup, but the received PA signal is more difficult to interpret due to its wide frequency bandwidth. To understand and correctly interpret a pulsed signal, it is necessary to carry out a theoretical analysis, taking into account such a specific way of the exciting signal modulation and high-rate relaxation processes that affect the measured PA signal.

This paper will consider the case when the excitation optical signal is given by one short pulse followed by a sufficiently long pause so that the excited system can fully relax. This means that the PA signal in the time domain can be modeled as the response to a single optical pulse.

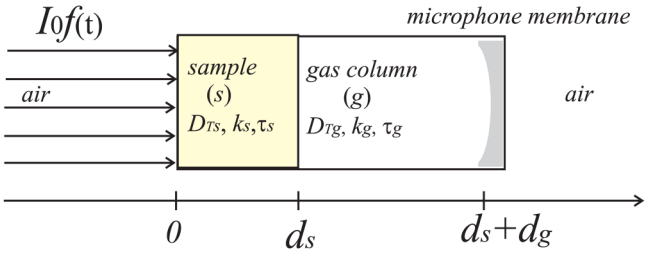

FIG. 1. Geometry of the problem in the transmission configuration of a sample-gas-microphone setup. A solid of thickness d_s (m) having an optical absorption coefficient β (m^{-1}) is surrounded by optically transparent air and supported by an electret microphone. The cell (microphone hole) of length d_g (m) contains an optically transparent gas. The surrounding air is taken to be thick so that its exterior boundaries are not important.

Existing theoretical models of the time-domain gas-microphone PA signal[31–35] do not take into account high-rate relaxation phenomena and might be insufficient for the analysis of experimental signals. A generalized model transmission PA response in a minimum volume cell including thermal relaxation is presented in this article. The spectral function of the PA signal is derived in Sec. II by using Laplace transform and thermal quadrupole formalism. In Sec. III, time-domain PA responses for a step function and short pulse are calculated and analyzed. It is shown that the derived model predicts the possible occurrence of overshoots and undershoots in the vicinity of the step changes of the excitation optical pulse. The similar phenomenon was observed by the experimental gas-microphone measurement of a thin Si plate that could not be explained by the existing models.[48] The relationship between thermal and geometrical properties of the semiconductor sample and the characteristics of time-domain PA signal are discussed. In the end, the most important conclusions are drawn.

A detailed description of the PA experiments on a thin Si plate and the processing of experimental measurements applying the derived model will be presented in Paper II of this paper.

II. THEORETICAL BACKGROUND

Optical, acoustic, and thermal processes occurring in a minimum volume PA cell excited by a light pulse of short duration are treated in one-dimensional approximation corresponding to the configuration illustrated schematically in Fig. 1.

A. Outline of the model

The increase in the cell temperature excited by the light pulse results in the change in gas pressure. The additional value of gas pressure in the cell is proportional to the average gas temperature, independent of the thermodynamic process (assumed to be adiabatic[1,43] or isochoric).[32,34] Only the coefficient of proportionality changes depending on the assumed model. In this paper, the gas overpressure is calculated for the case of an isochoric process, similar to the calculation given in Refs. 31, 32, and 34.

Under typical experimental conditions, the gas in the cell may be treated as an ideal gas and, consequently, the equation of state can be applied to it,

$$p(x, t) = R\rho_g(x, t)T_g(x, t), \tag{1}$$

where $\rho_g(x, t)$ (kg/m^3) and $T_g(x, t) = T_0 + \theta_g(x, t)$ (K) are the density of the gas and temperature in the one-dimensional enclosure (gas column), respectively, and $\theta_g(x, t)$ is the departure from the equilibrium temperature T_0. With symbol R being denoted as the universal gas constant, $p(x,t)$ (Pa) is the pressure fluctuation in the chamber. The average pressure in the chamber can be computed by taking the spatial average of $p(x,t)$. Rearranging Eq. (1) and recognizing that the spatial integral of $p(x,t)$ is the total mass of gas M_0 in the one-dimensional system and, therefore, constant,

TABLE I. The range of sound wavelengths in air in the audible frequency range of sound.

f (Hz)	20	50	100	500	1 000	5 000	10 000	20 000
λ(m)	17	6.8	3.4	0.68	0.34	0.068	0.034	0.017

results in

$$\int_{d_s}^{d_s+d_g} \frac{p(x,t)}{T_g(x,t)}dx = R\int_{d_s}^{d_s+d_g} \rho_g(x,t)dx = RM_0. \tag{2}$$

In the configuration shown in Fig. 1, the PA cell consists of an electret microphone chamber. The dimensions of this cell are of the order of a millimeter (d_g ranges from 1 to 4 mm; the microphone diameter is around 5 mm), and it is filled with gas, usually air. The speed of sound propagation is about 300 m/s in gaseous media. Using the relationship between the wavelength of sound and the frequency of the sound wave in the audible range, as shown in Table I, it can easily be concluded that the wavelength of sound is much larger than the linear dimensions of the cell, so it can be considered a small acoustic volume chamber (linear dimensions of the chamber are smaller than the wavelength of sound waves in the gas). Therefore, it can be considered that $p(x,t) \approx p(t)$ and, consequently, Eq. (2) becomes

$$\langle p(t)\rangle \int_{d_s}^{d_s+d_g} \frac{dx}{T_0\left(1+\frac{\theta_g(x,t)}{T_0}\right)} = RM_0. \tag{3}$$

Considering that there are small departures from the equilibrium temperature ($\theta_g(x,t)/T_0 << 1$) and expanding the denominator in terms of powers of $\theta_g(x,t)$ as well as putting $\langle p(t)\rangle = p_0 + \Delta p(t)$ lead to the following description of pressure fluctuation:

$$\Delta p(t) = \frac{p_0}{T_0 d_g}\int_{d_s}^{d_s+d_g} \theta_g(x,t)dx. \tag{4}$$

From Eq. (4), it can be concluded that for calculating the PA signal, it is necessary to calculate the average temperature variation inside the PA cell.

The sample is excited by a light pulse of duration t_p (s) and of an irradiance of I_0 (W/m^{-2}). Assuming that the light pulse comes from the negative side of the x axis to the sample of thickness d_s and of absorption coefficient β, and is absorbed as described by the Beer–Lambert law, as well as considering the nonradiative deexcitation processes following light absorption in the solid to be instantaneous,[49] the density function of the volume heat source takes the following form:

$$S(x,t) = (1-R_{rf})\eta I_0 \beta e^{-\beta x} f(t) = S_0 \beta e^{-\beta x} f(t), \tag{5}$$

where dimensionless parameters are as follows: R_{rf} is the coefficient of the optical reflection, η is the quantum coefficient of the conversion of electromagnetic energy into heat, and the function $f(t)$ describes the time shape of the incident light, with β (1/m) denoting the coefficient of optical absorption of the sample.

In the case of solids with high optical absorption coefficient, such as semiconductors, it can be assumed that all light is absorbed in a very thin layer close to the surface of the sample so that heat sources (excitation heat flux) are generated only in this thin layer. This means that it can be considered that there is a surface heat source;[17,18,45,50] that is, an optically induced excitation heat flux on the illuminated surface of the sample can be described by

$$S(x,t) = \lim_{\beta\to\infty}(1-R_{rf})\eta I_0 \beta e^{-\beta x} f(t) = S_0 f(t)\delta(x), \tag{6}$$

where $\delta(x)$ is Dirac's delta function; i.e., there is a surface heat source at the illuminated side of the sample during the duration of the pulse t_p.

With respect to air being a much better thermal insulator than the sample, thermal propagation across surrounding is not taken into account.

Under the conditions outlined above, the heat transfer equations including thermal relaxations for each of the regions $i = s, g$ (Fig. 1) can be written as[43–48,51–58]

$$\rho_i C_{pi}\frac{\partial \theta_i(x,t)}{\partial t} + \frac{\partial q_i(x,t)}{\partial x} = 0, \tag{7}$$

$$q_i(x,t) + \tau_i \frac{\partial q_i(x,t)}{\partial t} = -k_i \frac{\partial \theta_i(x,t)}{\partial x}, \tag{8}$$

where $\theta_i(x,t)$ (K) is the temperature departure from the initial ambient temperature T_0 and $q_i(x,t)$ (W/m^2) is the heat flux. In the above equations, symbols k_i(W/mK), C_{pi} (J/kg K), ρ_i (kg/m^3), and τ_i (s) signify the thermal conductivity, specific heat, density, and thermal relaxation time of the ith layer, respectively, and $k_i/(\rho_i C_{pi}) = D_{Ti}$ (m^2/s) is the thermal diffusivity.

The heat flux delayed constitutive relation given by Eq. (8) enables the inclusion of inertial thermal relaxation and the removes non-physical preposition of the classical theory of heat conduction about infinite heat propagation speed.[43,51–58] If thermal relaxations are neglected ($\tau_i = 0$), Eq. (8) is reduced to classic Fourier's constitutive relation and, consequently, heat conduction is described by classic parabolic diffusion theory[59] widely used in frequency photoacoustics.[1–28] This approximation is justified in the case when the frequency scale of the experiment is smaller than the inverse value of the inertial relaxation time. Unfortunately, this relaxation time and the associated heat propagation speed have not been determined so far for any material or structure at room temperature, and theoretical estimates range from a few seconds for biological tissues to a few femtoseconds for metals.[43,45,60,61] This means that it is not possible, for experiments based on heat propagation, to determine in advance whether it is necessary to take thermal relaxations into account or whether they can be neglected.

Recently, the values of inertial relaxation time have been measured for the graphene plane at low temperatures (above 100 and 200 K) in time-domain experiments based on the photothermal effect by using the theoretical model that includes thermal relaxations.[62,63] Starting from the facts that time-domain photoacoustics, as well as other PT techniques, are broadband and that the inertial relaxation time of either the semiconductor or gas is not known,

they are included in the derivation of the model for the time-domain PA signal.

Equations (7) and (8) are subject to the zero initial condition,

$$\frac{\partial \theta_i(x,t)}{\partial t}|t=0, \tag{9a}$$

$$\theta_i(x, t=0). \tag{9b}$$

Zero initial conditions are common in the consideration of heat transfer in many problems, whether one uses classical diffusion theory or one of the generalized theories.[43–45,50,59,64] Such conditions ensure the causality of the transport process and stability of solutions. The detailed study of the influence of initial conditions to heat transfer can be found in Refs. 65–67.

Assuming that surrounding air is a much better thermal insulator than the system sample-gas column, zero boundary conditions can be considered,[43,45,59]

$$q_s(x=0,t)=0, \tag{10a}$$

$$q_g(x=D,t)=0. \tag{10b}$$

We also suppose temperature and heat flux continuity at the boundaries between the sample and the gas column at all time points,

$$\theta_s(d_s,t)=\theta_g(d_s,t), \tag{11a}$$

$$q_s(d_s,t)=q_g(d_s,t). \tag{11b}$$

The solution to the problem described above may be obtained with different methods,[63,67–70] and the result will not depend on the chosen method. One of them is to use Laplace transform for the calculation of the spectral function of the PA signal and inverse Laplace transform for the calculation of the time-domain PA signal.

B. Spectral function of the PA signal

By applying the Laplace transform to expressions (7)–(8) and assuming that zero initial conditions can be applied [Eq. (9)], this system is reduced to the system of ordinary differential equations in a complex domain that is analogous with equations of propagation of voltage and current across the transmission line.[71–75] After solving this system of linear differential equations for each layer, complex representatives of temperature variations and heat flux for each layer from Fig. 1 are obtained as follows:

$$\bar{\Theta}_i(x)=\bar{\Theta}_{i1}ch[\bar{\sigma}_i(d_i-x)]+\bar{Z}_{ci}\bar{Q}_{i1}sh[\bar{\sigma}_i(d_i-x)], \tag{12}$$

$$\bar{Q}_i(x)=\frac{\bar{\Theta}_{i1}}{\bar{Z}_{ci}}sh[\bar{\sigma}_i(d_i-x)]+\bar{Q}_{i1}ch[\bar{\sigma}_i(d_i-x)], \tag{13}$$

where s is the complex frequency. In the above expressions, $\bar{\Theta}_{i1}$ and $\bar{Q}_{i1}$ are the complex representatives of temperature variations and heat flux at the end of the ith layer (at points d_s or d_s+d_g, see Fig. 1).

In the above expressions and further in the text, all complex variables are marked with overbar diacritic and their dependence on s is omitted for readability.

The propagation coefficient and the characteristic impedance of each layer are given by the following expressions:[71]

$$\bar{\sigma}_i=\sqrt{\bar{z}_i\bar{y}_i}, \tag{14}$$

$$\bar{Z}_{ci}=\sqrt{\frac{\bar{z}_i}{\bar{y}_i}}. \tag{15}$$

Parameters $\bar{z}_i$ and $\bar{y}_i$, longitudinal impedance and admittance, are introduced by using the analogy of the heat conduction process and propagation of voltage and current across the transmission line,[71]

$$\bar{z}_i=r_i+sl_i, \tag{16}$$

$$\bar{y}_i=g_i+sc_i, \tag{17}$$

where distributed (longitudinal) resistivity r_i, capacity c_i, inductivity l_i, and conductivity g_i are related to thermal properties of the ith layer by the following relations:[71]

$$r_i=\frac{1}{k_i}, \tag{18a}$$

$$c_i=\rho_i C_{pi}=\frac{k_i}{D_{Ti}}, \tag{18b}$$

$$l_i=\frac{\tau_i}{k_i}, \tag{18c}$$

$$g_i=0. \tag{18d}$$

By introducing Laplace transform into the expression for pressure fluctuations [Eq. (4)] and substituting Eqs. (12) and (13) in it, the following model of the spectral function of the pressure fluctuation is obtained,

$$\Delta\bar{P}(s)=\frac{p_0}{T_0}\frac{\bar{Z}_{cg}}{\bar{\sigma}_g d_g}(\bar{Q}_{g0}-\bar{Q}_{g1}), \tag{19}$$

where symbols $\bar{Q}_{g0}$ and $\bar{Q}_{g1}$ denote the heat flux at the beginning ($x=d_s$) and at the end of the gas column ($x=d_s+d_g$), respectively (see Fig. 1).

If we take into account the boundary condition $\bar{Q}_{g1}=0$ [Eq. (10b)], which assumes that there is no heat exchange between the PA cell and the surrounding, Eq. (19) is reduced to

$$\Delta\bar{P}(s)=\frac{p_0}{T_0}\frac{\bar{Z}_{cg}}{\bar{\sigma}_g d_g}\bar{Q}_{g0}. \tag{20}$$

As can be seen from Eq. (20), for the calculation of the PA signal, it is necessary to know the value of the heat flux at the boundary between the gas column and the optically heated sample

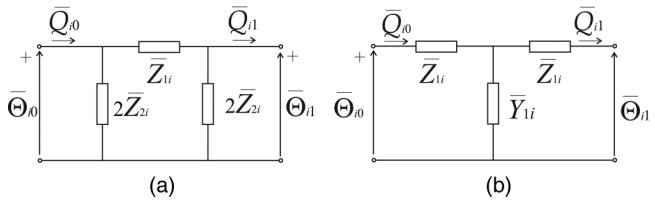

FIG. 2. Equivalent thermal quadrupole for the *i*th layer: (a) equivalent T network and (b) equivalent Π network.

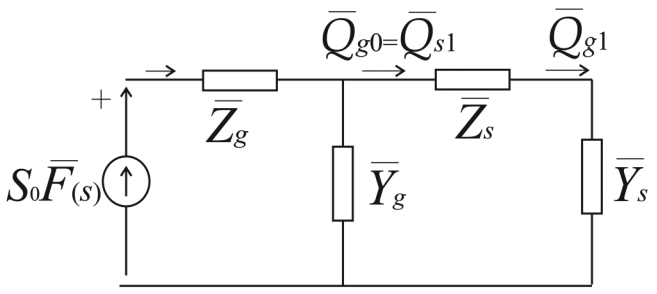

FIG. 3. Equivalent electrical circuit that represents the photothermally induced heat transfer across the system from Fig. 1 under the condition given by Eq. (26).

and not the entire profile of temperature and heat flux through the system shown in Fig. 1. For this calculation, it is suitable to apply the thermal quadrupole model.[71,76–79]

By using Eqs. (12) and (13), it can be shown that each layer can be represented by an equivalent Π or T network (Fig. 3),[71,72] the impedances of which, calculated from Eqs. (12) and (13), are given by the following expressions:

$$\bar{Z}_{1i} = \bar{Z}_i \frac{\sinh\left(\sqrt{\bar{Z}_i \bar{Y}_i}\right)}{\sqrt{\bar{Z}_i \bar{Y}_i}}, \tag{21}$$

$$\bar{Z}_{2i} = \frac{1}{\bar{Y}_i} \frac{\sqrt{\bar{Z}_i \bar{Y}_i}/2}{\tanh\left(\sqrt{\bar{Z}_i \bar{Y}_i}/2\right)}. \tag{22}$$

Parameters $\bar{Z}_i$ and $\bar{Y}_i$ are defined by distributed (longitudinal) impedance and admittance [Eqs. (16) and (17)], respectively, as well as layer thickness, d_i,

$$\bar{Z}_i = R_i + sL_i = r_i d_i + s l_i d_i = \left(\frac{d_i}{k_i} + s\frac{\tau_i}{k_i} d_i\right), \tag{23}$$

$$\bar{Y}_i = sC_i = sc_i d_i = s\frac{k_i}{D_{Ti}} d_i. \tag{24}$$

By applying Laplace transform to Eq. (6), the surface heat source can be represented by an equivalent ideal current source,

$$\bar{S}(s) = S_0 \bar{F}(s). \tag{25}$$

Considering the above calculations, the heat flux at the beginning of the gas column can be calculated by solving equivalent electrical circuits, which consist of two cascade related networks from Fig. 3, excited by the current source given by Eq. (25).

In the case of a very thin sample and minimum volume PA cell, the following condition is met:[68]

$$\bar{Z}_i \bar{Y}_i < 6 \quad i = s, g. \tag{26}$$

In that case, each thermal quadrupole (Fig. 2) can be reduced to a passive linear network: RC filter if the description of heat conduction is based on classic Fourier theory where $\tau_i = 0$ or RLC filter if the theory of heat conduction includes thermal relaxation, $\tau_i \neq 0$.[71] The equivalent electrical circuit in that case is shown in Fig. 3.

By solving the equivalent electrical circuit from Fig. 3, a relation can be established between the excitation flux and the heat flux at the beginning of the gas column that appears in the expression for the PA signal [Eq. (20)]. The transfer function of the system in Fig. 3 is

$$\bar{H}(s) = \frac{\bar{Y}_g}{\bar{Z}_g \bar{Y}_s \bar{Y}_g + \bar{Y}_s + \bar{Y}_g}. \tag{27}$$

By using Eqs. (23) and (24), for the case when thermal relaxations are included, the transfer function becomes

$$H(s) = \frac{K}{\frac{s^2}{\omega_n^2} + \frac{2\xi s}{\omega_n} + 1}. \tag{28}$$

Parameters K, ξ, and ω_n are the coefficient of amplification, the coefficient of attenuation of the system, and the natural (own) frequency of the system or inverse natural time constant of the system, respectively, calculated using Eqs. (23) and (24) as follows:

$$K = \frac{C_g}{C_g + C_s} = \frac{a}{a+1}, \qquad a = \frac{k_g}{k_s}\frac{D_{Ts}}{D_{Tg}}\frac{d_g}{d_s}, \tag{29}$$

$$\xi = \frac{R_g\sqrt{K}}{2}\sqrt{\frac{C_s}{L_g}} = \frac{1}{2}\sqrt{\frac{k_s}{k_g}}\frac{d_g}{\sqrt{D_{Ts}\tau_g}}\sqrt{\frac{a}{a+1}}\sqrt{\frac{d_s}{d_g}}, \tag{30}$$

$$\omega_n = \frac{1}{\sqrt{K}}\frac{1}{\sqrt{C_s L_g}} = \sqrt{\frac{k_g}{k_s}}\sqrt{\frac{D_{Ts}}{\tau_g}}\frac{1}{\sqrt{d_s d_g}}\sqrt{\frac{a+1}{a}}. \tag{31}$$

In the case when thermal relaxations are neglected, Eq. (28) is reduced to

$$\bar{H}(s) = \frac{K}{\tau s + 1}, \tag{32}$$

where

$$\tau = \frac{R_g C_g C_s}{C_g + C_s} = \frac{d_g^2}{D_{Tg}} \frac{1}{a+1}, \tag{33}$$

with a and K being dimensionless variables defined by Eq. (29).

The heat flux that enters into the PA cell (Fig. 3) is described by

$$\bar{Q}_{g0} = \bar{H}(s) S_0 \bar{F}(s). \tag{34}$$

By substituting Eq. (34) in Eq. (20), an approximate model of the spectral function of pressure fluctuation is obtained as follows:

$$\Delta\bar{P}(s) = S_0 \frac{p_0}{T_0} \frac{D_{Tg}}{k_g d_g} \frac{1}{s} H(s) \bar{F}(s). \tag{35}$$

In order to analyze the time response of the PA signal, it is necessary to take into account the transfer characteristic of the detector system. In the case of an electret microphone, which is used in transmission gas-microphone photoacoustics with minimum volume cell, the microphone membrane is a moving electrode of the capacitor, the movement of which, due to the fluctuation of pressure in the cell, leads to the voltage change in the capacitor, recorded via amplifiers as the PA signal. The simplest circuit that can describe the recorded voltage signal proportional to the pressure fluctuations in the PA cell[80,81] is shown in Fig. 4.

This circuit (Fig. 4) behaves as a high-pass RC filter when a periodic voltage is applied to its input,[80,81] which is widely used in high-frequency photoacoustics. However, in time-domain recording, its behavior in the transition process must be taken into account.

By analyzing the circuit shown in Fig. 4 in the Laplace domain, it is shown that the transformation of pressure into recorded voltage can be described by the following transfer function:

$$\bar{V}_{out} = A(s) \bar{V}_{in} = -sRC\bar{V}_{in}. \tag{36}$$

It can be concluded from [Eq. (36)] that the microphone behaves as an ideal inverting differentiator of voltage fluctuations at its input. Taking this into account as well as Eqs. (35) and (36), the spectral function of the recorded voltage can be described by the following expression:

$$\bar{S}(s) = A(s)\Delta\bar{P}(s) = AS_0 \frac{p_0}{T_0} \frac{D_{Tg}}{k_g d_g} H(s) \bar{F}(s), \tag{37}$$

where A is the detector system gain, which depends on the time constants of the microphone and microphone preamplifier.

As can be seen from the expressions given by Eqs. (28) and (32)–(37), the spectral function of the recorded PA signal (i.e., proportional to pressure fluctuations) is a real rational function, so its inverse Laplace transform can be found analytically.

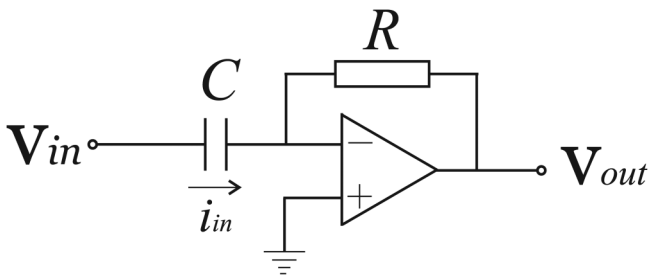

FIG. 4. The simplest circuit that can describe the recorded voltage signal by electret microphone that is proportional to the pressure fluctuations in the PA cell.

III. TIME-DOMAIN PA PULSES

In this section, transmission time-domain PA signals, recorded by a gas-microphone experimental setup with a minimum volume cell and produced by a step function or short pulse, are calculated.

The step function can be mathematically described by

$$f(t) = h(t) = \begin{cases} 0, & t < 0, \\ 1, & t \geq 0, \end{cases} \tag{38}$$

where $h(t)$ is Heaviside's function.[82] The Laplace transform of Heaviside's function is given by[82]

$$F(s) = \frac{1}{s}. \tag{39}$$

The short pulse function can be mathematically described by

$$f(t) = h(t) - h(t - t_p). \tag{40}$$

Its complex representative is obtained by the application of Laplace transform to Eq. (40),[82]

$$F(s) = \frac{1}{s}(1 - e^{-t_p s}). \tag{41}$$

Two cases are analyzed: when thermal relaxations in the gas are neglected and when their impact is taken into account.

A. PA signal neglecting thermal relaxation in PA cell

By substituting Eqs. (32) and (39) in Eq. (37), the spectral function of the normalized PA response to the step function is obtained in the case when thermal relaxations in the gas column are neglected,

$$\bar{S}_{n0}(s) = \frac{\bar{S}(s)}{P} \frac{1}{s} \frac{1}{\tau s + 1}, \tag{42}$$

where $P = AS_0 K \frac{p_0}{T_0} \frac{D_{Tg}}{k_g d_g}$ is the system gain that is equal to the steady value of the measured signal. In this way, the measured signal is normalized to its steady value.

By developing the function given by Eq. (42) into partial fractions and by solving the inverse Laplace transform for each partial fraction,[83] the normalized PA signal excited by a step function is obtained as follows:

$$y_0(t) = \left(1 - e^{-\frac{t}{\tau}}\right)h(t). \tag{43}$$

Figure 5 shows the PA signal described by Eq. (43) for three values of the parameter τ, which depends on the thermal and geometric properties of the sample and the gas column as described by Eq. (33).

As can be seen from Fig. 5, Eq. (43) predicts that the PA signal generated by step excitation approaches the steady value asymptotically, from below. The rate of approach to the steady value depends on the time constant of the system, τ. Two characteristic quantities are defined to estimate the influence of this time constant to the signal, described by Eq. (41): rise time t_u and settling time t_s (see Fig 5).

Rise time (t_u) is the time that elapses from the moment when the response reaches 10% of the steady state to the moment when the response reaches 90% of the steady state. Applying this definition to Eq. (43), the rise time is equal to

$$t_u = 2.2\tau. \tag{44}$$

Settling time (t_s) is defined as the time required for the response amplitude to decrease to the value less than 2% of the steady-state response value. Inserting the value 0.98 into Eq. (43), the settling time is obtained,

$$t_s = 4\tau. \tag{45}$$

Using these two characteristic quantities, it is possible to determine the time constant τ from the measured signal, and using the relationship between τ and the geometrical and thermal properties of the sample and the gas column [Eq. (33)], it is possible to determine these values or their ratios.

By substituting Eqs. (32) and (41) in Eq. (37), the spectral function of the normalized PA response to the short pulse function is obtained. By using solution given by Eq. (43), the normalized PA signal excited by a short pulse during the period t_p is obtained,

$$y_0(t) = \left(1 - e^{-\frac{t}{\tau}}\right)h(t) - \left(1 - e^{-\frac{t-t_p}{\tau}}\right)h(t - t_p). \tag{46}$$

Figure 6 shows the PA response to a short pulse given by Eq. (46) for the three values of the pulse width.

As can be seen from Fig. 6, the PA response will follow the excitation pulse only if the settling time of the system is less than the pulse width (blue line). In the opposite case, the steady value will not be reached (green and red lines) and for the larger values of the ratio of the pulse width (t_p) and time constant of the system (τ), the system is slowly relaxed to the equilibrium state after the excitation has stopped [falling time is equal to rise time, Eq. (44)].

It is important to note that the neglecting of thermal relaxation in the gas column leads to the PA signal that monotonically

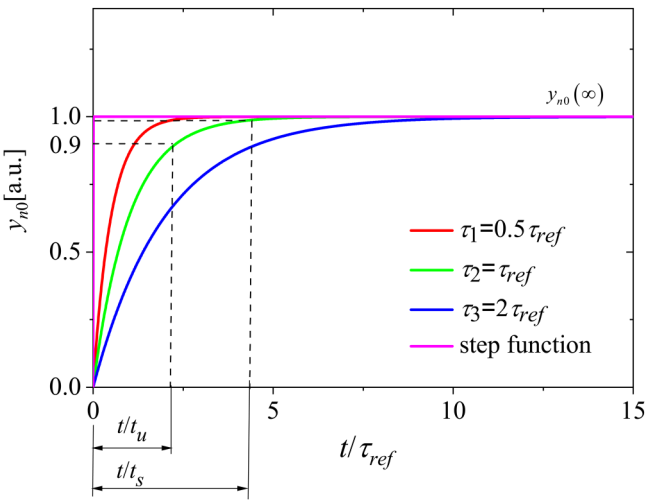

FIG. 5. PA signal normalized to the steady value, calculated on the basis of the derived model for step function excitation (magenta line) and in the case when thermal relaxations in the gas are ignored. Three values of the scaling time constant τ are considered: $\tau_1 = 0.5\tau_{ref}$ (red line), $\tau = \tau_{ref}$ (green line), and $\tau_3 = 2\tau_{ref}$ (blue line).

rises (due to the increasing step jump of the excitation) or falls (due to the decreasing step jump of the excitation) toward to steady or equilibrium values, respectively, all of which is also predicted by previous models, which ignore thermal relaxation either in the gas or in the sample.[32,34]

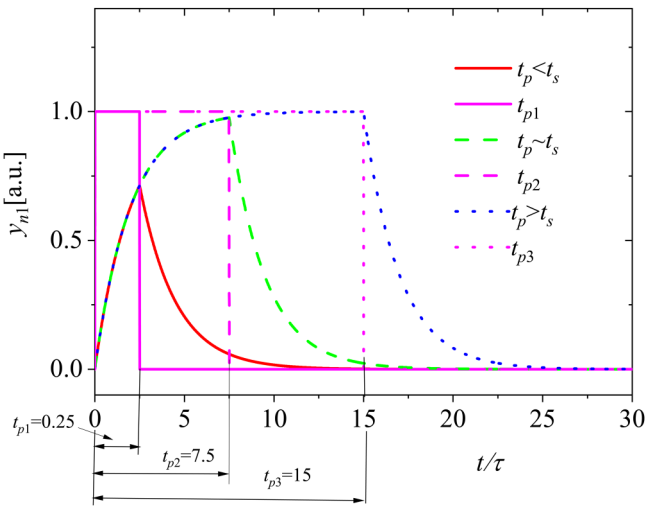

FIG. 6. PA signal normalized to the steady value, calculated on the basis of the derived model for short pulse excitation function (magenta line) and in the case when thermal relaxations in the gas are ignored. Three values of the scaled pulse width t_p/τ are considered: $t_{p1} = 0.25$ (red line), $t_{p2} = 7.5$ (green line), and $t_{p3} = 15$ (blue line).

B. PA signal including thermal relaxations in the PA cell

By substituting Eqs. (38) and (39) in Eq. (37), the spectral function of the normalized PA response to the step function is obtained in the case when thermal relaxations in the gas column are taken into consideration,

$$\bar{S}_n(s) = \frac{\bar{S}(s)}{P} = \frac{1}{s}\frac{1}{\frac{s^2}{\omega_n^2} + \frac{2\xi s}{\omega_n} + 1}. \tag{47}$$

By expanding the complex function given by Eq. (47) into partial fractions and solving the inverse Laplace transform for each fraction,[82,83] the normalized PA signal is obtained in time domain. The development of the function given by Eq. (47) into partial fractions depends on the root of the characteristic polynomial in the denominator of Eq. (47). Considering Eq. (30), the parameter ξ must be positive, so the polynomial in the denominator can only have negative real or conjugate complex solutions with a negative real part; i.e., poles of the transfer function given by Eq. (47) are located in the left part of the complex plane s. Besides, for a small volume PA cell and for thin samples, parameter ξ calculated by Eq. (26) must be smaller than unity. Only the case $0 < \xi < 1$ can be considered, when there are conjugate complex solutions of the characteristic polynomial in the left part of complex plane s. In that case, the normalized PA response to the step function becomes

$$y(t) = \left\{1 - \frac{1}{\sqrt{1-\xi^2}} e^{-\xi\omega_n t}\left[\cos\left(\omega_n\sqrt{1-\xi^2}\,t\right) + \frac{\xi}{\sqrt{1-\xi^2}}\sin\left(\omega_n\sqrt{1-\xi^2}\,t\right)\right]\right\}h(t). \tag{48}$$

The function given by Eq. (48) is shown in Fig. 7(a) for several values of ξ and in Fig. 7(b) for several values of ω_n [defined by Eqs. (30) and (31)].

As can be seen from Fig. 7, unlike the previous case, where the properties of the system from Fig. 1 affect only the promptness of the response to the step function; in this case, these properties affect, through the parameters ξ and ω_n, not only the intensity of the response rate but also its nature. Equation (48) predicts the occurrence of an overshoot of the PA signal in relation to its steady value and an oscillatory approach to the steady value with smaller and smaller deviations from it [green and blue curves in Figs. 7(a) and 7(b)]. The position of the first maximum depends on both parameters and is given by the following expression [calculated from Eq. (48)]:

$$t_{\max} \approx \frac{\pi}{\omega_n\sqrt{1-\xi^2}}. \tag{49}$$

The signal described by Eq. (48) oscillatory approach to steady values [Figs. 7(a) and 7(b)] with a period of damped oscillations that is twice longer than time at which the first maximum occurs [Eq. (49)]:

$$t_\pi \approx \frac{2\pi}{\omega_n\sqrt{1-\xi^2}}. \tag{50}$$

The extent of the overshoot depends only on ξ [Fig. 7(a)] and is given by the following expression:

$$\Pi = \frac{y_{\max} - y(\infty)}{y(\infty)} \times 100\% \approx e^{-\frac{\xi\pi}{\sqrt{1-\xi^2}}}100\%. \tag{51}$$

From Eq. (51), it can be seen that the increase in ξ [the damping of the system increases due to increasing either sample thickness or PA cell length, see Eq. (30)] decreases this overshoot.

The rise time of the signal, as well as the position of the first maximum, depends on both parameters. As ξ increases, the rise time increases, while as ω_n increases, the rise time decreases, and it can be described by the following expression [based on Eq. (48)]:

$$t_u \approx \frac{2.16\xi + 0.6}{\omega_n}. \tag{52}$$

By considering Eqs. (30), (31), and (51), the increase in the sample thickness or in the PA cell length affects increasing ξ and decreasing ω_n and, consequently, decreases the rise time.

The settling time for the transfer function described by Eq. (47) can be described by

$$t_s \approx \frac{4}{\xi\omega_n}. \tag{53}$$

As it can be seen from Eq. (53), it also depends on both parameters, ξ and ω_n, in the same way: if these parameters increase, the settling time decreases. It can be seen from Eqs. (30) and (31) that $\xi \sim \sqrt{d_s d_g}$ and $\omega_n \sim 1/\sqrt{d_s d_g}$. It means that geometrical properties of the system from Fig. 1 do not affect the settling time [see Eq. (53)]. This characteristic of the time-domain response depends on the ratio of thermal properties of the sample and gas as well as on the inertial relaxation time of gas.

The conducted analysis shows that from the recorded PA signal, it is possible to determine the parameters ξ and ω_n using the enumerated characteristic values and then, based on Eqs. (30) and (31), thermal and geometric properties of the optically excited sample.

Figure 8 shows the PA signal for the system from Fig. 1 excited by short pulses.

As it can be seen from Fig. 8, the derived model, which includes thermal relaxations in the gas column, predicts the occurrence of not only overshoots but also undershoots in the vicinity of

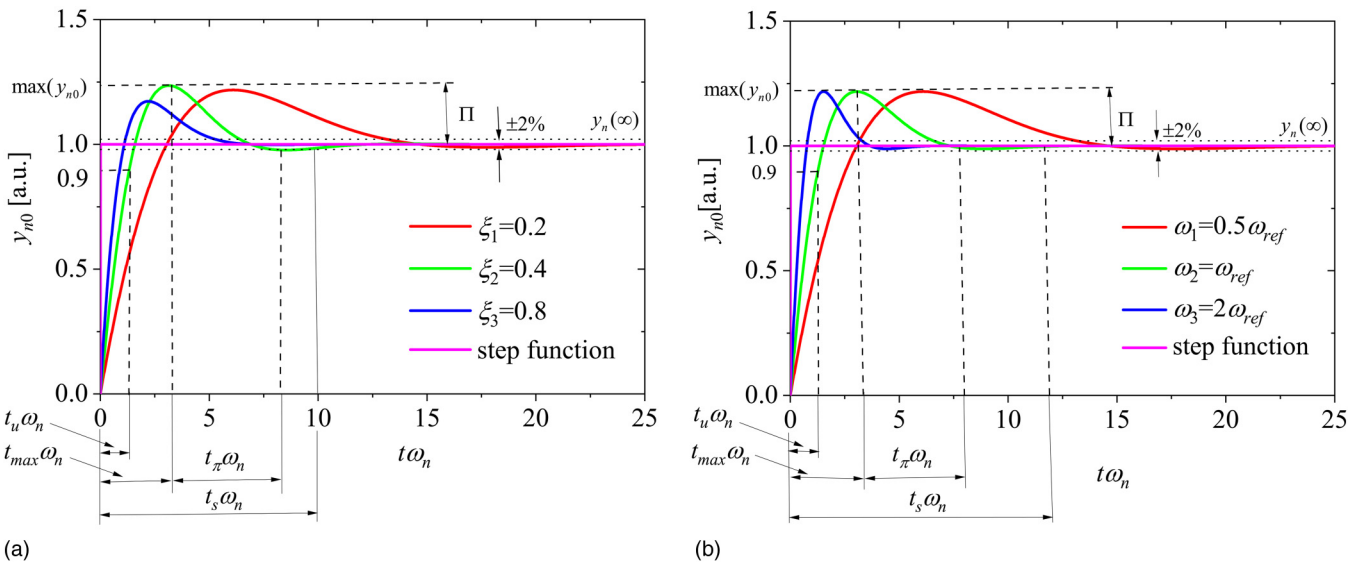

FIG. 7. PA signal normalized to the steady value, calculated on the basis of the derived model for the step excitation function (magenta line) and in the case when thermal relaxations in the gas are taken into account: (a) dependence on the attenuation coefficient ξ for $\omega_{ref} = 1s^{-1}$: $\xi_1 = 0.2$ (red line), $\xi_2 = 0.4$ (green line), and $\xi_3 = 0.8$ (blue line) and (b) dependence on the scaling natural frequency ω_n for $\xi = 0.5$: $\omega_1 = 0.5\omega_{ref}$ (red line), $\omega_2 = \omega_{ref}$ (green line), and $\omega_3 = 2\omega_{ref}$ (blue line).

steep changes in the excitation signal. If the settling time is shorter than the pulse length, the PA signal will follow the excitation signal fairly well [blue and green lines in Fig. 8], except near the steep changes. In the opposite case, the PA signal becomes distorted.

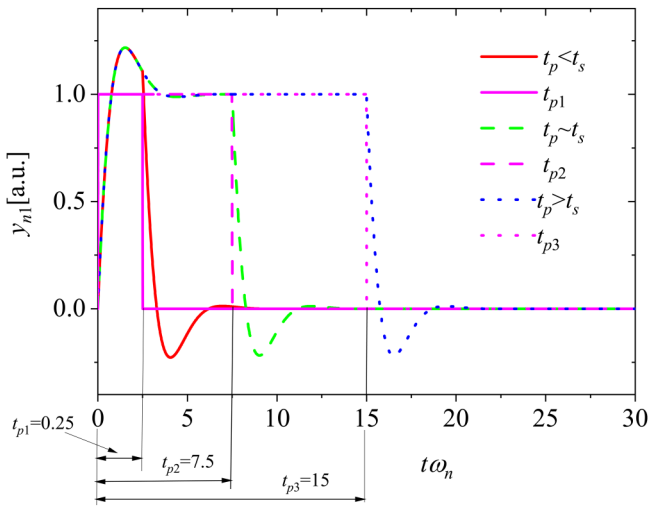

FIG. 8. PA signal normalized to the steady value, calculated on the basis of the derived model for the short pulse excitation function (magenta lines) and in the case when thermal relaxations in the gas are taken into account; three values of the scaled pulse width $t_p\omega_n$ are considered: $t_{p1} = 0.25$ (red line), $t_{p2} = 7.5$ (green line), and $t_{p3} = 15$ (blue line).

It is important to note that introducing the thermal relaxation model into the gas column leads to the PA signal that monotonically rises (at increasing step jump of excitation) up to the first maximum that is higher than the steady value of the signal (so-called overshoot) or falls (at decreasing step jump of excitation) up to the first minimum that is lower than equilibrium values (so-called undershoots). Approaching the steady or equilibrium value of the signal is oscillatory, in difference to the behavior of the PA signal in the case when the thermal relaxation in the gas column is neglected. The period and amplitudes of oscillations depend on ξ and ω_n.

Our experimental measurements of a thin Si membrane (thickness of 32 μm) by the time-domain PA experimental setup (pulse period 125 ms, pulse width 62.5 ms, duty cycle 50%, time resolution 100 μs) published in Ref. 48 show the existence of overshoots and undershoots similar to the PA signal predicted by a derived model that includes thermal relaxations into the PA cell (Figs. 7 and 8).

A detailed description of gas-microphone PA experiments in the time domain, normalization and synchronization of the measured signal, measurement resolution, sensitivity, and geometric and physical properties of the tested semiconductor membranes will be presented in Paper II of this paper, as well as an analysis of the measurement results using the derived model.

IV. CONCLUSIONS

A time-domain model of the gas-microphone PA signal recorded in a transmission configuration with a minimum volume cell was derived. The influence of the electret microphone on the PA signal, the finite length of the PA cell, and the thermal

relaxation in the sample and in the gas were taken into account. Characteristic quantities were proposed that relate the properties of the time-domain PA signal to the properties of the sample, in order to enable the inverse solution of time-domain PA problem and the estimation of the properties of the tested sample using such measurements.

It was shown that thermal relaxations in the gas significantly affect the shape of the time-domain PA signal in the case when the sample is thin and the length of the cell is much smaller than the wavelength of the acoustic wave in the cell. Due to the presence of these relaxations, overshoots and undershoots of the PA signal in relation to its steady or equilibrium (zero) values, respectively, as well as oscillatory approaching of the PA signal toward its steady or equilibrium value occur.

Such characteristics of the PA signal were observed during experimental gas-microphone measurements of thin Si membranes in a transmission configuration with a minimum volume cell[48] but could not be explained by the existing model. A detailed description of the experiment and the processing of experimental measurements using the derived model will be presented in Paper II of this paper.

ACKNOWLEDGMENTS

The authors acknowledge the Ministry of Science, Technological Development and Innovation of the Republic of Serbia (Contract No. 451-03-47/2023-01/200017) for the financial support.

AUTHOR DECLARATIONS

Conflict of Interest

The authors have no conflicts to disclose.

Author Contributions

Galovic S. P.: Conceptualization (equal); Formal analysis (equal); Investigation (equal); Methodology (equal); Software (equal); Supervision (equal); Validation (equal); Visualization (equal); Writing – original draft (equal); Writing – review & editing (equal). **K. Lj. Djordjevic:** Formal analysis (equal); Investigation (equal); Software (equal); Visualization (equal); Writing – original draft (equal); Writing – review & editing (equal). **M. V. Nesic:** Formal analysis (equal); Investigation (equal); Validation (equal); Writing – review & editing (equal). **M. N. Popovic:** Formal analysis (equal); Investigation (equal); Validation (equal). **D. D. Markushev:** Formal analysis (equal); Investigation (equal); Methodology (equal); Supervision (equal); Validation (equal). **D. K. Markushev:** Formal analysis (equal); Investigation (equal); Validation (equal). **D. M. Todorovic:** Conceptualization (equal); Methodology (equal); Resources (equal); Supervision (equal); Writing – original draft (equal).

DATA AVAILABILITY

The data that support the findings of this study are available from the corresponding author upon reasonable request.

REFERENCES

[1]A. Rosencwaig and A. Gersho, "Theory of the photoacoustic effect with solids," J. Appl. Phys. **47**(1), 64–69 (1976).
[2]P. Korpiun, B. Büchner, A. C. Tam, and Y. H. Wong, "Influence of gas viscosity on the photoacoustic signal in gas-microphone cells," J. Appl. Phys. **59**(8), 2944–2949 (1986).
[3]H. S. Bennett and R. A. Forman, "Absorption coefficients of highly transparent solids: Photoacoustic theory for cylindrical configurations," Appl. Opt. **15**(5), 1313–1321 (1976).
[4]L. C. Aamodt, J. C. Murphy, and J. G. Parker, "Size considerations in the design of cells for photoacoustic spectroscopy," J. Appl. Phys. **48**(3), 927–933 (1977).
[5]F. A. McDonald and G. C. Wetsel, "Generalized theory of the photoacoustic effect," J. Appl. Phys. **49**(4), 2313–2322 (1978).
[6]H. Vargas and L. C. M. Miranda, "Photoacoustic and related photothermal techniques," Phys. Rep. **161**(2), 43–101 (1988).
[7]S. Bialkowski, *Photothermal Spectroscopy Methods for Chemical Analysis* (John Wiley, New York, 1996), ISBN: 978-0-471-57467-5.
[8]A. C. Tam, "Applications of photoacoustic sensing techniques," Rev. Mod. Phys. **58**, 381–431 (1986).
[9]H. K. Park, C. P. Grigoropoulos, and A. C. Tam, "Optical measurements of thermal diffusivity of a material," Int. J. Thermophys. **16**(4), 973–995 (1995).
[10]A. P. Sarode and O. H. Mahajan, "Theoretical aspects of photoacoustic effect with solids: A review," Int. J. Sci. Adv. Res. Technol. **4**(2), 1237–1242 (2018), ISSN: 2395-1052.
[11]K. Dubyk, T. Borisova, K. Paliienko, N. Krisanova, M. Isaiev, S. Alekseev, V. Skryshevsky, V. Lysenko, and A. Geloen, "Bio-distribution of carbon nanoparticles studied by photoacoustic measurements," Nanoscale Res. Lett. **17**, 127 (2022).
[12]*Semiconductors and Electronic Materials*, edited by A. Mandelis and P. Hess (SPIE, Bellingham, WA, 2000).
[13]D. M. Todorović and P. M. Nikolić, "Investigation of carrier transport processes in semiconductors by the photoacoustic frequency transmission method," Opt. Eng. **36**(2), 432–445 (1997).
[14]D. M. Todorović, "Plasma, thermal, and elastic waves in semiconductors," Rev. Sci. Instrum. **74**(1), 582–585 (2003).
[15]M. D. Rabasović, M. G. Nikolić, M. D. Dramićanin, M. Franko, and D. D. Markushev, "Low-cost, portable photoacoustic setup for solid state," Meas. Sci. Technol. **20**(9), 095902 (2009).
[16]D. M. Todorović, B. Cretin, P. Vairac, Y. Q. Song, M. D. Rabasović, and D. D. Markushev, "Laser-excited electronic and thermal elastic vibrations in a semiconductor rectangular plate," Int. J. Thermophys. **34**(8–9), 1712–1720 (2013).
[17]J. A. Balderas-López, A. Mandelis, and J. A. García, "Normalized photoacoustic techniques for thermal diffusivity measurements of buried layers in multilayered systems," J. Appl. Phys. **92**(6), 3047–3055 (2002).
[18]J. A. Balderas-López and A. Mandelis, "Thermal diffusivity measurements in the photoacoustic open-cell configuration using simple signal normalization techniques," J. Appl. Phys. **90**(5), 2273 (2001).
[19]K. L. Djordjević, S. P. Galović, ŽM Ćojbašić, D. D. Markushev, D. K. Markushev, S. M. Aleksić, and D. S. Pantić, "Electronic characterization of plasma-thick n-type silicon using neural networks and photoacoustic response," Opt. Quantum Electron. **54**, 485 (2022).
[20]K. L. Djordjević, D. K. Markushev, S. P. Galović, D. D. Markushev, and J. Ordonez-Miranda, "Si plate radius influence on the photoacoustic signal processed by neural networks," J. Appl. Phys. **132**, 215701 (2022).
[21]K. L. Djordjević, S. P. Galović, M. N. Popović, M. V. Nešić, I. P. Stanimirović, Z. I. Stanimirović, and D. D. Markushev, "Use neural network in photoacoustic measurement of thermoelastic properties of aluminum foil," Measurement **199**, 111537 (2022).
[22]M. J. P. Valcárcel, A. J. Palacios, and J. J. Alvarado-Gil, "Determination of the thermophysical properties of polymers (PET) using photoacoustic spectroscopy," J. Mater. Sci. **34**, 2113–2119 (1999).

[23]J. L. Pichardo and J. J. Alvarado-Gil, "Open photoacoustic cell determination of the thermal interface resistance in two layer systems," J. Appl. Phys. **89**(7), 4070–4075 (2001).
[24]J. L. Pichardo-Molina and J. J. Alvarado-Gil, "Heat diffusion and thermolastic vibration influence on the signal of an open photoacoustic cell for two layer systems," J. Appl. Phys. **95**(11), 6450–6456 (2004).
[25]A. M. Mansanares, H. Vargas, F. Galembeck, J. Buijs, and D. Bicanic, "Photoacoustic characterization of a two-layer system," J. Appl. Phys. **70**(11), 7046–7050 (1991).
[26]V. V. Miletic, M. N. Popovic, S. P. Galovic, D. D. Markushev, and M. V. Nesic, "Photothermally induced temperature variations in a low-absorption sample via backside absorption," J. Appl. Phys. **133**, 075101 (2023).
[27]M. V. Nesic, M. N. Popovic, S. P. Galovic, K. L. Djordjevic, M. I. Jordovic-Pavlovic, V. V. Miletic, and D. D. Markushev, "Estimation of linear expansion coefficient and thermal diffusivity by photoacoustic numerical self-consistent procedure," J. Appl. Phys. **131**(10), 105104 (2022).
[28]M. N. Popovic, D. D. Markushev, M. V. Nesic, M. I. Jordovic-Pavlovic, and S. P. Galovic, "Optically induced temperature variations in a two-layer volume absorber including thermal memory effects," J. Appl. Phys. **129**, 015104 (2021).
[29]H. P. Hu, X. W. Wang, and X. F. Xu, "Generalized theory of the photoacoustic effect in multilayer material," J. Appl. Phys. **86**(7), 3953 (1999).
[30]X. Wang, H. Hu, and X. Xu, "Photo-acoustic measurement of thermal conductivity of thin films and bulk materials," J. Heat Transfer. **123**(1), 138–144 (2001).
[31]B. K. Bein and J. Pelzl, "Theory of signal generation in a photoacoustic cell," J. Phys. Colloq. **44**, C6-27–C6-34 (1983).
[32]A. Mandelis and B. S. H. Royce, "Time-domain photoacoustic spectroscopy of solids," J. Appl. Phys. **50**(6), 4330–4338 (1979).
[33]A. Mandelis and B. S. H. Royce, "Relaxation time measurements in frequency and time-domain photoacoustic spectroscopy of condensed phases," J. Opt. Soc. Am. **70**(5), 474 (1980).
[34]A. Domanowska and R. J. Bukowski, "Theoretical analysis of pulsed photoacoustic effect in solids," Int. J. Thermophys. **30**(5), 1536–1556 (2009).
[35]F. G. C. Bijnen, J. V. Dongen, J. Reuss, and F. J. M. Harren, "Thermoacoustic amplification of photoacoustic signal," Rev. Sci. Instrum. **67**(6), 2317–2324 (1996).
[36]S. Telenkov and A. Mandelis, "Signal-to-noise analysis of biomedical photoacoustic measurements in time and frequency domains," Rev. Sci. Instrum. **81**(12), 124901 (2010).
[37]B. Lashkari and A. Mandelis, "Comparison between pulsed laser and frequency-domain photoacoustic modalities: Signal-to-noise ratio, contrast, resolution, and maximum depth detectivity," Rev. Sci. Instrum. **82**(9), 094903 (2011).
[38]X. Wang, Y. Pang, G. Ku, X. Xie, G. Stoica, and L. V. Wang, "Noninvasive laser-induced photoacoustic tomography for structural and functional *in vivo* imaging of the brain," Nat. Biotechnol. **21**(7), 803–806 (2003).
[39]M. Xu and L. V. Wang, "Photoacoustic imaging in biomedicine," Rev. Sci. Instrum. **77**(4), 041101 (2006).
[40]C. Li and L. V. Wang, "Photoacoustic tomography and sensing in biomedicine," Phys. Med. Biol. **54**(19), R59–R97 (2009).
[41]Z. Xie, S. Jiao, H. F. Zhang, and C. A. Puliafito, "Laser-scanning optical-resolution photoacoustic microscopy," Opt. Lett. **34**(12), 1771–1773 (2009).
[42]Z. Xie, C. Tian, S.-L. Chen, T. Ling, C. Zhang, L. J. Guo, P. L. Carson, and X. Wang, "3D high resolution photoacoustic imaging based on pure optical photoacoustic microscopy with microring resonator," Proc. SPIE **8943**, 894314 (2014).
[43]S. Galović and D. Kostoski, "Photothermal wave propagation in media with thermal memory," J. Appl. Phys. **93**(5), 3063–3070 (2003).
[44]D. D. Markushev, M. D. Rabasović, M. V. Nesic, M. N. Popovic, and S. P. Galovic, "Influence of thermal memory on thermal piston model of photoacoustic response," Int. J. Thermophys. **33**(10–11), 2210–2216 (2012).
[45]S. Galović, Z. Šoškić, M. Popović, D. Čevizović, and Z. Stojanović, "Theory of photoacoustic effect in media with thermal memory," J. Appl. Phys. **116**(2), 024901 (2014).
[46]M. N. Popovic, M. V. Nesic, M. Zivanov, D. D. Markushev, and S. P. Galovic, "Photoacoustic response of a transmission photoacoustic configuration for two-layer samples with thermal memory," Opt. Quantum Electron. **50**(9), 1–10 (2018).
[47]J. Ordóñez-Miranda and J. J. Alvarado-Gil, "Frequency-modulated hyperbolic heat transport and effective thermal properties in layered systems," Int. J. Therm. Sci. **49**(1), 209–217 (2010).
[48]K. L. J. Djordjevic, S. P. Galovic, M. V. Nesic, D. M. Todorovic, M. N. Popovic, D. D. Markushev, and D. K. Markushev. "Transmission pulse photoacoustic set-up for characterization of solids," in *21st International Symposium INFOTEH-JAHORINA* (IEEE, 2022), see https://infoteh.etf.ues.rs.ba/zbornik/2022/radovi/O-8-3.pdf.
[49]V. A. Sablikov and V. B. Sandomirskii, "The photoacoustic effect in semiconductors," Phys. Status Solidi A **120**(2), 471–480 (1983).
[50]K. L. Djordjevic, D. Milicevic, S. P. Galovic, E. Suljovrujic, S. K. Jacimovski, D. Furundzic, and M. Popovic, "Photothermal response of polymeric materials including complex heat capacity," Int. J. Thermophys. **43**(5), 68 (2022).
[51]D. D. Joseph and L. Preziosi, "Heat waves," Rev. Mod. Phys. **61**(1), 41–73 (1989).
[52]D. D. Joseph and L. Preziosi, "Addendum to the paper 'heat waves' [Rev.: Mod. Phys. 61, 41 (1989)]," Rev. Mod. Phys. **62**(20), 375–391 (1990).
[53]D. Jou, J. Casas-Vazquez, and G. Lebon, "Extended irreversible thermodynamics," Rep. Prog. Phys. **51**, 1105–1179 (1988).
[54]C. Cattaneo, "Sur une forme de l'equation de la chaleur eliminant le paradowe d'une propagation instantanee," C. R. Acad. Sci. **247**, 431–433 (1958).
[55]P. Vernotte, "Sur quelques complications possible dans les phenomenes de conduction de la chaleur," C. R. Acad. Sci. **252**, 2190 (1961).
[56]I. A. Novikov, "Harmonic thermal waves in materials with thermal memory," J. Appl. Phys. **81**(3), 1067–1072 (1997).
[57]S. L. Sobolev, "Local non-equilibrium transport models," Phys. Usp. **167**(10), 1095–1106 (1997).
[58]S. L. Sobolev and W. Dai, "Heat transport on ultrashort time and space scales in nanosized systems: Diffusive or wave-like?," Materials **15**(12), 4287 (2022).
[59]H. S. Carslaw and J. C. Jaeger, *Conduction of Heat in Solids* (Oxford University Press, Oxford, 1959), ISBN: 0 19 8533 68 3.
[60]K. Mitra, S. Kumar, A. Vedevarz, and M. K. Moallemi, "Experimental evidence of hyperbolic heat conduction in processed meat," J. Heat Transf. **117**(3), 568–573 (1995).
[61]A. Vedavarz, S. Kumar, and M. K. Moallemi, "Significance of non-Fourier heat waves in conduction," J. Heat Transf. **116**(1), 221–224 (1994).
[62]Z. Ding, K. Chen, B. Song, J. Shin, A. A. Maznev, K. A. Nelson, and G. Chen, "Observation of second sound in graphite over 200 K," Nat. Commun. **13**, 285 (2022).
[63]S. Huberman, R. A. Duncan, K. Chen, B. Song, V. Chiloyan, Z. Ding, A. A. Maznev, G. Chen, and K. A. Nelson, "Observation of second sound in graphite at temperatures above 100 K," Science **364**(6438), 375–379 (2019).
[64]A. Camacho de la Rosa and R. Esquivel-Sirven, "Causality in non-Fourier heat conduction," J. Phys. Commun. **6**, 105003 (2022).
[65]J. Ordonez-Miranda and J. J. Alvarado-Gil, "On the stability of the exact solutions of the dual-phase lagging model of heat conduction," Nanoscale Res. Lett. **6**, 327 (2011).
[66]P. M. Jordan, W. Dai, and R. E. Mickens, "A note on the delayed heat equation: Instability with respect to initial data," Mech. Res. Commun. **35**, 414–420 (2008).
[67]K. Zhukovsky, "Operational approach and solutions of hyperbolic heat conduction equations," Axioms **5**(4), 28 (2016).
[68]W. Shen and S. Han. "Hyperbolic heat conduction in composite materials," in *8th AIAA/ASME Joint Thermophysics and Heat Transfer Conference* (AIAA/ASME, 2002).
[69]A. D. Polyanin, "Functional separable solutions of nonlinear convection–diffusion equations with variable coefficients," Communications in Nonlinear Science and Numerical Simulation **73**, 379–390 (2019).
[70]E. R. Monteiro, E. N. Macêdo, J. N. N. Quaresma, and R. M. Cotta, "Integral transform solution for hyperbolic heat conduction in a finite slab," Int. Commun. Heat Mass Transf. **36**(4), 297–303 (2009).
[71]S. Galovic, Z. Soskic, and M. Popovic, "Analysis of photothermal response of thin solid films by analogy with passive linear electric networks," Therm. Sci. **13**(4), 129–142 (2009).

[72]Z. Suszyński. "Thermal model based on the electrical analogy of the thermal processes," in *Proceedings of the 10th International Conference on Photoacoustic and Photothermal Phenomena* (AIP Publishing, 1999).
[73]D. Y. Tzou, "An engineering assessment to the relaxation time in thermal wave propagation," Int. J. Heat Mass Transf. **36**(7), 1845–1851 (1993).
[74]P. Hui and H. S. Tan, "Modelling of thermal diffusivity measurement of diamond thin films using a pulsed laser technique," Surf. Coat. Technol. **62**(1–3), 361–366 (1993).
[75]G. Chen and P. Hui, "Pulsed photothermal modeling of composite samples based on transmission-line theory of heat conduction," Thin Solid Films **339**(1–2), 58–67 (1999).
[76]D. Maillet, S. André, J. C. Batsale, A. Degiovanni, and C. Moyne, *Thermal Quadrupoles: Solving the Heat Equation Through Integral Transforms* (John Wiley and Sons, 2000), ISBN: 0 471 98320 9.
[77]J. C. Krapez and E. Dohou, "Thermal quadrupole approaches applied to improve heat transfer computations in multilayered materials with internal heat sources," Int. J. Therm. Sci. **81**, 38–51 (2014).
[78]J. Pailhes, C. Pradere, J. L. Battaglia, J. Toutain, A. Kusiak, A. W. Aregba, and J. C. Batsale, "Thermal quadrupole method with internal heat sources," Int. J. Therm. Sci. **53**, 49–55 (2012).
[79]A. Salazar and R. Celorrio, "Application of the thermal quadrupole method to the propagation of thermal waves in multilayered cylinders," J. Appl. Phys. **100**(11), 113535 (2006).
[80]S. M. Cristescu, D. C. Dumitras, D. C. A. Dutu, "Characterization of a resonant photoacoustic cell using the acoustic transmission line model," Proc. SPIE **4068**, 261 (2000).
[81]L. Mota, M. G. da Silva, V. P. de Souza, H. Vargas, V. F. Guimarães, and H. R. Paes, "On the use of photoacoustic technique for monitoring the thermal properties of lanthanum strontium cobalt ferrite–yttria stabilized zirconia two-layer systems," Thin Solid Films **519**(2), 938–942 (2010).
[82]F. Oberhettinger and L. Badii, *Tables of Laplace Transforms* (Springer Berlin, Heidelberg, 1973), ISBN: 978–3-642-65645-3.
[83]M. Stojic, *Continuous System of Automatic Control (in Serbian)* (Naučna Knjiga, Belgrade, 1990).

Journal of Applied Physics

RESEARCH ARTICLE | JUNE 15 2023

Analysis of plasma-elastic component of time-domain photoacoustic response FREE

Special Collection: Semiconductor Physics: Plasma, Thermal, Elastic, and Acoustic Phenomena

Ivanka Stanimirović ; Dragana Markushev ; Zdravko Stanimirović ; Slobodanka Galović ; Katarina Djordjević

Journal of Applied Physics 133, 235701 (2023)
https://doi.org/10.1063/5.0152713

Journal of Applied Physics ARTICLE scitation.org/journal/jap

Analysis of plasma-elastic component of time-domain photoacoustic response

Cite as: J. Appl. Phys. 133, 235701 (2023); doi: 10.1063/5.0152713
Submitted: 31 March 2023 · Accepted: 30 May 2023 ·
Published Online: 15 June 2023

Ivanka Stanimirović,[1,a)] Dragana Markushev,[2] Zdravko Stanimirović,[1] Slobodanka Galović,[1] and Katarina Djordjević[1]

AFFILIATIONS

[1]"Vinča" Institute of Nuclear Sciences-National Institute of the Republic of Serbia, University of Belgrade, P.O. Box 522, 11000 Belgrade, Serbia
[2]Institute of Physics, University of Belgrade, Pregrevica 118, 11080 Belgrade, Serbia

Note: This paper is part of the Special Topic on Semiconductor Physics: Plasma, Thermal, Elastic, and Acoustic Phenomena.
[a)]**Author to whom correspondence should be addressed:** ivanka.stanimirovic@vin.bg.ac.rs

ABSTRACT

The plasma-elastic component of the photoacoustic response in the time-domain of thin semiconductor samples excited by long electromagnetic radiation pulses is analyzed in detail. The plasma-elastic component model assumes that ambipolar diffusion can be approximated by the minority carrier diffusion. The results obtained show that the plasma-elastic component in thin semiconductor samples affects photoacoustic measurements in the time domain, which is important for the photoacoustic determination of semiconductor electronic properties.

I. INTRODUCTION

As in other materials, illumination by a modulated light induces a thermal response in semiconductors. Light absorption leads to time-dependent heating of the semiconductor sample and, hence, to a time-dependent change in the temperature distribution. Time-dependent heat flux is present on the surfaces as well as in the bulk of the sample.[1–10] However, the effect of quasi-free electron and hole generation occurs only in semiconductors.

If the energy of a photon is equal to or greater than the bandgap of the material ($\varepsilon = h\nu_i \geq \varepsilon_g$), such a photon promotes an electron from the conduction band into the valence band, and the electron–hole pair is generated.[11] The generation is the strongest on the surface of the material, where the majority of the light is absorbed and the resulting electron–hole pairs are called photogenerated or excess carriers.[12–21] Diffusion of carriers through the semiconductor material along the gradient, in the direction of lower concentrations, affects the temperature distribution along the depth of the sample, as well as the temperature gradient, thus affecting the thermal diffusion and thermoelastic component of the photoacoustic signal.[22–29]

In the late 1990s, Todorović and Nikolić[31] noticed the existence of another effect in semiconductors that is a direct consequence of the excess carrier photogeneration. They noticed that the photogeneration of excess carriers is followed by higher concentrations of excess carriers, not in the entire semiconductor sample, but in places where the light is absorbed.

For photogeneration induced by a harmonically modulated light source, due to the charge carrier motion, periodic charge concentrations are being formed at the ends of the semiconductor sample, higher on the illuminated side and lower on the non-illuminated side of the sample. The interactions of charge carriers with the semiconductor lattice are greater at locations where charge carrier concentrations are higher and smaller at locations where charge carrier concentrations are lower. These interactions cause periodic bending of the sample that results in gaseous sample compression and sound creation. By analyzing sound, it is possible to obtain the plasma-elastic parameter of the sample: the electronic deformation coefficient for the material in question. In this way, a new photoacoustic signal component in semiconductor photoacoustics is introduced, called plasma-elastic component.[22–30] Consequently, the total photoacoustic signal, induced by the harmonically modulated illumination of the semiconductor sample and detected by the microphone,

is composed of three components: thermal diffusion, thermoelastic, and plasma-elastic components. Among other things, the prevalence of the particular component depends on the concentration of photogenerated charge carriers, the surface properties, i.e., the velocity of the surface recombination, the charge carrier lifetime, the thickness of the sample, but also the modulation frequency of the excitation.[22]

Previous research has shown that the effects of plasma-elastic components become significant at high modulation frequencies ($\omega > 1/\tau$, τ being the charge carrier lifetime). Therefore, it can be expected that, for pulse excitation, this effect will become significant on a time scale shorter than the carrier lifetime ranging from microsecond for doped semiconductors to milliseconds for pure samples.[11,31–34] In addition, it is comparable to a time scale where the photoacoustic signal in the time domain can be recorded.[34]

In this paper, in the second section, a brief overview of the theoretical model of the spectral function of the plasma-elastic component of the photoacoustic signal, generated by the time-dependent monochromatic excitation, is given. Results obtained by the analysis of the plasma-elastic component of the photoacoustic response in the time-domain are presented and discussed in the third section. Finally, the most important findings are presented in fourth section.

II. THEORETICAL MODEL OF THE SPECTRAL FUNCTION FOR THE PLASMA-ELASTIC COMPONENT OF THE PHOTOACOUSTIC RESPONSE

The model of charge carrier transport in semiconductor materials used in this study is based on the assumption that the photogenerated charge carrier concentration is much lower than the concentration of charge carriers due to doping. Therefore, charge carrier transport can be described by minority carrier transport.[11]

The transport of photogenerated charge carriers in type n semiconductors is generally described as a diffusion process. The source of minority carriers in a semiconductor can be given as

$$S(x, t) = G(x, t) - R(x, t), \tag{1}$$

where minority carrier (hole) photogeneration is G and recombination R. Therefore, the ambipolar minority charge transport equation for the zero electrical field becomes[11,27–30]

$$\frac{\partial n(x, t)}{\partial t} = D_E \frac{\partial^2 n(x, t)}{\partial x^2} + G(x, t) - R(x, t), \tag{2}$$

where D_E is the minority carrier diffusion coefficient. Assume that the round semiconductor sample of radius R and thickness l ($R \gg l$) is a semi-transparent material illuminated on the front surface with an absorption coefficient β ($\beta \to \infty$) (Fig. 1). In this case, charge carriers are transported along the single axis (x-axis) and the photogeneration of minority carriers becomes a boundary condition. Light intensity, G and R, for modulated excitation[31,32] are

$$I = I_0 f(t), \tag{3}$$

$$G(x, t) = 0, \tag{4}$$

$$R(x, t) = \frac{n(x, t)}{\tau}, \tag{5}$$

where I_0 is the intensity of the incident light, f is the light source modulation function, and $n(x,t)$ is the charge carrier concentration along the x-axis. The charge carrier concentration change can be expressed as

$$\frac{\partial n(x, t)}{\partial t} = D_E \frac{\partial^2 n(x, t)}{\partial x^2} - \frac{n(x, t)}{\tau}. \tag{6}$$

Due to the linearity of Eq. (6), the Laplace transform can be performed and the change in the photogenerated minority carrier concentration can be written as

$$\tilde{n}(x, s) = \mathcal{L}\{n(x, t)\}\ . \tag{7}$$

As a result, the equation describing the dynamic component of the photogenerated charge carrier volume becomes

$$\frac{d^2 \tilde{n}(x)}{dx^2} - \frac{\tilde{n}(x)}{L^2} = 0, \tag{8}$$

with the complex minority carrier diffusion length

$$L = L_p / \sqrt{(1 + s\tau)}, \tag{9}$$

where the minority carrier diffusion length is

$$L_p = \sqrt{D_E \tau}, \tag{10}$$

with τ being the minority carrier (hole) lifetime.

Considering that Eq. (8) is an ordinary linear differential equation of the second order, its general solution can be written as[27–30]

$$\tilde{n}(z) = A_1 e^{\frac{z}{L}} + A_2 e^{\frac{-z}{L}}, \tag{11}$$

where A_1 and A_2 are constants obtained using the following boundary conditions:

$$D_{\frac{d\tilde{n}(z)}{dz}}\Big|_{z=0} = S_g \tilde{n}(0) - \frac{I_0}{2} \frac{1}{D_E \tau} F(s) \tag{12a}$$

and

$$D_E \frac{d\tilde{n}(z)}{dz}\Big|_{z=l} = -S_b \tilde{n}(l), \tag{12b}$$

where surface recombination velocities are being introduced in the front (S_g, $x = 0$) and back (S_b, $x = l$) side of the sample.

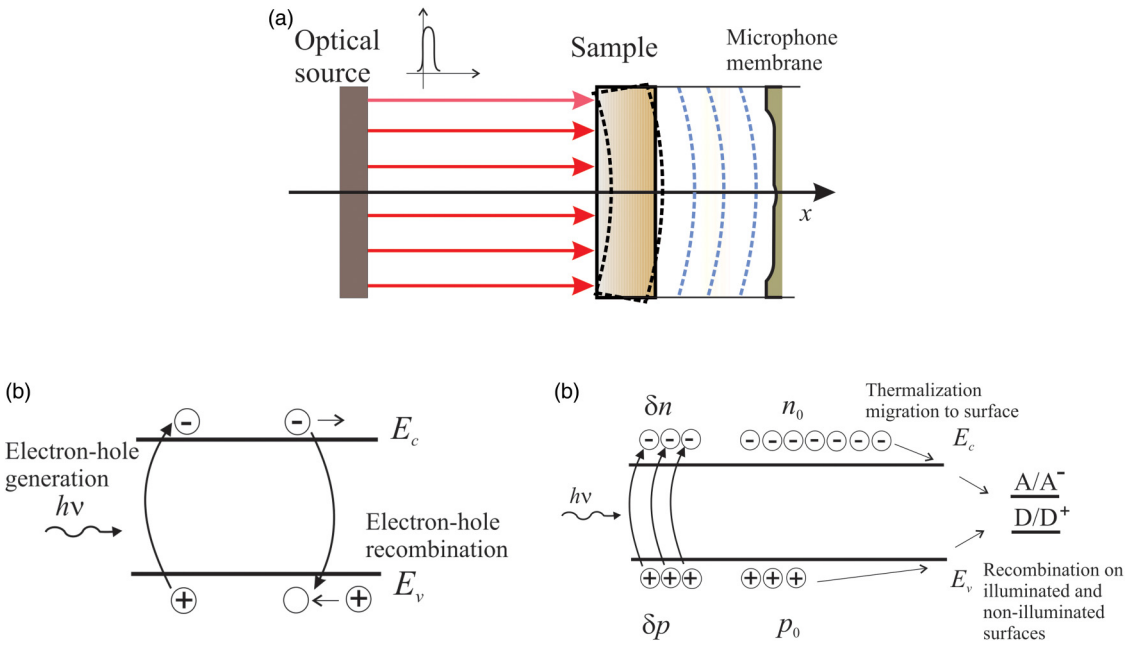

FIG. 1. (a) Schematic representation of the transmission configuration (optical source: single very short duration Gaussian pulse, wavelength: 660 nm—red light), (b) electron–hole generation and recombination, and (c) generation of excess carriers.

The integration constants are

$$A_1 = \frac{I_0}{\varepsilon_g D_E} \frac{\left(\frac{D_E}{L} - S_g\right) e^{\frac{-l}{L}}}{\left(\frac{D_E}{L} + S_g\right)\left(\frac{D_E}{L} + S_b\right) e^{\frac{l}{L}} - \left(\frac{D_E}{L} - S_g\right)\left(\frac{D_E}{L} - S_b\right) e^{\frac{-l}{L}}}, \tag{13}$$

$$A_2 = \frac{I_0}{\varepsilon_g D_E} \frac{\left(\frac{D_E}{L} + S_b\right) e^{\frac{l}{L}}}{\left(\frac{D_E}{L} + S_g\right)\left(\frac{D_E}{L} + S_b\right) e^{\frac{l}{L}} - \left(\frac{D_E}{L} - S_g\right)\left(\frac{D_E}{L} - S_b\right) e^{\frac{-l}{L}}}. \tag{14}$$

Since photogenerated charge carriers cause plasma-elastic bending of the sample, the sample surface displacement along the x-axes $\tilde{u}_z^{ED}(r, -l)$ becomes[21]

$$\tilde{u}_z^{ED}(r, -l) = d\frac{6R^2}{l^3}\left(1 - \frac{r^2}{R^2}\right)\left(\int_0^l x\tilde{n}(x)dx - \frac{l}{2}\int_0^l \tilde{n}(x)dx\right), \tag{15}$$

where d denotes the pressure dependence on the bandgap energy ε_g at the constant temperature

$$d = \frac{1}{3}\left(\frac{\partial \varepsilon_g}{\partial p}\right)_T. \tag{16}$$

The plasma-elastic component of the photoacoustic signal induced by the electronic deformation (electronic strain) is[21,26–28]

$$\tilde{S}^{ED} = \frac{\gamma P_0}{V_0} d \int_0^R 2\pi r \tilde{u}_z^{ED}(r, -l)dr, \tag{17}$$

where γ is the adiabatic constant, P_0 is the equilibrium pressure of the air in the microphone, $V_0 = r_0^2 \pi l_g$ is the photoacoustic cell volume, r_0 is the microphone radius, and l_g is the length of the photoacoustic cell.

Equations (17) and (15) show that the plasma-elastic component of the photoacoustic signal depends on the concentration moment [integral on the left in Eq. (15)] reduced by the mean carrier concentration along the sample [integral on the right of Eq. (15)].

Based on Eqs. (11) and (13)–(17), the plasma-elastic component of the photoacoustic signal can be expressed as follows:

$$\tilde{S}^{ED} = \frac{\gamma P_0}{V_0} 3\pi d \frac{R^4}{l^3}\left\{A_1 L\left[e^{\frac{l}{L}}\left(\frac{l}{2} - L\right) + \left(\frac{l}{2} + L\right)\right] - A_2 L\left[e^{\frac{-l}{L}}\left(\frac{l}{2} + L\right) + \left(\frac{l}{2} - L\right)\right]\right\}. \tag{18}$$

III. RESULTS AND DISCUSSION

In order to find the plasma-elastic component of the photoacoustic signal in the time domain, the Invlap method for numerical inversion of the Laplace transform was used.

Calculations have been carried out for silicon type n whose parameters are presented in Table I.[11,21]

The plasma-elastic component of the photo-acoustic response depends mainly on the surface quality of the semiconductor sample that is being determined by the front and back surface recombination velocities S_g and S_b, respectively, sample thickness l and, using the diffusion length of minority carriers L_p [Eq. (10)], by the lifetime of minority carriers τ. The ratio l/L_p determines the plasma thickness of the sample. For plasma-thin samples, $l/L_p < 1$, and for plasma-thick ones, $l/L_p > 1$. Another important parameter is the volume recombination velocity [D_E/L from Eqs. (13) and (14)]. Both components depend on the carrier lifetime [Eqs. (9) and (10)].

In order to analyze the plasma-elastic component of the time-domain photoacoustic response, calculations were performed for three semiconductor samples with different lifetimes of minority carriers ($\tau_1 = 10^{-8}$ s, $\tau_2 = 10^{-6}$ s, and $\tau_3 = 10^{-4}$ s), of different thicknesses (10 μm, 100 μm, and 1 mm), and surface qualities (passivated or active).

In Fig. 2, plasma-elastic components of time-domain photoacoustic responses for pure semiconductor samples ($\tau_1 = 6 \times 10^{-4}$ s) are given. It can be seen that the plasma-elastic responses are of the same shape but of different orders of magnitude. For the fixed value of the volume recombination velocity, in the beginning, the sample experiences negative straining, it bends toward the light source causing the underpressure in the photoacoustic cell. Over time, the system relaxes and tends towards a stationary state, depending on the surface recombination velocities. For $S_g = 24$, regardless of the S_b value, the system reaches a straining-free stationary state. For $S_g = 2$, regardless of the S_b value, the system oscillates around the stationary state. With the increase in the sample thickness straining decreases, the decrease is non-linear. The decrease is greater for plasma thick samples.

TABLE I. N-type Si sample parameters used in performed calculations.

Parameter	Fixed values
Sample radius (R)	5×10^{-3} m
Minority carrier diffusion coefficient (D_E)	$1{,}2 \times 10^{-3}$ m^2 s^{-1}
Adiabatic constant (γ)	1,4
Inner microphone radius (r_0)	4×10^{-3} m
Photoacoustic cell length (l_g)	2×10^{-3} m
Equilibrium pressure (P_0)	101 kPa
Absorption coefficient (β)	2.58×10^5 m^{-1}
Pressure dependence on the bandgap energy (d)	-9×10^{-31} m^3
Intensity of the incident light (I_0)	150 W/m^2
Excitation energy (ε)	1.88 eV
Energy gap (ε_g)	2,1 eV
Parameter	**Variables**
Sample thickness (l)	10 μm, 100 μm, 1 mm
Lifetime of minority carriers (τ)	10^{-8}, 10^{-6}, 10^{-4} s
Front surface recombination velocity (S_g)	2, 24 m/s
Back surface recombination velocity (S_b)	2, 24 m/s

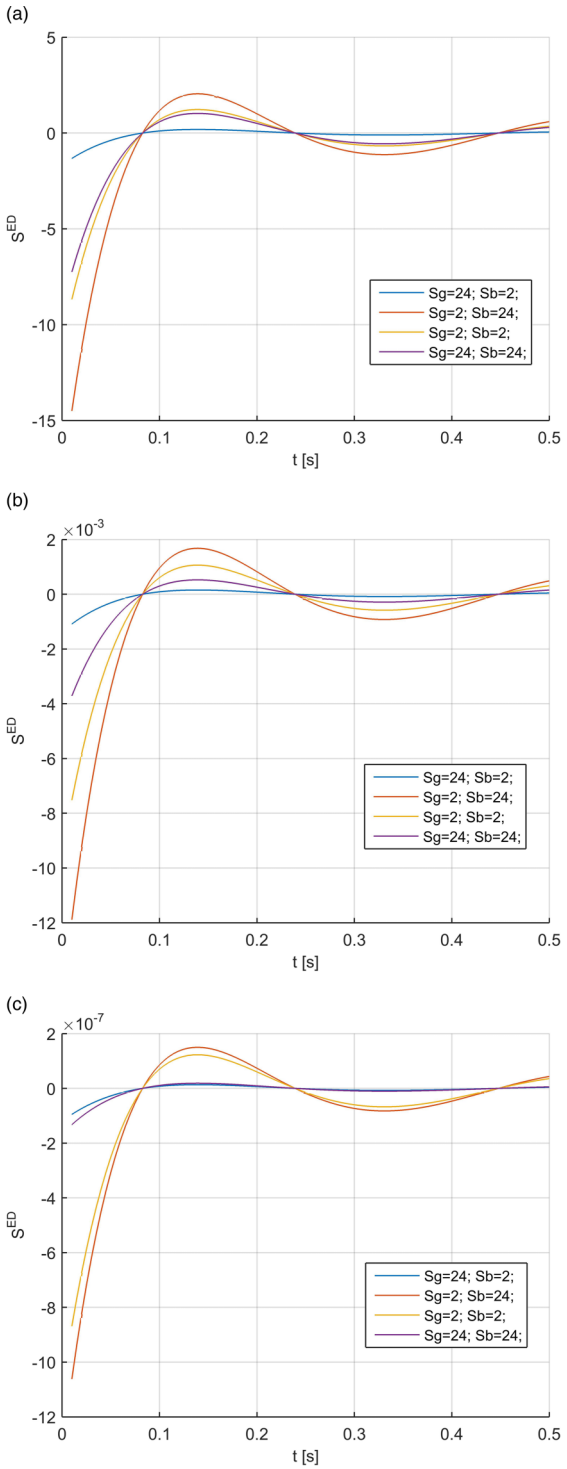

FIG. 2. Plasma-elastic components of time-domain photoacoustic responses for pure semiconductor samples ($\tau_1 = 6 \times 10^{-4}$ s) of different thicknesses: (a) $l = 10^{-5}$, (b) $l = 10^{-4}$, and (c) $l = 10^{-3}$ m.

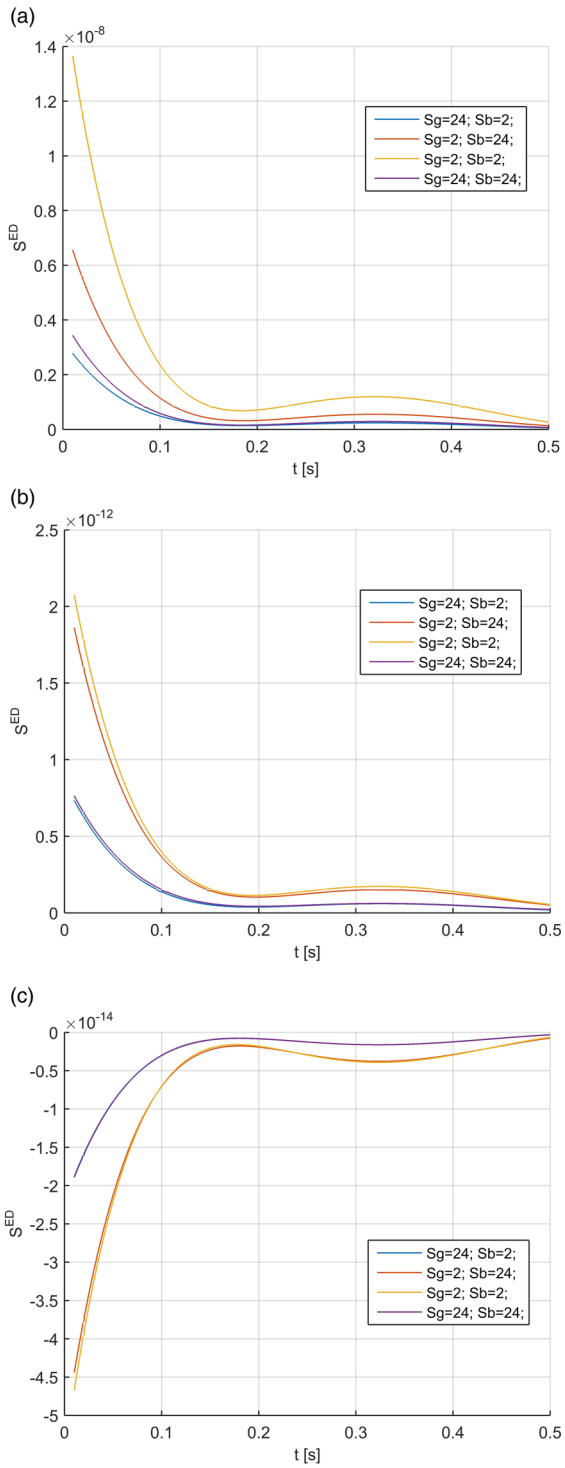

FIG. 3. Plasma-elastic components of time-domain photoacoustic responses for doped semiconductor samples ($\tau_2 = 6 \times 10^{-6}$ s) of different thicknesses: (a) $l = 10^{-5}$, (b) $l = 10^{-4}$, and (c) $l = 10^{-3}$ m.

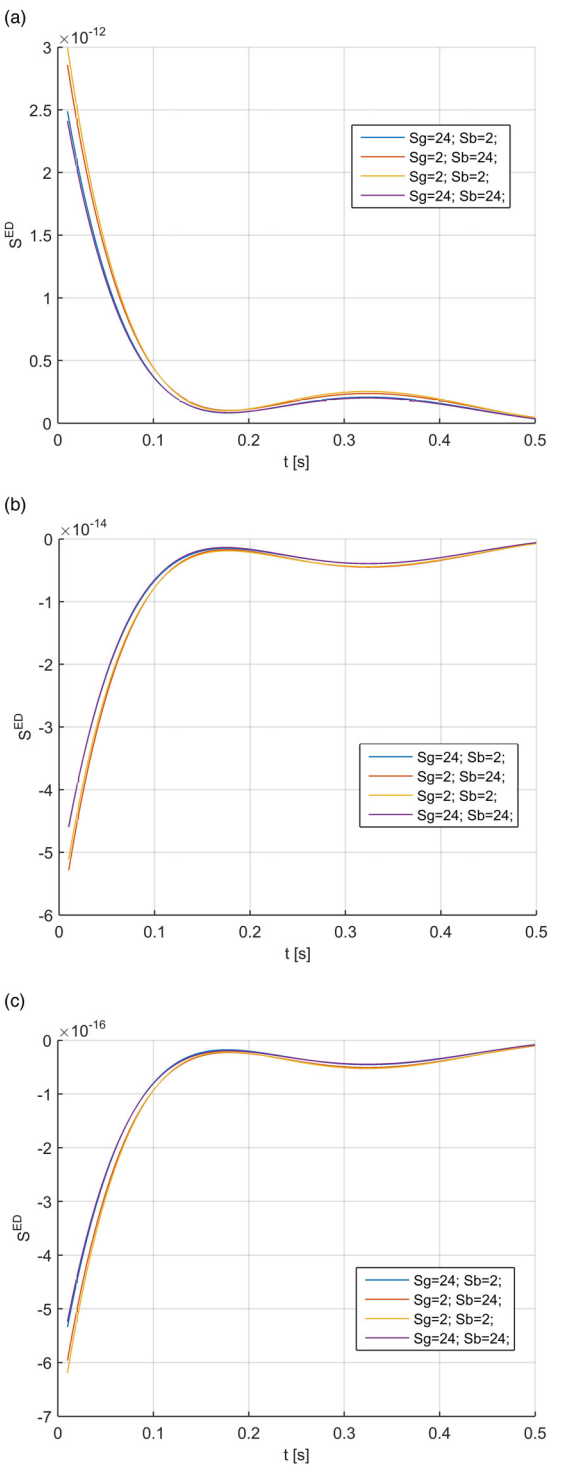

FIG. 4. Plasma-elastic components of time-domain photoacoustic responses for highly impure semiconductor samples ($\tau_3 = 6 \times 10^{-8}$ s) of different thicknesses: (a) $l = 10^{-5}$, (b) $l = 10^{-4}$, and (c) $l = 10^{-3}$ m.

In Fig. 3, plasma-elastic components of time-domain photoacoustic responses for doped/impure semiconductor samples ($\tau_2 = 6 \times 10^{-6}$ s) are given. Differences in the shape of plasma-elastic components can be observed for samples of different thicknesses. When compared to Fig. 2, the volume recombination velocity and diffusion length are smaller but fixed for all three sample thicknesses. Also, the straining is smaller. With the increase in thickness straining decreases non-linearly. For $S_g = 24$, deflection is the lowest and the system requires the least amount of time to achieve the stationary state. When two thinner samples are in question, a variation in shape can be noticed due to the lower volume recombination velocity value. In the beginning, the straining is positive, the sample bends away from the light source and an overpressure is created. Over time, the system reaches a stationary state with the exception of the thickest sample. In thinner samples, a greater number of electrons reach the back surface, creating the negative concentration gradient that affects the bending direction. With the increase in sample thickness, regardless of the lower value of the volume recombination, the electrons recombine before they reach the back side, there is no change in the concentration gradient sign and sample behavior is similar to that shown in Fig. 2.

In Fig. 4, plasma-elastic components of time-domain photoacoustic responses for heavily doped/impure semiconductor samples ($\tau_3 = 6 \times 10^{-8}$ s) are given. The plasma-elastic component is given for samples with even lower diffusion length and volume recombination velocity values. Therefore, the strains are even smaller in comparison to those shown in Fig. 3. With the increase in sample thickness, strains exhibit a non-linear decrease, similar to the previous two figures. At such low volume recombination velocity values, differences in samples with $S_g = 24$ (blue and black line) cannot be noticed. The behavior closely resembles that of Fig. 3, for the thinnest sample, for given fixed diffusion length and volume recombination velocity values (lower than in Figs. 2 and 3). There is a concentration gradient inversion because a larger number of electrons are able to reach the unilluminated side of the sample due to a low volume recombination velocity value. However, for thicker samples, electrons recombine before they can reach the back surface and there is no gradient inversion. Initially, straining causes overpressure, and over time, the system relaxes to a stationary state.

Performed analysis shows that surface recombinations, sample doping (via the charge carrier lifetime), and sample thickness have a significant influence on the shape and size of the plasma-elastic component of the photoacoustic response.

IV. CONCLUSIONS

Based on the model of the plasma-elastic component of the photoacoustic response, an analysis was conducted to examine the behavior of this component for single long optical pulse excitation of semiconductor samples. It is shown that the plasma-elastic component tends to a stationary value that is influenced by the sample thickness, the charge carrier lifetime (determined by the sample purity and doping), and the surface recombination velocity (determined by surface qualities that can be passive or active).

It has been found that the shortening of the charge carrier lifetime, which is related to increased impurities or higher doping of the semiconductor sample, decreases the plasma-elastic component of the photoacoustic response. The increase in the sample thickness also reduces the component in question. The dependencies are not linear, for a small increase in thickness or a shorter carrier lifetime, the plasma-elastic component decreases exponentially. For thin samples with low volume recombination rate (short lifetime), i.e., for samples of lower purity, the inversion of the concentration gradient can occur as well as the change of the bending direction of the sample within the short time interval after excitation. Surface recombinations described by their velocities (related to surface qualities) also affect strain amplitudes. Recombinations on the illuminated surface have a greater impact on the plasma-elastic component for greater volume recombination velocity values (in samples of higher purity and/or lower doping).

The observed effects, even though the recorded signals are low, are important. Deconvolution of the effect allows characterization of the electronic properties of semiconductors and, at the same time, the application potential of the photoacoustic method is increased.

ACKNOWLEDGMENTS

This work was financially supported by the Ministry of Science, Technological Development and Innovations of the Republic of Serbia (Contract No. 451-03-47/2023-01/200017).

AUTHOR DECLARATIONS

Conflict of Interest

The authors have no conflicts to disclose.

Author Contributions

Ivanka Stanimirović: Conceptualization (equal); Formal analysis (equal); Investigation (equal); Methodology (equal); Software (equal); Validation (equal); Visualization (equal); Writing – original draft (equal); Writing – review & editing (equal). **Dragana Markushev:** Conceptualization (equal); Formal analysis (equal); Investigation (equal); Methodology (equal). **Zdravko Stanimirović:** Formal analysis (equal); Investigation (equal); Software (equal); Validation (equal); Visualization (equal); Writing – original draft (equal); Writing – review & editing (equal). **Slobodanka Galović:** Formal analysis (equal); Investigation (equal); Supervision (equal); Validation (equal); Writing – original draft (equal); Writing – review & editing (equal). **Katarina Djordjević:** Formal analysis (equal); Investigation (equal); Methodology (equal); Supervision (equal); Validation (equal); Writing – original draft (equal); Writing – review & editing (equal).

DATA AVAILABILITY

The data that support the findings of this study are available from the corresponding author upon reasonable request.

REFERENCES

[1]Rosencwaig and A. Gersho, "Theory of the photoacoustic effect with solids," J. Appl. Phys. **47**(1), 64–69 (1976).
[2]H. Vargas and L. C. M. Miranda, "Photoacoustic and related photothermal techniques," Phys. Rep. **161**(2), 43–101 (1988).

[3]A. C. Tam, "Applications of photoacoustic sensing techniques," Rev. Mod. Phys. **58**, 381–431 (1986).
[4]A. P. Sarode and O. H. Mahajan, "Theoretical aspects of photoacoustic effect with solids: A review," Int. J. Sci. Adv. Res. Technol. **4**(2), 1237–1242 (2018).
[5]K. L. Djordjevic, D. Milicevic, S. P. Galovic, E. Suljovrujic, S. K. Jacimovski, D. Furundzic, and M. Popovic, "Photothermal response of polymeric materials including complex heat capacity," Int. J. Thermophys. **43**(5), 68 (2022).
[6]K. L. Djordjevic, D. K. Markushev, S. P. Galović, D. D. Markushev, and J. Ordonez-Miranda, "Si plate radius influence on the photoacoustic signal processed by neural networks," J. Appl. Phys. **132**, 215701 (2022).
[7]K. L. Djordjevic, S. P. Galović, ŽM Ćojbašić, D. D. Markushev, D. K. Markushev, S. M. Aleksic, and D. S. Pantic, "Electronic characterization of plasma-thick n-type silicon using neural networks and photoacoustic response," Opt. Quantum Electron. **54**(8), 485 (2022).
[8]A. Somer, A. Gonçalves, T. V. Moreno, G. K. d. Cruz, M. L. Baesso, N. Astrath, and A. Novatski, "Photoacoustic signal with two heating sources: Theoretical predictions and experimental results for the open photoacoustic cell technique," Meas. Sci. Technol. **31**, 075202 (2020).
[9]A. Somer, F. Camilotti, G. F. Costa, C. Bonardi, A. Novatski, A. V. C. Andrade, and G. K. Cruz, "Effects of the photogenerated processes influence on photoacoustic signal generation using open photoacoustic cell technique," J. Appl. Phys. **114**(6), 063503 (2013).
[10]S. Wang, *Fundamentals of Semiconductor Theory and Device Physics* (Prentice-Hall International, Englewood Cliffs, NJ, 1989), Vol. XVI, p. 864. ISBN 0-13-344425-2.
[11]P. M. Nikolić and D. M. Todorović, "Photoacoustic and electroacoustic properties of semiconductors," Prog. Quantum Electron. **13**(2), 107–189 (1989).
[12]D. M. Todorovic and P. M. Nikolic, "Investigation of carrier transport processes in semiconductors by the photoacoustic frequency transmission method," Opt. Eng. **36**(2), 432 (1997).
[13]Y. G. Gurevich and I. Lashkevych, "Sources of fluxes of energy, heat, and diffusion heat in a bipolar semiconductor: Influence of nonequilibrium charge carriers," Int. J. Thermophys. **34**, 341–349 (2013).
[14]I. N. Volovichev, G. N. Logvinov, O. Y. Titov, and Y. G. Gurevich, "Recombination and lifetimes of charge carriers in semiconductors," J. Appl. Phys. **95**(8), 4494–4496 (2004).
[15]Y. G. Gurevich and O. L. Mashkevich, "The electron-phonon drag and transport phenomena in semiconductors," Phys. Rep. **181**(6), 327–394 (1989).
[16]T. S. Gredeskul, Y. G. Gurevich, and O. L. Mashkevich, "Разогрев носителей тока и фононов постоянным электрическим полем," Fiz. Tekh. Poluprovodn. **23**(10), 1895–1898 (1989). https://www.mathnet.ru/eng/phts3587.
[17]I. N. Volovichev, L. Villegas-Lelovsky, G. González de la Cruz, and Y. G. Gurevich, "The effect of carrier diffusion and recombination in semiconductors on the photoacoustic signal," Phys. B **304**(1-4), 410–422 (2001). North-Holland.
[18]I. C. Ballardo Rodriguez, B. El Filali, O. Y. Titov, and Y. G. Gurevich, "Influence of thermal nonequilibrium on recombination, space charge, and transport phenomena in bipolar semiconductors," Int. J. Thermophys. **41**(5), 65 (2020).
[19]O. Y. Titov and Y. G. Gurevich, "Temperature gradient and transport of heat and charge in a semiconductor structure," Low Temp. Phys. **47**(7), 550–554 (2021).
[20]S. Kumar, "Effect of the confined plasma on thermal wave fild in semiconductor devices," in *Progress in Photothermal and Photoacoustic Science and Technology—Semiconductors and Electronic Materials*, edited by A. Mandelis and P. Hess (SPIE Press, Bellingham, WA, 2000), Vol. 4, pp. 175–198.
[21]D. M. Todorović and P. M. Nikolic, "Carrier transport contribution on thermoelastic and electronic deformation in semiconductors," in *Progress in Photothermal and Photoacoustic Science and Technology—Semiconductors and Electronic Materials*, edited by A. Mandelis and P. Hess (SPIE Press, Bellingham, WA, 2000), Vol. 4, pp. 271–315.
[22]D. M. Todorović, P. M. Nikolić, M. Smiljanić, R. Petrović, A. I. Bojičić, D. G. Vasiljević-Radović, and K. T. Radulović, "Investigation of the photoacoustic effect in metal-semiconductor system," in *Proceedings of the 10th International Conference on Photoacoustic and Photothermal Phenomena* (AIP, 1999).
[23]D. M. Todorovic and M. Smiljanic, "Theory of photoacoustic effect in metal-semiconductor system," in *Analytical Sciences Conference: 11th International Conference on Photoacoustic and Photothermal Phenomena* (AIP, 2001), Vol. 17.
[24]D. M. Todorović, B. Cretin, P. Vairac, Y. Q. Song, M. D. Rabasović, and D. D. Markushev, "Laser-Excited electronic and thermal elastic vibrations in a semiconductor rectangular plate," Int. J. Thermophys. **34**(8–9), 1712–1720 (2013).
[25]D. M. Todorović, P. M. Nikolić, M. D. Dramićanin *et al.*, "Photoacoustic frequency heat-transmission technique: Thermal and carrier transport parameters measurements in silicon," J. Appl. Phys. **78**(9), 5750–5755 (1995).
[26]D. K. Markushev, D. D. Markushev, S. M. Aleksic, D. S. Pantic, S. P. Galovic, D. M. Todorovic, and J. Ordonez-Miranda, "Effects of the photogenerated excess carriers on the thermal and elastic properties of n-type silicon excited with a modulated light source: Theoretical analysis," J. Appl. Phys. **126**(18), 185102 (2019).
[27]D. K. Markushev, D. D. Markushev, S. Galović *et al.*, "The surface recombination velocity and bulk lifetime influences on photogenerated excess carrier density and temperature distributions in n-type silicon excited by a frequency-modulated light source," Facta Univ. Ser. Electron. Eng. **31**(2), 313–328 (2018).
[28]D. K. Markushev, D. D. Markushev, S. M. Aleksic *et al.*, "Effects of the photogenerated excess carriers on the thermal and elastic properties of n-type silicon excited with a modulated light source: Theoretical analysis," J. Appl. Phys. **126**(12), 185102 (2019).
[29]P. M. Nikolic and D. M. Todorovic, "An investigation of semiconducting materials using a photoacoustic methods," *SANU Monographs* (Serbian Academy of Sciences and Arts, Belgrade, 2001), Vol. DCXLVIII Book 40.
[30]M. Isaiev, V. Kuryliuk, A. Kuzmich, and R. Burbelo, "Photothermal transformation in heterogeneous semiconductors structures under its pulse laser irradiation: Role of electron-hole diffusion," Arch. Metall. Mater. **58**(4), 1351–1354 (2013).
[31]M. Maliński, J. Zakrzewski, and F. Firszt, "Photoacoustic spectroscopy of surface defects states of semiconductor samples," Eur. Phys. J. Spec. Top. **153**(1), 251–254 (2008).
[32]K. L. Djordjević, S. P. Galović, Ž.M. Ćojbašić, D. D. Markushev, D. K. Markushev, S. M. Aleksic, and D. S. Pantic, "Electronic characterization of plasma-thick n-type silicon using neural networks and photoacoustic response," Opt. Quantum Electron. **54**(8), 485 (2022).
[33]D. M. Todorović, M. D. Rabasović, and D. D. Markushev, "Photoacoustic elastic bending in thin film—Substrate system," J. Appl. Phys. **114**(21), 213510 (2013).
[34]K. Lj. Djordjevic, S. P. Galovic, M. V. Nesic, D. M. Todorovic, M. N. Popovic, D. D. Markushev, and D. K. Markushev, "Transmission pulse photoacoustic set-up for characterization of solids," in *21st International Symposium INFOTEH-JAHORINA, 16–18 March 2022*, (FEE, University of Sarajevo, Bosnia and Herzegovina, 2022).

Journal of Applied Physics

Si plate radius influence on the photoacoustic signal processed by neural networks

Cite as: J. Appl. Phys. **132**, 215701 (2022); https://doi.org/10.1063/5.0123041
Submitted: 27 August 2022 • Accepted: 04 November 2022 • Published Online: 05 December 2022

Katarina Lj. Djordjevic, Dragana K. Markushev, Slobodanka P. Galović, et al.

AIP Publishing

Journal of Applied Physics ARTICLE scitation.org/journal/jap

Si plate radius influence on the photoacoustic signal processed by neural networks

Cite as: J. Appl. Phys. **132**, 215701 (2022); doi: 10.1063/5.0123041
Submitted: 27 August 2022 · Accepted: 4 November 2022 ·
Published Online: 5 December 2022

Katarina Lj. Djordjevic,[1,a)] Dragana K. Markushev,[2] Slobodanka P. Galović,[1] Dragan D. Markushev,[2] and Jose Ordonez-Miranda[3]

AFFILIATIONS

[1]"VINČA" Institute of Nuclear Sciences—National Institute of the Republic of Serbia, University of Belgrade, PO Box 522, 11000 Belgrade, Serbia
[2]Institute of Physics Belgrade, National Institute of the Republic of Serbia, University of Belgrade, Pregrevica 118, 11080 Belgrade (Zemun), Serbia
[3]LIMMS, CNRS-IIS UMI 2820, The University of Tokyo, Tokyo 153-8505, Japan

[a)]**Author to whom correspondence should be addressed:** katarina.djordjevic@vin.bg.ac.rs

ABSTRACT

The effect of the sample radius on the total photoacoustic signal processed by neural networks trained with undistorted and distorted signals is carefully analyzed for modulation frequencies from 20 Hz to 20 kHz. This is done for signals generated for a 400-μm-thick Si n-type plate, whose radius varies from 2 to 7 mm. It is found that the networks trained with both undistorted or distorted signals yield the best predictions for sample radii between 2 and 3 mm, which is close to the used microphone aperture radius of 1.5 mm. The network trained only with undistorted signals gives the best results for sample radii comparable to the microphone dimensions. The obtained results of neural networks in the prediction of Si-plate radius indicate the experimental necessity to use samples with radii slightly over to a microphone aperture.

I. INTRODUCTION

The photoacoustic effect is the effect of the sound appearance due to the illumination of a sample with an optical beam whose intensity is time-dependent.[1–5] Numerous non-destructive methods for the characterization and imaging of various solids, multilayer structures, microelectronic and photonic devices, soft matter, and biological tissues are based on this effect.[6–22] The use of neural networks in photoacoustics has become very popular recently, especially in imaging within biomedical applications.[23–25] Significant progress has been made, also, in photoacoustics of solids with different types of networks both in material characterization and in the development of experimental procedures.[26–28] Networks have proven to be a very effective tool for predicting the physical characteristics of solid samples.[29–31] Within the framework of multiparameter fitting in photoacoustics, the networks most often predicted the values of the sample parameters, such as thermal diffusion (D_T) and thermal expansion (α_T) together with the thickness of the sample (l).[32,33] These parameters are important because they occur when calculating the temperature distributions of the sample and all components of the photoacoustic signal (PAS) generated by the periodic illumination of the sample.

It has long been known that the geometric parameters of the sample are very important for the correct interpretation of the photoacoustic signal in the frequency domain.[34–36] If the circular plate shape samples are tested, one of such parameters is its radius R_s. It explicitly appears in the equation for calculating the thermoelastic and plasmaelastic components of the photoacoustic signal of a semiconductor so that its influence on the shape of the total signal through these two components can be extremely significant.[32,33] In this paper, the analysis of the influence of the semiconductor sample radius changes on all components of the photoacoustic signal, thermodiffusion (TD), thermoelastic (TE), and plasmaelastic (PE), is presented based on the theoretical model of a composite piston[1–3] that serves to form an appropriate base of photoacoustic signals for neural network training.[26,27] The tested sample is an Si n-type 400 μm thick wafer, classified as a plasma-thick sample—a sample with a thickness larger than the diffusion length of free

carriers.[32,33] Plasma-thick semiconductor samples have a thermal response of known and characteristic patterns of behavior of the total signal and its components in the modulation frequencies ranging from 20 Hz to 20 kHz.[33] These patterns include domination of the TD component at lower frequencies and the TE component at higher frequencies, while the PE component's influence on the total signal is negligible.

The basic idea of this paper is to determine which type of neural network gives better predictions in the case of a change in the radius of the sample: one that is trained by distorted signals or by signals undistorted with instrumental deviations.[37–39] This analysis is very important because its results can give the possibility of working with distorted signals, which significantly simplifies and speeds up the process of characterization of the tested samples. Both types of network training signals were obtained theoretically, and the final verification of network efficiency was tested on experimental data. The conclusions of this analysis indicate, in experimental terms, the importance of the choice of sample radius about the dimensions of the microphone as a photoacoustic cell and a signal detector. Also, based on the obtained network predictions, a conclusion can be drawn on the justification of using approximations in the theoretical model of the composite piston, especially those related to the equality of a microphone aperture and sample radii.

II. THEORETICAL INTRODUCTION

The theoretical model of the composite piston presented in this paper is adapted to the experimental setup of an open photoacoustic cell (OPC).[32,33,37,40] It is assumed that a frequency-modulated light source of wavelength 660 nm illuminates the Si n-type plate. Due to the photoacoustic effect of the absorbed modulated light and the sample interaction, a sound is recorded by an open photoacoustic cell in the transmission configuration (Fig. 1).

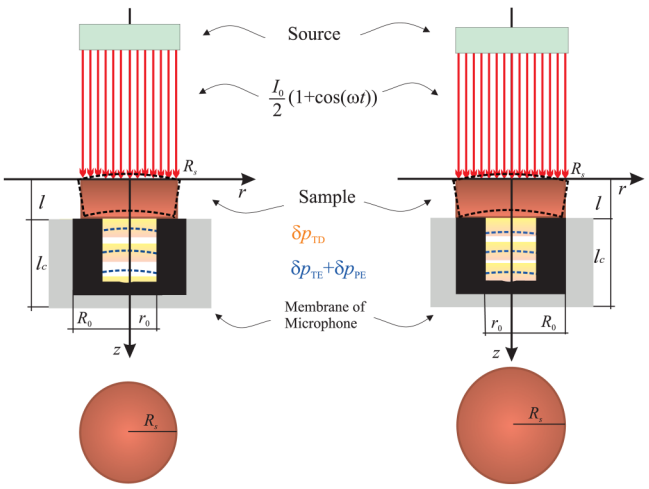

FIG. 1. Simple ideal scheme of the transmission configuration of an open photoacoustic cell with an electret microphone and samples of different radii.

The photoacoustic signal detector is assumed to be an electret microphone (ECM 30B, Jin In Electronics Co., Ltd.) with a radius of $R_0 = 4.9$ mm and an aperture radius of $r_0 = 1.5$ mm.[33] The sample is placed directly on the microphone with points of support that are slightly smaller but close to the radius of the sampleR_s so that the microphone at the same time can serve as a measuring cell of minimal volume $V_0 = \pi r_0^2 l_c$, where l_c is the distance from the microphone aperture to its membrane (length of OPC) (see Fig. 1).

The measured signal in the transmission configuration and in the frequency range from 20 Hz to 20 kHz is a sound signal that occurs due to the photoacoustic effect in the sample itself and is usually distorted by the influence of used instruments and the different types of noise. The signal, thus, measured is called the distorted signal $S_{\text{total}}(f)$. If a well-known signal correction procedure[33,37–39] is applied to such a signal, the so-called true or undistorted signal $\delta p_{\text{total}}(f)$ can be obtained, generated from an illuminated sample. The theoretical model that fully describes the undistorted signals is based on the composite piston model.[1–3] This model explains that the total photoacoustics signal $\delta p_{\text{total}}(f)$ of a semiconductor is equal to the sum of its components: thermodiffusion $\delta p_{\text{TD}}(f)$, thermoelastic $\delta p_{\text{TE}}(f)$, and plasmaelastic $\delta p_{\text{PE}}(f)$,[33,40]

$$\delta p_{\text{total}}(f) = \delta p_{\text{TD}}(f) + \delta p_{\text{TE}}(f) + \delta p_{\text{PE}}(f). \tag{1}$$

The thermodiffusion component can be written as follows:[33,41]

$$\delta p_{\text{TD}}(t) = \frac{\gamma p_0}{l_c}\frac{\mu_g}{\sqrt{2}T_0} T(l)\, e^{i\left(\omega t - \frac{\pi}{4}\right)}, \tag{2}$$

where $\omega = 2\pi f$, f is the modulation frequency, γ is an adiabatic ratio, p_0 and T_0 are the ambient pressure and temperature, μ_g is the thermal diffusion length of the surrounding gas, $T_s(l)$ (see Appendix A) is the dynamic temperature component at the back sample surface, l is the sample thickness, and l_c is the length of the cell (microphone).

Due to different temperature values on the illuminated and non-illuminated side of the silicon sample, its periodic bending and expansion occur. The effect of bending and spreading is most simply described by cylindrical (z, r) coordinates so that the thermoelastic component $\delta p_{\text{TE}}(f)$ of the photoacoustic signal can be written in the form[33,40]

$$\delta p_{\text{TE}}(f) = \alpha_{\text{T}} \frac{3\pi p_0 \gamma}{V_0}\frac{R_s^4}{l^3}\int_{-l/2}^{l/2} zT(z)dz, \tag{3}$$

where $T(z)$ is the temperature distribution in the sample along the z-axes (see Appendix A), α_{T} is the coefficient of thermal expansion, V_0 is the microphone (cell) volume, and R_s is the sample radius. In most of the theoretical analyses, the $R_s \approx R_0$ approximation is taken to simplify the analysis.[32,33,37,39]

By modulated illumination of the sample with the light of proper wavelength, free carriers (electrons and holes) are generated, which leads to additional stress and periodic bending of the sample. The influence of phototgenerated carriers on the bending of the sample is described by the plasmaelastic component

$\delta p_{PE}(f)$,[33,40]

$$\delta p_{PE}(f) = d_n \frac{p_0 \gamma}{V_0} \frac{3\pi R_s^4}{l^3} \int_{-l/2}^{l/2} z\, \delta n_p(z) dz, \tag{4}$$

where $\delta n_p(z)$ is the minority carrier density (see Appendix B) and d_n is the coefficient of electronic deformation. Analyzing Eqs. (3) and (4), one can see that $\delta p_{TE}(f)$ and $\delta p_{PE}(f)$ depend on R_s^4, meaning that small changes in R_s lead to large changes in $\delta p_{TE}(f)$ and $\delta p_{PE}(f)$.

It must be borne in mind that during the measurement, there are many signal distortions due to the influence of the used instruments (microphones and accompanying electronics). These distortions have signal filtering characteristics and are described, in the low-frequency range, by the function of the first-order low-pass filter $H_e(f)$ in the form[37,39]

$$H_e(f) = -\frac{\omega\tau_{c1}}{(1 + i\omega \cdot \tau_{c1})} \cdot \frac{\omega\tau_{c2}}{(1 + i\omega \cdot \tau_{c2})}, \tag{5}$$

where $\omega = 2\pi f$, f is the modulation frequency, and $\tau_{c1} = (2\pi f_{c1})^{-1} = R_1 C_1$ and $\tau_{c2} = (2\pi f_{c2})^{-1} = R_2 C_2$ are the time constants and RC characteristics of the microphone and accompanying electronics (usually sound-card or lock-in).

In the high-frequency range, these distortions are described by the function of the second-order low-pass filter $H_a(f)$ in the form[37,39]

$$H_a(f) = \frac{\omega_{c3}^2}{\omega_{c3}^2 + i\delta_{c3}\omega_{c3}\omega - \omega^2} + \frac{\omega_{c4}^2}{\omega_{c4}^2 + i\delta_{c4}\omega_{c4}\omega - \omega^2}, \tag{6}$$

where δ_k is the damping factor ($k = c3, c4$), ω_{c3} is the microphone cut-off frequency, and ω_{c4} is the characteristic frequency, which depends on the geometry of the microphone body.

The total measured signal $S_{total}(f)$ can be written as a product of $\delta p_{total}(f)$, $H_e(f)$, and $H_a(f)$,[33,37,39]

$$S_{total}(f) = \delta p_{total}(f) H_e(f) H_a(f). \tag{7}$$

Characteristic parameters $H_e(f)$ and $H_a(f)$ can be obtained either from the microphone manual or by independent measurements.[33,37,39] By finding them, $H_e(f)$ and $H_a(f)$ can be removed from $S_{total}(f)$ in Eq. (7) so that the required $\delta p_{total}(f)$ can be obtained,[33,37] which is further described by the composite piston theory [Eqs. (1)–(4)].

III. NEURAL NETWORKS

Our motive for the study of neural networks is their use in the precise characterization of the properties of the tested materials. In the process of supervised learning by connecting the data of input neurons (values of photoacoustic signals) with the data of output neurons (radius), the weights are adjusted to the moment when the output becomes increasingly like the desired data values. In our work with networks so far, we have learned that for the sake of prediction, we need to present undistorted data to the trained network, the data that are adapted to the theoretical model used to create the training base. This assumes that during the processing of experimental results, we must also count on the signal correction procedure. If it turns out that signal correction is not required to determine some of the sample parameters (expected in the case of only R_s changes), this will mean significant time savings. Therefore, in this paper, we will try to train networks with distorted (NN1) and undistorted (NN2) photoacoustic signals with the desire to determine the radius of the investigated sample, as a very important experimental parameter. Our goal is to see if there are differences in the prediction of the radius of the sample of such formed networks and whether, based on that, we can speed up the process of processing experimental data.

For the sake of simplicity and based on the problem we want to solve, we decided that both networks used here have the simplest architecture, the so-called shallow networks: input layer, one hidden layer, and output layer.[26,27] The input layer was determined by 144 neurons ($i = 72$ values of the photoacoustic signal amplitude A_i and $i = 72$ values of the photoacoustic signal phase φ_i characteristic), the hidden layer was determined by 10 neurons, and the output layer was determined by one neuron (the prediction of R_s, Fig. 2). The choice of the neural network architecture ensures good accuracy and optimal training time. Due to the better precision of the neural network, we adjusted the amplitudes by logarithmic normalization $20\log_{10} A_i$ to obtain the phase value range (A_i represents amplitudes normalized to unit pressure).

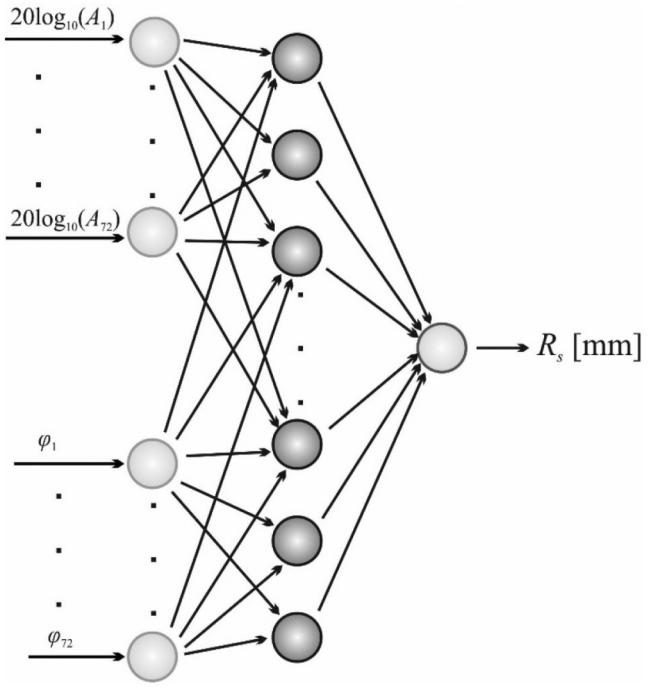

FIG. 2. Representation of a single-layer neural network used for the analysis of distorted and undistorted photoacoustic signals that depend on the radius of silicon samples.

IV. RESULTS AND DISCUSSION

A. Signal database formation

Due to the high sensitivity of these components to R_s changes in the total photoacoustic signal, we formed a "small" base of 26 undistorted $\delta p_{\text{total}}(f)$ and 26 distorted $S_{\text{total}}(f)$ theoretical photoacoustic signals obtained by Eqs. (1)–(7). As we said earlier, we assume that the sample is an Si n-type plate, 400 μm thick. Bases are determined by amplitude–phase characteristics in the frequency domain from 20 Hz to 20 kHz, changing R_s from 2 to 7 mm in the steps of 0.2 mm. To simplify our considerations, we assumed that the excitation light intensity $I_0 = \text{const}$. The dependences of the (a) amplitudes and (b) phases of $S_{\text{total}}(f)$ and $\delta p_{\text{total}}(f)$ signals on R_s in the frequency domain are clearly shown in Figs. 3 and 4, respectively. The influence of R_s is clearly expressed in both figures at frequencies $f > 100$ Hz in the amplitudes (saddle shape) and in phases (distend areas). The black arrows indicate the directions of changes due to the R_s value increase. Unchanged amplitudes and phases in the low-frequency region ($f < 100$ Hz) indicate an area where $S_{\text{total}}(f)$ and $\delta p_{\text{total}}(f)$ are insensitive to R_s changes.

Figures 3 and 4 clearly show the instrumental influences as electronic filtering [Eq. (5)] at lower frequencies (H_e at $f < 100$ Hz) and acoustic filtering [Eq. (6)] at higher frequencies (H_a at $f > 5$ kHz).[33,37–39] Electronic filters H_e reduce amplitudes [Figs. 3 and 4(a)] and raises phases [Figs. 3 and 4(b)] at low frequencies. Acoustic filters are characterized by resonant peaks in both amplitudes and phases. The parameters that define H_e and H_a are not dependent on R_s and are constant during its changes. Therefore,

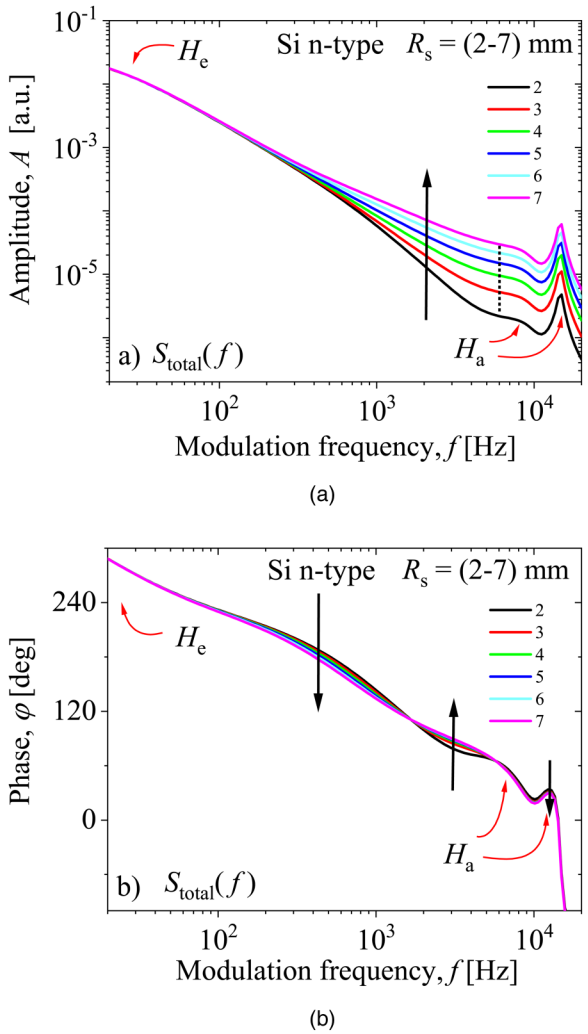

FIG. 3. The bases of distorted PA signal $S_{\text{total}}(f)$: (a) amplitudes, A, and (b) phase, φ, from an Si n-type as a function of simple radius R_s and modulation frequency f.

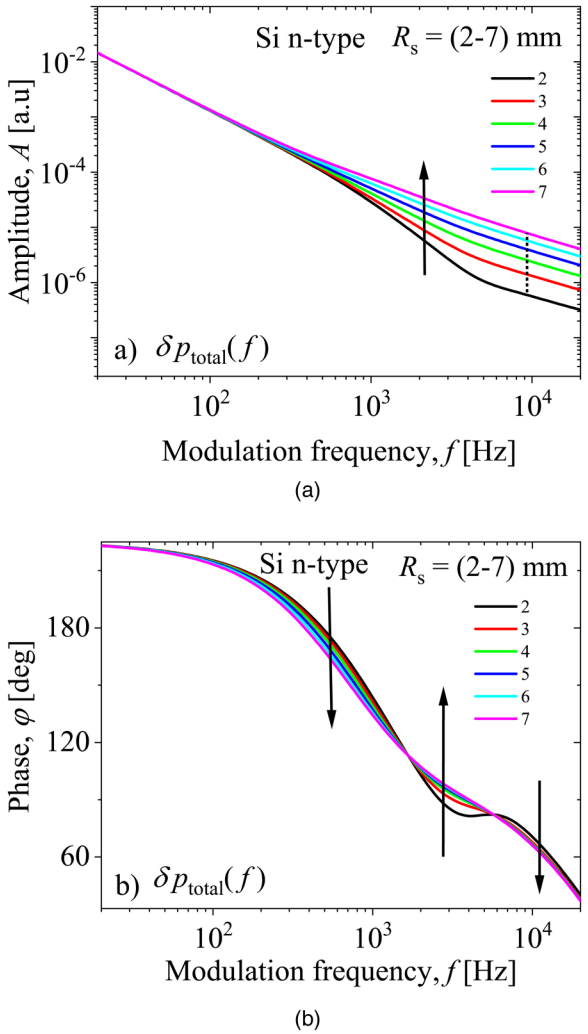

FIG. 4. The bases of undistorted PA signal $\delta p_{\text{total}}(f)$: (a) amplitudes, A, and (b) phase, j, from an Si n-type as a function of simple radius R_s and modulation frequency f.

the reasons for changing $S_{total}(f)$ and $\delta p_{total}(f)$ by changing R_s are the same and consist of the following: both signals are characterized with a saddle shape in amplitudes, which is more pronounced for $R_s = 2$ mm, while with an increasing radius, the saddle shape slowly disappears, and at $R_s = 7$ mm, it completely vanishes.

The insensitivity of the $S_{total}(f)$ and $\delta p_{total}(f)$ signals to R_s changes at lower frequencies allows one the possibility of, so-called, signal self-normalization that can contribute to the better performance of network training. On the other hand, the saddle shape of the $S_{total}(f)$ and $\delta p_{total}(f)$ signals is a typical pattern of plasma-thick silicon sample behavior in the frequency domain (strong TD and TE influence), allowing one to obtain better network parameter prediction. Both mentioned signal characteristics, insensitivity, and saddle shape are the reason why, in this paper, we decided to create a training base with distorted and undistorted signals of the plasma-thick samples, expecting efficient neural network optimization.

The question may be asked why the signal $S_{total}(f)$ and $\delta p_{total}(f)$ changes in amplitudes and phases due to R_s variations are most visible at $f > 100$ Hz. The explanation can be given by the theory based on the composite piston model [Eqs. (1)–(4)], in which the radius of the sample does not affect all components of the photoacoustic signal equally. Changes in R_s do not affect changes in the amplitude of the $\delta p_{TD}(f)$ component at all [Fig. 5(a)], but they do change the amplitudes of $\delta p_{TE}(f)$ [Fig. 6(a)] and $\delta p_{PE}(f)$ components [Fig. 7(a)]. In both $\delta p_{TE}(f)$ and $\delta p_{PE}(f)$ cases, the amplitudes increase with R_s. In all cases [Figs. 5(b), 6(b) and 7(b)], phases do not change at all.

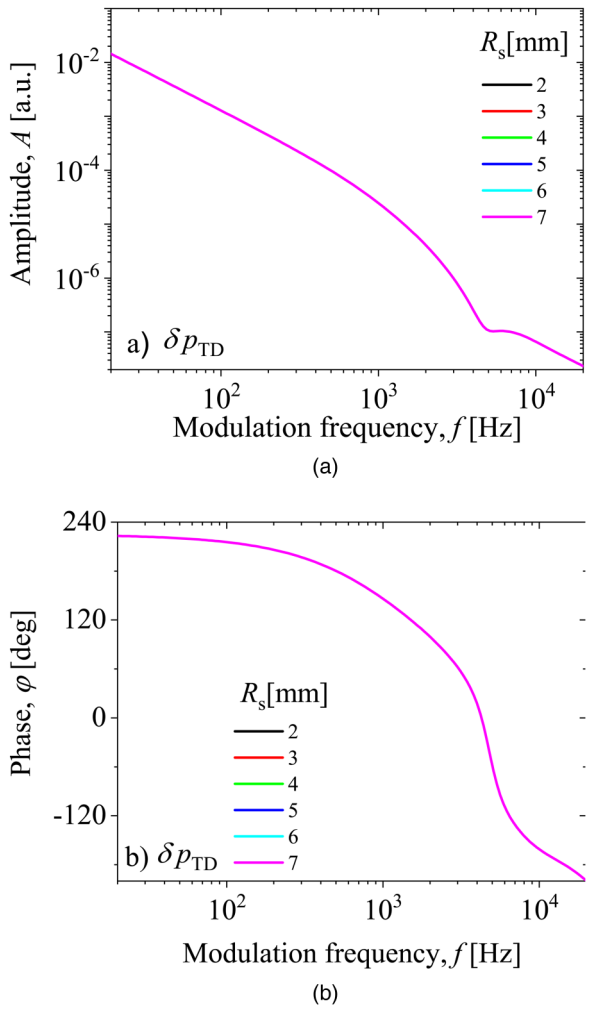

FIG. 5. Thermodiffusion component $\delta p_{TD}(f)$ (a) amplitudes A and (b) phases φ as a function of simple radius R_s and modulation frequency f.

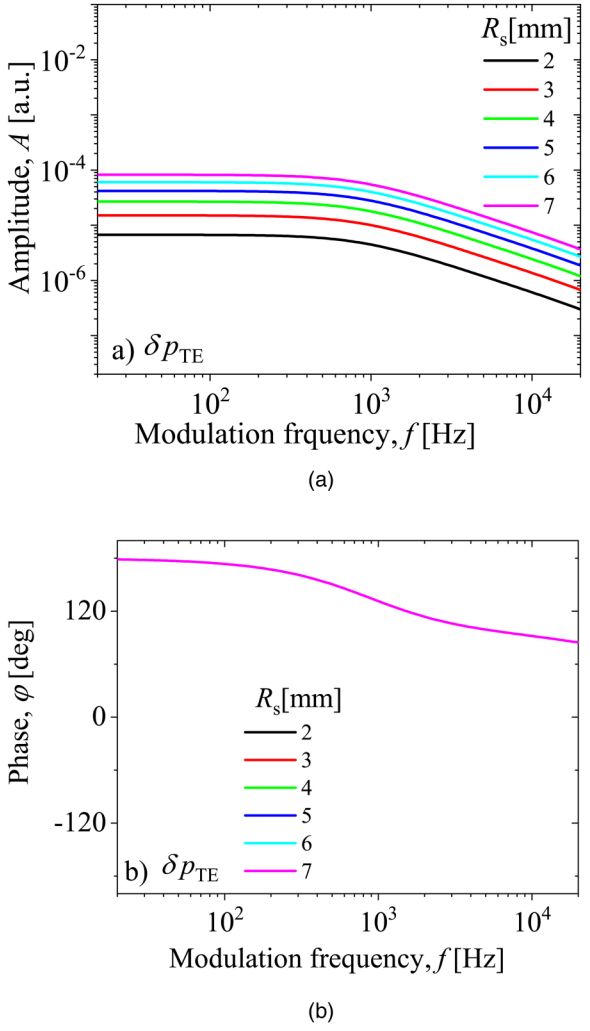

FIG. 6. Thermoelastic component $\delta p_{TE}(f)$ (a) amplitudes A and (b) phases φ as a function of simple radius R_s and modulation frequency f.

To fully understand what presented signal component amplitude and phase changes mean, it is necessary to draw all the components and the total signal together because not only the values of the components are important but also their mutual relationship, which is shown in Fig. 8. This figure shows the amplitudes and phases of total signals and their components for $R_s = 2$ mm (solid lines) and $R_s = 7$ mm (dashed lines). The amplitude changes of the $\delta p_{PE}(f)$ component (blue) are smaller in absolute values compared to the changes in $\delta p_{TE}(f)$ (green). This is the reason why $\delta p_{PE}(f)$ components do not affect the change in the total signal $\delta p_{total}(f)$ (black). Therefore, only the mutual relationship between $\delta p_{TD}(f)$ (red) and $\delta p_{TE}(f)$ (green) amplitudes drives the $\delta p_{total}(f)$ behavior in the frequency domain.

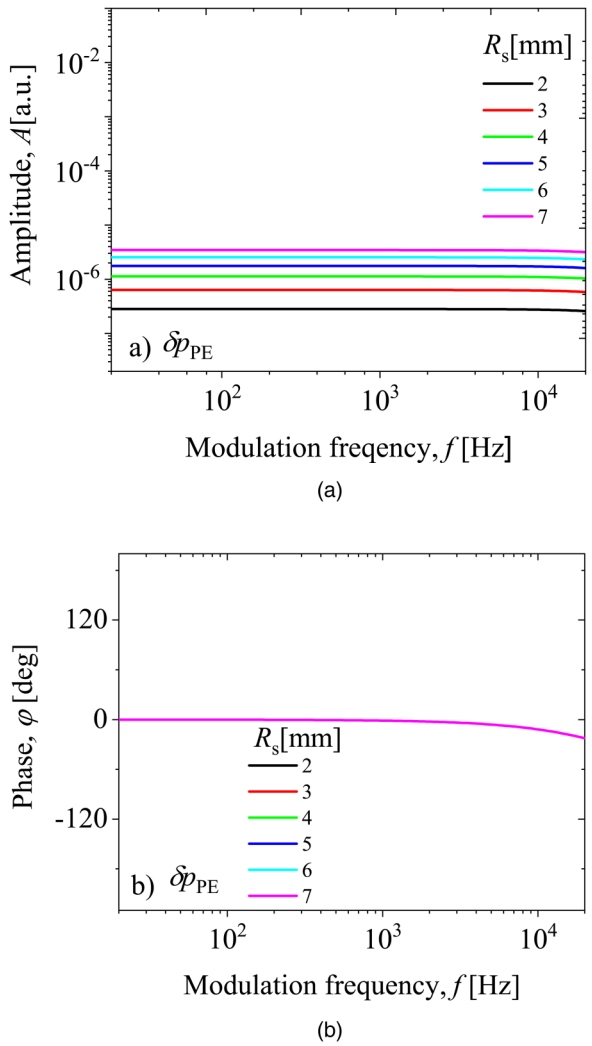

FIG. 7. Plasmaelastic component $\delta p_{PE}(f)$ (a) amplitudes A and (b) phases φ as a function of simple radius R_s and modulation frequency f.

If $R_s = 2$ mm, the intersection of $\delta p_{TD}(f)$ and $\delta p_{TE}(f)$ is at $f \sim 2.4$ kHz, and therefore, $\delta p_{total}(f)$ (solid black) has a saddle shape at higher frequencies. When $R_s = 7$ mm, the intersection of $\delta p_{TD}(f)$ and $\delta p_{TE}(f)$ is at $f \sim 600$ Hz, and therefore, $\delta p_{total}(f)$ (dashed black) is flattened (it has lost its saddle shape). Changes in the total signal for these and all other R_s values used to make the presented base will be visible in the range $f > 200$ Hz. The same conclusion was states for the distorted $S_{total}(f)$ signal, too. The analysis of the change of radius outside the range from 2 to 7 mm shows the loss of the influence of thermoelastic components on the total signal in the case of $R_s < 2$ mm and their dominance in the total signal for $R_s > 7$ mm.

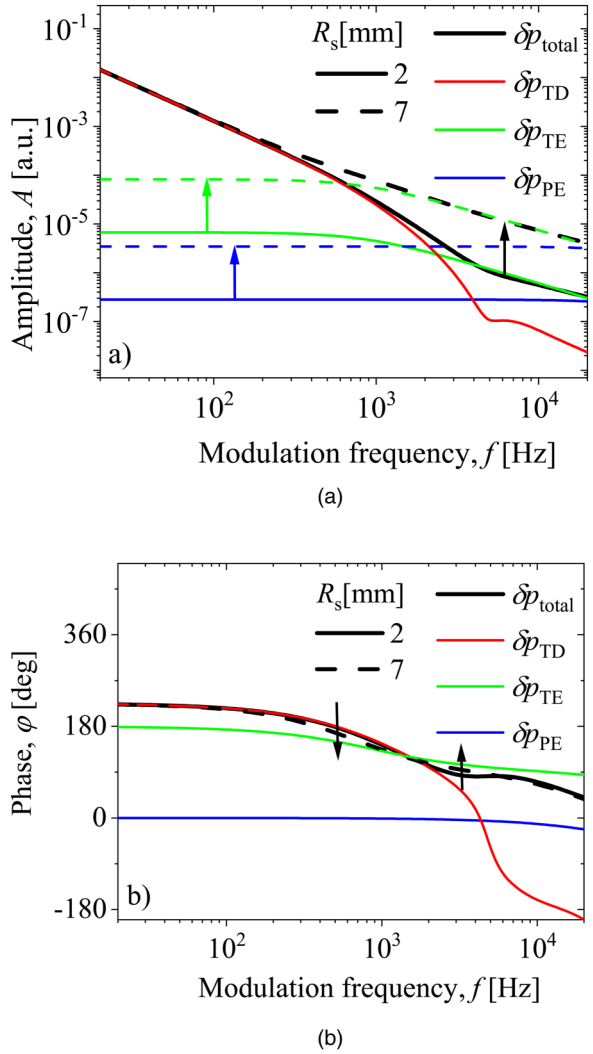

FIG. 8. The tendency of changes in (a) amplitudes A and (b) phases φ of total photoacoustic signals $\delta p_{total}(f)$ (black lines) with its components: thermodiffusion $\delta p_{TD}(f)$ (red lines), thermoelastic $\delta p_{TE}(f)$ (green lines), and plasma elastic $\delta p_{PE}(f)$ (blue lines) for 400 μm thick Si samples of radius $R_s = 2$ mm and $R_s = 7$ mm.

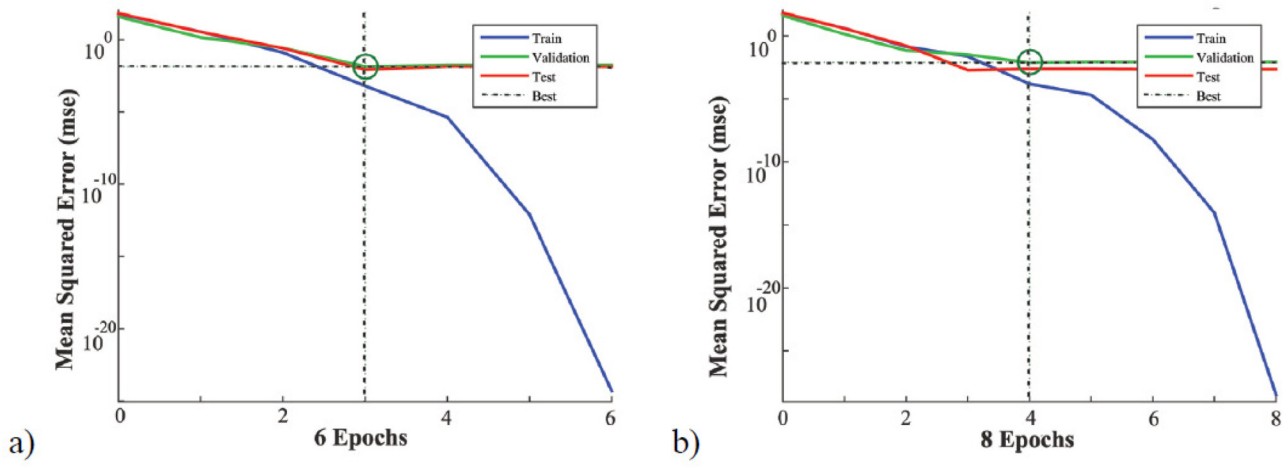

FIG. 9. Network performance results: (a) NN1 trained on distorted FA signals and (b) NN2 trained on undistorted FA signals.

The presented theoretical analysis of the total signal behavior by changing the radius of the sample shows that it makes sense to use both undistorted and distorted total signals to recognize R_s values because their amplitudes change significantly with changes in R_s only at higher modulation frequencies. The low-frequency range can be used as the total signal self-normalization range due to the absence of any R_s influences on the total signal.

B. Network prediction results

The training results of NN1 neural networks trained by the base of distorted (Fig. 3) and NN2 trained with the base of undistorted (Fig. 4) signals are presented by the mean square error (MSE) dependence of the number of epochs in Fig. 9. During network training, bases are divided into a training base, a testing base, and a validation base, based on which the generalized capabilities of networks are determined. To ensure the best performance of the networks, the criterion of interrupting the MSE deviation of individual curves is activated. The NN1 network stopped its work in three epochs with the best validation performance of 0.014 063 [Fig. 9(a)], while the NN2 network stopped its work in four epochs, with the best validation performance of 0.007 580 5 [Fig. 9(b)].

TABLE I. The results of NN1 and NN2 neural network predictions of the sample radius with relative (%) errors. The asterisk denotes the predictions for experimentally measured PASs.

R_s (mm)	NN1 R_s (mm)	rel % error, NN1	NN2 R_s (mm)	rel % error, NN2
2.1	2.1356	1.6933	2.1023	0.1086
2.5	2.4849	0.6048	2.5400	1.5996
2.9	2.9038	0.1319	2.8572	1.4745
3.3	3.2037	2.9183	2.8572	0.3332
3.7	3.8832	4.9527	3.7098	0.2650
4.1	4.1947	2.3089	4.1427	1.0416
4.5	4.7968	6.5967	4.5426	0.9470
4.9	4.8915	0.1740	4.5426	7.2936
5.3	5.3213	0.4014	5.1965	1.9530
5.7	5.6535	0.8155	5.6941	0.1028
6.1	6.0561	0.7190	6.1364	0.5964
6.5	6.4283	1.1034	6.1364	5.5942
6.9	6.8216	1.1358	6.8506	0.7156
4.54*	4.7976	5.6749	4.6644	2.7398
2.63*	2.6521	0.8315	2.6247	0.2014

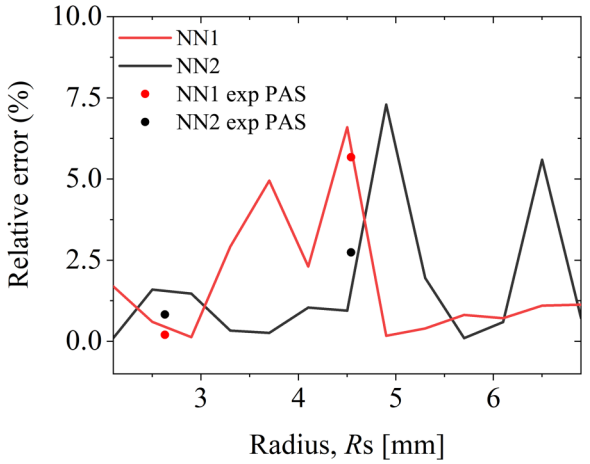

FIG. 10. Dependence of relative% error prediction of NN1 (red line) and NN2 (black line) networks on the sample radius for the tests of theoretical results and experimental verification [NN1 (red dots) and NN2 (black dots)].

To evaluate the neural networks' (NN1 and NN2) ability to predict, we formed additional distorted and undistorted signal bases with values from 2.1 to 6.9 mm, formed using a step of 0.4 mm. These additional bases are used for network testing. In this way, we obtained 13 distorted + 13 undistorted test signals evenly distributed throughout the range of R_s changes. The results of the neural network test on these signals are shown in Table I. The obtained relative errors are at the experimental measurement level of accuracy, which shows that for the network analysis of certain properties of samples, large photoacoustic signal databases are not necessary.

For the sake of clarity, the results in Table I are presented in Fig. 10. It can be seen, based on the relative error percentage for NN1 and NN2 (Table I and Fig. 10), that the prediction is good only in limited sample radius areas. A more accurate prediction of NN1 (low % value of relative error) is for samples having $R_s \leq 3$ mm and samples with a radius larger than the microphone dimension ($R_s \geq 5$ mm). A more precise prediction of the NN2 network ranges in a much wider range of radius values ($R_s \leq 4.5$ mm), while for higher values of R_s, it give poorer predictions. The largest (%) relative errors are made by both NN1 and NN2 networks for the radius of the sample in the range (4.0–5.5) mm, i.e., about a value equal to the radius of the microphone $R_0 = 4.9$ mm. These results lead to the conclusion that both networks give the best predictions when the value of R_s approaches the value of the microphone aperture radius ($r_0 = 1.5$ mm). This confirms the justification of the approximations $R_s = r_0$ taken here with the experimental configuration of the open cell. In general, the results show that for experimental work, it is best to take samples whose dimensions are smaller than the dimensions of the microphone (R_0).

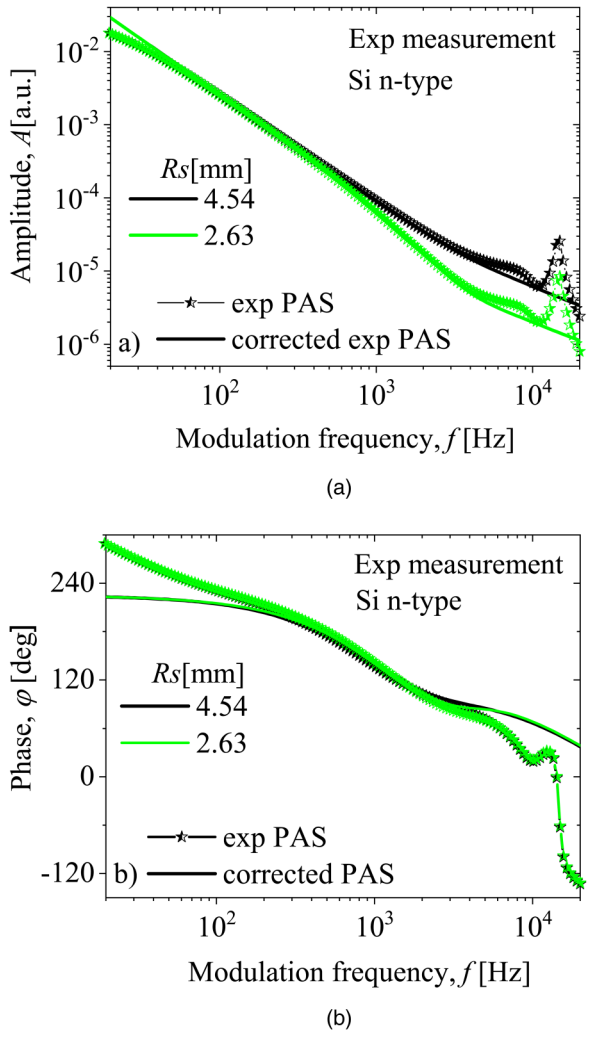

FIG. 11. Experimental result of the (a) amplitude I (b) phase of distorted (star) and undistorted (line) photoacoustic signals presented to NN2 and NN1, respectively, for a sample of 400 μm thick silicon n-type with a radius of $R_s = 4.54$ mm (black) and $R_s = 2.63$ mm (green).

To confirm the previous results, both networks presented the experimental results of distorted and undistorted signals of a sample that had a radius approximately equal to the microphone radius $R_s \approx R_0$ and with a sample radius close to the aperture radius $R_s \geq r_0$.

The results of network prediction in the case of the signal from Fig. 11 (black for $R_s = 4.54$ mm and green for $R_s = 2.63$ mm) obtained using the open photoacoustic cell experimental setup are shown in Table I with an asterisk and in Fig. 10 with dots (red for NN1 and black for NN2). Based on the experimental results, it can be concluded that the prediction of the experimentally corrected photoacoustic signals by the NN2 network is more accurate. Therefore, it can be recommended that networks trained on undistorted signals (NN2) should be used in determining R_s of the tested sample only with values smaller than the microphone radius R_0.

V. CONCLUSION

We have shown that the radius of the sample R_s is a very important parameter that can lead to changes in the shape of the amplitude and phase of the total photoacoustic signal and its elastic components (plasma elastic and thermoelastic) in the frequency domain from 20 Hz to 20 kHz. The analysis includes the total signals with respect to the influence of measuring instruments (distorted signals) and those generated directly by the illuminated sample (undistorted signals). It was found that the largest changes in the total signal due to R_s changes occur in its thermoelastic component amplitude, bearing in mind that the amplitude is proportional to R_S^4. It means that total signal amplitude changes are expected to find only at modulation frequencies $f > 100$ Hz, while at lower frequencies, the total signal amplitude remains the same; i.e., it is not sensitive to R_s changes at all. As it is expected, changes in the PE component amplitude are found to not affect total signal behavior. It was also found that amplitudes of the signals that are distorted under the influence of measuring instruments have similar behavior due to R_s changes. It was determined that the radius of the sample does not affect the change of the thermodiffusion component and that the largest changes in the total undistorted and distorted signals are due to changes in the relationship

between the thermodiffusion and thermoelastic components, which are noticeable in the modulation frequency domain of $f > 100$ Hz. The same relationship changes the phase of total signals in the entire frequency domain.

Numerical simulation created bases of distorted and undistorted signals depending on the sample radius in the range of changes from 2 to 7 mm with a change step of 0.2 mm, which were used for NN1 and NN2 network training, respectively. Through training, it has been shown that both networks achieve satisfactory accuracy after only a few epochs. This means that shallow networks can achieve acceptable performance even with databases created from a small amount of data. Undistorted and distorted signals, out of the base, having the same range of R_s but with a different step of its changes are presented to such trained networks due to the test.

Predictions of both NN1 and NN2 networks proved to be the best for small values of R_s in the range (2–3) mm, close to the dimensions of the microphone aperture ($r_0 = 1.5$ mm). This result indicates the justification of the theoretical approximation, which assumes that $R_s = r_0$. In that case, the correction of the measured signal due to the instrumental influences is not necessary to obtain correct network prediction, which means that the experimental data analysis procedure can be simplified.

When R_s values approach the microphone radius R_0 region, the NN2 network trained with undistorted signals gives better predictions. Both networks give poorer predictions for samples whose radii are larger than R_0. This result leads to the conclusion that the samples used in open photoacoustic cell configuration, whose radii are not larger than the dimensions of the microphone, should be used.

ACKNOWLEDGMENTS

We acknowledge the financial support from the Ministry of Education, Science and Technology Development of the Republic of Serbia (Contract No. 451-03-09/2021-14/200017).

AUTHOR DECLARATIONS

Conflict of Interest

The authors have no conflicts to disclose.

Author Contributions

Katarina Lj. Djordjevic: Conceptualization (equal); Data curation (equal); Formal analysis (equal); Investigation (equal); Methodology (equal); Software (equal); Validation (equal); Visualization (equal); Writing – original draft (equal). **Dragana K Markushev:** Data curation (equal); Formal analysis (equal); Investigation (equal); Resources (equal); Software (equal); Visualization (equal). **Slobodanka Galovic:** Funding acquisition (equal); Investigation (equal); Methodology (equal); Project administration (equal); Supervision (equal); Validation (equal); Writing – review & editing (equal). **Dragan Darivoye Markushev:** Conceptualization (equal); Funding acquisition (equal); Methodology (equal); Project administration (equal); Resources (equal); Supervision (equal); Validation (equal); Visualization (equal); Writing – original draft (equal); Writing – review & editing (equal). **Jose Ordonez-Miranda:** Conceptualization (equal); Methodology (equal); Supervision (equal); Validation (equal); Visualization (equal); Writing – review & editing (equal).

DATA AVAILABILITY

The data that support the findings of this study are available from the corresponding author upon reasonable request.

APPENDIX A: PERIODIC TEMPERATURE COMPONENT IN AN Si SAMPLE

Following the geometry of the problem presented in Fig. 1, we are enabled to use the 1D diffusion equation to describe the temperature changes within the investigated Si sample along the heat propagation axis (z axis),[8,32,33]

$$\frac{\mathrm{d}^2 T_s(z)}{\mathrm{d}z^2} - \sigma^2 T_s(z) = -\frac{1}{k}\left[\frac{\varepsilon - \varepsilon_g}{\varepsilon}\beta I_0 \exp(-\beta z) - \frac{\varepsilon_g}{\tau}\delta n_p(z)\right]. \quad \text{(A1)}$$

The solution $T_s(z)$ to Eq. (3) can be given as a sum of thermalization $T_{\mathrm{therm}}(z)$, bulk $T_{\mathrm{br}}(x)$, and surface $T_{\mathrm{sr}}(x)$ recombination components,[8,32]

$$T_s(z) = T_{\mathrm{therm}}(z) + T_{\mathrm{br}}(z) + T_{\mathrm{sr}}(z), \quad \text{(A2)}$$

defined as

$$T_{\mathrm{therm}}(z) = \frac{I_0}{k}\frac{\varepsilon - \varepsilon_g}{\varepsilon}\frac{\beta}{\beta^2 - \sigma^2}\left[b\frac{e^{\sigma(z-l)} + e^{-\sigma(z-l)} - e^{-\beta l}(e^{\sigma z} + e^{-\sigma z})}{e^{\sigma l} - e^{-\sigma l}} - e^{-\beta z}\right], \quad \text{(A3)}$$

$$T_{\mathrm{br}}(z) = \frac{\varepsilon_g B_1}{\tau k \sigma^2}\left\{\frac{B_2 e^{\sigma z} + B_3 e^{-\sigma z}}{e^{\sigma l} - e^{-\sigma l}} - \frac{1}{c^2 - 1}\left[\frac{\delta n_p(z)}{B_1} + \frac{b^2 - c^2}{b^2 - 1}e^{-\beta z}\right]\right\}, \quad \text{(A4)}$$

$$T_{\mathrm{sr}}(z) = \frac{2\varepsilon_g}{k\sigma}\frac{s_1 \delta n_p(0)\cos h[\sigma(z-l)] + s_2 \delta n_p(l)\cos h(\sigma z)}{e^{\sigma l} - e^{-\sigma l}}, \quad \text{(A5)}$$

where constants are

$$b = \frac{\beta}{\sigma},\ c = \frac{1}{L\sigma},$$

$$B_1 = \frac{\beta I_0}{\varepsilon D_p(\beta^2 - L^{-2})},$$

$$B_2 = B_4 e^{-\sigma l} + B_5,$$

$$B_3 = B_4 e^{\sigma l} + B_5,$$

and

$$B_4 = -c\frac{\frac{1}{B_1}[\delta n_p(l) - \delta n_p(0)\cosh(l/L)] - \cosh(l/L) + e^{-\beta l}}{\sinh(l/L)\cdot(c^2 - 1)} - \frac{b}{b^2 - 1},$$

$$B_5 = c\frac{\frac{1}{B_1}[\delta n_p(l)\cos h(l/L) - \delta n_p(0)] - 1 + e^{-\beta l}\cos h(l/L)}{\sin h(l/L)\cdot(c^2-1)} + \frac{be^{-\beta l}}{b^2-1}.$$

Here, $\sigma = (1+i)/\mu$ is the complex heat diffusion coefficient, $\mu = \sqrt{D/\pi f}$ the thermal diffusion length of the semiconductor, β the semiconductor absorption coefficient, and D the thermal diffusivity. Also, $L = L_p/(1+i2\pi f\tau_p)^{1/2}$ is the complex excess carrier diffusion length, $L_p = \sqrt{D_p\tau_p}$ the minority excess carrier diffusion length, i the complex unit, $\delta n_p(z)$ the photogenerated minority carrier (hole) dynamic density component, D_p the hole diffusion coefficient, τ_p the hole lifetime, and s_1 and s_2 are the surface recombination velocities at front and rear sample surfaces, respectively.

Total temperature and its components at the rear (nonilluminated) side of the sample ($z = l$, $e^{-\beta l} \to 0$) can be written as[8,32]

$$T_s(l) = T_{\text{therm}}(l) + T_{\text{br}}(l) + T_{\text{sr}}(l), \tag{A6}$$

where

$$T_{\text{therm}}(l) = \frac{I_0}{k\sigma}\frac{\varepsilon - \varepsilon_g}{\varepsilon}\frac{\beta^2}{\beta^2-\sigma^2}\frac{1}{\sin h(\sigma l)}, \tag{A7}$$

$$T_{\text{br}}(z) = \frac{\varepsilon_g}{\tau k\sigma^2}\frac{\beta I_0}{\varepsilon D_p(\beta^2 - L^{-2})}\left\{\frac{B_2e^{\sigma l} + B_3e^{-\sigma l}}{2\sin h(\sigma l)} - \frac{1}{c^2-1}\frac{\delta n_p(z)}{B_1}\right\}, \tag{A8}$$

$$T_{\text{sr}}(l) = \frac{\varepsilon_g}{k\sigma}\frac{s_1\delta n_p(0) + s_2\delta n_p(l)\cos h(\sigma l)}{\sin h(\sigma l)}. \tag{A9}$$

APPENDIX B: PERIODIC CARRIER DENSITIES IN AN Si SAMPLE

Considering that the used Si membranes (Fig. 1) are the low-level injection n-type semiconductors (minority carriers are used to explain carrier dynamics), the dynamic part of the 1D diffusion equation (important for sound wave generation) that explains carrier transport in membranes can be written in the form[8,32,33]

$$\frac{\mathrm{d}^2\delta n_p(z)}{\mathrm{d}z^2} - \frac{\delta n_p(z)}{L^2} = -\frac{\beta I_0}{\varepsilon D_p}e^{-\beta z}, \tag{B1}$$

where $L = L_p/(1+i2\pi f\tau_p)^{1/2}$ is the complex excess carrier diffusion length, $L_p = \sqrt{D_p\tau_p}$ the excess carrier diffusion length, i the complex unit, $\delta n_p(z)$ the photogenerated minority (hole) dynamic density component, D_p the hole diffusion coefficient, and τ_p the hole lifetime. The solution $\delta n_p(z,f)$ of Eq. (B1) is given by[8,32,33]

$$\delta n_p(z) = A_+e^{z/L} + A_-e^{-z/L} - Ae^{-\beta z}, \tag{B2}$$

where $A = I_0/(\varepsilon D_p\beta)$, and the integration constants $A_\pm$ are defined by[8,32,33]

$$A_\pm = \frac{A}{\nu_D}\frac{\nu_\beta(\nu_D \pm s_2)e^{\mp l_2/L} - \nu_D(\nu_\beta - s_2)e^{-\beta l_2}}{(\nu_D + s_2)e^{l_2/L} - (\nu_D - s_2)e^{-l_2/L}}, \tag{B3}$$

depending strongly on the relative ratio of the characteristic diffusion speeds $\nu_D = D_p/L$ and $\nu_\beta = \beta D_p$.

REFERENCES

[1] A. Rosencwaig and A. Gersho, "Photoacoustic effect with solids: A theoretical treatment," Science **19**(4214), 556–557 (1975).
[2] A. Rosencwaig and A. Gersho, "Theory of the photoacoustic effect with solids," J. Appl. Phys. **47**, 64 (1976).
[3] F. A. McDonald and G. C. Wetsel, "Theory of photothermal and photoacoustic effects in condensed matter," Phys. Acoust. **18**, 167–277 (1988).
[4] L. Rousset, F. Lepoutre, and L. Bertrand, "Influence of thermoelastic bending on photoacoustic experiments related to measurements of thermal diffusivity of metals," J. Appl. Phys. **54**, 2383 (1983).
[5] A. C. Tam, "Applications of photoacoustic sensing techniques," Rev. Mod. Phys. **58**, 381 (1986).
[6] H. Vargas and L. C. M. Miranda, "Photoacoustic and related photothermal techniques," Phys. Rep. **161**, 43–101 (1988).
[7] S. Bialkowski, *Photothermal Spectroscopy Methods for Chemical Analysis* (John Wiley, New York, 1996), ISBN: 978-0-471-57467-5.
[8] D. M. Todorović and P. M. Nikolic, in *Progress in Photothermal and Photoacoustic Science Technology: Semiconductors and Electronic Materials*, edited by A. Mandelis and P. Hess (SPIE Press, Bellingham, WA, 2000), pp. 271–315, ISBN-13: 978-0819435064.
[9] N. E. Souza Filho, A. C. Nogueira, J. H. Rohling, M. L. Baesso, A. N. Medina, A. P. L. Siqueira, J. A. Sampaio, H. Vargas, and A. C. Bento, "Investigation of doped calcium aluminosilicate glass: A coupling between thermal-expansion and thermal-diffusion models for assessment of nonradiative relaxation time and characteristic diffusion time," J. Appl. Phys. **106**(9), 093105 (2009).
[10] J. L. Pichardo, E. Marín, J. J. Alvarado-Gil, J. G. Mendoza-Alvarez, A. Cruz-Orea, I. Delgadillo, G. Torres-Delgado, and H. Vargas, "Photoacoustic measurements of the thermal properties of $Al_yGa_{1-y}As$ alloys in the region $0 < y < 0.5$," Appl. Phys. A **65**, 69–72 (1997).
[11] M. Nesic, M. Popovic, and S. Galovic, "Developing the techniques for solving the inverse problem in photoacoustics," Atoms **7**(1), 24 (2019).
[12] M. Pawlak, S. Pal, S. Scholz, A. Ludwig, and A. D. Wieck, "Simultaneous measurement of thermal conductivity and diffusivity of an undoped $Al_{0.33}Ga_{0.67}As$ thin film epitaxially grown on a heavily Zn doped GaAs using spectrally-resolved modulated photothermal infrared radiometry," Thermochim. Acta **662**, 69–74 (2018).
[13] S. Galović, Z. A. Stojanović, D. Čevizović, and M. Popović, "Photothermal microscopy: A step from thermal wave visualization to spatially localized thermal analysis,"J. Microsc. **232**(3), 558–561 (2008).
[14] A. Somer, M. N. Popovic, G. K. da Cruz, A. Novatski, E. K. Lenzi, and S. P. Galovic, "Anomalous thermal diffusion in two-layer system: The temperature profile and photoacoustic signal for rear light incidence," Int. J. Thermal Sci. **179**, 107661 (2022).
[15] M. N. Popovic, M. V. Nesic, M. Zivanov, D. D. Markushev, and S. P. Galovic, "Photoacoustic response of a transmission photoacoustic configuration for two-layer samples with thermal memory," Opt. Quantum Electron. **50**(9), 330 (2018).
[16] S. Galović, Z. Šoškić, M. Popović, D. Čevizović, and Z. Stojanović, "Theory of photoacoustic effect in media with thermal memory," J. Appl. Phys. **116**(2), 024901 (2014).
[17] K. Huang, Y. Zhang, J. Lin, and P. Huang, "Nanomaterials for photoacoustic imaging in second near-infrared window," Biomater. Sci. **7**, 472–479 (2019).

[18]A. Somer, F. Camilotti, G. F. Costa, C. Bonardi, A. Novatski, A. V. C. Andrade, V. A. Kozlowski, Jr., and G. K. Cruz, "The thermoelastic bending and thermal diffusion processes influence on photoacoustic signal generation using open photoacoustic cell technique," J. Appl. Phys. **114**(6), 063503 (2013).
[19]A. Somer, A. Gonçalves, T. V. Moreno, G. K. da Cruz, M. L. Baesso, and N. G. C. Astrath, "Photoacoustic signal with two heating sources: Theoretical predictions and experimental results for the open photoacoustic cell technique," Meas. Sci. Technol. **31**(7), 075202 (2020).
[20]J. A. Balderas-Lopez and A. Mandelis, "Self-normalized photothermal technique for accurate thermal diffusivity measurements in thin metal layers," Rev. Sci. Instrum. **74**, 5219 (2003).
[21]M. Isaiev, G. Mussabek, P. Lishchuk, K. Dubyk, N. Zhylkybayeva, G. Yar-Mukhamedova, D. Lacroix, and V. Lysenko, "Application of the photoacoustic approach in the characterization of nanostructured materials," Nanomaterials **12**, 708 (2022).
[22]L. Villegas-Lelovsky, G. Gonzalez de la cruz, and Yu. G. Gurevich, "Electron and phonon thermal waves in semiconductors: The effect of carrier diffusion and recombination on the photoacoustic signal," Thin Solid Films **433**, 371–374 (2003).
[23]A. DiSpirito, T. Vu, M. Pramanik, and J. Yao, "Sounding out the hidden data: A concise review of deep learning in photoacoustic imaging," Exp. Biol. Med. **246**(12), 1355–1367 (2021).
[24]M. Nešić, P. Gusavac, M. Popović, Z. Šoškić, and S. Galović, "Thermal memory influence on the thermoconducting component of indirect photoacoustic response," Phys. Scr. **T149**, 014018 (2012).
[25]E. M. A. Anas, H. K. Zhang, C. Audigier, E. M. Boctor *et al.*, "Robust photoacoustic beamforming using dense convolutional neural networks," in *Simulation, Image Processing, and Ultrasound Systems for Assisted Diagnosis and Navigation. POCUS 2018, BIVPCS 2018, CuRIOUS 2018, CPM 2018*, Lecture Notes in Computer Science, edited by D. Stoyanov (Springer, Cham, 2018), p. 11042.
[26]K. L. Djordjevic, D. D. Markushev, ŽM Ćojbašić, and S. P. Galović, "Inverse problem solving in semiconductor photoacoustics by neural networks," Inverse Probl. Sci. Eng. **29**, 248–262 (2021).
[27]K. L. Djordjevic, D. D. Markushev, Ž. M. Ćojbašić *et al.*, "Photoacoustic measurements of the thermal and elastic properties of n-type silicon using neural networks," Silicon **12**, 1289–1300 (2020).
[28]M. I. Jordović-Pavlović, M. M. Stanković, M. N. Popović *et al.*, "The application of artificial neural etworks in solid-state photoacoustics for the recognition of microphone response effects in the frequency domain," J. Comput. Electron. **19**, 1268–1280 (2020).
[29]R. E. A. Goodall and A. A. Lee, "Predicting materials properties without crystal structure: Deep representation learning from stoichiometry," Nat. Commun. **11**, 6280 (2020).
[30]T. Hu, H. Song, T. Jiang, and S. Li, "Learning representations of inorganic materials from generative adversarial networks," Symmetry **12**(11), 1889 (2020).
[31]K. K. Tho, S. Swaddiwudhipong, Z. S. Liu, and J. Hua, "Artificial neural network model for material characterization by indentation," Model Simul. Mater. Sci. Eng. **12**(5), 1055 (2004).
[32]D. K. Markushev, D. D. Markushev, S. M. Aleksic, D. S. Pantic, S. P. Galovic, D. M. Todorovic, and J. Ordonez-Miranda, "Effects of the photogenerated excess carriers on the thermal and elastic properties of n-type silicon excited with a modulated light source: Theoretical analysis," J. Appl. Phys. **126**(18), 185102 (2019).
[33]D. K. Markushev, D. D. Markushev, S. M. Aleksic, D. S. Pantic, S. P. Galovic, D. M. Todorovic, and J. Ordonez-Miranda, "Experimental photoacoustic observation of the photogenerated excess carrier influence on the thermoelastic response of n-type silicon," J. Appl. Phys. **128**, 095103 (2020).
[34]A. Lachaine, "Thermal analysis by photoacoustic phase measurements: Effect of sample thickness," J. Appl. Phys. **57**(11), 5075–5077 (1985).
[35]G. Wang, Y. Chang, G. Ma, Q. Gua, X. Li, and G. Zhang, "Relation between photoacoustic signal and sample thickness," J. Appl. Phys. **73**(11), 7275–7279 (1993).
[36]R. Burbelo, D. Andrusenko, M. Isaiev, and A. Kuzmich, "Laser photoacoustic diagnostics of advanced materials with different structure and dimensions," Arch. Metall. Mater. **56**(4), 1157 (2011).
[37]D. D. Markushev, M. D. Rabasovic, D. M. Todorovic, S. Galovic, and S. E. Bialkowski, "Photoacoustic signal and noise analysis for Si thin plate: Signal correction in frequency domain," Rev. Sci. Instrum. **86**, 035110 (2015).
[38]M. N. Popovic, M. V. Nesic, S. Ciric-Kostic, M. Zivanov, D. D. Markushev, M. D. Rabasovic, and S. P. Galovic, "Helmholtz resonances in photoacoustic experiment with laser-sintered polyamide including thermal memory of samples," Int. J. Thermophys. **37**(12), 116 (2016).
[39]S. M. Aleksić, D. K. Markushev, D. S. Pantić, M. D. Rabasović, D. D. Markushev, and D. M. Todorović, "Electro-acoustic influence of the measuring system on the photoacoustic signal amplitude and phase in frequency domain," FU Phys. Chem. Technol. **14**(1), 9–20 (2016).
[40]M. V. Nešić, M. N. Popović, and S. P. Galović, "Influence of thermal memory on the thermoelastic bending component of photoacoustic response," Hem. Ind. **65**(3), 219–227 (2011).
[41]A. Domanowsk and R. J. Bukowski, "Theoretical Analysis of Pulsed Photoacoustic Effect in Solids," Int. J. Thermophys. **30**, 1536 (2009).

Journal of Applied Physics

Enhancement of the thermoelastic component of the photoacoustic signal of silicon membranes coated with a thin TiO_2 film

Cite as: J. Appl. Phys. **131**, 085105 (2022); https://doi.org/10.1063/5.0079902
Submitted: 25 November 2021 • Accepted: 07 February 2022 • Published Online: 23 February 2022

D. K. Markushev, D. D. Markushev, S. M. Aleksić, et al.

Journal of Applied Physics ARTICLE scitation.org/journal/jap

Enhancement of the thermoelastic component of the photoacoustic signal of silicon membranes coated with a thin TiO_2 film

Cite as: J. Appl. Phys. **131**, 085105 (2022); doi: 10.1063/5.0079902
Submitted: 25 November 2021 · Accepted: 7 February 2022 ·
Published Online: 23 February 2022

D. K. Markushev,[1] D. D. Markushev,[1] S. M. Aleksić,[2,a)] D. S. Pantić,[2] S. P. Galović,[3] D. V. Lukić,[1] and J. Ordonez-Miranda[4]

AFFILIATIONS

[1]Institute of Physics, University of Belgrade, Pregrevica 118, 11080 Belgrade-Zemun, Serbia
[2]Faculty of Electronic Engineering, University of Niš, Aleksandra Medvedeva 14, 18000 Niš, Serbia
[3]Vinča Institute of Nuclear Sciences, P.O. Box 522, 11001 Belgrade, Serbia
[4]LIMMS, CNRS-IIS UMI 2820, The University of Tokyo, Tokyo 153-8505, Japan

Note: This paper is part of the Special Topic on Non-Invasive and Non-Destructive Methods and Applications Part I – Festschrift.
[a)]**Author to whom correspondence should be addressed:** sanja.aleksic@elfak.ni.ac.rs

ABSTRACT

The reduction of the photogenerated charge carriers' influence in periodically illuminated thin silicon membranes is investigated by using the experimental setup of an open photoacoustic cell in the standard range of modulation frequencies from 20 Hz to 20 kHz. It is confirmed that the deposition of a 200 nm thin film of titanium dioxide on the 30- and 50 μm silicon membrane leads to a large increase of the thermoelastic component of the photoacoustic signal, which restores the flexibility lost to the membrane under the influence of photogenerated carriers. The effect of the thermoelastic component enhancement is analyzed by observing the displacement of the tested samples along the heat propagation axis, depending on the carrier density and temperature differences on the illuminated and unilluminated sides, for different membrane thicknesses and a constant film thickness. It is found that the effect of enhancement of several orders of magnitude is more visible in thinner membranes due to higher ratios between the film and membrane thicknesses.

INTRODUCTION

It is well known that the illumination of semiconductors with a modulated light source can generate charge carriers that cause different types of thermal responses.[1–5] There are various spectroscopic methods within photothermal sciences that can be used to analyze such thermal responses.[6–12] In our previous articles,[13–15] we showed that photoacoustics (PA) is a method by which different thermal responses of semiconductors can be clearly observed under the strong influence of photogenerated carriers by analyzing different patterns of behavior of photoacoustic signals and their components. It was observed that the influences of carriers on the thermal response are most intense in semiconductor membranes having the shape of circular plates with a thickness smaller than the sample carrier diffusion length (so-called plasma-thin samples). A strong decrease in the amplitude of the thermoelastic component and a decrease in the total phase of the photoacoustic signal were observed as a typical pattern of the PA signal behavior in the frequency domain.[13,14] In practical terms, it means that the degree of bending of the illuminated semiconductor membrane decreases under the influence of photogenerated carriers. This is a very significant effect that can affect the reliability, accuracy, and sensitivity of MEMS sensors (e.g., pressure sensors), in which silicon membranes are an integral part.[15] Among the others, the zero and span calibration shifts are the most frequent errors caused by Si membrane illumination. They may be sufficient to cause unacceptable mistakes in the sensor operation process so their avoidance is the ultimate manufacturing goal.

One very important question also arises: is there a way to significantly reduce the influence of photogenerated carriers on the bending degree of illuminated semiconductor membranes?

Our research shows that this can be done by coating the silicon membranes with a thin transparent film on the membrane illuminated side. Such a film should be made of a material that does not generate charge carriers at the light source wavelength, transparent to allow direct membrane excitation, having a thickness relatively large enough to be visible in photoacoustic measurements. Titanium dioxide (TiO_2), with which we already have experience in working with plasma-thick samples,[16,17] appears to be a good thin film candidate.

Here, we measure and analyze photoacoustic signals (amplitudes and phases) generated by the single- (silicon membranes 30- and 50 μm thick) and two-layer samples (30- and 50 μm thick silicon membrane substrate + thin TiO_2 film of constant 200 nm thickness) and monitor the behavior of their thermoelastic components. This is done by using an open photoacoustic cell operating in the transmission configuration with modulation frequencies from 20 Hz to 20 kHz. The relationship between the PA signal thermoelastic component and the thermoelastic bending degree is studied by using the sample displacement as a parameter involved in the applied theoretical model.

THEORETICAL BACKGROUND

The thermal response of a semiconductor sample illuminated by a modulated light source is a consequence of several processes. The first one is the process of light absorption resulting in an increase in the internal energy which leads to the sample heating and temperature gradient formation. Due to the mentioned gradient formation, the thermal-diffusion process starts to transfer heat through the sample periodically changing its temperature in the bulk and on its surfaces. At the same time, the temperature difference on the illuminated and nonilluminated side of the sample results in the process of sample periodic, the so-called thermoelastic bending. In addition, the generation of free carriers on the illuminated side of the sample results in their diffusion through the semiconductor material, periodically changing their concentrations within and on its surfaces. Different concentrations of carriers on different sides of the sample lead to its periodic bending process, the so-called plasma-elastic bending.

All of the mentioned processes are incorporated in the theoretical model of composite pistons,[18,19] the well-known model of photoacoustics. Although this model is basically made for single-layer samples consisting of a pure arbitrary material, it can be easily adapted to multi-layer structures as well. The typical scheme used for thermal response analysis of a two-layer sample (Si substrate + TiO_2 thin film) irradiated from one side by the modulated light source is presented in Fig. 1. The presented scheme is used for the explanation of 1D heat transfer along the heat flow axes parallel to the sample thickness. The samples used in the presented investigation have cylindrical symmetry so cylindrical coordinates are a reasonable choice and heat transfer is assumed to take place along the z axis.

The photoacoustic response of the two-layer sample irradiated with the modulated light source (Fig. 1)[16,17,20] can be theoretically described by the total PA signal $\delta p_{\text{total}}(f)$ defined with the simple equation:[13,14]

$$\delta p_{\text{total}}(f) = \delta p_{\text{TD}}(f) + \delta p_{\text{TE}}(f) + \delta p_{\text{PE}}(f), \tag{1}$$

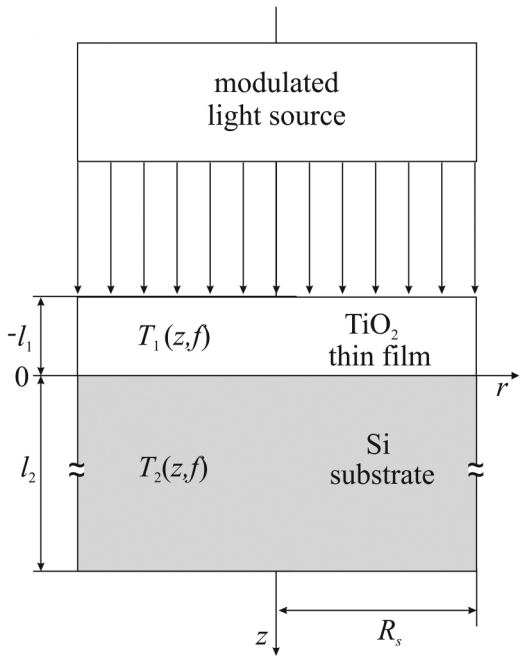

FIG. 1. The simplest scheme of the two-layer sample irradiated by a modulated light source. l_1 and l_2 ($l_1 \ll l_2$) are the thicknesses of the thin film (TiO_2) and the substrate (Si), respectively. R_s is the sample radius, $T_1(z,f)$ is the temperature in the thin film, and $T_2(z,f)$ is the temperature in the substrate.

where f is the modulation frequency and $\delta p_{\text{TD}}(f)$, $\delta p_{\text{TE}}(f)$, and $\delta p_{\text{PE}}(f)$ are the thermal diffusion (TD), thermoelastic (TE), and plasma-elastic (PE) PA signal components, respectively. Using a simple 1D theoretical model,[13,16,17,20] these components can be written as

$$\delta p_{\text{TD}}(f) = \frac{p_0 \gamma_g}{\sigma_g l_c} \frac{T_2(l_2, f)}{T_0}, \tag{2}$$

$$\delta p_c(f) = \frac{\gamma p_0}{V_0} \int_0^{R_s} 2\pi r U_{z,c}(r, z)\mathrm{d}r, \quad c = \text{TE, PE}, \tag{3}$$

where γ is the adiabatic constant, p_0 and T_0 are the equilibrium pressure and temperature of the air in the microphone, $\sigma_g = (1+i)/\mu_g$, μ_g is the thermal-diffusion length of the air, l_c is the PA cell length, $T_2(l_2, f)$ is the dynamic temperature variation at the substrate rear (nonilluminated) surface,[18–20] V_0 is the photoacoustic cell volume, and $U_{z,c}(r,z)$ is the sample displacement along the z axis.

$U_{z,c}(r,z)$ of the two-layer sample at the back surface, $z = l_2$, important in a transmission photoacoustic measurements, can be written in a general form as[16,17,20]

$$U_{z,c}(r, z) = \frac{C_c}{2}(R_s^2 - r^2), \quad c = TE, PE, \tag{4}$$

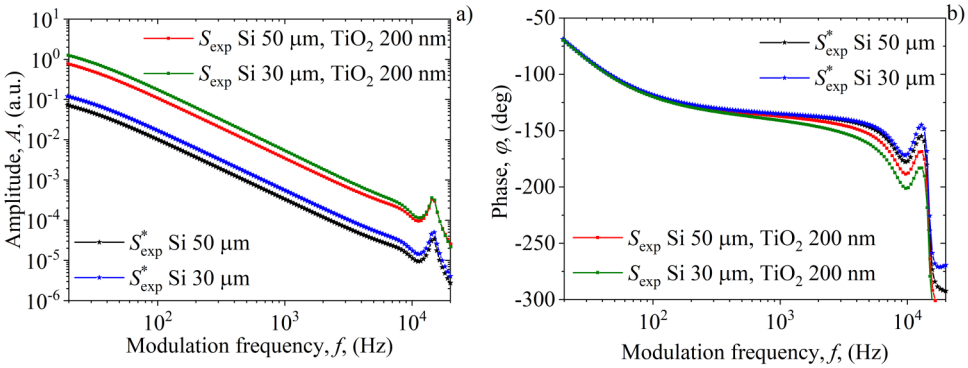

FIG. 2. Experimental photoacoustic signal (a) amplitude A and (b) phase φ of Si membranes with $S_{exp}(f)$ and without $S^*_{exp}(f)$ thin TiO_2 film as a function of modulation frequencies f.

where R_s is the sample radius and

$$C_{TE} = 6\frac{A_1 + A_2 + E_1E_2[\alpha_{T1}l_2(2M_{T1} - l_2N_{T1}) + \alpha_{T2}l_1(2M_{T2} + l_1N_{T2})]}{E_1^2l_1^4 + E_2^2l_2^4 + 2E_2E_1l_2l_1(2l_2^2 + 3l_2l_1 + 2l_1^2)}, \tag{5a}$$

$$C_{PE} = 6d_nE_2\frac{[E_1l_1(2M_n + l_1N_n) + E_2l_2(2M_n - l_2N_n)]}{E_2^2l_2^4 + E_1^2l_1^4 + 2E_2E_1l_2l_1(2l_2^2 + 3l_2l_1 + 2l_1^2)}. \tag{5b}$$

Here, $A_1 = E_1^2l_1(2M_{T1} + l_1N_{T1})\alpha_{T1}$, $A_2 = E_2^2l_2(2M_{T2} - l_2N_{T2})\alpha_{T2}$, E_1 and E_2 are Young's modulus of the film and the substrate, respectively, d_n is the coefficient of electronic deformation, and M_{T1}, M_{T2}, M_n, N_{T1}, N_{T2}, and N_n are defined as[16,17,20]

$$M_{T1} = \int_{-l_1}^{0} zT_1(z,f)\mathrm{d}z,\ M_{T2} = \int_{0}^{l_2} zT_2(z,f)\mathrm{d}z,$$
$$M_n = \int_0^{l_2} z\delta n_p(z,f)\mathrm{d}z, \tag{6}$$

$$N_{T1} = \int_{-l_1}^{0} T_1(z,f)\mathrm{d}z,\ N_{T2} = \int_{0}^{l_2} T_2(z,f)\mathrm{d}z,$$
$$N_n = \int_0^{l_2} \delta n_p(z,f)\mathrm{d}z, \tag{7}$$

where $T_1(z,f)$ is the temperature in the thin film, $T_2(z,f)$ is the temperature in the substrate, and $\delta n_p(z,f)$ is the photogenerated minority carrier density. M_{T1} and M_{T2} are the first moments of the temperature change, and M_n is the first moment of the photogenerated minority carriers change along the $z$axis. N_{T1} and N_{T2} are the average temperature changes and N_n is the average photogenerated minority carriers change along the z axis.

In the case of one-layer sample (Fig. 1, substrate only), Eqs. (1)–(7) reduce to[13,14,18]

$$\delta p^*_{total}(f) = \delta p^*_{TD}(f) + \delta p^*_{TE}(f) + \delta p^*_{PE}(f), \tag{8}$$

$$\delta p^*_{TD}(f) = \frac{p_0\gamma_g}{\sigma_g l_c}\frac{T_2(l_2,f)}{T_0}, \tag{9}$$

$$U^*_{z,TE}(r,z) = \alpha_{T2}\frac{6(R_s^2 - r^2)}{l_2^3}M_{T2},\ M_{T2} = \int_0^{l_2}\left(z - \frac{l_2}{2}\right)T_2(z,f)\mathrm{d}z, \tag{10a}$$

$$U^*_{z,PE}(r,z) = d_n\frac{6(R_s^2 - r^2)}{l_2^3}M_n,\ M_n = \int_0^{l_2}\left(z - \frac{l_2}{2}\right)\delta n_p(z,f)\mathrm{d}z, \tag{10b}$$

$$\delta p^*_{TE}(f) = \alpha_{T2}\frac{\gamma p_0}{V_0}\frac{3\pi R_s^4}{l_2^3}\int_0^{l_2}\left(z - \frac{l_2}{2}\right)T_2(z,f)\mathrm{d}z, \tag{11}$$

and

$$\delta p^*_{PE}(f) = d_n\frac{\gamma p_0}{V_0}\frac{3\pi R_s^4}{l_2^3}\int_0^{l_2}\left(z - \frac{l_2}{2}\right)\delta n_p(z,f)\mathrm{d}z. \tag{12}$$

RESULTS AND DISCUSSION

To check the influence of thin films on the bending degree of illuminated silicon membranes, we measured the amplitude $A(f)$ and phase $\varphi(f)$ of the photoacoustic signal $S(f) = A(f)\exp[i\varphi(f)]$ as functions of the modulation frequency f within the 20 Hz–20 kHz range.[13,16,17] Measurements were carried out for two thicknesses of membranes (50 and 30 μm) with (S_{exp}) and without (S^*_{exp}) the 200 nm-thick TiO_2 thin film coating, illuminated with the laser diode light source having 660 nm wavelength and intensity of $I_0 = 10\ \mathrm{W/m^2}$. The results of such measurements are presented in Fig. 2. All substrate samples used in the presented investigation are made from the same n-type Si wafer ($\langle 100\rangle$, 3–5 Ωcm) in the form of thin circular plates (membranes) having the radius $R_s = 30$ mm. The TiO_2 thin films were deposited on Si membranes using RF sputtering technique.[16]

The amplitudes and phases of the measured photoacoustic signals $S^*_{exp}(f)$ and $S_{exp}(f)$ shown in Figs. 2(a) and 2(b), respectively, were obtained using an open photoacoustic cell apparatus operating in the transmission mode, described in detail in our previous

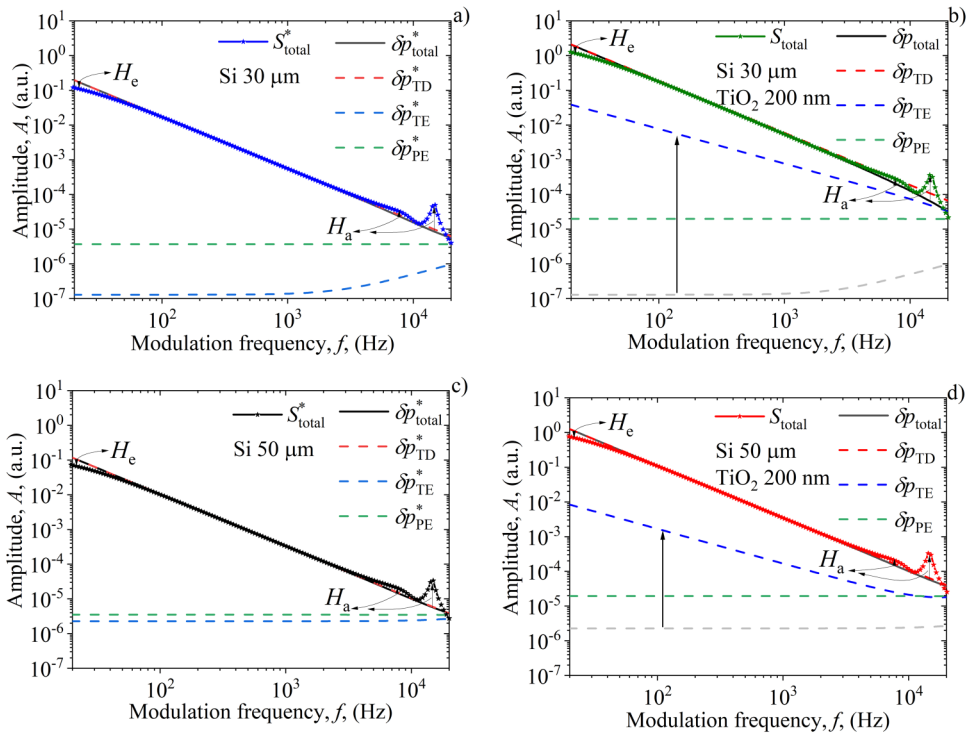

FIG. 3. Experimental (asterisks) and corrected (solid line) total photoacoustic signals along with the corresponding components (dashed lines) for the amplitudes A of the Si membranes without $S_{exp}(f)$ [(a) and(c)] and with $S_{exp}(f)$ [(b) and(d)] a thin TiO_2 film, as functions of the modulation frequency f.

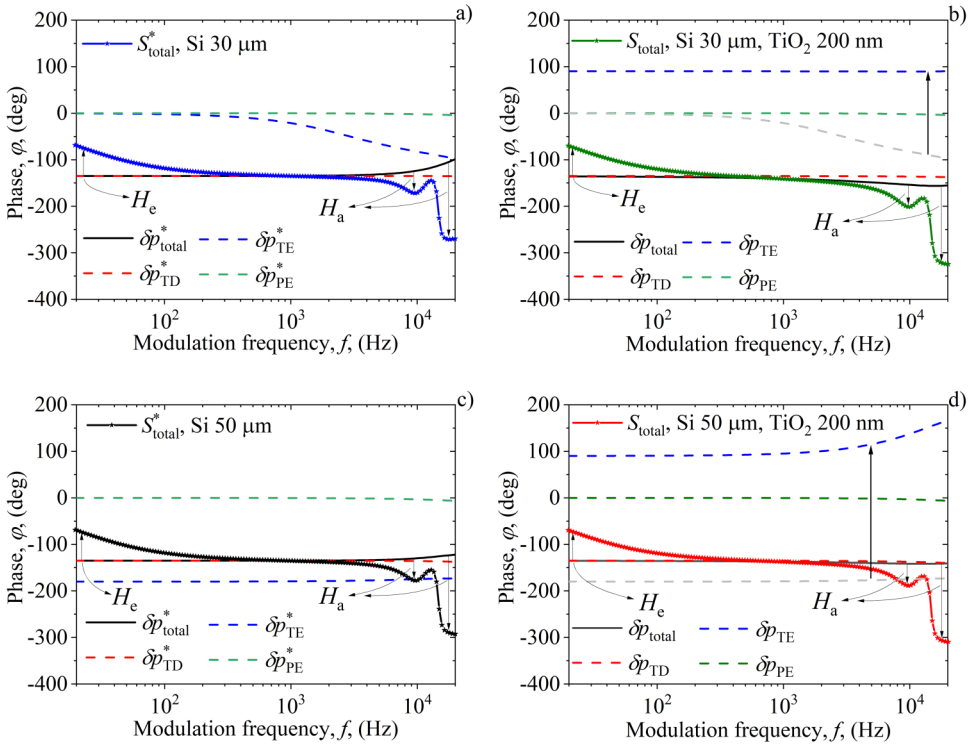

FIG. 4. Experimental (asterisks) and corrected (solid line) total photoacoustic signals along with the corresponding signal components (dashed lines) for the phases φ of the Si membranes without $S_{exp}(f)$ [(a) and(c)] and with $S_{exp}(f)$ [(b) and(d)] a thin TiO_2 film, as functions of the modulation frequency f.

TABLE I. Basic Si and TiO_2 parameters obtained after signal correction procedure.

	Si	TiO_2
β (10^5/m)	(2.6 + 0.2)	(1.8 + 0.4)
D_T (10^{-6} m^2/s)	(9.0 + 0.1)	(3.9 + 0.5)
α_T (10^{-6}/K)	(2.6 + 0.2)	(11 + 2)
k (W/mK)	(150 + 2)	(10 + 3)

articles.[13,14] All these signals are a complex combination of the "real" photoacoustic signals $\delta p^*_{\text{total}}(f)$ [Eq. (8)] and $\delta p_{\text{total}}(f)$ [Eq. (1)] that come directly from the illuminated samples and their electronic $H_e(f)$ and acoustic $H_a(f)$ deviations caused by the influence of measuring instruments[13,20] (Appendix A),

$$S^*_{\text{exp}}(f) = \delta p^*_{\text{total}}(f) H_e(f) H_a(f) \tag{13}$$

and

$$S_{\text{exp}}(f) = \delta p_{\text{total}}(f) H_e(f) H_a(f). \tag{14}$$

The influence of measuring instruments can be simply described as electronic filtering (H_e) which reduces the signal amplitude in the low-frequency range, and acoustic filtering (H_a) which generates typical signal peaks at higher frequencies (Figs. 3 and 4, Appendix A), usually recognized as shaped, or tailored, microphone frequency response.[21] The measured signals $S^*_{\text{exp}}(f)$ and $S_{\text{exp}}(f)$ are corrected by the well-known procedure of recognizing and removing H_e and H_a[13,21] in order to obtain $\delta p^*_{\text{total}}(f)$, $\delta p_{\text{total}}(f)$, and corresponding basic sample parameters: coefficient of optical absorption β, thermal diffusivity D_T, coefficient of thermal expansion α_T, and thermal conductivity k. The results of such procedures are presented in Table I. They are in accordance with the literature values obtained by different methods[22–25] and our previous research.[13,16] Other important parameters, like Young's modulus of the film ($E_1 = 280$ GPa) and the substrate ($E_2 = 137$ GPa), the coefficient of electronic deformation ($d_n = -9.0 \times 10^{-31}$ m^3) and photogenerated carriers' lifetime ($\tau = 6 \times 10^{-6}$ s) are taken from the same literature.[13,16,22–25]

Based on the composite piston theory,[18] obtained $\delta p^*_{\text{total}}(f)$ and $\delta p_{\text{total}}(f)$ are disassembled into three signal components—TD, TE, and PE, whose amplitudes and phases are shown in Figs. 3(a), 3(c), 4(a), and 4(c) in the case of single-layer [Si membranes, Eqs. (8)–(12)] and Figs. 3(b), 3(d), 4(b), and 4(d) in the case of two-layer systems [Si membrane + thin TiO_2 film, Eqs. (1)–(7)].

The changes in the mutual relationships of the photoacoustic signal components are clearly visible in Figs. 3 and 4. They are caused by the deposition of a thin TiO_2 film on both membrane thicknesses. Larger mutual relationship changes are detected in the case of the thinner substrate (30 μm), where the amplitude of the total signal decreases at higher frequencies more intensely (up to 35% lower values) in the case of the two-layer system [Fig. 3(b)] compared to the pure silicon [Fig. 3(a)]. In the case of the thicker substrate (50 μm), total amplitude decrease is much lower: up to 5% lower values in the case of the two-layer system [Fig. 3(d)] at middle frequencies compared to the pure silicon [Fig. 3(c)]. At the same time, the total phase in pure silicon [Fig. 4(a) and 4(c)] at higher frequencies increases, but in the case of a two-layer system [Figs. 4(b) and 4(d)], total phase decreases. One can conclude that explained effects of the total PA amplitudes and phases behavior in the frequency domain are more intense in the case of thinner substrates.[13,14]

Comparing Figs. 3(a), 3(c) and 3(b), 3(d), it is obvious that the amplitude of the thermoelastic component (blue dashed line) undergoes the greatest changes: (a) for pure silicon, under the action of photogenerated carriers, TE amplitude at low frequencies drops to $\sim 10^{-7}$ [Fig. 3(a)] and $\sim 10^{-6}$ [Fig. 2(c)], changing its functional dependence at higher frequencies[13,14] and (b) TE amplitude of the two-layer system increases up to $\sim 10^{-1}$ [Fig. 3(b)] and $\sim 10^{-2}$ [Fig. 3(d)] at lower frequencies, decreasing in the entire frequency domain up to $\sim 10^{-4}$ [Fig. 3(b)] and $\sim 10^{-5}$ [Fig. 2(d)] at higher frequencies. For clarity, in Figs. 3(b) and 3(c), the thermoelastic components of the pure silicon samples are marked with dashed gray lines so that the increase in the thermoelastic component, which is indicated by arrows, can be more noticeable.

In phases (Fig. 4), as in amplitudes, the thermoelastic component (blue dashed line) suffers the largest changes, which is indicated by the arrows in Figs. 4(b) and 4(d), where the dashed gray line represents the thermoelastic component phase of pure silicon samples [Figs. 4(a) and 4(c)].

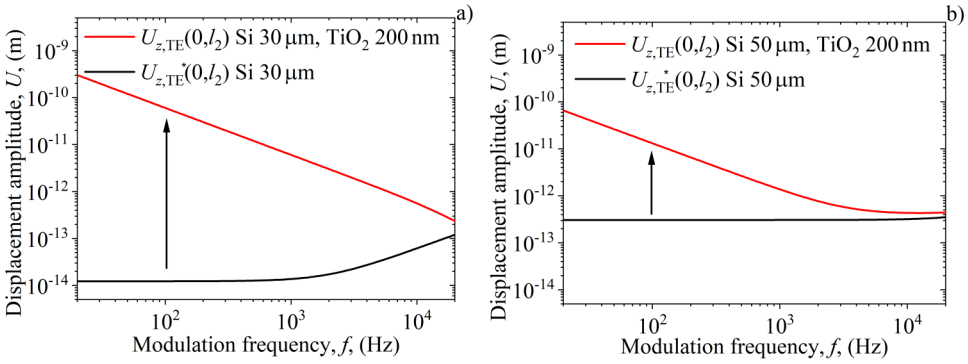

FIG. 5. Thermoelastic displacements of the (a) 30 and (b) 50 μm Si membranes with $U_{z,TE}(r, z)$ and without $U^*_{z,TE}(r, z)$ a thin TiO_2 film, as functions of modulation frequency f.

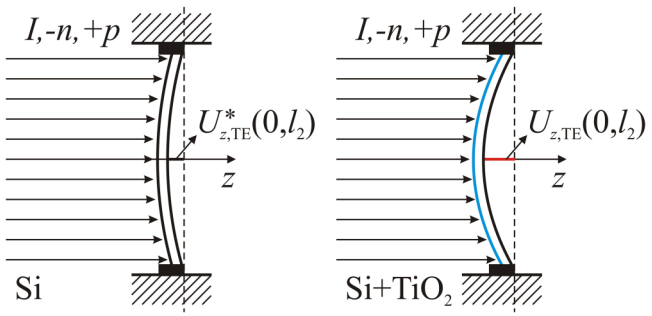

FIG. 6. Schemes of the thermoelastic displacement of the irradiated Si membranes with $U_{z,\mathrm{TE}}(r, z)$ and without $U^{\star}_{z,\mathrm{TE}}(r, z)$ a thin TiO_2 film (blue line), where photogenerated electrons (–*n*) and holes (+*p*) are present.

Analyzing Eqs. (3) and (11), one can conclude that the presented thermoelastic component amplitude behavior in all cases (Fig. 3) was guided by the displacements of the sample along the *z*axis $U_{z,\mathrm{TE}}(r, z)$. Following such behavior, the results of $U^{\star}_{z,\mathrm{TE}}(r, z)$ [Eq. (10a)] and $U_{z,\mathrm{TE}}(r, z)$ [Eqs. (4)–(6)], for both substrate thicknesses in the case of $z = l_2$ and $r = 0$ in the whole range of modulation frequencies are presented in Fig. 5, where clear differences can be seen between "pure" and "coated" membranes.

In the generalized scheme, displacements of membranes of different thicknesses with and without a thin film (Fig. 5) can be simply represented as in Fig. 6. Regardless of the thickness of the substrate, the $U^{\star}_{z,\mathrm{TE}}(r, z) < U_{z,\mathrm{TE}}(r, z)$ ratio will always apply.

To find the cause of differences between $U^{\star}_{z,\mathrm{TE}}(r, z)$ and $U_{z,\mathrm{TE}}(r, z)$, one needs to analyze the changes in C_{TE} values [Eq. (5a)]. It is obvious that these changes depend on the mutual relationships between M_{T1} and N_{T1} and M_{T2} and N_{T2}. Changes in the first moments and/or average temperature changes can lead to the changes in C_{TE} and, thus, in $U_{z,\mathrm{TE}}(r, z)$ changes. The first moments and average temperatures depend on the temperature distribution in the sample, and temperature distribution depends on the density distribution of the photogenerated carriers. This is the reason why one can attribute all changes in $U^{\star}_{z,\mathrm{TE}}(r, z)$ and $U_{z,\mathrm{TE}}(r, z)$ behavior to changes in differences in the photogenerated carrier densities $\Delta\delta n^{\star}_p$, $\Delta\delta n_p$, and temperatures $\Delta T^{\star}_2$, ΔT_2, at the substrate surfaces (illuminated, $z = 0$, and nonilluminated, $z = l_2$) defined by

$$\Delta\delta n^{\star}_p = \delta n^{\star}_p(0) - \delta n^{\star}_p(l_2),\ \Delta\delta n_p = \delta n_p(0) - \delta n_p(l_2)$$

and

$$\Delta T^{\star}_2 = T^{\star}_2(0) - T^{\star}_2(l_s),\ \Delta T_2 = T_2(0) - T_2(l_s).$$

The analysis results are presented in Table II, where all carrier densities (Appendix B) and substrate temperatures (Appendix C) correspond to the calculated sample displacements $U^{\star}_{z,\mathrm{TE}}(0, l_2)$ and $U_{z,\mathrm{TE}}(0, l_2)$ (Fig. 5) for both substrate thicknesses l_2 and three characteristic modulation frequencies (100, 1000, and 20 000 Hz). One must always bear in mind that $T_1(0) = T_2(0)$ (Fig. 1) is one of the boundary conditions for temperature calculations (Appendix B).

The results presented in Table II show that the film deposition on the substrate reduces the differences in carrier density ($\Delta\delta n_p < \Delta\delta n^{\star}_p$) and temperatures ($\Delta T_2 < \Delta T^{\star}_2$) on the illuminated and unilluminated sides of the sample. These reductions indicate a decrease in the influence of free carriers, i.e., an increase in the degree of bending (flexibility) which is the main goal of this work. The influence of carrier and temperature decrease on $U_{z,\mathrm{TE}}(0, l_2)$ is larger at lower frequencies, while at higher ones, such an influence is reflected through the dominant mutual relationship between M_{T2} and N_{T2}: the impact of the film becomes insignificant. Also, $U_{z,\mathrm{TE}}(0, l_2)$ is larger for thinner substrates, which is expected, since $U_{z,\mathrm{TE}} \sim l_2^{-3}$ [Eqs. (4), (5), and (10)].

CONCLUSIONS

The enhancement of the thermoelastic component of the photoacoustic signal measured by using an open photoacoustic cell for plasma-thin silicon samples with a thin layer of TiO_2 has been studied. The photoacoustic theory for two-layer samples consisting of a substrate in the form of 30- and 50-μm thick Si membranes, and a 200 nm-thick TiO_2 film has been used in the data analysis. These substrate thicknesses are smaller than the diffusion length of the heat carriers, while the film is thick enough to be well visible for photoacoustic measurements. It has been found that the TiO_2 film

TABLE II. Temperatures at sample surfaces (illuminated and nonilluminated), their differences and ratios, together with sample displacements of Si and Si + TiO_2 at characteristic modulation frequencies.

f (Hz)	$\Delta\delta n^{\star}_p(10^{18}\ \mathrm{m}^{-3})$	$\Delta\delta n_p(10^{18}\ \mathrm{m}^{-3})$	$\Delta T^{\star}_2\ (10^{-10}\ \mathrm{K})$	$\Delta T_2\ (10^{-10}\ \mathrm{K})$	$U^{\star}_{z,\mathrm{TE}}(0, l_2)\ (10^{-13}\ \mathrm{m})$	$U_{z,\mathrm{TE}}(0, l_2)(10^{-13}\ \mathrm{m})$
$l_2 = 30\ \mu$m						
100	3.083 53	2.974 50	−14.99	−13.573	0.1232	609.41
1000	3.083 45	2.974 42	−155.92	−141.16	0.1381	152.96
20 000	3.055 48	2.947 44	−2926.2	−2636.7	1.2131	2.3370
$l_2 = 50\ \mu$m						
100	4.906 65	4.733 15	−12.67	−4.21	3.065	132.52
1000	4.906 37	4.732 88	−138.26	−43.7	2.5486	13.4
20 000	4.801 61	4.631 83	−1626.9	−101.3	3.3993	4.43

enhances both the amplitude and phase of the thermoelastic component of the photoacoustic signal of the entire two-layer system. This enhancement is a direct consequence of the sample displacement along the heat propagation axis, such that larger displacements are obtained for the thinner substrate (30 μm). This is reasonable as the displacement of a two-layer sample is inversely proportional to the (thickness)^3 of the substrate. Based on the analysis of the photogenerated carrier densities and temperature differences at the illuminated and nonilluminated sides of the samples, for three characteristic modulation frequencies, it has been shown that the displacement of two-layer samples is larger than that of the single-layer ones. The TiO_2 film, therefore, suppresses the influence of the photogenerated carriers and enhances the bending of the sample described by the thermoelastic component of the photoacoustic signal. The obtained results, thus, show that the loss of flexibility of Si samples induced by photogenerated carriers can be overcome by depositing a thin transparent TiO_2 film on the illuminated Si side, which can be useful for developing MEMS and the electronic industry in general.

ACKNOWLEDGMENTS

This work was supported by the Ministry of Education, Science and Technological Development of the Republic of Serbia, within the institutional financing, Contract No. 451-03-09/2021-14/200017.

AUTHOR DECLARATIONS

Conflict of Interest

The authors have no conflicts to disclose.

DATA AVAILABILITY

The data that support the findings of this study are available from the corresponding author upon reasonable request.

APPENDIX A: THE INFLUENCE OF MEASURING INSTRUMENTS ON THE PHOTOACOUSTIC SIGNAL

The photoacoustic signal generated by the sample excited by the modulated light source contains various influences of the instruments used in its measurement. A detailed analysis determines that such influences arise mostly from the microphones used in measurements and accompanying electronics. These effects are reflected in signal distortion due to different types of filtering at low and high frequencies.[13,21]

At low frequencies (<1 kHz), the PA signal is distorted in a way typical for the high-pass filters: amplitude decreases and phase increases with decreasing frequencies (Fig. 7). The degree of distortion is described by the cascade connection of the *RC* low-pass filters. Each filter corresponds to one instrument with characteristic *RC* values. Therefore, low-frequency filtering of photoacoustic signals is called electronic filtering described by the $H_e(f)$ function,[13,21]

$$H_e(f) = -\frac{\omega\tau_{c1}}{(1+i\omega\tau_{c1})} \times \frac{\omega\tau_{c2}}{(1+i\omega\tau_{c2})}, \tag{A1}$$

where $\omega = 2\pi f$, f is the modulation frequency, and $\tau_{c1} = (2\pi f_{c1})^{-1} = R_1C_1$ and $\tau_{c2} = (2\pi f_{c2})^{-1} = R_2C_2$ are the time constants and *RC* characteristics of the microphone (A1) and signal processing electronics (A2) (usually the sound-card or lock-in).

At high frequencies (>1 kHz), the PA signal is distorted in a way typical for the low-pass filters: sharp jumps and falls of amplitude and phase values occur which gives typical peak structure responses (Fig. 8). The size and shape of peaks with characteristic frequencies and dumping factors are described by the sum of low-frequency *RCL* filters. Since the peaks are a typical high-frequency microphone response caused by its acoustic characteristics, filtering in the high-frequency region is called acoustic filtering described by the function $H_a(f)$,[13,21]

$$H_a(f) = \frac{\omega_{c3}^2}{\omega_{c3}^2 + i\delta_{c3}\omega_{c3}\omega - \omega^2} + \frac{\omega_{c4}^2}{\omega_{c4}^2 + i\delta_{c4}\omega_{c4}\omega - \omega^2}, \tag{A2}$$

where δ_k is the damping factor ($k = c3,c4$), ω_{c3} is the microphone cut-off frequency, and ω_{c4} is the characteristic frequency which depends on the geometry of the microphone body.

Characteristic PA signal distortion, $H_e(f)$ and $H_a(f)$, parameters calculated from our presented and previous measurements,[13] used here to draw Figs. 7 and 8, are presented in Table III.

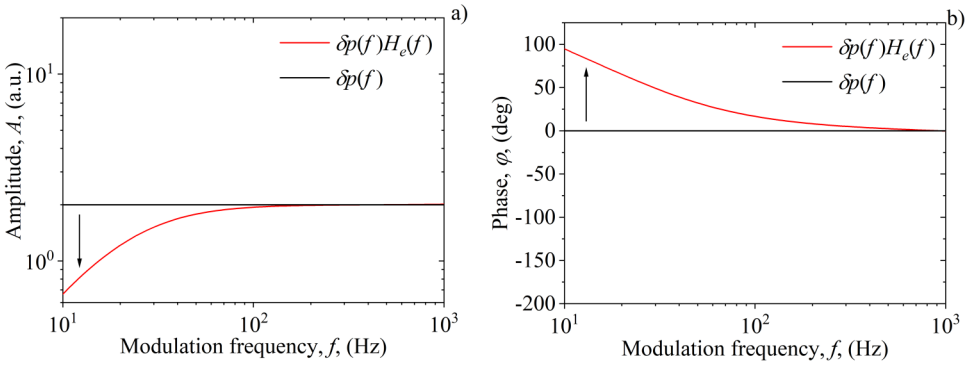

FIG. 7. Typical signal distortion (red line) of the (a) amplitude A and (b) phase φ for modulation frequencies $f < 1$ kHz.

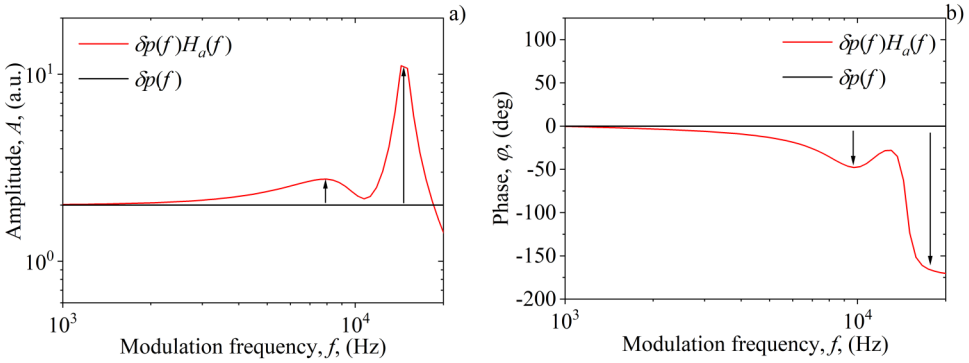

FIG. 8. Typical signal distortion (red line) at high frequencies with (a) amplitude A and (b) phase φ behavior at modulation frequencies $f > 1$ kHz.

APPENDIX B. PERIODIC CARRIER DENSITIES IN THE SI SUBSTRATE

Within photoacoustics, photogenerated carrier density calculations are based on Fick's second law of diffusion, assuming that electrons and holes are generated in pairs as identical particles neglecting their electrical nature. Considering that the used Si membranes (Fig. 1) are the low-level injection n-type semiconductors (minority carriers are used to explain carrier dynamics), the dynamic part of the 1D diffusion equation (important for sound wave generation) that explains carrier transport in membranes can be written in the form[13–15]

$$\frac{\mathrm{d}^2\delta n_p(z,f)}{\mathrm{d}z^2} - \frac{\delta n_p(z,f)}{L^2} = -\frac{\beta I_0}{\varepsilon D_p} e^{-\beta z}, \tag{B1}$$

where $L = L_p/(1 + i2\pi f\tau_p)^{1/2}$ is the complex excess carrier diffusion length, $L_p = \sqrt{D_p\tau_p}$ is the excess carrier diffusion length, i is the complex unit, $\delta n_p(z,f)$ is the photogenerated minority (holes) dynamic density component, D_p is the holes diffusion coefficient, and τ_p is their lifetime. The solution $\delta n_p(z,f)$ of Eq. (17) is given by[13–15]

$$\delta n_p(z) = A_+ e^{z/L} + A_- e^{-z/L} - Ae^{-\beta z}, \tag{B2}$$

where $A = I_0/(\varepsilon D_p\beta)$ and the integration constants $A_\pm$ are defined by[13–15]

$$A_\pm = \frac{A}{v_D}\frac{v_\beta(v_D \pm s_2)e^{\mp l_2/L} - v_D(v_\beta - s_2)e^{-\beta l_2}}{(v_D + s_2)e^{l_2/L} - (v_D - s_2)e^{-l_2/L}}, \tag{B3}$$

TABLE III. Characteristic PA signal distortion He and Ha parameters used to obtain Figs. 7 and 8.

Characteristic frequency f_{c1} (Hz)	25
Characteristic frequency f_{c2} (Hz)	5
Characteristic frequency f_{c3} (Hz)	9400
Characteristic frequency f_{c4} (Hz)	14 700
Damping factor δ_{c3}	0.6
Damping factor δ_{c4}	0.08

depending strongly on the relative ratio of the characteristic diffusion speeds $v_D = D_p/L$ and $v_\beta = \beta D_p$.

APPENDIX C. PERIODIC TEMPERATURE DISTRIBUTIONS IN THE THIN TiO_2 FILM AND THE SI SUBSTRATE

Periodic temperature distributions in the thin film (1-TiO_2) and the substrate (2-Si) illuminated by the modulated light source (Fig. 1) can be obtained by solving the thermal-diffusion equations in the form[16,17,20]

$$\frac{\partial^2 T_1(z,f)}{\partial z^2} - \frac{i\omega}{D_{T1}} T_1(z,f) = -\frac{1}{k_1}\beta_1(1 - R_1)I_0 e^{-\beta_1 z} \tag{C1}$$

and

$$\frac{\partial^2 T_2(z,f)}{\partial z^2} - \sigma_2^2 T_2(z,f) = -\frac{\varepsilon_g}{k_2\tau_2} n_p(z,f) - \frac{\beta_2 I}{k_2} \times \frac{\varepsilon - \varepsilon_g}{\varepsilon} e^{-\beta_2 z}, \tag{C2}$$

where $\omega = 2\pi f$, f is the modulation frequency, I_0 is the incident light intensity, $I = (1 - R_1)(1 - R_2)e^{-\beta_1 l_1} I_0$, R_1 is the film reflection coefficient, R_2 is the substrate reflection coefficient, $\sigma_1 = \sqrt{i\omega/D_{T1}}$ is the film complex thermal diffusivity, D_{T1} is the film thermal-diffusion coefficient, $\sigma_2 = \sqrt{i\omega/D_{T2}}$ is the substrate complex thermal diffusivity, D_{T2} is the substrate thermal-diffusion coefficient, k_1 is the thin film heat conduction coefficient, k_2 is the substrate heat conduction coefficient, β_1 is the film absorption coefficient, β_2 is the substrate absorption coefficient and $\delta n_p(z,f)$ is the photogenerated minority carrier dynamic density component [Eq. (18)].

The general solutions of Eqs. (17) and (18) can be written in the form[20]

$$T_1(z,f) = A_1 e^{\sigma_1 z} + A_2 e^{-\sigma_1 z} + A_3 e^{-\beta_1 z} \tag{C3}$$

and

$$T_2(z,f) = B_1 e^{\sigma_2 z} + B_2 e^{-\sigma_2 z} + B_3 n_p(z,f) + B_4 e^{-\beta_2 z}, \tag{C4}$$

where the constants A_3, B_3, and B_4 are given as

$$A_3 = -\frac{\beta_1 I_0(1-R_1)}{k_1(\beta_1^2-\sigma_1^2)},\quad B_3 = -\frac{\varepsilon_g}{k_2\tau_{p2}\left(\sigma_2^2-\frac{1}{L^2}\right)},$$

$$B_4 = -\frac{\beta_2(1-R_1)(1-R_2)e^{-\beta_1 l_1}I_0}{\varepsilon(\beta_2^2-\sigma_2^2)}\left(\frac{B_3}{D_p}-\frac{\varepsilon-\varepsilon_g}{k_2}\right).$$

Constants A_1, A_2, B_1, and B_2 can be found by solving the following boundary conditions:[20]

$$\begin{aligned}
&\text{(a)} \quad -k_1\left.\frac{\partial T_1(z,f)}{\partial z}\right|_{z=-l_1} = 0,\\
&\text{(b)} \quad T_1(0,f) = T_2(0,f),\\
&\text{(c)} \quad -k_2\left.\frac{\partial T_2(z,f)}{\partial z}\right|_{z=0} = s_F n_p(0,f)\varepsilon_g - k_1\left.\frac{\partial T_1(z,f)}{\partial z}\right|_{z=0},\\
&\text{(d)} \quad -k_2\left.\frac{\partial T_2(z,f)}{\partial z}\right|_{z=l_2} = -s_R n_p(l_2,f)\varepsilon_g,
\end{aligned} \tag{C5}$$

where s_F and s_R are the substrate surface recombination speeds at the front ($z=0$) and rear ($z=l_2$) surfaces, respectively. Based on our previous investigations,[13–17,20] the analysis of the two-layer optical properties shows that the multiple optical reflections can be neglected in the Si substrate,[13] but must be taken into account in the case of the thin TiO_2 film. This is the reason why the film reflection coefficient R_1 is calculated here using[16,17]

$$R_1 = r_F + (1-r_F)^2 r_R \times \frac{e^{-2\beta_1 l_1}}{1-r_F r_R e^{-2\beta_1 l_1}}, \tag{C6}$$

where r_F and r_R are the front and rear thin-film reflectivity coefficients, respectively.

REFERENCES

[1]M. Kaviany, *Heat Transfer Physics*, 2nd ed. (Cambridge University Press, Cambridge, 2014), ISBN 978-1-107041783.
[2]D. K. Ferry, *Semiconductors, Bonds and Bands* (IOP Publishing Ltd, Bristol, 2013).
[3]I. Lashkevych, O. Titov, and Y. G. Gurevich, "Recombination and temperature distribution in semiconductors," Semicond. Sci. Technol. **27**, 055014 (2012).
[4]S. Volz, *Microscale and Nanoscale Heat Transfer (Topics in Applied Physics)* (Springer, 2010), ISBN 978-3642071584.
[5]S. S. Li, "Excess carrier phenomenon in semiconductors," in *Semiconductor Physical Electronics*, edited by S. S. Li (Springer, New York, 2006).
[6]S. E. Bialkowski, N. G. C. Astrath, and M. A. Proskurnin, "Photothermal spectroscopy methods," in *Chemical Analysis: A Series of Monographs on Analytical Chemistry and Its Applications* (John Wiley & Sons, New York, 2019), ISBN: 9781119279075.
[7]M. Pawlak, "Photothermal, photocarrier, and photoluminescence phenomena in semiconductors studied using spectrally resolved modulated infrared radiometry: Physics and applications," J. Appl. Phys. **126**, 150902 (2019).
[8]D. Foumier, A. C. Boccara, A. Skumanish, and N. M. Amer, "Photothermal investigation of transport in semiconductors: Theory and experiment," J. Appl. Phys. **59**, 787 (1986).
[9]Y. G. Gurevich and I. Lashkevych, "Sources of fluxes of energy, heat, and diffusion heat in a bipolar semiconductor: Influence of nonequilibrium charge carriers," Int. J. Thermophys. **34**, 341 (2013).
[10]Y. G. Gurevich and J. E. Velázquez-Pérez, "The role of non-equilibrium charge carriers in thermoelectric cooling," J. Appl. Phys. **114**, 033704 (2013).
[11]*Photoacoustic and Thermal Wave Phenomena in Semiconductors*, edited by A. Mandelis (Elsevier, New York, 1987).
[12]Semiconductors and Electronic Materials, in *Progress in Photothermal and Photoacoustic Science and Technology*, edited by A. Mandelis and P. Hess (SPIE Press, Washington, 2000).
[13]D. K. Markushev, D. D. Markushev, S. M. Aleksić, D. S. Pantić, S. P. Galović, D. M. Todorović, and J. Ordonez-Miranda, "Experimental photoacoustic observation of the photogenerated excess carrier influence on the thermoelastic response of n-type silicon," J. Appl. Phys. **128**, 095103 (2020).
[14]D. K. Markushev, D. D. Markushev, S. M. Aleksić, D. S. Pantić, S. P. Galović, D. M. Todorović, and J. Ordonez-Miranda, "Effects of the photogenerated excess carriers on the thermal and elastic properties of n-type silicon excited with a modulated light source: Theoretical analysis," J. Appl. Phys. **126**, 185102 (2019).
[15]D. K. Markushev, D. D. Markushev, S. P. Galovic, S. M. Aleksic, D. S. Pantic, and D. M. Todorovic, "The surface recombination velocity and bulk lifetime influences on photogenerated carrier density and temperature distributions in n-type silicon excited by a frequency-modulated light source," FU Ser. Elec. Energ. **31**(2), 313–328 (2018).
[16]D. M. Todorović, M. D. Rabasović, D. D. Markushev, and M. Sarajlić, "Photoacoustic elastic bending in thin film–substrate system: Experimental determination of the thin film parameters," J. Appl. Phys. **116**, 053506 (2014).
[17]D. M. Todorović, M. D. Rabasović, and D. D. Markushev, "Photoacoustic elastic bending in thin film–substrate system," J. Appl. Phys. **114**, 213510 (2013).
[18]F. A. McDonald and G. C. Wetsel, Jr, "Theory of photothermal and photoacoustic effects in condensed matter," in *Physical Acoustics* (Academic Press, 1988), Vol. 18, Chap. 4, pp. 167–277.
[19]A. Rosencwaig, "Thermal wave characterization and inspection of semiconductor materials and devices," in *Photoacoustic and Thermal Wave Phenomena in Semiconductors*, edited by A. Mandelis (Elsevier Publishing Company, 1987), pp. 97–135.
[20]N. Jovančić, D. K. Markushev, D. D. Markushev, S. M. Aleksić, D. S. Pantić, D. Korte, and M. Franko, "Thermal and elastic characterization of nanostructured Fe_2O_3 polymorphs and TiO_2-coated Fe_2O_3 using open photoacoustic cell," Int. J. Thermophys. **41**, 90 (2020).
[21]D. D. Markushev, M. D. Rabasović, D. M. Todorović, S. Galović, and S. E. Bialkowski, "Photoacoustic signal and noise analysis for Si thin plate: Signal correction in frequency domain," Rev. Sci. Instrum. **86**, 035110 (2015).
[22]M. H. Shinen, S. A. A. AlSaati, and F. Z. Razooqi, "Preparation of high transmittance TiO_2 thin films by sol-gel technique as antireflection coating," J. Phys. Conf. Ser. **1032**, 012018 (2018).
[23]A. Kot, M. Radecka, D. Dorosz, and K. Zakrzewska, "Optically active TiO_2:Er thin films deposited by magnetron sputtering," Materials **14**, 4085 (2021).
[24]I. Sta, M. Jlassi, M. Hajji, M. F. Boujmil, R. Jerbi, M. Kandyla, M. Kompitsas, and H. Ezzaouia, "Structural and optical properties of TiO_2 thin films prepared by spin coating," J. Sol-Gel Sci. Technol. **72**, 421–427 (2014).
[25]See https://www.azom.com/properties.aspx?ArticleID=1179 for information about the thermoelastic properties of TiO_2.

Silicon
https://doi.org/10.1007/s12633-022-01723-6

ORIGINAL PAPER

Photoacoustic Analysis of Illuminated Si-TiO_2 Sample Bending Along the Heat-Flow Axes

S. M. Aleksić[1] · D. K. Markushev[2] · D. D. Markushev[2] · D. S. Pantić[1] · D. V. Lukić[2] · M. N. Popović[3] · S. P. Galović[3]

Received: 30 November 2021 / Accepted: 26 January 2022

Abstract
This paper describes the influence of thin transparent film on thermal and elastic characteristics of the two-layer sample consisting of the silicon substrate and thin TiO_2 film using analysis of photoacoustic signals and their components in the 20 Hz – 20 kHz frequency domain. Through thermoelastic component changes, it was found that the thin film significantly changes the thermal state of the substrate and makes the degree of its bending increase drastically. The relationships between the thermoelastic component, the displacement along the heat flux axis and the difference of carrier density and temperatures on the different sides of the sample are described. It has been shown that the addition of a thin transparent film to a silicon substrate can effectively reduce the influence of photogenerated carriers in the substrate, especially on its degree of flexibility and restore it efficiently.

Keywords Photoacoustic · Illumination · Si-TiO2 · Bending · Thermoelastic

1 Introduction

It is a well-known thing in photoacoustics that modulated optical irradiation of the semiconductor sample from one side can be used to excite a sample due to the absorption of the part of radiation energy. Such optical excitation followed by nonradiative energy transfer results in sample heating from the irradiated side, changing its temperature. Temperature change results in thermal gradient between irradiated and nonirradiated sides of the sample generating heat transport between them [1–6]. In the most simplified case of a sample in the form of a plate, if one side of the plate is irradiated, heat is transferred along with the sample thickness axe - 1D transfer. Knowing the temperatures on both plate sides (surfaces) allows one to calculate thermal diffusion (TD) and thermoelastic (TE) photoacoustic signal components generated from the sample [7–11].

If the optical source emitted light with the proper wavelength, photogenerated charge carriers transfer occurs, too, parallel to the heat transfer process within the semiconductor sample [12–14]. Knowing the carrier densities on both sides of the sample allows one to calculate plasmaelastic (PE) photoacoustic signal component and recalculate, at the same time, TD and TE components, knowing that charge carriers are also energy carriers that change temperatures within the sample and at its sides. In the end, all mentioned components TD, TE and PE are the constitutive part of the total PA signal used in our measurements [15–17].

In our previous research, we show that specific temperature behavior patterns exist in PA signal amplitude and phase when the semiconductor is under the strong influence of photogenerated carriers [18, 19]. Such an effect is reflected in the amplitude decrease of the PA signal TE component, which is more pronounced in plasma-thin samples (samples whose thickness is less than the diffusion length of the photogenerated carriers). Decrease of the thermoelastic component amplitude results in smaller sample displacement along the heat-flow axes i.e. smaller bending. It indicates that photogenerated carriers change (reduce) the flexibility degree of semiconductors, especially thin ones. Flexibility change can affect the correct operation of some MEMS devices by changing their sensitivity at a constant temperature.

✉ S. M. Aleksić
sanja.aleksic@elfak.ni.ac.rs

[1] Faculty of Electronic Engineering, University of Niš, Aleksandra Medvedeva 14, Niš 18000, Serbia

[2] Institute of Physics, University of Belgrade, Pregrevica 118, Belgrade-Zemun 11080, Serbia

[3] Vinča Institute of Nuclear Sciences, P.O. Box 522, Belgrade 11001, Serbia

Published online: 09 February 2022

In this article, we will show that the deposition of a thin layer of titanium-dioxide on the illuminated side of silicon plates can almost completely attenuate the effect of photogenerated carriers and restore their flexibility. A complete analysis of the PA signal and the behavior of its components is given using temperatures on the illuminated and nonilluminated side in the case of the plasma-thin silicon plate samples with (Fig. 1a) and without (Fig. 1b) a thin TiO_2 film. Comparative analysis of the plate displacements along the heat flow axis is given, too, considering displacement as a parameter directly connected to the sample flexibility degree. The influence of photogenerated carrier densities and temperature differences on the mentioned displacements is also given in order to show the direct influence of the electronic and thermal state of the tested samples on their thermoelastic bending properties.

2 Theoretical Model

The aim of this research is to analyze the photoacoustic response of a two - layer system illuminated by a modulated light source [20–26]. The investigated system is presented in Fig. 1a and consists of a thin TiO_2 film (first layer) deposited on a silicon wafer (second layer). The TiO_2 film is considered as a dielectric transparent material while the wafer is considered as semi-transparent semiconductor – n-type silicon. Such a distiction is based on the assumption that the illumination will be performed by a light source of such a wavelength (red laser diode) which will excite only the substrate but not the film. The thickness of the film (l_f) is assumed to be much less than the thickness of the wafer (l_s): $l_f << l_s$. The radius R_s of both layers was taken as the same. Also, the thickness of the wafer is taken to be much smaller than its radii: $R_s >> l_s$. In order to simplify all derivations, it is assumed that the complete two-layer system has cylindrical symmetry, so the heat transfer can be analyzed only in one dimension around the z-axis, the so-called 1D transfer. It means that all carrier density and temperature distribution calculations along both layers are based on the dynamic part of 1D diffusion equations solving (static part does not participate in photoacoustic signal generation).

In the case of the thin TiO_2 film (first layer) as a transparent dielectric volume absorber, the dynamic part of the 1D heat diffusion equation has the form [24–26]:

$$\frac{\partial^2 T_F(z,f)}{\partial z^2} - \frac{i\omega}{D_{TF}} T_F(z,f) = -\frac{1}{k_F}\beta_F\left(1-R_F\right)I_0 e^{-\beta_F z}, \tag{1}$$

where $\omega = 2\pi f$, f is the modulation frequency, I_0 is the incident light intensity, R_F is the film optical reflection coefficient, D_{TF} is the film thermal diffusion coefficient, k_1 is the film heat conduction coefficient, and β_F is the film absorption coefficient. The general solution of Eq. (1) can be written in the form [26]:

$$T_F(z,f) = A_1 e^{\sigma_F z} + A_2 e^{-\sigma_F z} + A_3 e^{-\beta_F z}, \tag{2}$$

where $\sigma_F = \sqrt{i\omega/D_{TF}}$ is the complex thermal diffusivity of the film, and constant A_3 is given as [26]:

$$A_3 = -\frac{\beta_F I_0\left(1-R_F\right)}{k_F\left(\beta_F^2 - \sigma_F^2\right)}.$$

The temperature distribution T_2 (z,f) in the second layer as a semitransparent n-type Si semiconductor can be obtained solving the dynamic part of 1D heat diffusion equation given in the form [24–26]:

$$\frac{\partial^2 T_s(z,f)}{\partial z^2} - \sigma_s^2 T_s(z,f) = -\frac{\varepsilon_g}{k_s \tau_s} n_p(z,f) - \frac{\beta_s I}{k_s}\cdot\frac{\varepsilon-\varepsilon_g}{\varepsilon} e^{-\beta_s z}, \tag{3}$$

where $I = \left(1-R_F\right)(1-R)e^{-\beta_f l_f} I_0$, $n_p(z,f)$ is the minority carrier density along the z – axes, ε_g is the substrate energy gap, ε is the incident light photon energy, R is the substrate

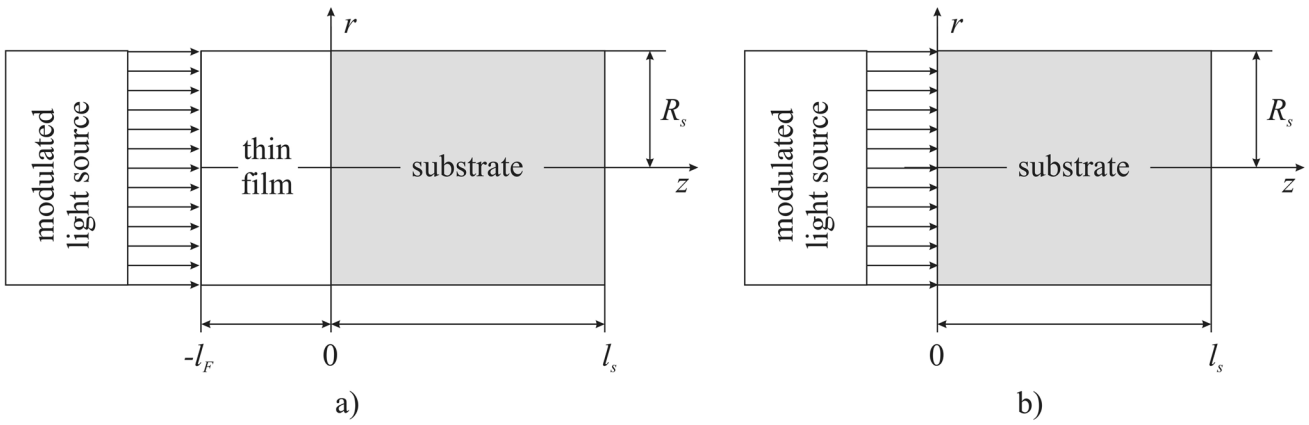

Fig. 1 The principal scheme of an investigated **a**) two-layer **b**) one-layer system

optical reflection coefficient, $\sigma_s = \sqrt{i\omega/D_{Ts}}$ is the substrate complex thermal diffusivity, D_{Ts} is the substrate thermal diffusion coefficient, k_s is the substrate heat conduction coefficient, τ_s is the bulk minority carrier lifetime and β_s is the substrate optical absorption coefficient.

The general solution of Eq. (3) can be written in the form [26]:

$$T_s(z,f) = B_1 e^{\sigma_s z} + B_2 e^{-\sigma_s z} + B_3 n_p(z,f) + B_4 e^{-\beta_s z}, \tag{4}$$

where.

$$B_3 = -\frac{\varepsilon_g}{k_s\tau_s\left(\sigma_s^2 - \frac{1}{L^2}\right)},\ B_4 = -\frac{\beta_2(1-R_F)(1-R)e^{-\beta_F l_F} I_0}{\varepsilon\left(\beta_s^2 - \sigma_s^2\right)}\left(\frac{B_3}{D_p} - \frac{\varepsilon - \varepsilon_g}{k_s}\right),$$

and $L = \sqrt{\frac{D_p\tau_s}{1+i\omega\tau_s}}$ is the complex minority carrier diffusion length (D_p is the diffusion coefficient of minority carriers).

Constants A_1, A_2, B_1 and B_2 can be found solving the boundary conditions [26]:

$$\begin{aligned} &\text{a)} -k_F \left.\frac{\partial T_F(z,f)}{\partial z}\right|_{z=-l_F} = 0, \quad \text{b)}\ T_F(0,f) = T_s(0,f), \\ &\text{c)} -k_s \left.\frac{\partial T_s(z,f)}{\partial z}\right|_{z=0} = s_1 n_p(0,f)\varepsilon_g - k_F \left.\frac{\partial T_F(z,f)}{\partial z}\right|_{z=0}, \\ &\text{d)} -k_s \left.\frac{\partial T_s(z,f)}{\partial z}\right|_{z=l_s} = -s_2 n_p(l_s,f)\varepsilon_g, \end{aligned} \tag{5}$$

where s_1 and s_2 are the substrate surface recombination speeds at the front ($z=0$) and rear ($z=l_2$) surfaces, respectively.

Using Eqs. (1–5) one can calculate T_s (l_s,f), the temperature at nonilluminated substrate side ($z=l_s$, see Fig. 1) which can be used to calculate thermodiffusion (TD) component of the photoacoustic signal, given in the form [23–26].

$$\delta p_{\mathrm{TD}}(f) = \frac{p_0\gamma_g}{\sigma_g l_c}\frac{T_2(l_2,f)}{T_0}, \tag{6}$$

where γ_g is the adiabatic constant, p_0 and T_0 are the equilibrium pressure and temperature of the air in the microphone, $\sigma_g = (1+i)\mu_g$, $\mu_g$is the thermal diffusion length of the air and l_c is the PA cell length.

Continuing calculation with the same Equations, one can find temperatures of the film T_F (-l_F,f), T_F (0,f) and substrate T_s (0,f) and T_s (l_s,f), assuming that $n_p(0,f)$ and $n_p(l_s,f)$ are calculated before (Appendix II). Knowing all mentioned temperatures and densities one can calculate the sample displacements $U_{z,c}(r,z)$ along the z-axes at $r=0$ and $z=l_s$ (back-side displacement), which can be used in the calculation of thermoelastic (TE) and plasmaelastic (PE) photoacoustic signal components.

The $U_{z,c}(r,z)$ can be written in a general form as [26]:

$$U_{z,c}(r,z) = \frac{C_c}{2}\left(R_s^2 - r^2\right), c = \mathrm{TE}, \mathrm{PE}, \tag{7}$$

where R_s is the sample radius and

$$\begin{aligned} C_{\mathrm{TE}} &= 6\frac{A_1 + A_2 + E_F E_s\left[\alpha_{TF} l_s\left(2M_{TF} - l_s N_{TF}\right) + \alpha_{Ts} l_F\left(2M_{Ts} - l_F N_{Ts}\right)\right]}{E_F^2 l_F^4 + E_s^2 l_s^4 + 2E_s E_F l_s l_F\left(2l_s^2 + 3l_s l_F + 2l_F^2\right)}, \\ C_{\mathrm{PE}} &= 6d_n E_s\frac{\left[E_F l_F\left(2M_n - l_F N_n\right) + E_s l_s\left(2M_n - l_s N_n\right)\right]}{E_s^2 l_s^4 + E_F^2 l_F^4 + 2E_s E_F l_s l_F\left(2l_s^2 + 3l_s l_F + 2l_F^2\right)}. \end{aligned} \tag{8}$$

Here $A_F = E_F^2 l_F\left(2M_{TF} + l_F N_{TF}\right)\alpha_{TF}, A_2 = E_s^2 l_s\left(2M_{Ts} - l_s N_{Ts}\right)\alpha_{Ts}$, E_F and E_s are the Young's modulus of the film and substrate, respectively, α_{TF} and α_{Ts} are the film and substrate coefficient of thermal expansion, d_n is the coefficient of electronic deformation and M_{TF}, M_{Ts}, M_n, N_{TF}, N_{Ts} and N_n are defined as [16, 17, 20].

$$M_{TF} = \int_{-l_F}^{0} z\cdot T_F(z,f)\mathrm{d}z,\ M_{Ts} = \int_0^{l_s} z\cdot T_s(z,f)\mathrm{d}z,\ M_n = \int_0^{l_s} z\cdot \delta n_p(z,f)\mathrm{d}z, \tag{9.a}$$

$$N_{TF} = \int_{-l_F}^{0} T_F(z,f)\mathrm{d}z.\ N_{Ts} = \int_0^{l_s} T_s(z,f)\mathrm{d}z,\ N_n = \int_0^{l_s} \delta n_p(z,f)\mathrm{d}z. \tag{9.b}$$

In general, the $U_{z,c}(r,z)$ exhibit parabolic thermoelastic and plasmaelastic displacement representing bending. Such bending produces the back-side acoustic waves with pressures [24–26].

$$\delta p_{\mathrm{TE}}(f) = \frac{\gamma p_0}{V_0}\int_0^{R_s} 2\pi r U_{z,\mathrm{TE}}(r,z)\mathrm{d}r, \tag{10.a}$$

$$\delta p_{\mathrm{PE}}(f) = \frac{\gamma p_0}{V_0}\int_0^{R_s} 2\pi r U_{z,\mathrm{PE}}(r,z)\mathrm{d}r, \tag{10.b}$$

which can be detected with a microphone as a thermoelastic, $\delta p_{\mathrm{TE}}(f)$, and plasmaelastic, $\delta p_{\mathrm{PE}}(f)$, photoacoustic signal components.

Knowing that the microphone integrates all signal components into one, so called total photoacoustic signal $\delta p_{\mathrm{total}}(f)$, one can write it as [24–26]:

$$\delta p_{\mathrm{total}}(f) = \delta p_{\mathrm{TD}}(f) + \delta p_{\mathrm{TE}}(f) + \delta p_{\mathrm{PE}}(f), \tag{11}$$

In the case of one-layer (Fig. 1b) Eqs. (6–11) are reduced to [17–19].

$$\delta p^*_{\mathrm{TD}}(f) = \frac{p_0\gamma_g}{\sigma_g l_c}\frac{T_s^*(l_s,f)}{T_0}, \tag{12}$$

$$U^*_{z,\mathrm{TE}}(r,z) = \alpha_T\frac{6\left(R_s^2 - r^2\right)}{l_s^3}\int_0^{l_s}\left(z - \frac{l_s}{2}\right)\cdot T_s^*(z,f)\mathrm{d}z, \tag{13.a}$$

$$U^*_{z,\mathrm{PE}}(r,z) = d_n \frac{6\left(R_s^2 - r^2\right)}{l_s^3} \int_0^{l_s} \left(z - \frac{l_s}{2}\right) \cdot \delta n_p(z,f)\mathrm{d}z, \tag{13.b}$$

$$\delta p^*_{\mathrm{TE}}(f) = \alpha_T \frac{\gamma p_0}{V_0} \frac{3\pi R_s^4}{l_s^3} \int_0^{l_s} \left(z - \frac{l_s}{2}\right) \cdot T^*_s(z,f)\mathrm{d}z, \tag{14}$$

$$\delta p^*_{\mathrm{PE}}(f) = d_n \frac{\gamma p_0}{V_0} \frac{3\pi R_s^4}{l_2^3} \int_0^{l_2} \left(z - \frac{l_2}{2}\right) \cdot \delta n(z,f)\mathrm{d}z. \tag{15}$$

$$\delta p^*_{\mathrm{total}}(f) = \delta p^*_{\mathrm{TD}}(f) + \delta p^*_{\mathrm{TE}}(f) + \delta p^*_{\mathrm{PE}}(f), \tag{16}$$

3 Results and Discussion

The experimental set-up used here is based on the well-known transmission open-cell model where a miniature electrets microphone is used as a PA cell. The investigated sample is mounted directly onto the front surface of the microphone. Modulated optical source (656 nm laser diode) is controlled by the sensitive photodiode and is used for sample excitation. The computer is used as the measurement control unit and data storage at the same time [18, 19, 26].

All investigated samples (one- and two-layer) have the form of thin circular plates with 40 μm thick Si n-type substrate and 200 nm thin TiO_2 film (Fig. 1). Substrates are taken from the same wafer while the film is deposited on the substrate with a conventional RF sputtering technique.

Knowing that experimental photoacoustic signal $S_{\mathrm{total}}(f)$ can be represented by the simple formula [18, 24–26].

$$S_{\mathrm{total}}(f) = A_{\mathrm{total}}(f)\exp\left[i\varphi_{\mathrm{total}}(f)\right], \tag{17}$$

the obtained measured data-set contains two features: amplitudes $A_{\mathrm{total}}(f)$ and phases $\varphi_{\mathrm{total}}(f)$ in the modulation frequency f range from (20 – 20 k) Hz. Our experience shows that even these two features are in different ranges, both $A_{\mathrm{total}}(f)$ and phases $\varphi_{\mathrm{total}}(f)$ are features of equal importance. Due to that fact and simplicity, the results presented here will include only amplitudes of the PA signal and its components.

All experimental signals obtained with $S_{\mathrm{total}}(f)$ and without $S^*_{\mathrm{total}}(f)$ thin TiO_2 film (Fig. 2a) are corrected due to the distortions induced by the instrumental filtering (*RC* at low, acoustic at high modulation frequencies), flicker noise and coherent deviations (crosstalk signals). After the proper correction procedure (explained in detail in [18, 26, 27]), corrected signals $\delta p_{\mathrm{total}}(f)$ and $\delta p^*_{\mathrm{total}}(f)$ are obtained (Fig. 2b) representing the "true" PA signals generated by the two- and one-layer sample, respectively, free from any kinds of deviations. Finally, total signals are fitted with the proper theoretical model (Eq. (6–16)) to obtain all PA signal components (TD, TE and PE, Figs. 3a and b). The accuracy of fitting procedure is ±8%. Fitting parameters are divided into three different groups; measured, literature and fitted ones. Layer thicknesses ($l_f = 200$ nm and $ls = 40$ μm) and radius ($R_s = 3$ mm) together with the substrate surface recombination speeds at the front illuminated ($s_1 = 2$m/s) and back nonilluminated ($s_2 = 24$m/s) surfaces are taken as independently and previously measured parameters [26, 27], respectively. Young's modulus of the film ($E_1 = 280$GPa) and substrate ($E_2 = 137$GPa), together with the film ($\beta_F = 1.8\times10^5\mathrm{m}^{-1}$) and substrate ($\beta_s = 2.6\times10^5\mathrm{m}^{-1}$) optical absorption coefficients, and substrate band gap ($\varepsilon_g = 1.78\times10^{-19}$J) are taken from the literature [18, 19].

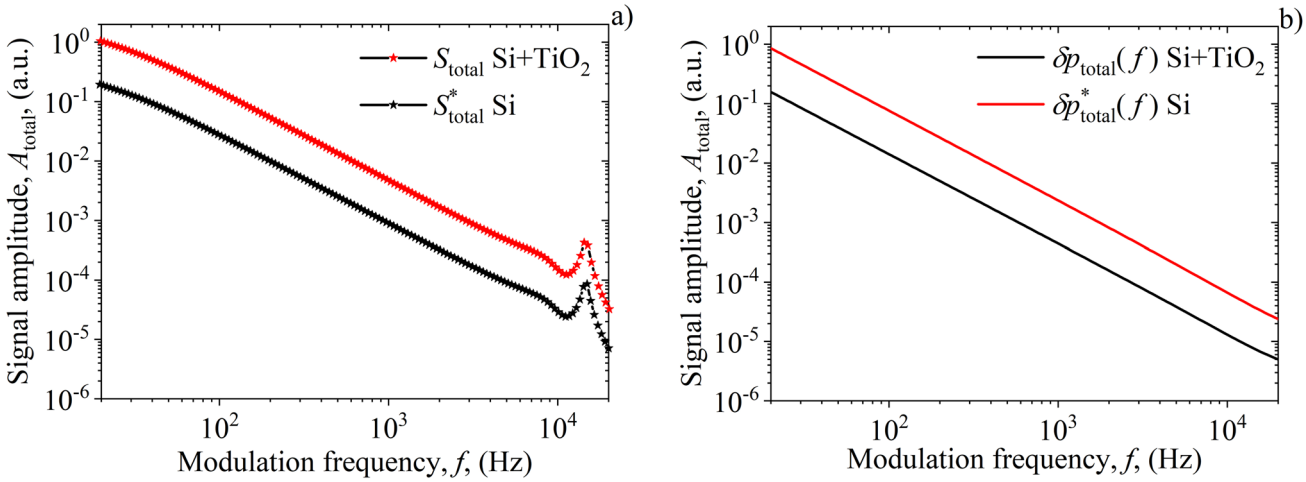

Fig. 2 Results of the **a**) measured (S_{total} and S^*_{total}, asterisks) and **b**) corrected ($\delta p_{\mathrm{total}}$ and $\delta p^*_{\mathrm{total}}$, solid lines) photoacoustic signals for pure 40 μm silicon (Si) and same silicon coated with 200 nm thin-film (Si + TiO_2) in frequency f domain

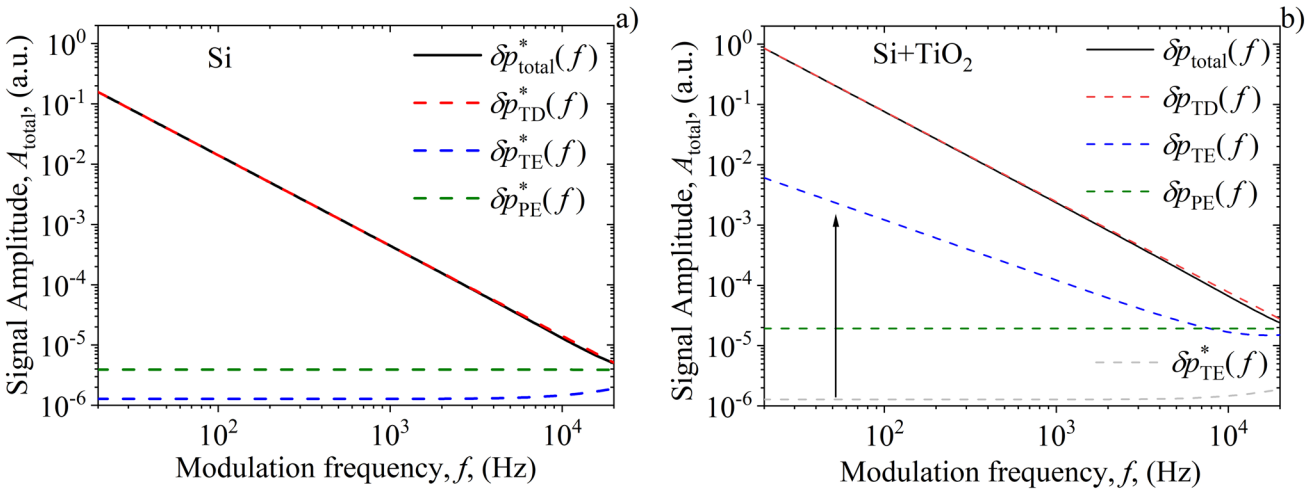

Fig. 3 Decomposition of the corrected photoacoustic signals (dp_{total} and dp^*_{total} – Fig. 2) on their components a) δp^*_{TD}, δp^*_{TE}, and δp^*_{PE}, and b) δp_{TD}, δp_{TE}, and δp_{PE}, in frequency f domain

Thermal diffusivity, thermal expansion, thermal conductivity and optical reflections of both layers together with substrate layer diffusion coefficient of minority carriers, coefficient of electronic deformation and photogenerated carriers bulk lifetime are taken as fitting parameters. Their obtained values are presented in Table 1.

The results of photoacoustic signal decomposition shown in Fig. 3a agrees with the results of our previous research [18, 19] based on the typical photoacoustic response of plasma-thin silicon samples - samples whose thickness is less than the diffusion length of their minority carriers. The characteristic of this response is a large decrease in the TE component (blue dash) at low, and its peak-like growth at high frequencies, leaving TD component (red dash) to dominate in $\delta p^*_{total}(f)$ (solid black, Eq. (16)) in the whole frequency range ($\delta p^*_{TD}(f) >> \delta p^*_{PE}(f) > \delta p^*_{TE}(f)$). It was found, in the same articles [18, 19], that the decrease in the TE component is a consequence of the heat transfer effect called "temperature equalizing" on oposite sides of the illuminated sample caused by the movement of photogenerated carriers. It is obvious from Fig. 3b that $\delta p_{TE}(f)$ component of the two-layer sample suffers drastically changes compared to $\delta p^*_{TE}(f)$ of the one-layer one (arrow pointing the change), indicating that sample bending is much larger in the two-layer sample due to the existence of a thin TiO_2 film. This is a good example of how thin film on Si substrate can restore (enhance) sample bending degree attenuated by the influence of the photogenerated carriers in semiconductors.

The differences between $\delta p_{TE}(f)$ and $\delta p^*_{TE}(f)$ are driven by the sample displacements $U_{z,\,TE}(r,z)$and $U^*_{z,TE}(r,z)$ (Fig. 4a, Eqs. (7–9, 13)) along the z-axes (axes of the heat-flow), which frequency behavior is controlled by the differences of carrier densities$\Delta\delta n_p(z) = \delta n_p(0) - \delta n_p(l_s)$ and $\Delta\delta n^*_p(z) = \delta n^*_p(0) - \delta n^*_p(l_s)$ (Fig. 4b), and temperatures $\Delta T(z) = T_s(0) - T_s(l_s)$ and $\Delta T^*(z) = T^*_s(0) - T^*_s(l_s)$, (Fig. 5a) at illuminated ($z = 0$) and nonilluminated ($z = l_s$) sample surfaces, together with temperature ratios $R_T = T_s(0)/T_s(l_s)$ and $R^*_T = T^*_s(0)/T^*_s(l_s)$, (Fig. 5b), obtained with Eqs. (18–22) and (1–5), respectively. Here we must remind that the illuminated sample bends in two ways due to the formation of two gradients: temperature gradient and gradient of photogenerated carriers. Under the experimental conditions, we used in the presented research, bending under the influence of photogenerated carriers does not suffer significant changes

Table 1 Two-layer sample characteristic parameters obtained by photoacoustics

parameters	value	
	Si	TiO_2
thermal diffusivity, D_T (m^2s^{-1})	$(9.0 \pm 0.1) \times 10^{-5}$	$(3.7 \pm 0.2) \times 10^{-6}$
thermal expansion, α_T (K^{-1})	$(2.6 \pm 0.2) \times 10^{-6}$	$(11 \pm 3) \times 10^{-6}$
thermal conductivity, k ($Wm^{-1}\,K^{-1}$)	(150 ± 15)	(11 ± 2)
optical reflection, R	(0.30 ± 0.02)	(0.20 ± 0.02)
diffusion coefficient of minority carriers, D_p (m^2s^{-1})	$(1.2 \pm 0.2) \times 10^{-3}$	
coefficient of electronic deformation, d_n (m^3)	$(-9.0 \pm 0.1) \times 10^{-31}$	
excess carrier bulk lifetime, τ(s)	$(6.0 \pm 0.3) \times 10^{-6}$	

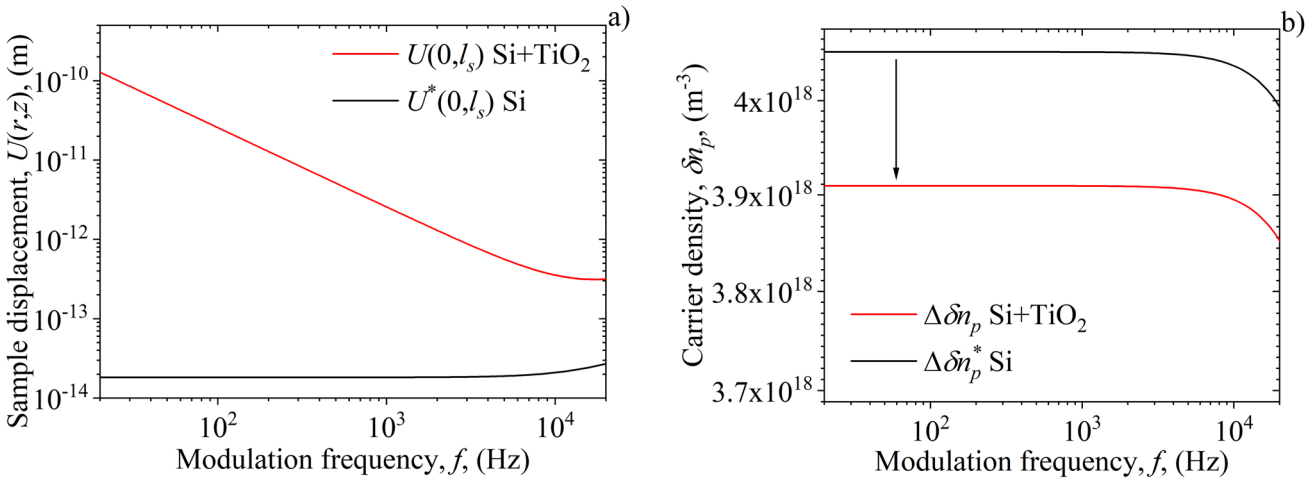

Fig. 4 Results of **a**) sample displacement with ($U(0,l_s)$) and without ($U^*(0,l_s)$) thin film together with **b**) carrier density differences $\Delta\delta n_p$ and $\Delta\delta n_p^*(0)$ in the frequency f domain that corresponds to TE signal components presented in Fig. 3

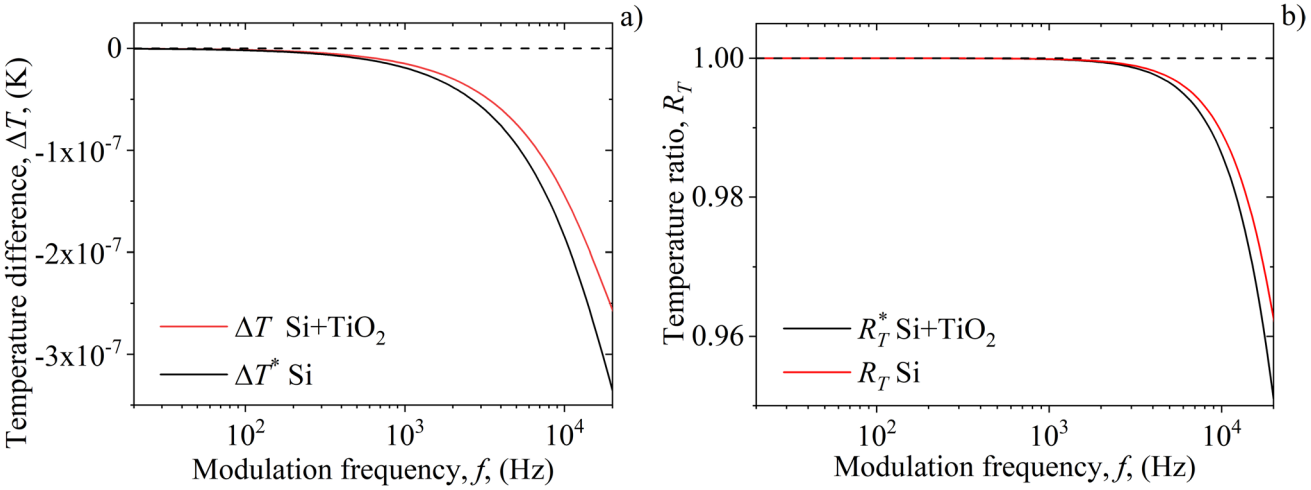

Fig. 5 Results of **a**) temperature difference of illuminated (0) and unilluminated (l_s) side of silicon with (ΔT) and without (ΔT^*) thin film, together with **b**) temperature ratios R_T and R_T^* from the same sides of the sample in the frequency f domain

by applying a thin film to the substrate (see green dashed lines in Figs. 3a and b), while bending due to the temperature changes, the so-called thermoelastic bending, is significant and dominant. Although the carrier density and temperature differences (Fig. 4b and 5a), together with temperature ratios (Fig. 5b) are small, such differences conducted the $U_{z,\mathrm{TE}}(r,z)$ and $U^*_{z,\mathrm{TE}}(r,z)$, significantly change their behavior in the frequency domain. Larger changes are in lower frequencies, smaller at higher ones. Such displacement behavior confirms the previously obtained results in the analysis of the behavior patterns of the thermoelastic component of the photoacoustic signal of plasma-thin samples under the influence of photogenerated carriers. The greater the difference between the temperatures of the illuminated and unilluminated side of the sample, the smaller the value of the TE component and vice versa.

4 Conclusions

In the presented article, the photoacoustics analysis of the influence of thermal state changes on silicon-TiO$_2$ sample bending along the heat-flow axes is presented. The 40 mm thick silicon plates were used as the basic sample. Their thickness was chosen to be less than the value of the diffusion length of the photogenerated carriers (plasma-thin samples), which allows one clear visibility of the bending reducing effect of the plates due to the strong carrier influence. Part of the plates was used as the substrates covered

by 200 nm transparent thin TiO_2 films. The film thickness is chosen not only to be visible in photoacoustic measurements but to keep transparency, too. In this way, single-layer (silicon plates) and double-layer samples (silicon plates + thin film) were obtained which has been used in this investigation.

The whole research is based on the analysis of amplitudes and phases of the total photoacoustic signal (response) and its components generated by illumination of the mentioned samples in the frequency domain from 20 Hz to 20 kHz. It has been observed that the largest changes in the photoacoustic response of a two-layer sample come from the thermoelastic component that increases rapidly compared to the same component of a single-layer sample, especially in the low-frequency region. It has been shown that such behavior of the thermoelastic component is directly related to the displacements of the sample along the heat-flow axis which is a consequence of the sample thermoelastic bending. It has also been shown that larger displacements are a consequence of small changes in the photogenerated carriers caused by the thin film. Knowing that changes in the carrier density result in larger changes in temperature differences and ratios between the illuminated and unilluminated sides of the sample, it was concluded that the sample displacement behavior in the frequency domain is conducted by the simultaneous changes of carrier density and temperatures on both sides of the sample.

As a general conclusion, one can say that covering plasma-thin silicon plates with a transparent TiO_2 film of nanometer thickness leads to overcoming the problem of reducing the bending degree of plates due to the influence of photogenerated carriers. Such covering increases the bending degree of the plates and restores their flexibility, which is a very important feature for various MEMS devices that use silicon membranes of similar thicknesses.

Appendix

Appendix I. General presentation of thermoelastic bending

Generally speaking, thermoelastic bending of the illuminated sample produces a parabolic mirror characterized by the curvature

$$\left.\frac{\partial^2 U_z(r,z)}{\partial r^2}\right|_{r=0} = -\alpha_T \frac{12}{l^3} M_T. \tag{18}$$

The photoacoustic and thermal mirror responses are subsequently interrelated through

$$\delta p_{\mathrm{TE}} = -\frac{\gamma p_0}{V_0}\frac{\pi R^4}{4}\left.\frac{\partial^2 U_z(r,z)}{\partial r^2}\right|_{r=0}. \tag{19}$$

If one wants to represent in general such parabolic thermal mirror curvature graphically, it would look like in Fig. 6:

Figure 6a shows a cross-section of the initial, equilibrium state of the nonilluminated Si membrane ($\Delta T_a = 0$). Figure 6b shows the equilibrium state of the same membrane illuminated by the light of such a wavelength that does not generate free carriers. The membrane is curved, and the degree of curvature is defined by the displacement of the sample U_{zb} along the heat transfer axis, which is proportional to the temperature difference ΔT_b. In Fig. 6c, the same membrane is illuminated by the light of a wavelength that generates free carriers (electrons, n, and holes, p). The displacement U_{zc} is smaller than U_{zb} because the carriers efficiently transfer heat from the illuminated to the nonilluminated side of the sample, thus reducing the temperature difference between these sides. In Fig. 6d, the same membrane is illuminated with the light as in Fig. 6c, but covered with a thin transparent film on the illuminated side. The thin film absorbs one part of the light energy and reduces the number of photogenerated carriers in the semiconductor. In such way, the temperature difference decreases and the displacement of the sample U_{zd} increases, approaching the value of U_{zb}.

Appendix II. Photogenerated carrier distribution in silicon

Following the ambipolar transport model that describes the nonequilibrium, coupled motion of electrons and holes (photogenerated free carriers) drifting and diffuse together without external influence, photoacoustics theoretical model is based on Fick's laws of carrier diffusion. Here, carriers act as heat (not charge) carriers participating in the calculation of temperature distributions in the tested sample. In the case of low-level injection n-type silicon the equation used for carrier concentration distribution within and at sample surfaces is given in the form [20, 21]:

$$\frac{\mathrm{d}^2 \delta n_p(x,f)}{\mathrm{d}x^2} - \frac{\delta n_p(x,f)}{L^2} = -\frac{\beta I_0}{\varepsilon D_p} e^{-\beta x}, \tag{20}$$

where $L = L_p/(1 + i2\pi f\tau_p)^{1/2}$ is the complex excess carriers diffusion length, $L_p = \sqrt{D_p \tau_p}$ is the excess carrier diffusion length, and $\delta n_p(x,f)$ is the photogenerated minority dynamic concentration component.

The solution of the Eq. (5) can be found in the form [20, 21]:

$$\delta n_p(x,f) = A_+ e^{xL^{-1}} + A_- e^{-xL^{-1}} + A_\beta e^{-\beta x}, \tag{21}$$

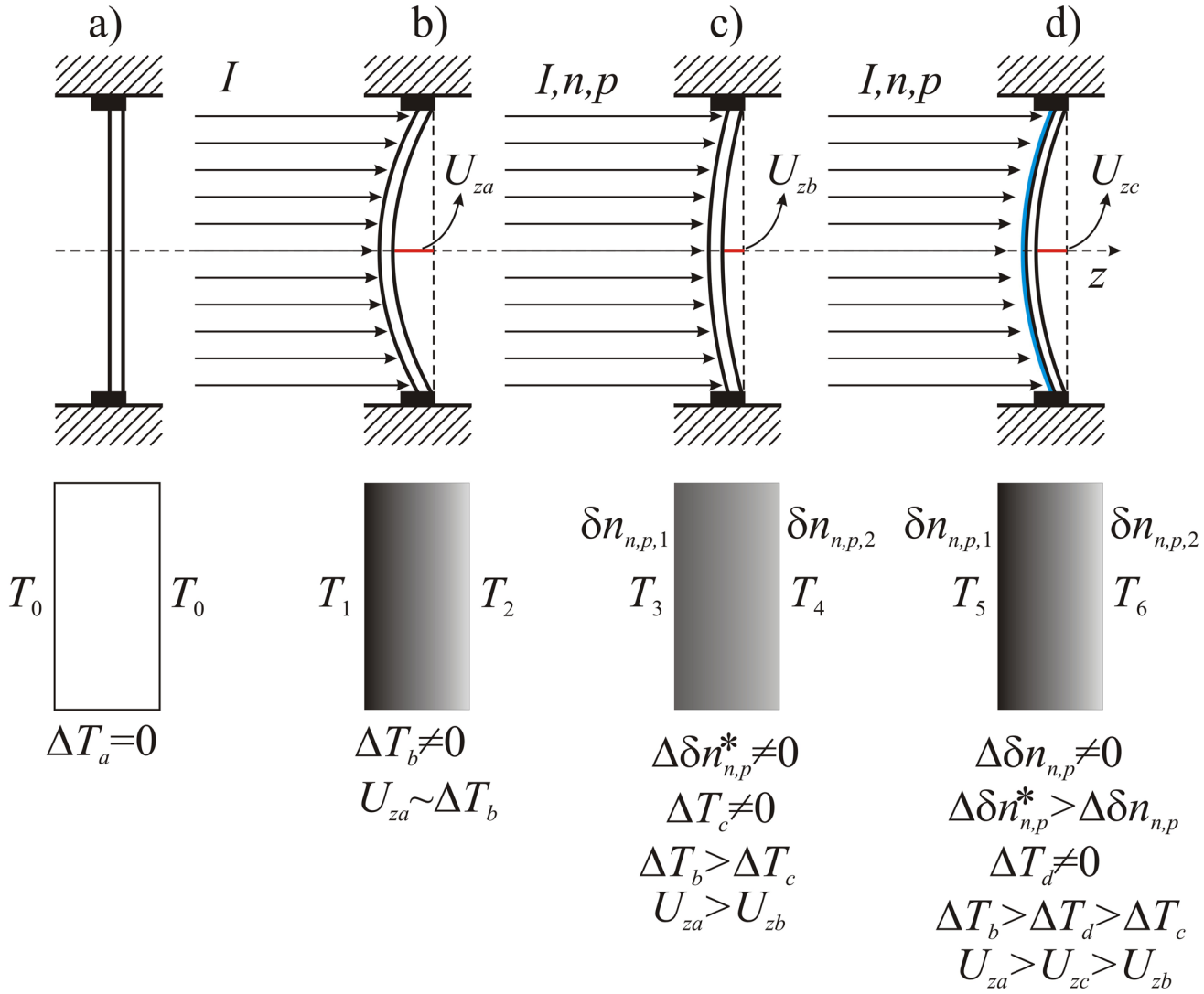

Fig. 6 Simplified scheme of different degrees of silicon sample bending with and without a thin film under the influence of illumination and photogenerated carriers

The A_β is the solution of the inhomogeneous part of the differential equation, and $A_+$and $A_-$are the integration constants calculated from the boundary conditions, which are given in the form:

$$A_\pm = \pm\frac{A_\beta}{A_L}\left[(1\mp\sigma_1)(1+\beta L\sigma_2)e^{-\beta l} - (1\pm\sigma_2)(1+\beta L\sigma_1)e^{\pm lL^{-1}}\right], \tag{22}$$

$$A_L = (1+\sigma_1)(1+\sigma_2)e^{lL^{-1}} - (1-\sigma_1)(1-\sigma_2)e^{-lL^{-1}} \tag{23}$$

$$A_\beta = \frac{I_0}{\varepsilon v_D}\frac{\beta L}{L^{-2}-\beta^2}, \tag{24}$$

where $\sigma_m = D_p(s_m L)^{-1}$ is the dimensionless parameter which depends on the Si surface recombination speed s_m at front ($m=1$) and back side ($m=2$) of sample, and $v_D = D_p L^{-1}$ is the diffusion velocity of the photogenerated minority carriers.

Acknowledgments This work was supported by the Ministry of Education, Science and Technological Development of the Republic of Serbia within the institutional financing, contract number 451-03-09/2021-14/200017.

Authors' Contributions Not applicable' for that section.

Data Availability Not applicable' for that section.

Declarations

Ethics Approval and Consent to Participate All authors ethically approve and give consent to participate.

Consent for Publication All authors give full consent for publication.

Research Involving Human Participants and/or Animals Not applicable.

Conflict of Interest There is no conflicts of interests among different authors.

References

1. Bialkowski SE, Astrath NGC, Proskurnin MA (2019) Photothermal spectroscopy methods, chemical analysis: a series of monographs on analytical chemistry and its applications. Wiley, New York ISBN: 9781119279075
2. Volz S (2010) Microscale and nanoscale heat transfer (topics in applied physics). Springer ISBN: 978–3642071584
3. Kaviany M (2014) Heat transfer physics2nd edn. Cambridge University Press, Cambridge ISBN: 978–1-107041783
4. Ordóñez-Miranda J, Alvarado-Gil JJ (2012) Determination of thermal properties for hyperbolic heat transport using a frequency-modulated excitation source. Int J Eng Sci 50:101–112. https://doi.org/10.1016/j.ijengsci.2011.08.012
5. Tikhonov AN, Samarski AA (1990) Equations of mathematical physics. Dover Publications, New York ISBN-13: 978–0486664224
6. Wang L, Zhou X, Wei X (2008) Heat conduction: mathematical models and analytical solutions. Springer-Verlag, Berlin Heidelberg
7. Rosencwaig A, Gersho A (1976) Theory of the photoacoustic effect with solids. J Appl Phys 47:64–69
8. Mcdonald FA, Wetsel JGC (1978) Generalized theory of the photoacoustic effect. J Appl Phys 49:2313–2322
9. Rosencwaig A "Thermal wave characterization and inspection of semiconductor materials and devices," in Photoacoustic and Thermal Wave Phenomena in Semiconductors, edited by A. Mandelis (Elsevier Publishing Company, 1987), pp. 97–135
10. Sablikov A, Sandomirskii VB (1983) The photoacoustic effect in semiconductors. Phys Status Solidi B 120:471
11. Mandelis A (2001) Diffusion waves fields: mathematical methods and green functions. Springer, New York
12. Pawlak M (2019) Photothermal, photocarrier, and photoluminescence phenomena in semiconductors studied using spectrally resolved modulated infrared radiometry: physics and applications. J Appl Phys 126:150902
13. Gupta KM, Gupta N (2016) Carrier transport in semiconductors. Advanced Semiconducting Materials and Devices, Part of the Series Engineering Materials. Springer International Publishing, Springer Cham Heidelberg, New York, Dordrecht, London, pp 87–144
14. Miranda LCM (1982) Theory of the photoacoustic effect in semiconductors influence of carrier diffusion and recombination. Appl Opt 21:2923
15. Todorovic DM, Nikolic PM, Dramicanin MD, Vasiljevic DG, Ristovski ZD (1995) Photoacoustic frequency heat-transmission technique: thermal and carrier transport parameters measurements in silicon. J Appl Phys 78:5750
16. Todorović DM, Nikolić PM, Bojičić AI, Radulović KT (1997) Thermoelastic and electronic strain contributions to the frequency transmission photoacoustic effect in semiconductors. Phys Rev B 55(23):15631–15642
17. Todorović DM, Nikolić PM (2000) Semiconductors and electronic materials, Progress in Photothermal and photoacoustic science and technology. Optical Engineering Press, New York, pp 273–318
18. Markushev DK, Markushev DD, Aleksic SM, Pantic DS, Galovic SP, Todorovic DM, Ordonez-Miranda J (2020) Experimental photoacoustic observation of the photogenerated excess carrier influence on the thermoelastic response of n-type silicon. J Appl Phys 128:095103. https://doi.org/10.1063/5.0015657
19. Markushev DK, Markushev DD, Aleksic SM, Pantic DS, Galovic SP, Todorovic DM, Ordonez-Miranda J (2019) Effects of the photogenerated excess carriers on the thermal and elastic properties of n-type silicon excited with a modulated light source: Theoretical analysis. J Appl Phys 126(18):185102. https://doi.org/10.1063/1.5100837
20. Fernelius NC (1980) Extension of the Rosencwaig-Gersho photoacoustic spectroscopy theory to include effects of a sample coating. J Appl Phys 51:650–654
21. Fujii Y, Moritani A, Nakai J (1981) Photoacoustic spectroscopy theory for multi-layered samples and interference effect. Jpn J Appl Phys 20:361–367
22. Hu H, Zhang W, Xu J, Dong Y (2008) General analytical solution for photoacoustic effect with multilayers. Appl Phys Lett 92:014103
23. Popovic MN, Markushev DD, Nesic MV, Jordovic-Pavlovic MI, Galovic SP (2021) Optically induced temperature variations in a two-layer volume absorber including thermal memory effects. J Appl Phys 129:015104. https://doi.org/10.1063/5.0015898
24. Todorović DM, Rabasović MD, Markushev DD, Sarajlic M (2014) Photoacoustic elastic bending in thin film-substrate system: experimental determination of the thin film parameters. J Appl Phys 116:053506. https://doi.org/10.1063/1.4890346
25. Todorović DM, Rabasović MD, Markushev DD (2013) Photoacoustic elastic bending in thin film—substrate system. J Appl Phys 114:213510. https://doi.org/10.1063/1.4839835
26. Jovančić N, Markushev DK, Markushev DD, Aleksić SM, Pantić DS, Korte D, Franko M (2020) Thermal and elastic characterization of nanostructured Fe_2O_3 polymorphs and TiO_2-coated Fe_2O_3 using open photoacoustic cell. Int J Thermophys 41:90. https://doi.org/10.1007/s10765-020-02669-w
27. Markushev DD, Rabasović MD, Todorović DM, Galović S, Bialkowski SE (2015) Photoacoustic signal and noise analysis for Si thin plate: signal correction in frequency domain. Rev Sci Instrum 86:035110. https://doi.org/10.1063/1.4914894

Радови Драгана К. Маркушев

Часописи

М23

FACTA UNIVERSITATIS
Series: **Electronics and Energetics** Vol. 36, Nº 4, December 2023, pp. 485 - 497
https://doi.org/10.2298/FUEE2304485S

Original scientific paper

ELECTRO-ACOUSTIC ANALOGIES BETWEEN THERMOELASTIC COMPONENT OF THE PHOTOACOUSTIC SIGNAL AND LOW-PASS RC FILTER

Neda Lj. Stanojevic[1], Dragana K. Markushev[2], Sanja M. Aleksic[1], Dragan S. Pantic[1], Dragan V. Lukic[2], Marica N. Popovic[2], Dragan D. Markushev[2]

[1]Faculty of Electronic Engineering, University of Niš, Niš, Serbia
[2]Institute of Physics, University of Belgrade, Belgrade-Zemun, Serbia

Abstract. *This paper presents a new approach to the thermal characterization of aluminum, based on the electro-acoustic analogy between the thermoelastic component of the photoacoustic signal and the passive RC low-pass filter. The analogies were used to calculate the characteristic thermoelastic cut-off frequencies of the photoacoustic component and obtain their relationship with the thickness of the aluminum samples. Detailed numerical analysis showed that the required relationship is linear in the log-log scale and can serve as a reference curve for the given material. The results of the numerical analysis were also confirmed experimentally.*

Key words: *electro-acoustic, thermoelastic component, photoacoustic signal, RC filter*

1. INTRODUCTION

Photoacoustics, as one of the very sensitive detection methods within photothermal sciences, is based on the photoacoustic effect [1,2]. The photoacoustic effect is the effect of the formation of sound waves after the interaction of light and the matter of the periodically illuminated sample in any aggregate state. In this article, we will deal with the analysis of solid samples. The sound generated in solids after light-matter interaction is usually called a photoacoustic signal. It is a complex combination of at least two components: thermo-diffusion and thermoelastic [3,4]. If a plate-shaped solid sample is illuminated by a modulated light source from one side, the thermo-diffusion component is generated by the periodic expansion and contraction of a thin layer of air adjacent to the unilluminated surface of the sample. On the other hand, periodic bending of the same sample occurs because of different temperatures at illuminated and nonilluminated sample surfaces. Such bending causes the

Received February 13, 2023; revised April 10, 2023; accepted May 03, 2023
Corresponding author: Neda Stanojevic
Faculty of Electronic Engineering, University of Niš, Aleksandra Medvedeva 14, 18000 Niš, Serbia
E-mail: neda.stanojevic@elfak.ni.ac.rs

compression of the gas in the sample vicinity, changing gas pressure, and thus the thermoelastic component is generated [5,6]. Both components bring physical characteristics of the illuminated sample material, usually given in the terms of different coefficients: thermal diffusion, D_T, thermal conduction k, linear thermal expansion α_T, etc.

The thermoelastic component of the photoacoustic signal is specific in that its frequency response, both amplitude, and phase, is very similar to the frequency response of a low-pass RC filter [7-10]. Therefore, in this paper, we will try to establish an electro-acoustic analogy between the thermoelastic response and the response of a passive RC low-pass filter. We will show that the amplitude and phase graphs of the thermoelastic component can be understood as Bode plots and analyzed with the same transfer function as the aforementioned RC filter. Also, we will show that characteristic cut-off frequencies obtained from such an analysis can be used to obtain the thermal diffusion coefficient of the material from which the examined sample is made.

2. THEORETICAL BACKGROUND

2.1. Theory of thermoelastic bending

A typical photoacoustic setup for material characterization (an open-cell setup) involves illuminating the sample with a modulated light source intensity (pure sinusoid I, Fig.1, with frequency $\omega=2\pi f$, f is the modulation frequency) [5,11-13]. The sample is surrounded by air and placed on top of the microphone. Illumination leads to a change in the thermal state of the sample, which results in different temperatures on its illuminated and non-illuminated sides. Different temperatures cause the sample to bend (see Fig.1). The bending is periodic and elastic, following the rhythm of the light source modulation. The bending of the sample described in this way is called thermoelastic bending. Theory of thermoelastic bending [14,15] derived equations describing the thermoelastic bending of a uniform-thickness plate being heated.

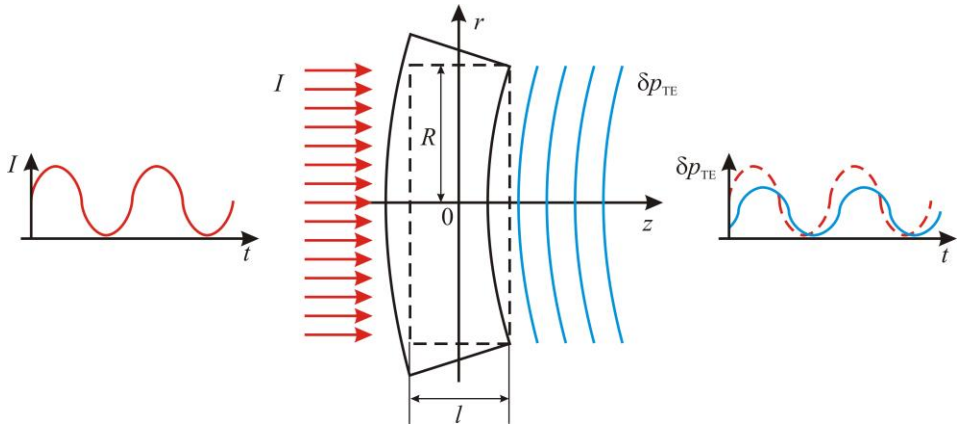

Fig. 1 The basic scheme of the open-cell setup shows the thermoelastic bending of a periodically illuminated sample of thickness l, radius R, and the thermoelastic sound component δp_{TE} generation and propagation along the z - axis (axis of heat propagation)

Thermoelastic bending produces a back-side acoustic wave, so-called thermoelastic component of the photoacoustic signal δp_{TE} (pure sinusoid, same frequency as *I*, different amplitude and phase), with a pressure detected by the microphone membrane defined as [16,17]:

$$\delta p_{\mathrm{TE}} = \alpha_T \frac{\gamma p_0}{V_0} \frac{3\pi R^4}{l^3} M_T \,, \tag{1}$$

where α_T is the coefficient of linear thermal expansion, γ, p_0 and V_0 are the adiabatic constant, pressure and volume of the air in microphone, respectively, and M_T is the first moment of the plate temperature change along the z - axis, defined as [15-17]:

$$M_T = \int_{-l/2}^{l/2} z T_s(z,\omega)\,\mathrm{d}z \,. \tag{2}$$

Here $T_s(z,\omega)$ is the temperature distribution along the z - axis. When M_T is calculated in the case of a surface absorber, it can be written as [15-17]:

$$M_T = \frac{I_0}{k\sigma_i^3} \cdot \left[\tanh\left(\frac{\sigma_i l}{2}\right) - \frac{\sigma_i l}{2} \right], \tag{3}$$

where I_0 is the amplitude of excitation, k is the thermal conductivity of the sample material, and $\sigma_i = (1+j)\sqrt{\omega / 2D_T}$ is the complex thermal diffusion coefficient (j is the imaginary unit, D_T is the diffusion coefficient).

Being the complex number, δp_{TE} has an amplitude A_{TE} and a phase φ_{TE} (see Appendix I). Usually, their common modulation frequency f response plots are presented as in Fig. 2.a (A_{TE}) and Fig. 2.b (φ_{TE}), where calculations are performed for the pure aluminum circular plate sample having the thickness, $l = 100\ \mu m$, and a radius, $R = 2.5\ mm$, with basic thermal properties given in Table I [17,18].

Table 1 Aluminum sample parameters used in Eq. (1-3)

Thermal conductivity, k / (W/mK)	237
Heat capacity, C / (J/kgK)	900
Density, ρ / (kg/m^3)	2700
Heat diffusion D_T / (10^{-5} m^2/s)	9.75
Linear thermal expansion, α_T / (10^{-6} 1/K)	23.1

Since δp_{TE} represent sound, the A_{TE} values can also be represented in decibels (dB), Figure 2a (A_{dB}), using the equation:

$$A_{\mathrm{dB}} = 20 \log \frac{A_{\mathrm{TE}}}{A_{\mathrm{TE}}^{\max}} \,, \tag{4}$$

where A_{TE}^{max} is the maximal amplitude value in the given frequency domain. Corresponding phase φ values are represented in Figure 5b. Both quantities, A_{dB} and φ, have the same shape in the frequency domain as A_{TE} and φ_{TE}, but different numerical values.

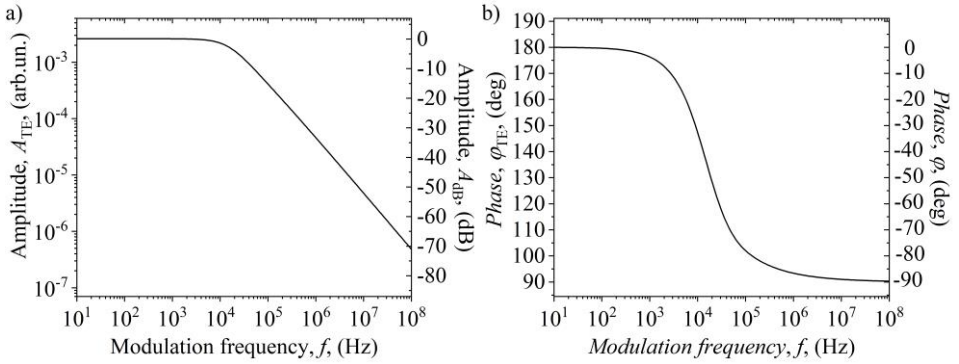

Fig. 2 a) Amplitudes A_{TE} and b) phases φ_{TE} of the photoacoustic signal thermoelastic component δp_{TE} (Eq. (1)) as a function of the modulation frequency f. Amplitude A_{dB} in decibels (Eq.(4)) and corresponding phase φ values were depicted, also

2.2. Low-pass RC filter

Analyzing δp_{TE} response from Figure 2, one can see that our photoacoustic system can pass certain frequencies while attenuating others. In other words, our system acts as a filter, so the analogy can be made with a passive low-pass RC filter, presented in Figure 3 in (a) time and (b) frequency domain [7-10]. Here, U_{in} is an input voltage, U_{out} is an output voltage (voltage across the capacitor), $Z_R = Z$ is the resistor impedance, and $Z_C = 1/sC$ is the capacitor impedance, where s is a complex number $s = \sigma + j\omega$ (j is the imaginary unit, σ is the exponential decay constant, and ω is the sinusoidal angular frequency).

By viewing the circuit (Figure 3b) as a voltage divider, and considering a special case of sinusoidal steady state in which the input (red line) and output (blue line) voltage consists of a pure sinusoid (no exponential decay, $\sigma = 0$, $s = j\omega$), the transfer function $H(j\omega)$ from the input voltage to the voltage across the capacitor can be given in the form [7-10]:

$$H(j\omega) = \frac{U_{out}(j\omega)}{U_{in}(j\omega)} = \frac{1}{1 + j\omega RC} = \frac{1}{1 + j\dfrac{\omega}{\omega_0}} \tag{5}$$

assuming zero initial conditions, where $\omega_0 = 1/RC$ is the cut-off frequency, a boundary frequency at which energy flowing through the circuit begins to be attenuated. As a complex number, $H(j\omega)$ has an amplitude $|H(j\omega)|$ and the phase φ which can be presented in the forms:

$$\left|H(j\omega)\right| = \frac{1}{\sqrt{1 + \left(\dfrac{\omega}{\omega_0}\right)^2}} \tag{6}$$

and

$$\varphi = -\arctan\left(\frac{\omega}{\omega_0}\right) \tag{7}$$

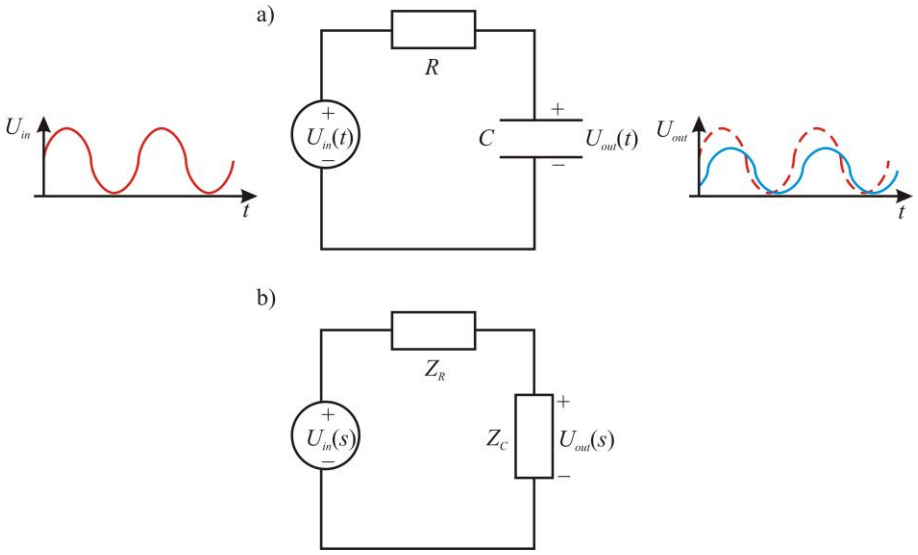

Fig. 3 A simple scheme of RC low - pass filter in a) time and b) frequency domain.

Usually, the magnitude A is calculated in decibels (dB) using [7-10]:

$$A = 20\log\left|H\left(j\omega\right)\right| \tag{8}$$

The standard representations of a given low-pass RC filter A and φ are Bode plots [19,20] (Figure 4), obtained using Eq.(6-8), taking into account that $\omega_0 = 2\pi f_0$, and $f_0 = 1.5 \cdot 10^4\ s^{-1}$.

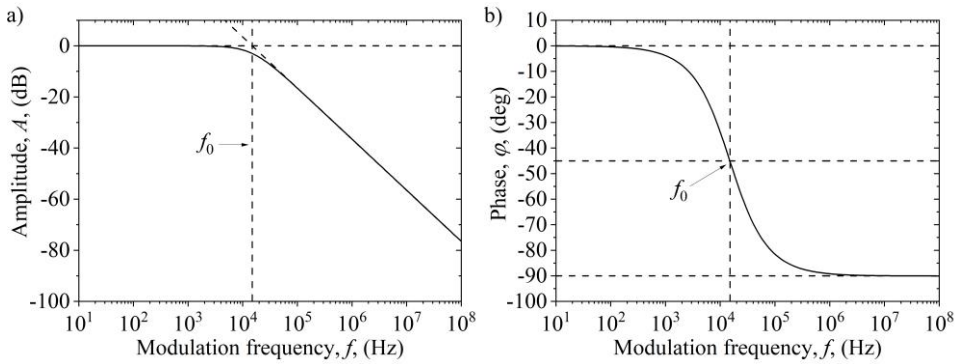

Fig. 4 Bode a) amplitude A and b) phase φ plots of the RC low-pass filter response in frequency domain. Dashed auxiliary lines define the position of f_0

3. RESULTS AND DISCUSSION

3.1. Theoretical procedure

Based on the introductory remarks, both the photoacoustic system (Figure 1) and the low - pass RC filter (Figure 3) can be considered as the linear time - invariant (*LTI*) systems [21,22] whose frequency responses after sinusoidal inputs (excitations) are shown in Figures 2 and 4. The cut - off frequency f_{TE} of the thermoelastic component can be found, using the Bode diagrams from Figure 2 for $l = 100\,\mu m$ and $R = 2.5\,mm$ values, in two ways: 1) approximately, finding the intersection of the amplitude asymptotes (dashed lines in Figure 5a), and/or 2) explicitly, by fitting the amplitude (Figure 5.a) with a function y_{TE}, based on Eqs. (6) and (8), given in the form:

$$y_{\mathrm{TE}} = 20\log\left(\left(1+\left(\frac{x}{m}\right)^2\right)^{-\frac{n}{2}}\right) \tag{9}$$

where, $x = f$ is the modulation frequency, and m and n are fitting parameters, $f_{TE} = m$ and the slope is $n/2$. This expression is commonly used in electronics to describe the cascade connection of the RC filters, but in our case, it is intended to cover a slope, different to the RC filter. The results of the δp_{TE} amplitude fitting procedure (Figure 5a, blue line) are as follows: $f_{TE} = (15660\pm60)$ and $n = (9786\pm6)\cdot10^{-4}$. The value of f_{TE} is depicted in Figures 5.a.b, using dashed vertical line.

Applying the obtained f_{TE} value in A (Eq. (8)) and φ (Eq. (7)) one can calculate corresponding low - frequency bandpass RC filter responses (red lines in Figure 5.a, and Figure 5.b, respectively). Obvious discrepancies between blue and red lines can be observed at higher frequencies for both amplitudes and phases. This result is only a consequence of the fact that real systems (photoacoustics) are not the ideal analogies (RC filters).

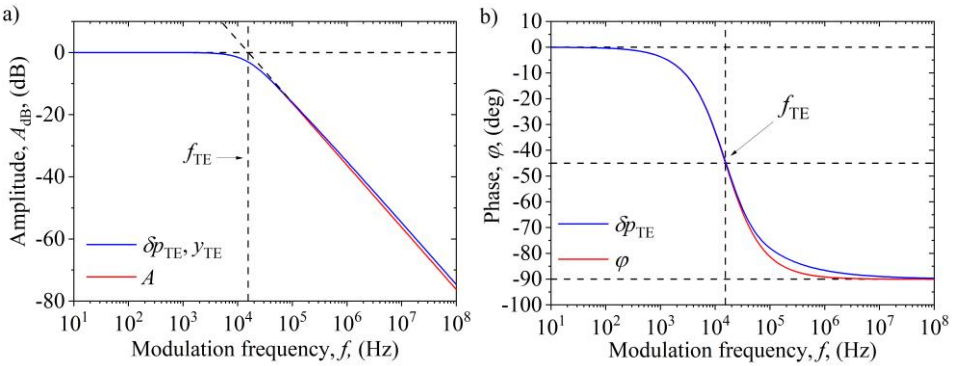

Fig. 5 Bode a) amplitude and b) phase plots of the photoacoustic signal thermoelastic component δp_{TE} obtained theoretically (Eq. (1)) in the case of aluminum circular plate having the thickness l and radius R, with basic thermal parameters which are given in Table I. Cut-off frequency f_{TE} is obtained using y_{TE} fit (Eq. (9)). Red line A is obtained using Eq. (8) and f_{TE}

Using the same procedure, we can fit thermoelastic components for aluminum samples of the same shape but different thicknesses: from l_{min} = 10 to 100 μm in steps of 10 μm, and from 100 to l_{max} = 1000 μm in steps of 100 μm (Figure 6). All presented thermoelastic components of the photoacoustic signals are obtained using Eq. (4) and sample parameters are given in Table 1.

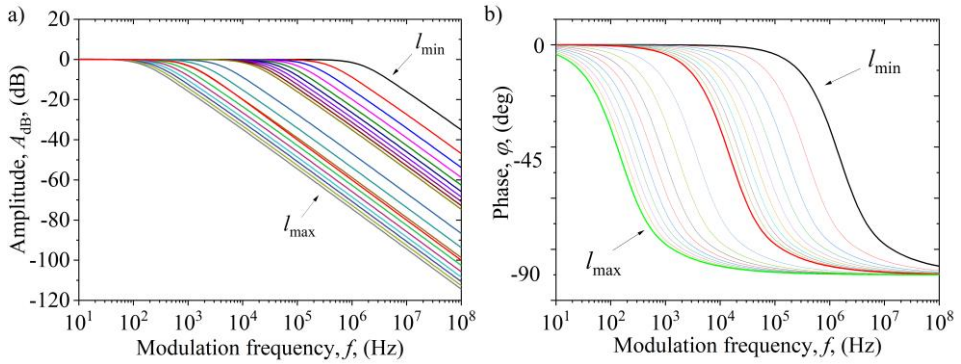

Fig. 6 Bode a) amplitude and b) phase plots of the photoacoustic signal thermoelastic component δp_{TE} obtained theoretically (Eq. (1)) in the case of aluminum circular plate with different thicknesses l and constant radius R, with basic thermal parameters which are given in Table 1

The fitting results obtained by Eq. (9) are shown in Table II, based on which the dependence of f_{TE} on the sample thickness l is drawn (red line, Figure 7).

Table 2 Fitting results of an aluminum sample estimation of cut - off frequency as a function of sample thickness.

Sample thickness l / ($\times 10^{-6}$ m)	Cut-off frequency f_{TE} / (Hz)
10	1480460
20	376097
30	168860
40	95666.5
50	61560.5
60	42936.7
70	31658.7
80	24313.1
90	19261.3
100	15638.0
200	3965.95
300	1776.11
400	1004.17
500	645.126
600	449.404
700	331.063
800	256.923
900	204.806
1000	167.771

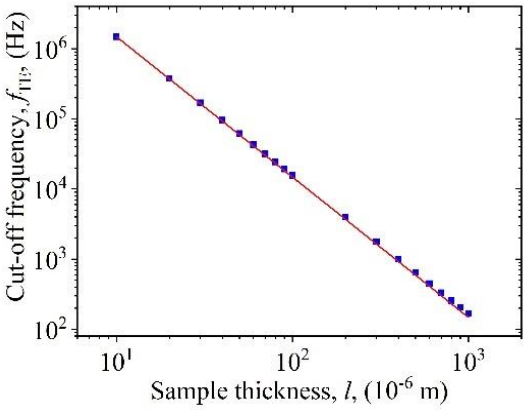

Fig. 7 Log-log scale of f_{TE} dependence on sample thickness l. Red line represent the fit line obtained using Eq. (11)

Mathematically, the dependence of f_{TE} on l in a logarithmic scale (Figure 7) can be obtained by finding the value of $\sigma_i\, l/2$ in the square bracket of Eq. (3), in the case of $f=f_{TE}$, using:

$$\frac{|\sigma_i| l}{2} = b \tag{10}$$

or

$$f_{\mathrm{TE}} = \frac{2}{\pi} \cdot \frac{D_T}{l^2} \cdot b^2 \tag{11}$$

considering that $|\sigma_i| = \sqrt{\omega / D_T}$, and $\omega = \omega_{\mathrm{TE}} = 2\pi f_{\mathrm{TE}}$. Fitting the data from Figure 7 with Eq. (11) (red line), it is obtained that $b = 1.545$. Obtained data fit line represents the reference value of the aluminum samples considered as surface absorbers. It can be used to check the validity of measurements and deviations from theoretical model and/or literature values due to various sample impurities, physical damages, etc.

3.2. Experimental validation

To validate the suggested δp_{TE} analysis procedure based on electro-acoustic analogy with low - pass RC filter and Eq.(11), we measured and analyzed the photoacoustic response of aluminum sample in 20 Hz – 20 kHz modulation frequency f domain, using a typical open-cell photoacoustic experimental set-up (see Appendix II). The investigated sample was circular in shape, having a thickness, $l = 155\ \mu m$, and a radius, $R = 2.5\ mm$. The results of such analysis are shown in Figures 8 - 11. Using the well-known method of the signal "cleaning" from the instrumental influence [23-25], we obtained the "real" signal δp (blue line, Figure 8) from the measured experimental values S_{exp} (Figure 8, asterisks), within the experimental error of 5 %.

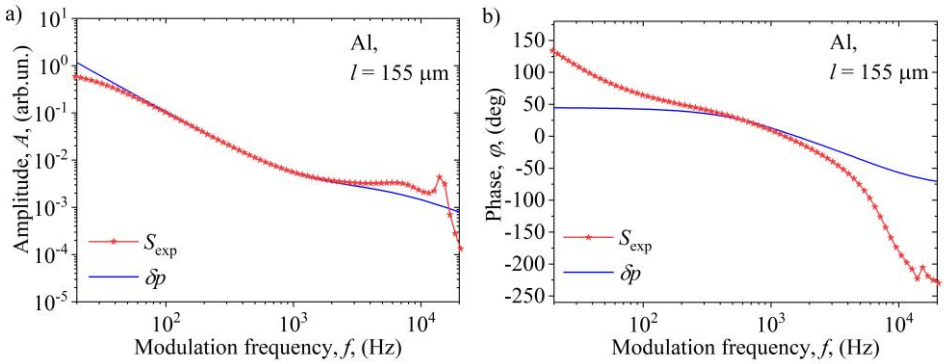

Fig. 8 a) Amplitude and b) phase of the aluminum A_1 sample experimental signal S_{exp} (asterisks) and the "real" signal δp (blue line), signal freed from the instrumental influences

Applying the composite piston model on the "real" signal δp [4,16,17], both components were obtained: thermo-diffusion, δp_{TD}, and thermoelastic, δp_{TE}, (Figure 9, green and red lines, respectively). One must take into account that model suggest simple relationship: $\delta p = \delta p_{\mathrm{TD}} + \delta p_{\mathrm{TE}}$. Obtained frequency response of these components correspond to the thermal characteristics of the investigated sample given in Table I.

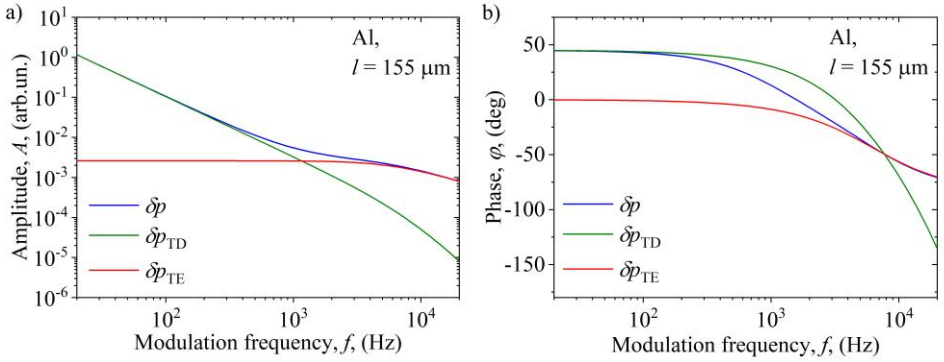

Fig. 9 a) Amplitude and b) phase of the "real" δp signal and its components (thermo-diffusion, δp_{TD}, and thermoelastic, δp_{TE}), obtained using the composite piston model [4,16,17]

Analyzing obtained thermoelastic component with Eq. (12) (Figure 10), the value $f_{TE155} = (6275 \pm 325)$ *Hz* is obtained for the measured sample.

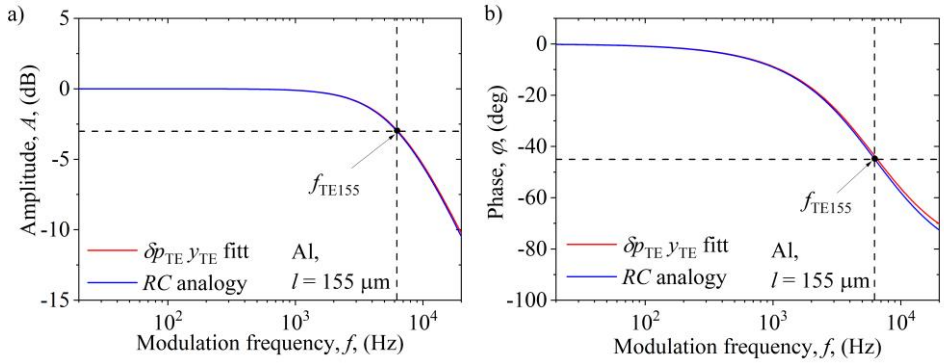

Fig. 10 Analysis of a) amplitude A and b) phase φ of δp_{TE} using Eq. (9) (red line) and the analogue curve of the RC low - pass filter obtained by equations (7) and (8) and frequency $f_0 = f_{TE155}$

The value of f_{TE155} is plotted on the dependence graph $f_{TE} = f(l)$ (Figure 11, blue line) copied from Figure 7 (red line). It is obvious from Figure 11 that the full matching of f_{TE155} with the blue line confirms the correctness of Eq. (11).

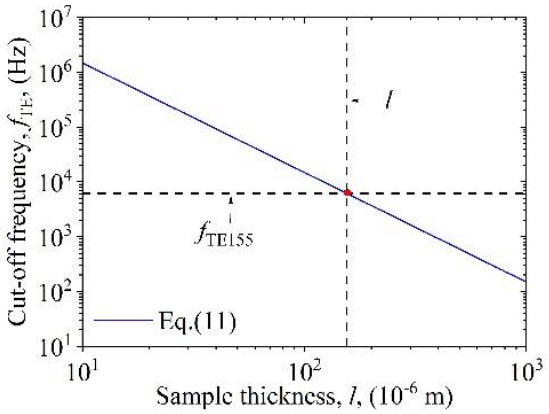

Fig. 11 Dependence of the characteristic thermoelastic cut-off frequency, f_{TE}, on the thickness of the sample, l, with the value of f_{TE155} (red circle) of the experimental *Al* sample having a thickness of 155 microns

4. CONCLUSIONS

In this paper, we have shown that it is possible to make an analogy between the response of the thermoelastic component of the photoacoustic signal in the frequency domain and the frequency response of the low - pass RC filter because both systems behave as linear time - invariant systems. It was established that the thermoelastic component could be numerically processed by a function created based on of the RC filter transfer function. As a result of such processing, the characteristic cut - off

frequency f_{TE} of the thermoelastic component is obtained, the value of which changes by changing the thickness of the tested sample. It was observed that the dependence of f_{TE} on sample thickness l in a logarithmic scale is linear, and that f is proportional to $1/l^2$. The proportionality coefficient contains the value of the thermal diffusion coefficient D_T and the numerical value of the constant b that defines the value of temperature moment M_T in the case when $f = f_{TE}$. Since both D_T and b constants are related to the tested sample, the dependence $f_{TE} \sim 1/l^2$ can be used to define a reference curve for the thermal characterization of the sample material. To confirm the slope of the reference curve, the photoacoustic response of a 155 μm thick aluminum sample was measured with the open-cell experimental set-up, and its thermoelastic component was processed. The obtained value of f_{TE} entirely coincides with the established reference curve of aluminum obtained by theoretical analysis, thus confirming the correctness of the newly established methodology for the thermal characterization of the material.

The importance of the presented article is that it can serve as a basis for the future application of electro-acoustic analogies in the description of transport processes both in physics and electronics [26] (for example, characterization of semiconductors through the contribution of excess carriers) and in medical sciences [27,28] (transport and exchange of energy by diffusion, the transmission of information by the nervous system, modelling axons as electrical cables, forming axon circuits, etc.).

Acknowledgement: *This work has been supported by the Ministry of Education, Science and Technological Development of the Republic of Serbia and by the Institute of Physics Belgrade, through the grant by the Ministry of Science, Technological Development and Innovations of the Republic of Serbia.*

REFERENCES

[1] D. Almond and P. Patel, *Photothermal Science and Techniques*, Chapman & Hall, London, 1996.
[2] S. E. Bialkowski, N. G. C. Astrath, M. A. Proskurnin, *Photothermal Spectroscopy Methods for Chemical Analysis*, 2nd Edition, New York: John Wiley, 2019.
[3] A. Rosencwaig and A. Gersho, "Theory of the photoacoustic effect with solids", *J. Appl. Phys.*, vol. 47, p. 64-69, 1976.
[4] F. McDonald and G. Wetsel, "Generalized theory of the photoacoustic effect", *J. Appl. Phys.*, vol. 49, pp. 2313-2322, 1978.
[5] L. F. Perondi and L. C. M. Miranda, "Minimal-volume photoacoustic cell measurement of thermal diffusivity: Effect of the thermoelastic sample bending", *J. Appl. Phys*, vol. 62, no. 7, pp. 2955-2959, 1987.
[6] A. L. Glazov and K. L. Muratikov, "Generalized thermoelastic effect in real metals and its application for describing photoacoustic experiments with al membranes", *J. Appl. Phys.*, vol. 128, no. 9, p. 095106, 2020.
[7] L. D. Paarman, *Design and analysis of analog filters*, Kluwer Academic Publishers, USA, 2001.
[8] L. E. Frenzel Jr., *Principals of Electronic Communications Systems*, Fourth Edition, McGraw-Hill, 2016.
[9] C. K. Alexander, M. N. O. Sadiku, *Fundamentals of electric circuits*, McGraw-Hill Education, USA, 2017.
[10] Okawa Electric Design (2019), *RC Low-pass Filter Design Tool*. Available at: http://sim.okawa-denshi.jp/en/CRlowkeisan.htm
[11] A. Somer, F. Camilotti, G. Costa, C. Bonardi, A. Novatski, A. Andrade, V. Kozlowski Jr and G. Cruz, "The thermoelastic bending and thermal diffusion processes influence on photoacoustic signal generation using open photoacoustic cell technique", *J. Appl. Phys.*, vol. 114, no. 6, p. 063503, 2013.
[12] A. Somer, A. Gon¸calves, T. V. Moreno, G. K. da Cruz, M. L. Baesso, N. G. C. Astrath and A. Novatski, "Photoacoustic signal with two heating sources: theoretical predictions and experimental results for the open photoacoustic cell technique", *Meas. Sci. Technol.*, vol. 31, no. 7, p. 075202, 2020.

[13] J. A. Balderas-Lopez and A. Mandelis, "Thermal diffusivity measurements in the photoacoustic open-cell configuration using simple signal normalization techniques", *J. Appl. Phys.*, vol. 90, no. 5, pp. 2273-2279, 2001.
[14] B. A. Boley and J. H. Weiner, *Theory of Thermal Stresses*, Wiley, New York, 1960.
[15] G. Roussett, F. Lepoutre and L. Bertrand, "Influence of thermoelastic bending on photoacoustic experiments related to measurements of thermal diffusivity of metals", *J. Appl. Phys.*, vol. 54, pp. 2383-2391, 1983.
[16] D. D. Markushev, J. Ordonez-Miranda, M. D. Rabasovic, M. Chirtoc, D. M. Todorovic, S. E. Bialkowski, D. Korte and M. Franko, "Thermal and elastic characterization of glassy carbon thin films by photoacoustic measurements", *The European Phys. J. Plus*, vol. 132, no. 33, pp. 1-9, 2017.
[17] D. D. Markushev, J. Ordonez-Miranda, M. D. Rabasović, S. Galović, D. M. Todorović and S. E. Bialkowski, "Effect of the absorption coefficient of aluminium plates on their thermoelastic bending in photoacoustic experiments", *J. Appl. Phys.*, vol. 117, p. 245309, 2015.
[18] J. R de Laeter, et al, "Atomic weights of the elements: Review 2000", *Pure Appl. Chem.*, vol. 75, pp. 683-800, 2003.
[19] W. M C. Sansen, *Analog design essentials.* Dordrecht, The Netherlands: Springer. pp. 157-163.
[20] R. K. Rao Yarlagadda, *Analog and Digital Signals and Systems*. Springer Science & Business Media. 2010, p. 243.
[21] C. L. Phillips, J. M. Parr and E. A. Riskin, *Signals, systems and Transforms.* Prentice Hall. 2007.
[22] J. P. Hespanha, *Linear System Theory*. Princeton University Press, 2009.
[23] D. D. Markushev, M. D. Rabasović, D. M. Todorović, S. Galović and S. E. Bialkowski, "Photoacoustic signal and noise analysis for Si thin plate: Signal correction in frequency domain", *Rev. Sci. Instrum.*, vol. 86, p. 035110, 2015.
[24] M. N. Popovic, M. V. Nesic, S. Ciric-Kostic, M. Zivanov, D. D. Markushev, M. D. Rabasovic, S. P. Galovic, "Helmholtz Resonances in Photoacoustic Experiment with Laser-Sintered Polyamide Including Thermal Memory of Samples", *Int. J. Thermophys.*, vol. 37, p. 116, 2016.
[25] S. M. Aleksić, D. K. Markushev, D. S. Pantić, M. D. Rabasović, D. D. Markushev and D. M. Todorović, "Electro-acoustic influence of measuring system on the photoacoustic signal amplitude and phase in frequency domain", *FU Phys Chem Tech*, vol. 14, no. 1, pp. 9-20, 2016.
[26] S. Galovic, Z. Soskic and M. Popovic, "Analysis of photothermal response of thin solid films by analogy with passive linear electric networks", *Thermal Sci.*, vol. 13, no. 4, pp. 129-142, 2009.
[27] R. Deaton, M. Garzon and R. Yasmin, "Systems of axon-like circuits for self-assembled and self-controlled growth of bioelectric networks", *Sci. Reports*, vol. 12, p. 13371, 2022.
[28] P. Alcami and A. El Hady, "*Axonal Computations*", *Front. Cell. Neurosci.*, vol. 13, p. 413, 2019.

APPENDIX I

Considering Eqs (1-3) the expression for δp_{TE} can be written in the form

$$\delta p_{TE} = \alpha_T \frac{\gamma I_0 p_0}{2V_0 k} \frac{3\pi R^4}{(\sigma_i l)^2} \cdot \left[\frac{\tanh\left(\frac{\sigma_i l}{2}\right)}{\frac{\sigma_i l}{2}} - 1 \right], \tag{12}$$

as a complex number δp_{TE} has its amplitude and phase, whose analytical expressions are complicated. But, for electro-acoustic analogies [26], with the series expansion of the expression in square brackets, one can obtain a simplified expression for δp_{TE} of the form

$$\delta p_{TE} = -3\pi\alpha_T \frac{\gamma I_0 p_0 R^4}{16 V_0 k} \cdot \left[\frac{1}{1 + j\frac{\omega}{\omega_{TE}}} \right], \tag{13}$$

whose amplitudes and phases are given as

$$A_{TE}(j\omega) = \left|\delta p_{TE}(j\omega)\right| \sim \frac{1}{\sqrt{1+(\omega/\omega_{TE})^2}}, \text{ and } \varphi = -\arctan\left(\frac{\omega}{\omega_{TE}}\right). \quad (14)$$

Here $\omega_{\mathrm{TE}} = D_T / (l/2b)^2$, and $\sqrt{2} \le b < \sqrt{6}$, depending on number of terms in series expansion.

APPENDIX II. EXPERIMENTAL SET-UP

The experimental setup of the open-cell used in this work is presented in Figure 12. It is a homemade non-commercial setup, explained in detail somewhere else [23,24]. As a light source, a red laser diode with a wavelength of 650 nm, modulated by a frequency generator from the control unit, was used. The photodiode controls the operation of the laser diode and its signal is recorded by the signal processing unit. As a sample, a thin circular aluminum plate, 3 mm in diameter and 155 microns thick, was used, and placed on the microphone's opening. The sample and the microphone together form the so-called photoacoustic cell of minimal volume.

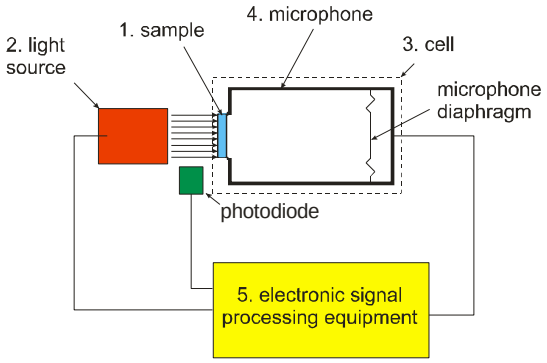

Fig. 12 Simple scheme of the open-cell photoacoustics experimental setup used in our measurements.

The sound created by the illumination of the sample spreads through the air in the cell to the microphone membrane, which records it as a photoacoustic signal, converts it into a voltage signal and forwards it to the signal processing unit for further processing. The PC is used simultaneously as a control (frequency generator) and a signal processing unit. (lock-in amplifier). As a replacement for the instrument, the computer's sound card emulates the lock-in amplifier's operation, with which we record the amplitude and phase of the measured signal (the signal from the photodiode is used as a reference signal).

Радови Драгана К. Маркушев

Конференције

М33

2025 IEEE 34th INTERNATIONAL CONFERENCE ON MICROELECTRONICS

PROCEEDINGS

Niš, Serbia
October 13th-16th, 2025

organized by
Faculty of Electronic Engineering, University of Niš

IEEE Serbia and Montenegro Section- ED/SSC Chapter

in cooperation with
Serbian Academy of Sciences and Arts- Branch in Niš

under the co-sponsorship of
IEEE Electron Devices Society

under the auspices of
Serbian Ministry of Science, Technological Development, and Innovation
Society for ETRAN

IEEE Catalog No. CFP25432-PRT
ISBN 979-8-3315-1416-7

Published by

Electron Devices Society

of the

INSTITUTE OF ELECTRICAL AND ELECTRONICS ENGINEERS, INC.

IEEE Catalog Number:	CFP25432-PRT
ISBN:	979-8-3315-1416-7

STEERING COMMITTEE

Asia & Pacific
S.S. Chung, National Chiao Tung University, Taiwan
P. Balasubramanian, Nanyang Technological University, Singapore
S. Dimitrijev, Griffith University, Australia
H. Iwai, Tokyo Institute of Technology, Japan
S. K. Mohapatra, National Institute of Technology, India
R. Huang, Peking University, China
S. Oda, Tokyo Institute of Technology, Japan
M. K. Radhakrishnan, NanoRel, India
H. Wong, City University of Hong Kong, Hong Kong

Europe, Africa & Middle East
D. Danković, University of Niš, Serbia
V. Davidović, University of Niš, Serbia
S. Deleonibus, CEA/LETI, France
G. Golan, Ariel University, Israel
V. Liberali, University of Milan, Italy
A. Nathan, Cambridge University, UK
A. Nikiforov, NRNU MEPhI, Russia
A. Paskaleva, Bulgarian Academy of Sciences, Bulgaria
S. Selberherr, Technical University of Vienna, Austria
Z. Stamenković, University of Potsdam, Germany

America
V. Arora, Wilkes University, PA, USA
R. Sedaghat, Ryerson University, Canada
M. Estrada, CINVESTAV, Mexico
A. Lakhtakia, Pennsylvania State University, USA
M. Mustafa Hussein, UC Berkeley, USA
B. Nikolic, University of California, Berkeley, CA, USA
A. Ortiz-Conde, University Simon Bolivar, Venezuela
R. Singh, Clemson University, SC, USA
J. Stathis, IBM Research, NY, USA

PROGRAMME COMMITTEE

Co-Chairmen:
D. Danković, University of Niš, Serbia
V. Davidović, University of Niš, Serbia

Vice-Chairmen:
S. Dimitrijev, Griffith University, Australia
Z. Stamenković, University of Potsdam, Germany
S. Selberherr, Technical University of Vienna, Austria
H. Wong, City University of Hong Kong, Hong Kong

Conference Secretariat:
S. Veljković, University of Niš, Serbia
N. Mitrović, University of Niš, Serbia
M. Marjanović, University of Niš, Serbia
E. Živanović, University of Niš, Serbia

Corresponding Members:

I. Adesida, University of Illinois at Urbana-Champaign, USA
G. Angelov, Technical University of Sofia, Bulgaria
M. Aleksandrova, Technical University of Sofia, Bulgaria
V. Benda, Technical University of Prague, Czech Republic
D. Bertozzi, University of Manchester, United Kingdom
M. Blyzniuk, Melexis, Ukraine
D. Boychenko, National Research Nuclear University MEPhI, Russia
A. Cerdeira, CINVESTAV-IPN, Mexico
B. Djezzar, Centre de Développement des Technologies Avancées, Algeria
S. Djorić-Veljković, University of Niš, Serbia
R. Długosz, University of Technology and Life Sciences, Poland
L. Dobrescu, Politehnica University of Bucharest, Romania
A. Dziedzic, Technical University of Wroclaw, Poland
D. Fleetwood, Vanderbilt University, USA
D. Flores, National Centre of Microelectronics, Spain
T. Grasser, Technical University of Vienna, Austria
V. Grimalsky, Autonomous University of Morelos, Mexico
J. Iannacci, Center for Sensors and Devices, Trento, Italy
A. Ionescu, Swiss Federal Institute of Technology, Switzerland
M. Janicki, Lodz University of Technology, Poland
S. Jit, Indian Institute of Technology (BHU) Varanasi, India
G. Jovanović Doleček, Institute INAOE, Mexico
L. Kessarinskiy, SPELS, Moscow, Russia
D. Kouvatsos, NCSR Demokritos, Greece
M. Krstić, IHP Microelectronics, Germany
J. Kuo, National Taiwan University, Taiwan
T. R. Lenka, National Institute of Technology Silchar, India
J. Lutz, Technical University of Chemnitz, Germany
Z. Marinković, University of Niš, Serbia
V. Melikyan, SYNOPSYS, Armenia
V. Milovanović, University of Kragujevac, Serbia
E. Miranda, Universitat Autonoma de Barcelona, Spain
G. Mura, University of Cagliari, Italy
A. Napieralski, Technical University of Lodz, Poland
J. Nikolić, University of Niš, Serbia
T. Nikolić, University of Niš, Serbia
N. Novkovski, University “St Cyril and Methodius”, North Macedonia
G. Papaioanou, National Kapodistrian University of Athens, Greece
Z. Perić, University of Niš, Serbia
Z. Petrović, Institute of Physics, Serbia
S. Poriazis, Phasetronic Laboratories, Greece
M. Potrebić Ivaniš, University of Belgrade, Serbia
A. Prijić, University of Niš, Serbia
Z. Prijić, University of Niš, Serbia
G. Ristić, University of Niš, Serbia
D. Sekulić, University of Novi Sad, Serbia
S. Stanković, Institute of Nuclear Sciences "Vinča", Serbia
G. Stojanović, University of Novi Sad, Serbia
G. Tagliapietra, FBK Trento, Italy
T. Suligoj, University of Zagreb, Croatia
M. Topič, University of Ljubljana, Slovenia
J. Trontelj, University of Ljubljana, Slovenia
J. Vobecky, ABB Switzerland Ltd. Semiconductors, Switzerland
P. Yu, University of California at San Diego, USA
F. Vargas, IHP Microelectronics, Germany
D. Vasiljević Radović, University of Belgrade, Serbia
V. Vukić, University of Novi Sad, Serbia
M. Zwolinski, University of Southampton, United Kingdom

Applicaton of RC Analogies in the Framework of Thermal Characterization of Materials Assigned for Electronics

Dragana K. Markushev
Institute of Physics
University of Belgrade
Belgrade, Serbia
dmarkusev@ipb.ac.rs
ORCID: 0000-0003-1270-4606

Neda Lj. Branković
Faculty of Electronic Engineering
University of Niš
Niš, Serbia
neda.brankovic@elfak.ni.ac.rs
ORCID: 0000-0001-5328-5466

Slavica M. Kovačević
Institute of Physics
University of Belgrade
Belgrade, Serbia
slavica.kovacevic@ipb.ac.rs
ORCID: 0009-0008-7502-250X

Sanja M. Aleksić
Faculty of Electronic Engineering
University of Niš
Niš, Serbia
sanja.aleksic@elfak.ni.ac.rs
ORCID: 0000-0003-4414-6442

Dragan D. Markushev
Institute of Physics
University of Belgrade
Belgrade, Serbia
draganmarkushev@gmail.com
ORCID: 0000-0002-0330-3600

***Abstract*—This paper is based on the use of RC analogies and the development of a theoretical model that can be employed as a laboratory exercise for thermal characterization of materials in electronics. Investigation and analysis of the method have demonstrated that it is reliable and non-destructive for the samples under study. Since the thermoelastic component of a photoacoustic signal (sound) can be approximated by an *RC* circuit, and a mathematical framework for this method has been established, thermal diffusivity and thermal conductivity—both dependent on sample thickness—as well as the cut-off frequency, can be determined. The results obtained so far through mathematical analysis, numerical simulations, and experiments have shown a high degree of consistency and reliability. Compared to conventional techniques, it offers excellent reliability, reduced complexity, and strong agreement between theory and experiment, confirming its potential for accurate, efficient, reliable, and universal thermal characterization of a wide range of materials.**

Keywords—photoacoustic, RC circuit, analogies, thermal characterization.

I. Introduction

Managing heat in modern electronic devices is one of the most important challenges in science and engineering. Electronic components keep getting smaller, while energy dissipation increases. Efficient heat transfer and removal are crucial for protecting device performance, stability, and lifetime. For this reason, the thermal characterization of materials plays a central role not only in electronics but also in fields such as energy technologies, industrial applications, and even biomedical systems. In these areas, precise temperature control is required.

It is an also well-known fact that all materials assigned for electronics can be viewed as thermal systems that serve to transfer, store, or remove heat. These properties are crucial because thermal effects are inherent to all significant processes in electronic components and systems. In all materials, heat transfer is described by diffusion processes, with two characteristic parameters: the temperature difference, ΔT, of the heated and unheated side of the sample, and the thermal diffusion coefficient of the material, D_T, from which the sample is made [1,2].

One of the most suitable techniques for the thermal characterization of materials is photoacoustics. This is due to its high sensitivity, non-destructive nature, and ability to probe a wide range of materials, including thin films, composites, and layered structures. The technique is based on the fundamental photoacoustic effect - absorption of modulated light in a material leads to localized heating, which in turn generates an acoustic wave. Alexander Graham Bell first discovered this in the 1880s. Over the decades, this effect has evolved from a scientific curiosity into a powerful diagnostic tool in material science and solid-state physics.

Examination of sound, which is generated during the process of illuminating a material, is the crucial information to analyzing its periodic changes in thermal state and also it is the basis of this work. The shape of that audio signal, created in periodically illuminated material, as well as the values of its amplitudes and phases, gives a thermal image of the material and provides information about its ability to transfer heat. A simple scheme of the theoretical model on which the research is based is shown in Fig. 1 [3].

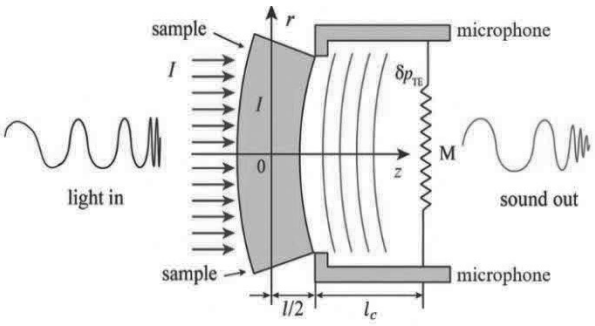

Fig. 1. A simple scheme of the theoretical model. The sinusoidal input represents modulated light, and the sinusoidal output represents sound.

The modulated light source uniformly illuminates the front surface of the sample, which has a circular shape with thickness l and radius R. The absorbed light energy on the

This work has been supported by the Ministry of Science, Technological Development and Innovation of the Republic of Serbia [Grant Number: 451-03-137/2025-03/ 200102].

979-8-3315-1418-1/25/$31.00 ©2025 IEEE

illuminated surface and in the nearby volume is converted into thermal energy, which is then transferred through the sample along the *z*-axis (1D transfer), altering the thermal state of the semiconductor. This change creates a temperature difference between the illuminated and non-illuminated sides of the sample, resulting in its so-called thermoelastic bending. The bending occurs periodically, following the rhythm of the modulated light, and periodically changes the air pressure near the non-illuminated side of the sample (mechanical piston effect). This pressure variation generates sound, i.e., the thermoelastic component $\delta p_{TE}(j\omega)$ of the photoacoustic signal is produced [3].

The thermoelastic component of the photoacoustic signal, which relies on changes in the mentioned parameters D_T and ΔT, is particularly suitable for rapid material characterization. A simplified theoretical model underlying photoacoustics can be a significant aid in the analysis of experimental data and the calculation of the corresponding physical quantities, which are affected by their values, and describe important thermophysical properties of the material, known as transport and thermophysical parameters. The most important parameters are the thermal conductivity, k, and the thermal diffusivity, D_T, where k is the heat transfer property of the material sample, while D_T quantifies the material's ability to conduct thermal energy relative to its ability to store it.

The results of the photoacoustic analysis are usually given through the analysis of amplitudes and phases of the obtained sound in the frequency domain from 20 Hz to 20 kHz. Although there is a tendency to use a simplified theoretical model, frequency-domain photoacoustic heat flow measurements in solid samples suggest that it is necessary to analyze a larger number of thermophysical and mechanical parameters of the tested samples parameters that can be extracted simultaneously, using the total photoacoustic signal and its components. A recently developed method, which aims to simultaneously avoid complex multi-parameter matching, is based on electroacoustic analogies between a low-pass RC filter and the thermoelastic (TE) photoacoustic response of a sample [2-4]. This method extracts only one component of the photoacoustic signal for analysis (the thermoelastic), by introducing only one matching parameter (the cut-off frequency, f_c), as the only characteristic value of the thermoelastic response.

The focus of this work is to provide a theoretical overview of photoacoustics with an emphasis on the analogy between thermal and electrical systems. By establishing electroacoustic analogies, the thermoelastic component of the photoacoustic signal can be described in terms of a low-pass RC filter model. This simplified but powerful theoretical approach allows for the extraction of key thermophysical parameters of materials using only a single characteristic parameter – the cut-off frequency. The goal of this paper is therefore to highlight the theoretical background of photoacoustics, explain the derivation of the thermoelastic signal in terms of diffusion processes, and demonstrate the usefulness of electroacoustic analogies in material characterization.

II. Theoretical Background

Apart from physical models, the characterization of materials with photoacoustics can also be done by establishing appropriate electroacoustic analogies. Namely, in the physical sense, the temperature changes and transport of heat in the material are described by the 1D diffusion equation [2]:

$$\frac{\partial^2 T_s(x,t)}{\partial x^2} = \frac{1}{D_T}\frac{\partial T_s(x,t)}{\partial t}, \tag{1}$$

where the temperature field in the case of period illumination is expressed as:

$$T_s(x,t) = T_{\mathrm{amb}}(x) + T_{st}(x) + T_s(x)e^{j\omega t}. \tag{2}$$

Here, $T_{\mathrm{amb}}(x)$ is the ambient temperature, $T_{st}(x)$ is the static temperature component of the sample, $T_s(x)$ is the dynamic temperature component of the sample, $\omega = 2\pi f$ is the angular modulation frequency, j is the imaginary unit and the above mentioned $D_T = k/(\rho C_V)$, where k is the thermal conductivity, ρ the density and C_V the volumetric thermal capacity of the material. The dynamic solution of Eq. (1) in the frequency domain, which is also responsible for creating sound in the illuminated material, in the case of surface absorbers has the form [2]:

$$T_s(x) = \frac{I_0}{k\sigma_\omega}\frac{cosh[\sigma_\omega(x-l/2)]}{sinh(\sigma_\omega l)}, \tag{3}$$

where I_0 is the light intensity, $\sigma_\omega = (1+j)\sqrt{\pi f/D_T}$ is the complex wave vector of heat diffusion, l is the thickness of the sample, and f is the modulation frequency.

To make the analogy with electrical systems, one can find in literature that Eq. (1) is similar in form to the Maxwell (telegraph) equation of an electromagnetic field, which, given in terms of the voltage $u(x,t)$ between the lines, reads [3]:

$$\frac{\partial^2 u(x,t)}{\partial x^2} = rc\frac{\partial u(x,t)}{\partial t}, \tag{4}$$

where $r = dR/dx$ is the distributed resistance, and $c = dC/dx$ – the distributed capacitance of the line. One can establish an analogy between Eq. (1) and Eq. (3) as an analogy between two distributed parameter systems, by introducing the following relationships: $u \leftrightarrow T$, $c \leftrightarrow \rho C_V$, and $r \leftrightarrow 1/k$. This analogy shows that heat diffusion in solids can be treated as an electrical low-pass filtering process, where heat conduction plays the role of resistance, and thermal storage the role of capacitance.

Based on the established analogies, the diffusion process, which establishes the flow of heat through a material, can be described in the $j\omega$ domain by a simpler model, the low-frequency bandpass RC filter whose transfer function has the form [3,4]:

$$H(j\omega) = \frac{1}{1+j\frac{\omega}{\omega_c}}, \tag{5}$$

where $\omega_c = 2\pi f_c$ is the so-called cut-off frequency of the filter. For low frequencies ($f \ll f_c$), the material can follow the periodic illumination almost completely, leading to strong photoacoustic signals with negligible phase shift. Conversely, for high frequencies ($f \gg f_c$), the penetration depth decreases, and the signal is strongly attenuated with a phase lag approaching -90^o [5].

On the other hand, the analytical form of the equation that describes the thermoelastic component of the photoacoustic

signal $\delta p_{TE}(j\omega)$ in the $j\omega$ domain can also be reduced to the form of the transfer function of the RC low-pass filter [3]:

$$\delta p_{TE}(j\omega) = \frac{3\pi}{2}\frac{I_0\gamma_g p_0 \alpha_T R_S^4}{V_0 k(\sigma l)^2}\left[\frac{tanh(\sigma l/2)}{(\sigma l/2)} - 1\right], \quad (6)$$

from which it follows:

$$\delta p_{TE}(j\omega) = \frac{3\pi}{2}\frac{I_0\gamma_g p_0 \alpha_T R_S^4}{V_0 k}\left[\frac{1}{1+j\frac{\omega}{\omega_c}}\right], \quad (7)$$

whose amplitudes are $|\delta p_{TE}(j\omega)|$ and phases $< (\delta p_{TE}(j\omega))$ given in the form [2,3]:

$$|\delta p_{TE}(j\omega)| \to \frac{1}{\sqrt{1+\left(\frac{f}{f_c}\right)^2}} \quad (8)$$

and

$$\iota < (\delta p_{TE}(j\omega)) \to -arctan\left(\frac{f}{f_c}\right), \quad (9)$$

which represents a complete analogy with the amplitudes and phases of $H(j\omega)$ (Eq. (4)). Using the last two equations, the amplitudes and phases shown in Fig. 2 were obtained for different thicknesses of the tested sample, while Table I presents the basic parameters for aluminum as the material from which the samples were made.

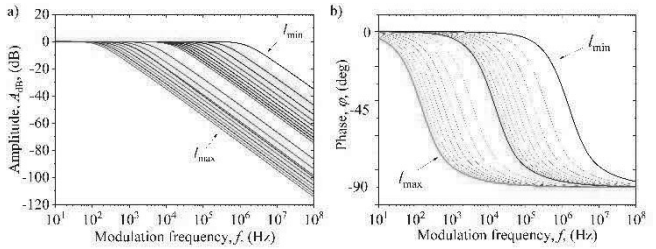

Fig. 2. Based on the Eq. 7, a) amplitudes, A_{dB} (Eq. 8), and b) phases, φ (Eq. 9), of aluminum thermoelastic frequency responses are depicted, for different thicknesses l of the sample in the form of circular plates, having constant radius R and thermal parameters given in Table I [5,6].

TABLE I. ALUMINUM SAMPLE PARAMETERS

Thermal conductivity, k / (W/mK)	237
Heat capacity, C / (J/kgK)	900
Density, ρ / (kg/m^3)	2700
Heat diffusion DT / (10^{-5} m^2/s)	9.75
Linear thermal expansion, αT / (10^{-6} 1/K)	23.1

III. RESULTS AND DISCUSSION

According to the established analogy model, any material that functions as a surface absorber exhibits a characteristic RC response in the frequency domain. The frequency response of the RC filter (Fig. 2), based on the analogies established using Eq. (4), can assist in the thermal characterisation of the material in question. Therefore, it is important to determine whether this statement is purely theoretical or whether the material can be characterised using actual RC parameters.

To assess the practical applicability of RC material characterisation, consider the example of aluminium from our previous work [5]. Based on the Table II that provides the reference curve for aluminium, and using the simple relationship $\tau = RC = 1/(2\pi f_c)$, the connection between f_c and RC values can be determined (Table II). By using standard resistor (100 Ω, 1-100 kΩ) and capacitor (1-100 nF) values, commonly available for measuring the frequency characteristics of RC filters in laboratories [7], we observe that the τ values for thicknesses of 10, 100, and 1000 micrometres correspond to combinations of R = 100 Ω with C = 1 nF, 100 nF and 10 μF, respectively.

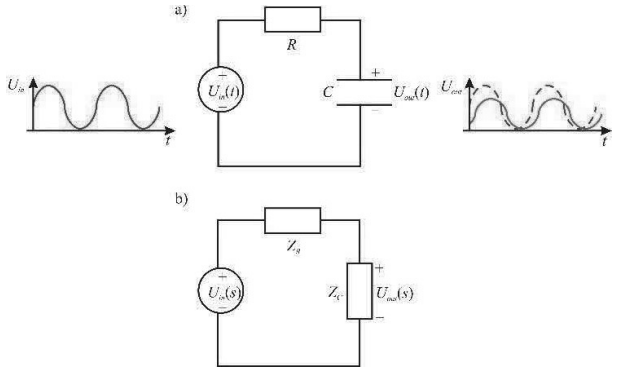

Fig. 3. A simple scheme of RC low-pass filter in a) time, and b) frequency domain [5,6].

TABLE II. FITTING RESULTS OF AN ALUMINUM SAMPLE ESTIMATION OF CUT-OFF FREQUENCY AND RC TIME CONSTANT AS A FUNCTION OF SAMPLE THICKNESS [5]

Sample thickness l / ($\times 10^{-6}$ m)	Cut-off frequency f_c / (Hz)	Time constant t/($\times 10^{-7}$ s)
10	1480460	1.07418
20	376097	4.29673
30	168860	9.66765
40	95666.5	17.18693
50	61560.5	26.85458
60	42936.7	38.6706
70	31658.7	52.63499
80	24313.1	68.74774
90	19261.3	87.00885
100	15638.0	107.41834
200	3965.95	429.67335
300	1776.11	966.76504
400	1004.17	1718.6934
500	645.126	2685.45843
600	449.404	3867.06014
700	331.063	5263.49852
800	256.923	6874.77358
900	204.806	8700.88532
1000	167.771	10741.83372

The obtained result confirms the correctness of the established analogies between the photoacoustic response and the RC filter response of a low-pass filter, demonstrating that

photoacoustic methods of characterising electronic materials can be developed, among others, through the laboratory exercises in electrical engineering for undergraduate students.

IV. Conclusion

Based on the analogies established in the presented way, several conclusions can be drawn. From the side of photoacoustics, the analytical form of $\delta p_{TE}(j\omega)$ (Eq. 6) was obtained based on the assumption that the analogy with RC filters exists, connecting the cut-off frequency f_c. and filters' time constant $\tau = RC$. On the other hand, there is a connection between the cut-off frequency, the thickness of the examined sample through and heat diffusion coefficient D_T. The presented approach to connecting the RC characteristics of electronic circuits with the photoacoustic response and thermal properties of tested material samples opens up the opportunity for developing new and advanced methods of rapid characterisation, as well as various types of student exercises. These would enable students to find real-world applications of photoacoustics and establish a direct link with specific chapters in electronics. By establishing such analogies, one can easily arrive at effective methods of material characterization, which not only determine its thermal characteristics but can also predict its behavior under special conditions of storage or heat removal [2,3].

References

[1] O. Ye, O.V. Pogorelov, E.M. Filatov, I.V.K. Rudenko, M.V. Dyakin, "Characterization methods of heat flows in solids," Progress Phys. Met., vol. 24, no. 2, pp. 239-281, 2023.

[2] D. K. Markushev, N. Lj. Brankovic, S. P. Galovic, K. Lj. Djordjevic, S. M. Aleksic, D. S. Pantic, and D. D. Markushev, "The cut-off frequency – a key concept in the heat flow measurements based on the thermoelastic photoacoustic response," Measurement, vol. 248, pp. 1-11, 2025.

[3] N. Stanojevic, D. K. Markushev, S. M. Aleksić, D. S. Pantić, S. P. Galović, D. D. Markushev, and J. Ordonez-Miranda, "Thermal characterization of n-type silicon based on an electro-acoustic analogy", J. Appl. Phys., vol. 133, pp. 1-12, 2023.

[4] D. K. Markushev, N. Branković, S. M. Aleksić, D. S.Pantić, S. P. Galović, D. D. Markushev, and J. Ordonez Miranda, "The influence of excess free carriers as heat carriers on the n-type silicon thermoelastic photoacoustic responses explained by electro-acoustic analogies", Int. J. Thermophys., vol. 45, no. 107, pp. 1-23, 2024.

[5] N. Lj. Stanojevic, D. K. Markushev, S. M. Aleksic, D. S. Pantic, D. V. Lukic, M. N. Popovic, and D. D. Markushev, "Electro-acoustic analogies between thermoelastic component of the photoacoustic signal and low-pass RC filter", FU: Elec. Energ. vol. 36 no 4, pp. 485-497, 2023.

[6] D. Markushev, N. Branković, S. Aleksić, D. Pantić, A. Pantić, and D. Markushev, "How to use sound as a powerful tool for new materials characterization", Proc. of the 11th International Conference IcETRAN, 2024, pp. 1-4.

[7] P. Pejović, „Laboratorijske vežbe iz električnih merenja", elektronski udžbenik, Elektrotehnički fakultet Univerziteta u Beogradu, Predrag Pejović, Beograd, 2018, Available: https://www.etf.bg.ac.rs/uploads/files/udzbenici/Predrag_Pejovic_Laboratorijske_vezbe_iz_elektricnih_merenja.pdf.

2024 11th International Conference on Electrical, Electronic and Computing Engineering (IcETRAN) | 979-8-3503-8699-8/24/$31.00 ©2024 IEEE | DOI: 10.1109/ICETRAN62308.2024.10645150

PROCEEDINGS

11th International Conference IcETRAN

Niš, Serbia, June 03 - 06, 2024.

ORGANIZED BY:

Society for ETRAN

University of Niš, Faculty of Electronic Engineering

UNDER THE AUSPICES:

Ministry of Science, Technological Development and Innovations of the Republic of Serbia (NITRA)

TECHNICAL SPONSORS:

IEEE – Institute of Electrical and Electronics Engineers, USA

IEEE Region 8 Europe, Middle East, and Africa

IEEE Serbia and Montenegro Section,

IEEE Bosnia and Herzegovina Section

IEEE Industrial Electronics Society

IEEE S&M Section Chapter of the Microwave Theory and Technology Society

IEEE S&M Section Chapter of the Computer Society

SUPPORTED BY

Power Electronics Society of Serbia

CIRED Serbia

TELFOR, Serbia

Society for Microwave Technique, Technologies and Systems, Serbia

2024 11th International Conference on Electrical, Electronic and Computing Engineering (IcETRAN) 3-6 June 2024
Niš, Serbia

Additional copies may be ordered from:

IEEE Service Center
445 Hoes Lane
Piscataway, NJ 08855-1331 USA

+1 800 678 IEEE (+1 800 678 4333)
+1 732 981 1393
+1 732 981 9667 (FAX)
email: customer-services@ieee.org

IEEE Catalog Number: CFP24UWD-ART
ISBN: 979-8-3503-8699-8

2024 11th International Conference on Electrical, Electronic and Computing Engineering (IcETRAN) | 979-8-3503-8699-8/24/$31.00 ©2024 IEEE | DOI: 10.1109/ICETRAN62308.2024.10645174

Committees

IcETRAN 2024, Niš, Serbia, 3-6 June 2024

CONFERENCE CHAIRS:

Prof. Vladimir Katić, *Life Senior Member, IEEE*, Novi Sad, Serbia

Prof. Dragan Mančić, Niš, Serbia

Conference Co-Chair:

Academician, Prof. Slobodan Vukosavić, *Senior Member, IEEE*, Belgrade, Serbia

INTERNATIONAL SCIENTIFIC COMMITTEE

Chairs

Prof. Platon Sovilj, *Member, IEEE*, Novi Sad, Serbia

Prof. Nebojša Dončov, *Senior Member, IEEE*, Niš, Serbia

Co-chair:

Prof. Aleksandra Smiljanić, Belgrade, Serbia

Members of the ISC (preliminary list)

Prof. Emilia Ambrozini, Milan, Italy

Prof. Karsten Berns, Keiserslautern, Germany

Prof. Vincent Bonnet, Paris, France

Prof. Đurađ Budimir, London, England

Prof. Pasquale Daponte, *Fellow, IEEE,* Sania, Italy

Prof. Dragan Denić, Niš, Serbia

Prof. Rafael Dima, Lyon, France

Prof. Nebojša Dončov, *Senior Member, IEEE*, Niš, Serbia

Prof. Strahinja Došen, *Member, IEEE*, Aalborg, Denmark

Academician SASA Antonije Đorđević, Belgrade, Serbia

Academician MASA Igor Đurović, Podgorica, Montenegro

Prof. Željko Đurović, Belgrade, Serbia

Prof. Ovidiu Florin Caltun, Iasi, Romania

Principal Research Fellow Zoran Jakšić, Belgrade, Serbia

Prof. Đorđe Janaćković, Belgrade, Serbia

Corres. member SASA Branislav Jelenković, Belgrade, Serbia

Prof. Gojko Joksimović, *Senior Member, IEEE*, Podgorica, Montenegro

Prof. Nikola Jorgovanović, Novi Sad, Serbia

Prof. Helan Karatza, Thessaloniki, Greece

Prof. Vladimir Katić, *Life Senior Member, IEEE*, Novi Sad, Serbia

Prof. Zora Konjović, Novi Sad, Serbia

Prof. Miroslav Krstić, *Fellow, IEEE*, San Diego, California, USA

Prof. Jozef Lacko, Budapest, Hungary

Prof. Theodore Laopoulos, Thessaloniki, Greece

Prof. Emil Levi, *Fellow, IEEE*, Liverpool, England

Prof. Christos Mademlis, Thessaloniki, Greece

Prof. Guido Maione, *Senior Member, IEEE*, Bari, Italy

Research Associate Nebojša Malešević, Lund, Sweden

Prof. Dragan Mančić, Niš, Serbia

Principal Research Fellow Branko Matović, Belgrade, Serbia

Prof. Gyula Mester, Budapest, Hungary

Prof. Miomir Mijić, Belgrade, Serbia

Prof. Bratislav Milovanović, Niš, Serbia

Prof. Nebojša Mitrović, *Member, IEEE*, Čačak, Serbia

Research Associate Dragana Nikolić, Belgrade, Serbia

Prof Albena Paskaleva, Sofia, Bulgaria

Prof. Alesandro Pizano, Calgari, Italy

Prof. Predrag Petković, Niš, Serbia

Principal Research Fellow Predrag Petrović, Belgrade, Serbia

Academician SASA Zoran Lj. Petrović, Belgrade, Serbia

Academician SASA Zoran Popović, Belgrade, Serbia

Prof. Veljko Potkonjak, Belgrade, Serbia

Prof. R.E. Precup, Timisoara, Romania

Prof. Renato Procopio, *Senior Member, IEEE*, Genova, Italy

Prof. Božidar Radenković, *Member, IEEE*, Belgrade, Serbia

Academician SASA Velimir Radmilović, Belgrade, Serbia

Prof. Branimir Reljin, *Life Senior Member, IEEE*, Belgrade, Serbia

Prof. Danijela Ristić-Durrant, Bremen, Germany

Prof. Romain Serizel, Vandœuvre-les-Nancy, France

Prof. Vladimir Srdić, Novi Sad, Serbia

Dr. Biljana Stošić, *Senior Member, IEEE*, Niš, Serbia

Prof. Paul Sotiriadis, Athens, Greece

Prof. Petar Uskoković, Podgorica, Montenegro

Prof. Boban Veselić, *Senior Member, IEEE*, Niš, Serbia

Prof. Sanja Vraneš, Belgrade, Serbia

Academician SASA Slobodan Vukosavić, *Senior Member, IEEE*, Belgrade, Serbia

Prof. Franz Zotter, Graz, Austria

LOCAL ORGANIZING COMMITTEE:

Chair:

Prof. Dragan Mančić, Niš, Serbia

Members of the LOC (preliminary list)

Prof. Danijel Danković, *Member, IEEE*, Niš, Serbia

Prof. Dragan Denić, Niš, Serbia

Prof. Nebojša Dončov, *Senior Member, IEEE*, Niš, Serbia

Prof. Vesna Javor, *Member, IEEE*, Niš, Serbia

Prof. Zlatica Marinković, *Senior Member, IEEE*, Niš, Serbia

Nikola Mihajlović, Niš, Serbia

Prof. Bratislav Milovanović, Niš, Serbia

Prof. Milutin Petronijević, *Member, IEEE*, Niš, Serbia

Dr. Biljana Stošić, *Senior Member, IEEE*, Niš, Serbia

Prof. Boban Veselić, *Senior Member, IEEE*, Niš, Serbia

SPECIAL SESSIONS PROGRAM COMMITTEE

Prof. dr Platon Sovilj, *Member, IEEE*, Novi Sad, Serbia, Chair

Prof. dr Aleksandra Smiljanić, Belgrade, Serbia, Co-chair

Prof. dr Nebojša Arsić, Kosovska Mitrovica, Serbia

Prof. dr Vladimir Katić, *Life Senior Member, IEEE*, Novi Sad, Serbia

Prof. dr Gyula Mester, Budapest, Hungary

Asst. Prof. Manuela Minetti, Genova, Italy

Prof. dr Milutin Petronijević, *Member, IEEE*, Niš, Serbia

Prof. dr Jelica Protić, Belgrade, Serbia
Dr. Ivana Radonjić-Mitić, Niš, Serbia

Prof. dr Milesa Srećković, Belgrade, Serbia

PUBLICATION CHAIR:

Prof. Danijel Danković, *Member, IEEE*, Niš, Serbia

TREASURER:

Prof. Boban Veselić, *Senior Member, IEEE*, Niš, Serbia

EXHIBITION CHAIR:

Prof. Milutin Petronijević, *Member, IEEE*, Niš, Serbia

INFORMATION CONTACT:

Mrs. Mirjana Jovanic, Belgrade, Serbia

SUPPORT AND TECH.

Awarded papers support and promotion:

Prof. Milić Đekić, Čačak, Serbia

Technical support:

Assoc. Prof. dr Marko Rosić, Čačak, Serbia

Uzahir Ramadani, Belgrade, Serbia

Nikola Mihajlović, Niš, Serbia

Aleksandar Rašković, Belgrade, Serbia

Boban Milijić, Belgrade, Serbia

Marko Vujadinović, Belgrade, Serbia

IcETRAN SECRETARIAT:

Mrs. Mirjana Jovanic, Belgrade, Serbia

Mr. Zlatko Jarnevic, Belgrade, Serbia

How to use sound as a powerful tool for new materials characterization

Dragana Markushev
Institute of Physics Belgrade, National Institute of the Republic of Serbia
Pregrevica 118, 11000 Beograd, Serbia
dragana.markusev@ipb.ac.rs
https://orcid.org/0000-0003-1270-4606

Neda Branković
Faculty of Electronic Engineering, University of Niš,
Aleksandra Medvedeva 14, 18000 Niš, Serbia
neda.brankovic@elfak.ni.ac.rs
https://orcid.org/0000-0001-5328-5466

Sanja Aleksić
Faculty of Electronic Engineering, University of Niš,
Aleksandra Medvedeva 14, 18000 Niš, Serbia
sanja.aleksic@elfak.ni.ac.rs
https://orcid.org/0000-0003-4414-6442

Dragan Pantić
Faculty of Electronic Engineering, University of Niš,
Aleksandra Medvedeva 14, 18000 Niš, Serbia
dragan.pantic@elfak.ni.ac.rs
https://orcid.org/0000-0003-2696-3879

Aleksandar Pantić
Faculty of Electronic Engineering, University of Niš,
Aleksandra Medvedeva 14, 18000 Niš, Serbia
aleksandar.pantic@elfak.ni.ac.rs
https://orcid.org/0000-0003-2351-498X

Dragan Markushev
Institute of Physics Belgrade, National Institute of the Republic of Serbia
Pregrevica 118, 11000 Beograd, Serbia
dragan.markushev@ipb.ac.rs
https://orcid.org/0000-0002-0330-3600

2024 11th International Conference on Electrical, Electronic and Computing Engineering (IcETRAN) | 979-8-3503-8699-8/24/$31.00 ©2024 IEEE | DOI: 10.1109/ICETRAN62308.2024.10645122

***Abstract*— This article will cover the fundamentals of solid-state photoacoustics, which involves sound wave generation by the sample illuminated with a modulated light source, and various sound applications within the characterization of the sample in the solid phase. Among the many sound components, the thermoelastic component is beneficial for establishing a generalized model to characterize the solid. Based on electro-acoustic analogies, the simplest analysis of the thermoelastic component in the frequency domain gives a relationship between the characteristic cut-off frequency of the mentioned component and the corresponding thickness of the investigated sample. The proportionality coefficient in this relationship represents the thermal diffusion coefficient for the sample material. This simple relation can be established for any material in the solid phase, allowing one to establish the generalized method aimed at material characterization. Such a method is reliable and precise and can be used in various branches of science and industry, from the analysis of new materials to material quality control in electrical and electronic engineering.**

Keywords — photoacoustic, sound wave, thermoelastic component, temperature distribution, electro-acoustic analogies, thermal diffusion, cut-off frequency

I. Introduction

To advance modern technologies, it is crucial to have devices, research methods, and computational approaches that perform better and can be applied across various applications. To enhance the function and performance of these devices, it is essential to investigate the properties of related materials, composites, and applications [1-3]. This article explores new trends in the characterization and quality control of new materials. Such advancements can ultimately lead to the developing of more advanced and efficient technologies.

For many years, photoacoustic spectroscopy has been a leading non-destructive method for characterizing various solid phase materials [4]. Photoacoustics is based on the photoacoustic effect, which involves the generation of sound by a periodically illuminated material [5]. The method is characterized by its ability to extract a large number of optical, thermal, and mechanical parameters from experimental data, using a well-known theoretical model of a composite piston. Experimental data consists of amplitudes and phases of the total sound signal picked up by the microphone. This signal consists of at least two components, thermal-diffusion and thermoelastic one, to which these parameters are distributed. The parameters obtained are characteristics of the investigated material.

Despite the large number of parameters that make photoacoustics a very powerful method, the plethora of these parameters makes it challenging because fitting them does not always result in a unique solution. In other words, the combination of parameters obtained through fitting may satisfy an amplitude curve that appears correct but suggests a different material altogether. To overcome this challenge, it is necessary to analyze both amplitudes and phases simultaneously. This is a more complicated and time-consuming task.

In search of simpler and faster solutions, a recent paper introduces a new methodology in the photoacoustic characterization of materials [6]. The novelty is that the total signal is not used for characterization, but one of its components - the thermoelastic one. And what is even more important, is that the thermoelastic component is characterized by only one parameter, the so-called cut-off frequency, f_0. The f_0 depends on the thickness of the investigated sample, l, and serves to establish a reference curve for the tested material. The coefficient of proportionality between f_0 and l is the thermal diffusion coefficient, D_T. In this article, a brief overview of a new material characterization method based on sound analysis using thermoelastic photoacoustic components will be provided.

II. Theoretical Background

A. The Photoacoustic Signal Structure

A photoacoustic signal, $dp(f)$, is a sound signal composed of at least two components: thermodiffusion, $\delta p_{TD}(f)$, and thermoelastic, $\delta p_{TE}(f)$. According to the composite piston theory, the most widely recognized theory of photoacoustics, the δp_{TD} component is generated due to the formation of a thermal piston, and the $\delta p_{TE}(f)$ component is generated due to the creation of a mechanical piston. Both pistons are formed behind the sample being illuminated. Based on this theoretical model one can write [7]:

$$\delta p(f) = \delta p_{TD}(f) + \delta p_{TE}(f), \quad (1)$$

where

$$\delta p_{TD}(f) = \frac{I_o \gamma p_o \sqrt{D_g D_T}}{2\pi l_c T_o k f \sinh(\sigma l)} e^{-i\frac{\pi}{4}}, \quad (2)$$

and

$$\delta p_{TE}(f) = \alpha_T \frac{3\pi p_o I_o \gamma}{V_o k \sigma^3} \frac{R^4}{l^3} \left[\tanh\left(\frac{\sigma l}{2}\right) - \frac{\sigma l}{2}\right]. \quad (3)$$

Here, I_0 is the amplitude of the illuminated light, γ is the adiabatic exponent of air, p_0 , V_0 and T_0 are the air pressure, volume and temperature within the cell (microphone), respectively, D_g and D_T are thermal diffusivities of the air and sample, respectively, l_c is the length of the cell (distance between the sample and microphone diaphragm), α_T is the sample thermal expansion coefficient, k is the sample heat conduction coefficient, l is the sample thickness, R is the sample radius, f is the modulation frequency, and σ is the complex heat diffusion coefficient ($\sigma = (i+1)/\mu$, $\mu = (D_T/\pi f)^{1/2}$, i is the imaginary unit).

The standard procedure in material characterization by photoacoustics consists of the following [7]. The sample response to modulated illumination is usually presented by photoacoustic signal amplitude, A, and phase, φ, as measured points marked by black solid ones in Figure 1 (idealized case). Multiparameter fitting procedure based on (1-3) will give $\delta p(f)$ (red solid line), and both $\delta p_{TD}(f)$ and $\delta p_{TE}(f)$ components (dashed lines) on the same Figure, together with most of the calculated parameters mentioned in previous paragraph.

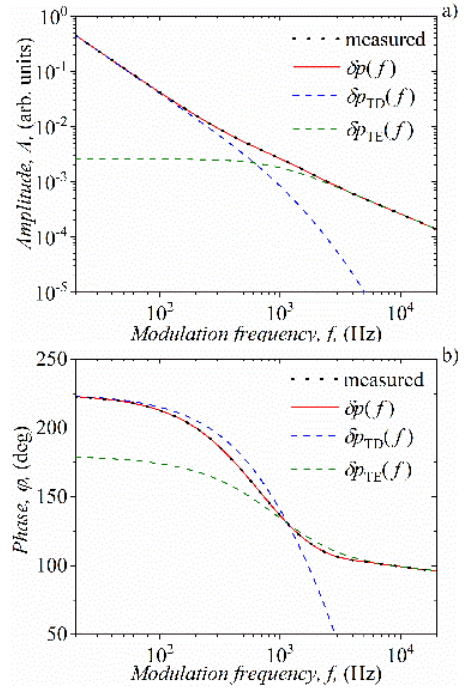

Fig. 1. Measured and fitted photoacoustic signal and its components a) amplitudes, A, and b) phases, φ, as a function of modulated frequency, f, for an arbitrary material of thickness, l, in the form of thin plate.

B. The Concept of Cut-Off Frequency

In the beginning, it was mentioned that photoacoustics provides a large number of physical parameters that can be time-consuming and complex to analyze. To simplify things, researchers are looking for simpler characterization models that focus on analyzing individual components of the photoacoustic signal rather than the total one [6].

One useful component of the photoacoustic signal is the thermoelastic component (3), which is effective in developing a generalized model for material characterization in the solid state. This method is based on the concept of cut-off frequency f_0, a unique parameter that describes both the amplitude and phase of the thermoelastic component (Figure 2). There are three techniques based on which one can extract and define the cut-off frequency of the thermoelastic component. First relies on the frequency at which the temperature difference ΔT between the illuminated and non-illuminated sides of the sample is at its maximum. Second relies on the use of electro-acoustic analogies [8] between the response of the low-frequency RC filter and the thermoelastic photoacoustic response. The third is based on the intersection of the amplitude asymptotes and the inflection point of the phase.

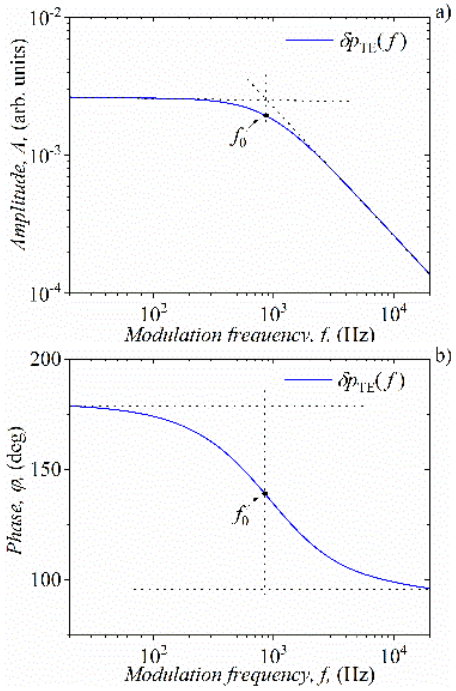

Fig. 2. Thermoelastic component a) amplitude, A, and b) phase, φ, as a function of modulated frequency, f, for an arbitrary material of thickness, l, in the form of thin plate, with cut-off frequency, f_0, defined with asymptotes (amplitude) and inflection point (phase).

Whatever technique is used, the simplest analysis of the thermoelastic component in the frequency domain shows a dependence between the cut-off frequency and the corresponding thickness of the investigated sample. In Figure 3 the results of such analysis are presented for an arbitrary material in the l_{min} = 10 μm to l_{max} = 1000 μm thickness range.

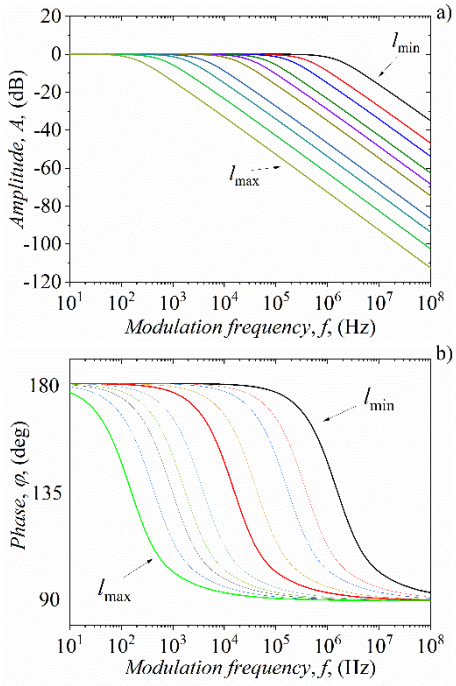

Fig. 3. The dependence between the thermoelastic component shape in the frequency domain (the cut-off frequency possition) and the corresponding thickness, l, of the investigated sample, as a function of the modulation frequency, f.

If we create a logarithmic plot of the cut-off frequency, f_0, against the sample thickness, l, we will observe that the resulting dependence can be represented by a straight line (Figure 4). The slope of this line is defined by l^{-2}. The coefficient of proportionality between f_0 and l^{-2} is thermal diffusion coefficient D_T of the material being tested.

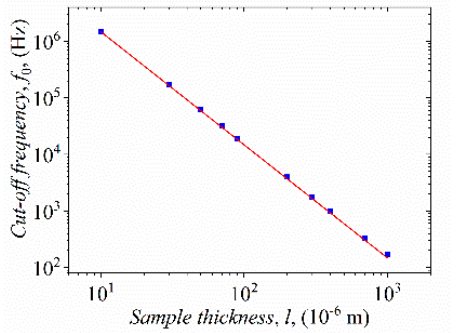

Fig. 4. The resulting dependence between f_0 and l creating the reference curve for the given material.

This simple relation between f_0 and l can be derived from the composite piston model and written as [6]

$$f_0 = \frac{2}{\pi}\frac{D_T}{l^2}b^2 \ , \qquad (4)$$

where b is, so called, calibration factor, depending on the technique used to establish the analogy.

Such a relation can be established for any material in the solid phase (D_T corresponds to the given material), allowing the formation of a generalized photoacoustic method of material characterization based on one sound component analysis. Any deviation from the obtained straight line along the x-axis indicates geometric changes in the sample (e.g. thickness). In contrast, deviations along the y-axis indicate changes in the structure of the sample (e.g. impurities, defects, etc.).

III. Results and Dicussion

Efficient methods aimed at material characterization can be done using sound. One of them is based on the thermoelastic component of the photoacoustic signal. This method involves measuring the amplitudes and phases of the total sound signal detected by the microphone in approximately 80 equidistant points in the range of modulation frequencies from 20 Hz to 20 kHz. The measurement results are then fitted using the theoretical model of the composite piston and the model of recognition of the influence of measuring instruments [9]. The influence of the instruments is removed to obtain the total photoacoustic signal generated in the illuminated sample of the given thickness [10]. The total signal is then divided into thermodiffusion and thermoelastic components. For the obtained thermoelastic component, the cut-off frequency is determined as the frequency corresponding to the maximum temperature difference between the illuminated and non-illuminated parts of the sample. For the specified sample thickness, the obtained cut-off frequency is plotted on the graph with the reference curves of different materials. Matching the value of this frequency and the thickness of the sample with the corresponding reference curve, the unknown material is recognized. Possible disadvantages or advantages of this material, such as defects, impurities, etc., are defined based on the deviation from the ideal curve.

A. Experimental set-up

Experimental photoacoustic spectroscopy of solids often uses a transmission configuration of a photoacoustic cell with minimal volume taking the microphone body as its cell [9-11]. This configuration allows for frequency analysis of samples illuminated from only one side by a modulated light source from the optical spectrum. The scheme of this configuration is shown in Figure 5.

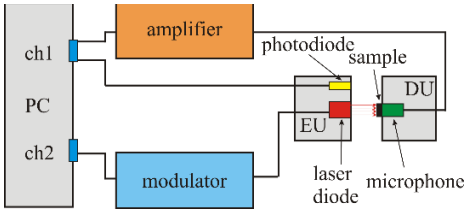

Fig. 5. Simple sheme of the minimal volume experimental set-up.

The excitation unit (EU) consists of a diode (LED or laser diode) and a photodiode. The frequency generator modulates the light intensity of the diode. The photodiode controls the diode's operation. The signal from the photodiode serves as a reference signal that measures how much the microphone signal lags behind the modulated source.

The detection unit (DU) consists of a microphone as a detector and a cell. The sample is placed on the opening of the microphone, and the diode illuminates the sample uniformly. The sample is formed as a flat plate, with a thickness much smaller than its width and length, allowing simple 1D heat flow analysis along the sample thickness (x-axis). The sound wave is transmitted through a narrow air tunnel between the sample and the microphone membrane. Since this configuration detects

sound behind the sample and on the opposite side from the excitation source, it is called a transmission configuration.

Control and signal processing unit is used to control the modulation of the diode and to process the signals coming from the photodiode and the microphone.

B. Measurement Data Analysis

To prove the accuracy and effectiveness of the method that characterizes materials using sound by analyzing the cut-off frequency of the thermoelastic photoacoustic component, we will examine the experimental data of aluminum and silicon samples with thicknesses of 40 and 400 microns. We chose these two materials because their D_T values are similar, which makes it necessary to differentiate them to verify the correctness of the method. To analyze the measured data, three independent steps need to be taken. The first step is to remove instrumental deviations from the measured signal to obtain δp (1). The second step is to extract the thermoelastic component δp_{TE} (3) from δp and find f_0 (4). Finally, the third step is to compare the obtained results with the reference curves of aluminum and silicon.

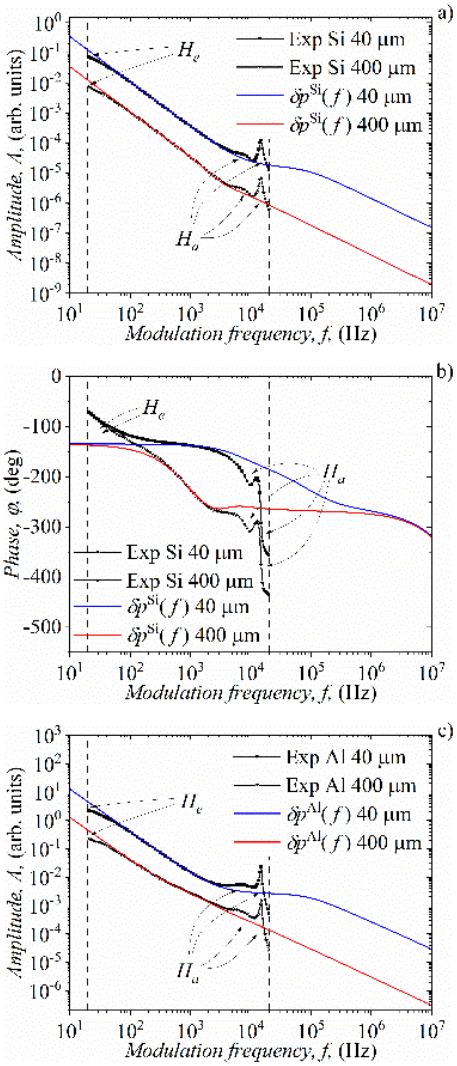

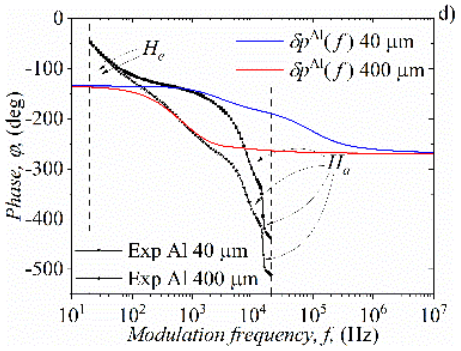

Fig. 6. a,c) Amplitudes, A, and b,d) phases, φ, of the distorted experimental signal, and $\delta p(f)$ signal after signal correction procedure, clear from all instrumental deviations H_e and H_a in the frequency domain, in the case of silicon (Si - a,b) and aluminum (Al - c,d).

The accuracy of photoacoustic measurements can be affected by the measuring chain consisting of interconnected instruments such as detectors, modulators, and amplifiers. These instruments transmit the signal from the sample to the PC as a receiver. The measuring chain can introduce distortion to the measurement which can be caused by various factors such as electronic, H_e, or acoustic, H_a, filtering properties of the microphone, accompanying electronics, random noise, and parasitic currents. These factors can interfere with the measured signal (symbols) at lower (H_e) or higher (H_a) frequencies and substantially impact the results (see Figure 6). To address this issue, we use a signal correction procedure (SCP) [10] to identify and eliminate any signal disturbances. This process ensures that only the relevant signal δp remains (solid line), which can be fitted with a well-known theoretical model of the composite piston, and extrapolated to the larger frequency range.

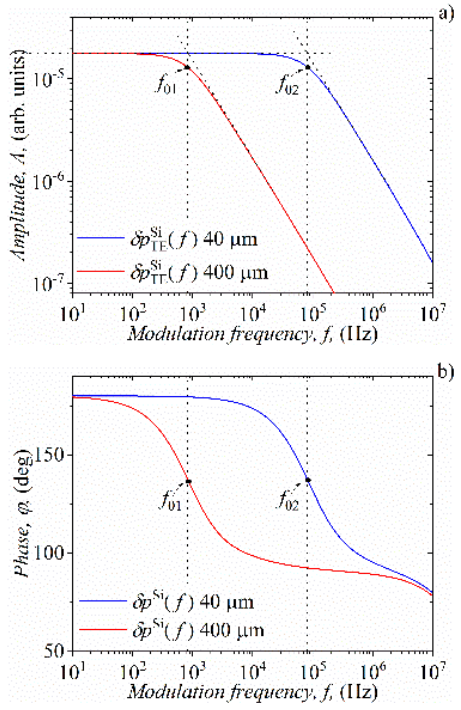

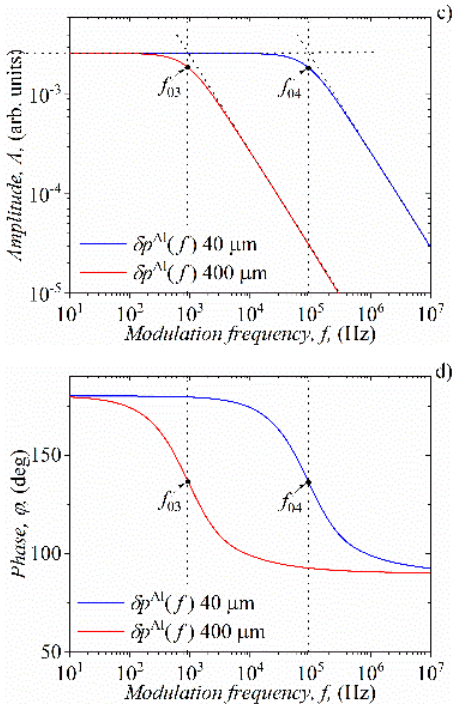

Fig. 7. Thermoelastic component a,c) amplitudes, A, and b,d) phases, φ, in the frequency domain with obtained cut-off frequencies f_{01}, f_{02}, f_{03}, and f_{04} , in the case of silicon (Si - a,b) and aluminum (Al - c,d).

After fitting the δp using the composite piston model, the components (2-3) of the photoacoustic signal can be obtained. Singling out the thermoelastic components (Figure 7), one can easily obtain the matching cut-off frequencies f_{01}, f_{02}, f_{03}, and f_{04} for the corresponding sample thicknesses, using one of two mentioned techniques. In Figure 8 cut-off frequencies are found using the maximal temperature difference method (ΔT_{max}).

C. Material Characterization

After finding all the cut-off frequencies from Figure 8, one can enter their values, for the corresponding sample thicknesses, on the graphs of the aluminum and silicon reference curves presented in Figure 8 (solid lines). By comparing the data with the reference curves, we can accurately confirm the type of material being examined. Reading the results presented in Figure 8 it is obvious that f_{01} and f_{02} (red asterisks) corresponds to the silicon, while f_{03} and f_{04} (blue asterisks) corresponds to the aluminum sample. Any deviations from the reference curves, either horizontally or vertically, suggest irregularities in the material's thermal, mechanical, optical, transport or structural properties. All the mentioned properties are essential when it comes to materials characterization, whether they are completely new or it is about improving the characteristics of existing ones.

IV. Conclusions

This paper shows how sound, especially one of its components, can be a powerful tool in developing advanced methods of characterizing new materials. It is shown that by extracting the thermoelastic component and analyzing it based on only one parameter, the cut-off frequency, a set of reference curves for different materials defined based on the thermal diffusion coefficient can be obtained. The validity of this method was experimentally confirmed in the cases of silicon and aluminum in thick and thin samples. Its great possibilities were pointed out when characterizing single-layer and multi-layer samples, thin films and bulk materials. Determination of thermal, optical, transport and structural properties is the main task of this method, and special attention should be directed to weakly absorbing organic, inorganic, hybrid and nanomaterials, which are rough or highly scattered and their analysis by conventional techniques is rather difficult.

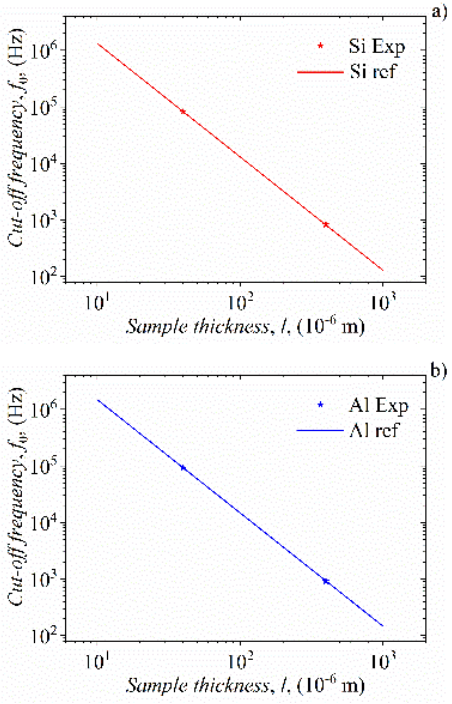

Fig. 8. Typical reference curves in the case of silicon (Si – a) and aluminum (Al – b) and experimentaly obtained cut-off frequencies (asterisks) from Figure 7.

Acknowledgment

The authors acknowledge funding provided by the Institute of Physics Belgrade, and Faculty of Electronic Engineering Niš through the grant (grant number 451-03-65/2024-03/200102) by the Ministry of Science, Technological Development and Innovations of the Republic of Serbia.

References

[1] J. K. Wessel, Handbook of advanced materials: enabling new designs, John Wiley & Sons, Inc., Hoboken, New Jersey, 2004.

[2] J. Xu, H. C. Wu, J. Mun, R. Ning, W. Wang, G. N. Wang, S. Nikzad, H. Yan, X. Gu, S. Luo, D. Zhou, J. B. Tok, Z. Bao, "Tuning Conjugated Polymer Chain Packing for Stretchable Semiconductors", Advanced Materials, 2022, 34, 2104747, https://doi.org/10.1002/adma.202104747

[3] M. R. Clary, S. N. Cantu, J. A.-C. Liu, B. A. Evans, "Magnetic Reprogramming of Self-Assembled Hard-Magnetic Cilia", Advanced Materials Technologies, 2024, 9, 2302243, https://doi.org/10.1002/admt.202302243

[4] S. E. Bialkowski, N. G. C. Astrath, M. A. Proskurnin, Photothermal Spectroscopy Methods for Chemical Analysis, 2nd Edition New York: John Wiley, 2019.

[5] S. Krishnaswamy, "Photoacoustic Characterization of Materials", in: Sharpe, W. (eds) Springer Handbook of Experimental Solid Mechanics, Springer Handbooks. Springer, Boston, MA, 2008.

[6] N. Stanojevic, D. K. Markushev, S.M. Aleksić, D.S. Pantić, S.P. Galović, D. D. Markushev, J. Ordonez-Miranda, "Thermal characterization of n-type silicon based on an electro-acoustic analogy", Journal of Applied Physics, 133, 245102 (2023), https://doi.org/10.1063/5.0152495

[7] D. K. Markushev, D. D. Markushev, S. M. Aleksic, D. S. Pantic, S. P. Galovic, D. M. Todorovic, and J. Ordonez-Miranda, "Effects of the photogenerated excess carriers on the thermal and elastic properties of n-type silicon excited with a modulated light source: Theoretical analysis", Journal of Applied Physics, 126 (18), 185102 (2019), https://doi.org/10.1063/1.5100837

[8] D. Maillet, Thermal quadrupoles: solving the heat equation, John Wiley & Sons, Chichester, West Sussex, 2000.

[9] D. K. Markushev, D. D. Markushev, S. M. Aleksic, D. S. Pantic, S. P. Galovic, D. M. Todorovic, and J. Ordonez-Miranda, "Experimental photoacoustic observation of the photogenerated excess carrier influence on the thermoelastic response of n-type silicon", Journal of Applied Physics, 128, 095103 (2020), https://doi.org/10.1063/5.0015657

[10] D. D. Markushev, M. D. Rabasović, D. M. Todorović, S. Galović, and S. E. Bialkowski, "Photoacoustic signal and noise analysis for Si thin plate: Signal correction in frequency domain", Review of Scientific Instruments, 86, 035110 (2015), https://doi.org/10.1063/1.4914894

[11] M. D. Rabasović, M. G. Nikolić, M. D. Dramićanin, M. Franko and D. D. Markushev, Low-cost, portable photoacoustic setup for solid samples, Measurement Science & Technology, 20, (2009) 095902 (6pp), doi:10.1088/0957-0233/20/9/0959

BOOK OF ABSTRACTS

BOOK OF ABSTRACTS

22nd International Conference on Photoacoustic and Photothermal Phenomena

ISBN 978-989-33-6212-9

Organizing Committee

CHAIR:
Carlos Serpa (University of Coimbra)

Luis Arnaut (University of Coimbra)
João Pina (University of Coimbra)
Fábio Schaberle (University of Coimbra)
Lígia Gomes da Silva (University of Coimbra)
Adelino Pereira (University of Coimbra)
Amílcar Duque Prata (University of Coimbra)
Daniela Amado (University of Coimbra)
Diogo Pereira (University of Coimbra)
Otávio Augusto Chaves (University of Coimbra)

1 2 9 0
UNIVERSIDADE D COIMBRA

CLL
COIMBRA LASER LAB

PHOTOMEDICINE AND REACTIVITY
COIMBRA CHEMISTRY CENTRE - INSTITUTE OF MOLECULAR SCIENCES

International Scientific Committee

Nelson Astrath (Brazil)
Bertrand Audoin (France)
Mauro L. Baesso (Brazil)
Peter Burgholzer (Austria)
Stanislav Emelianov (USA)
Mladen Franko (Slovenia)
Christ Glorieux (Belgium)
Vitaliy Gusev (France)
Daniel Lanzillotti Kimura (France)
Bincheng Li (China)
Roberto Li Voti (Italy)
Boris Majaron (Slovenia)
Andreas Mandelis (Canada)
Ernesto Marin (Mexico)
Alexei Maznev (USA)
Arantza Mendioroz (Spain)
Vasilis Ntziachristos (Germany)
Alberto Oleaga (Spain)
Michał Janusz Pawlak (Poland)
Mikhail Proskurnin (Russia)
Daniel Razansky (Switzerland)
Pascal Ruello (France)
Agustin Salazar (Spain)
Vincenzo Spagnolo (Italy)
Masahide Terazima (Japan)
Dragan Todorovič (Serbia)
Chenglong Wang (China)
Lihong Wang (USA)
Oliver Wright (Japan)
Perry Xiao (Unied Kingdom)
Vladimir Zharov (USA)
Ugo Zammit (Italy)

International Steering and Advisory Board

P16 - The cut-off frequency - a key concept in the thermoelastic photoacoustic response

Markushev DK(1)*, Brankovic N(2), Galovic SP (3), Djordjevic KLj(3), Aleksic SM(2), Pantic DS(2), Markushev DD(1)

(1) Institute of Physics Belgrade-National Institute of the Republic of Serbia, University of Belgrade, Belgrade, Serbia.

(2) Department of Microelectronics, Faculty of Electronic Engineering, University of Nis, Nis, Serbia.

(3) Vinca Institute of Nuclear Sciences-National Institute of the Republic of Serbia, Belgrade, Serbia.

* dragana.markusev@ipb.ac.rs

Background

It is a well-known fact that the photoacoustic analysis in the frequency domain was always multi-parametric and that it managed to extract many thermal and mechanical quantities of the investigated samples, such as D_t as the coefficient of thermal diffusion, k as the coefficient of heat conduction, α_t as the coefficient of linear thermal expansion, l and R as the sample thickness and radius, respectively, etc, using the total photoacoustic signal and its components [1-3]. Although multiparameter fitting has numerous advantages, it has a significant drawback: the combination of fitting parameters may not always be unique. As a consequence, both amplitudes and phases must be used simultaneously. There is no correct way to single out only one or the other. Additionally, it is necessary to measure independently at least one or two parameters with different methods (l and/or R for example) to be included in the fitting process of the experimental data as constants.

Methods

We have recently developed a new method of material characterization based on electro-acoustic analogies between the low-pass *RC* filter and the thermoelastic (TE) photoacoustic response of the sample [4]. This method introduces the cut-off frequency, f_c, the characteristic value of the thermoelastic response. By establishing a relationship between the cut-off frequency and the square of the thickness of the sample, we can obtain the reference curve of the sample material, knowing that the proportionality parameter between f_c and l^2 is the thermal diffusivity coefficient, D_t, of the investigated material. It is important to point out that while electroacoustic analogies have the advantage of simplicity, they are only an approximation. There is a margin of error of $\pm 10\%$ when determining f_c using this method. It is also worth noting that the concept of f_c can be somewhat unclear.

ISBN: 978-989-33-6212-9

Results

In this paper, we present the concept of f_c based on the parabolic heat conduction equation (PHCE) applied for temperature variation calculation within the sample and on its surfaces [2,3]. The f_c refers to the frequency at which the temperature difference ΔT between the illuminated and non-illuminated sample sides is at its maximum for a given sample thickness. A persuasive representation of the f_c concept is shown in Figure 1, displaying TE amplitude responses alongside the corresponding temperature differences for a thick (a-1000 μm) and thin (b-10 μm) aluminium sample. The maximal value of temperature difference corresponds to the f_c position in the frequency domain (fall to 0.707 of the thermoelastic component amplitude).

Conclusions

The cut-off frequency concept of thermoelastic photoacoustic response has proven effective for several reasons. First, it allows the TE response to be described with only one parameter. Secondly, it allows the obtaining of reference curves for different materials, enabling effective material quality control, necessary when creating advanced materials for certain purposes. Thirdly, it connects with the maximum temperature difference on the illuminated and non-illuminated side of the tested sample, which gives an insight into the efficiency of heat transport in materials at different modulation frequencies. Finally, this concept applies to any solid material.

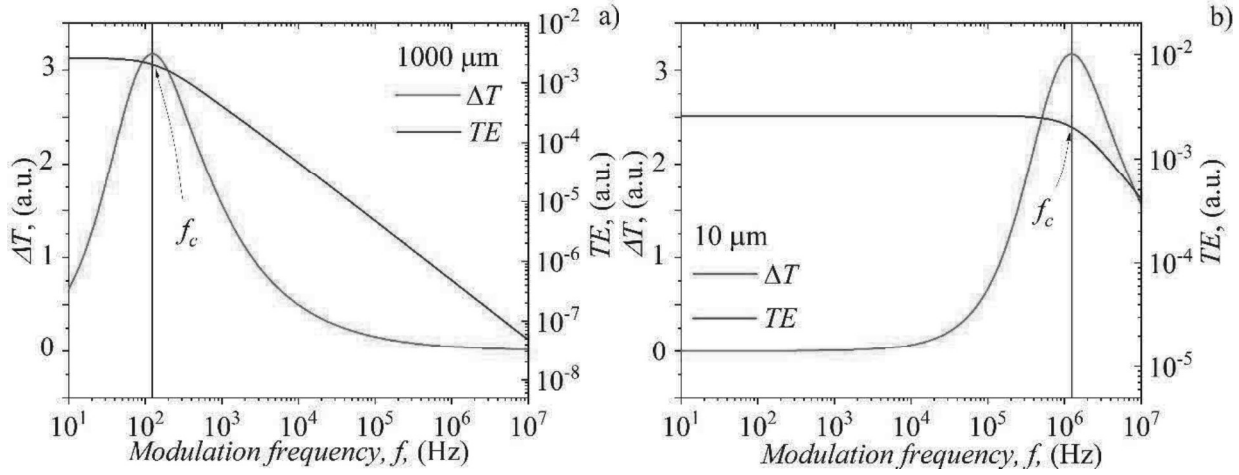

Fig. 1. Thermoelastic amplitude responses *TE* and corresponding temperature differences ΔT as a functions of modulation frequencies *f*, with assumed cut-off frequency f_c position in the case of a) thick (1000 μm) and b) thin (10 μm) aluminium sample.

ISBN: 978-989-33-6212-9

References

[1] K.Lj.Djordjevic, S.P. Galović, M.N. Popović, M.V. Nešić, I.P.Stanimirović, Z.I. Stanimirović, D.D. Markushev, Use Neural Network in Photoacoustic Measurement of Thermoelastic Properties of Aluminum foil, Measurement, 119, (2022), https://doi.org/10.1016/j.measurement.2022.111537

[2] A. Rosencwaig and A. Gersho, Theory of the photoacoustic effect with solids, Journal of Applied Physics, 47, 64–69 (1976), https://doi.org/10.1063/1.322296

[3] F. McDonald and G. Wetsel, Generalized theory of the photoacoustic effect, Journal of Applied Physics, 49, 2313 (1978), https://doi.org/10.1063/1.325116

[4] N. Stanojevic, D. K. Markushev, S.M. Aleksić, D.S. Pantić, S.P. Galović, D. D. Markushev, J. Ordonez-Miranda, Thermal characterization of n-type silicon based on an electro-acoustic analogy, Journal of Applied Physics, 133, (2023), https://doi.org/10.1063/5.0152495

ISBN: 978-989-33-6212-9

P46 - Machine Learning optimal photoacoustic characterisation of aluminium using thermoelastic response

Kovacevic SS(1), Jordovic-Pavlovic MI(2)*, Popovic MN(3), Markushev DD(3), Dobardzic EF(1), Markushev DK(3)

(1) Faculty of Physics, University of Belgrade, Belgrade, Serbia.

(2) Faculty of Mechanical and Civil Engineering in Kraljevo, University of Kragujevac, Kraljevo, Serbia.

(3) Institute of Physics Belgrade - National Institute of the Republic of Serbia, University of Belgrade, Belgrade, Serbia.

* jordovicpavlovic.m@mfkv.kg.ac.rs

Background

The photoacoustic method for material characterization is non-destructive, offering high potential for industrial applications [1]. This paper introduces two techniques to reduce the number of experimental points required to train a neural network (NN) to predict sample parameters from thermoelastic responses of aluminium samples accurately. By minimizing input features, the measurement time for photoacoustic characterization can be reduced from hours to minutes. For this case, 67000 simulated thermoelastic responses were used. Each simulation represents an aluminium sample's thermoelastic response measured at 300 modulation frequencies, with the sample having a specific thickness l and cut-off frequency f_{TE}. Input features for the NN are amplitudes and phases of these thermoelastic signals where each modulation frequency has a corresponding amplitude and phase. There are 600 features (300 amplitudes and 300 phases). The output features of the NN are thickness ranging from $l = (10 - 1000)\ \mu\text{m}$ and cut-off frequency ranging from $f_{TE} = (0.149 - 1{,}481)\ \text{kHz}$. Two techniques for reducing the number of input features were proposed: principal component analysis (PCA) [2] and genetic algorithms (GA) [3]. The study demonstrates that using only five input features, corresponding to five different modulation frequencies, is sufficient for precise and accurate prediction of sample parameters.

Results

During data pre-processing, the amplitudes were converted to logarithmic values and then maximum absolute scaling was applied to all 600 features. Logarithmic values of both output values were taken, and then maximum absolute scaling was done. The neural network had an input layer with 5 neurons, one hidden layer with 5 neurons and an output layer with 2 neurons, corresponding to the output variables l and f_{TE}. The two extracted feature groups were used on the same model with the same hyperparameters during training. GA are in their nature stochastic, so reproducibility is not to be expected in their case. In Fig 1. are the predicted values vs true values for thickness and cut-off frequency, done on previously unseen data (validation set). GA extracted variables perform better than those obtained by PCA, with 1000 epochs and a learning rate of 10^{-4}, the mean relative errors for l and f_{TE} are $0{,}04\%$ and $0{,}12\%$

ISBN: 978-989-33-6212-9

respectively. For PCA extracted variables the mean relative errors are slightly higher, 0,07% and 0,17% for l and f_{TE}.

Conclusion

Current analysis shows that an NN with 5 thermoelastic signal points as input features predicts the aluminium sample's thickness and cut-off frequency with adequate precision and accuracy. Genetic algorithms are better suited for feature extraction of photoacoustic signals used for material characterisation. PCA performs well for thicker samples, but as the sample gets thinner, the relative error for prediction grows. NNs trained on GA-extracted features perform well for both thick and thin samples. It should be noted that GA neural networks were trained on features corresponding to modulation frequencies far outside of the photoacoustic range of 20 Hz to 20 kHz.

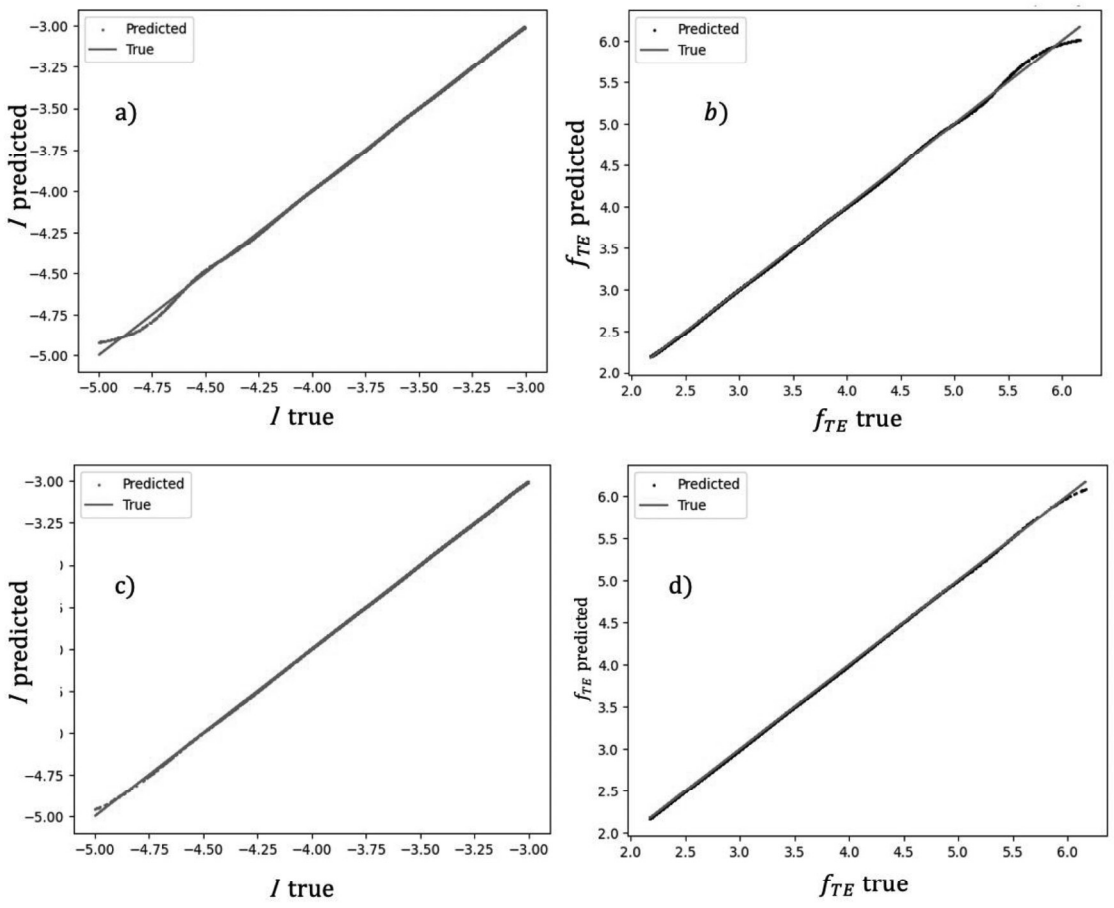

Fig. 1. Predicted vs true values for thickness l and cut-off frequency f_{TE} for PCA extracted variables (a and b) and for GA extracted variables (c and d)

ISBN: 978-989-33-6212-9

References

[1] Djordjevic, K.L., Galovic, S.P., Jordovic-Pavlovic, M.I., Nesic M.V., Popovic M.N., Cojbasic Z.M., Markushev D.D., Photoacoustic optical semiconductor characterization based on machine learning and reverse-back procedure, Optical and Quantum Electronics, 52, 247 (2020)., 52, 247 (2020) https://doi.org/10.1007/s11082-020-02373-x

[2] F. Song, Z. Guo, D. Mei, Feature selection using principal component analysis, Conference on System Science, Engineering Design and Manufacturing Informatization (2010) Yichang, Hubei China, https://ieeexplore.ieee.org/document/5640135.

[3] H Yoshida, R Leardi, K Funatsu, K Varmuza,"Feature selection by genetic algorithms for mass spectral classifiers", Analytica Chimica Acta, Volume 446, Issues 1–2 (2021) https://doi.org/10.1016/S0003-2670(01)00910-2.

ISBN: 978-989-33-6212-9

P61 - Photoacoustic characterization of Poly-L-Lactide

Popovic MN (1)*, Markushev DD (1), Milicevic D (2), Markushev DK (1) , Djordjevic KLj (2), Galovic SP (2)

(1) Institute of Physics Belgrade, National Institute of the Republic of Serbia, University of Belgrade, Pregrevica 118, Belgrade (Zemun) 11080, Serbia

(2) Vinca Institute of Nuclear Sciences-National Institute of the Republic of Serbia, University of Belgrade, Mike Petrovica Alasa 12-14, Belgrade (Vinca) 11351, Serbia.

* marica.popovic@ipb.ac.rs

Abstract

The photothermal effect is the phenomenon that describes the absorption of the incident electromagnetic radiation and its conversion into heat in different non-radiative relaxation and de-excitation processes. This way generated heat causes the disruption of the thermodynamic state of the sample (pressure, temperature, density), which propagates through the sample and the nearby environment, producing many detectable phenomena. Photoacoustic is a first set, non-destructive and versatile photothermal technique, that measures the air pressure oscillations in the photoacoustic cell occurred as a consequence of the periodic sample heating exposed to a modulated light beam.

In this paper, the dependence of the photoacoustic response on the level of crystallinity of Poly-(L-lactide) (PLLA) samples is investigated. By varying the cooling conditions following the compression molding process, two kinds of PLLA samples with significant differences in microstructure and crystallinity were prepared; samples quenched in ice-water mixture had a crystallinity of 20%, while ones slowly cooled down had a high crystallinity of over 70%. These samples have substantial discrepancies in optical properties (transparency, color, and others), as the crystallinity significantly impacts the optical behavior of polymers.

The theory-mathematical models of thermoconducting and thermoelastic components of total photoacoustic presser are derived based on the generalized theory of heat conduction [3,4,5]. The total pressure is obtained as the sum of those two components. It is discussed thermaly opaque (thermal diffusion length is smaller than the thickness of the sample) and thermaly transparent sample (sample tikness is smaller than the thermal diffusion lenght) dependence on the coefficient of the optical absorpcion. Figure 1 shows the amplitudes of the photoacoustic response and its two components as a function of frequency for different values of the optical absorption coefficient. It can be observed that for values of optical absorbance (product of the coefficient of optical absorption and thickness) greater than 1.5, all three components change their behavior.

ISBN: 978-989-33-6212-9

Based on the analysis performed in the paper, it can be concluded that different sample preparation methods can be distinguished and that the photoacoustic response can be related to their crystallinity. By further analysis of the data, it is possible to establish an exact relationship between the photoacoustic response and the degree of crystallinity of the material and determine the coefficient of optical absorption of polylactide.

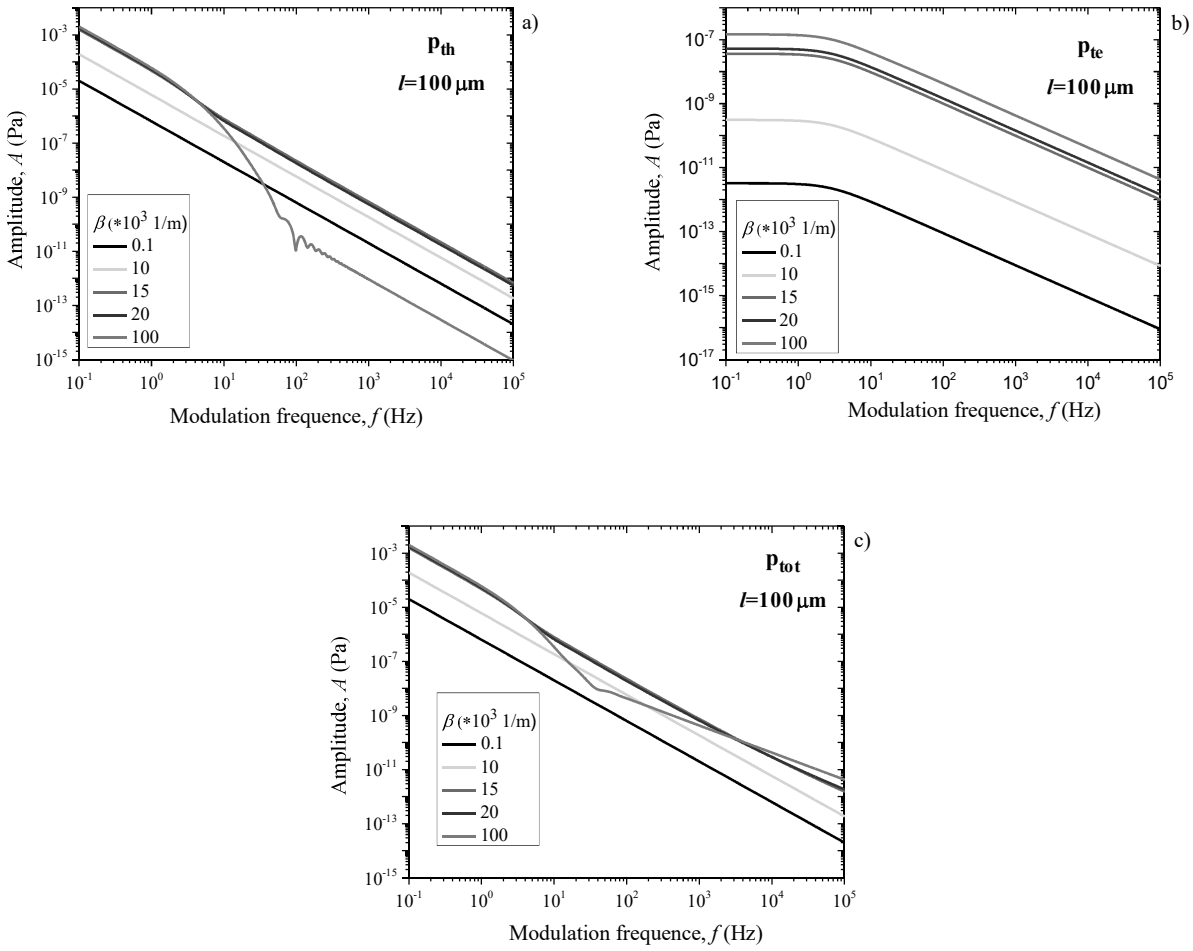

Fig. 1. Amplitude characteristics of the photoacoustic response (c) and its components: a) thermoconducting component and b) thermoelastic component

ISBN: 978-989-33-6212-9

References

[1] Milicevic, D. and Suljovrujic, E. (2017), The influence of the preparation conditions and filler content on thermal properties of poly-l-lactide and hydroxyapatite/poly-l-lactide nanocomposite. *Polym. Int*, 66: 1275-1283. https://doi.org/10.1002/pi.5382

[2] Edin Suljovrujic & Dejan Milicevic, On the enthalpy of melting of poly(l-lactide), *International Journal of Polymer Analysis and Characterization*, 24:5, 381-388, (2019) DOI: 10.1080/1023666X.2019.1598635

[3] S. Galović and D. Kostoski, "Photothermal wave propagation in media with thermal memory," *Journal of Applied Physics*,. 93(5), 3063–3070 (2003). DOl: 10.1063/1.1540741

[4] Galović, S., Šoškić, Z., Popović, M., Cevizović, D., & Stojanović, Z, Theory of photoacoustic effect in media with thermal memory. *Journal of Applied Physics*, *116*(2), (2014). https://doi.org/10.1063/1.4885458

[5] Nesic, M., Galovic, S., Soskic, Z., Popovic, M., & Todorovic, D. M, Photothermal thermoelastic bending for media with thermal memory. *International Journal of Thermophysics*, *33*(10–11), 2203–2209 (2012). https://doi.org/10.1007/s10765-012-1237-6

ISBN: 978-989-33-6212-9

PROCEEDINGS OF SCIENCE

Evaluation of Thermophysical Properties of Semiconductors by Photoacoustic Phase Neural Network

Katarina Lj Djordjevic[a], Slobodanka P Galović[a], Miroslava I Jordović-Pavlović[b], Dragan D Markushev[c], Dragana K Markushev [c], Mioljub V Nešić[a], and Marica N Popović[c]

a „VINČA" Institute of Nuclear Sciences - National Institute of the Republic of Serbia University of Belgrade, Mike Petrovica Alasa 12-14, 11351 Vinča, Belgrade, Serbia

b College of Applied Sciences Užice, Trg svetog Save 34, 31000 Uzice, Serbia

c Institute of Physics Belgrade, National Institute of the Republic of Serbia, Pregrevica 118, 11080 Belgrade (Zemun), Serbia

E-mail: katarina.djordjevic@vin.bg.ac.rs

Abstract: The idea of this paper is to develop a method for determination thermal diffusivity, linear expansion coefficient and thickness of a semiconductor sample from photoacoustic phase measurement by using neural network. The neural network has been trained on photoacoustic phases obtained from a theoretical model for semiconductors Si n-type in the range of 20Hz to 20kHz. The accuracy of the prediction of the experimental signal by the phase neural network was analyzed depending on the application of random Gaussian noise to the input base of photoacoustic signals.

Key words: photothermal, photoacoustics, phases, artificial neural networks, optimization, random Gaussian noise, experimental data processing

11th International Conference of the Balkan Physical Union (BPU11),
28 August - 1 September 2022
Belgrade, Serbia

PoS(BPU11)157

1. Introduction

Photoacoustics is a non-destructive technique that considers the effects of the interaction of light and matter. In the most cases, it is non-contact experimental setup and requires little preparation of samples for the experiment. With the experimental setup of the open photoacoustic cell, the photoacoustic response is recorded with a microphone directly placed on the sample [1-6]. The photoacoustic response (amplitude-phase characteristics) can be used by standard analysis to determine the sample's optical, thermal, elastic and many other properties. Most often, in the analyzes of the results of various photoacoustic settings, only the amplitude characteristics in a narrower frequency range are considered, cutting off the frequency ranges where there is the detection of instrumental influences [7-9].

By developing theoretical-simulation models [10-17] of physical effects that exist in a modulated illuminated sample that affects the formation of a signal detected by a microphone, it was possible to develop algorithms for the inverse determination of the parameters of the analyzed sample [18-21]. A neural network algorithm is based on a working replica of the human brain in process of learning from the given data. The structure of neural networks consists of connected neurons that are placed in three layers: input, hidden and output. During training through the neural network, forward and backward, input layer values and output layer values connect. In our case, the phases of photoacoustic signals with the aim of characterizing the sample.The application of neural networks in the inverse solution of the photoacoustic problem showed high precision in determining the parameters from the experimentally recorded signal in the range of 20 to 20kHz. The question arises as to how precisely it is possible to determine parameters from experimentally recorded phases[22], and whether it is possible to apply some optimization method in the application of neural networks.

2. Theoretical background

The sample considered is a circular silicon wafer whose radius is significantly greater than its thickness, which ensures one-dimensional energy transport based on Fourier's law of heat conduction. In the photoacoustics of semiconductors, three effects that lead to the formation of a photoacoustic signal are considered: thermodiffusion, thermoelasticity and plasmaelasticity. The thermodiffusion effect is a consequence of heat conduction through the sample and depends on the thermal diffusivity of the semiconductor sample. The thermoelastic effect is a consequence of mechanical stress caused by photothermally induced temperature gradient within the sample and depends on thermal expansion coefficient and thickness. The plasmaelastic effect is a consequence of the mechanical stress that occurs due to the appearing of concentration gradient of photogenerated carriers. The most influential physical effects create a sound that is experimentally measured and well described by a theoretical simulation model. By changing the parameter in the theoretical simulation model of thermal diffusivity, expansion in the range of 10% from literary values of pure silicon sample and thickness in the range of 100 to 1000 microns, the phase base of >5000 photoacoustic signals is obtained, which is shown in Figure 1a) in degrees (deg) [13-21]. The database was used to train the phase neural network NN0, Figure 1b). In the process of training the NN0 network, an algorithm is activated that connects the data of the input layer, phase φ_1-φ_{72}, with the data of the output layer, thermal diffusivity D_T, thermal expansion α_T and sample thickness l. The number of input neurons 72 is determined by the number of values of the experimentally measured photoacoustic signal. The hidden layer is a

single layer, and has 50 neurons. During the time of one epoch, all the data of the input and output databases are used once. By back propagation, correction is made until the minimum error is reached.

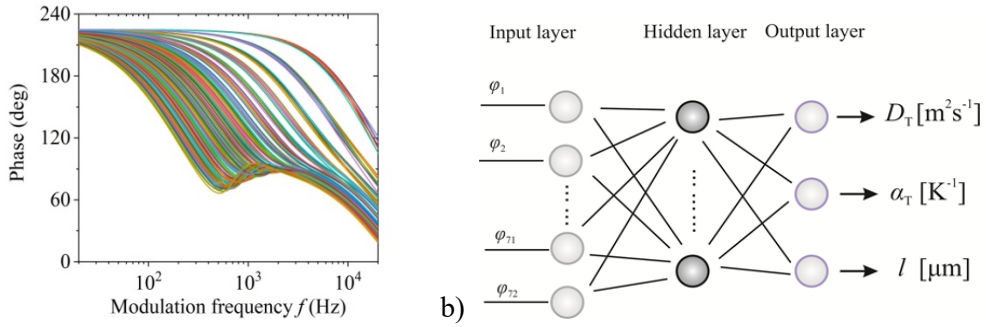

Figure 1. a) phase base of photoacoustic signals, b) neural network architecture.

3. Results and discussion

Phase neural network NN0, after training on the basis, Figure 1, achieved exceptional performance of 1.7246×10^{-6} in 1000 epochs, which provides high precision with errors <1% on simulated signals and errors of 30%, 16% and 15% on experimentally recorded signals in the prediction of parameters of thermal diffusivity D_T^{ANN}, expansion α_T^{ANN} and thickness l^{ANN} **..**In addition to the neural network NN0, neural networks NN1-5 were also formed by the application random Gaussian noise in degrees % from 1-5 with the aim of adapting the signal base, Figure 1a, to the experimental conditions [5-7].

The basic characteristics of networks NN1-5 are that their training time, which is determined by the number of epochs, decreases (from 44 to 5 epochs) and that their performance decreases (increases from 1.58×10^{-2} to 7.0721×10^{-2}), with increasing % added Gaussian noise (1-5%). In front of the basic characteristics, as a requirement for further use, their precision and time of prediction of parameters of thermal diffusivity, expansion and thickness are imposed. The accuracy of the prediction of these three parameters on the theoretical photoacoustic signals is lost, the errors increase from $\sim 10^{-2}$ to 11%, while the accuracy in the prediction of the experimental signals becomes better, decreasing to 30%, 16% and 15% at error values <2% in parameter predictions D_T^{ANN}, α_T^{ANN} and l^{ANN}, respectively.

Practical application of formed networks NN0-5 is a test on recorded experimental photoacoustic signals. The results show that the most optimal network for predicting sample parameters from measured photoacoustic signals is a network that has a degree of added random Gaussian noise with a value between 3 and 4%, which fits with the most common measurement uncertainty of photoacoustic phases.

4. Conclusion

The presented results show that it is possible to determine the thermoelastic properties of semiconductors based on the measurement of the phases of the photoacoustic signal when the inverse photoacoustic problem is solved using neural networks. Phase networks without adding noise, although they have a high accuracy on the numerical experiment data, do not show a high accuracy in the real experiment. By adding the Gaussian noise to the base, the networks are trained faster and a much higher accuracy is obtained in determining all sample parameters. Be-

sides, prediction errors show that the optimal adding Gaussian noise is between 3 and 4% corresponding to the uncertainty of the experimental phase measurement.

Acknowledgments
We are thankful for the financial support of this research by Ministry of Science, Technological Development and Innovation of the Republic of Serbia, grant numbers 451-03-47/2023-01/200017.

References

1. M. D. Rabasović, M. G. Nikolić, M. D. Dramićanin, M. Franko and D. D. Markushev, Low-cost, portable photoacoustic setup for solid state, Meas. Sci. Technol.,**20**,9, (2009) https://doi.org/10.1088/0957-0233/20/9/095902
2. L. Rousset, F. Lepoutre, L. Bertrand, Influence of thermoelastic bending on photoacoustic experiments related to measurements of thermal diffusivity of metals, J. Appl. Phys. **54**, 2383 (1983) https://doi.org/10.1063/1.332352
3. A.C.Tam, Applications of photoacoustic sensing techniques. Rev. Mod. Phys. **58**, 381 – (1986) https://doi.org/10.1103/RevModPhys.58.381
4. H. Vargas, L.C.M. Miranda, Photoacoustic and related photothermal techniques. Phys. Rep. **16**, 43–101 (1988) https://doi.org/10.1016/0370-1573(88)90100-7
5. Perondi L.F.; Miranda L.C.M.; Minimal-volume photoacoustic cell measurement of thermal diffusivity: Effect of the thermoelastic sample bending J. Appl. Phys. **1997**, 62(7), 2955–2959. https://doi.org/10.1063/1.339380
6. Somer A.; Camilotti F.; Costa G.F.; Bonardi C.; Novatski A.; Andrade A.V.C.; … Cruz G.K. The thermoelastic bending and thermal diffusion processes influence on photoacoustic signal generation using open photoacoustic cell technique J. Appl. Phys. **2013**, 114(6), 063503(4) https://doi.org/10.1063/1.4817655
7. Markushev, D. D., Rabasović, M. D., Todorović, D. M., Galović, S., & Bialkowski, S. E. (2015). Photoacoustic signal and noise analysis for Si thin plate: Signal correction in frequency domain. Review of Scientific Instruments, 86(3), 035110. https://doi.org/10.1063/1.4914894
8. Popović M.N.; Nešić M.V.; Cirić-Kostić S.; et al. Helmholtz resonances in photoacoustic experiment with laser-sintered polyamide including thermal memory of samples Int. J. Thermophys. 2016, 37:116(9). https://doi.org/10.1007/s10765-016-2124-3
9. Aleksić S.M.; Markushev D.K.; Pantić D.S.; et al. Electro-acoustic influence of the measuring system on the photoacoustic signal amplitude and phase in frequency domain Facta Univ. Ser.: Phys Chem Technol 2016, 14(1):9–20. https://doi.org/10.2298/FUPCT1601009A
10. A. Rosencwaig, A. Gersho, Photoacoustic effect with solids: A theoretical treatment, Science, **19** (4214) 556-557 (1975) https://doi.org/10.1126/science.190.4214.556
11. A. Rosencwaig, A. Gersho,Theory of the photoacoustic effect with solids, J. Appl. Phys. **47**, 64 (1976) https://doi.org/10.1063/1.322296
12. F.A. McDonald, G C. Wetsel, Theory of Photothermal and Photoacoustic Effects in Condensed Matter, Physical Acoustics, **18,** 167-277 (1988) https://doi.org/10.1016/B978-0-12-477918-1.50010-2
13. D.M. Todorović and P.M. Nikolic, in Prog. Photothermal Photoacoust. Sci. Technol. - Semicond. Electron. Mater., edited by A. Mandelis and P. Hess (SPIE Press, Bellingham, Washington, USA, 2000), pp. 271–315 ISBN-13: 978-0819435064
14. A. Somer, F. Camilotti, G.F. Costa, C. Bonardi, A. Novatski, A.V.C. Andrade, V.A. Kozlowski Jr, G.K. Cruz, The thermoelastic bending and thermal diffusion processes influence on photoacoustic signal generation using open photoacoustic cell technique, Journal of Applied Physics **114** (6), 063503 (2013) http://dx.doi.org/10.1063/1.4817655
15. Markushev D.K.; Markushev D.D.; Aleksić S.M.; Pantić D.S.; Galović S.P.; Todorović D.M.; Ordonez-Miranda J. Experimental photoacoustic observation of the photogenerated excess carrier influence on the thermoelastic response of n-type silicon *J. Appl. Phys.* **2020**, 128(9) 095103(9). https://doi.org/10.1063/5.0015657
16. Markushev D.K.; Markushev D.D.; Aleksić S.; Pantić D.S.; Galović S.; Todorović D.M.; Ordonez-Miranda J. Effects of the photogenerated excess carriers on the thermal and elastic properties of n-type silicon excited with a modulated light source: Theoretical analysis *J. Appl. Phys.* **2019**, 126(18)185102(12). https://doi.org/10.1063/1.5100837
17. L. Villegas-Lelovsky, G. Gonzalez de la Cruz, Yu. G. Gurevich, Electron and phonon thermal waves in semiconductors: the effect of carrier diffusion and recombination on the photoacoustic signal, Thin Solid Films 433,371-374, (2003) https://doi.org/10.1016/S0040-6090(03)00396-1
18. M. Nesic, M. Popovic, K. Djordjevic, V. Miletic, M. Jordovic-Pavlovic, D. Markushev and S. Galovic. Development and comparison of the techniques for solving the inverse problem in photoacoustic characterization of semiconductors. Opt Quant Electron 53, 381 (2021). https://doi.org/10.1007/s11082-021-02958-0
19. K. Lj. Djordjevic, D. D. Markushev, Ž. M. Ćojbašić, S. P. Galović, Photoacoustic measurements of the thermal and elastic properties of n-type silicon using neural networks, Silicon (2019) 12(3) https://doi.org/10.1007/s12633-019-00213-6
20. K. Lj. Djordjevic, D. D. Markushev, Ž. M. Ćojbašić, S. P. Galović, Inverse problem solving in semiconductor photoacoustics by neural networks, Inverse Probl. Sci. Eng. (2020) 29(2):1-15, https://doi.org/10.1080/17415977.2020.1787405
21. Djordjevic, K. L., Galovic, S. P., Jordovic-Pavlovic, M. I., Cojbasic, Z. M., & Markushev, D. D. (2020). Improvement of Neural Networks Applied to Photoacoustic Signals of Semiconductors with Added Noise. Silicon, 13(9), 2959–2969. https://doi.org/10.1007/s12633-020-00606-y
22. PESSOA JR, O. F. ; CESAR, C. L. ; PATEL, N. A. ; VARGAS, H. ; GUIZONI, C. C. ; MIRANDA, L. C. M. . Two-beam Photoacoustic Phase Measurement of the Thermal Diffusivity of Solids. Journal of Applied Physics, v. 59, n.4, p. 1316-1318, 1986.

13th INTERNATIONAL SCIENTIFIC CONFERENCE

SCIENCE AND HIGHER EDUCATION IN FUNCTION OF SUSTAINABLE DEVELOPMENT

5th - 8th June 2023, Hotel Slatina, Vrnjacka Banja, Serbia

CONFERENCE PROCEEDINGS

home :: about SED :: program :: committee :: sponsors and partners :: ISBN

13th INTERNATIONAL CONFERENCE

SCIENCE AND HIGHER EDUCATION IN FUNCTION OF SUSTAINABLE DEVELOPMENT

5th - 8th June 2023, Hotel Slatina, Vrnjacka Banja, Serbia

Organizing and Scientific Committee SED 2023

ORGANIZING COMMITTEE

- **Ljubica Diković**, PhD – President of Organizing Committee;
- **Ljiljana Trumbulović**, PhD – Vice-President of Organizing Committee;
- **Aleksandar Milovanović**, PhD;
- **Snežana Aksentijević**, PhD;
- **Milovan Milivojević**, PhD;
- **Đorđe Đuričić**, PhD;
- **Zorica Tanasković**, PhD;
- **Željko Karganović**, spec. dr med.;
- **Predrag Popović**, MSc;
- **Slobodanka Stankov**, PhD;
- **Biljana Đuričić**, Mr;
- **Ivana Marinković**, MSc;
- **Dragana Knežević**, MSc;
- **Aleksandar Pujović**, MSc;
- **Marijana Milutinović**, MSc;
- **Ana Đokić**;
- **Milisav Šuljagić**;
- **Mirjana Selaković**, MSc;
- **Marina Vulović**;
- **Marija Jezdović**, spec;

SCIENTIFIC COMMITTEE

- **Srećko Stopić**, PhD, Associate Professor, IME Process Metallurgy and Metal Recycling, RWTH Aachen University (Germany)
- **Milan Antonijević**, PhD, Full Professor, School of Science, University of Greenwich, England (United Kingdom)
- **Drahoslav Lančarič**, PhD, Vice-Rector for Science and Research, Slovak University of Agriculture, Nitra (Slovakia)
- **Plamen Zahariev**, PhD, Associate Professor, University of Ruse "Angel Kanchev", Ruse, Bulgaria
- **Nina Bencheva**, PhD, Associate Professor, University of Ruse "Angel Kanchev", Ruse, Bulgaria
- **Josef Caslavsky**, PhD, Full Professor, Global Change Research Institute of the Czech Academy of Sciences (Czech Republic)
- **Mátyás Ando**, PhD, Full Professor, Institute of Mechanical Engineering Technology, Szent István University, Budapest (Hungary)
- **Polonca Trebše**, PhD, Research Associate, University of Ljubljana (Slovenia)
- **Irena Grmek Kosnik**, PhD, Assistant Professor, National Laboratory of Health, Environment and Food, Institute of Public Health, Kranj (Slovenia)
- **Stefan Žun**, PhD, Lecturer of Higher Education, Šolski Center Kranj (Slovenia)
- **Michalis Koniordos**, PhD, Professor, Technological Educational Institute of Piraeus, Athens (Greece)
- **Radomir Zejak**, PhD, Full Professor, University of Montenegro, Faculty of Civil Engineering, Podgorica (Montenegro)
- **Marija Knežević**, PhD, Associate Professor, Dean of the Faculty of Tourism and Hotel Management, University of Business Studies, Banja Luka (Republic of Srpska, Bosnia and Herzegovina)
- **Aleksandar Stojanović**, PhD, Associate Professor, Faculty of Economics, Pale, University of East Sarajevo (Republic of Srpska, Bosnia and Herzegovina)
- **Vladimir Popović**, PhD, Full Professor, Dean of the Faculty of Mechanical Engineering, University of Belgrade, Belgrade (Serbia)
- **Srdan Kolaković**, PhD, Full Professor, Faculty of Technical Sciences, University of Novi Sad, Novi Sad (Serbia)
- **Marica Popović**, PhD, Research Associate Professor, Institute of Physics, Belgrade (Serbia)
- **Dragana Markushev**, PhD, Research Associate Professor, Institute of Physics, Belgrade (Serbia)
- **Katarina Đorđević**, PhD, Research Associate Professor, Vinča Institute of Nuclear Sciences, Belgrade (Serbia)
- **Goran Marinković**, PhD, Associate Professor, Faculty of Technical Sciences, University of Novi Sad, Novi Sad (Serbia)
- **Branko Savić**, PhD, Professor of Vocational Studies, Higher Education Technical School of Professional Studies, Novi Sad (Serbia)
- **Tatjana Marinković**, PhD, Professor of Vocational Studies, Academy of Applied Technical Studies, Belgrade (Serbia)

- **Ljubica Diković**, PhD, Professor of Vocational Studies, Western Serbia Academy of Applied Studies, Užice (Serbia)
- **Ljiljana Trumbulović**, PhD, Professor of Vocational Studies, Western Serbia Academy of Applied Studies, Užice (Serbia)
- **Radomir Stojanović**, PhD, Professor of Vocational Studies, Western Serbia Academy of Applied Studies, Užice (Serbia)
- **Đorđe Đuričić**, PhD, Professor of Vocational Studies, Western Serbia Academy of Applied Studies, Užice (Serbia)
- **Zorica Tanasković**, PhD, Professor of Vocational Studies, Western Serbia Academy of Applied Studies, Užice (Serbia)
- **Dejan Milivojević**, PhD, Professor of Vocational Studies, Western Serbia Academy of Applied Studies, Užice (Serbia)
- **Milovan Milivojević**, PhD, Professor of Vocational Studies, Western Serbia Academy of Applied Studies, Užice (Serbia)
- **Nataša Ćirović**, PhD, Professor of Vocational Studies, Western Serbia Academy of Applied Studies, Užice (Serbia)
- **Ivana Ćirović**, PhD, Professor of Vocational Studies, Western Serbia Academy of Applied Studies, Užice (Serbia)
- **Vesna Vasović**, PhD, Professor of Vocational Studies, Western Serbia Academy of Applied Studies, Užice (Serbia)
- **Snežana Aksentijević**, PhD, Professor of Vocational Studies, Western Serbia Academy of Applied Studies, Užice (Serbia)
- **Zorica Sagić**, PhD, Professor of Vocational Studies, Western Serbia Academy of Applied Studies, Užice (Serbia)
- **Vesna Marjanović**, PhD, Professor of Vocational Studies, Western Serbia Academy of Applied Studies, Užice (Serbia)
- **Gordana Lazić**, PhD, Professor of Vocational Studies, Western Serbia Academy of Applied Studies, Užice (Serbia)
- **Momčilo Vasiljević**, PhD, Professor of Vocational Studies, Western Serbia Academy of Applied Studies, Užice (Serbia)
- **Ivana Bojović**, PhD, Professor of Vocational Studies, Western Serbia Academy of Applied Studies, Užice (Serbia)
- **Sandra Stojadinović Jovanović**, PhD, Professor of Vocational Studies, Western Serbia Academy of Applied Studies, Užice (Serbia)
- **Aleksandar Milovanović**, PhD, Professor of Vocational Studies, Western Serbia Academy of Applied Studies, Užice (Serbia)
- **Ivana Čeković**, PhD, Professor of Vocational Studies, Western Serbia Academy of Applied Studies, Užice (Serbia)
- **Slobodanka Stankov**, PhD, Professor of Vocational Studies, Western Serbia Academy of Applied Studies, Užice (Serbia)
- **Aleksandar Dimitijević**, PhD, Professor of Vocational Studies, Western Serbia Academy of Applied Studies, Užice (Serbia)
- **Jelena Andrić**, PhD, Professor of Vocational Studies, Western Serbia Academy of Applied Studies, Užice (Serbia)
- **Slavka Mitričević**, PhD, Professor of Vocational Studies, Western Serbia Academy of Applied Studies, Užice (Serbia)
- **Miroslava Jordović Pavlović**, PhD, Professor of Vocational Studies, Western Serbia Academy of Applied Studies, Užice (Serbia)
- **Mladen Vićentić**, PhD, Professor of Vocational Studies, Western Serbia Academy of Applied Studies, Valjevo (Serbia)
- **Ilja Stanišević**, PhD, Professor of Vocational Studies, Western Serbia Academy of Applied Studies, Valjevo (Serbia)
- **Slobodan Ilić**, PhD, Professor of Vocational Studies, Western Serbia Academy of Applied Studies, Valjevo (Serbia)
- **Snežana Rakić**, PhD, Professor of Vocational Studies, Western Serbia Academy of Applied Studies, Valjevo (Serbia)
- **Marina Janković Perić**, PhD, Professor of Vocational Studies, Western Serbia Academy of Applied Studies, Valjevo (Serbia)

home :: about SED :: program :: committee :: sponsors and partners

Principal Component Analysis in Processing Photoacoustic Measurement Data

Miroslava Jordović Pavlović[1], PhD; Kristina Milojević[1]BSc; Dragana Markušev[3],PhD;Dragan Markušev[3],PhD;
[1]Western Serbia Academy of Applied Studies, departmant Uzice, Serbia, miroslava.jordovic-pavlovic@vpts.edu.rs
[1] Western Serbia Academy of Applied Studies, departmant Uzice, Serbia, kristinamilojevic123@gmail.com
[2]Institute of Physics, Laboratory for Photoacoustic, Belgrade, Serbia, dragana.markushev@ipb.ac.rs
[2] Institute of Physics, Laboratory for Photoacoustic, Belgrade, Serbia, dragan.markushev@ipb.ac.rs

Abstract:*Researchers often come across the problems of storing and processing massive data sets in machine learning tasks, as it is a time-consuming process and difficulties to interpret also arises. Not every feature of the data is necessary for predictions. These redundant data can lead to bad performances or overfitting of the model. Through this article implementation of an unsupervised learning technique, Principal Component Analysis for dimensionality reduction in preprocessing phase of photoacoustic measurement data processing is presented. It helped model deal effectively with these issues to an extent and provided sufficiently accurate prediction results.*

Keywords:*principal component analysis, simulated data, photoacoustic, measurement, neural network*

1. INTRODUCTION

Massive datasets are very common in machine learning, often with high dimensionality which includes measurements on many variables. Having a large number of features can pose many problems, and the most frequent is overfitting which reduces the ability to generalize beyond the training set. Question is how many features are irrelevant due to correlations and duplications compering with other features? Contemporary Machine Learning (ML) techniques in its preprocessing phase usually involve some of widely used mathematical procedures that reduces dimensionality. PCA is one of these mathematical procedures which main characteristic is transformation of a set of features in a dataset into a smaller number of features called principal components while at the same time trying to retain as much information in the original dataset as possible.

The Principal Component Analysis (PCA) reduction in the number of attributes is obtained by removing redundant information. PCA tries to reduce redundancy by combining the original attributes into new attributes in order to decrease the covariance, and as a result the correlation between the attributes of a data set. To do this, transformation matrix operations from linear algebra are used. These operations transform the attributes in the original data set, which can have high linear correlation, to attributes that are not linearly correlated. These are called the principal components. Each principal component is a linear combination of the original attributes. The components are ranked according their variance, from the largest to the smallest. Next, a set of components is selected, one by one, starting with the component with the largest variance and following the ranking. At each selection, the variance of the data with the selected components is measured. No new components are selected once the increase in the variance is small or a predefined number of principal components has been selected [1], [2], [3].
Advantages of using PCA are [1], [2], [3]:

- •Removes correlated features. PCA removes all the features that are correlated, a phenomenon known as multi-collinearity. If the number of features is large, finding correlated features is time consuming.
- •Improves machine learning algorithm performance. With the number of features reduced with PCA, the time taken to train ML model is now significantly reduced.
- •Reduce overfitting. By removing the unnecessary features in the dataset, PCA contributes to overcome overfitting.

On the other hand, PCA has its disadvantages [1], [2], [3]:

•Independent variables are now less interpretable. Each of PCA reduced component isnow a linear combination of original features, which makes it less readable and interpretable.
•Information loss. Data loss may occur in case of not proper choice the right number of components.
•Feature scaling. Because PCA is a variance maximizing technique, PCA requires features to be scaled prior to processing.

The article presents discussion on a convenience of use of PCA technique in processing photoacoustic measurement data.
Photoacoustics is one of phototermal methods which aim is physical characteristics determination of measured sample. It is experimental life science that has, in the recent years, an explosion of the data available from experiments, especially a simulated experimental values or numerical experiments. In our previous work, [4] the potential of using simulated data in photoacoustics is proved and became practice in designing machine learning models for decision making. A mainstay of simulated data generation is developed theoretical-mathematical model of photoacoustic response. Validity of created data is obtained due to experimental experience and expert knowledge. Numerical experiments imitate proximately all experimental conditions. Hundreds of measurements for a single experiment are reported and therefore the statistical methods face challenging tasks when dealing with such high dimensional data.

2. PROBLEM DESCRIPTION

Database that we investigate in the paper consists of 270 000 records. Each record has 200 instances of amplitude and 200 instances of phase obtained by sampling amplitude and phase characteristics of simulated photo acoustic response at defined points of frequency axe [4]. Photoacoustic response hides, among other harmful influences, the influence of measurement system, represented as distortions. The main part of measurement system in the photoacoustic experiment has microphone as a detector [5]. Without going into deeper analysis and explanations of photoacoustic experiment, some general truths will be represented here. Microphone has the greatest impact to distortions, its response in the frequency and time domain differs due to construction, geometry and membrane type, and two identical microphones do not exist in practice. Having these facts in mind it is obvious why a lot of our research attention is focused to the correction of distorted photo acoustic signal where distortions are mainly caused by microphone [6] [7].

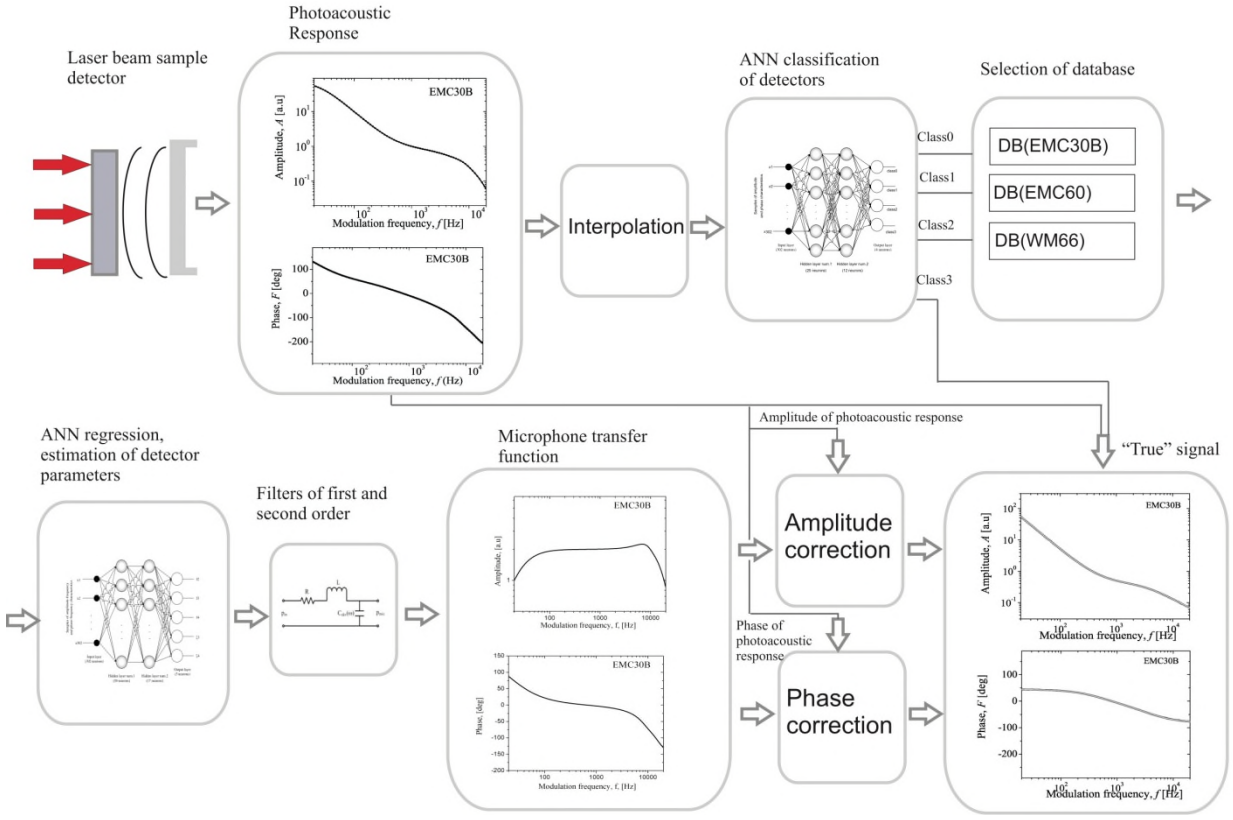

Figure 1: The block sheme of distorted photoacoustic measurement signal autocorrection method [6]

In Figure 1, a block scheme of the autocorrection of distorted photoacoustic signal is presented. The PA response of the experimental setup measured in a certain number of points represents the input signal. Input signal is first interpolated to some points that correspond to the number of neural network input vector elements. The interpolated PA response is an input of the classification model. The output is the type of microphone used as a detector in the setup. Further more, class of microphone determines the corresponding database. Regression model, trained on the selected database, gives the targeted microphone parameters. Results of corrections are amplitude and phase characteristic of the "true" PA signal. In the case of class 3 (IM) regression is not executed, experimental signal is the "true" PA signal. Detail analysis of the method is explained in our previous work [6]. In this paper focus is dimensionality reduction of the input vector.
The dataset is generated using well defined preset of three electret microphones frequently used in photoacoustic experiment and ideal microphone (microphone of ideal characteristics) used as a reference [4]. Visualization of the dataset in the form of scatter diagram, is given in Figure 2. Each point on a scatter diagram is one point of 200 points that corresponds to one curve of 270,000 curves in the database. Different classes of microphone are presented with different colors.

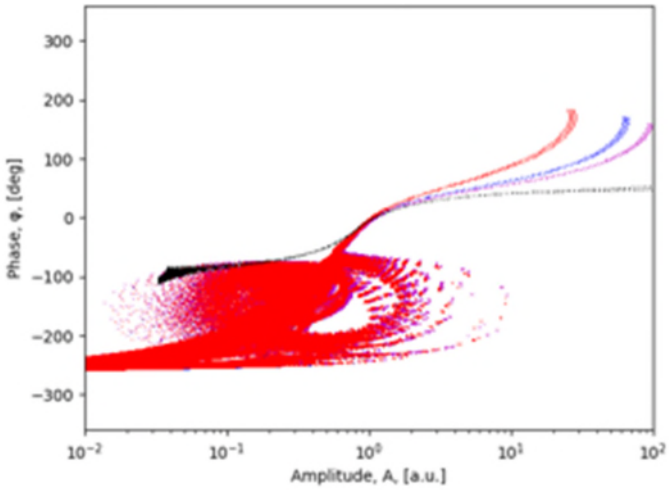

Figure 2: Scatter diagram of the data set [4]

3. RESULTS AND DISCUSSION

PCA applied on whole dataset (400 features) provides promising results of retained variance, Figure 3. It means that the dimensionality reduction could be done even to 2 components, where retained variance is 99.55%. Results for 4 and 6 components are 99.89%, 99.96% respectively.

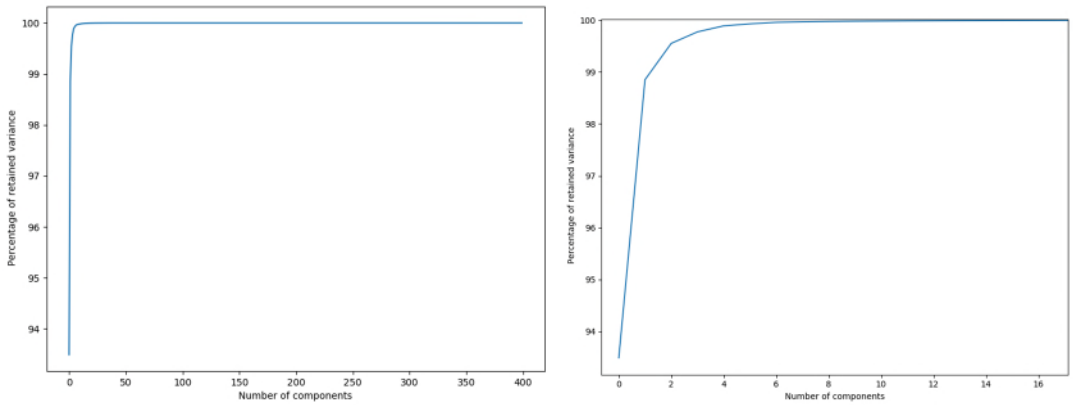

Figure 3: Retained variance in realtion to number of components

Regarding literature suggestions [8] [9] [10], 99% of retained variance means preserved information in the data set, it can be concluded that the idea of dimensionality reduction of input vector is justified. Furthermore the decision on the number of PCA components could be choice of nearest result to 99% and that means 2 components.
Validity of proposed dimensionality reduction is checked on classification model for recognition of microphone type perfomance.Input vector is reduced in accordance with proposed dimensionality reduction.

Training, validation and test sets are obtained randomly because dataset is first shuffled and then divided into training, validation and test set. Generalization of the results is obtained on that way, thus 243 000 records or 90% of the total number of records belongs to the training set, 13500 records or 5% belong to the validation set and the rest belongs to the test set.
Comparison of the classification model performance with [4] and without of dimensionality reduction done in preprocessing phase is presented in Table 1. Analyzing the table it can be concluded that the accuracy of the model is slately lower in the case of dimensionality reduction but it is still a very good result. The implementation of PCA technique is thus proven to be the adequate dimensionality reduction technique regarding the PA experiment request for precision and real time work.

	Trainaccuracy(%)	Dev accuracy(%)	Test accuracy(%)	Number of epochs	Prediction time (ms)
Perfomance of the model without dimensionality reduction	99.99	99.99	99.99	100	14ms
Perfomance of the model with dimensionality reduction	99.21	99.12	99.15	100	13ms

Table 1: Performance of the classification model with and without the dimensionality reduction

The reliability of the classification model is tested on independent data tests. Sixteen different independent data sets, meaning for different amplitude and phase characteristics for each type of microphone were created, where the microphone parameter values differed from those on which the network was trained, but in the given parameter range. Results are presented in Table 2. According to table our model is reliable, it recognizes the microphone type precisely and gives an answer regarding the microphone type in real time.

Test	1	2	3	4	5	6	7	8	9	10	11	12	13	14	15	16
Class.	1	3	0	2	1	2	3	0	2	3	1	2	1	0	3	0
Accuracy	T	T	T	T	T	T	T	T	T	T	T	T	T	T	T	T

Table 2: Indepedent data tests, T means true

4. CONCLUSION

The paper discusses the results of PCA technique application in the preprocessing phase of PA measurement data processing. The change in performance of classification model is negligible compering to classification model without dimensionality reduction.It can be concluded thatPCA is suitable for implementation regarding PA experiment request for precision and real time work. Managing and exploratory analysis of the dataset are now much easier. However, interesting question came up during this research. Is there a possibility of reduction in the number of measurement points and thus simplifying the measurement procedure in real experiments? Such a reduction would significantly reduce the measurement time and researcher engagement. Unfortunately, PCA is not suitable for solving this problem. PCA component is a linear combination of original features, so the number of features is not changed, the same as number of measurement points, but its interpretation is. Solution of araised problem will need further investigation.

REFERENCES

[1] Pavel Pořízka, Jakub Klus, Erik Képeš, David Prochazka, David W. Hahn, Jozef Kaiser, „On the utilization of principal component analysis in laser-induced breakdown spectroscopy data analysis, a review“, Spectrochimica Acta Part B: Atomic Spectroscopy,Volume 148, 2018,Pages 65-82, ISSN 0584-8547, https://doi.org/10.1016/j.sab.2018.05.030.
[2] Konishi, T., Matsukuma, S., Fuji, H. *et al.* Principal Component Analysis applied directly to Sequence Matrix. *Sci Rep*9, 19297 (2019). https://doi.org/10.1038/s41598-019-55253-0
[3] Daoqiang Zhang, Zhi-Hua Zhou, (2D)2PCA: Two-directional two-dimensional PCA for efficient face representation and recognition, Neurocomputing, Volume 69, Issues 1–3, 2005, Pages 224-231, ISSN 0925-2312, https://doi.org/10.1016/j.neucom.2005.06.004.

[4] Jordović-Pavlović M., Kupusinac A., Galović S., Markushev D., Nešić M., Djordjević K., Popović M., Potential of Using Simulated Data in Processing Photoacoustic Measurement Data. In: Proceedings of 8th In- ternational Conference on Electrical, Electronic, and Computing Engineering (IcETRAN), ISBN 978-86- 7466-894-8 (2021),
[5] M. D. Rabasovic, M. G. Nikolic, M. D. Dramicanin, M. Franko, and D. D. Markushev, "Low-cost, portable photoacoustic setup for solid samples," Meas. Sci. Technol., vol. 20, no. 9, p. 95902, 2009.
[6] M. I. Jordovic-Pavlovic et al., "Computationally intelligent description of a photoacoustic detector," Opt. Quantum Electron., vol. 52, no. 5, pp. 1–14, 2020.M. Nesic et al., "Development and comparison of the techniques for solving the inverse problem in photoacoustic characterization of semiconductors," Opt. Quantum Electron., vol. 53, no. 7, p. 381, 2021.
[7] M. I. Jordović-Pavlović, M. M. Stanković, M. N. Popović, Ž. M. Ćojbašić, S. P. Galović, and D. D. Markushev, "The application of artificial neural networks in solid-state photoacoustics for the recognition of microphone response effects in the frequency domain," J. Comput. Electron., vol. 19, no. 3, pp. 1268–1280, 2020.
[8]Shalev-Shwartz, S. and S. Ben-David, *Understanding machine learning: From theory to algorithms.* Under- standing Machine Learning: From Theory to Algorithms, 2014: p. 1-397.
[9] Bishop, C.M., Pattern Recognition and Machine Learning. 2006
[10] Martel, E., et al., Implementation of the Principal Component Analysis onto high-performance computer facilities for hyperspectral dimensionality reduction: Results and comparisons. Remote Sensing, 2018.
[11] M. Nesic et al., "Development and comparison of the techniques for solving the inverse problem in photoacoustic characterization of semiconductors," Opt. Quantum Electron., vol. 53, no. 7, p. 381, 2021
[12] M. V. Nesic, M. N. Popovic, S. P. Galovic, K. Lj. Djordjevic, M. I. Jordovic-Pavlovic, V. V. Miletic, and D. D. Markushev, Estimation of linear expansion coefficient and thermal diffusivity by photoacoustic numerical self-consistent procedure, March 2022, Journal of Applied Physics, https://doi.org/10.1063/5.0075979
[13] K.Lj. Djordjević, S.P. Galović, M.N. Popović, M.V. Nešić, I.P. Stanimirović,Z.I. Stanimirović, D.D. MarkushevUse Neural Network in Photoacoustic Measurement of Thermoelastic Properties of Aluminum foil, Measurement (2022) 111537, 0263-2241https://doi.org/10.1016/j.measurement.2022.111537
[14] K. Lj. Djordjevic, S. P. Galovic, M. I. Jordovic-Pavlovic, Z. M. Cojbasic, D. D. Markushev, Improvement of Neural Networks Applied to Photoacoustic Signals of Semiconductors With Added Noise, Silicon,https://doi.org/10.1007/s12633-020-00606-y.

Радови Драгана К. Маркушев

Конференције

М34

RAP
CRETE 2025

INTERNATIONAL CONFERENCE ON RADIATION APPLICATIONS
IN PHYSICS, CHEMISTRY, BIOLOGY, MEDICAL SCIENCES, ENGINEERING AND ENVIRONMENTAL SCIENCES

rap-conference.org

BOOK OF ABSTRACTS

May 26-30, 2025
Hellenic Centre of Marine Research
Gournes - Heraklion
Crete | Greece

A new and straightforward method for thermal quality control of radiation shielding materials based on photoacoustic thermoelastic response

Dragan Markushev, Dragana Markushev

Institute of Physics Belgrade, Belgrade, Serbia

Introduction. Radiation shielding materials are various mixtures of elements that serve to block or keep radiation dose as low as reasonably achievable. It was found that thermal properties are one of the factors that influence the design, selection, and use of shielding for radioactive material, so the development of methods for their thermal quality control is gaining more and more importance. In this article, we will present a new and straightforward method for the thermal quality control of shielding materials, based on their thermoelastic photoacoustic response in the modulation frequencies domain from 20 Hz to 20 kHz.

Methods and Materials. In our experiment, we used an open-cell transmission setup to analyze the total photoacoustic signal of radiation shielding materials (aluminium and high-density polyethylene) with thicknesses l ranging from 10 to 1000 microns. Our objective was to determine the position of the maximum temperature difference $\Delta Tmax$ between the illuminated and non-illuminated sides of the sample within the specified frequency range. This $\Delta Tmax$ position also represents the cut-off frequency position f_c of the sample's thermoelastic response - a constitutive component of the total photoacoustic signal. By plotting the dependencies of $\Delta Tmax = f(l)$ and $f_c = f(l)$ on a log-log scale, we can establish linear relationships that allow us to calculate the sample's thermal conductivity k and thermal diffusivity D_T. By comparing potential deviations from the reference curves, we can deduce the thermal quality of the investigated materials and identify any alterations from the required properties due to manufacturing defects.

Conclusion. This presentation aims to demonstrate that the proposed new and straightforward methodology for assessing the thermal quality control of radiation shielding materials, based on the thermoelastic photoacoustic response, holds significant promise for heat flow analysis. This method allows for calculating thermal transport parameters in aluminium and high-density polyethylene. These properties are essential for the advanced materials development assigned for radiation shielding and their non-destructive thermal analysis.

Acknowledgments: The authors acknowledge funding provided by the Institute of Physics Belgrade, through the grant by the Ministry of Education, Science, and Technological Development of the Republic of Serbia.

Reduction of a set of thermoelastic photoacoustic parameters used for shielding material characterization

Dragana Markushev, Dragan Markushev

Institute of Physics Belgrade, Belgrade, Serbia

Introduction. The frequency domain photoacoustic characterization of solids has traditionally relied on multiparameter fitting to extract investigated samples' thermal, optical, and mechanical properties. While this method has proven effective, it also has its drawbacks. Therefore, a growing focus is on finding alternative, simpler sound processing methods with fewer parameters. Our recent research has demonstrated that analogue electrical circuits can be useful for the straightforward study of photoacoustic systems and processes. Using this analogy, one can represent the thermoelastic photoacoustic response with just one parameter instead of the large number in traditional photoacoustic theory. Even though the analogy is approximative, this approach retains the original behaviour of the thermoelastic response.

Methods and Materials. The method used in this study is based on electroacoustic analogies of thermal systems, where heat is transferred and stored, and can be described using *RC* circuits of various complexity. It is based on the similarity between the thermoelastic response of the illuminated material (lead, iron, aluminium, high-density polyethylene) and the response of the low-frequency *RC* filter in the frequency domain. We discovered that the filter we mentioned is defined by a single parameter, the cut-off frequency, and found a similar point in the thermoelastic response. Using the analytical form of the thermoelastic component equation, we linked the cut-off frequency to the sample's thermal and mechanical properties. This allowed us to create referent curves using data from existing literature to characterize various materials intended for radiation protection.

Conclusion. With this presentation, we want to show that the proposed reduction of a set of thermoelastic photoacoustic parameters is nothing but the transformation from a multi- to one-parameter analysis retaining some meaningful properties of the original data, ideally close to its original one. By reducing the number of parameters and discretizing thermal systems, where heat is transferred and stored through various physical processes, it has been demonstrated that all thermal processes can be represented using *RC* circuits of varying complexity It was found that reducing parameters is essential in establishing an efficient thermal characterization method, knowing that thermal properties are an important factor influencing the design, selection, and use of shielding for radioactive material.

Acknowledgments: The authors acknowledge funding provided by the Institute of Physics Belgrade, through the grant by the Ministry of Education, Science, and Technological Development of the Republic of Serbia.

ISBN-978-86-81652-07-7

CPPTA

BOOK OF ABSTRACTS

4th Conference on Photoacoustic and Photothermal Theory and Applications

22-25 September 2025, Warsaw (Poland)

ORGANIZING COMMITTEE

Tomasz Starecki (conference chair)
Anna Kaźmierczak-Bałata (co-chair)
Wiktor Porakowski
Oleksandra Zhyhylii
Patrycja Hojczyk
Barbara Kozielewska

SCIENTIFIC COMMITTEE

Juan Jose Alvarado-Gil
Guillaume Aoust
Nelson Astrath
Stephen Bialkowski
Zoltán Bozóki
Peter Burgholzer
Mihai Chirtoc
Dorin Dadarlat
Gerald Diebold
Danièle Fournier
Mladen Franko
Slobodanka Galović
Jérôme Gateau
Christ Glorieux
Vitali Gusev
Bernhard Lendl
Roberto Li Voti
Yufei Ma
Srivalleesha Mallidi
Andreas Mandelis
Antonio Manzanares
András Miklós
Matthew O'Donnell
Jose Ordonez-Miranda
Kumar Patel
Mikhail A. Proskurnin
Manijeh Razeghi
Amir Rozenthal
Markus Sigrist
Vincenzo Spagnolo
Masahide Terazima
Dragan M. Todorović
Lihong V. Wang
Marcus Wolff
Shu-yi Zhang
Vladimir Zharov
Zbigniew Bielecki
Jerzy Bodzenta
Alina Dudkowiak
Mirosław Maliński
Janusz Ryczkowski
Tomasz Starecki
Zbigniew Suszyński

Transsmision Photoacoustic Response of Coated Polymer Samples Measured With Minimum Volume Cell

M.N. Popovic[1], S.P. Galovic[2], D.K. Markushev[1], E. Suljovrujic[2], D.D. Markushev[1]

[1]Institute of Physics – National Institute of the Republic of Serbia, University of Belgrade
[2]Vinca Institute of Nuclear Sciences – National Institute of the Republic of Serbia, University of Belgrade

marica.popovic@ipb.bg.ac.rs

The photoacoustic (PA) investigation of polymer samples, particularly in a transmission configuration using a minimal-volume cell, often necessitates additional sample preparation due to the generally low optical absorption coefficient of polymers. To improve photothermal efficiency, a thin dye coating, typically less than 10 μm thick, is applied to the sample. This coating not only enhances absorption but also protects the detector, which could otherwise be exposed to optical excitation if the sample is transparent or semi-transparent in the minimal-volume cell configuration. To ensure that also the optical properties could be measured (not just thermal and mechanical properties) after this preparation, the experiment is set up so that the coated surface remains unilluminated, while the optical excitation is directed onto the uncoated side of the sample [1,2].

This study analyzes the effects of sample thickness and thermal relaxation time on the photoacoustic (PA) response. Using a model of optically induced temperature variations in a sample with an unilluminated coated surface, and examining the thermoelastic component of the PA signal linked to thermal moments and surface displacement, it is evaluated both individual and total components of the PA response. The findings indicate that sample absorbance significantly influences the thermoelastic signal more than the thermoconducting component, thereby affecting the overall PA response. Sample thickness modifies the relative contributions of these components within the measured range, while the thermal relaxation time establishes the frequency of appiriance periodic oscillations in the PA signal due to thermal memory effects in the polymer.

Our results indicate that by varying the sample thickness, it is possible to probe not only optical, mechanical, and standard thermal properties such as thermal conductivity and thermal diffusivity, but also memory-related properties associated with the finite speed of heat propagation in polymeric materials, within the PA frequency range corresponding to the audio spectrum (20 Hz to 20 kHz).

References

[1] V. V. Miletic et al., *J. Appl. Phys.* **133**, 075101 (2023).
[2] M. N. Popovic et al., *Int. J. Therm. Sci.* **211**, 109689 (2025).

BOOK OF ABSTRACTS

BOOK OF ABSTRACTS

22nd International Conference on Photoacoustic and Photothermal Phenomena

ISBN 978-989-33-6212-9

Organizing Committee

CHAIR:
Carlos Serpa (University of Coimbra)

Luis Arnaut (University of Coimbra)
João Pina (University of Coimbra)
Fábio Schaberle (University of Coimbra)
Lígia Gomes da Silva (University of Coimbra)
Adelino Pereira (University of Coimbra)
Amílcar Duque Prata (University of Coimbra)
Daniela Amado (University of Coimbra)
Diogo Pereira (University of Coimbra)
Otávio Augusto Chaves (University of Coimbra)

1 2 9 0
UNIVERSIDADE D COIMBRA

CLL
COIMBRA LASER LAB

PHOTOMEDICINE AND REACTIVITY
COIMBRA CHEMISTRY CENTRE - INSTITUTE OF MOLECULAR SCIENCES

International Scientific Committee

Nelson Astrath (Brazil)
Bertrand Audoin (France)
Mauro L. Baesso (Brazil)
Peter Burgholzer (Austria)
Stanislav Emelianov (USA)
Mladen Franko (Slovenia)
Christ Glorieux (Belgium)
Vitaliy Gusev (France)
Daniel Lanzillotti Kimura (France)
Bincheng Li (China)
Roberto Li Voti (Italy)
Boris Majaron (Slovenia)
Andreas Mandelis (Canada)
Ernesto Marin (Mexico)
Alexei Maznev (USA)
Arantza Mendioroz (Spain)
Vasilis Ntziachristos (Germany)
Alberto Oleaga (Spain)
Michał Janusz Pawlak (Poland)
Mikhail Proskurnin (Russia)
Daniel Razansky (Switzerland)
Pascal Ruello (France)
Agustin Salazar (Spain)
Vincenzo Spagnolo (Italy)
Masahide Terazima (Japan)
Dragan Todorovič (Serbia)
Chenglong Wang (China)
Lihong Wang (USA)
Oliver Wright (Japan)
Perry Xiao (Unied Kingdom)
Vladimir Zharov (USA)
Ugo Zammit (Italy)

International Steering and Advisory Board

OC19 - Influence of excess charge carriers recombination to time-resolved photoacoustic response of semiconductor

Galovic S [1]*, Markushev D K [2] , Markushev D D [2] , Djordjevic K [1], Popovic M [2], Suljovrujic E [1], Todorovic D [3]

(1) Vinca Institute of Nuclear Sciences-National Institute of the Republic of Serbia, University of Belgrade, Belgrade, Serbia.

(2) Institute of Physics-National Institute of the Republic of Serbia, University of Belgrade, Belgrade, Serbia.

(3) Institute for Multidisciplinary Research, University of Belgrade, Belgrade, Serbia.

* bobagal@vin.bg.ac.rs

Abstract

When a semiconductor sample is illuminated by a monochromatic source, part of the excitation electromagnetic energy is absorbed, and part of the absorbed energy is converted into heat due to non-radiative deexcitation-relaxation processes, leading to thermalization of the sample. However, if the energy of the excitation photons is greater than the width of the energy gap in semiconductors, part of the absorbed excitation energy is spent on exciting electrons from the valence to the conduction zone, leaving in the valence zone an excess of positively charged quasi-particles, so-called holes. Therefore, an electric field is established in the optically excited semiconductor sample [1].

Under the influence of this field, the photogenerated excess of electrons in the conduction zone recombines with the photogenerated excess of holes in the valence zone, transferring its kinetic energy to the crystal lattice. This means that part of the absorbed electromagnetic energy, spent on the generation of excess charge carriers, is indirectly (through the recombination process) converted into heat, forming an additional heat source in illuminated semiconductors [2].

Considering both types of heating of a semiconductor sample it can be concluded that the temperature variations on the sample surfaces, and consequently pressure fluctuations in the gaseous environment of the photothermally excited semiconductor, depend not only on the thermal properties of the sample that manage heat transfer but also on its electronic characteristics that manage recombination processes of the photogenerated excess charge [3].

In this paper, the model of the spectral function of the photoacoustic response of optically opaque and thermally thin semiconductor sample that includes surface recombination of excess charge carriers was derived based on electro-thermal analogy [4,5]. By application of inverse Laplace transform to the model the theoretical description of the time-resolved photoacoustic signal generated by a train of optical pulses of various duty cycles was obtained. The model was validated by comparing with time–resolved

ISBN: 978-989-33-6212-9

photoacoustic measurement with a minimum volume cell [6] of thin doped silicon membrane of the thickness of 40 micrometers.

The analysis of pulsed photoacoustic signal shows that the influence of photo-generated carriers is small in the short-time limit and pronounced in the long-time limit indicating that it is possible to deconvolve the contribution of recombination processes and deexcitation relaxation processes to the indirect PA signal by adjusting the duty cycle of the optical excitation. It means that time-resolved photoacoustic enables simultaneous measurement thermal and electronic properties of semiconductors.

Acknowledgements

The authors are grateful to the Ministry of Science, Technological Development and Innovations of the Republic of Serbia (Contract No. 451-03-66/2024-03/ 200017) for the financial support.

References

[1] S. Wang, Fundamentals of semiconductr theory and device physics, Prentice-Hall International Editions, NJ USA 1989 Available form: ISBN 0–13–344425–2

[2] D.M. Todorović, P.M. Nikolić, Semiconductors and Electronic Materials Progress in Photothermal and Photoacoustic, Science and Technology Chapter 9; Optical Engineering Press: New York, NY, USA (2000) Volume PM74, pp. 273–318. ISBN 9780819435064.

[3] K.L. Djordjevic, S.P. Galović, Ž.M Ćojbašić,D.D. Markushev,D. K. Markushev, S. M. Aleksic, and D. S.Pantic, Electronic characterization of plasma-thick n-type silicon using neural networks and photoacoustic response, Opt. Quantum Electron.54(8), 485 (2022). https://doi.org/10.1007/s11082-022-03808-3

[4] S. Galovic, Z. Soskic, M. Popovic. Analysis of Photothermal Response of Thin Solid Films By Analogy with Passive Linear Electric Networks. Thermal Science, 13(4),129-142 (2009) https://doi.org/10.2298/TSCI0904129G

[5] S.P. Galovic , K.Lj. Djordjevic ,M.V. Nesic , M.N. Popovic , D.D. Markushev , D.K. Markushev , D.M. Todorovic , Time-domain minimum-volume cell photoacoustic of thin semiconductor layer. I. Theory, J. App. Phys. 133,245701 (2023) https://doi.org/10.1063/5.0152519

[6] K.LJ. Djordjevic, S.P. Galovic, M.V. Nesic, D.M. Todorovic, M.N. Popovic, D.D.Markushev, D.K. Markushev. Transmission pulse photoacoustic set-up for characterization of solids, in 21st International Symposium INFOTEH-JAHORINA, 16-18 March (2022) https://infoteh.etf.ues.rs.ba/zbornik/2022/radovi/O-8-3.pdf

ISBN: 978-989-33-6212-9

ICPPP21 International Conference on Photoacoustic and Photothermal Phenomena

June 19 - 24, 2022
Bled, Slovenia

BOOK OF ABSTRACTS

https://indico.ung.si/event/5/

ORGANIZERS:

- UNIVERSITY OF NOVA GORICA
- UNIVERSITY OF LJUBLJANA
- JOŽEF STEFAN INSTITUTE

University of Ljubljana

Jožef Stefan Institute

Abtracts of the ICPPP21 Conference 2022

ICPPP21
19 – 24 June 2022, Bled, Slovenia

Organizing and Programme Committee

Chair:
Mladen Franko (University of Nova Gorica, Slovenia)

Vice-Chairs:
Dorota Korte (University of Nova Gorica, Slovenia)
Boris Majaron (Jožef Stefan Institute; University of Ljubljana, Slovenia)
Rok Petkovšek (University of Ljubljana, Slovenia)

Members:
Hanna Budasheva (University of Nova Gorica, Slovenia)
Humberto Cabrera (The Abdus Salam International Centre for Theoretical Physics, Italy)
Aljaž Čujec (University of Nova Gorica, Slovenia)
Petra Makorič (University of Nova Gorica, Slovenia)
Claudia D'ercole (University of Nova Gorica, Slovenia)
Petra Makorič (University of Nova Gorica, Slovenia)
Griša Močnik (University of Nova Gorica, Slovenia)
Nives Štefančič (University of Nova Gorica, Slovenia)
Iain R. White (University of Nova Gorica, Slovenia)
Nadja Lovec Santaniello (University of Nova Gorica, Slovenia)
Neža Golmajer Zima (Jožef Stefan Institute, Slovenia)
Martina Bergant Marušič (University of Nova Gorica, Slovenia)
Maria Chiara Magnano (University of Nova Gorica, Slovenia)
Martina Bergant Marušič (University of Nova Gorica, Slovenia)
Swapna Nair Sindhu (University of Nova Gorica, Slovenia)

International Scientific Committee:
Juan José Alvarado-Gil (Mexico)
Nelson Astrath (Brazil)
Bertrand Audoin (France)
Mauro L. Baesso (Brazil)
Jerzy Bodzenta (Poland)
Peter Burgholzer (Austria)
Mihai Chirtoc (France)
Nicu D. Dadarlat (Romania)
Gerald Diebold (USA)
Stanislav Emelianov (USA)
Mladen Franko (Slovenia)
Christ Glorieux (Belgium)
Xinxin Guo (Canada)
Vitaliy Gusev (France)
Daniel Lanzillotti Kimura (France)
Bincheng Li (China)

International Steering and Advisory Board:
Walter Arnold (Germany)
Stephen E. Bialkowski (USA)
Gabriel Bilmes (Argentina)
Paolo G. Bison (Italy)
Silvia Braslavsky (Germany)
Edson Corrêa da Silva (Brazil)
Danièle Fournier (France)
Yuri Gurevich (Mexico)
Frans J.M. Harren (Holland)
Peter Hess (Germany)
Alexander A. Kolomenskii (USA)
Jean-Claude Krapez (France)
Junyan Liu (China)
John F. McClelland (USA)
Humphrey Maris (USA)
Fulvio Mercuri (Italy)

Characterization of TiO_2 thin films deposited on silicon membranes using neural networks

Djordjević KLj[(1)*], Markushev DK[(2)], Popovic MN[(2)], Nesic MV[(1)], Galović SP[(1)], Lukić DV[(2)], Markushev DD[(2)]

(1) University of Belgrade, „VINČA" Institute of Nuclear Sciences - National Institute of the Republic of Serbia, University of Belgrade, PO box 522, 11000 Belgrade, Serbia
(2) University of Belgrade, Institute of Physics Belgrade, National Institute of the Republic of Serbia, Pregrevica 118, 11080 Belgrade (Zemun), Serbia

*Corresponding author's email: katarina.djordjevic@vin.bg.ac.rs

Background – This paper presents a theoretical analysis of the possibility of thermal characterization of a thin TiO_2 film deposited on a 30 μm thick Si membrane as a wafer in the frequency domain of photoacoustics from 20 Hz to 20 kHz. For this purpose, photoacoustic signals generated by such a sample were used (Figure 1) in which the membrane parameters were known and constant, while the film parameters were changed in the ranges of thickness $l_f = (475-525)\,\mathrm{nm}$, thermal expansion coefficient $\alpha_f = (1.045-1.155)\cdot 10^{-5}\,\mathrm{K^{-1}}$, and thermal diffusivity $D_f = (3.515-3.885)\cdot 10^{-6}\,\mathrm{m^2 s^{-1}}$. It can be seen from the Figure 1 that changes in the signal amplitude for the given changes in the film parameters cannot be noticed, while in the phase such changes are clearly noticeable. Within the classical approach of photoacoustic signal processing, non-distinguishing of amplitudes requires the introduction of an additional process of their normalization. In this paper, we will show that well-trained neural networks have no problem distinguishing signal amplitudes and that networks recognize precisely the parameters of thin films on such signals, knowing that the thickness of the films can be two orders of magnitude thinner than their wafers.

Results – The neural networks used in this paper were trained with the basis of photoacoustic signals from Figure 1. The supervised learning algorithm was used by connecting the data of the frequency amplitude-phase characteristics of the input layer signals with the values of the given parameters of the output layer change. The network architecture is very simple and consists of one input (144 neurons), one hidden (10 neurons), and an output layer (3 neurons). The number of input layer neurons corresponds to 144 points that define the photoacoustic signal (72 amplitudes + 72 phases). The three neurons of the output layer are connected to the thin-film parameters: l_f, α_f and D_f. In the case of the thin film thickness, the obtained network performances are 4.3106 x 10^{-6} for 4 epochs, in the case of coefficient of thermal expansion 3.567 x 10^{-5} for 7 epochs, and in the case of thermal diffusivity 0.0044842 for 4 epochs. The prediction of neural networks on test signals with errors of less than 1% shows that the networks are sensitive to small changes in TiO_2 parameters.

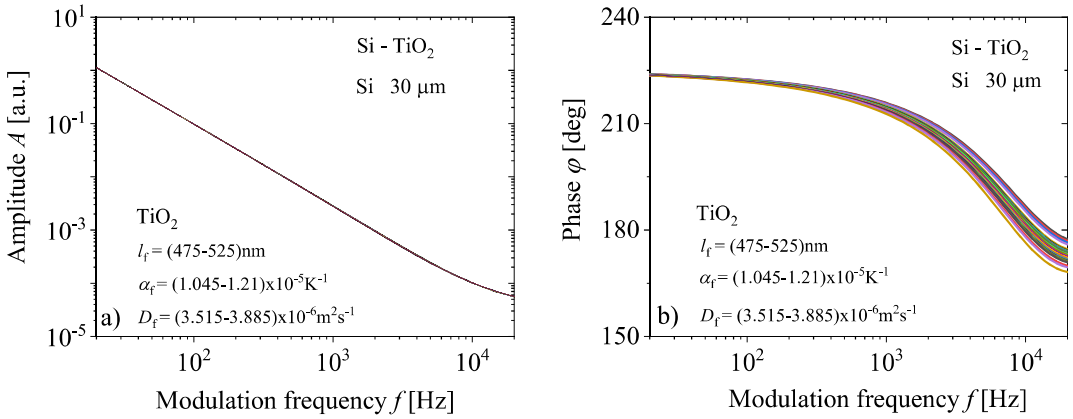

Fig. 1. Photoacoustic signals: a) amplitudes and b) phases of the two-layer model of the TiO2 layer on the Silicon sample obtained by changing the parameters of thickness l_f, expansion α_f and diffusivity D_f of the TiO_2 layer.

Conclusions – Our analysis shows that neural networks have a significant sensitivity to changes in the characteristics of thin layers of TiO_2 deposited on silicon membranes. This fact points to the possibility that neural networks, in combination with photoacoustics, can be a powerful tool in characterizing thin single-layer or multilayer coatings, important for the production of MEMS and NEMS sensors, as well as for the electronics and automotive industries in general.

References

[1] D.M. Todorović, M.D. Rabasović, and D.D. Markushev, Photoacoustic elastic bending in thin film—Substrate system, J. Appl. Phys. 114 (2013) 213510. doi: 10.1063/1.4839835.

[2] N. Jovančić, D. K. Markushev, D.D. Markushev, S.M. Aleksić, D.S. Pantić, D. Korte, M. Franko, Thermal and Elastic Characterization of Nanostructured Fe2O3 Polymorphs and TiO2-Coated Fe2O3 Using Open Photoacoustic Cell, Int. J. Thermophys. 41 (2020) 90. https://doi.org/10.1007/s10765-020-02669-w.

[3] K. Lj. Djordjevic, D.D. Markushev, Ž.M. Ćojbašić, et al. Photoacoustic Measurements of the Thermal and Elastic Properties of n-Type Silicon Using Neural Networks. Silicon (2019) doi:10.1007/s12633-019-00213-6.

[4] K. Lj. Djordjevic, D.D. Markushev, Ž.M. Ćojbašić, S.P. Galović, Inverse problem solving in semiconductor photoacoustics by neural networks, Inv. Prob. Scie. En. 29 (2020) 248 - 262. https://doi.org/10.1080/17415977.2020.1787405.

[5] S.M. Aleksić, D.K. Markushev, D.D. Markushev, D.S. Pantić, D.V. Lukić, M.N. Popović, S.P. Galović, Photoacoustic Analysis of Illuminated Si-TiO_2 Sample Bending Along the Heat-Flow Axes. Silicon (2022). https://doi.org/10.1007/s12633-022-01723-6.

Thermoelastic and optical properties of PLLA estimated by photoacoustic measurements

Nešić MV(1)*, Miletic VV(2), Milicevic DS(1), DjordjevicKLj(1), Jordovic-Pavlovic MI(3), Markushev DK(4), Popovic MN(4)

(1) "VINCA" Institute of Nuclear Sciences - National Institute of the Republic of Serbia, University of Belgrade, PO box 522, Belgrade 11351, Serbia
(2) Faculty of Philosophy, University of East Sarajevo, Pale 71420, Bosnia and Herzegovina
(3) Faculty of information technology, Metropolitan University, Belgrade, Serbia
(4) Institute of Physics, University of Belgrade, Pregrevica 118, Belgrade 11080, Serbia

*Corresponding author's email: mioljub.nesic@vin.bg.ac.rs

Polylactides, like all polymers, are materials with low coefficient of optical absorption. Transmission photoacoustic measurements on such materials require that a transparent sample be coated with a thin layer of good optical absorption, such as ink, dye or metal foil, in order to ensure optical opacity and to protect the microphone. The photoacoustic response of the Poly-(L-lactide) (PLLA), on which a thin layer of ink dye was previously applied, is measured in a minimum volume cell transmission configuration for two different positions of the two-layer sample: 1) the absorption layer is directly illuminated and 2) the transparent polymeric layer is directly illuminated. Thermal diffusivity, linear expansion coefficient and optical absorption coefficient of PLLA are determined by applying the boundary model of photoacoustic response for a two-layer sample in the case of optically thick and thermally thin absorption layer and self-consistent procedure for the inverse solution of the photoacoustic problem is derived. The obtained properties are in the range of literary expectations.

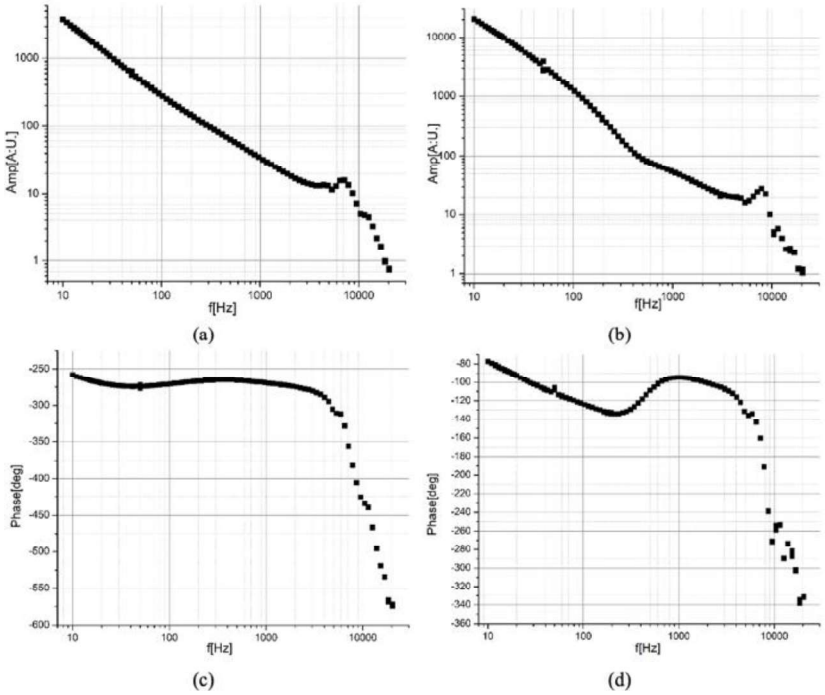

Fig. 1. Experimentally obtained photoacoustic response of 516 μm thick PLLA sample, coated with black acrylic dye 44 μm thick. Amplitude and phase characteristics when front-side illuminated **(a,c),** and when back-side illuminated **(b,d).**

References

[1] Popovic, M.N., Nesic, M. V, Zivanov, M., Markushev, D.D., Galovic, S.P.: Photoacoustic response of a transmission photoacoustic configuration for two-layer samples with thermal memory. Opt. Quantum Electron. 50, 1–10 (2018). https://doi.org/10.1007/s11082-018-1586-x.

[2] Ordóñez-Miranda, J., Alvarado-Gil, J.J.: Frequency-modulated hyperbolic heat transport and effective thermal properties in layered systems. Int. J. Therm. Sci. 49, 209–217 (2010). https://doi.org/https://doi.org/10.1016/j.ijthermalsci.2009.07.005.

[3] Popovic, M.N., Nesic, M. V., Markushev, D.D., Jordovic-Pavlovic, M.I., Galovic, S.P.: Optically induced temperature variations in a two-layer volume absorber including thermal memory effects. J. Appl. Phys. (2021). https://doi.org/10.1063/5.0015898.

[4] Nesic M. V., Popovic M. N., Galovic S. P., Djordjevic K. Lj.,Jordovic-Pavlovic M. I., Miletic V. V., Markushev, D.D.,Estimation of linear expansion coefficient and thermal diffusivity by photoacoustic numerical self-consistent procedure, J. Appl. Phys. – accepted for publication.

[5] Milicevic, D., Suljovrujic, E.: The resistance of poly-(l-lactide) to gamma radiation: effect of initial preparation and crystallinity. Polym. Bull. 77 (2020). https://doi.org/10.1007/s00289-019-02880-2.

Estimation of heat propagation speed in the thin graphene-oxide foil by photoacoustic spectroscopy

Misovic A(1), Nesic MV(1), Djordjevic KL(1)*, Markushev DK(2), Popovic MN(2), Markushev DD(2), Galovic SP(1)

(1) University of Belgrade, "VINČA" Institute of Nuclear Sciences - National Institute of the Republic of Serbia, PO box 522, 11000 Belgrade, Serbia
(2) University of Belgrade, Institute of Physics Belgrade, National Institute of the Republic of Serbia

Pregrevica 118, 11080 Belgrade (Zemun), Serbia

*Corresponding author's email: katarina.djordjevic@vin.bg.ac.rs

The amplitudes and phases of photoacoustic signal measured for the thin foil of graphene oxide (about 20 micrometers) in dependence of modulation frequencies of excitation laser beam are presented. Measurements were performed in a gas-microphone photoacoustic transmission configuration with an open cell of minimum volume [1]. Periodic changes in amplitude and phase at frequencies higher than 4 kHz (Fig.1) were interpreted as a possible consequence of thermal resonances in the sample, which occur due to the thermal memory of graphene oxide [2]. Based on both, the generalized model of photoacoustic response for media with thermal memory [2,3] and the presented measurements, the velocity and diffusion lengths of heat propagation in graphene oxide were determined. The estimated value of the heat propagation speed indicates the presence of relaxation phenomena in graphene oxide whose rate is of the same order of magnitude as in polymeric materials [4] and which are much slower than those in crystalline solids. It is in agreement with existing knowledge about structure properties of graphene oxide [5,6].

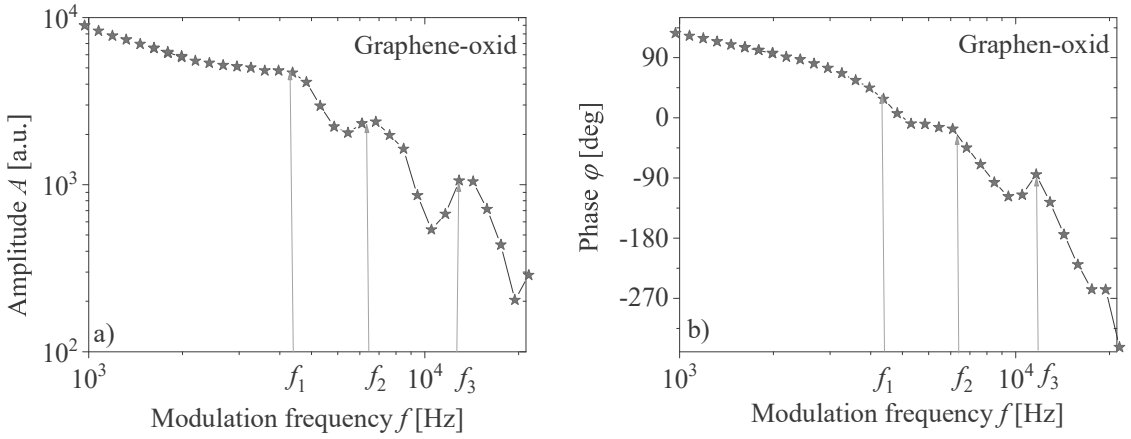

Fig. 1. Experimental measurements of **(a)** amplitudes and **(b)** phases of photoacoustic response of graphene-oxide foils which thickness is 20 micrometers. Measurements were performed in a gas-microphone photoacoustic transmission configuration with an open cell of minimum volume

References

[1] M.D. Rabasović, M.G. Nikolić, M.D. Dramićanin, M. Franko, D.D. Markushev, Low-cost, portable photoacoustic setup for solid state, Meas. Sci. Technol, 20 (2009) 9. doi:10.1088/0957-0233/20/9/095902.

[2] S. Galović, D. Kostoski, Photothermal wave propagation in media with thermal memory. Journal of Applied Physics, 93:5 (2003) 3063-3070. doi:10.1063/1.1540741.

[3] S. Galović, Z. Šoškić, M. Popović, D. Čevizović, Z. Stojanović, Theory of photoacoustic effect in media with thermal memory, J. Appl. Phys., 116:2 (2014) 024901. https://doi.org/10.1063/1.4885458.

[4] A. Saiter, H. Couderc, J. Grenet, Characterisation of structural relaxation phenomena in polymeric materials from thermal analysis investigations, J. Therm. Anal. Calorim. 88:2 (2007) 483-488. https://doi.org/10.1007/s10973-006-8117-x.

[5] D.Y. Kornilov, S.P. Gubin, Graphene Oxide: Structure, Properties, Synthesis, and Reduction (A Review), Russ. J. Inorg. Chem., 65 (2020) 1965–1976. https://doi.org/10.1134/S0036023620130021.

[6] A.T. Dideikin, A.Y. Vul, Graphene Oxide and Derivatives: The Place in Graphene Family, Front. Phys. 28 (2019) https://doi.org/10.3389/fphy.2018.00149.

The reduction of neural network input vector for efficient optimization of photoacoustic calibration

Jordovic-Pavlovic MI[(1)*], Popovic MN[(2)], Galovic SP[(3)], Djordjevic KLj[(3)], Nesic MV[(3)], Markushev DK[(2)], Markushev DD[(2)]

(1) Faculty of information technology, Metropolitan University, Belgrade
(2) Institute of Physics, University of Belgrade, Belgrade - Zemun, Serbia
(3) Vinca Institute of Nuclear Sciences- National Institute of the Republic of Serbia, University of Belgrade, Belgrade, Serbia

*Corresponding author's email: miroslava.pavlovic@metropolitan.ac.rs

The research presented in this paper is part of an effort to improve the process of calibration procedure optimization of model - dependent diagnostic techniques (transmission frequency photoacoustics) using a machine learning approach. A regression model for recognizing the characteristics of a microphone as a photoacoustic detector has already been developed and significant results have been obtained, first in reducing the influence of measuring instruments, then in significantly reducing the processing time of measured data, reaching the so-called work in real time, while maintaining the basic requirements - to make measurements reliable and accurate. Testing the model under different conditions (theoretical or experimental signals, with and without noise, different types of microphones, different samples) we found that the accuracy of the model is high and that the processing speed of measured data does not change significantly by reducing the input vector dimension of the machine learning algorithm. The question is how far can the reduction go without losing the quality of measurements? Computational intelligence algorithms - artificial neural networks and principal component analysis of main characteristics (amplitude and phase), supplemented by discussion of their correlations and expert knowledge can indicate a solution: the data set can be reduced to 10 characteristics, which means that the measurement procedure is reduced to 5 measuring points. We confirmed this assumption in this paper with satisfactory accuracy and reliability by a regression model for the characterization of three types of microphones. It has been shown that the procedure of measuring and characterizing a microphone can be performed simply and quickly by measuring at 5 defined points. At the same time, the problem of different number of measuring points is generalized by a new reduced set of characteristics.

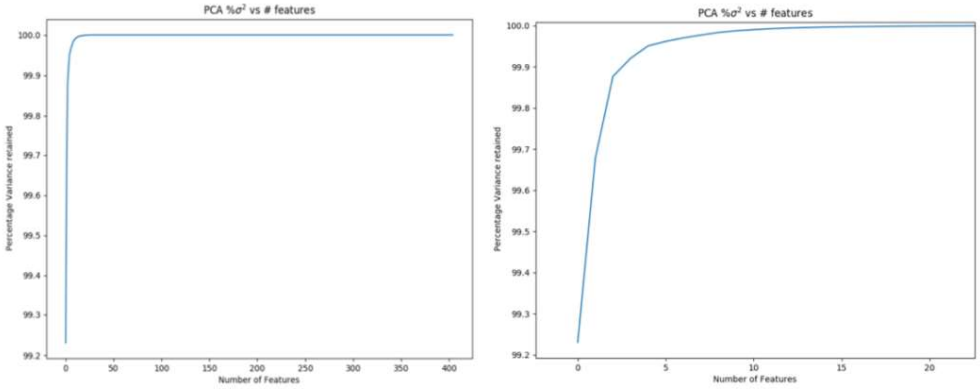

Fig. 1. *a. Reduced dataset variance depending of number of features, analyzed for microphone ECM30B (dataset original dimension: 400 x 67 500), b. zoom of diagram a. to lower number of features*

Table 1. Regression model performance on reduced data set for three types of microphones

Average deviation from the accurate value expressed in percentage of the accurate value on the test set, microphone ECM30B, accuracy of the regression model 97.8 %					
Parameter	f_2	f_3	f_4	ξ_3	ξ_4
Average deviation	0.05664359	0.13738047	0.0719733	1.290471	1.2778711
Average deviation from the accurate value expressed in percentage of the accurate value on the test set, microphone ECM60, accuracy of the regression model 98.32 %					
Parameter	f_2	f_3	f_4	ξ_3	ξ_4
Average deviation	0.06761368	0.08670316	0.05289495	0.85380656	1.0646605
Average deviation from the accurate value expressed in percentage of the accurate value on the test set, microphone WM66, accuracy of the regression model 98.02 %					
Parameter	f_2	f_3	f_4	ξ_3	ξ_4
Average deviation	0.0737425	0.13992077	0.08633012	1.1550651	1.2725114

References

[1] M.I. Jordović-Pavlović, M.M. Stanković, M.N. Popović, Ž.M. Ćojbašić, S.P. Galović, D.D. Markushev, The application of artificial neural networks in solid-state photoacoustics for the recognition of microphone response effects in the frequency domain, J. Comput. Electron., 19:3 (2020) 1268–1280. https://doi.org/10.1007/s10825-020-01507-4.

[2] M.I. Jordovic-Pavlovic et al., Computationally intelligent description of a photoacoustic detector, Opt. Quantum Electron., 52:5 (2020) 1–14. https://doi.org/10.1007/s11082-020-02372-y.

[3] T. I. Jolliffe, J. Cadima, "Principal component analysis: a review and recent developments," Philos. Trans. R. Soc. A Math. Phys. Eng. Sci., vol. 374, no. 2065, (Apr. 2016). doi: 10.1098/rsta.2015.0202

[4] E. Martel et al., Implementation of the Principal Component Analysis onto high-performance computer facilities for hyperspectral dimensionality reduction: Results and comparisons, Remote Sens., 10: 6 (2018). doi: 10.3390/rs10060864.

https://indico.ung.si/event/5/

UNIVERZA V NOVI GORICI
SCIENTIA VINCES 1995

University *of Ljubljana*

Jožef Stefan Institute